europhysics conference abstracts

23rd European Physical Society Conference on

Controlled Fusion and Plasma Physics

Kiev, 24-28 June,1996

Editors: D.Gresillon, A.Sitenko and A.Zagorodny

Contributed Papers, Part II

Published by: The European Physical Society

Series Editor: Prof. R.Pick, Paris

Managing Editor: G.Thomas, Geneva

Volume 20C

Part II

europhysics conference abstracts

23rd European Physical Society Conference on

Controlled Fusion and Plasma Physics

Kiev, 24-28 June,1996

Editors: D.Gresillon, A.Sitenko and A.Zagorodny

Contributed Papers, Part II

Published by: The European Physical Society
Series Editor: Prof. R.Pick, Paris
Managing Editor: G.Thomas, Geneva

Volume 20C
Part II

EUROPHYSICS CONFERENCE ABSTRACTS is published by the European Physical Society

23rd European Physical Society Conference on

Controlled Fusion and Plasma Physics

Bogolyubov Institute for Theoretical Physics, Kiev, Ukraine

24-28 June 1996

Editors: D Gresillon, A.Sitenko and A.Zagorodny

PREFACE

The 23rd EPS Conference on Controlled Fusion and Plasma Physics was organized on behalf of the European Physical Society by the National Academy of Sciences of Ukraine, State Committee on Science, Technologies, and Industrial Policy of Ukraine, and the Bogolyubov Institute for Theoretical Physics (BITP) in Kiev, Ukraine.

The 1996 Conference included the topics: A - Tokamaks, B - Stellarators, C - Alternative Magnetic Confinement, D - Plasma Edge Physics, E - Plasma Heating and Current Drive, F - Diagnostics, G - Basic Collisionless Plasma Physics, H - High Intensity Laser Produced Plasmas and Inertial Confinement, I - Astrophysical and Geophysical Plasmas, J - Low-Temperature Plasmas.

The Conference Proceedings are published in three parts, including:

Part I - Topic A; Part II - Topics B,C,D,E;
Part III - Topics F.G,H,I,J, and postdeadline papers.

The four-page papers are arranged within topical groups in the ascending order of file numbers. An exception is made for 24 contributions which were selected for oral presentation at the Conference. Such papers are presented at the beginning of each topical group.

According to EPS Plasma Physics Division regulations, the Conference Proceedings contain the four-page papers of all those contributions for which at least one author was a registered participant at the Conference. There are 371 papers which satisfy this condition. The three parts of the proceedings will be mailed to all registered participants of the Conference.

The papers of five Review Lectures and 21 Topical Lectures will be published in a special issue of the journal "Plasma Physics and Controlled Fusion", which will also be mailed to all registered participants.

D.Gresillon, A.Sitenko, A.Zagorodny

July 1996

Program Committee

D.Gresillon	(Ecole Polytechnique, CNRS, Palaiseau France - *Chairman*)
G.Fussmann	(MPI fur Plasmaphysik, Bereich Berlin, Germany)
X.Garbet	(CEA, Cadarache, France)
C.Hidalgo	(CIEMAT Fusion, Madrid, Spain)
L.Kovrizhnykh	(General Physics Institute, Moscow, Russia)
S.Prager	(University of Wisconsin, Madison USA)
A.Sitenko	(BITP, Kiev, Ukraine)
F.Sluijter	(Eindhoven University, The Netherlands - *Chairman of the EPS PlasmaPhysics Division*)
M.Tendler	(Royal Institute. of Technology, Stockholm, Sweden)
P.Thomas	(JET Joint Undertaking, Abingdon, UK)
H.Weisen	(CRPP-EPFL, Lausanne, Switzerland)
J.Winter	(KFA, Juelich, Germany)

Local Organizing Committee

A.Sitenko	*Chairman*
A.Zagorodny	*Vice-Chairman*
O.Pavlichenko	*Vice-Chairman*
I.Goutych	*Scientific Secretary*
G.Bugrij	
Yu.Chutov	
S.Fomina	
O.Kocherga	
Ya.Kolesnichenko	
V.Krol'	
A.Polozov	
P.Schram	
P.Sosenko	
K.Stepanov	
I.Yakimenko	

CONTENTS

PART I

PART II

PART III

B

STELLARATORS

Edge turbulence and transport barrier associated with the H-mode in the W7-AS stellarator

E. Holzhauer *, J. Baldzuhn, S. Fiedler, J. Geiger, M. Hirsch, R. Jaenicke, Ch. Konrad, A. Weller, W7-AS team and NBI team
Max-Planck-Institut für Plasmaphysik, EURATOM Ass., D-85748 Garching, FRG
** Institut für Plasmaforschung, Univ. Stuttgart, D-70569 Stuttgart, FRG*

H-mode operation in W7-AS

In the modular stellarator W7-AS (R_0 = 2.0m, a ≤ 0.18m) H-mode operation is achieved in a net currentless plasma with either ECRH or NBI heating at B_{tor}=2.5T and B_{tor} =1.25T [1]. The operational range is characterized by narrow windows of the edge rotational transform ι_a (around ι_a=0.525 and ι_a=0.475) where the plasma minor radius is comparatively large and determined by the inner separatrix of a natural island chain. For this well defined plasma boundary the connection length decreases to a value of some meters within a radial distance of Δr≈1cm outside the LCFS. As a consequence a strong radial variation of the radial electric field and the concomitant velocity shear layer exist already under L-mode conditions. This is considered as a favourable preconditioning for the L-H transition[1]. At ι_a=0.525 the H-mode is achieved already at the lowest available heating power, 200kW of ECRH (one gyrotron) or 340kW of NBI (one source) respectively. At the L-H transition the poloidal impurity rotation measured with spectroscopy increases towards the electron diamagnetic flow direction corresponding to a change of the negative radial electric field by $\Delta E_{rad} \approx$ -100V/cm. In analogy to tokamaks the transition into the H-phase is characterized by the appearance of an edge transport barrier. However the improvement of *global* confinement is comparatively small ($\Delta W_{dia}/W_{dia} < 30\%$) and achieved only after a quiescent H-mode of sufficient length (t>30ms) is established. Here we concentrate on the temporal and spatial behaviour of the edge transport barrier and the associated changes of fluctuations in density and magnetic field.

Edge transport barrier in the L- and H-phase

The existence of a barrier for particle and heat transport in the H-phase is confirmed by various diagnostics: In the H-phase the density gradient around and inside the separatrix increases as measured with Thomson scattering, Li-beam, reflectometry and Langmuir probes indicating an improvement of particle confinement. Electron temperature profiles obtained from ECE show the build-up of an edge pedestal inside the LCFS. The corresponding results obtained with several SX-channels are shown in Fig.1. The increase of the edge ion temperature is determined spectroscopically from the broadening of the impurity lines. Similar results are obtained with the LENA diagnostic. The transport barrier is characterized by the so-

called pivot-point inside of which density and temperature start to increase after the transition whereas they decreases outside.

In most cases the H-mode is reached through a "dithering" phase characterized by an almost periodic modulation of the transport barrier indicated e.g. by the H_α signal originating outside the LCFS. A typical repetition frequency is 2 kHz. The transient phase of deteriorated energy confinement can be clearly identified by ECE and SX-diagnostics. The modulation of T_e is only noticable in the ECE channels up to 5 cm inside the separatrix demonstrating the edge localized character of the phenomenon. The concomitant changes of the density gradient inside the separatrix are seen with the reflectometer.

Edge turbulence at the L-H transition

Fluctuation diagnostics show that plasma turbulence is strongly suppressed in the H-mode: The density fluctuations in the gradient region and around the separatrix are measured by reflectometry and microwave scattering. For radial positions inside the separatrix the spectral power of broadband density turbulence is reduced in the H-mode by more than one order of magnitude. Magnetic fluctuations observed with Mirnov coils (frequency range f≤600kHz) mounted close to the vessel wall are reduced on a similar scale. This reduction is observed for all available poloidal and toroidal coil positions. As an example Fig. 2 shows turbulent signal power for two coils at toroidal positions separated by 174 °. The magnetic field fluctuations are correlated within Δt<3μs.

The dithering L-H transition is characterized by periodic burst-like phenomena lasting 100 - 200 μs each with typical repetition frequency around 2 kHz. In the short intervals between the bursts fluctuation power of both density and magnetic turbulence is strongly reduced and the frequency spectra are identical to those in the fully developed H-mode. Therefore these quiescent time windows (≈300μs) are interpreted as short phases where the plasma *edge* is in an H-state.

If a dithering burst appears the spectral power of the *broadband density fluctuations* increases by up to two orders of magnitude within several 10 microseconds. This high measured fluctuation level is almost independent of the radial penetration depth of the reflectometer. In contrast in a stationary L-mode the measured fluctuation level typically decreases if the nominal cut-off layer is shifted deeper into the plasma. Together with the bursts in density turbulence bursts of *incoherent magnetic broadband fluctuations* are observed. In addition to the broadband turbulence the spectra of magnetic fluctuations show other types of instability (e.g. global Alfven modes). In particular a quasi coherent precursor activity (f≈400kHz) is observed starting 50μs before the well defined onset of the density turbulence. *H_α emission* in the SOL begins to rise within <30μs with the bursts of density fluctuations demonstrating the fast deterioration of the transport barrier.

At the drop in turbulence the improvement of the transport barrier measured with ECE, SX and reflectometry is found to occur on a timescale of ≈100μs (Fig.3). As a burst appears edge electron temperature displayed by the SX channel in Fig.3 increases within a few ten microseconds as a result of the rapid outflux of heat as the transport barrier is disturbed. Thus in the plasma edge region no clear separation in time between the changes in turbulence $\tilde{n}_e, \tilde{B}$ and in plasma background parameters n_e, T_e can be found.

It is proposed that the dithering phase does not constitute a simple switching between two states corresponding to equilibrium L- and H- phases: The precursor activity and the radial extent of the level of density turbulence several cm inside the separatrix indicate that the dithering bursts are similar to the high-frequency ("grassy") ELMs seen in tokamaks[2].

Edge localized Modes

Typically after a quiescent H-phase of several tenths of millisecond length, single or quasi-periodic ELMs (typical repetition rates 50 and 100 Hz) appear. The duration of these phenomena is $\tau \leq 0.5$ms. Broadband density and magnetic turbulence increases far above L-mode level. No clear coherent precursor activity has been identified in the fluctuations of density and magnetic field. With the multichannel SX-camera the T_e profiles are found to flatten initially around a pivot point about 2.5 cm inside the separatrix. This position corresponds to the maximum of the pressure gradient before the ELM. The breakdown of the transport barrier manifests itself in ECE as sudden decrease of T_e in the channel ≈2cm inside the separatrix. Correspondingly a cold pulse can be followed until ≈5 cm inside the separatrix ($v_r \approx 25$m/s). In some cases an ELM triggers an L-phase of several ms duration ("compound ELM") characterized by both a level of broadband turbulence and of H_α emission comparable to stationary L-mode. During this phase the T_e-profiles measured with ECE remain flattened until the fluctuations return to H-mode level.

Conclusions

The H-mode in W7-AS is characterized by an edge transport barrier displaying a fast switching during transient phenomena like dithering ("grassy") ELMs at the L-H transition and ELMs after a quiescent H-phase. Macroscopic profiles and microscopic fluctuations simultaneously change on a timescale of 100μs indicating an interdependence which looks like a closed loop process. The similarity between these edge phenomena in W7-AS stellarator and the findings in tokamaks underlines the generic behaviour of the H-mode transition as an edge phenomenon in toroidal devices.

References

[1] Wagner et al., Plasma Phys. Control. Fusion 36 (1994) A61.
[2] H. Zohm, Plasma. Phys. Control. Fusion 38, 105-128, (1996).

Fig. 1

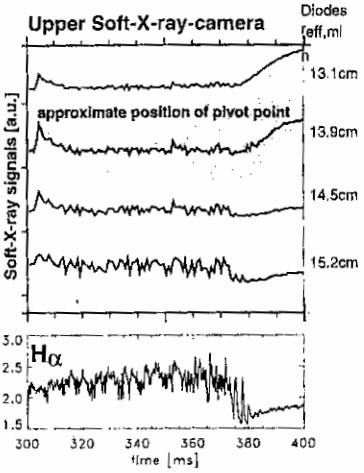

Fig. 3

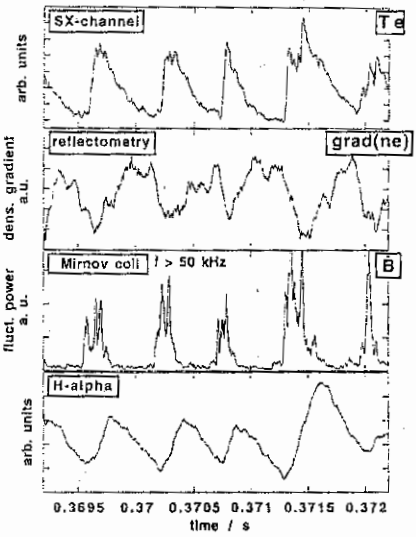

Fig. 2

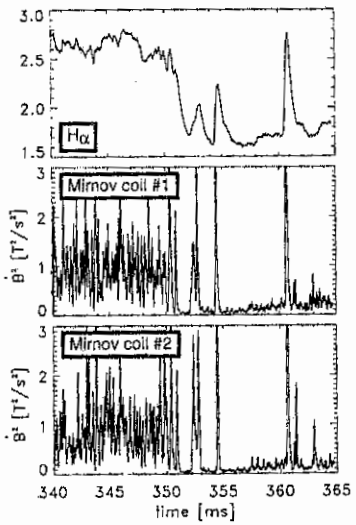

Fig. 1 : Development of SX-signal around the pivot point (r_{eff}=14cm) during the L-H transtion.

Fig. 2 : Synchronous temporal behaviour of magnetic signal power during a dithering L-H transition: Mirnov coil #1 and #2 are separated by 174° in toroidal direction. After a quiescent phase single ELMs occur.

Fig. 3 : Dithering phase : H_α-monitor and SX-channel (outside transport barrier) indicate the quasi-periodic build-up and detoriation of the barrier. The corresponding steepening and flattening of the density gradient is measured from the time-delay signal of reflectometry. As an example for turbulent edge activity the fluctuation power of a Mirnov signal is given. The short intervals of high fluctuation activity correspond to the detoriation of the barrier.

REVIEW OF EXPERIMENTAL INVESTIGATIONS ON THE U-3 AND U-3M TORSATRONS

E.D.Volkov

Institute of Plasma Physics,
National Science Center "Institute of Plasma and Technology"
Kharkov 310108,Ukraine

The U-3 (l=3, m=9, R=1m, a≈0,09 m, t(a)≈0,3, Bo<1 T) and U-3M (l=3, m=9, R=1m, a≈0,12 m, t(a)=0,4, Bo<1,5 T) torsatrons were built for a plasma heating and confinement studies in the torsatron magnetic configuration with, special emphasis on a helical divertor operation. The modernized U-3M torsatron has two additional inner vertical field coils and more exactly manufactured and strengthened helical winding. To realize the divertor magnetic systems of these devices were placed inside a large vacuum chamber.

The plasma is produced and heated by RF fields in the ion cyclotron range of frequencies $\omega<\omega_{ci}$ [1]. The frame type antenna (FTA) has been used for plasma production and heating in the range of values $1.10^{12}<n_e<8.10^{12}$ cm^{-3} and $0,45<B_0<1,3$ T.

The energy stored in the plasma column as well as the unidirectional current generated in the plasma and radiation losses are proportional to RF power at $P_{RF}<250$ kW. At the higher P_{RF} there is a saturation of the plasma energy content on the level~200÷250 J. Accordingly the $<\beta>$ value saturated too, but the global energetic lifetime, τ_E^G, decreased at the P_{RF} more than 300 kW. These phenomena are connected with the excitement of relax-type oscillations in the plasma [2]. These oscillations can be suppressed by the vertical field change (the shift of a plasma column to the major axis of torus). There is an optimum on the vertical field value for plasma parameters (Fig.1). At the optimal vertical field value $<\beta>$~0,6% was obtained [3].

The low density plasma confinement studies were carried out at magnetic field values up to 1,3 T. Measured values of τ_E^G are in a good agreement with τ_E^G LHD scaling (Fig.2) [4].

Attempts to increase the plasma density above 8.10^{12} cm^{-3} in the case of FTA using led to the degradation of plasma parameters during RF discharge. to understand the reasons of a density restriction we paid attention to ion and electron distribution function measurements. The energy

spectra of charge exchange neutrals measured in tangential and perpendicular directions to the toroidal plane show a two-temperature ion distribution. Doppler broadening of the CV line indicates that these impurity ions are in equilibrium with the lower temperature part of the hydrogen ion distribution (T_{i1}) during the whole RF pulse duration. By changing the entrance slit width of the longitudinal NPA a qualitative picture of the spatial localization of ions with T_{i1} and T_{i2} has been obtained (Fig.3). With density increase the region of localization of high energy ions (T_{i2}) moves on the outside. Measurements of ECE spectrum show that high energy electrons are generated at the plasma edge (Fig.4). With density increase the region of the localization of fast electrons moves on the outside too.

It is necessary to notice one very interesting phenomenon. The peculiarities on the right wing of spectrum correspond to electron temperature increase in magnetic is lands [5].

In order to study antenna system parameters and to optimize plasma build-up scenarios in a torsatron self-consistent numerical modeling with two codes (1-D RF code and O-D transport code linked one to another) has been performed. It was shown that the efficiency of plasma heating by the FTA is reduced with the plasma density rise due to the power deposition profile shift to the plasma periphery.

To avoid this effect a compact three-half-turn antenna (THTA) was proposed [6]. The power deposition profile of the THTA is better than that of the FTA at the high density. It is necessary to notice that long wavelength mode excitation by the THTA has been deliberately reduced in order to avoid plasma periphery heating in the high density regime. During FTA and THTA simultaneous operation the increase of n_e up to 3.10^{13} cm^{-3} was observed but in this case there was a large impurity influx.

The transition to a qualitatively new stage of plasma discharge was observed during the THTA pulse joined to the FTA pulse (Fig.5). The significant rise of plasma density during the THTA pulse was observed mainly at the plasma core while the ion saturation current, j_i, registered by the external Langmuir probes dropped sharply. The signal of the H_β line measured outside the plasma core decreased at the same time. The measurements of the plasma density radial distribution showed that the density profile steepened near the periphery. During the THTA operation the high energy neutral signal was not observed in the CX measurements (the high energy tail disappeared). But we could not maintain such a discharge in a quasistationary state due to impurity accumulation during FTA pulse.

To avoid the target plasma production stage the crankshaft type antenna was proposed and tested at low power level (P_{RF}<100 kW) [7]. We hope that using this antenna will allow us to realize the quasistationary maintenance of H-like regime of a plasma confinement.

The research described in this publication was made possible in part by Grants N 7000 and 7200 from the International Science Foundation and by International Soros Science Education Program through Grant N SPU 062014.

References.

1. Bakaev V.V. et al. Proc. of the 10 th Int.Conf. on Plasma Phys. and Contr. Nucl. Fus. Research. London, 1984, IAEA, Vienna, 1985, v.2, p.397.
2. Nazarov N.I. et al. Lett. to Journ. Exp. and Teor.Phys. 1987, v.45, N 1, 20.
3. Nazarov N.I. et al. Sov.Journ. of Plasma Phys. 1993, v.15, 1028.
4. Volkov E.D. et al. Proc. of the 14 th Int. Conf. on Plasma Phys. and Contr. Nucl. Fus. Research. Wurzburg, 1992, IAEA, Vienna, 1993, v. 2, 679.
5. Volkov E.L. et al. Proc. of the 23 d EPS Conf. on Contr. Fus. and Plasma Phys. 1996, Kiev.
6. Lysoivan A.I. et al. 5 the Int. Toki Conf., Toki, Japan, 1993. Fusion Eng. and Design 1995, 26, 185.
7. Moiseenko V.E. et al. Proc. of the 21 st EPS on Contr. Fus. and Plasma Phys. Montpellier, 1994, v.18 B, 980.

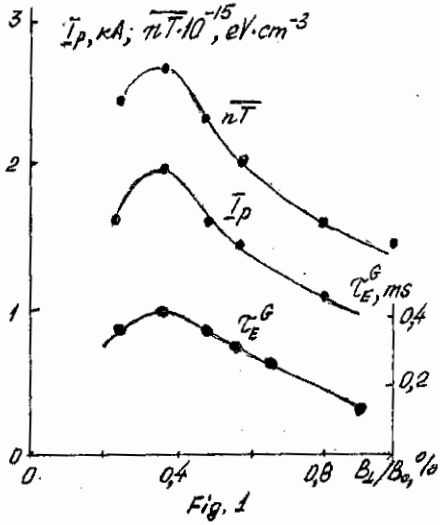

Fig. 1

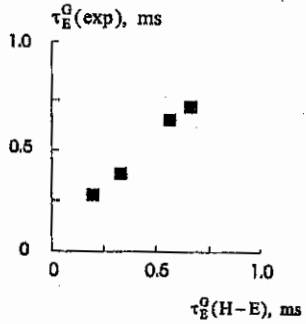

Fig. 2

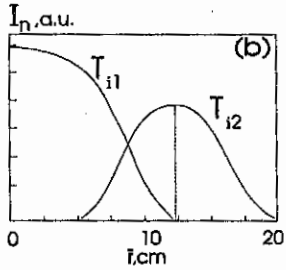

Fig. 3

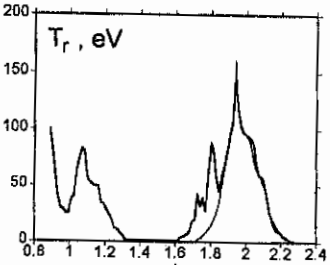

Fig. 4

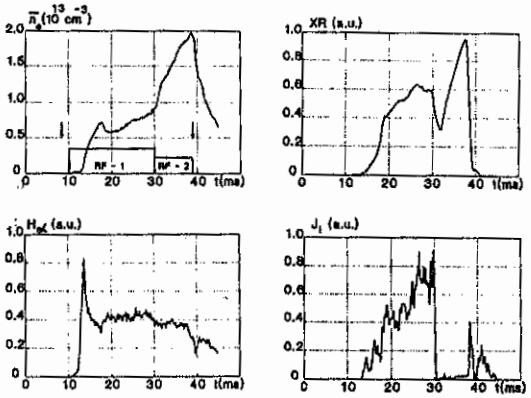

Fig. 5

GUIDING CENTER MOTION OF COLLISIONLESS α-PARTICLES IN A HELIAS REACTOR CONFIGURATION

A.V. Zolotukhin, C. D. Beidler, F. Herrnegger, J. Kißlinger, H. Wobig

Max-Planck-Institut für Plasmaphysik, IPP-Euratom Association
D-85748 Garching bei München, Germany

The guiding center motion of collisionless α-particles is studied for the Helias Reactor configuration (HSR) (Fig.1 for vacuum case (a) and for finite β case (b)). The fusion α-particles have a normalized Larmor radius of ρ/a=1/30 where a is the minor radius of a last closed magnetic surface. Effects due to the electric field are not taken into account. Effects of the modular ripple are included.

The present computations of α-particle trajectories under the plasma conditions are done for the parabolic pressure profile and a rather small β-value (β_0=3%) to study the finite β effect on the α-particle motion in real coordinates. A similar study will be done for higher β values in the order of <β>≈5% which is more realistic for the Helias Reactor.

The coil system of the magnetic configuration HSR is described in [1] and is characterized as follows: major radius R=22 m, minor radius of the last closed magnetic surface a=1.8 m, average magnetic field on the axis B_0=5 T, number of field periods m=5 and 10 coils per field period. The mirror ratio $(B_1-B_2)/(B_1+B_2)$ is about 10% on the magnetic axis and about 18% at the boundary with the aspect ratio $A=R/a$=12.4; B_1 and B_2 are the absolute value of the magnetic field at φ=0 (bean-shaped cross section) and φ=π/5 (triangular cross section). Rotational transform profiles for the vacuum and finite β cases are shown in Fig.2.

The radial distribution of the magnetic field is obtained from the contour plots of B on several magnetic surfaces (see Fig.3) and is used for predictions of the particle behavior. The separatrices (Fig.4) divide the space (r, E/μ) in regions where particles are passing ($E/\mu>B_{max}$), trapped ($E/\mu<B_{sep}$) or transient ($B_{sep}<E/\mu<B_{max}$) where they can overcome the local field maximum $B_{sep,max}$ and extend their path over several field periods. These estimations are consistent with the loss cone diagram which is obtained from launching test particles. The majority of particles are passing particles. As is shown in [2,3] the comparison of drift surfaces for co- and counter passing particles demonstrates the high degree of drift optimization in the Helias configuration. Trapped α-particles are characterized by a pitch parameter value $\gamma \geq 0.9$ ($\gamma \equiv v_\perp/v$, where v and $v_\perp$ are the total particle velocity and the velocity perpendicular to the magnetic field, respectively). There is a difference in the behavior of trapped α-particles which start under identical conditions in vacuum and finite β cases (Fig.5). In the vacuum case the particle becomes trapped in the modular ripple and its orbit then intersects the first wall. The confinement time is not larger than 6 ms. In the finite β case the particle does not escape the confinement region during the computation (≥ 8 ms). This single example illustrates the general improvement of α-particle behavior under plasma conditions.

The interaction of thermonuclear particles with the first wall of the device is of interest for fusion reactors. For tokamaks [4, 5] the distribution of α-particle flux on the first wall is highly non-uniform in the poloidal angular coordinate. To get a map of the intersection points of lost α-particles orbits with the vacuum chamber in HSR, the particles were launched from the different cross sections of the magnetic surfaces with average radii r/a=0.2 and 0.4 ($\gamma \geq 0.9$). Particles which start in the bean-shaped cross section (φ=0°, maximum of B) are passing and their trajectories do not intersect the first wall.The footprints of lost α-particles in the vacuum case

are found in "hot spots" which correspond to particles ($\gamma \approx 0.95$ to 0.97) which are trapped in modular ripples and drift upward and to particles ($\gamma \geq 0.97$) with large radial drift (see Fig.6). A next step of this study will be to take into account the location of the divertor plates.

References.

1. C.D.Beidler, G.Grieger, E.Harmeyer, J.Kißlinger, N.Karulin, W.Maurer, J.Nührenberg, F.Rau, J.Sapper, H.Wobig, Helias Reactor Studies, IPP Report No.IPP2/30 (Oct. 1995).
2. E.Harmeyer, J.Kißlinger, A.Montvai, F.Rau, H.Wobig. Proc. 2nd Ringberg Workshop on W VII-X, June 1988, p.79-96
3. A.V.Zolotukhin, F.Herrnegger, H.Wobig. Proc. 6th Ringberg Workshop on W VII-X and Helias Reactors, Nov.1996, p.178-186.
4. V. Ya. Gologorod'ko, V.A.Yavorskij, Nuclear Fusion, **29**, No.6 (1989), p.1025-1029.
5. S. J. Zweben et al., Nuclear Fusion, **35**, No.12 (1995), p.1445-1455.

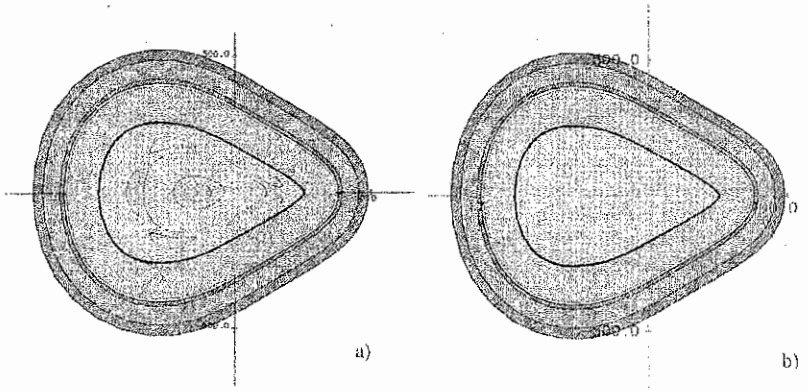

Fig.1. Poincaré plot of magnetic surfaces. Cross section of plasma, blanket, shield and coil system in the planes φ=36° for the vacuum (a) and β_0=3% case (b).

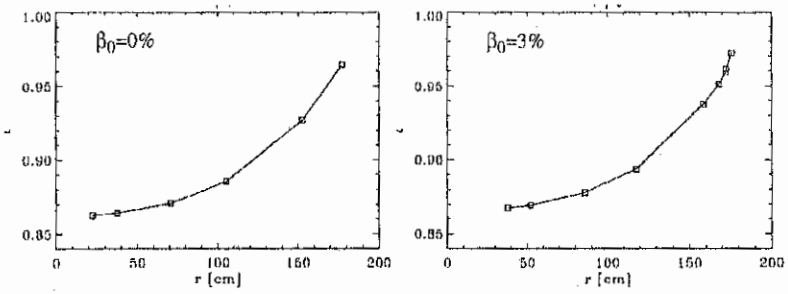

Fig.2. Rotational transform as a function of the minor radius of the magnetic surface.

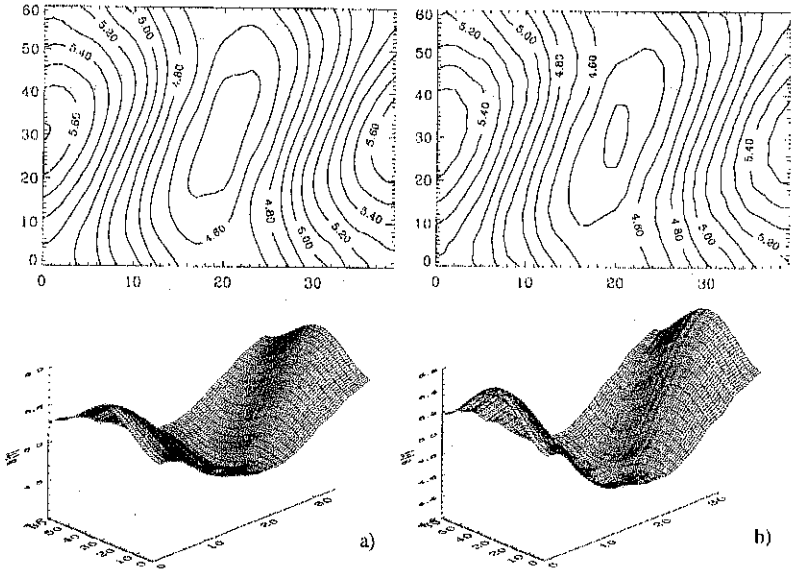

Fig.3. B-contours and B-surface for the magnetic surface with radius r/a=0.4 in the angular coordinartes (υ, ϕ) for the vacuum (a) and finite β case (b). The value ϕ=40 corresponds to toroidal angle φ=36°; υ=60 is one turn in the poloidal direction. The labels on the B-contours are magnetic field values in T.

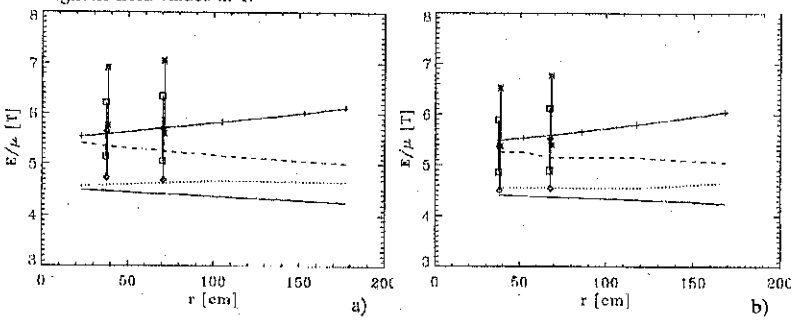

Fig.4. Radial structure of the magnetic field for vacuum (a) and finite β (b) configurations; B_{min} (solid line) and B_{max} (solid line with crosses) are minimum and maximum values of B at the magnetic surface, $B_{sep,min}$ (dotted line) and $B_{sep,max}$ (dashed line) are field values at saddle points in the B-contour plot with local field minimum and maximum, respectively. Lines with asterisks, diamonds and squares show the E/μ ranges for α-particles which start in three planes φ=0°, 36°, 54°, respectively; the pitch-parameter $\gamma=v_{\perp}/v$ is in the range 0.9 to 0.97. E and μ are the energy and adiabatic invariant of the α-particle.

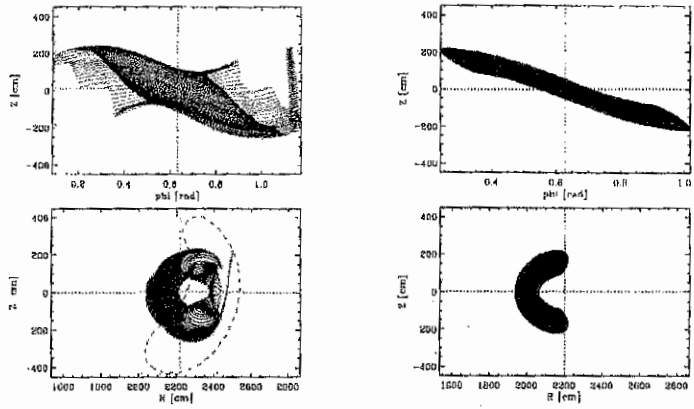

Fig.5. Trajectories of α-particles (γ=0.95, radius of launch surface r/a=0.2, starting toroidal coordinate φ_0=0.628) in planes (φ, Z), (R, Z) in the vacuum (a) and finite β case (b). The dashed line is the cross section of first wall which the trajectory intersects.

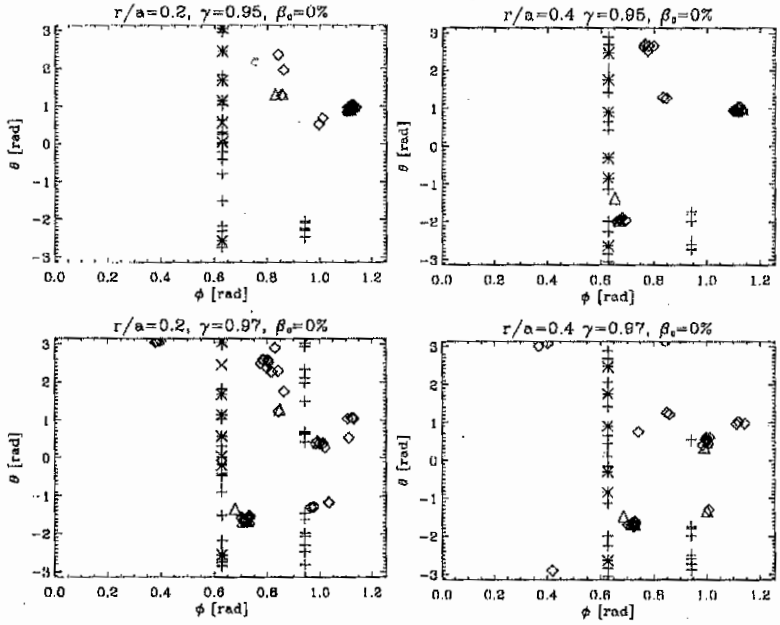

Fig.6. Footprints of the lost α-particles on the first wall. Crosses and x's are the starting positions on the magnetic surfaces for particles with positive (in the direction of a magnetic field) and negative parallel velocity at the starting point , diamonds and triangles are the intersection points respectively.

Neoclassical Transport in High-Mirror Advanced Stellarators

C.D. Beidler, H. Maaßberg
Max-Planck-Institut für Plasmaphysik, IPP-EURATOM Association
D-85748 Garching bei München, Germany

A.A. Shishkin
Institute for Plasma Physics, Kharkov Institute of Physics and Technology
310108 Kkarkov, Ukraine

Large magnetic-field ripple is generally considered to be detrimental for neoclassical transport. Numerical simulations have shown, however, that the introduction of a large "toroidal mirror" term in the B-Fourier spectrum of a stellarator configuration can significantly improve the neoclassical confinement, both in the collisional (plateau) and collisionless (long-mean-free-path) regimes [1]. The transport properties of such High-Mirror Advanced Stellarators are of particular interest both for the future W7-X experiment and for stellarator reactor studies [2].

In general, the magnetic field, $B(r,\theta,\varphi)$ (with r being the effective radius, θ and φ the poloidal and toroidal angles in Boozer co-ordinates, respectively), is described by $B/B_0 = 1 + \sum_{m,n} b_{m,n} \cos(m\theta - nN\varphi)$ where $b_{m,n}(r) \propto r^m$ is the Fourier coefficient with respect to the poloidal (m) and toroidal (n) modes, and N is the number of field periods. The model field analyzed in this work is given by only three Fourier harmonics: the average toroidal curvature, $b_{1,0}$, the toroidal mirror term, $b_{0,1}$, and the helical ripple, $b_{1,1}$. The (gyro-averaged) drift-kinetic equation (DKE) is solved using the "local diffusive ansatz" $f = f_0 + f_1$. Here, $f_0(r,\theta,\varphi,v^2)$ is the "equilibrium" distribution function including the transport effects along magnetic field lines due to small poloidal and toroidal electric fields on the flux surfaces, $-\nabla\Phi_1$, and is given by

$$\underline{v}_\parallel \cdot \underline{\nabla} f_0 + \dot{v}\frac{\partial f_0}{\partial v} = C(f_0) \qquad \text{which yields} \qquad f_0 = e^{-\frac{q\Phi_1}{T}} f_M(r,v^2) \tag{1}$$

where $\dot{v}$ is the acceleration term ($\propto \underline{B}\cdot\underline{\nabla}\Phi_1$), C the Coulomb collision term, $f_M(r,v^2)$ is the usual Maxwellian driving the neoclassical transport in 1st order, Φ_1 the 1st order potential ($\Phi = \Phi_0(r) + \Phi_1(\theta,\varphi)$ with $|\Phi_1| \ll |\Phi_0|$), and $T(r)$ the temperature. In this context, all terms with $(\underline{B}\times\underline{\nabla}B)\cdot\underline{\nabla}\Phi$ are neglected (the ∇B-drift in a strong radial electric field leads to a change in the perpendicular energy). In the 1st order DKE, the terms related to $\partial f_1/\partial r$ and $\partial f_1/\partial v$ are omitted with respect to the equivalent terms in f_0, and the Coulomb term, C, is approximated by the simple pitch-angle collision operator (the pitch $p = v_\parallel/v$). These last assumptions allow a mono-energetic treatment of the problem. Additionally, the poloidal component of the ∇B drift is neglected with respect to the 0th order $E\times B$ drift. Then, the 1st order DKE is given by

$$\left(\frac{pv}{B}\underline{B} + \frac{1}{B^2}\underline{B}\times\underline{\nabla}\Phi_0\right)\cdot\underline{\nabla} f_1 - v\frac{1-p^2}{2}\left(\frac{q}{B}\frac{2}{mv^2}\underline{B}\cdot\underline{\nabla}\Phi_1 + \frac{1}{B^2}\underline{B}\cdot\underline{\nabla}B\right)\frac{\partial f_1}{\partial p}$$

$$-C(f_1) = -\left(\underline{v}_{\nabla B} + \underline{v}_{E\times B}\right)_r f_0'. \tag{2}$$

Here, f_0' is the radial derivative (under the constaint of invariant total energy) which drives all the neoclassical transport in combination with the radial components of

$v_{\nabla B} = (mv^2/2qB)\,(1+p^2)\,\underline{B}\times\underline{\nabla}B$ and $v_{E\times B} = \underline{B}\times\underline{\nabla}\Phi_1/B^2$. In the next two sections, i.e., for the plateau and the LMFP regime, the 1st oder DKE is analyzed with the Φ_1 terms omitted. The final section presents the self-consistent neoclassical theory in both orders for the plateau regime where Φ_1 is determined by the quasi-neutrality condition on the flux surface, and the radial electric field, $-\Phi_0'$, from the ambipolarity condition for the particle fluxes.

Plateau Transport

With Fourier representations of B (real), of $f_1 = \sum_{m,n} f_{m,n}(p)\,\exp(i(m\theta - nN\varphi))$ and of the normalized 1st order potential $(2q/mv^2)\,\Phi_1 = \sum_{m,n}\phi_{m,n}\,\exp(i(m\theta - nN\varphi))$, a system of 1st order DKE's for the modes m, n is obtained.

$$-\frac{1-p^2}{2}\sum_{m',n'}(m'\iota - n'N)\left\{\frac{1}{2}\,b_{m',n'}\,(f'_{m-m',n-n'} - f'_{m+m',n+n'}) + \phi^*_{m',n'}\,f'_{m-m',n-n'}\right\}$$

$$+\big((m\iota - nN)\,p + m\epsilon^*\big)\cdot f_{m,n} + i\,\nu^*\widehat{C}(f_{m,n}) \;=\; \frac{\gamma^*}{2}\,m\left\{(1+p^2)\,b_{m,n} + \phi_{m,n}\right\} \quad (3)$$

with $\widehat{C} = d/dp\,(1-p^2)\,d/dp$, $\epsilon^* = \Phi_0'/\varepsilon B v$, $\nu^* = \nu R/v$ and $\gamma^* = (qv/mB\varepsilon)\,f_0'$ and $\varepsilon = r/R$. In eq. (3), terms of order ε^2 from $\underline{B}\times\underline{\nabla}$ are neglected.

The mode coupling term ($\sum$) originates from the $\dot{p}$ term in the DKE and is neglected in the traditional analytic theory for the plateau regime. As a consequence, helical contributions add to the transport coefficient resulting from the $b_{1,0}$ term. Direct mode coupling with the mirror term $b_{0,1}$ appears only between the $f_{1,0}$ and $f_{1,1}$ modes. The transport properties cannot be improved by the $n = 1$ mirror term in helical configurations with $m > 1$. The $f_{0,1}$ mode is negligible since the mode coupling is only small ($\propto \iota\, b_{1,0} f'_{1,1}$), and a direct drive (r.h.s. of eq. (3)) is missing. Thus, the 1st order DKE in the plateau regime of a High-Mirror Advanced Stellarator described by the $b_{0,1}$, $b_{1,0}$ and $b_{1,1}$ modes is given by

$$\left[p\begin{pmatrix}\iota & \\ & \iota - N\end{pmatrix} + \epsilon^* + i\,\nu^*\widehat{C}\right]\begin{Bmatrix} f_{1,0} \\ f_{1,1}\end{Bmatrix} + \frac{1-p^2}{4}\,N\,b_{0,1}\begin{Bmatrix} -f'_{1,1} \\ f'_{1,0}\end{Bmatrix} = \gamma^*\,\frac{1+p^2}{2}\begin{Bmatrix} b_{1,0} \\ b_{1,1}\end{Bmatrix}. \quad (4)$$

For small radial electric fields, $\epsilon^* \ll \iota$, the mode coupling is only efficient if the relation $\iota\,|b_{1,1}| \sim |(\iota - N)\,b_{1,0}|$ holds, i.e., if the "toroidal plateau" and the "helical plateau" values of the mono-energetic transport coefficients are roughly comparable. E.g., for the W7-X configurations with $\iota \simeq 1$, $N = 5$ and $b_{1,1}/b_{1,0} \simeq 2$, mode coupling by the toroidal mirror term $b_{0,1}$ is efficient. For small ι and/or high N, the "helical plateau" is much lower than its "toroidal" counterpart, and no possibility exists for optimization with the mirror term. Reduction of the transport is only obtained if $b_{0,1}$ and $b_{1,1}$ are of different signs (which is the case for W7-X) while degradation is found if $b_{0,1}\cdot b_{1,1} > 0$. The dependence of the mono-energetic transport coefficient on $b_{0,1}$ obtained numerically with three modes from eq. (3) (by a simple complex-valued matrix difference scheme) is in full agreement with DKES code [3] results (see [1], Fig. 5). Finally, the mode coupling effect disappears at larger $\epsilon^* > \iota$ since $\Im(f_{1,0})$ (the sin component being relevant for transport) is strongly reduced beyond the "toroidal resonance" at $\epsilon^* = \iota$. Consequently, no optimisation of the "helical plateau" value for W7-X configurations is found for very large radial electric fields.

Long-Mean-Free-Path Transport

In the LMFP regime, the mode coupling becomes detrimental to a straightforward solution of the DKE; e.g., the DKES code (which solves eq. (3) with $\phi_{m,n} = 0$) must use hundreds of $f_{m,n}$ to obtain a convergent solution in the (m, n) Fourier space. This problem may be eliminated in situations where the rapid drift motion along field lines is a (nearly) periodic function of the local helical ripple. Using the appropriate time average, the DKE simplifies to the *Ripple-Averaged* Kinetic Equation, the solution of which may be described by a very small harmonic spectrum and which requires tiny computational resources [4]. On the other hand, the conventional ripple-averaged theory employs simplifications which limit its usefulness for predictive transport calculations. One such simplification is the assumption of negligible rotational transform per field period (i.e., $\iota/N = 0$). Under this assumption, functions of the poloidal angle $\theta = \theta_0 + (\iota/N)\zeta$ are treated as constants with respect to the ripple average (which is performed along a field line — and thus at constant θ_0 — over functions of $\zeta \equiv N\varphi$). A reformulation of the ripple-averaged theory which avoids this assumption is made possible by introducing a change of variables $\theta = \theta_n + (\iota/N)(\zeta - \zeta_n)$, where $\theta = \theta_n$ specifies a local minimum of B. Additionally, B is expressed as a function of θ_n by approximating the "true" magnetic field by a model consisting of two sinusoidal "half ripples" with extrema identical to those of the "true" B; these extrema are found numerically to high accuracy. This approach leaves the basic formalism of the ripple-averaged theory largely unchanged although the complexity of individual quantities increases significantly due to the non-symmetry of the model field.

The importance of avoiding the assumption $\iota/N = 0$ may be demonstrated by solving the ripple-averaged kinetic equation for localized particles in the $1/\nu$ regime (the more collisional end of the LMFP regime where the transport coefficients scale inversely with collision frequency). Figure 1 presents the results for the advanced stellarator W7–X ($\iota/N \approx 0.2$) expressed in terms of the "effective helical ripple" (in the $1/\nu$ regime, the mono-energetic diffusion coefficient is given by $D = (4/9\pi)(2\epsilon_{eff})^{3/2}(v_d^2/\nu)$ where v_d is the radial drift velocity [5]). Three configurations are considered which differ only in that the mirror term, $b_{0,1}$, has been changed by a constant amount. A significant mirror term serves to confine the majority of localized particles in the "straight" portion of each field period. Clearly, neoclassical transport in such "drift-optimized" W7–X configurations is described accurately using a ripple-averaged formalism only if the assumption $\iota/N = 0$ is avoided.

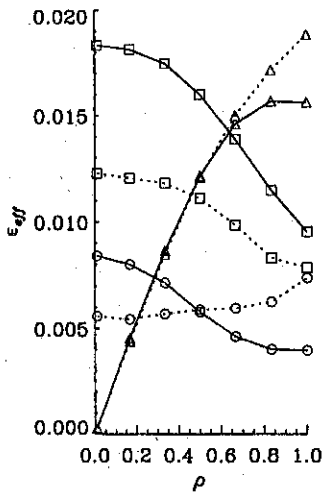

Figure 1. *The effective helical ripple for $1/\nu$ transport is shown as a function of normalized radius for* **W7-X**. *The configurations "low mirror" with $b_{0,1}(\rho = 0) = 0$ ($\triangle$), "standard" with $b_{0,1}(\rho = 0) = 0.046$ ($\circ$), and "high mirror" with $b_{0,1}(\rho = 0) = 0.092$ ($\square$) are shown. Solid lines indicate the results obtained when non-zero ι/N is accounted for, dotted lines the results under the conventional assumption $\iota/N = 0$.*

Self-Consistent Neoclassical Transport

The 1st order potentials, Φ_1, are driven by the inhomogeneity of the density on flux surfaces due to the ∇B drift in the DKE (2). The transport is affected by the Φ_1 terms in both orders, f_0 and f_1. For the particle flux in 0th order, the radial components of $\Phi_1 \underline{v}_{\nabla B}$ (Φ_1 from the linearized Boltzmann factor; see eq. (1)) and $\underline{B} \times \underline{\nabla} \Phi_1 / B^2$ cancel exactly after energy convolution and flux surface averaging. For the energy flux density, however, a 0th order term is obtained: $q^\Phi = -(nT/2rB) \sum_{m,n} mb_{m,n} \Im(\phi_{m,n})$ with $\Im(\phi_{m,n})$ being the transport-relevant sin component. In a simple description [6], the $\phi_{m,n}$ modes are mainly driven by the ion density inhomogeneity, and, as a consequence, the q^Φ flux may increase up to the ion level, i.e., $q^\Phi/q_e(\Phi_1 = 0)$ is of the order of $\sqrt{m_i/m_e}$.

For the plateau transport, the 1st order DKE (3) with the $b_{0,1}$, $b_{1,0}$ and $b_{1,1}$ components is solved numerically for the three modes $f_{1,0}$, $f_{1,1}$ and $f_{2,1}$ for both electrons and ions. After energy convolution, the 1st order densities $n^{e,i}_{m,n}$ are obtained. The quasi-neutrality condition (with 0th and 1st order included) leads to $n_0 e \phi_{m,n} (T_e + z_i T_i) = n^{i}_{m,n} - n^{e}_{m,n}$ where $\phi_{m,n}$ is used in the DKE (3) for the next iteration step until convergence is reached. As a result, the 1st order density inhomogeneity driven by the ∇B drift is reduced by the transport within flux surfaces, i.e., by the Φ_1 term. This reduction depends on the value of the $b_{0,1}$ term. The 1st order particle and energy fluxes (related to the $f_{m,n}$ modes) are only slightly affected. The 0th order q^Φ term can significantly exceed the 1st order q_e flux at very small radial electric fields.

Taking the ambipolarity condition into account, however, q^Φ is found to be of minor importance: q^Φ has a similar dependence on the radial electric field, $E_r = -\nabla \Phi_0$, as the ion flux density, Γ_i. For the typical plateau scenarios, $\Gamma_i(E_r) = 0$ is a very good estimate for the ambipolar E_r^a (since $\Gamma_i \gg \Gamma_e$ for $E_r = 0$). As the integrand for Γ_i is only weighted with the radial component of the ∇B drift with respect to the integrand for $n^{i}_{m,n}$, the ion $\phi_{m,n}$ modes must be reduced at $E_r \simeq E_r^a$. Thus, both the density inhomogeneities and the 1st order potentials become small at E_r^a leading to $q^\Phi \simeq 0$. This result is in contradiction to [6]. *Anomalous* electron heat transport cannot be explained within the theory of self-consistent neoclassical transport.

The effects of Φ_1 on neoclassical transport in the LMFP regime remain to be investigated. These effects are likely to be of greater importance since ions and electrons occupy different collision frequency regimes which, especially for Advanced Stellarators, may have quite different degrees of optimization with respect to neoclassical transport.

[1] H. Maaßberg et al., Phys. Fluids B **5** (1993) 3728.
[2] G. Grieger et al., Fusion Tech. **21** (1992) 1037.
[3] W.I. van Rij and S.P. Hirshman, Phys. Fluids B **1** (1989) 563.
[4] C.D. Beidler and W.D. D'haeseleer, Plasma Phys. Control. Fusion **37** (1995) 463.
[5] C.D. Beidler et al., EPS 1994, ECA **18B II** (1994) 568.
[6] M. Taguchi, J. Phys. Soc. Japan **62** (1993) 2976.

3 MW Neutral Injection into the Stellarator Wendelstein7-AS - Heating efficiency at high-beta operation -

F.-P. Penningsfeld, J. Geiger, W. Ott, E. Speth, W7-AS Team, NI Team

Max-Planck-Institut für Plasmaphysik, D-85748 Garching, Germany

Abstract

With 3 MW of neutral power and a new non-resonant RF method of plasma start-up, W7-AS is now equipped for the investigation of high-β plasmas over a wide range of magnetic fields ($0.5 < B_0 < 2.5$ T). With full beam power, a maximum central beta of 4% at 1.27 T was obtained, however the aim of hitting the beta limit, expected at about 4.5%, by lowering the magnetic field, was not reached. In contrast to Lackner-Gottardi scaling, where $\beta \propto n^{0.6} p^{0.4} B^{-1.2}$ can be expected, no increase in $<\beta>$ was seen even at reduced B despite constant neutral input power. In this paper it is shown, that one of the reasons for this behaviour is a degradation of the heating power with decreasing magnetic field; not due to transmission or reionisation losses of the neutral beams, but due to increasing fast ion orbit losses with decreasing magnetic field.

Introduction

The power level of Neutral Beam Injection (NBI) into the W7-AS Stellarator has been increased from 1.5 to 3.0 MW in order to extend the accessible range of plasma parameters in this device. The beta values achieved at 1.5 MW were about a factor 2 below the equilibrium limit. Furthermore, since the energy confinement time in W7-AS scales favourable with density and the maximum density obtained increases with power, this was an additional incentive for upgrading the beam power.

Therefore, the number of ion sources was increased from 4 to 8 which doubled the available neutral power. Experiments with the upgraded power began in spring 1995. The extended parameter regimes are still being explored. This paper reports the present status.

In an attempt to understand the experimental findings, the computations of the heating efficiency had to be repeated and extended because the plasma limiters have been changed to inner limiters and the magnetic field range of NI discharges was widened up by start-up with 900 MHz RF. The variations of the flux surfaces with increasing β became much stronger than earlier [1]. The vacuum magnetic field configuration as used previously was therefore no longer appropriate for the computation of the beam deposition in the plasma. A series of FAFNER runs [2] with finite-beta plasma configurations and variations of the magnetic field had to be done. The main results are a somewhat more favourate heating efficiency at low plasma densities than earlier and a strong reduction of the heating efficiency for low magnetic field operation.

Status of the 3MW Neutral Injection on W7AS

Total and neutral power of 45 kV H^0-beams delivered into the torus were measured by a reinstalled calorimeter inside the torus for one box. The results confirm the estimated power transmissions per source for not fully optimized divergence and beam steering. Comparison of single

source operation with and without magnetic field of W7-AS show a reduction by reionization of about 12% mainly caused by high pressure in the front part of the NI-box, not in the duct itself. It was confirmed, that a common operation of all sources over 0.3 s, limited by the inertial calorimeter plate, does not show beam blocking.

NI heating efficiency for $\beta > 0$ in W7-AS

Two motivations lead to a resumption of calculations with FAFNER to update the heating profiles of NBI in W7-AS: the change of the limiter geometry and the high Shafranov shift due to the higher beta values obtained. The variations between vacuum field and finite beta equilibrium flux surfaces, as shown in fig.1, are dominated by the large increase of the plasma cross section and by the Shafranov shift of about 7.5 cm in the $\phi = 0^o$ plane for highest beta obtained up to now [1]. Lower and upper limiter used in earlier campaigns were removed and the plasma now is only controlled by the inner limiter and the vertical field. To clarify the effect of these modifications on the global NI heating efficiency, especially as function of the magnetic field strength and target density, the Monte-Carlo code FAFNER [2] was used, not only in 3D guiding centre but also in real orbit calculation at very low fields, where the gyro radius of fast ions starting nearly parallel to B (pitch angle of the starting ions is in the range of $22^o < \gamma < 35^o$) becomes greater than the |grad pl - region of typical 2-3 cm in the outer part of high density NI discharges.

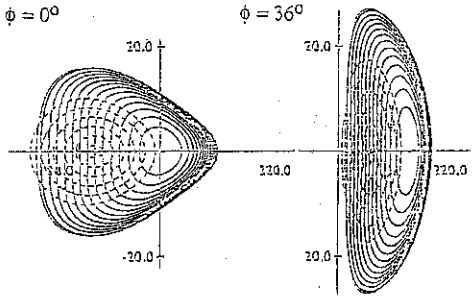

fig. 1: Comparison of vacuum field (dashed) and finite beta equilibrium flux surfaces at the toroidal angles $\phi = 0^o$ and $\phi = 36^o$

The calculations use the measured density and temperature profiles with $n_e(0) = 1.8*10^{20}$ m^{-3}, $T_e(0) = 350$ eV with full beam power, where the obtained $<\beta>$ was 1.8%. For density and temperature scans, these central values are scaled. The results for the global NI heating efficiency as a function of the line density $\int ndl$ for co and counter beams of inner and outer sources for 1.25T are shown in fig.2a. The maximum beta obtained corresponds to $\int ndl = 0.64*10^{20}$ m^{-2}.

Fig.2b shows the corresponding results for the vacuum field (β=0 , B = 1.25T) as used before, including the inner limiters, but using a fixed radial position. This radial position corresponds to a beta value of about $<\beta> \approx 0.75\%$ of the new data set. Therefore, the differences between both results are low (< 10% for $\int ndl > 0.3*10^{20}$ m^{-2}).

For lower line densities the results differ somewhat more, depending on the source position,

because the target plasma moves to the inner limiters and shrinks in diameter typically by a factor of 1.5 (see fig.1 also).

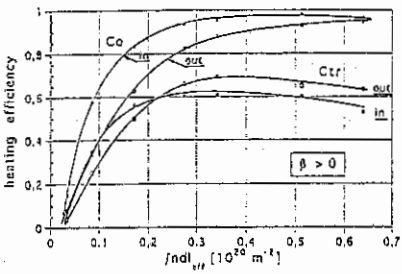

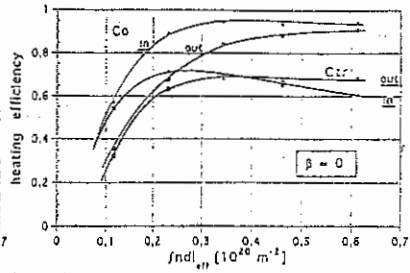

fig2.a: heating efficiency as function of line density using flux surfaces of the corresponding beta for all types of NI sources .

fig.2b: heating efficiency versus ∫ndl for β=0 as used up to now with the effect of inner limiter; (n,T)-profiles in both cases are similar

The radial heating profiles for co and counter beams (each 1.5 MW neutral power) obtained by FAFNER in guiding center approximation are shown in fig.3. For $\int ndl > 0.10*10^{20}$ m^{-2} the counter beams deliver only half of the power of the co beams in the inner plasma region with $r/a \leq 0.3$. The high beta studies done so far, show a central heating power of about 5.4 W/cm^3 (co + counter) in a wide density range of $0.34 < \int ndl < 0.64$ [10^{20} m^{-2}].

fig.3: NI/W7AS heating profiles p(r) for various line densities including Shafranov shift. left (right) side shows the contribution of all four co (counter) beams (each for 1.5 MW).

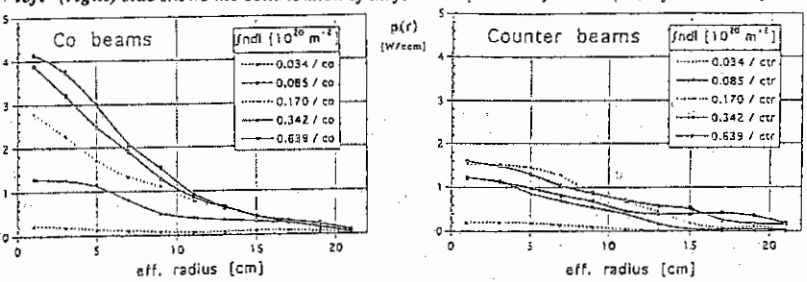

Results of real orbit calculations for low field operation

When the magnetic field strength is lowered, $<\beta> \propto n^{0.6} P^{0.4} B_0^{-1.2}$ should increase as long as plasma heating power P and confinement are not deteriorated. However, the B_0-dependence of the heating efficiency η shows a strong drop at about 0.5 T for co beams and at ≈1.0 T for counter beams (see fig.4). The calculations were done for a fixed target density of

$n_e(0) = 1.0*10^{20}$ m^{-3} and temperature of $T_e(0) = 350$ eV using real orbit calculations for the first toroidal orbit of each particle.

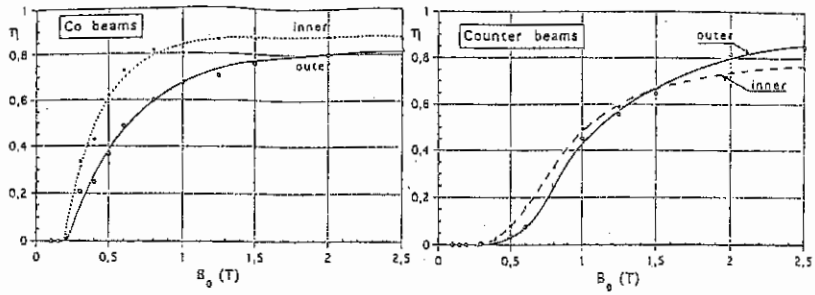

fig.4 : Heating efficiency for NI/W7AS as function of the magnetic field B_0 for inner and outer sources of co and counter beams with real orbit calculation for the first toroidal orbit.

The heating efficiency of all 8 sources together (4 co and 4 counter beams) as a function of the magnetic field B_0 is shown fig.5 for the same target conditions. Below 1T the NI-heating drops strongly and reduces $P = \eta(B_0) * 3.0$ [MW] from ≈ 2.2 MW at 1.25 T to 1.0 MW at B_0= 0.6 T. These M-C-results are in good agreement with a newly published paper on orbital aspects at low field in CHS [3]. The dependence $\eta = \eta(B)$ as shown in fig.5 explains at least qualitatively that no increase of <β> was found when the field strength was lowered (see also [4]).

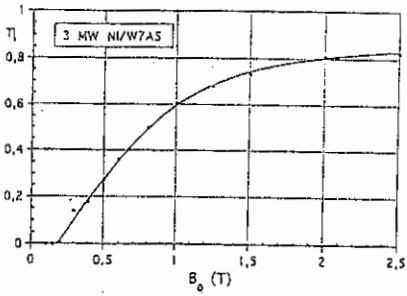

fig.5: heating efficiency for all 8 sources of NI / W7-AS for same target as used in fig.4

Up to now the real orbit calculations were done without a radial electric field, because for B > 1.0 T no essential effects were seen in earlier calculations [5]. But at low magnetic field operation a strong radial E-field may influence the orbits again. A study of this effect is under way.

References

[1] *R.Jaenicke et al.*, High power heating experiments on the Wendelstein 7AS Stellarator, Plasma Phys.&Contr.Fus., **37**, A163, 1995
[2] *F.-P. Penningsfeld* : NBI studies for W7-AS using the 3D computer code FAFNER 11th Conf. on Contr.Fus.&Plasma Phys., vol 7d, part II, pp323, Aachen, Sept. 1983
[3] *S.Murakami et al.*, Orbital aspects of reachable β values in NBI heated HELIOTRON / TORSATRONS, Nucl.Fus., **36**,no3,letters pp359, 1996
[4] *J.V. Hofmann et al., Stellarator optimization studies in W7-AS, TL of this conference*
[5] *A.Teubel, F.-P. Penningsfeld* Influence of the electric field on the heating efficiency in W7-AS, Proc.19th EPS. Conf.Plas.Phys., **16c**, part 1, p 537, 1992

Neoclassical Transport Predictions for Stellarators in the Long-Mean-Free-Path Regime

H. Maaßberg, C.D. Beidler, M. Kaiser, E.E. Simmet

Max-Planck-Institut für Plasmaphysik, IPP-EURATOM Association
D-85748 Garching bei München, Germany

The off-diagonal term in the neoclassical transport matrix, which is related to the particle flux, becomes essential in the stellarator long-mean-free-path (LMFP) regime. Strong temperature gradients can drive the density profile hollow, i.e., a positive density gradient related to the diagonal term in the transport matrix has to compensate this off-diagonal drive in order to fulfil the particle balance. As a consequence, central heating with peaked temperature profiles can make an active density profile control by central particle refuelling mandatory. This effect will become essential for the larger stellarator devices of the next generation since recycling as well as gas puffing can affect only the plasma edge region of typically a few centimeters. This neoclassically predicted outward particle flux driven by the temperature gradients is experimentally confirmed in W7-AS discharges in the LMFP regime [1].

Necessity of an Active Density Profile Control

With a particle source, S_p, within the bulk plasma, e.g., by NBI and/or by pellets, a particle flux density, $\Gamma_{ex} = \frac{1}{r}\int_0^r r' S_p\, dr'$, is externally driven. Then, the ambipolarity condition, $\Gamma_e = \Gamma_i = \Gamma_{ex}$, with the neoclassical particle fluxes is given by

$$\Gamma_{ex} = -n\Big\{D_{11}^{e,i}\big(\frac{n'}{n} \pm \frac{E_r}{T}\big) + D_{12}^{e,i}\frac{T'}{T}\Big\}, \qquad (1)$$

with + (-) for electrons (ions). Here, $T_e = T_i = T$ and $n_e = n_i = n$ was assumed for simplicity. The neoclassical transport coefficients, D_{jk}^{α} (with $j,k = 1,2$ and $\alpha = e, i$) are obtained by energy convolution of the mono-energetic transport coefficients. For various magnetic field configurations, the databases of these mono-energetic transport coefficients calculated by DKES code [2] are fitted based on traditional analytic theory [3] with axisymmetric contributions in the plateau collisionality regime taken into account. Inverting eq. (1) leads to

$$\begin{Bmatrix} n'/n \\ E_r/T \end{Bmatrix} = -\frac{1}{2}\Big\{\frac{D_{12}^e}{D_{11}^e} \pm \frac{D_{12}^i}{D_{11}^i}\Big\}\frac{T'}{T} - \frac{\Gamma_{ex}}{2n}\Big\{\frac{1}{D_{11}^e} \pm \frac{1}{D_{11}^i}\Big\}, \qquad (2)$$

where the ratio of the transport coefficients is much less sensitive to the radial electric field, E_r, than the D_{jk}^{α} itself. Several roots of eq. (2) with respect to E_r may exist: the "electron root" at large $E_r > 0$ with both the electron and ion transport coefficients being significantly reduced, the "ion root" at moderate $E_r < 0$ (for $T_e \simeq T_i$) where mainly the ion D_{jk}^i are decreased, and an unstable root inbetween. The 1st term of the r.h.s. of eq. (2) (with the - sign for E_r) is typically positive, and the "electron root" is forced for very small Γ_{ex}. For large Γ_{ex}, the "ion root" is obtained due to $D_{11}^e < D_{11}^i$.

Assuming "pure" collisionality regimes, the normalized off-diagonal terms, $\delta_{off}^{\alpha} = D_{12}^{\alpha}/D_{11}^{\alpha}$, are easily obtained: $\delta_{off}^{\alpha} = 7/2$ for the $1/\nu$ regime, $\delta_{off}^{\alpha} = 3/2$ in the plateau regime, $\delta_{off}^{\alpha} = 1/2$ for the $\sqrt{\nu}$ regime, and, finally, $\delta_{off}^{\alpha} = -1/2$ for the tokamak-like ν regime. As these regimes overlap in the energy convolution, the values of δ_{off}^{e} and δ_{off}^{i} as

given in Fig. 1 for an ambipolar particle flux Γ_{ex} estimated from the condition $n' = 0$ reflect mainly the dependence on E_r. With decreasing collisionality, $\nu^* \propto n/T^2$, the electrons enter deeply the $1/\nu$ regime since the effect of the "ion root" E_r on the D^e_{jk} is small. The ion coefficients are mainly determined by the $\sqrt{\nu}$ regime which is very pronounced for the high-mirror advanced stellarator configuration under consideration [3].

For the typical LMFP conditions, $\delta^e_{off} > \delta^i_{off}$ holds with the tendency of driving the density profile hollow. For the case of no central particle refuelling, i.e., $\Gamma_{ex} = 0$, eq. (2) gives for the pressure gradient

$$p' = -\frac{1}{2}(\delta^e_{off} + \delta^i_{off} - 2)nT', \tag{3}$$

with $p' > 0$ (for $T' < 0$) if $\delta^e_{off} + \delta^i_{off} > 2$ which holds in the stellarator LMFP regime. Please note in this context, that $\delta^e_{off} + \delta^i_{off} \approx 0$ (or even negative) in the deep tokamak banana regime. An inverted pressure profile, i.e., $p' > 0$, is in strong conflict with the MHD stability condition based on magnetic well, $V'' < 0$. Then, the typically stabilizing term, $p'V''$, becomes destabilizing. Consequently, the condition $p' < 0$ is mandatory leading to the requirement of an active density profile control, i.e., sufficiently large Γ_{ex}.

Quantitative Estimates

An estimate of the necessary particle refuelling rate can be obtained in a local (i.e., at a fixed radius, r) solution of the ambipolarity condition for a required n'/n, for given density and "heating power". Here, the "heating power", or more precisely, the total heat flux density, $q_t = q_e + q_i$, over the flux surface of effective radius, r, given by

$$q_{e,i} = -nT\left\{D^{e,i}_{21}\left(\frac{n'}{n} \pm \frac{E_r}{T}\right) + D^{e,i}_{22}\frac{T'}{T}\right\}, \tag{4}$$

is used. For the example shown in Fig. 1, a W7-X configuration with high toroidal mirror ($\simeq 10\,\%$) [4] was selected. At about half the plasma radius ($r = 0.27$ m, $R = 5.5$ m), a (normalized) temperature gradient $rT'/T = 1$ was assumed which corresponds to a fairly peaked T profile. The physical dependence of all the results on the local T'/T, however, turned out to be fairly small (e.g., a steeper T'/T decreases T at given heat flux Q_t). Full density control with $n' = 0$ was assumed. The necessary refuelling rate, i.e., the total ambipolar particle flux, scales roughly with the heating power for the 3 densities in Fig. 1. Please note in this context, that full NBI heating with a mean energy of 60 keV just fulfils this request ($\simeq 10^{20}$ particles/s and per MW heating power). The temperature increases only slightly with Q_t in the LMFP regime, nearly independent on density. At the high Q_t values, the electron transport coefficients deeply within the $1/\nu$ regime exceed the ion ones, and, consequently, the E_r of the "ion root" ($E_r < 0$) decreases since only a small E_r is sufficient to reduce the D^i_{jk} to the electron level ($D^i_{22} \simeq D^e_{22}$ at the low collisionbaities, ν^*). Consequently, the density dependence of the heat flux disappears in the deep $1/\nu$ regime. For both the normalized quantities, δ^e_{off} and δ^i_{off}, as well as for the "convective" term, $T\Gamma_{ex}/q_t$, versus the collisionality ν^*, nearly no additional density dependence is found with the ambipolar E_r taken into account.

"Electron Root"

Only for the lower densities, an "electron root" was found from the ambipolarity condition. In order to decide if this root can be realized, additional thermodynamic arguments have to be considered. On the basis of the poloidal force balance with a shear viscosity term included, a generalized heat production which has to be minimized is derived [5]. The Euler-Lagrange form of this variational principle leads to a diffusion equation for the radial

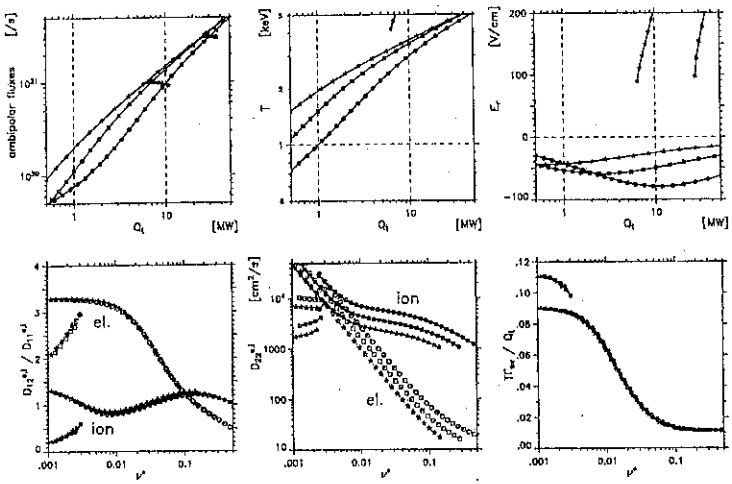

Fig. 1: *Ambipolar particle flux ($n' = 0$ assumed), temperature ($T_e = T_i$), ambipolar E_r vs. heat flux, Q_t (upper plots, from left to right), the norm. off-diagonal transport matrix terms, $\delta^e_{\rm off}$ and $\delta^i_{\rm off}$, the heat diffusivities, D^e_{22} and D^i_{22}, and (for reference) the norm. "convective" heat flux $T\Gamma_{\rm ex}/Q_t$ vs. collisionality, ν^* (lower plots, from left to right) for the high mirror W7-X configuration at an effective radius of $r = 27$ cm. Densities ($n_e = n_i$): $5 \cdot 10^{19}\ m^{-3}$ ($\star$), $1 \cdot 10^{20}\ m^{-3}$ ($\blacksquare$), and $2 \cdot 10^{20}\ m^{-3}$ ($\bullet$).*

electric field which is suited for integration in a predictive neoclassical code. For a "local" analysis, i.e., at one radius, however, the minimization of the generalized heat production with respect to the shear layer position (the width is assumed to be sufficiently narrow) leads to the condition

$$\int_{E_r^i}^{E_r^e} (\Gamma_i - \Gamma_e)\, dE_r = 0, \tag{5}$$

with E_r^i (E_r^e) being the "ion" ("electron") roots. On the other hand, with the integral of eq. (5) being positive, the "ion root" will be realized. From this argument, the "electron root" solutions of Fig. 1 cannot be expected. In the integral of eq. (5), however, the assumptions for the "local diffusive ansatz" in the neoclassical theory are violated at least for the ions at $E_r \simeq 0$, and direct losses have to be taken into consideration. From this point of view, the usual neoclassical ansatz may lead to an underestimation of Γ_i for very small E_r supporting the prediction of the "ion root". Furthermore, a Kelvin-Helmholtz-like instability may be driven at the highly localized poloidal shear layer and may suppress the "electron root" feature. As a consequence, neoclassical transport predictions should not rely only on the optimistic prospects of the "electron root".

"Ion Root"

For the "ion root" in the deep LMFP regime (with $D^i_{jk} \simeq D^e_{jk}$), the total heat flux scales with $T^{9/2}$, comp. Fig. 1. This unfavourable scaling makes stellarator optimization

with respect to neoclassical confinement mandatory. For reactor scenarios based on the "ion root", very high densities at moderate temperatures are favourable. However, the negative E_r may lead to the problem of impurity accumulation. Assuming full density profile control with $n' = 0$, the "ion root" E_r can be estimated from $\Gamma_i \simeq 0$ (since $\Gamma_e(E_r) = \Gamma_i(E_r) \ll \Gamma_i(0)$): $E_r \simeq \delta^i_{\rm off} T'$. For the impurities, Z, stationary conditions with $\Gamma_Z = 0$ (no inner sources) leads to highly peaked profiles

$$\frac{n'_Z}{n_Z} \simeq (Z\,\delta^i_{\rm off} - \delta^Z_{\rm off})\,\frac{T'}{T}, \tag{6}$$

since $Z\,\delta^i_{\rm off} - \delta^Z_{\rm off} \gg 1$ for high Z. It seems to be unlikely that $Z\,\delta^i_{\rm off} - \delta^Z_{\rm off} < 0$ (which is the case in the deep banana regime in tokamaks) can be achieved by stellarator optimization. The negative radial electric fields of the "ion root" result in a strong inward term for the high Z impurities. For the "electron root", on the contrary, no accumulation problems are expected.

Predictive Neoclassical Transport Codes

Neoclassical theory for fairly general stellarator configurations seems to be sufficiently developed, so that the predictive neoclassical transport modelling is the natural next step. A first attempt was done by implementing the ASTRA code [6] in a stellarator specific version [7]. The neoclassical transport matrix with the analytical respresentation [3] is used. The ambipolar E_r is obtained by direct iteration which is only stable for the "ion root". So far, the diffusion equation for E_r (corresponding to the poloidal force balance with the shear viscosity included) is not implemented. This problem is being treated by an other code which is still under development.

This stellerator specific ASTRA code version will be used to describe the transient phenomena in case of pellet injection used for the necessary active density profile control. In particular, the refuelling rate required to control the density profile in the bulk part of the plasma may be in conflict with the global density control if a transport barrier develops at the outer radii. Finally, on the basis of self-consistent density and temperature profiles together with the ambipolar radial electric field, the severe problem of impurity transport has to be treated.

Acknowledgements

We like to acknowledge helpful discussions with Dr. N.E. Karulin and Dr. J. Geiger.

References

[1] H. Maaßberg et al., Plasma Phys. Control. Fusion **35** (1993) B319.

[2] W.I. van Rij and S.P. Hirshman, Phys. Fluids B **1** (1989) 563.

[3] C.D. Beidler et al., EPS 1994, ECA **18B II** (1994) 568.

[4] C.D. Beidler et al., this conference.

[5] H. Maaßberg et al., Phys. Fluids B5 (1993) 3627.

[6] G.V. Pereverzev et al., *ASTRA - An Automatic System for Transport Analysis in a Tokamak* (1991) IPP-Report 5/42.

[7] N.E. Karulin, *Transport Modelling of Stellarators with ASTRA* (1994) IPP-Report 2/328.

Stability of W7-AS Configurations with Reduced Vacuum Magnetic Well

J.Geiger, A.Weller, R.Jaenicke, W7-AS Team, NBI-Team
Max-Planck-Institut für Plasmaphysik, IPP-EURATOM-Association,
D-85748 Garching, Germany

Introduction: Wendelstein 7-AS is a modular low shear stellarator with 5 field periods, a major radius of about 2m and a minor radius of about 18cm. W7-AS is an intermediate step towards a fully optimized low shear stellarator like the projected W7-X. The Pfirsch-Schlüter-currents in W7-AS are already reduced by the smaller average toroidal curvature compared to a classical stellarator, although not in the extend as in W7-X. This partial optimization results in better equilibrium properties (reduced Shafranov shift), and in a better stability behaviour since the PS-currents are driving terms for ideal (Mercier-) and resistive interchange modes. Stability at low β is usually provided by a vacuum magnetic well of up to 2%. This is in contrast to the torsatron/heliotron line of stellarators which are stabilized against Mercier modes by a strong shear inevitably leading to a large number of rational surfaces inside the plasma. A low shear stellarator tries to avoid low order rational surfaces. With respect to resistive interchange modes torsatrons/heliotrons are unstable due to a magnetic hill in their magnetic configurations at least at outer radii. Resistive interchange modes are thus thought to cause most of the turbulent transport in the gradient regions of such machines [1].

To study the importance of interchange stability for W7-AS an investigation of the predicted ideal and resitive interchange stability limits had been started for the accessible magnetic configurations of W7-AS [2]. We extend this study in particlar to configurations with vanishing vacuum magnetic well. These are more unstable with respect to Mercier and resistive interchange modes than the configurations for low and medium β-experiments. We discuss this stability analysis in comparison with experimental results.

Configurational space of W7-AS: A magnetic configuration of W7-AS is determined by the currents in the four coil systems, namely in the modular coils (I_m), in the large special coils (I_5) located in the region of strongest toroidal curvature ("elliptical" cross section), the toroidal field coils (I_t) and in the vertical field coils (I_v). Therefore, the magnetic configuration is defined by three coil current ratios: I_v/I_m (the vertical field) is related to the position of the magnetic axis and reduces the vacuum magnetic well in inward shifted configurations. I_t/I_m (additional toroidal field) can be used to control the rotational transform ι, and I_5/I_m determines the toroidal ripple, r_t[2], of the magnetic field strength B as defined by its Fourier components in Boozer coordinates. The "standard" configuration is defined by $I_5/I_m = 1$ and has ($r_t \approx 0$). Configurations with $r_t < 0$ have an increased magnetic field strength in the "elliptical" plane. Thus, trapped particles are shifted out of the region of strong curvature, so that trapped particle modes are expected to be not important. Additionally, a negative toroidal ripple reduces the vacuum magnetic well in W7-AS.

Equilibrium calculations for stability analysis: We analysed inward shifted "standard" configurations at $\iota_{vac} \approx 0.34 - 0.35$, and about 0.4, and "ripple" configurations with $r_t = -20\%$ at $\iota_{vac} \approx 0.34 - 0.35$ where high-β discharges had been performed. In earlier experiments top and bottom limiters in the "elliptical" plane determined the plasma boundary, and vertical fields with $B_z/B_0 \leq 0.011$ had been applied for position control (B_0 = mean magnetic field strength). Experiments in the last campaign without these limiters and with the upgraded NBI (8 injectors instead of 4, i.e. almost doubled input power) required higher vertical fields. Values of $B_z/B_0 \approx 0.012 - 0.025$ were used in both the "standard" and the "ripple" configuration. The plasma boundary was determined by new limiters on the inner torus wall.

Free-boundary equilibria were calculated with the NEMEC-code [3] assuming pressure profiles

proportional to $(1-s)$ and $(1-s)^2$, s being the normalized toroidal flux ($s \approx (r_{eff}/a_{eff})^2$), resulting in $\beta_0/ < \beta > \approx 2$ and 3, respectively ($< \ldots >$ denotes the volume average). The first profile shape is more typical for heating with NBI, the second one for ECR heating. The plasma boundary was chosen to touch the inner limiters for the converged equilibrium. In the calculation we neglected toroidal net current densities, i.e. the bootstrap current, ohmically and NBI driven currents. This is reasonable for high density, low temperature plasmas at high β with balanced NBI. Fig.1 shows that the PS-currents have considerable influence on the plasma position and the ι-profile at high β due to the low ι-values of W7-AS.

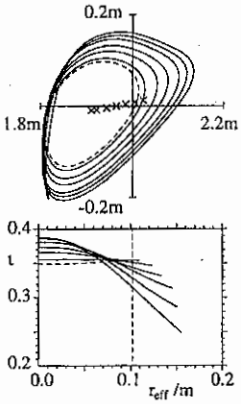

Figure 1: *Change of the plasma boundary and axis and of the ι-profile for the standard configuration at $\iota = 0.35$, $B_z/B_0 = 0.025$. The profile shape is (1-s) with $\beta_0 = 0, 0.3, 1, 1.7, 2.4, 3.2, 4\%$.*

The vacuum magnetic well of the considered configurations was reduced to marginality by the applied vertical fields. This effect was even pronounced in the "ripple" configuration where a vacuum magnetic hill can be achieved for $B_z/B_0 \geq 0.015$. In the standard configuration vertical fields with B_z/B_0 of about 0.025 are required.

Stability analysis of configurations with marginal magnetic vacuum well: For low shear stellarators the stability criterion for resistive interchange modes is in a good approximation given by [4]

$$(p'V'' - < j_\perp^2 >_s - < j_\parallel^2 >_s) > 0 \quad ,$$

if the modes are localized around rational flux surfaces and if toroidal net currents are neglected. Here, $< \ldots >_s = \int d\theta d\phi (\ldots \sqrt{g}/|\nabla s|^2)$ and $(\ldots)' \equiv d(\ldots)/ds$. We note that the "peeling modes", which are resonant ideal free boundary modes localized at the plasma boundary have the same stability criterion as the resistive interchange modes at the plasma boundary [5]. Therefore, whenever a resistive interchange unstable region extends to the plasma boundary, "peeling modes" may be present. The less strict Mercier criterion for ideal interchange has an additional stabilizing term depending on the global shear ι' and is given by

$$\left[\frac{\iota'}{2} + < \sqrt{g}B^2 >_s < \frac{j_\parallel}{B|\nabla s|^2} >_s\right]^2 + < \sqrt{g}B^2 >_s < \frac{1}{|\nabla s|^2} >_s (p'V'' - < j_\perp^2 >_s - < j_\parallel^2 >_s) > 0$$

with the above assumption of no toroidal net-currents. The idea of shear stabilization in torsatrons and heliotrons is obvious in this formulation.

The stability analysis was performed using the JMC-code [4] which evaluates the Mercier- and the resistive interchange stability criterion on the flux surfaces using Boozer coordinates. The results for the resistive and ideal interchange modes are shown in Fig. 2. Since we are more interested in "general" stability boundaries we did not resolve unstable regions due to low order rationals in the ι-profile [4].

For the "standard" cases at $\iota = 0.35$ and 0.4 we see that for configurations, which are stable at low β, the resistive interchange unstable region is growing from the boundary towards the inside. For those which have an unstable region even for $\beta = 0$ the magnetic well generated by β stabilizes the central part of the plasma leaving the outer fourth to third of the plasma unstable. The configuration with the large toroidal ripple shows qualitatively the same behaviour, but the unstable regions are intruding further towards the plasma center for comparable vertical fields.

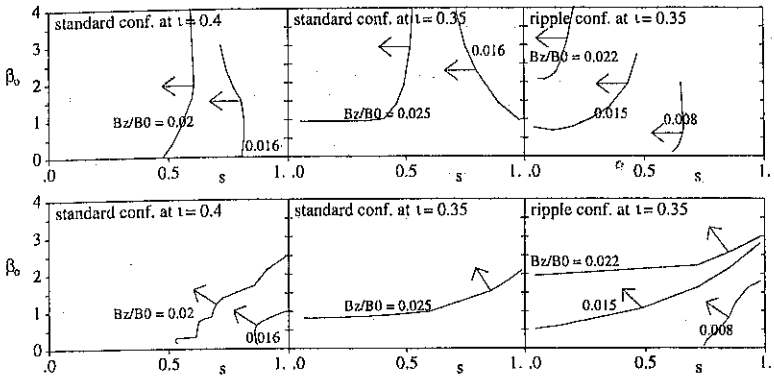

Figure 2: *Resistive (upper picture) and ideal (lower picture) interchange boundaries for the different configurations. The arrows point into the stable plasma region.*

For the cases, which had been considered previously [2], Mercier stability did not pose any problem. It is different in the cases considered here. For the standard configuration the Mercier criterion starts to play a role at vertical fields of about $B_z/B_0 \approx 0.016$ depending on ι (stable for $\iota = 0.35$, but a small unstable region for $\iota = 0.4$). For low β, the unstable region grows from the boundary towards the axis with increasing vertical fields, but is stabilized at higher β-values. Since the finite-β magnetic well is not sufficient to stabilize the resistive interchange modes, the important part for the stabilization of the Mercier modes is the shear part, which also involves the parallel current density. This last part can be important for Mercier stability in regions where the shear vanishes.

A comparison of the stability with respect to the two different β-profiles shows that the narrower profile is more unstable with respect to resistive interchange modes. This is due to the different finite-β well deepening. However, the stability boundaries with respect to Mercier modes are comparable.

Experimental results: High-β experiments had been performed in the configurations analyzed above. Most discharges used vertical fields with $B_z/B_0 \leq 0.017$ in the "standard" configuration but a variety of values of the rotational transform ι around the above values. In the case of the ripple configurations discharges have been performed only in the ones considered in the stability analysis. Generally, after a start-up with 70GHz ECRH at half field ($B_0 = 1.25T$), the NBI was switched on in steps from 2 to 4 to 8 or from 2 to 8 injectors with a total heating power of 2.2MW. The peak densities raised depending on the field strength to values of nearly $2 \cdot 10^{20} m^{-3}$ and electron temperatures of 400eV. These values justify the assumption on the internal toroidal net current densities at least in the moderate to high β-phases of the discharges. The maximum $< \beta >$-values were about $1.6 - 1.8\%$ for the standard configurations with peaking factors of about 2.2 regardless of the inward shift.

Even in the configurations with $r_i = -20\%$ the maximum β-values ranged between 1.4 and 1.6% for 5 and 6 NB-injectors with about the same β-peaking. Experiments using a nonresonant start-up (900MHz Rf-heating) at lower main fields (1.0T and 0.8T) did not lead to the naively expected higher $< \beta >$-values. However, as reported in [6], this "β-limit" is mainly due to the degrading heating efficiency of the counter NB-injectors at fields below 1.25T and, additionally,

to the scaling of the maximum achievable density $n_{max} \sim B_0$.

Although various MHD-activities have been observed in the Mirnov- and soft X-ray diagnostics in the high-$< \beta >$ discharges no general β-limiting phenomena have been observed. However, in a sequence of discharges in the "standard" configuration with $B_z/B_0 \geq 0.017$ a burst type, broad band MHD-activities occured, correlated to relaxations in the energy signal and to profile relaxations seen by the SX-ray diagnostic. Because of the reduced resistive interchange stability of these highly inward shifted configurations resistive interchange modes together with the peeling modes could be candidates for this type of activity. The appropriate low order rationals at the plasma boundary, which could be the origin of such relaxation processes, might have been generated by the deformation of the ι-profiles due to the high-β-values. Nevertheless, the identification is unsure since it is not clear why this type of activity was not observed in the strongly inward shifted ripple cases which are more unstable in this aspect.

Other significant MHD-activities observed are coherent modes at low frequencies ($f \leq 10kHz$) with $k_\parallel \approx 0$ which are presumably driven by the plasma pressure. Some have been identified by the SX-ray diagnostic with mode numbers (e.g. (n,m)=(1,3),(1,2)) corresponding to low order rationals of ι inside the plasma. However, these modes did not show any significant influence on the confinement. Moreover, their appearance does not depend on high $< \beta >$ values, but it is also known to appear at medium values[7]. Coherent mode activity above 15kHz was observed, too, and is thought to be mainly driven by fast beam particles [8].

Summary: We have extended the stability studies to magnetic configurations of W7-AS with strongly reduced vacuum magnetic well. Depending on the inward shift (vertical field strength), and/or the toroidal magnetic ripple, these configurations can be Mercier unstable at low β stabilizing themselves at higher β. They are generally also resistive interchange unstable in the outer half of the minor radius. Experimentally, relaxation phenomena have only been observed in the highly inward shifted standard cases. The observed burst type, broad band MHD-activity may be due to resistive interchange or "peeling" modes. However, their identification is far from being sure. Especially, their absence in the more unstable "ripple" configurations is not understood. From these results, the importance of resistive interchange as a soft, β-"limiting" instability seems to be questionable for W7-AS. However, torsatrons/heliotrons have a much higher shear at outer radii. This may lead to a stronger radial coupling of resitive modes due to the smaller distances between resistive instabilities on rational surfaces. From the view of the stability analysis, the Mercier unstable regions at low β would be more interesting than the high β phases. However, since the emphasis in the experiments was on stability limits at high β, only few data are available to judge on this subject, and a separate experimental investigation of these cases should be started. Internal toroidal current densities may then be included, and alter the ideal stability boundaries due to the induced shear.

References

1. Harris J.H. *et al.*, Proc. IAEA Conf. Plasma Physics and Controlled Nuclear Fusion , Würzburg, 1992, IAEA-CN-56/C-1-3
2. Geiger J. *et al.*, (Proc. 21st Euro. Conf. Montpellier, 1994), Part I (1994), 372.
3. Hirshman S.P., van Rij W.I. and Merkel P. (1986) Comput. Phys. Comm. 43, 143
4. Nührenberg J. and Zille R. Theory of Fusion Plasmas (Varenna, 1987), Editrice Compositori, Bologna (1988), 3.
5. D.Lortz, Nucl.Fusion 15 (1975),49
6. Penningsfeld F.P. et al, this conference
7. Weller A. *et al.*, (Proc. 19th Euro. Conf. Innsbruck, 1992), Part I (1992), 549.
8. Weller A. *et al.*, (Proc. 21st Euro. Conf. Montpellier, 1994), Part I (1994), 488.

Radiative boundary studies in the Wendelstein 7-AS stellarator

R. Brakel, H. Hacker, D. Hildebrandt*, R. Burhenn, A. Elsner, S. Fiedler, L. Giannone, C. Görner, P. Grigull, H. J. Hartfuß, A. Herrmann*, G. Kühner, U. Stroth, A. Weller, R. C. Wolf*, W7-AS Team, ECRH-Group#, NBI-Group

*Max-Planck-Institut für Plasmaphysik, EURATOM Association, Garching and *Berlin, FRG*

#Institut für Plasmaforschung, Universität Stuttgart, FRG

1. Introduction

Radiative edge cooling is widely considered necessary for power exhaust of future steady state fusion devices in order to prevent target overload by high heat flux densities. Configurational flexibility enables two approaches to radiative power exhaust to be examined in W7-AS: (1) A boundary photosphere of the core plasma may be established by injecting impurities from the edge into limiter bounded magnetic configurations. Experimentally, a steady state radiation level is adjusted by nitrogen injection from a valve, feedback controlled via VUV line emission. (2) Impurities may specifically be injected and eventually confined into magnetic boundary islands in order to provide a local heat sink, topologically separated from the core plasma. In this approach impurities are transiently released from a fast reciprocating erosion probe in a boundary region with magnetic islands. Impurity source and transport properties, the location of impurity radiation and its impact on global confinement and on power balance have been studied for both scenarios. Boundary photosphere studies are presented in detail; first results on the radiating island approach are discussed in ref. [1].

2. Comparative impurity radiation modeling

Figure 1 shows radiation profiles of the low-Z impurities nitrogen and neon and, for comparison, of the medium-Z impurity titanium as calculated with a 1D impurity radiation and transport code (IONEQ [2]). The total radiated power is kept fixed at the arbitrary value $P(r_w)$ = 100kW. Electron density and temperature profiles used in the calculation are those taken at 0.4s from the nitrogen fuelled discharge in Fig.3, which is simultaneously heated by 300kW ECRH and 650kW NBI (line averaged density $\langle n_e \rangle = 8 \times 10^{19} m^{-3}$, $T_e(0)$ = 1000eV, $T_e(a)$ = 25eV, major radius R = 2m, effective minor radius of the last closed magnetic surface (LCMS) a = 0.18m and of the wall r_w = 0.20m, impurity diffusion coefficient $D = 0.5 m^2/s$).

For nitrogen and neon the maximum of the emissivity Q(r) is localized close to but inside the LCMS. A second maximum deeper inside the confinement region significantly contributes to the power loss P(r), which explains the experimentally observed degradation of energy confinement even in the case of nitrogen (see below). For the same total power loss the central concentration is about twice as high for nitrogen, but the central dilution as expressed by the increase of Z_{eff} is the same as for neon. In view of the requirement of low radiation within the plasma core, nitrogen, radiating closer to the edge than neon and being completely ionized in the center, should be favourable for relatively small devices such as W7-AS.

The titanium radiation is more smoothly distributed over the plasma cross section. A strong reduction of the effective heating power P_{heat}-P_{rad} has to be expected in the core. Therefore, medium Z impurities are not suited for edge cooling in W7-AS under the given discharge

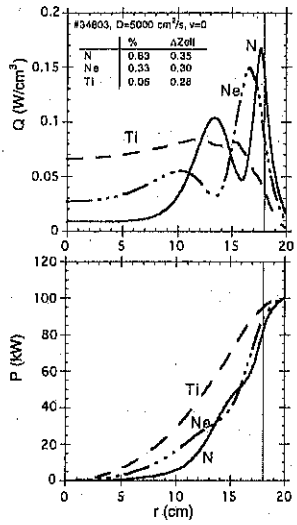

Fig.1: Local emissivity Q(r) and radiated power $P(r) = 4\pi^2 R \int Q r dr$ calculated for the impurities nitrogen, neon and titanium. The vertical line indicates the limiter position.

conditions, i.e. limiter bounded plasmas with modest electron temperatures, unless penetration into the core is prevented, e.g. by trapping of the impurity ions in edge localized islands or by screening due to a high edge density and/or diffusivity.

3. Nitrogen recycling and fuelling

Radiation feedback control requires effective impurity particle exhaust. Because impurities cannot be effectively removed by external pumps during a plasma discharge in W7-AS at present, particle removal must rely on wall pumping, i.e. on a recycling coefficient significantly below one. Therefore nitrogen, which is expected to have a low recycling coefficient, was finally chosen as impurity rather than neon, which has previously been used in tokamaks equipped with a pumped limiter [3] or a divertor [4].

Nitrogen is injected into the plasma from an absolutely calibrated valve at the outboard side of the wall. The gas flow can be adjusted either to a programmed flow rate or, by feedback control, to produce a programmed radiation level. The intensity of the 765Å line of NIV, measured along a central chord by a VUV-spectrometer, has been used as the feedback parameter. The gas flow is monitored by the 4631Å line of NI, the spectrometer viewing along the gas flow direction.

Wall pumping of nitrogen proved to be sufficiently high for feedback control. Decay times after turning off the gas feed at the end of a phase of constant flow rate were of the order $\tau_1^* = 25$ms for Be-like NIV (ECRH heated discharge, $P_{ECRH} = 260$kW, $\langle n_e \rangle = 4 \times 10^{19} m^{-3}$). The central chord soft-X radiation exhibited a bi-exponential decay. The fast decay time of about $\tau_2^* = 25$ms is attributed to H- and He-like nitrogen. The slow decay time of about $\tau_3^* = 70$ms is attributed to the transport of fully ionized particles from the plasma center, becoming radiative after recombination into H- and He-like ions.

In steady state, the probability f_z that an injected impurity atom is confined in the plasma in the ionization state z is $f_z = N_z/(\tau_z^* \Phi)$, with the impurity flow rate Φ, the effective ion confinement time τ_z^*, and the number of ions N_z. We use $\tau_z^* = \tau_1^*$ for ions up to Be-like, τ_2^* for H- and He-like and τ_3^* for fully stripped ions. For the previous discharge parameters an increase in soft-x radiation by an amount of 25kW is observed when nitrogen is puffed at a rate of $\Phi = 2.3 \times 10^{20}$atoms/s. This increase can be modeled ($D = 0.2 m^2/s$) by a total number of 1.4×10^{18} nitrogen ions, where stripped ions contribute 57%, H- and He-like ions 36%, and ions up to Be-like 7%. The central nitrogen concentration is 2.5%. From these data a total fuelling efficiency Σf_z of only 15% is calculated.

Because the fuelling efficiency is low, a large amount of nitrogen has to be introduced into the vessel, which due to the high sticking probability leads to the shot-to-shot build-up of an intrinsic nitrogen reservoir. However, this reservoir settled at a stationary radiation level an order of magnitude lower than that resulting from injection. Short (10min) helium glow discharge cleaning was not effective in reducing this internal reservoir, but it decreased after stellarator discharges without external nitrogen puff. Therefore long-term contamination of the vessel with nitrogen was not observed.

4. Experimental radiation profiles

Radiation profiles across poloidal cross sections are measured by two 30-channel bolometer arrays, two 36-channel soft-x ray cameras and, spectrally resolved, by a VUV-spectrometer combined with a rotating mirror. On the inboard side the NIV and NV VUV-radiation shells are close to the LCMS in accordance with the expectations from modeling. On the outboard side these shells extend much further outward. This poloidal asymmetry can be related to the local perturbation introduced by the gas puff, which is located at the outboard wall in a toroidal distance of only 8° from the VUV observation plane. The evident difference in Fig. 3 between the time evolutions of the NIV-intensity, which is used for feedback control, and the radiation power is probably caused by the same local perturbation.

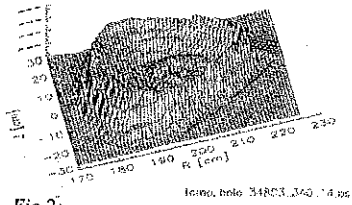

Fig.2: Radiation profile at 0.34s for the nitrogen fuelled discharge in Fig.3 (tomographic reconstruction of bolometry data).

The poloidal distribution of the total radiation is shown in Fig.2. In the equatorial plane (z=0) the LCMS is located at R = 178cm (inboard) and R = 215cm (outboard). Nitrogen fuelling strongly increases the edge radiation. In a reference discharge without nitrogen injection, intrinsic low-Z impurities (boron and carbon, W7-AS is operated with graphite limiters and boronized wall) provide an already hollow radiation pattern, but at much lower level.

5. Power balance

The radiated power P_{rad} and the power P_{lim} conducted to the limiters are derived from the local bolometry and thermography [5] measurements assuming toroidal symmetry. Time traces for the discharge with nitrogen puff and the unperturbed reference discharge are shown in Fig. 3. In the quasi steady phase ($|dW/dt| << P_{heat} = 950kW$) P_{rad} and P_{lim} are strictly correlated such that the sum is constant. The power accountability exceeds 85%, which gives confidence in the symmetry assumption. The radiated power fraction can be increased from 20% to more than 60% causing a corresponding reduction of the limiter load. The electron temperature near the LCMS as measured by a Langmuir probe decreased from 75 to 25 eV, the edge density increased by up to 30%. During the injection phase, both, the plasma stored energy and the central electron temperature degrade continously with increasing radiation. The discharge recovers instantaneously on the nitrogen confinement time scale when the nitrogen puff is stopped. If the radiation level is increased further the discharge becomes radiatively unstable and starts to collapse softly from the outside. The maximum fraction of radiated power which

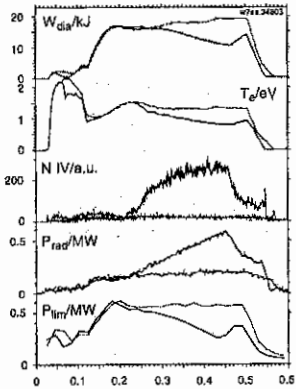

Fig.3: Diamagnetic energy, central electron temperature, NIV intensity, radiated power and power conducted to the limiters for a nitrogen fuelled discharge and an unperturbed reference discharge. Heating power is 950kW.

could be maintained in quasi steady state depended on heating power and increased from 33% at 180kW (ECRH) to about 60% at 1MW (ECRH+NBI).

The nitrogen radiation shell occupies a significant fraction of the confinement volume and reduces the effective heating power $P = P_{heat}-P_{rad}$. Therefore the degradation of the stored plasma energy can qualitatively be explained by the global W7-AS energy confinement scaling [6] $\tau_E \sim P^{-0.55}$, i.e. $W \sim P^{0.45}$. Electron heat transport in the core seems not to be affected. The heat diffusivity $\chi_e(r)$ from a local transport analysis is similar for both discharges, with and without nitrogen puff. The analysis accounts for a radially distributed heat sink by using the radiation profile of Fig.1 scaled to the total radiation power from the experiment. The temperature profile predicted for the nitrogen fuelled discharge with $\chi_e(r)$ from the reference discharge and additional radiative losses agrees well with the experimental one (Fig. 4). For the prediction the edge temperature is set to the experimental value.

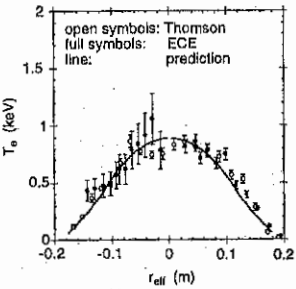

Fig.4: Experimental and predicted electron temperature.

5. Summary and conclusion

Nitrogen has been proven to be appropriate for radiative edge cooling studies in relatively small devices such as W7-AS which are not equipped with active pumping capabilities. Recycling and radiation properties are in accordance with expectations. Long-term contamination with nitrogen was not observed in spite of the high sticking probability. Injection into limiter bounded plasmas provided hollow radiation profiles, reduced the limiter load and strongly cooled the edge plasma. Electron transport analysis does not indicate enhanced heat transport. The degradation of the stored plasma energy with increasing radiation power is rather explained by a reduction of the effective heating power. This seems to limit the radiative stability and thus the maximum radiated power fraction which could be achieved in steady state (up to 60%, increasing with heating power). Detachment from the limiters ($P_{lim} \rightarrow 0$) could not yet be realized in steady state.

References

[1] D. Hildebrandt et al., Proc. 12th PSI Conference, St-Raphael, France (1996), to be published
[2] A. Weller et al., JET-Report,JET-IR-(87)10
[3] U. Samm et al., Plasma Phys. Control. Fusion, **35** (1993) B167
[4] A. Kallenbach et al., Nucl. Fusion, **35** (1995) 1231
[5] R. C. Wolf et al., this conference
[6] U. Stroth et al., Nucl. Fusion, in press

Ion Cyclotron Resonance Heating Experiments on the Stellarator W7-AS

G. Cattanei, *D.A. Hartmann, D.A. Rasmussen†, J.F. Lyon†, V. Plyusnin‡,*
ICRH-Team, W7AS-Team
Max-Planck-Institut für Plasmaphysik, Euratom Association, 85478 Garching, Germany
†Oak Ridge National Laboratory, Oak Ridge, Tennessee 37831, USA
‡Kharkov Institute of Physics and Technology, Kharkov 310108, Ukraine

Ion cyclotron resonance heating (ICRH) has, for the first time, successfully been demonstrated on the stellarator W7-AS. A novel broad antenna [1,2] designed to excite a narrow spectrum of fast waves was used. Two different heating scenarios were investigated: second harmonic heating of neutral beam heated hydrogen plasmas and hydrogen-minority heating of ECRH deuterium plasmas. Both scenarios showed plasma heating without a significant concurrent increase in plasma density or impurity radiation loss. In addition, it was possible to sustain the plasma with ICRH alone.

The ICRH antenna, shown in Fig. 1, is located on the high field side in the elliptical cross-section of the non-axisymmetric plasma. It has four feeders that allow operation in 0- and π- phasing. Typically it is operated in π-phasing. Then the poloidal current has an almost sinusoidal distribution in the toroidal direction and excites a narrow $k_\parallel \approx 6\mathrm{m}^{-1}$ spectrum of fast waves. During the Spring 1995 opening of the torus vessel the feeders to the antenna, shown in Fig. 2, were closed off against plasma penetration. This eliminated anomalously high loading of the antenna during plasma operation observed previously [3] and increased the maximum rf-voltage at which electrical breakdown (arcing) occurred. Most plasma targets had $\iota \approx 0.33$ and were shaped by inside limiters. In those plasmas the distance from the antenna to the fast-wave cutoff is about 6 cm and the observed antenna plasma loading is only about 0.5 Ω. Voltages of up to 55 kV for 400 msec, corresponding to a maximum power of about 400 kW at the antenna, have been achieved after extensive conditioning. Real time visual observation of the antenna during plasma operation and inspection after the vacuum break confirmed that arcs did not occur in the antenna, but only in the feeders and in the transmission lines.

In the second harmonic hydrogen heating scenario with a neutral beam heated target plasma an increase in the diamagnetic energy of about 10 % (0.6 kJ) was obtained. The central hydrogen temperature was about 800 eV and central electron densities were $6 \times 10^{19}\mathrm{m}^{-3}$. One estimates

that about 60 % of the power P radiated from the antenna is found in the plasma, if P is the generator power reduced by the ohmic losses in the antenna and $P^{-0.6}$-scaling of the energy confinement time is invoked. Under good wall conditions, the plasma density could be kept constant during the rf-pulse, even though the H_α-observation indicated enhanced outgassing at the antenna. The impurity radiation inferred from the bolometer did not increase. An increase in the flux of hydrogen atoms with energies between 10 keV and 33 keV was observed; however, no significant increase in the bulk hydrogen temperature was observed. Maximum heating occurred if the location of the second harmonic resonance coincided with the center of the plasma; almost no heating occurred if the resonance was outside of the plasma. The antenna loading was independent of the location of the resonance even though a rf-probe (located half-way around the torus) detected a wave signal only if the resonance was outside of the plasma. Heating at 0-phasing showed similar increases in the diamagnetic energy as in π-phasing and no enhanced impurity radiation. No significant heating was observed in ECRH plasmas of the same density, presumably because the hydrogen temperature of the target plasma was too low (about 350 eV).

In the H-minority heating scenario with an ECRH target deuterium plasma an increase in the diamagnetic energy of about 15 % (1 kJ) was obtained. This corresponds to absorption of about all of the radiated power P. Fig. 3 shows a typical example of a plasma shot. The spectroscopically estimated H/D ratio was about 10%. The line-of-sight averaged deuterium temperature rose from 300 eV to 400 eV; the central electron temperature rose slightly. Energetic hydrogen atoms with energies up to 33 keV were observed. The impurity radiation did not increase.

In this heating scenario it was possible to sustain an ECRH-created plasma with ICRH alone for as long as 500 msec. The duration of the ICRH-only phase of the plasma was solely limited by arcing in the transmission lines. An almost steady state condition could be obtained about 200msec into the ICRH-only phase of the discharge. Typical parameters were diamagnetic energy of 2 kJ, average electron density of $4. \times 10^{19} m^{-3}$, central electron temperature of 300 eV, and central deuterium temperature of 350 eV.

An example of an ICRH sustained plasma is shown in Fig. 4 starting at 400 msec. The generator frequency and the approximate H/D-ratio were such that both, the H-resonance and the ion-ion-resonance were located inside of the plasma volume, as shown in Fig. 2. The average electron density first rose by increased outgassing of the antenna but returned towards the initial value near the end of the ICRH plasma. The central electron temperature dropped rapidly within

an energy confinement time and then stayed constant throughout the ICRH phase. The total radiation measured with bolometers stayed constant, even though an accumulation of iron and chromium could be inferred from VUV observation; yet soft X-ray measurements indicated that $Z_{\rm eff}$ did not increase. We can therefore conclude that, at least in the range of parameters investigated, the ICRH sustained plasma is not hampered either by uncontrolled density increase or by enhanced impurity production.

The plasma density profile, measured with Lithium beam diagnostic, Langmuir probes, microwave reflectometry and Thomson scattering, was narrower and had steeper edges during the ICRH sustained plasma than during comparable ECRH heated plasmas. The transition between these two profiles occured within approximately one energy confinement time. Further narrowing of the plasma was observed on a longer time-scale. The resulting increase of the distance from the antenna to the fast wave cutoff could explain the decrease of the antenna plasma loading and therefore the decrease in diamagnetic energy. A radial electric field of about -1.5 kV/m built up at the beginning of the ICRH phase of the discharge, presumably due to increased high-energy hydrogen losses as indicated by CX measurements.

References:

[1] G.Cattanei et al., Stellarator News, Issue 25, January 1993, p.3.

[2] G. Cattanei and the W7-AS Team. Topical Conference on Radiofrequency Heating and Current Drive of Fusion devices. (Brussels 1992) p. 121.

[3] M. Ballico et al., IAEA Technical Committee Meeting on Stellarators and Other Helical Confinement Systems, Garching (1993), p. 413.

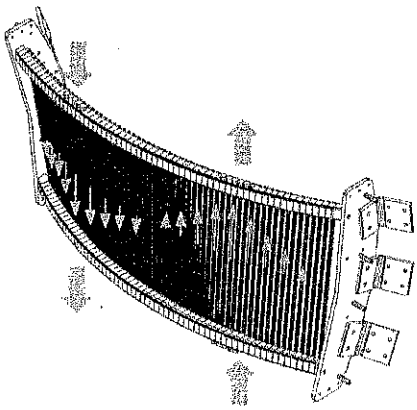

Figure 1. ICRH antenna shown without Faraday screen.

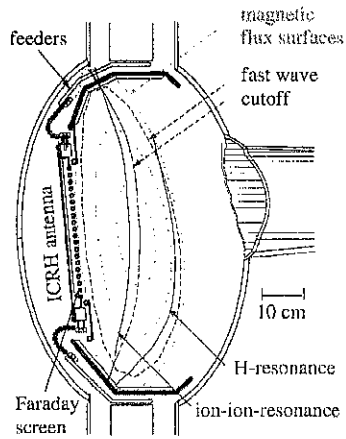

Figure 2. Poloidal cross-section through the ICRH antenna. Resonances and cutoffs shown for the ICRH plasma in Fig.3.

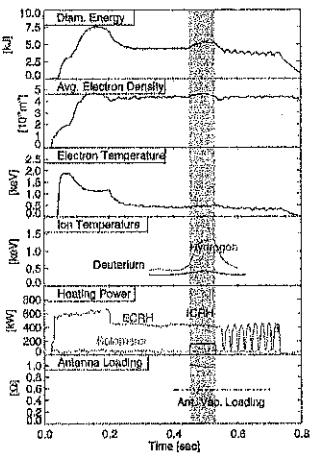

Figure 3. Time trace of shot 33882. Ion temperatures infered from unweighted line-of-sight average of CX fluxes. B_T = 2.5T, ι=0.34.

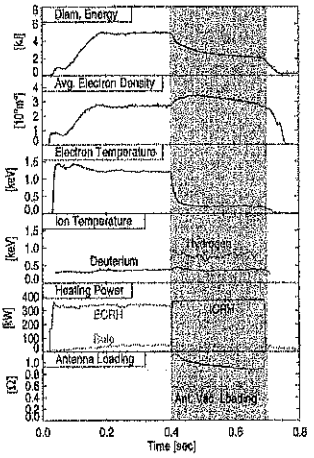

Figure 4. Time trace of shot 33634. Ion temperatures infered from unweighted line-of-sight average of CX fluxes. B_T = 2.5T, ι=0.34.

Global stability of $n = 1$ external modes for plasmas with helical boundary deformation and net toroidal current

A. Ardelea and W. A. Cooper
CRPP/EPFL, Association Euratom/Confederation Suisse,
Lausanne, Switzerland

1 Introduction

The global stability of plasmas with helical boundary deformation and non null net toroidal current is tested against external $n = 1$ (n toroidal mode number) modes with the aim of seeing whether these modes can be stabilized at values of β inaccessible for the classical tokamak. L=2,3 configurations with several aspect ratios and different numbers of equilibrium field periods are considered. A large variety of toroidal current densities are taken into acount and Mercier stability is also investigated.

2 Equilibrium and Stability

The 3D equilibria with nested magnetic surfaces and single magnetic axis are generated with the VMEC code [1] [2]. Input parameters are : N_{per} the number of equilibrium field periods, ϵ the inverse aspect ratio, $J'(s)$ the toroidal current density profile, $p(s)$ the pressure profile and $\Phi(s)$ the toroidal flux function. Here s represents the radial coordinate (choosen proportional to Φ i.e. $d\Phi/ds = cst$) . The plasma boundary is specified as:

$$R(s=1,u,v) = \sum_{m_b,n_b} R_{m_b n_b}(s) cos(m_b u - n_b N_{per} v)$$

$$Z(s=1,u,v) = \sum_{m_b,n_b} Z_{m_b n_b}(s) sin(m_b u - n_b N_{per} v)$$

The Fourier amplitudes of the inverse coordinates R (the distance from major axis) and Z (the distance from midplane) obtained from VMEC together with $\Phi'(s)$ and $\Psi'(s)$ which are the radial derivatives of the toroidal and poloidal magnetic flux functions, form the input to the stability code TERPSICHORE [4]. The variational formulation of the linear MHD stability of 3D plasmas on which TERPSICHORE is based is described in detail in [3]. The variational equation is written as:

$$\delta W_p + \delta W_v - \omega^2 \delta W_k = 0$$

with

$$\delta W_p = \frac{1}{2}\int\int\int d^3x \left\{ Q^2 + \Gamma p (\vec{\nabla}\cdot\vec{\xi})^2 + \vec{j}\wedge\vec{\xi}\cdot\vec{Q} + (\vec{\xi}\cdot\vec{\nabla}p)(\vec{\nabla}\cdot\vec{\xi}) \right\}$$

$$\delta W_v = \frac{1}{2}\int\int\int d^3x \left|\vec{\nabla}\wedge\vec{A}\right|^2 \qquad \delta W_k = \frac{1}{2}\int\int\int d^3x \vec{\xi}\cdot\rho_M\cdot\vec{\xi}$$

where δW_p, δW_v, δW_k and ω^2 represent the potential energy in the plasma, the magnetic energy in the vacuum region, the kinetic energy and the eigenvalue of the system. The perturbations have been assumed to evolve as $exp(i\omega t)$ and the system is unstable to MHD modes when $\omega^2 < 0$. $\vec{\xi}$ is the displacement vector, $\vec{Q}$ stands for the perturbed magnetic field and $\vec{A}$ represents the perturbed vector potential. TERPSICHORE reconstructs the MHD equilibrium and maps it to the Boozer coordinate system (s,θ,ϕ). The displacement vector expressed as [3]:

$$\vec{\xi} = \sqrt{g}\xi^s \vec{\nabla}\theta\wedge\vec{\nabla}\phi + \eta\frac{\vec{B}\wedge\vec{\nabla}S}{B^2} + \left[\frac{J(s)}{\Phi'(s)B^2}\eta - \mu\right]\vec{B}$$

with (ξ^s,η,μ) the (radial,binormal,parallel) components. By imposing the incompressibility constraint $\vec{\nabla}\cdot\vec{\xi} = 0$ to get rid of the positive definite term $\Gamma p(\vec{\nabla}\cdot\vec{\xi})^2$ from δW_p, the parallel component μ is

eliminated as a variable from the problem and the two remaining components of the perturbation are expanded in truncated Fourier series,

$$\xi^s(s,\theta,\phi) = \sum_l \xi_l(s) sin(m_l\theta - n_l\phi) \qquad \eta(s,\theta,\phi) = \sum_l \eta_l(s) cos(m_l\theta - n_l\phi)$$

where m_l and n_l are the poloidal and toroidal mode numbers, l being the index of an (m,n) pair.

3 Configurations under study

Configurations of the type $L = 2$ and $L = 3$ have been studied i.e. the plasma boundary has been prescribed according to the following equations

$$L=2 \quad \begin{cases} R(s=1,u,v) &= R_0 + cosu + \delta\left(cos(u) + cos(u - 2N_{per}v)\right) \\ Z(s=1,u,v) &= sinu - \delta\left(sin(u) + sin(u - 2N_{per}v)\right) \end{cases}$$

$$L=3 \quad \begin{cases} R(s=1,u,v) &= R_0 + cosu + \delta\left(cos(2u - N_{per}v) + cos(2u - 3N_{per}v)\right) \\ Z(s=1,u,v) &= sinu - \delta\left(sin(2u - N_{per}v) + sin(2u - 3N_{per}v)\right) \end{cases}$$

δ being a measure of the boundary deformation.
In a geometry with N_{per} field periods the configuration repeats itself N_{per} times when going in the toroidal direction. It follows that modes with toroidal number n are only coupled to modes with n, $n \pm N_{per}$, $n \pm 2N_{per}$, etc. There are a total of $N_{fam} = N_{per}/2$ families ($N_{fam} = (N_{per} - 1)/2$ families) of modes for configurations with even (odd) number of field periods [5], [6]. If k labels one of these families the modes belonging to it will have toroidal mode number given by

$$n = n_i(k, N_{per}) = iN_{per} \pm k \quad i = .., -1, 0, 1, .. \quad k \in \{1, N_{fam}\}.$$

The following remarks can be made: 1) N_{fam} increases with the number of field periods. If $N_{per} \leq 3$ there is a single family (with all n 's), if $N_{per} = 4, 5$ there are two families and so on. 2) the coupling between modes with close values of n is restricted to configurations with small N_{per}. 3) if N_{per} is even the familiy $k = N_{fam} = N_{per}/2$ contains less modes than the other families. For practical/technical reasons which result from the observations above, we have limited the computation to configurations with $N_{per} = 4, 5$ and 7 ($N_{per} = 3, 6$ were left aside). Several values have been taken for the aspect ratio $1/\epsilon = 5, 8, 10, 13, 17$. The toroidal current density was prescribed with

$$J^l(s) = a_1\left(1 - s^{a_2}\right)^{a_3} + a_4\left(1 - s^{a_5}\right)^{a_6}$$

the six parameters $a_{1,..,6}$ offering a large choice of profiles; a_4, a_5 and a_6 were taken nonzero only for hollow $J^l(s)$ profiles. All the computations were made at $\beta = 1\%$ with a pressure profile given by $p(s) = p_0[(1-s)^2 + (1-s^2)^2]$ (p#1). Some configurations have been studied with $p(s) = p_0(1 - s^2)$ (p#2).
We proceeded as follows : for a given configuration characterized by L, N_{per}, ϵ, a sequence of equilibra with fixed $J^l(s)$ and β was generated, each equilibria resulting from a different choice of the deformation parameter δ. In general the starting point was $\delta = 0$ (corresponding to the circular tokamak), then at each step δ was increased and the stability analysis was done.

4 Results

The numerical study has showed that a helical triangular deformation of plasma can stabilize $n = 1$ global modes (we considered the cases for which the circular tokamak is unstable with respect to the modes studied). The observations below apply to the $(m,n) = (2,1)$ mode.
- it was found that a stability window $[\delta_{min}, \delta_{max}]$ may exist depending sensibly on equilibrium parameters (see *Fig.3,4*). In fact by increasing δ, q decreases and stabilization is lost when the minimum of the security factor q_{min} is less than one somewhere in the plasma. This happens at $\delta \simeq \delta_{max}$.
- if the equilibrium is such that q_{min} is already low at $\delta = 0$ then increasing δ may not stabilize the plasma.
- increasing/decreasing $J^l(s)$ but keeping it's profile the same (by changing only a_1), new stability windows are obtained. The representation of these stability windows in a (q_{axis}, q_{edge}) plane gives a stability area (see *Fig.3,4*). It's left (small q_{axis}) and lower (small q_{edge}) margins are limited by the

condition $q_{min} > 1.0$, and the upper margin corresponds to $\delta \simeq \delta_{min}$. The right limit (large q_{axis}) is not well defined; this topic will be discussed below.
- in general the stability area is situated under the diagonal $q_{edge} = q_{axis}$ and in the region limited by $q_{edge} \leq 1.5$ but for strong and peaked currents, stable plasmas are obtained with $q_{axis} < q_{edge}$. Small currents require more deformation for stabilization (bigger δ_{min}) than large currents. Peaked current profiles ($a_2 < 1.5$) yield compact areas, situated mostly in the $1.0 < q_{axis} < 1.5$ region. Broader currents ($a_2 > 5$) give areas elongated in the q_{axis} direction. The biggest stability areas were produced with hollow currents ($sign(a_1) \neq sign(a_4)$ shifted towards large q_{axis}.
- $N_{per} = 7$ produces the least extended stable zones. Although beeing different in details, $N_{per} = 4$ and $N_{per} = 5$ give comparable stability zones ($N_{per} = 4$ is slightly better).
- configurations with $L = 2$ give better results than those with $L = 3$ but require much larger values of the deformation parmeter. ($\delta_{min}^{L=2} \simeq 0.3 - 0.35$ compared with $\delta_{min}^{L=3} \simeq 0.1 - 0.15$)
- with respect to the aspect ratio, the best results were obtained for $1/\epsilon = 8$ and 10. The largest $1/\epsilon = 17$ and the smallest $1/\epsilon = 5$ gave reduced stability zones.
- a different pressure profile (p#2 instead of p#1) does not bring major changes to the size or position of the stability area.
It is not obvious to determine the right-side boundary (low-current, high q_{axis}) of the stability area. The p#1 profile produces equilibria with large Shafranov shifts $\Delta_{sh} \simeq 12 - 18\%$ and for low, peaked currents at high apect ratio the circular tokamak equilibrium does not even exist. On the other hand increasing the helical deformation diminishes the Shafranov shift; for $L = 2$ configurations Δ_{sh} is diminished by a factor of 2 (even 3) when going from $\delta = 0$ to $\delta \in [\delta_{min}, \delta_{max}]$.
However working with currents which are lower and lower causes VMEC to produce equilibria with inacceptable Δ_{sh} i.e. $\geq 15 - 20\%$. When these values are encountered stability investigation for smaller currents is stopped. For peaked currents at high $1/\epsilon$ such problems may appear for $q_{axis} \geq 1.5$, whereas for hollow currents it is possible to continue beyond $q_{axis} \geq 2$.
The p#2 parabolic pressure profile was introduced with the aim of reducing the Shafranov shift. It effectively brought down these large Δ_{sh} to more acceptable values of $6 - 9\%$. but again we could not continue toward lower currents, because the null pressure gradient at the flux surfaces near the axis caused increasing problems in computing the equilibrium.
- Mercier stability at $\delta = 0$ depends on the equilibrium parameters. Configurations have been found for which the Mercier criterion can be satisfied for δ between zero and a maximun value δ_M. For $\delta > \delta_M$ more and more surfaces become Mercier unstable. The aim was to have $\delta_M > \delta_{min}$ which, in general, was not the case. The highest values for δ_M were obtained with low, peaked currents and p#1 profiles. The Mercier criterion was satisfied only for configurations with $L = 3$, $N_{per} = 4, 5$ $1/\epsilon \geq 8$ and small currents. Unfortunately this corresponded to the points at the right limit of the stable zone in the (q_{axis}, q_{edge}) plane i.e. at large Δ_{sh} (more than 15%).

References

[1] S.P.Hirshman, U.Schwenn, J.Nührenberg - J. Comput. Phys. 87, 396 (1990)

[2] S.P.Hirshman, O.Betancourt - J. Comput. Phys. 96, 99 (1991)

[3] W.A.Cooper - "Variational formulation of the linear MHD stability of 3D Plasmas with noninteracting hot electrons" - Plasma Physics and Controlled Fusion, vol 34, No 6, pp.1011-1036, 1992

[4] D.V.Anderson, W.A.Cooper, R.Gruber, S.Merazzi, U.Schwenn - Terpsichore: a 3-dimensional ideal magnetohydrodynamic stability program - Scient. Comp. on Supercomputer II ,159 (1990)

[5] W.A.Cooper,G.Y.Fu and all - "Global external ideal MHD instabilities in 3D plasmas"- Proceedings of the joint Varenna-Lausanne international workshop, (1990) p.165

[6] C.Nuhrenberg - Physics of Plasmas 3 (1996) p 2401

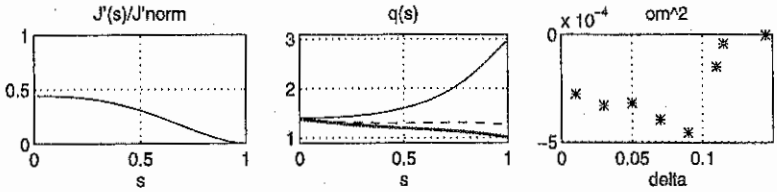

Fig.1 $J'(s)$ profile, q profile and the most unstable eigenvalue ω^2 as a function of δ for a configuration characterized by $L = 3, N_{per} = 5, 1/\epsilon = 10$ at $\beta = 1\%$, pressure profile p#2 and toroidal current density given by $J'(s)/J'_{norm} = 0.440 * (1 - s^{2.5})^2$. q decreases with δ; the three curves in the middle plot represent q at $\delta = 0.0$ (circ.tokamak), $\delta = 0.115$ (last unstable ω^2) and $\delta = 0.145$ (first unstable ω^2 after the stability window). For this last value $q_{min} = q_{edge} < 1$. q_{axis} barely changes with δ.

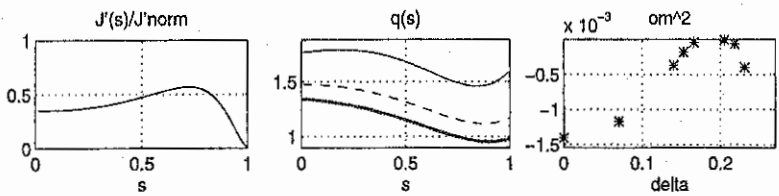

Fig.2 The same as above for $L = 2, N_{per} = 5, 1/\epsilon = 10, \beta = 1\%$, pressure profile p#1 and toroidal current density given by $J'(s)/J'_{norm} = 0.75 * (1 - s^{10})^2 - 0.4 * (1 - s^{2.5})^2$. q is represented for $\delta = 0.0$, $\delta = 0.166$ and $\delta = 0.231$. q_{axis} decreasses strongly with δ.

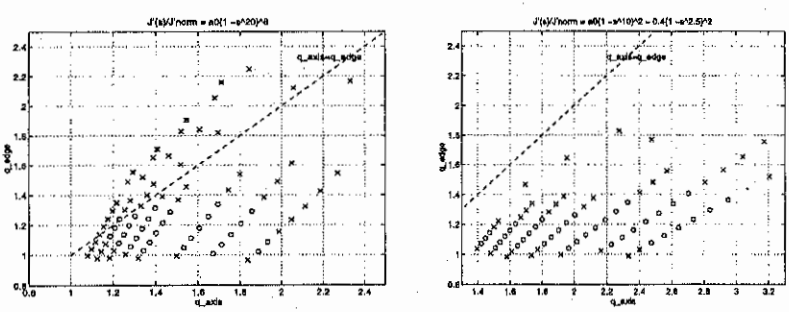

Fig.3,4 **Left plot:** stability area for $L = 2, N_{per} = 5, 1/\epsilon = 10, \beta = 1\%$, pressure profile p#1 and toroidal current densities having the form $J'(s)/J'_{norm} = a_1 * (1 - s^{20})^8$. Each oblique line corresponds to a fixed a_1 value and represent (q_{axis}, q_{edge}) pairs at different δ's. Unstable points are represented with the labels $\times$, stable points byo and $*$ correspond to the circular tokamak $\delta = 0$. The stable zone gets narrower and probably will close for a smaller current.
Right plot: the same for $L = 2, N_{per} = 5, 1/\epsilon = 10, \beta = 1\%$, pressure profile p#2 and toroidal current densities having the form $J'(s)/J'_{norm} = a_1 * (1 - s^{10})^2 - 0.4 * (1 - s^{2.5})^2$. The "." marker represent an eigenvalue near marginal stability.

Superposition of ECH on NBI Plasma in Heliotron E

T. Mizuuchi, H. Zushi** , K. Nagasaki, K. Kondo**, F. Sano, S. Besshou**, H. Okada, C. Christou, Y. Ijiri, T. Senju, K. Yaguchi, S. Kobayashi, K. Toshi, K. Sakamoto, S. Sudo[(1)], K. Ida[(1)], B. J. Peterson[(1)], K.Watanabe[(1)], S. Kado[(2)], Y. Kurimoto , H. Funaba, T. Hamada and T. Obiki

** Plasma Physics Laboratory, Kyoto University, Gokasho, Uji, 611 Japan*
(1) National Institute for Fusion Science, Nagoya, Japan
(2) Interdisciplinary Graduate School of Engineering Science, Kyushu University, Kasuga, Japan

ABSTRACT

In order to improve ion heating efficiency during NBI heating, the superposition of ECH pulse on NBI plasma has been investigated in Heliotron E. It was observed that $\Delta T_i > 0$ for ECH overlapping with rather broad power deposition profile but $\Delta T_i < 0$ for center focused ECH case.

1. Introduction

Increasing the electron temperature during NBI heating is preferable for ion heating since it can enlarge the ion heating power through the ion-electron energy transfer and change of NBI input-power sharing between electrons and ions. The electron cyclotron resonance heating is one effective method to increase T_e. Moreover, The buildup of positive radial electric field E_r, which is usually observed in ECH-only plasma in Heliotron E[1], can reduce the loss-cone for beam ions. The neo-classical theory predicts the improvement of ion heat transport in the case of $E_r > 0$. However, the degradation of particle confinement, which is frequently observed during ECH phase in many toroidal devices, might cause negative effect. The combination heating of ECH and NBI has been investigated in Heliotron E.

2. Experiments

2.1 ECH plasma

In this study, two different types of ECH are examined. One is a fundamental ECH (f_{ECH} = 53 GHz, $P_{ECH} \leq 0.5$ MW) [2]. Because of the TE02 mode and/or non-focused linearly polarized Gaussian beams in this case, it is not so effective to heat the plasma locally. The other one is a 2nd harmonic ECH (f_{ECH} = 106 GHz, $P_{ECH} \leq 0.4$ MW) with the linearly polarized Gaussian beam[3]. The *1/e* beam waist of this highly focused beam is

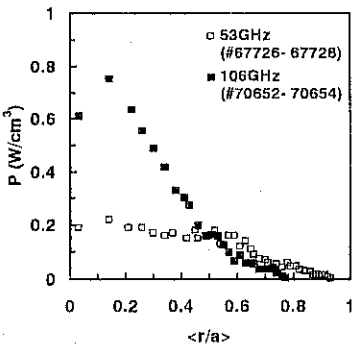

Fig.1 Experimental power deposition profile. $P_{ECH}^{53GHz} = 0.26\ MW, P_{ECH}^{106GHz} = 0.31\ MW$

Present address
*** Graduate School for Energy Science ,Kyoto University, Uji, Japan*
** Institute of Advanced Energy, Kyoto University, Uji, Japan*

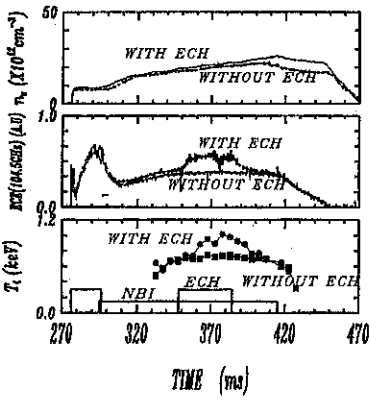

Fig.2(a) Time evolution of $\overline{n_e}$, $T_{e,ECE}$ and T_i^{NPA} for the 53 GHz ECH case.

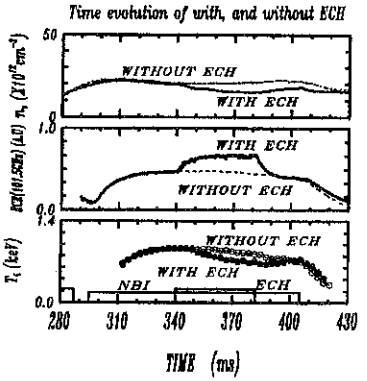

Fig.2(b) Time evolution of $\overline{n_e}$, $T_{e,ECE}$ and T_i^{NPA} for the 106 GHz ECH center heating case.

the port[2]. During the combination heating phase of NBI and ECH, T_i^{NPA} became higher than this scaling as shown in Fig.3 (■). The increase of E_r during the ECH pulse, $\Delta E_r \equiv E_r^{NBI+ECH} - E_r^{NBI} > 0$, is observed by a Langmuir probe measurement[6] and rotation measurements of magnetic and density fluctuation modes[4]. The change of the energy spectra of less than 0.02 m ($<< a_p$) and the single pass power absorption is estimated at ~ 100 %, leading to local electron heating. A comparison of $T_e(r)$ and $n_e(r)$ between 106 GHz (P_{ECH} ~ 0.3 MW) and 53 GHz (P_{ECH} ~ 0.4 MW) cases shows that T_e in the 106 GHz case is much higher and it has a peaked profile. The observed peaked profile is associated with the power deposition profile. As shown in Fig. 1, the experimentally estimated power deposition is higher in the central region and the profile is peaked in the 106 GHz case. The density profile is, however, very broad for both cases indicating the presence of the density "pump-out" phenomena.

2.2 Superposition of ECH on NBI plasma

When the 53 GHz ECH (P_{ECH} ~ 0.45 MW) was superposed to NBI plasma ($P_{ionized}$ ~ 0.7 MW), both of T_i^{NPA} and T_e was increased as shown in Fig.2(a)[4,5], where T_i^{NPA} denotes the center ion temperature estimated by CX-flux energy spectra. The value of T_i^{NPA} for NBI-only plasma can be scaled as a function of $P_{ionized} / \overline{n_e}$ (the zone between two dashed lines in Fig.3), where $P_{ionized}$ is the initially ionized neutral beam power injected through

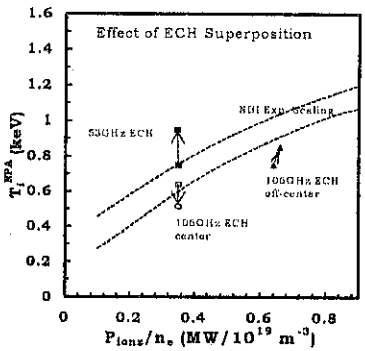

Fig.3 T_i^{NPA} vs. $P_{ionized}/\overline{n_e}$.

the CX-flux, which is considered to correspond to the modification of the loss-cone structure for trapped beam ions, is also consistent with buildup of $\Delta E_r \geq 0$ by ECH[7]. Although the increases of Hα-signal and the probe currents at the plasma edge and at the wall indicate the degradation of the particle confinement, the ECH pulse does not decrease $\overline{n_e}$. The normalized density profile is not changed by the ECH pulse within the accuracy of the inversion process from the 7ch. line density data, as shown in Fig.4(a),.

On the other hand, the 106 GHz ECH superposition decreased T_i^{NPA} as in Fig. 2(b) and Fig.3 (□). In contrast to the 53 GHz case, $\overline{n_e}$ was decreased and the density profile became very broad during ECH (see Fig.4(b)). This indicates the strong particle "pump-out" in the core region caused by the high power density of the microwaves. Both of the particle "pump-out" and resultant flat density profile would reduce the NBI ion heating efficiency in the core region. Figure 5 shows the profile of T_i measured by CXRS. The ion temperature only in the central region was decreased by ECH overlapping. As for $T_e(r)$, however, the highly focused ECH increased T_e mainly in the center region as shown in Fig.6.

To examine the effect of the different power deposition profile between the 53 GHz and the 106 GHz cases, the resonance position for the 106 GHz microwaves was shifted from the plasma center to <r/a> ~ 0.3 - 0.4 by moving plasma position or tilting the microwave-beam direction. In these off-center ECH cases, $\Delta T_i \geq 0$ was observed (▲ in Fig.3). Both of the decreasing of $\overline{n_e}$ and broadening of $n_e(r)$ were mild compared to that in the center heating case (see Fig.4(c)). The change of the energy spectra of the CX-flux suggests $\Delta E_r \geq 0$ although the change of the edge-E_r from the probe measurement is small also in this case as that in the center heating case.

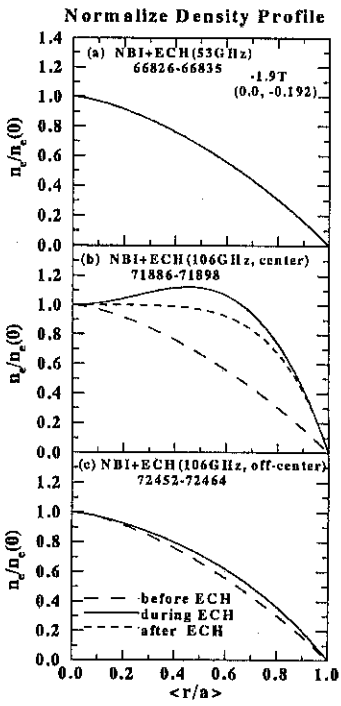

Fig.4 Change of density profile by the superposition of ECH to NBI plasma.

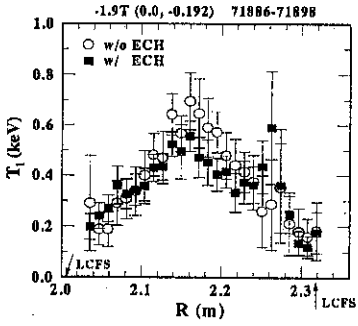

Fig.5 Change of $T_i(R)$ by the superposition of ECH(106 GHz, center) to NBI plasma.

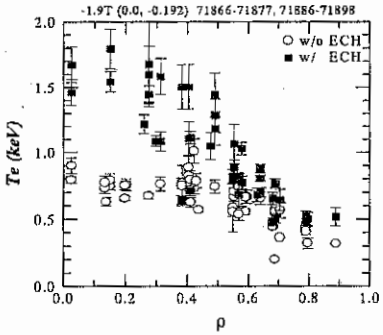

Fig.6 Change of T_e by the superposition of ECH(106 GHz, center) to NBI plasma.

3. Discussion

Since the high T_i-mode in Heliotron E seems to closely relate with peaked density profile[8], to keep the peaked density profile is one of important "techniques" to get high ion heating. From this point of view, superposition of highly center-focused ECH beam, which is accompanied by strong flattening of $n_e(r)$, is not preferred even if it produces better central electron heating. On the other hand, the change of E_r in the peripheral region can modify the orbit of high energy trapped ions more than ΔE_r in the central region[7]. In experiments, apparent change of edge plasma potential is usually observed for overlapping of the ECH with broad power deposition profile. Broad power deposition might be preferable to build up of $\Delta E_r > 0$, although the detailed mechanism of E_r buildup by ECH is still under investigation.

4. Summary

In order to improve ion heating efficiency during NBI heating, the superposition of ECH pulse on NBI plasma has been investigated. Different effects of ECH on the center ion temperature are observed. A key to explain these different observations is the balance between the gain from $\Delta T_e > 0$, $\Delta E_r > 0$ and the loss from the particle "pump-out" and/or resultant flattering of the density profile. This study suggests that the balance of them depends on the power deposition profile of superposed microwaves.

Acknowledgment

The authors are grateful to the other members of the Heliotron E supporting group for their excellent arrangement of the experiments.

[1] T.Obiki, et al., in Plasma Phys. and Cont. Nucl. Fusion Research 1988 (Proc. 12th Int. Conf., Seville, 1988), Vol.2, IAEA, Vienna (1989) 337.

[2] K.Uo, et al., in Plasma Phys. and Cont. Nucl. Fusion Research 1986 (Proc. 11th Int. Conf., Kyoto, 1986), Vol.2, IAEA, Vienna (1987) 355.

[3] K.Nagasaki, et al., in this conference

[4] T.Obiki, et al., in Plasma Phys. and Cont. Nucl. Fusion Research 1994 (Proc. 15th Int. Conf., Seville, 1994), Vol.1, IAEA, Vienna (1995) 757.

[5] T.Obiki, et al., Trans. Fusion Tech. (Proc. 6th Int. Toki Conf., Toki, 1995), 27 (1995) 85.

[6] T.Mizuuchi, et al., in 10th Int. Conf. Stellarators (IAEA Tech. Com. Meeting, CIEMAT, Madrid, Spain, 1995)

[7] S.Kurimoto, in preparation for publication.

[8] K.Ida, et al., Phy. Rev. Let., 76 (1996) 1268.

Parameter Study of 106GHz Second Harmonic ECH Plasma in Heliotron-E

K. Nagasaki, H. Zushi, S. Kobayashi, K. Sakamoto, F. Sano, K. Kondo, T. Mizuuchi, S. Besshou, H. Okada, Y. Kurimoto, H. Funaba, T. Hamada, T. Obiki, K. Ida[A], **K. Watanabe**[A], A. Isayama[B], S. Kado[C], G. Denisov[D], A. Goldenberg[D], V. Kurbatov[D] and V. Orlov[D]

Plasma Physics Laboratory, Kyoto University, Uji, Kyoto 611, Japan

A. National Institute for Fusion Science, Nagoya 464-01, Japan

B. Japan Atomic Energy Research Institute, Naka 801-1, Japan

C. Interdis. Graduate School of Engineering Science, Kyushu Univ., Kasuga 816, Japan

D. Institute of Applied Physics, Nizhny Novgorod, Russia

1. Introduction

106GHz second harmonic ECH experiments have been made in Heliotron-E. Replacing one of the 53GHz ECH systems, a new 106GHz ECH system was introduced using a gyrotron of 0.5MW 0.2sec Gaussian beam output and HE11 waveguide transmission line. The focused Gaussian beam (beam waist, r=2cm) is perpendicularly launched from the outside of the torus. By combining another 106GHz ECH system [1], the total power of P_{ECH}=550kW can be launched into a plasma. The features of 106GHz ECH are that the X-mode cut-off density is twice as much as in the 53GHz fundamental O-mode ECH, and that it has a good single pass absorption. According to ray tracing calculations, the single pass absorption of the X-mode is nearly 100%, and the power deposition can be localized at the desired resonance region, making it possible to investigate the relation between the plasma profile and the power deposition. In this paper, we will show the experimental results of the 106GHz ECH compared with the previous ECH, and the dependence of plasma parameters on the resonance position and polarization.

2. Improvement of plasma parameters

Compared with the 53GHz fundamental ECH in which the O-mode cut-off density was $3.5\times10^{19}m^{-3}$ at 400kW ECH, The accessible electron density was extended up to $\bar{n}_e=5.0\times10^{19}m^{-3}$, and $n_e(0)$ reached the X-mode cut-off density, $7.0\times10^{19}m^{-3}$, at P_{ECH}=250−350kW. The density profile was broad or slightly hollow, which has been usually observed in tokamaks and helical systems[2]. Figure 1 shows the density dependence of the central electron temperature, Te(0), and averaged ion temperature, $\bar{T}i$, in the 53GHz fundamental and 106GHz second harmonic ECH at standard configurations. Here Te(0) and $\bar{T}i$ were measured with Thomson scattering system and neutral particle analyzer, respectively. The electron temperature was improved over the confinement region, and its profile was more peaked. The

peaking factor, η =Te(0)/Te(a/2), was η =2.6±0.6 in the 106GHz ECH, while it was η =2.0±0.5 in the 53GHz ECH. Te(0) reached 2.8keV in low density ($\bar{n}_e$=0.5×$10^{19}$$m^{-3}$), inwardly shifted (Δv=-2cm) plasma. $\bar{T}i$ was not increased with the electron density, but kept constant around 250eV in contrast to the theoretical prediction of collisional coupling between electrons and ions. The global stored energy, Wp, calculated from the measured plasma profiles, increased with the increase of the electron density up to $\bar{n}_e$=3.0×$10^{19}$$m^{-3}$, then saturated around 8kJ at the higher density in a similar way in SOC regime of tokamaks. The energy confinement time was improved by 10-50% compared to the LHD scaling [3] as shown in Fig. 2. The fraction of the energy deposited in the ions increased from 15% at low density, $\bar{n}_e$=0.8 ×$10^{19}$$m^{-3}$, up to 30% at high density, $\bar{n}_e$=4.0×$10^{19}$$m^{-3}$. The total radiation power was 30% of the heating power except for the nearly cut-off density.

The second harmonic ECH has a narrower magnetic field regime for plasma production and heating than the fundamental ECH. As shown in Fig.3, this property is commonly observed in the 35GHz, 53GHz and 106GHz, three different frequencies of ECH in Heliotron-E. The accessible magnetic field regime is the narrowest in the 106GHz ECH. This is because the launched beam is focused Gaussian for the 106GHz ECH, while it was TE02 mode or non-focused Gaussian for the 35GHz and 53GHz ECH. The lower limit of magnetic field for the plasma production agrees well with a drastic decrease of the single pass absorption from 98% at B(0)=1.88T to 2% at B(0)=1.84T evaluated from the ray tracing calculation.

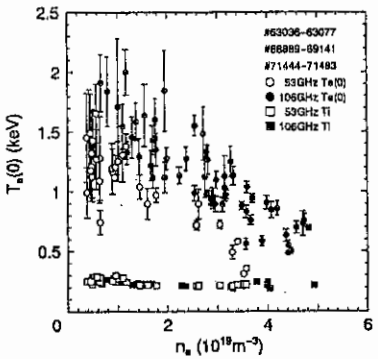

Fig.1 ne dependence of Te(0) and $\bar{T}i$ in 53GHz and 106GHz ECH plasmas.

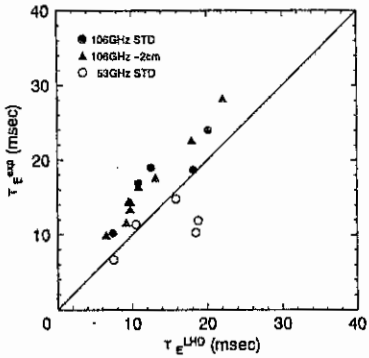

Fig.2 Comparison of global energy confinement time with LHD scaling.

3. Dependence on Power deposition

The relation between Te profile and power deposition can be investigated by moving the resonance position which is a function of the magnetic field strength, additional fields and

launching angle. Since the magnetic field contour is a saddle geometry at the plasma central region, control of the field strength makes the injected beam propagate with/without crossing the resonance layer. The difference between the single pass absorption and the multi-pass absorption from the chamber wall would be clear. When the magnetic field strength at the center, B(0), scans from 1.86T to 1.96T, then the resonance layer moves from the high field side to the low field side. The lower the field strength is, the less focused beam crosses the resonance layer. As shown in Fig.4, the Te profile was changed from a peaked one (η=2.4 at B(0)=1.90T) to a broad one (η=1.4 at B(0)=1.86T), indicating that the peakedness of the Te profile depends on the power deposition profile. Off-axis heating was performed by moving the magnetic axis by ~8cm with using additional vertical field, or by tilting the launching angle. The main power deposition is located at r/a=0.43 in the former and r/a=0.24 in the latter. The profile measurement showed that the Te profile was hollow and its peak position corresponded to the resonance position.

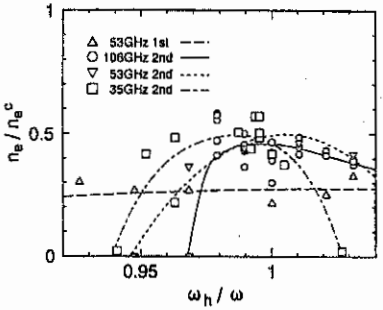

Fig.3 Magnetic field regime for plasma production. ne^c, ω_h and ω are cut-off density, central resonance and wave frequencies, respectively.

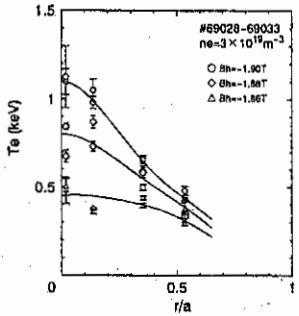

Fig.4 Te profile of 106GHz ECH plasma. The electron density is fixed as $\bar{n}_e$ =3.0 $\times 10^{19} m^{-3}$.

The difference between single-pass and multi-pass absorption can also investigated by controlling the polarization of the launched wave. The polarizer is installed on the mirror miter bend in the HE11 transmission line, rotating the electric field direction of the launched wave by 180° with the linear polarization almost remained. Figure 5 shows the dependence of Te on the mirror rotation angle. The Te profile was changed from a peaked one to a broad one as observed in the B scan experiment. Te(0) decreased from 2keV to 1keV, while the change in Te(a/2) was weak. Another important point is that the rotation angles, θ =0°, 90°, for the maximum Te(0) correspond to the 60° tilting of the electric field in respect to the resonant

magnetic field, meaning that the effective heating condition is not perpendicular to the resonant magnetic field. This experimental result is in good agreement with theoretical calculations including magnetic shear effects on the wave propagation [4]. In moderate or strong magnetic shear configurations such as heliotron/torsatron, the O- and X-modes do not propagates independently through the plasma, and they rotate with the magnetic field. For effective single pass absorption, the polarization should be controlled by taking into account the magnetic shear effects.

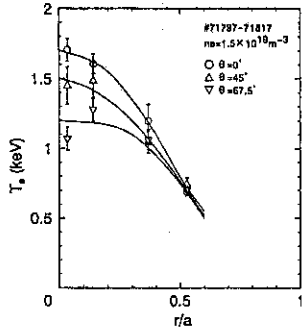

Fig.5(a) Te profile change by controlling rotation angle of polarizer mirror. The electron density is fixed as $\bar{n}_e = 1.5 \times 10^{19} m^{-3}$.

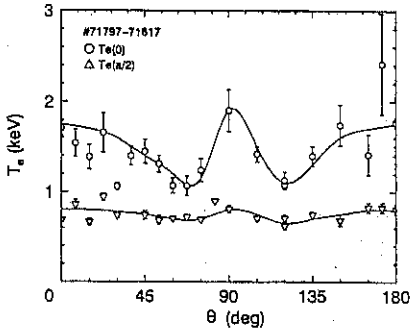

Fig.5(b) Dependence of Te(0) and Te(a/2) on rotation angle of polarizer mirror. .

4. Summary

The 106GHz second harmonic ECH experiments were performed in Heliotron-E. The plasma parameters such as stored energy, accessible electron density and electron temperature were improved compared to the 53GHz fundamental ECH. The relationship between the electron temperature profile and the power deposition were investigated by controlling the magnetic field, beam injection angle and polarization. Modification of the power deposition leads to a change in the Te profile. The importance of the magnetic shear in heliotron/torsatron configurations were also shown.

References

[1] K. Nagasaki, et al., 22nd EPS Conf. on Controlled Fusion and Plasma Physics, Bournemouth, (1995) 19C Part I, p.141

[2] H. Zushi, et al., Nucl. Fusion 28 (1988) 1801

[3] S. Sudo, et al., Nucl. Fusion 30 (1990) 11

[4] K. Nagasaki, et al., Rev. Sci. Instrum. 66 (1995) 3432

EFFECT OF HIGH-ENERGY PARTICLES ON GAE MODES IN A STELLARATOR

Zh.N.Andrushchenko
Scientific Center "Institute for Nuclear Research", the National Ukrainian Academy of Sciences, Kiev 252028, Ukraine

1. Introduction

Many theoretical and experimental works strongly indicate the existence of global Alfven eigenmodes (GAE) with a characteristic real frequency ω below the minimum of the Alfven continuum spectrum. These modes can exist in the case of nonzero shear only. Therefore, GAE modes in stellarators with shear can be excited [1]. The modification of the Alfven spectra by energetic particles is expected.

Let us consider the stellarator with shear ($S = a\mu'/\mu$), flat magnetic axis and circular "in average" magnetic surfaces. As in previous studies [2,3], we describe the background plasma modes in the cylindrical approximation. The equation for small oscillations describing GAE with $m \gg 1$ has the form [2]:

$$\hat{L}\,X \equiv \left[\frac{1}{a^2}\frac{d}{da}\left(a^3\left(\frac{\omega^2}{v_A^2}-k_\parallel^2\right)\frac{d}{da}\right)-\frac{m^2}{a}\left(\frac{\omega^2}{v_A^2}-k_\parallel^2\right)+\omega^2\frac{d}{da}\left(\frac{1}{v_A^2}\right)\right] X = 0, \quad (1)$$

where X is the radial displacement of the plasma column, a is radial coordinate in the stream coordinate system with "straightening force lines" [4], $k_\parallel = (m\mu-n)/R$, m and n are the poloidal and toroidal numbers, $\mu = 1/q$ is the rotation transform, R is the large radius. The taking into account the magnetic well in such stellarator gives us the following modification of Eq.(1)

$$\hat{L}\,X - W\,X = 0, \quad (2)$$

where

$$W = \frac{2P'm^2}{R^2B_0^2}\left(1+\mu^2(1+S)-\frac{\mu J'}{2\pi B_0}\frac{R}{a}-\frac{RB_0^2V_0''}{2}-\frac{a\mu_v''+3\mu_v'}{2\mu}\frac{R\Delta}{a}\right), \quad (3)$$

P is the plasma pressure, B_0 and J are the toroidal magnetic field and the longitudinal current, V_0'' and μ_v are the vacuum

magnetic well and vacuum rotation transform, Δ is magnetic surface center shift relative to geometric axis, $' \equiv d/da$.

We consider the high-energy particles to be a small perturbation on the mode mentioned, which are already exist in the background plasma. The contribution of high-energy particles is described in our model by equation:

$$\hat{L}\,X - W\,X - Q = 0 \tag{4}$$

where

$$Q = \frac{2im}{aRB_0^2}\left(\frac{\partial \delta P}{\partial \vartheta}\cos\vartheta + a\,\frac{\partial \delta P}{\partial \vartheta}\sin\vartheta\right), \tag{5}$$

δP is perturbed particle pressure, ϑ is poloidal angle.

2. GAE spectrum in a stellarator

We start with Eq.(1) and look for localized modes at $a = a_0$, where ω_A^2 attains its minimum value. Expanding ω_A^2 around $a = a_0$ and using the designations:

$$x = a - a_0, \qquad L^2 = \frac{2\omega_A^2}{(\omega_A^2)''}, \qquad \Delta^2 = \frac{2(\omega_A^2 - \omega^2)}{(\omega_A^2)''}, \qquad \xi = \frac{x}{\Delta}, \qquad \varphi \equiv X, \tag{6}$$

we represent Eq.(2) in the form:

$$\frac{d}{d\xi}\left[(1+\xi^2)\,\frac{d\varphi}{d\xi}\right] + G\,\varphi - \Gamma^2(1+\xi^2)\,\varphi = 0, \tag{7}$$

with boundary conditions

$$\varphi\big|_{\xi\to\pm\infty} = 0 \tag{8}$$

Here

$$G = L^2\left(\frac{2Sm}{a_0^2(n-m\mu)} + \frac{1}{a_0 k_\parallel^2}\,W\right), \qquad \Gamma^2 = \frac{m^2}{a_0^2}\,\Delta^2. \tag{9}$$

With help of variables z, $\Psi(z)$ ($\xi = sh\,z$, $\varphi = (ch\,z)^{-1/2}\Psi(z)$) the Eq.(7) may be reduced to the Schrödinger equation

$$\frac{d^2\Psi}{dz^2} + \left(\mathcal{E} - U(z)\right)\Psi = 0 \tag{10}$$

with potential $U(z)$ and energy $\mathcal{E}$:

$$U(z) = \Gamma^2\,ch^2 z + (4ch^2 z)^{-1}, \qquad \mathcal{E} = G - \frac{1}{4}. \tag{11}$$

The condition for existence of GAE coincides with the existence of an energy level in the potential (11) and is given by inequality

$$G - \frac{1}{4} > 0 \tag{12}$$

The spectrum of GAE and dispersion relations for a tokamak plasma were studied previously [5, 6]. Following [65], we find:

$$\omega_1^2 = \omega_A^2\left(1 - \frac{a_0^2}{m^2L^2}\,\mathcal{E}^2 f_1\right), \qquad f_1 = \frac{2^4}{e^2}\,exp\left(-\frac{(n+1/2)\pi}{\sqrt{\mathcal{E}}} - \frac{1}{2\mathcal{E}}\right), \tag{13}$$

if $\frac{2Sm}{n-m\mu} > \frac{a_0^2}{2L^2} + \frac{m^2\Delta^2}{L^2} - \frac{a_0}{k_\parallel^2} W$, and

$$\omega_2^2 = \omega_A^2 \left(1 - \frac{a_0^2}{m^2L^2} \varepsilon f_2\right), \quad f_2 = \frac{2^6}{e^4} \exp\left(-\frac{(2n+1)\pi}{\sqrt{\varepsilon}}\right), \qquad (14)$$

if $\frac{2Sm}{n-m\mu} > \frac{a_0^2}{4L^2} + \frac{m\Delta a_0}{L^2} - \frac{a_0}{k_\parallel^2} W$.

3. Effect of high-energy particles

Let us consider high-energy particle influence on the spectrum of GAE in a stellarator. For simplicity we subdivide all particles into circulating and trapped groups and investigate the effect of each group on modes mentioned above separately.

3.1. Circulating particle effect. The equation for GAE in a stellarator with circulating particles can be written as:

$$\frac{d}{d\xi}\left((1 + \xi^2 - \Delta_C)\frac{d\varphi}{d\xi}\right) + G\varphi - \Gamma^2(1 + \xi^2 - \Delta_C)\varphi = 0, \qquad (15)$$

where Δ_C describes the circulating particle contribution:

$$\Delta_C = \frac{\omega L^2}{4R^2k^2B_\parallel^2\Delta_0^2}(I_+ + I_-), \qquad (16)$$

$$I_\pm = \left(\frac{\partial F}{\partial E} + \frac{m}{a\omega\omega_b}\frac{\partial F}{\partial a}\right)\int M\left(v_\parallel^2 + \frac{v_\perp^2}{2}\right)^2 \frac{dv}{\omega - v_\parallel\left(k_\parallel \pm \frac{1}{qR}\right)},$$

ω_b is ion cyclotron frequency, F and E are equilibrium distribution function and energy of high-energy particles, $v_\parallel$ and $v_\perp$ are their longitudinal and transverse velocities.

For α-particles with Maxwellian distribution function, the analytical expression for the growth rate can be found:

$$\frac{\gamma_C}{\omega_{1,2}} = -\frac{\beta_\alpha}{4R^2k_\parallel^2}\frac{1}{8\sqrt{\pi}}\left(1 - \frac{\omega_{*\alpha}}{\omega}\right)F\left(\frac{v_A}{v_\alpha}\right) \qquad (17)$$

where

$$\omega_{*\alpha} = \frac{\kappa m T_\alpha}{a\omega_b M_\alpha}, \quad \kappa = -\frac{d\ln P}{da}, \quad \beta_\alpha = \frac{8\pi n_\alpha T_\alpha}{B_0^2}, \quad F(x) = x(1+2x^2+2x^4)\exp(-x^2),$$

$\omega_{1,2}$ are determined by Eqs. (13) and (14) respectively. It is easy to see that circulating α-particles can destabilize GAE in stellarator if $\omega < \omega_{*\alpha}$.

3.2. Trapped particle effect. The taking into account the toroidally trapped particles gives us the following equation

for GAE:

$$\frac{d}{d\xi}\left[(1+\xi^2)\frac{d\varphi}{d\xi}\right] + (G - \Delta_{tr})\varphi - \Gamma^2(1+\xi^2)\varphi = 0, \qquad (18)$$

where

$$\Delta_{tr} = \frac{Hm^2L^2}{R^2k_\parallel^2 B_0^2 a_0^2} I, \qquad (19)$$

$$I = \int \frac{\omega}{\omega-\omega_D}\left(\frac{\partial F}{\partial E} + \frac{m}{a\omega\omega_b}\frac{\partial F}{\partial a}\right)\frac{1}{|v_\parallel|} B_0 E^2 d\mu\, dE\, \overline{\cos\vartheta}^2,$$

$$\omega_D = \frac{Em}{a\omega_b R}\overline{\cos\vartheta}, \qquad \overline{(\ldots)} = \oint(\ldots)\,d\vartheta/v_\parallel / \oint d\vartheta/v_\parallel.$$

For α-particles with Maxwellian distribution function we obtain the following expression for growth rate of GAE:

$$\frac{\gamma_{tr}^{(1)}}{\omega_A} = \frac{\beta_\alpha}{4R^2k_\parallel^2}\left(\frac{\omega}{\omega_D}\right)^{5/2}\left[\frac{\omega}{\omega_D} + R\left(\kappa - \frac{1}{2a}\right)\right]exp\left(-\frac{\omega}{\omega_D}\right)\frac{\pi}{\gamma\left(\frac{3}{2},1\right)}\,\varepsilon f_1 \qquad (20)$$

and

$$\frac{\gamma_{tr}^{(2)}}{\omega_A} = \frac{\beta_\alpha}{4R^2k_\parallel^2}\left(\frac{\omega}{\omega_D}\right)^{5/2}\left[\frac{\omega}{\omega_D} + R\left(\kappa - \frac{1}{2a}\right)\right]exp\left(-\frac{\omega}{\omega_D}\right)\frac{\pi}{\gamma\left(\frac{3}{2},1\right)}\,f_2, \qquad (21)$$

where ω_1, f_1 and ω_2, f_2 are given by Eqs.(13) and (14), $\gamma\left(\frac{3}{2},1\right) = \int_0^1 x^{1/2}e^{-x}dx$. It is seen that trapped α-particles can both stabilize and destabilize GAE modes in a stellarator, in dependence on sign of expression in square brackets, namely on plasma and device parameters.

References

1. A.Weller, D.A.Spong, R.Jaenicke, Phys.Rev.Lett., **72** (1994), 1220.
2. S.M.Mahajan, D.W.Ross, G.-L.Chen. Phys.Fluids, **26** (1983), 2195.
3. Y.M.Li, S.M.Mahajan, D.W.Ross, Phys.Fluids, **30**(1987),1466.
4. V.D.Pustovitov, W.D.Shafranov, in Problems of Plasma Theory. Vol. 15 (1987), 146.
5. B.N.Kuvshinov, A.B.Mikhailovskii, S.V.Nazarenko et al. Preprint IAE-4753/6.
6. O.K.Cheremnykh, S.M.Revenchuk. Plasma Phys. and Contr. Fusion, **34** (1992), 55.

Highest β in Quasisymmetric Stellarator

M.Yu. Isaev, M.I. Mikhailov, V.D. Shafranov, A.A. Subbotin,
M.Yokoyama[A], Y.Nakamura[B], M.Wakatani[B]

Russian Research Centre "Kurchatov Institute", 123182, Moscow, Russia

Faculty of Engineering[A] and Energy Science[B], Kyoto University, Uji, Japan

1. Introduction

Efforts in the search of the optimal on equilibrium and stability quasihelical symmetric (QS) configuration [1] were made in $3D$ calculations [1,2] and in the semianalytical considerations [3,4]. In this report the optimization problem for QS stellarators with small period number ($N = 4, N = 8$) is considered. We find QS configuration with maximum equilibrium and Mercier stability values of parameter $< \beta >= 2 < p > /B_0^2$. Here B_0 is the magnetic field strength on the magnetic axis. The used paraxial approximation permits to obtain equations for parameters of QS configurations: elongation E, angle between axis of the magnetic surface cross-section and the principal normal of the magnetic axis δ, shifts, and triangularities of magnetic surface cross-sections as the functions of the toroidal angle [3].

Form of the magnetic axis is the key object for our approximate optimization. It was shown in [3] that for large values of $\alpha = r_1 N/R$ (see below), near 1, there exists special type of QS configurations, $n_1 = 0$, where n_1 is QS type number parameter, n_1 equals to the number of magnetic surface cross-section turns on one system period with respect to the magnetic axis principal normal, with high $< \beta >$ limit on equilibrium and Mercier stability, $< \beta > \sim 8\%$ for $N = 4$ and $< \beta > \sim 16\%$ for $N = 8$. Magnetic surface cross-sections of such type of QS rotate simultaneously with the principal normal of the magnetic axis. This type of QS is analogous to the well-known Heliac systems, but in QS case magnetic surface cross-sections are changed along the toroidal angle in a certain way to fulfill the QS conditions. Quasisymmetry condition fulfillment does not decrease the magnetic well in such type of QS configurations.

2. Systems with the bumpy reference torus and the modulated pitch angle of the magnetic axis

The case of QS configuration with magnetic axis in the form of a helical line on the circular reference torus with minor and major radii r_1 and R was considered in [3]. Here we'll study QS systems with the magnetic axis on bumpy reference torus. Let minor radius of the reference torus be a function of cylindrical angle φ:

$$r(\varphi) = r_1(1 - \gamma \cos N\varphi_1(\varphi)), \tag{1}$$

where $r_1 =$ const, $\gamma =$ const is parameter of bumping. The effect of bumping can be canceled by the effect of second harmonic amplitude in the expansion of $r(\varphi)$, $z(\varphi)$. The same result can be obtained for the magnetic axis with modulated pitch angle

$$\varphi_1 = \varphi + \varepsilon_1 \sin N\varphi. \tag{2}$$

We selected triangularities of magnetic surface cross-sections in a special way to obtain equality of given value of $< \beta >$ on equilibrium and value of $< \beta >$ calculated from Mercier criterion. In Fig. 1 we show one of series of calculated $< \beta >$ limit on equilibrium and Mercier stability in paraxial approximation for 4-period QS configurations with various initial (at $\varphi = 0$) elongations E_0. Elongation E_0 equals to the ratio of large and small semiaxes of the magnetic

surface cross-section at $\varphi = 0$. In Fig.1 $\alpha = r_1 N/R = 1$. In each case we calculated dependencies of $< \beta >$ on E_0 for different values of second harmonic amplitude, proportional to the bumping parameter γ or modulation parameter ε_1.

As it is seen from these figures, each curve $< \beta >$ on E_0 has a maximum corresponding to the optimum value of ellipticity for equilibrium and stability. Maximum value of $< \beta >= 8.5\%$ has been obtained for $\alpha = 1$ for the magnetic axis without second harmonic. Fig.1 demonstrate that additional second harmonic (bumping or modulating pitch angle) decreases maximum value of $< \beta >$ and moves optimal ellipticity to 1 for positive sign of bumping and from 1 for negative sign of bumping.

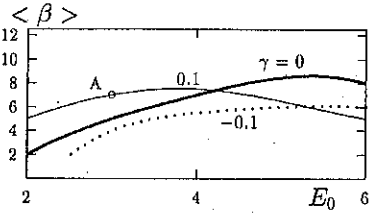

Fig. 1. The dependencies of equilibrium and Mercier stability $< \beta >$ limit on initial (at $\varphi = 0$) elongations E_0 for 4-period QS configurations with $\alpha = r_1 N/R = 1$. The cases $\gamma = 0$, 0.1, -0.1 are shown. Point "A" corresponds to curve 2 in Fig. 5.

3. The effect of other parameters of the magnetic axis

Here we investigate the effect of elongations of cross-section of the reference torus on equilibrium and Mercier stability, $z_1/r_1 \neq 1$ (r_1 and z_1 are horizontal and vertical sizes of cross-section of the reference torus). An example of these calculations for $N = 4$ is given in Fig. 2. As in the previous cases, we found that for each initial magnetic surface elongation E_0 there exists some optimal z_1/r_1. In particular, optimization on z_1/r_1 also allows to yield the values of $< \beta >\sim 7\%$ for reasonable magnetic surface elongation ($E \sim 3$).

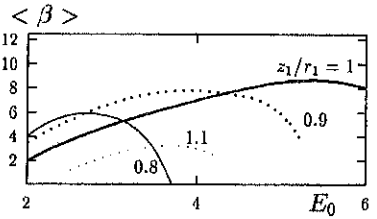

Fig. 2. The dependencies of equilibrium and Mercier stability $< \beta >$ limit on initial elongation E_0 for 4-period QS configurations with $\alpha = r_1 N/R = 1$. Curves correspond to different elongations of cross-section of the support torus. The cases with $z_1/r_1 = 1$, 0.8, 0.9, 1.1 are shown.

We have also investigated the possibility of improvement of equilibrium and Mercier stability conditions by combination of different methods of magnetic axis changes (flattening of the reference torus with modified pitch angle of the magnetic axis, with bumpy support torus and so on). We considered different harmonics of the magnetic axis pitch angle, i.e.

$$\varphi_1 = \varphi + \varepsilon_1 \sin N\varphi + \varepsilon_2 \sin 2N\varphi + \ldots \qquad (3)$$

The result of this research can be formulated as follows. If one found the configuration optimized on one of these parameters, the variation of any other parameter leads only to decrease of $< \beta >$ limit.

We found that $< \beta >$ limit depends on the behavior of δ (angle between axis of the magnetic surface cross-section and the principal normal of the magnetic axis) and E (elongation of the

magnetic surface) on the toroidal angle, φ. The smoother curves $\delta(\varphi)$ and $E(\varphi)$ are, the greater limiting $< \beta >$ one can yield.

Fig. 3 shows the behavior $E(\varphi)$ for different combinations of the magnetic axis modification parameters. Here the case $E_0 = 3$ is considered. Thin solid curves correspond to the case of circular reference torus without any magnetic axis modification. One can see that change of the parameter z_1/r_1 leads to more smooth curves. The optimal value is $z_1/r_1 = 0.92$. This case corresponds to maximum $< \beta >$ limit. Adding any magnetic axis pitch angle modification gets worse smooth and consequently, decreases $< \beta >$ limit.

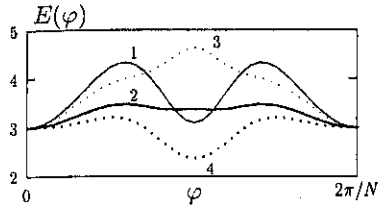

Fig. 3. The dependencies of E (elongation of the magnetic surface cross-section) on the toroidal angle. 4-period quasisymmetric configurations with $\alpha = r_1 N/R = 1$ is considered. Initial elongation is $E_0 = 3$.
1 - $z_1/r_1 = 1$, $\varepsilon_1 = 0$. 2 - $z_1/r_1 = 0.92$, $\varepsilon_1 = 0$ (maximum $< \beta >$). 3 - $z_1/r_1 = 0.92$, $\varepsilon_1 = 0.02$. 4 - $z_1/r_1 = 0.92$, $\varepsilon_1 = -0.02$.

4. VMEC equilibrium and Mercier stability calculations

To prove values of $< \beta >$ obtained in paraxial approximation we used fixed boundary version of 3D VMEC code [5] and stability code made by Y.Nakamura which calculates Mercier criterion $D_m > 0$ with the VMEC equilibrium quantities. We have found difficulties on the way of comparison of results obtained from paraxial approximation and from VMEC codes. First problem is to find right Fourier spectrum in cylindrical coordinates (cross-sections $\varphi = const$, φ - cylindrical angle) for the boundary which is obtained near magnetic axis in Mercier coordinates (cross-section $s = const$, s - magnetic axis length). Cross-sections $\varphi = const$ have complicated form in the middle of system period where the magnetic axis has large torsion and curvature. So the required number of harmonics for VMEC code increases, the convergence becomes poor.

Fig.4 demonstrate cross-sections obtained from paraxial approximation and Fourier representation of given configuration with 2 poloidal modes and 4 toroidal modes for 4-periods configuration with $\alpha = r_1 N/R = 1$, $\gamma = 0.1$.

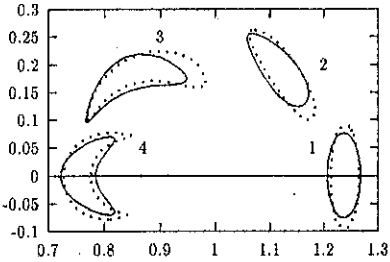

Fig. 4. Magnetic surface cross-sections $\varphi = const$. Dotted cross-sections are obtained from paraxial approximation, cross-sections shown by solid lines are obtained from Fourier representation of given configuration with 2 poloidal modes and 4 toroidal modes for 4-periods configuration with $\alpha = r_1 N/R = 1$, $\gamma = 0.1$.
1 - $\varphi = 0$, 2 - $\varphi = \pi/12$, 3 - $\varphi = \pi/6$, 4 - $\varphi = \pi/4$.

Next problem is connected with the difference between paraxial calculation method and VMEC calculation. In paraxial method we use fixed axis and find different boundaries for various plasma pressure. In VMEC calculation plasma boundary is fixed and the position of the magnetic axis depending on plasma pressure.

In our VMEC and Mercier stability calculation we used harmonics obtained from paraxial approximation for $< \beta >= 8\%$. The results show the increasing of stability zone with the increasing of $< \beta >$ value (see Fig.5). Fig.5 demonstrates that for $< \beta >= 8.8\%$ this configuration is Mercier stable in wide plasma region which confirms the results shown in Fig.1.

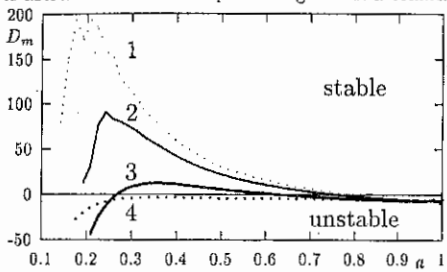

Fig. 5. The dependencies of D_m versus normalized plasma radius a for 4-period quasisymmetric configurations with $\alpha = r_1 N/R = 1$, $\gamma = 0.1$. $D_m > 0$ corresponds to Mercier stable zone. 1 - $< \beta >= 8.8\%$, 2 - $< \beta >= 6.88\%$, 3 - $< \beta >= 4.13\%$, 4 - $< \beta >= 1.56\%$.

5. Discussion

We have found examples of QS configurations with special magnetic axes which have the form of the helical line on bumping support torus or with modulated pitch angle. Adding second harmonic of toroidal angle to the magnetic axis makes possible to get high $< \beta >$ for not too high elongation at $\varphi = 0$. For large elongation at $\varphi = 0$ the second harmonic leads to additional modulations in curvature and torsion of the magnetic axis. This modulation decreases the maximum $< \beta >$ value.

Our paraxial analysis shows that in 4-periods QS stellarator $< \beta >$ limit on equilibrium and stability can be achieved on the level of 8%. It seems that $n_1 = 0$ type of QS which is close to Heliac-like configuration has some remarkable features:

1. Deep magnetic well even for a small number of system period.
2. Small neoclassical losses due to quasisymmetry which theoretically can be obtained.
3. High $< \beta >\sim 8\%$.

For $n_1 = 0$ type of QS systems further $3D$ - calculations of equilibrium, stability modes and transport coefficients should be made.

Acknowledgements

Russian authors thank Prof. F. Troyon for supporting this work, Drs. A. Cooper and S. Medvedev for help with 3D calculations. This work is supported by Russian Foundation of Fundamental Research, grant N 95-02-05519a.

References

[1] Nührenberg J., Zille R.// Phys. Lett. A, **129**, 113(1988).

[2] Yokoyama M., Nakamura Y., Wakatani M.// Transaction of Fus. Technology (Proc. of 6th Int. Toki Conf., Japan, 1994), **27**, 186(1995).

[3] Isaev M., Mikhailov M., Shafranov V., Subbotin A.// Proc. of 10th Int. Conf. on Stellarators, Madrid, 1995, p.278.

[4] Boozer A.// Plasma Phys. and Contr. Fus., **37** (1995), Suppl. 11A, A103, Invited Papers from 22nd EPS Conf. on Contr. Fus. and Plasma Phys. Bournemouth, UK, 1995.

[5] Hirshman S., et al.// Comput. Phys. Commun. **43** (1986) 143.

Electrostatic Fluctuations and Their Contribution to Particle Losses at the Plasma Boundary in the U-3M Torsatron

E.L. Sorokovoj, S.P. Bondarenko, A.V. Chechkin, V.V. Chechkin, L.I. Grigor'eva
N.I. Nazarov, I.B. Pinos, V.V. Plyusnin, K.S. Rubtsov, V.A. Rudakov, E.D. Volkov

Institute of Plasma Physics
National Science Center "Kharkov Institute of Physics and Technology",
310108 Kharkov, Ukraine

1. Introduction. The particle transport in the boundary plasmas of tokamaks and stellarators is known to be anomalously high. In particular, this has also been shown experimentally in the U-3M stellarator-torsatron [1]. In Ref. [2] a comparison has been made for some tokamaks and the ATF torsatron of local turbulence-induced particle transport at the plasma boundary with the total particle transport inferred from equilibrium parameters of the boundary plasma (in ATF - from spectral measurements). The measurements were carried out in ohmic discharges (tokamaks) and in an ECR heated currentless plasma (ATF).

In this report the results are presented of a similar comparison made on the U-3M torsatron. In view of the Ref. [2] results, the estimation of the contribution of low-frequency electrostatic turbulence to particle losses at the plasma boundary in the U-3M conditions is of special interest, as (i) a significant contribution to these losses might be made by the edge magnetic surface destruction, which is characteristic for U-3M [1], and (ii) the plasma in U-3M is produced and heated by RF fields ($\omega \leq \omega_{ci}$), when the low-frequency turbulence can be enhanced due to parametric interaction between regular RF pump waves and natural drift-type plasma oscillations [3].

2. Experimental conditions. The U-3M machine is an $l=3$ $m=9$ torsatron, $R=1$ m, $\bar{a}=0.12$ m, $\iota(\bar{a})/2\pi \approx 0.4$. The plasma with $\bar{n}_e \equiv 4\times10^{18}$ m^{-3}, $T_e(0) \approx 0.3$ keV, $T_i(0) \approx 0.1$ keV is supported with ~200 kW RF power launched into 100% hydrogen gas at a frequency of 5.4 MHz in multimode Alfven resonance regime ($B_\varphi = 0.45$ T, $\omega = 0.8\omega_{ci}(0)$), the RF pulse length is up to 60 ms.

The equilibrium parameters of the plasma and their fluctuations near the boundary of the confinement region were measured by a probe assembly consisting of 3 single Langmuir probes arranged in a poloidal line and spaced 2.8 mm apart.

The probes were introduced from l.f.s. along the major radius in a poloidal cross-section located 130° (3.25 field periods) toroidally away from the antenna leads.

Figure 1(a) represents the numerically calculated dependence of the connection length L_c on the minor radius r in the poloidal cross-section where the probes are installed. A sharp L_c decrease occurring at $r=12$ cm determines the boundary of the confinement region (there is no material limiter in U-3M).

The profiles of equilibrium values of floating potential, V_f , ion saturation current density, j_s , and electron temperature, T_e , are shown in Figs 1(b,c,d). Also, the possible trend of the plasma potential, V_p , as estimated from measured V_f and T_e , is shown in Fig. 1(b) (dashed curve), and the decay scales of the ion saturation current, L_j , and of the electron temperature, L_T , are indicated in Figs 1(c) and 1(d) respectively. It follows from Fig. 1(b) that the radial electric field, E_r , reverses its sign at $r\cong12$ cm, that is, a so-called shear layer exists at the plasma boundary [2].

3. **Characteristics of the SOL turbulence.** At the boundary of the confinement region ($r=12$ cm) the measured normalized levels of density (ion saturation current) and potential (floating potential) fluctuations, $\tilde{j}_s/j_s$ and $e\tilde{V}_f/T_e$, amount ~0.2 and ~ 0.5 respectively and grow when the probes are moved outwards (Fig. 2). The main intensity of the fluctuations in SOL falls in the range of 5 to 150 kHz. Generally, the power autospectra of the fluctuating signals in this range of frequencies consist of a broad band noise, on which several (~10) peaks are superimposed with a broad variety (from ~10 to ~-10 cm^{-1}) of poloidal wavenumbers. As follows from the form of joint spectra $S(k_\theta,\omega)$ [4] measured in different shots, the position of the plasma boundary can change within 0.5 cm from shot to shot. The spectra measured at $r=12$ cm and $r=12.5$ cm have the maximum width in k_θ . As the probes are moved away from the boundary, the spectra become more narrow and a more deterministic $k_\theta(\omega)$ dependence becomes apparent (cf., Fig. 3(a) and Fig. 3(b)).

As the computations of correlation dimension ν of probe signals show, at the boundary, in the region of maximum E_r gradient, the turbulence possesses a higher number of freedoms (ν≥10) than in other points of SOL (ν~5). This is in agreement with the form of joint spectra (Fig. 3) and might be an evidence of possible effect of the E_r gradient on excitation of drift-like oscillations near the boundary.

4. Comparison of turbulence-induced and total particle transports in SOL. Evaluated from density and perpendicular electric field correlation measurements in SOL, the spectral function of the radial particle flux density induced by the turbulence, $T(\omega)$ [5], can generally take both positive and negative values (Fig. 4). Nevertheless, the total, that is, frequency-integrated, flux density is positive (i.e., it

is directed outwards) and takes the value of $\tilde{\Gamma} \cong 1 \times 10^{20}$ $m^{-2}s^{-1}$ at the boundary $r = 12$ cm and the maximum value, $\tilde{\Gamma} \cong 2 \times 10^{20}$ $m^{-2}s^{-1}$, at $r = 14$ cm. To compare these quantities with the value of the total particle flux density through the boundary, we estimate the latter as [1]

$$\Gamma_\perp \approx i\left[m_h - \iota(\bar{a})/2\pi\right]\left(L_j/\pi R\right)\Gamma_\parallel \qquad (1)$$

Here, $m_h = 3$ is the number of turns of a single helical conductor, $\Gamma_\parallel$ is the particle flux density along a field line at the boundary (estimated as j_s/e at r=12 cm, Fig. 1(c)). Evaluated from Eq. (1), the value of $\Gamma_\perp$ amounts 4×10^{20} $cm^{-2}s^{-1}$, that is, it has the same order of magnitude as the local turbulence-driven particle flux density, similar to what has been observed in some other closed magnetic traps with other methods of plasma heating [2].

In conclusion, we note the following.

1) As the number of realizations of fluctuating signals was small, the fluctuations of electron temperature were neglected, and the probes were moved from shot to shot, the accuracy of determination of particle flux density from both fluctuating and equilibrium parameters was not high enough to judge the possible contribution of magnetic surface destruction to the anomalous transport.

2) All the probe measurements were carried out at a large distance from the antenna. Therefore, the information having been obtained should be supplemented in future with the data on characteristics of the SOL turbulence in a close proximity to the antenna, where the turbulence can be strongly affected by the RF wave processes associated with the near antenna field [6].

This research was in part supported by the State Committee on Science and Technologies of Ukraine under Projects No. 2/453 and No. 2.3/745.

References

[1] Chechkin, V.V., Fomin, I.P., Grigor'eva, L.I., *et al.*, Nucl. Fusion **36** (1996) 133.

[2] Tsui, H.Y.W., Wootton, A.J., Bell, J.D., *et al.*, Phys. Fluids B **5** (1991) 2491.

[3] Liu, C.S., Tripathi, V.K., Phys. Rep. **130** (1986) 145.

[4] Beall, J.M., Kim, Y.C., and Powers, E.J., J. Appl. Phys. **53** (1982) 3933.

[5] Powers, E.J., Nucl. Fusion **14** (1974) 749.

[6] Chechkin, V.V., Grigor'eva, L.I., Nazarov, N.I., *et al.*, Fusion Engrg. Des. **12** (1990) 171.

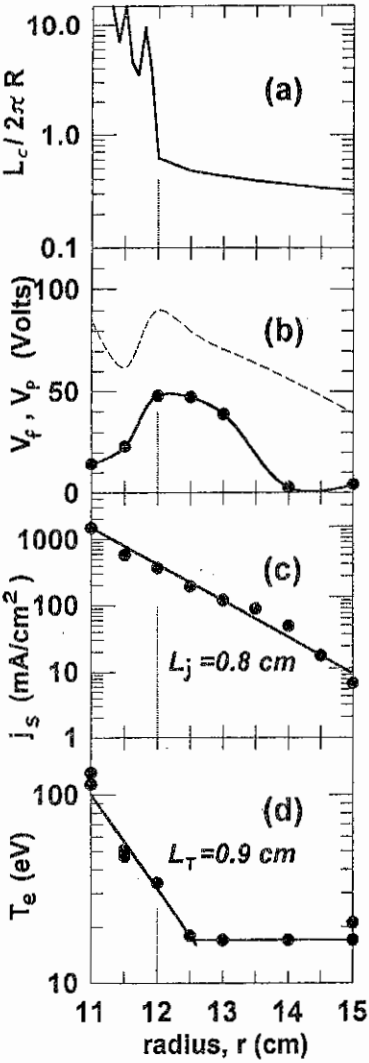

Fig.1

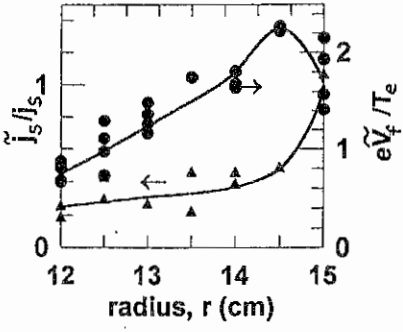

Fig. 2

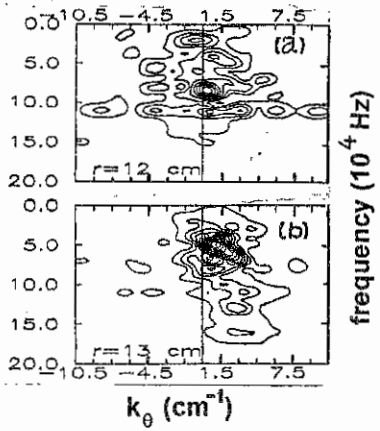

Fig. 3

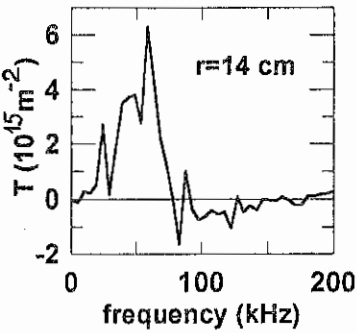

Fig. 4

Mercier criterion investigation in the region of the island magnetic surfaces of stellarators

V.V. Nemov
Institute of Plasma Physics, National Science Center "Institute of Physics and Technology", Kharkov 310108, Ukraine

For stellarator-type magnetic configurations there is a large probability of island magnetic surfaces to arise at rational values of the rotational transform, t. The present report deals with numerical investigation of MHD plasma stability in the region of such magnetic surfaces using the Mercier criterion. Two variants of magnetic configurations have been considered. The first variant represents the region of the "Uragan-3M" ("U-3M") torsatron configuration for $t=1/4$ and $B_1/B_0 \approx 1.2\%$ on the assumption of a slight eccentricity (2 mm) in position of two outer vertical-field compensation coils [1]. The second configuration variant is the "Helias"-type magnetic configuration [2] with the boundary magnetic surface determined by the equations and the parameters given in [2]. The method [3] based on the integration along magnetic field lines has been used to investigate the Mercier criterion. The case of low β but a finite local pressure gradient, ∇p, was considered (β is the gas kinetic-to-magnetic pressure ratio). In connection with this it is supposed that the magnetic surfaces are practically coincident with the vacuum magnetic surfaces, but here we take into account the effect of plasma currents governed by the local plasma-pressure gradient. One of the peculiarities of the report is that the plasma stability region boundaries are directly determined as functions of the plasma pressure gradient (p' value) for each magnetic surface considered. In calculations a set of ordinary differential equations is used, including the magnetic field line equations, $d\mathbf{r} / d\tau = \mathbf{B}_V$, equations [4] for the magnetic-surface function gradient, $\nabla\Psi$, and the following equations [3]:

$$d f^V_{GB} / d\tau = \nabla\Psi\nabla B^2_V / B^2_V|\nabla\Psi|^2, \qquad d f^V_{hS} / d\tau = h S_V,$$

$$d f^V_B / d\tau = B^2_V / |\nabla\Psi|^2, \quad d f^V_S / d\tau = S_V, \quad d f^V_{hB} / d\tau = h B^2_V / |\nabla\Psi|^2,$$

where $S = \dfrac{[\mathbf{B}\nabla\Psi]}{|\nabla\Psi|^2} \mathrm{rot} \dfrac{[\mathbf{B}\nabla\Psi]}{|\nabla\Psi|^2}$ (S_V is equal to S calculated for the vacuum magnetic field $\mathbf{B}_V$), and the function h is related to the longitudinal plasma current density $j_{||}$ as $j_{||} = p' h \mathbf{B}$ (the prime denotes the derivative with respect to Ψ) and is given by the equation $dh / d\tau = -2[\mathbf{B}\nabla B]\nabla\Psi / B^3$. The Mercier criterion is directly expressed through the $f^V_{GB}(\tau_m)$, $f^V_{hS}(\tau_m)$, $f^V_B(\tau_m)$, $f^V_S(\tau_m)$ and

$f^{V}_{hB}(\tau_m)$ values (τ_m is the upper limit of the integration interval). When integrating the differential equations, the $\nabla\Psi$ value at the initial points of integration was specified so that the inequality $p'<0$ should correspond to the plasma pressure decreasing in the direction of the exterior normal to each magnetic surface considered.

Concurrently with the Mercier criterion investigation for each magnetic surface considered calculations by the method of Ref. [5] were made for the parameter $\gamma_{||}/\gamma_{\perp}=\int j^2_{||}\delta V/\int j^2_{\perp}\delta V$ ($j_{||}$ and $j_{\perp}$ are the current density components, parallel and perpendicular to the magnetic field; the integrals imply integration over the volume of the layer between closely spaced magnetic surfaces).

For numerical calculations the vacuum magnetic field of both systems was approximated by the superposition of the toroidal harmonic functions containing the associated Legendre functions. For the "U-3M" we have used 33 terms in the helical winding field decomposition; the field of compensation coils was simulated in the same way as in [1]. For the "Helias" magnetic field the number of decomposition terms used was limited by the conditions $0 \le n \le 10$, $m = m_p M$, $|M| \le 10$, where n and m are the poloidal and toroidal harmonic numbers, m_p is the number of periods along the torus ($m_p=5$). In this case the decomposition coefficients were found by minimizing the magnetic field component which is normal to the given boundary magnetic surface [2].

The calculations were carried out in the cylindrical system of co-ordinates ρ, φ, z (the z axis is coincident with the principal axis of the torus). Fig.1 shows the magnetic surfaces cross-sections $\varphi=0$ for the "U-3M" magnetic field model ($x = \rho - R$, R=100 cm is the major radius of the torus, dimensions are given in cm). This picture is in good agreement with the numerical simulation of the perturbed configuration [1]. Two chains of the $t=1/4$ island surfaces (inner and outward) are seen. The region with a strongly stochastic behaviour of magnetic field lines lies in the configuration periphery, where small islands corresponding to $t=1/3$ are also seen. Fig.2 shows magnetic surfaces for the "Helias" configuration (in the $\varphi=0$ cross-sections and through a half of the field period, the dimensions are given in the same relative units as in [2]). The form of the magnetic surfaces is in good agreement with the boundary surface [2], which is also shown in Fig.2. For the "Helias" magnetic field model used the island surfaces corresponding to $t=5/8$ and $t=5/7$ turn out to be the most pronounced. Fig.2 also shows the $t=2/3$ islands which are however less pronounced. The rotational transform t increases towards the configuration boundary ($t>5/9$ in the center of the configuration).

The results of the investigation carried out for the net toroidal current-free case are as follows (each integration interval corresponds to 250 circuits around the z axis):

1. At a plasma pressure decreasing in the direction of the exterior normal to each magnetic surface considered ($p'<0$), the Mercier stability criterion is violated for the island magnetic surfaces corresponding to $t=1/4$ in the "U-3M" torsatron (for both the inner and outward island chains) and to $t=5/7$ in the "Helias" type configuration. Note that for the island magnetic surfaces the condition $p'<0$ corresponds to the local maximum of plasma pressure in the island center. For the $t=5/8$ island surfaces of the "Helias" configuration at $p'<0$ the Mercier criterion is satisfied, but it is violated if $p'>0$, i.e., at a local plasma pressure minimum in the island center. For the $t=2/3$ islands the Mercier criterion was not considered. The Mercier criterion violation occurs if the $|\nabla p|$ is larger than a certain boundary value of the order of $0.001\, p_0 / (a\beta)$, where p_0 is the plasma pressure in the column center and a is the average radius of the column.

2. The calculations for non-island surfaces, carried out for comparison, have shown that the Mercier criterion for these surfaces is satisfied for both types of the configurations at $p'<0$. For the "Helias" configuration this result agrees with the results obtained for non-rational surfaces in [2]. For "U-3M" it is in agreement with the existence of a vacuum magnetic well at $B_\perp/B_0 \approx 1.2\%$ [1]. If $p'>0$, i.e., at an increasing plasma pressure in the direction of the exterior normal to the magnetic surface, the Mercier criterion may be violated.

3. The calculations of the $\gamma_{||}/\gamma_\perp$ ratio have shown that for the non-island surfaces in the "Helias" configuration this parameter proves to be less than unity. This is in agreement with the results of Ref. [2]. For the island magnetic surfaces considered the $\gamma_{||}/\gamma_\perp$ parameter also proves to be less than unity, it only insignificantly exceeds its magnitude for the non-island surfaces. But for the "U-3M" configuration this parameter turned out to be significantly larger than unity. For the non-island surfaces its magnitude is of the order of $2/t^2$. But for the $t=1/4$ island surfaces and closely adjacent to them non-island surfaces this parameter reaches the values ranging from 200 to 700 (for the inner chain the $\gamma_{||}/\gamma_\perp$ ratio is larger than for the outward one). These values are by order of magnitude ten times larger than the $2/t^2$ value.

From the present results it follows that at the finite pressure gradient the parallel current density for the island magnetic surfaces considered turns out to be finite. This density appears to be finite too for the non-island surfaces which are directly adjacent to the island surfaces. In principle, the current density may

become infinite for the separatrices which separate the island surfaces from the adjacent to them non-island surfaces. But, as is known, in a three-dimensional inhomogeneous toroidal magnetic field, instead of a separatrix a stochastic layer is formed. Calculations of the plasma current in such layers were not carried out in this work. For "Helias" the width of the above-mentioned layers (in the $\varphi=0$ plane) did not exceed $0.001 \div 0.007$ (in relative units corresponding to Fig.2). In the "U-3M" case, for the outward $t=1/4$ island chain the width of the layer was about 1 or 2 mm.

The large value of the $\gamma_{||}/\gamma_{\perp}$ ratio for the $t=1/4$ island magnetic surfaces in the "U-3M" configuration corresponds to a significant increase in the $j_{||}$ distribution amplitude. Due to relatively small sizes of the islands, one may expect, as a main result of the $j_{||}$ increase, the perturbation of the magnetic configuration near the islands by the $j_{||}$ magnetic field and associated with it the change in the island sizes and the increase of the stochastic region embracing these islands.

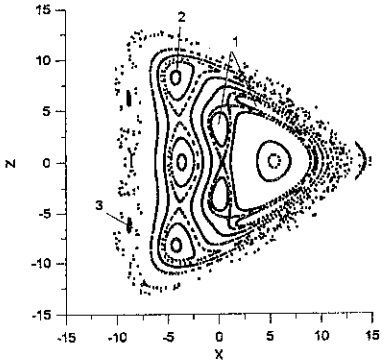

Fig.1. "U-3M" magnetic surfaces for the considered magnetic field perturbation: (1) inner t=1/4 islands, (2) outward t=1/4 islands, (3) t=1/3 islands.

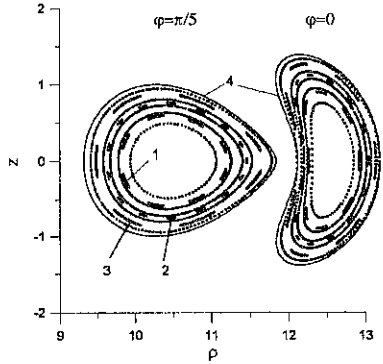

Fig.2. "Helias" magnetic surfaces: (1) t=5/8 islands, (2) t=2/3 islands, (3) t=5/7 islands, (4) boundary surface [2] *(solid line).*

References

[1] Lesnyakov G.G., Volkov E.D., Georgievskij A.V., et al. *Nucl. Fusion*, **32**, 2157 (1992).
[2] Nührenberg J., Zille R. *Phys. Lett. A*, **114**, 1291 (1986).
[3] Nemov V.V. *Plasma Physics Reports*, **21**, 5 (1995).
[4] Nemov V.V. *Nucl. Fusion*, **28**, 1727 (1988).
[5] Nemov V.V. *Nucl. Fusion*, 1992, **32**, 597 (1992).

CONFINEMENT OF CHARGED PARTICLES IN TORSATRONS AND HELIOTRONS WITH ADDITIONAL TOROIDAL MAGNETIC-FIELD RIPPLE

M. S. Smirnova
Institute of Plasma Physics, National Science Center
"Kharkov Institute of Physics and Technology"
310108, Kharkov, Ukraine

1. Introduction. One of the basic requirements for torsatrons of today is that charged particles should be confined during many periods of their motion around the device. Different methods applied for the realization of the magnetic configuration and its control in modern torsatrons and heliotrons complicate significantly the modulation of the magnetic field along a field line in such devices. The adequate representation for the magnitude of the real magnetic field requires, in this case, the following Fourier-expansion,

$$B/B_0 = \sum_{\substack{j=-\infty,\\ N=0}}^{\infty} \varepsilon_{N,j}(r)\cos(NM\phi - j\theta),$$

where the high-order N terms $\varepsilon_{N,j}$ with N>2 usually present. Being typical of a tokamak, such harmonics of the toroidal magnetic-field ripple, or the TF ripple, are also typical of torsatrons/heliotrons even without the TF coils (Fig.1) [1]. The main purpose of the present work is investigation of additional TF ripple effects on charged particle confinement in torsatrons.

2. Weak TF ripple effects on the helically trapped particle confinement. In a heliotron-type configuration without toroidal field coils, the TF ripple perturbation of the magnetic field usually is weak. In order to investigate the effect of such perturbation on the helically trapped particle orbits as the most dangerous for confinement in heliotrons, the following model for the magnitude of the magnetic field along the field line is used:

$$B/B_0 = 1 + \varepsilon_t \cos\theta + \varepsilon_H \cos\eta + \varepsilon_{NH} \cos(N\eta).$$

Here $\varepsilon_t = r/R$; $\eta = M\phi - l\theta - \xi$; $\cos\xi = C_1/\sqrt{C_1^2+D_1^2}$;

$$\varepsilon_h = \frac{1}{2\pi}\int_0^{2\pi} \sqrt{C_1^2 + D_1^2}\, d\theta; \quad C_1 = \varepsilon_{1,l} + \sum_{j=1} \left[\varepsilon_{1,l+j} + \varepsilon_{1,l-j}\right]\cos(j\theta);$$

$$D_1 = \sum_{j=1} \left[\varepsilon_{1,l+j} - \varepsilon_{1,l-j}\right] sin(j\theta); \qquad \varepsilon_H = \varepsilon_h\,(1 + \sigma_1 cos\theta);$$

$$\varepsilon_{Nh} = \frac{1}{2\pi} \int_0^{2\pi} \sqrt{C_N^2 + D_N^2}\; d\theta; \quad C_N = \varepsilon_{N,p} + \sum_{j=1} \left[\varepsilon_{N,p+j} + \varepsilon_{N,p-j}\right] cos(j\theta);$$

$$D_N = \sum_{j=1} \left[\varepsilon_{N,p+j} - \varepsilon_{N,p-j}\right] sin(j\theta); \qquad \varepsilon_{NH} = \varepsilon_{Nh}\,(1 + \sigma_N cos\theta);$$

$$\sigma_1 = \frac{1}{\pi\varepsilon_h} \int_0^{2\pi} \sqrt{C_1^2 + D_1^2}\; cos\theta d\theta; \quad \sigma_N = \frac{1}{\pi\varepsilon_{Nh}} \int_0^{2\pi} \sqrt{C_N^2 + D_N^2}\; cos\theta d\theta;$$

M is the helical field period number, and N×M is the TF ripple periodicity. Using the bounce-averaged equations of motion of helically trapped particles in the TF ripple-perturbed magnetic field [2] the following expressions for radial deviations of above particles from the initial flux surface can be derived:

$$\Delta r \sim \Delta r_0 \left\{1 - 2^{N+1}\, \varepsilon_{NH} / (\varepsilon_H)^2\right\},$$

$$\Delta r_{sb} \sim \left\{\Delta r_0 \left[1 - 2^{N+1}\, \varepsilon_{NH} / (\varepsilon_H)^2\right]\right\}^{1/2},$$

for deeply trapped passing bananas and for superbananas, respectively. Here $\Delta r_0 \sim 2\pi r\, \varepsilon_t / \varepsilon_H$ is the radial deviation from the initial flux surface of a deeply trapped particle in a configuration where the TF ripple harmonics are not taken into account. The comparison of expressions derived above with results of numerical integration of guiding center equations of particle motion in magnetic coordinates (Fig.2) shows good agreement between them.

3. Effects of a strong TF ripple. In the torsatron with TF coils such as the Uragan-2M torsatron, the TF ripple perturbation of the magnetic field usually is strong, i.e. the following inequality is correct: $|\varepsilon_{NH}| \geqslant \varepsilon_H / N^2$ [3]. Owing to the effect of such a perturbation, additional toroidal ripple wells in a torsatron occur, and particles of the respective energies can be trapped in these wells [3]. The computations show (Fig.3) that in torsatrons among all types of trapped particles (Fig.4),

toroidally ripple-trapped ones are the most dangerous for confinement as particles which have the largest radial deviations from the initial flux surface in the process of a drift.

4. Conclusions. (a). A weak TF ripple perturbation of a torsatron/heliotron magnetic field has been found affecting significantly radial deviations of helically trapped particles over the long-time period of their rotation around the device. As distinct from tokamaks, the presence of the TF ripple harmonics in the magnetic-field harmonic spectrum of a torsatron may improve the trapped particle confinement. In order that such an improvement may be possible, the TF ripple must be decreased to satisfy the inequality $|\varepsilon_{NH}| \leqslant \varepsilon_H^2 / 2^{N+1}$. If latter is not fulfilled, which is a characteristic feature of the heliotron magnetic field near the axis ($r/a_{pl} \leqslant 0.3$), then radial deviations of helical bananas increase significantly owing to the perturbation effect, becoming tens times greater than respective values for the case of the unperturbed torsatron configuration.

(b). Being generated by the TF coils, a strong TF ripple perturbation of a torsatron magnetic field leads to trapping of charged particles in toroidal ripple wells, and such a ripple increases the fraction of lost particles owing to poor confinement of toroidally ripple-trapped particles.

(c). Being weakly affected by both collisions and the radial electric field of the order $e\Phi/kT \sim 1$, the confinement of suprathermal trapped particles in heliotrons/torsatrons may be deteriorated significantly under the action of the TF ripple perturbation which give rise to direct losses of these particles. Thus, the presence of such a ripple in the magnetic-field of a heliotron of the pre-reactor or reactor size may lead to the decrease of the plasma heating efficiency as well as to the enhanced fusion product escape.

References. [1] TODOROKI J. J. Phys. Soc. Jpn 59 (1990) 2758. [2] SMIRNOVA M.S., Effect of High-Order Magnetic-Field Harmonics on the Trapped Particle Confinement in Torsatrons and Heliotrons, to be published in Nucl. Fusion. [3] SMIRNOVA M.S., Collisionless Particle Orbits in a Torsatron with the Complicated Magnetic -Field Harmonic Spectrum, to be published in Physics of Plasmas, vol.3, No 8 (1996).

Figure Captions. Fig.1. Magnetic-field harmonic spectra for the

Large Helical Device and the Uragan-2M torsatron. **Fig.2.** Radial deviations from the initial flux surface versus time of helically trapped particles in LHD. Guiding center equations of motion were integrated taking into account the full range of the magnetic -field harmonics (solid line) or ignoring the high-order N harmonics (dashed line). **Fig.3.** An example of the escaped toroidally ripple-trapped particle orbit in a torsatron with the strong TF ripple. **Fig.4.** A classification of the trapped particle orbits for a torsatron with additional toroidal ripple wells.

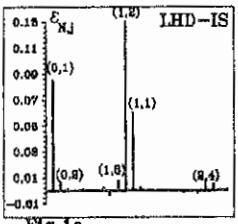

Fig.1a

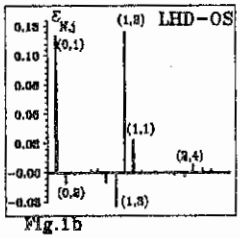

Fig.1b

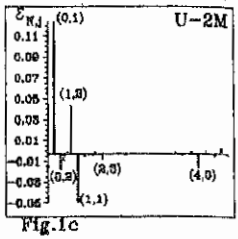

Fig.1c

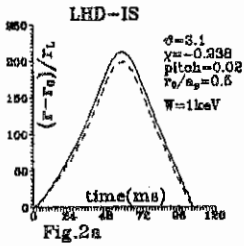

Fig.2a

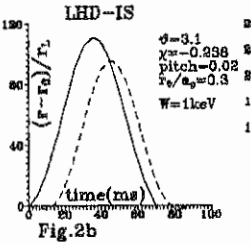

Fig.2b

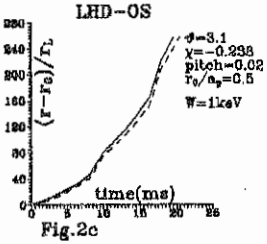

Fig.2c

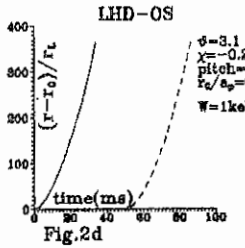

Fig.2d

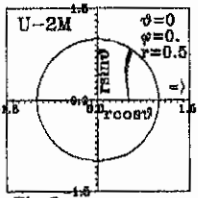

Fig.3

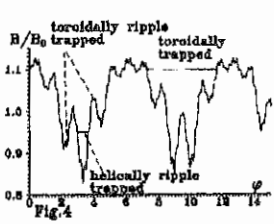

Fig.4

ANALYTICAL CALCULATIONS OF THE AVERAGE MAGNETIC WELL IN THE URAGAN-2M TORSATRON WITH DIFFERENT PROFILES OF PLASMA PRESSURE

Yu.K.Kuznetsov, I.B.Pinos, **V.I.Tyupa**
Institute of Plasma Physics
National Science Center Kharkov Institute of Physics and Technology,
310108 Kharkov, Ukraine

With the aid of formulas for averaging over magnetic surfaces general analytical expressions are deduced here to determine the average magnetic well in stellarator systems having regard to different plasma pressure profiles.

It has been known that the minimum of an average magnetic field is an important factor that exerts influence on the stability of a high-temperature plasma [1]. It has been demostrated by several authors [2, 3] that with an increasing gas-kinetic pressure there arises an average magnetic well resulting in plasma stabilization.

We have considered here the plasma pressure distribution of three types: $P_1 = P_o$, $P_2 = P_o(1-\Psi(r)/\Psi(r_o))$, $P_3 = P_o(1-\Psi(r)/\Psi(r_o))^2$, where $\Psi(r) = \int t(r) r dr$ is averaged function of vacuum magnetic surfaces. The distribution for the vacuum angle of rotational transform was chosen in the form $t(r) = t(r_o)[\alpha + (1-\alpha)\ r^2/r^2_o]$, where $\alpha = t(o)/t(r_o)$ is the ratio of the angle of rotation of field lines on the magnetic axis to that at the plasma boundary, r_o. The equations of averaged magnetic surfaces in the cylindrical coordinate frame (r, ϑ) are written as [4]:

$$\Psi_1 = t(r_o)\int[\alpha+(1-\alpha)\frac{r^2}{r_o^2}]rdr - \frac{\beta A_o r_o}{(1+\alpha)t(r_o)} r\cos\vartheta,$$

$$\Psi_2 = t(r_o)\int[\alpha+(1-\alpha)\frac{r^2}{r_o^2}]rdr - \frac{\beta A_o r_o}{(1+\alpha)t(r_o)}(1-\frac{1}{2}\frac{r^2}{r_o^2})r\cos\vartheta, \qquad (1)$$

$$\Psi_3 = t(r_o)\int[\alpha+(1-\alpha)\frac{r^2}{r_o^2}]rdr - \frac{\beta A_o r_o}{(1+\alpha)t(r_o)}[\frac{2}{3}\frac{2+\alpha}{1+\alpha} - \frac{r^2}{r_o^2} + \frac{2}{3(1+\alpha)}(\alpha\frac{r^4}{r_o^4} + \frac{1-\alpha}{4}\frac{r^6}{r_o^6})]r\cos\vartheta,$$

where $A_o = R/r_o$ is the aspect ratio, R is the major radius of torus. Here in after, the indices 1, 2, 3 in both the formulas and the plots refer to plasma pressures P_1, P_2, P_3, respectively.

The average magnetic well given by the following formula [5, 6]

$$\frac{V'(r_1)-V'(o)}{V'(o)} = \frac{B_{ot}}{<B(r_1)>} - 1, \qquad (2)$$

where $V'(r_1)$ and $V'(o)$ are the derivatives of specific volumes on the magnetic surface of radius r_1 and on the magnetic axis r_c in the (r_1, ϑ_1)

coordinate frame related to the magnetic axis. $B_{o1} = B_o /(1+r_c /R)$ is the longitudinal magnetic field on the magnetic axis,<B> is the longitudinal magnetic field averaged over magnetic surfaces.

The $B_{o1} /<B(r_1)>$ ratio is difined accordin to [5] as

$$\frac{B_{o1}}{<B(r_1)>} = \frac{\int_o^{2\pi} \frac{r_1 d\vartheta_1}{\partial\psi/\partial r_1}}{\int_o^{2\pi} \frac{B(r_1) r_1 d\vartheta_1}{B_{o1}\partial\psi/\partial r_1}} = \frac{\int_o^{\pi} \frac{d\vartheta_1}{1+b\cos\vartheta_1 + c\cos 2\vartheta_1 + d\cos 3\vartheta_1 + e\cos 4\vartheta_1}}{\int_o^{\pi} \frac{d\vartheta_1}{(1+f\cos\vartheta_1)(1+b\cos\vartheta_1 + c\cos 2\vartheta_1 + d\cos 3\vartheta_1 + e\cos 4\vartheta_1)}} =$$

$$= \frac{\int_o^{\infty} \frac{Ax^2+B}{x^4+px^2+q}dx + \int_o^{\infty} \frac{Cx^2+D}{x^4+p_1x^2+q_1}dx}{\frac{1+f_1}{2}\left[\int_o^{\infty} \frac{E_1 dx}{1+f_1x^2} + \int_o^{\infty} \frac{A_1x^2+B_1}{x^4+px^2+q}dx + \int_o^{\infty} \frac{C_1x^2+D_1}{x^4+p_1x^2+q_1}dx\right]}, \qquad (3)$$

where $B(r_1)/B_{o1} = 1/(1+f\cos\vartheta_1), f = r_1/R/(1+r_o/R), x = tg\vartheta_1/2,$ ψ is the magnetic surface function over the displaced magnetic axis, whose derivative is given by $\partial\psi/\partial r_1 = \alpha l(r_o)(1+b\cos\vartheta_1 + c\cos 2\vartheta_1 + d\cos 3\vartheta_1 + e\cos 4\vartheta_1)$.The coefficients a, b, c, d, e are difined as follows: for the $P_1 = P_o$case we have $a = \alpha + (1-\alpha)r_1^2/r_o^2 + 2(1-\alpha)r_c^2/r_o^2, b = 3(1-\alpha)/a\cdot r_c r_1/r_o^2, c = (1-\alpha)/a\cdot r_c^2/r_o^2, d = e = 0.$

In case $P_2 = P_o\{1-\Psi(r)/\Psi(r_o)\}$

$$a = \alpha + (1-\alpha)\frac{r_1^2}{r_o^2} + 2\frac{r_c^2}{r_o^2}\frac{1-(1-\alpha)r_1^2/2r_o^2}{1-3r_c^2/2r_o^2}; b = \frac{3r_1r_c}{2ar_o^2}\frac{\alpha+2(1-\alpha)(1-r_c^2/r_o^2)}{1-3r_c^2/2r_o^2};$$

$$c = \frac{1-\alpha}{a}\frac{r_c^2}{r_o^2}\frac{1-(1-\alpha)r_c^2/2r_o^2}{1-3r_c^2/2r_o^2}; d = e = 0.$$

For $P_3 = P_o\{1-\Psi(r)/\Psi(r_o)\}^2$, we have

$$a = \alpha + (1-\alpha)r_1^2/r_o^2 + 2(1-\alpha)r_c^2/r_o^2 - 2Nr_c/r_o\{-2 + 6M\alpha r_c^2/r_o^2 + 3M(1-\alpha)r_c^4/r_o^4 + 3M[2\alpha + 3(1-\alpha)r_c^2/r_o^2]r_1^2/r_o^2 + 3M(1-\alpha)r_1^4/r_o^4\},$$

$$b = r_1/ar_o\{3(1-\alpha)r_c/r_o - N[3(-1+9M\alpha r_c^2/r_o^2 + 15/2M(1-\alpha)r_c^4/r_o^4) + 5M[\alpha + 9/2(1-\alpha)r_c^2/r_o^2]r_1^2/r_o^2 + 7/4(1-\alpha)Mr_1^4/r_o^4]\},$$

$$c = r_c/ar_o\{(1-\alpha)r_c/r_o - N[-2 + 8\alpha Mr_c^2/r_o^2 + 9/2M(1-\alpha)r_c^4/r_o^4 + 4M[2\alpha + 4(1-\alpha)r_c^2r_o^2]r_1^2/r_o^2 + 9/2(1-\alpha)Mr_1^4/r_o^4]\},$$

$$d = -\frac{3MNr_c^2r_1}{ar_o^3}[\alpha + \frac{5}{4}(1-\alpha)\frac{r_c^2}{r_o^2} + \frac{5}{4}(1-\alpha)\frac{r_1^2}{r_o^2}], e = -\frac{MN(1-\alpha)}{a}\frac{r_c^3r_1^2}{r_o^5},$$

$$N = \frac{[\alpha + (1-\alpha)r_c^2/r_o^2]r_c/r_o}{\frac{2}{3}\frac{2+\alpha}{1+\alpha} - 3\frac{r_c^2}{r_o^2} + M[5\alpha\frac{r_c^4}{r_o^4} + \frac{7}{4}(1-\alpha)\frac{r_c^6}{r_o^6}]} = \frac{\beta A_o}{t^2(r_o)(1+\alpha)}, M = \frac{2}{3(1+\alpha)}, f_1 = \frac{1-f}{1+f}.$$

After integrating expression (3) we obtain the $B_{o1}/<B(r_1)>$ratio for the distributions $P_1 = P_o$ and $P_2 = P_o\{1-\Psi(r)/\Psi(r_o)\}$

$$\frac{B_{o1}}{<B(r_1)>} = \frac{\frac{1}{\sqrt{p+2\sqrt{q}}}(1+\frac{1}{\sqrt{q}})}{\frac{1+f_1}{2}[\frac{1}{\sqrt{p+2\sqrt{q}}}(A+\frac{B}{\sqrt{q}})+\frac{E}{\sqrt{f_1}}]} \qquad (4)$$

For the pessure distribution $P_3 = P_o(1-\Psi(r)/\Psi(r_o))^2$ we obtein

$$\frac{B_{o1}}{<B(r_1)>} = \frac{\frac{1}{\sqrt{p+2\sqrt{q}}}(A+\frac{B}{\sqrt{q}})+\frac{1}{\sqrt{p_1+2\sqrt{q_1}}}(C+\frac{D}{\sqrt{q_1}})}{\frac{1+f_1}{2}[\frac{1}{\sqrt{p+2\sqrt{q}}}(A_1+\frac{B_1}{\sqrt{q}})+\frac{1}{\sqrt{p_1+2\sqrt{q}}}(C_1+\frac{D_1}{\sqrt{q_1}})+\frac{E_1}{\sqrt{f_1}}]} \qquad (5)$$

For particular plasma pressure distributions the constants A, B, C, D, E, A_1, B_1, C_1, D_1, E_1 are calculated by the method of undetermined coefficients.

The calculations of the average magnetic well for different profiles of vacuum angles of rotational transform have shown that for l=3 stellatator systems ($\alpha=0$) the magnetic well value dependens only slightly on the plasma pressure profiles under study. Using the derived relations we have calculated the average magnetic well value for the Uragan-2M torsatron with the parameters $t(r_o)=0{,}43$, $\alpha=0{,}802$, $r_o=20{,}8$ cm, $A_o=8{,}17$. The figure shows average magnetic well values $B_{o1}/<B(r_1)>-1$ associated with different plasma pressure profiles as functions of the average radius r_1. The variable in the plots is the magnetic axis displacement r_c/r_o (a-$r_c/r_o=0{,}1$; b-$r_c/r_o=0{,}2$; c-$r_c/r_o=0{,}3$; d-$r_c/r_o=0{,}4$). It is evident from the figure that the average magnetic well value increases with increased r_c/r_o ratio, i.e. with rise in the plasma pressure. From the stand poin of attaining the maximum magnetic well value, it is $P_2 = P_o(1-\Psi(r)/\Psi(r_o))$ that appears to be the optimum plasma pressure distribution. In the mode of Uragan-2M operation considered the magnetic hill value can be negleted.

References

1. B.B.Kadomtzev. Fizika plazmy i problemy upravlyaemyh termoyadernyh reaktsij, Moscov, USSR Academy of Sciences, 1958, v.4, pp.16-23.
2. V.N.Pyatov, V.P.Sebko, V.I.Tyupa. Preprint KhFTI 76-25, Kharkov, 1976.
3. L.M.Kovrizhnykh, S.V.Shchepetov. Fiz. Plazmy, 1981, v.7, pp.419-427.
4. I.S.Danilkin, L.M.Kovrizhnyh, S.V.Shchepetov. Preprint FI AN N75, Moscow, 1981.
5. L.S.Solovyov, V.D.Shafranov. Vopr. Teor.Plazmy, Gosatomizdat, Moscov, 1967,v.5,pp.3-208.
6. Yu.K.Kuznetsov, I.B.Pinos, V.I.Tyupa. Preprint KhFTI 92-31, Kharkov, 1992.

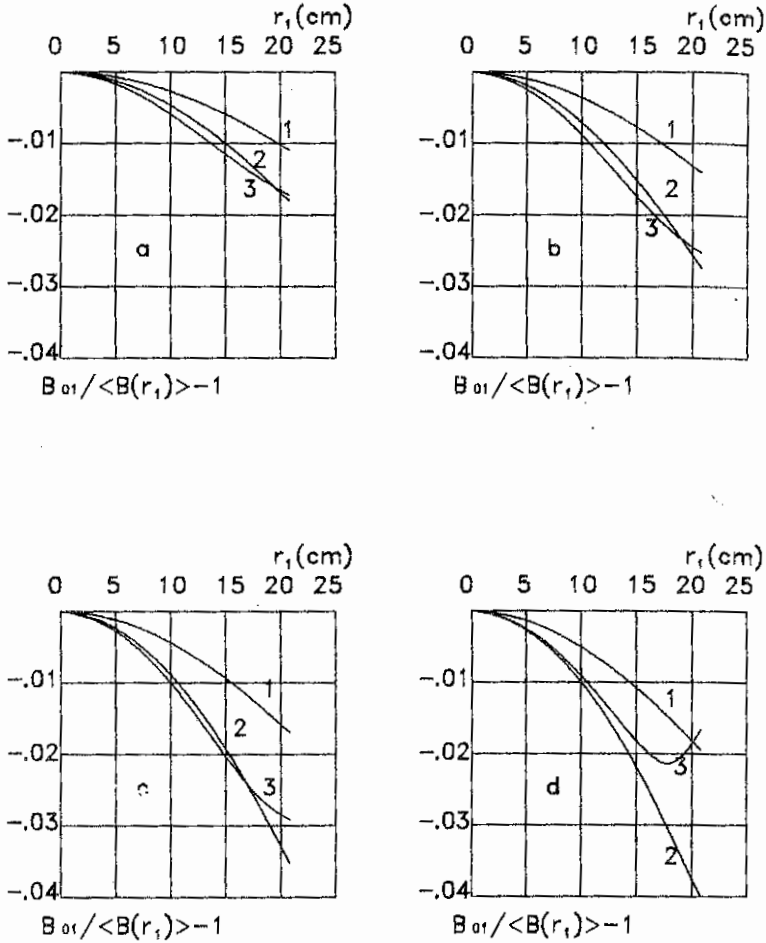

Average magnetic well distributions in the Uragan−2M torsatron.

INVESTIGATION OF PLASMA STABILITY RELATIVELY TO THE DEVELOPMENT OF QUASI FLUTE RESISTIVE MODES (G-MODES) IN STELLARATORS.

A.Ya. Omel'chenko, V.N.Kalyuzhnyj, V.V.Nemov

Institute of Plasma Physics, National Science Center "Khark-ov Institute of Physics and Technology", Kharkov 310108, Ukraine.

Finite plasma pressure and curvature of magnetic field lines are those factors which can lead to excitation of small-scale quasi-flute modes localized in the vicinity of magnetic surfaces in toroidal plasma configurations [1]. Effect of above mentioned factors is a reason of excitation of Mercier modes [2] in ideal plasma and resistive modes, in particular, g-modes [3,4] in plasma of finite conductivity. Instability of these modes limits a value of plasma pressure in magnetic trap. Conditions of excitation of Mercier modes and g-modes in arbitrary toroidal magnetic fields are determined by corresponding stability criterions. Numerical methods are nessesary to analyse these stability criterions owing to complicated 3-D geometry of magnetic field in stellarators. One of such methods, based on integration along magnetic field lines [5], was developed in [6] and used for calculations of Mercier criterion of plasma stability in "Uragan-2M" torsatron [6,7]. It was shown [6-8] that instability of Mercier modes in plasma of "Uragan-2M" torsatron can be suppresed as by increasing of plasma pressure or increasing the relative value of vertical magnetic field so under the influence of finite Larmour radius of ions.

As Mercier modes are stabilized in ideal plasma because of above mentioned factors, it is nessesary to carry out analysis of plasma stability relative to g-mode excitation taking into account the plasma resistence. In order to carry out such investigation, we transformed a known g-mode stability criterion [3], expressed in flow coordinates, to a new form, where all values are expressed in arbitrary coordinate system. For a plasma of small kinetic pressure p and small inhomogeneous length of plasma pressure as compared with values accordingly magnetic pressure and inhomogeneous length of confining magnetic field the g-mode stability criterion can be expressed in form

$$-V' p' \left\{ X_{GB} - X_{hS} + f_{\delta\varepsilon} \left[X_S + p' \left(f_{\delta\varepsilon} - X_{hB} \right) \right] \right\} > 0. \tag{1}$$

where

$$X_{GB} = f^V_{GB}(\tau_m) / f^V_B(\tau_m), \quad X_{hS} = f^V_{hS}(\tau_m) / f^V_B(\tau_m),$$
$$X_S = f^V_S(\tau_m) / f^V_B(\tau_m), \quad X_{hB} = f^V_{hB}(\tau_m) / f^V_B(\tau_m), \tag{2}$$

$$f_{\delta\varepsilon} = \kappa(\tau_m) / \kappa_2(\tau_m) - f_h(\tau_m) / f_L(\tau_m). \tag{3}$$

Here V is volume limited by magnetic surface under consideration, τ_m is upper limit of interval of integration as integrals on magnetic layer volume are

calculated, prime denotes the derivative with respect to Ψ (Ψ is the function of Ψ magnetic surface). In order to calculate functions $f_{GB}^V, f_{hS}^V, f_B^V, f_S^V$ and f_{hB}^V we use equations

$$df_{GB}^V/d\tau = \nabla\Psi\nabla B_V^2/B_V^2|\nabla\Psi|^2, \quad df_{hS}^V/d\tau = hS_V,$$
$$df_B/d\tau = B_V^2/|\nabla\Psi|^2, \quad df_S/d\tau = S_V, \quad df_{hB}/d\tau = hB_V^2/|\nabla\Psi|^2, \tag{4}$$

which were deduced in [6,7] for numerical calculation of Mercier criterion. Here $S_V = \{[\bar{B}_V\nabla\Psi]/|\nabla\Psi|^2\}rot\{[\bar{B}_V\nabla\Psi]/|\nabla\Psi|^2\}$, $\bar{B}_V$ is vacuum magnetic field. The values κ, κ_2, f_h and f_L are the solutions of equations

$$d\kappa/d\tau = hB^2, \quad d\kappa_2/d\tau = B^2, \quad df_h/d\tau = h, \quad df_L/d\tau = 1. \tag{5}$$

Equations (4)-(5) must be supplemented with magnetic field lines equations, equations for calculation of $\nabla\Psi$ and equation for function h

$$dh/d\tau = -2[\bar{B}\nabla B]\nabla\Psi/B^3, \tag{6}$$

Equating left-side of equation (1) to zero we can calculate two values of p', which determine the boundaries of stability zone. One of these values is zero ($p'=0$). Another one is determinated by expression

$$p_2' = -\frac{X_{GB} - X_{hS} + f_{8c}X_S}{f_{8c}(f_{8c} - X_{hB})}. \tag{7}$$

We used the obtained equations for calculation of g-mode stability in l=2 torsatron with parameters, which are similar to parameters of "Uragan-2M" torsatron [9] (major radius of torus R=170cm, average radius of torus r=44cm, number of helical field period on torus length m=4).

Examined configuration is similar to standard torsatron configuration with $k_\varphi = B_{\varphi 0}/B_0 = 0.375$ ($B_{\varphi 0}$ is longitudinal magnetic field of helical winding, B_0 is total longitudinal magnetic field). The calculations were carried out in cylindrical coordinate system ρ, φ, z (z axis coinsides with the major axis of the torus). G-mode stability was examined in currentless regimes, which were characterized by the following values of relative vertical magnetic field $B_\perp/B_0$: $B_\perp/B_0$=0%, 1% and 2%. Here $B_\perp$ is a homogeneous vertical magnetic field additional to torsatron magnetic field.

Table 1 shows results of calculations of some parameters in regimes in which total longitudinal equilibrium current is zero. We used the following simbols in Table 1: ι is rotation transform on the torus length (in 2π units), x_0 is coordinate of initial point of integration in the plane φ=0, (z_0=0, the average radius of examined magnetic surface $\bar{r}$ is given in brackets), D is normalized on V' left-side of criterion (1). The value $p'<0$ corresponds to plasma pressure

Table 1.

$B_\perp/B_0$	0		1%		2%	
$x_0(\bar{r})$,см	1.0(15.3)	2.0(18.9)	2.3(16.1)	3.1(19.1)	1.0(7.6)	3.7(17.1)
ι	0.662	0.737	0.720	0.760	0.720	0.772
$X_{GB}\times10^3$	1.153	0.575	0.544	0.608	0.693	1.079
$X_{hS}\times10^3$	0.888	1.573	0.501	1.132	-0.170	1.020
$X_S\times10^3$	1.415	2.039	0.975	1.307	0.185	0.600
X_{hB}	0.431	0.299	0.266	0.253	0.221	0.192
$f_{\delta\varepsilon}$	0.237	0.127	0.089	0.113	0.069	0.154
$p'_2\times10^3$	13.03	-33.68	0.011	-23.85	0.084	26.08
$D\times10^7$	6.46	-7.16	1.42	-3.60	8.87	1.58

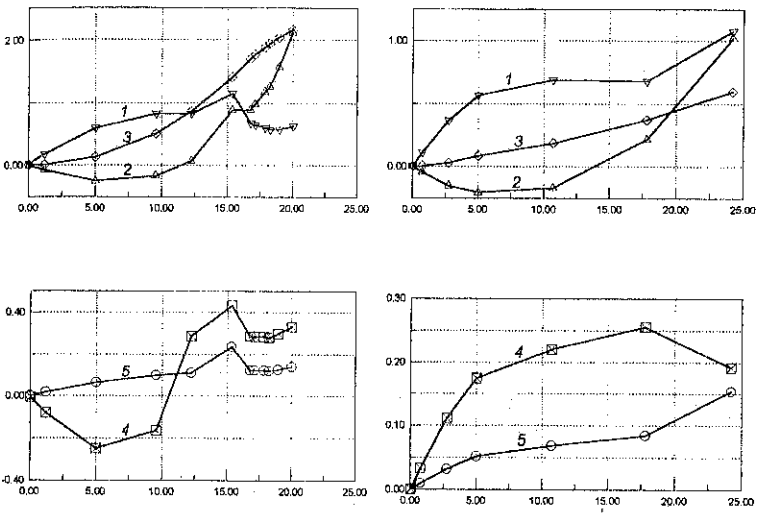

a) $B_\perp/B_0$ =0 b) $B_\perp/B_0$ =2%

Fig.1. The plot of $X_{GB}\times10^3$ (curve 1), $X_{hS}\times10^3$ (curve 2), $X_S\times10^3$ (curve 3), X_{hB} (curve 4) and $f_{\delta\varepsilon}$ (curve 5) for: a) $B_\perp/B_0$ =0; b) $B_\perp/B_0$ =2%.

decreasing in the direction of plasma periphery. The value D given in Table 1 was calculated at $p'/B^2 = -10^{-3}\text{cm}^{-1}$.

The following conclusions can be formulated from analysis of obtained results. G-mode stability criterion is realized in plasma region $\bar{r} < 16\text{cm}$ (average radius of plasma cord is 20cm) for currentless regime of plasma confinement in the case, when vertical magnetic field is zero ($B_\perp/B_0 = 0$) and plasma pressure decreases to plasma periphery. The violation of stability criterion take place at plasma periphery when $\bar{r} > 16\text{cm}$. A separation of plasma cord depending on radius value into stable and unstable zones determinated by radial distribution of functions $X_{GB}, X_{hS}, X_S, X_{hB}$ and f_{ss} (see fig.1a). All above mentioned functions give stabilizing contribution into g-mode stability criterion in central region of plasma cord ($\bar{r} < 11\text{cm}$). But in plasma region defined by condition $11\text{cm} < \bar{r} < 16\text{cm}$ function X_{hS} conncted with plasma current give destabilizing contribution into g-mode stability. However this destabilizing contribution is compensated by stabilizing contribution of function X_{GB} connected with the magnetic field structure. Destabilizing influence connected with plasma current increases at the plasma periphery ($\bar{r} > 16\text{cm}$) in accordance with fig.1a, just as stabilizing influence, determined by magnetic field structure, changes rather small. As a result plasma periphery becomes unstable becouse of g-mode excitation in the range of plasma pressure value from zero up to $p'/B^2 < 34\text{cm}^{-1}$ for plasma layer near $\bar{r} = 19\text{cm}$ and up to $p'/B^2 < 44\text{cm}^{-1}$ for plasma layer near $\bar{r} = 20\text{cm}$.

The additional vertical magnetic field with relative value $B_\perp/B_0 = 1\%$ leads to displacement of plasma cord and to magnetic surfaces deformation and to decreasing unstable zone width at plasma periphery (see Table 1). Further increasing of vertical magnetic field to value $B_\perp/B_0 = 2\%$ leads to total suppressing of g-mode instability at plasma periphery. As a result g-mode stability criterion is fulfilled everywhere inside the plasma.

Comparison of numerical dates of g-mode stability and dates of Mercier mode stability [7] shows that enfluence of vertical magnetic field of value $B_\perp/B_0 \approx 2\%$ results in suppressing of bouth types of unstable modes.

References

1. Shafranov V.D., Yurchenko E.I. *Zhurn. Exp. Teor. Fiz.* **53**, 1157 (1967).
2. Mercier C. *Nucl. Fusion Supl.* Part 2, 801 (1962).
3. Mikhailovskii A.B. Plasma instabilities in magnetic traps. M. Atomizdat (1978).
4. Glasser A., Green J.M., Jonson J.L. *Phys. Fluids* **18**, 875 (1975).
5. Nemov V.V. *Nucl. Fusion* **28**, 1727 (1988); **32**, 597 (1992).
6. Nemov V.V. *Plasma Physics Reports*, **21**, 5 (1995).
7. Kalyuzhnyj V.N., Nemov V.V. 10-th Stellarator Workshop, IAEA, 218 (1993).
8. Burdo O.S. et al. *Ukr. Fiz. Zhurn.* **40**, 317 (1995).
9. Bykov V.E. et al. *Vopr. Atom. Nauki Tekh.* **2**, 17 (1988).

NEW MODULAR HELICAL SYSTEM WITH PROPERTIES CLOSE TO A CONTINUOUS HELICAL TRAP

K.S.Rubtsov , V.A.Rudakov
Institute of Plasma Physics, National Science Center KIPT, Ukraine

The numerical code allowing to calculate the l=2 modular helical magnetic configurations with finite-sized conductors and with an arbitrary number of moduli was developed. The code is founded on using the Bio-Savar formula for magnetic field calculations. The modular design consists of the ensemble of one period parts of helical conductors having vertically located ends, which are connected by the connection parts with two pairs of poloidal currents. The system differs from K.Yamasakis design [1] by an additional pair of poloidal coils. In previous papers we used the helical parts of the moduli with horizontally located ends [2].Preferences of this system are realized in the possibility to receive the necessary poloidal field at technologically suitable positions of poloidal currents by the current distribution in the inner and the outer poloidal conductors.

The winding law of the helical coils is given by $\vartheta = M_j(\varphi - \varphi_j) + \alpha_j \sin\vartheta$, where φ and ϑ are the toroidal and poloidal coordinates; the subscript j denotes a number of helical conductors: (1) for a current on the inner side and (2) for the outer side of torus, φ_j is the φ - coordinate of the helical conductor at ϑ=0; M_j is the turn number of the helical current in the ϑ - direction at 2π interval in φ-direction (are not obligatory integer). The helical conductor makes exactly half a turn in ϑ direction independently on the conductor position and gap size between moduli. The M_j values for the helical currents, located inside and outside torus are determined with $M_1 = \frac{m(\pi + 2\alpha_1)}{2\pi(1 - m\delta/360)}$, $M_2 = \frac{m(\pi - 2\alpha_2)}{2\pi(1 - m\delta/360)}$, where δ is the gap between moduli in angular degree and m is the quantity of moduli. We use 9 filament currents for simulation of the finite-sized helical coils in the conventional continuous winding system and 6 filaments in the modular case. In the both cases, continuous winding and modular system, the transversal cross-section of helical conductors is kept without changing.

Fig 1 illustrates the 3D perspective view of the modular ensemble and the top view. The computer bundle calculation system in the one-filament case is shown. The flux surface calculations for the LHD-like ten-periodical system were done. The calculations are carried out for three kinds of magnetic systems: with finite-sized continuous helical winding, with one-filament helical winding and with finite-sized modular helical coils. The position of poloidal currents in all three cases corresponds to the following coordinates: $r_{in} = 2.7$m, $r_{ex} = 5.1$m, $z_* = \pm 1.6$m. The values of poloidal fields are taken to obtain the magnetic axis shift about -0.15m at $R_0 = 3.9$m. The helical coils radius was 0.978m. with the coil radial dimension $\Delta_r = 0.32$m. and the angular dimension at $\varphi = const$ was $\vartheta_h = 46°$. The total current in the helical conductor was taken $I_h = 7.8\,10^6$ A. Note, that the magnetic axis

positions are not changed practically at the same values of the poloidal currents for both cases of the modular systems (one-filament and six-filament helical currents). The pitch modulation α equals to 0.1 for the LHD device, but we used different sings of the same value α at the inner and at the outer sides of the modular system. We calculated the magnetic configurations for two values of the gap: 5 and 10 degrees. Figures 2-4 illustrate the flux surfaces in the conventional continuous winding case, in the modular systems with one-filament and with finite-sized helical conductors at the same sing and values of α. Fig. 5 shows the surfaces in the modular system with finite-sized helical conductors at the opposite sings of α ($\alpha_1 = -\alpha_2 = -0.1$). Fig. 6 shows the rotational angle dependencies versus the surface radius in the continuous winding system and in finite-sized modular systems at δ=5 and 10 degree ($\alpha_1 = \alpha_2 = 0.1$). The same dependencies for the modular system with $\alpha_1 = -\alpha_2 = -0.1$ are shown in Fig. 7. The case $\alpha_1 = \alpha_2$ has some advantages in a confinement volume and in a rotational transform. The advantages are not significant in comparison with one-filament modular systems, but in the finite-sized case they become very remarkable.

Presented data allows to do the following conclusions:

1. The useful volume in the modular system with the gap between moduli δ=5 degree is close to the useful volume of the conventional continuous helical winding system.

2. The modular system with equal values of the helical current modulation in the inner and outer sides of torus has some advantages over the case of opposite sign of α_{in} ($\alpha_1 = -\alpha_2$). This result contradicts to that one published in [3], where the case $\alpha_1 = -\alpha_2$ has advantages.

REFERENCES

[1] K. Yamazaki, J. Plasma and Fusion Research, vol. 70, ' 3 (1994), pp. 281.-288.
[2] E.D.Volkov et. al. VANT, ser. Termoyademy Sintez, (1991), vyp.1 p.42.(in Russian).
[3] K. Yamazaki and K.Y. Watanabe, Research Report, NIFS-279, (Apr.1994).

FIGURE CAPTIONS

Fig.1 Schematic drawing of 10-modular ensemble, (a)-3D-view and (b)-the top view.
Fig.2 Vacuum magnetic surfaces for LHD-like system with continuous finite-sized helical winding.
Fig.3 Magnetic surfaces of the one-filament modular system ($\delta = 5°, \alpha_1 = \alpha_2 = 0.1$).
Fig.4 Magnetic surfaces of the finite-sized modular case ($\delta = 5°, \alpha_1 = \alpha_2 = 0.1$).
Fig.5 Magnetic surfaces of the finite-sized modular system ($\delta = 5°$, $\alpha_1 = -\alpha_2 = -0.1$).
Fig.6 Rotational angle dependences versus the surface radius in the cotinuous winding system (1) and in finite-sized modular systems (2,3) at δ=5 and 10 degree ($\alpha_1 = \alpha_2 = 0.1$).
Fig.7 Rotational angle dependences versus the surface radius in the finite-sized modular systems at $\alpha_1 = -\alpha_2 = -0.1$ with δ=5 (1) and 10 degree (2).

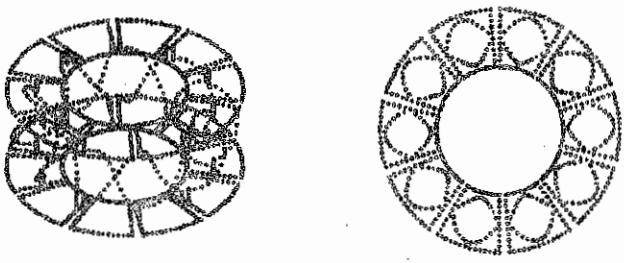

Fig.1

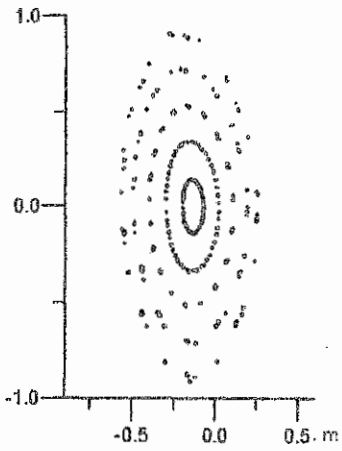

Fig.2

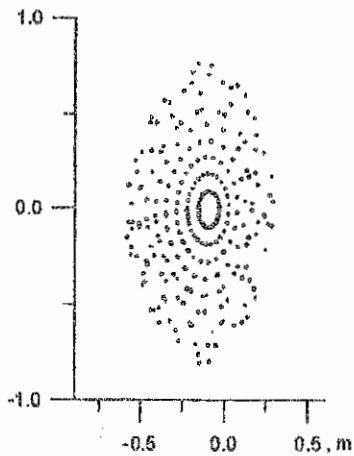

Fig.3

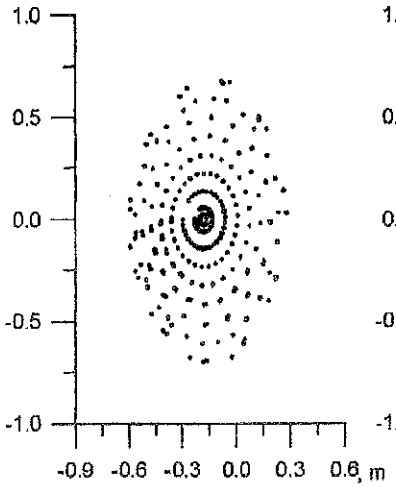

Fig.4

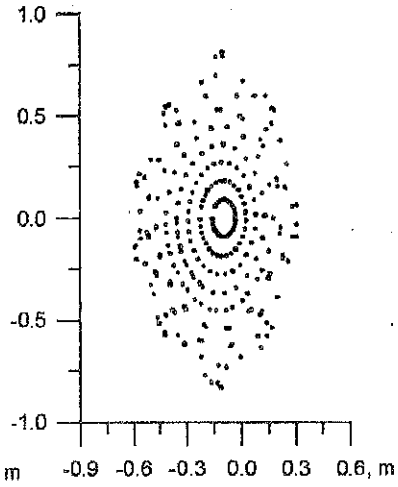

Fig.5

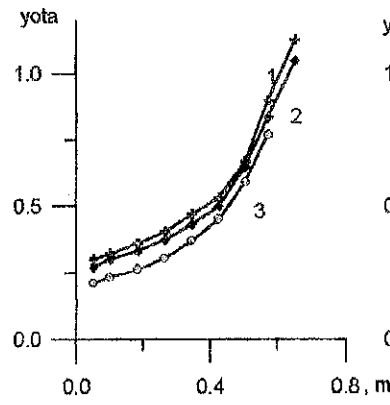

Fig.6

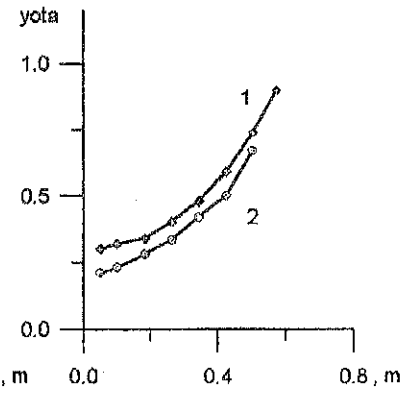

Fig.7

Studies of Magnetic Surfaces in the "Uragan-2M" Torsatron

G. G. Lesnyakov, D. P. Pogozhev, Yu. K. Kuznetsov, N. T. Besedin, E. D. Volkov, O. S. Pavlichenko

Institute of Plasma Physics,
National Science Center "Kharkov Institute of Physics and Technology",
310108, Kharkov, Ukraine

1. Introduction

The "Uragan-2M" ("U-2M") torsatron with an additional toroidal magnetic field was created for investigating the confinement of a collisionless plasma at reduced helical inhomogeneities of a magnetic field but still having a moderate shear and magnetic well.

Numerical calculations have shown that besides the magnetic configuration perturbations that are due to toroidicity and are responsible for the occurrence of "natural islands" around rational surfaces (rotational transforms divided by 2π are ι=4/7, 4/6, 4/5, 4/4) [1-5], there should take place the perturbations connected with the design of a helical winding (detachable joints and currentfeeds) [6].

The purpose of the present studies has been to experimentally determine the region of existence of closed magnetic surfaces in "U-2M" and also the extent to which the quality of magnetic surfaces depends on the design features of a helical winding.

2. Experimental setup

The magnetic system of the "U-2M" torsatron with an additional toroidal magnetic field [1-3] includes the l=2 helix with m=4 magnetic field periods and $A_h \approx 3.86$ aspect ratio, 16 coils of an additional toroidal magnetic field, 8 main poloidal coils to compensate the vertical magnetic field of the helix, 4 poloidal (trim) coils to control the residual vertical field. The major radius of torus is R_o=1.7 m. The minor radius of vacuum chamber is a_{ch}=0.34 m. The helix consists of two closed helical windings. Each of the two helical windings is split into two halves with an 18-deg poloidal gap in between, where the diagnostic ports are placed. The helical windings have detachable joints [6] which allow the windings disassemble into two toroidal halves. The coordinates of detachable joints differ by 180-deg in the toroidal angle. The commutating joints of busbars in the helical winding halves were made at detachable joints sites. Over the top and under the bottom of detachable joints on one side of the torus the currentfeeds are located.

The "U-2M" magnetic configuration parameters such as the average radius **r** of the last closed magnetic surfaces (LCMS), the angle of rotational transform and others, can be changed through the operation parameter K_φ ($K_\varphi = B_{th}/B_o$, $B_o = B_{th} + B_{tt}$, where B_{th} - toroidal magnetic field produced by the helix, and B_{tt} - additional toroidal magnetic field) and the average vertical magnetic field along the circular minor axis of the torus $\langle B_\perp \rangle / B_o$ that controls the magnetic axis shift (Δ) from the circular minor axis of the torus. Idealized calculations of

magnetic properties of the trap [1-3,5] have shown that in the range $0.29 \le K_\varphi \le 0.38$ the rotational transform can change from $\iota(r) \approx 0.4$ up to $\iota(r) \approx 0.75$ ($0.3 \le \iota(0) \le 0.57$ on the magnetic axis). The average magnetic well is $\delta V'/V' \approx -4\%$.

The structure of vacuum magnetic surfaces was investigated by the luminescent rod method [7,8] and the stellarator diode method [9,10]. The measurements were carried out in two poloidal cross-sections, spaced 45-deg apart in the toroidal angle. The horizontally located "elliptic" magnetic surfaces of the magnetic field half-period were mapped by the diode method. The vertical "elliptic" magnetic surfaces of the magnetic field period were mapped by the scanning luminescent rod method. The measurements have been performed in steady-state magnetic fields $0.08 \le B_o \le 0.15$ T.

3. Experimental data and computer simulation results

Over a range of $K_\varphi = 0.295$-0.38 the mapping of magnetic surface structure was carried out for 6 regimes: 1) $K_\varphi = 0.295$, $\langle B_\perp \rangle / B_o = 1.8\%$; 2) $K_\varphi = 0.313$, $\langle B_\perp \rangle / B_o = 1.86\%$; 3) $K_\varphi = 0.322$, $\langle B_\perp \rangle / B_o = 1.89\%$; 4) $K_\varphi = 0.34$, $\langle B_\perp \rangle / B_o = 1.95\%$; 5) $K_\varphi = 0.36$, $\langle B_\perp \rangle / B_o = 2.02\%$; 6) $K_\varphi = 0.375$, $\langle B_\perp \rangle / B_o = 2.09\%$. The results for the average radius of LCMS r and the magnetic axis position under these regimes are shown in Fig. 1. On mapping magnetic surfaces near the boundary of the confinement volume the step of measurements was decreased so that the error in LCMS r determination should not exceed 1-1.5 cm (dotted curve). The calculations of the magnetic field structure by idealized models of configuration [1-3,5], and with the help of the models [4,6] that are close in the description to the magnetic system design, have shown islands of resonances $\iota = 4/7$, $4/6$, $4/5$, $4/4$ for the regimes with $\iota(0) \ge 0.5$ on the magnetic axis. The inclusion of design features of both the detachable joints of the helix and the currentfeeds in model [4] has predicted the occurrence of two, significant in size, islands of the resonance $\iota = 1/2$ [6]. The mapping has shown that the reduction in K_φ (at $K_\varphi < 0.38$) causes the motion of islands of resonance $\iota = 1/2$ in a radial direction, from center to periphery, with a simultaneous reduction in the average width of islands. It has turned out that under regimes with $0.3 \le K_\varphi \le 0.33$ ($\iota(0) < 0.5$) there are no resonant magnetic surfaces, Fig. 2a,b. This is of importance, because the regimes without islands are especially attractive for starting work with a plasma, Fig. 2a,b and Fig. 3a,b.

For $K_\varphi = 0.295$ three islands of resonance $\iota = 1/3$ (15 cm < r < 19 cm) were detected, Fig. 2c. The numerical simulation with the use of model [6] has shown practically a complete coincidence between experimental and numerical position and size values of islands of resonance $\iota = 1/3$, Fig. 3. Another resonant magnetic surface in this regime is the surface $\iota = 2/5$. However, it is not mapped in experiment, because it should be cut off by RF antenna, target plates and vacuum chamber.

The diode measurements of magnetic surfaces were carried out under regimes with $K_\varphi = 0.375$ ($\langle B_\perp \rangle / B_o = 1.85\%$) and $K_\varphi = 0.295$ ($\langle B_\perp \rangle / B_o = 1.85\%$), see also the first results of [3]. The results of one-dimensional scanning of the magnetic surfaces of these two extreme

regimes by the emitter are in agreement with the average LCMS radii obtained by the scanning luminescent rod method. The radial distribution of emission current along the minor axis of an ellipse (chord is R_0-10 cm) in regime K_φ=0.295 is presented in Fig. 4. The ratio of emission currents of the thermionic emitter, measured outside and for the central part of CMS, reaches three orders of magnitude and it is one of CMS quality estimates.

4. Conclusions

Magnetic surfaces with r=19.5-20.5 cm (K_φ=0.295) were measured in the vacuum chamber of "Uragan-2M", where the computer simulated magnetic surfaces with r=22 cm only can be placed. Regimes under which there are no islands are limited by a range $0.3 \le K_\varphi \le 0.33$. A strong suppression of the emitter current (by three orders of magnitude) in the diode method represents one of the qualitative estimates of closed magnetic surfaces for regimes with $0.295 \le K_\varphi \le 0.38$. In the explanation of the radial position and size of islands of resonances ι=1/2, 1/3 it was the consideration of design features of helical detachable joints and current feeds that appeared essential in the numerical simulation of the "U-2M" magnetic system.

The research described in this publication was made possible in part by Grants N U2T 000 and N UA 7000 from the International Science Foundation, by the International Soros Science Education Program through Grant N SPUO62014.

References

1. Bykov V.E., et al., Fus. Technology **17** 140 1990)
2. Pavlichenko O.S., IAEA Techn. Comm. Meet. On Stellarators and other Helical Confinement Systems, Garching, Germany, 1993, IAEA, Vienna, 60 (1993)
3. Pavlichenko O.S. for the U-2M group, Pl. Phys. and Contr. Fusion. **35** B223 (1993)
4. Besedin N.T., et al., Vopr. Atom. Nauki i Tekh., Ser. Termoyad. Sintez, Moskva (Probl. of Atomic Science and Technique), 1987, N.3, p. 18 (in Russian)
5. Bykov V.E., et al., IIP-Report IIP 2/301, 1989
6. Besedin N.T., et al., Vopr. Atom. Nauki i Tekh., Ser. Termoyad. Sintez, Moskva (Probl. of Atomic Science and Technique), 1991, N.1, p. 48 (in Russian)
7. Hailer H., et al., 14th EPS Conf., Madrid, 1987, **11 D, I**, 423
8. Lesnyakov G.G., et al., Nuclear Fusion **32** 2157 (1992)
9. Dikij A.G., et al., Fizika Plasmy (Sov. J. Plasma Phys.) **14** 279 (1988)
10. Volkov E.D., et al., IAEA Techn. Comm. Meet. On 8th Stellarator Workshop, Kharkov, USSR, 1991, IAEA, Vienna, 429 (1991)

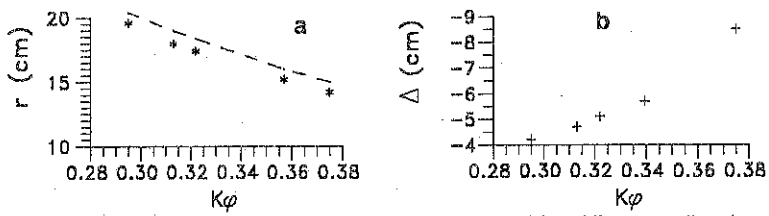

Fig. 1. *Average radius of the last closed magnetic surface (a) and the magnetic axis shift (b) from the circular minor axis of the torus inward as a function of K_φ for regimes with current I_{trim}=const .*

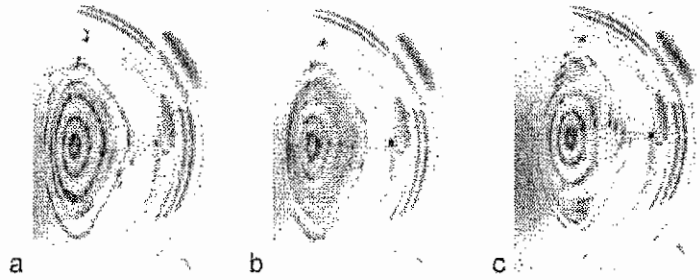

Fig. 2. *Measured electron drift surface cross-sections: (a)* K_{φ} =0.322, $\langle B_{\perp} \rangle / B_0$ =2.09%; *(b)* K_{φ} =0.313, $\langle B_{\parallel} \rangle / B_0$ =1.86%; *(c)* K_{φ} =0.295, $\langle B_{\perp} \rangle / B_0$ =1.8%.

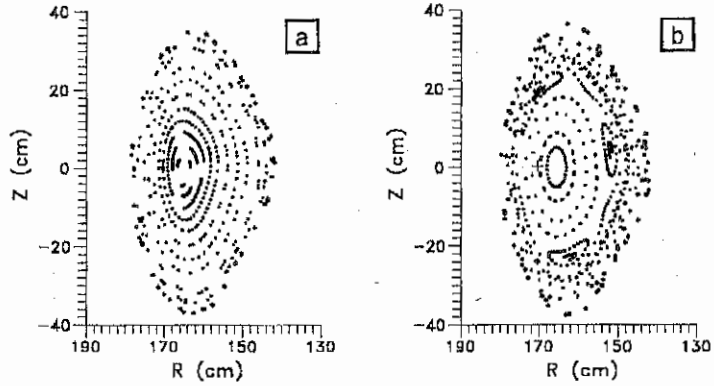

Fig. 3. *Calculated magnetic flux surfaces: (a)* K_{φ} =0.31, $\langle B_{\parallel} \rangle / B_0$ =1.86%; *(b)* K_{φ} =0.295, $\langle B_{\perp} \rangle / B_0$ =1.85%; *(c) rotational transform profile for regime* K_{φ} =0.31, *see (a).*

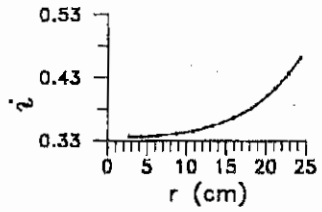

Fig. 3c.

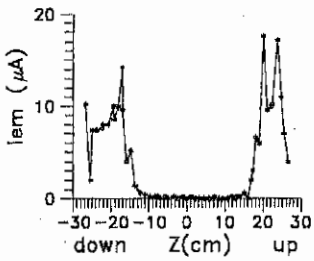

Fig. 4. *Electron emitter current profile for vertical scan at wide part of horisontally located "elliptic" magnetic surfaces, regime* K_{φ} =0.295, $\langle B_{\perp} \rangle / B_0$ =1.85%.

Progress in Reactor Heliotron/Torsatron Physics Study

O.Motojima, K.Y.Watanabe, A.Sagara, K.Yamazaki
(National Institute for Fusion Science, Toki, Japan),
A.A.Shishkin, A.V.Zolotukhin, M.S.Smirnova, I.N.Sidorenko
(Institute of Plasma Physics, National Scientific Center "Kharkov Institute of Physics and Technology ",Kharkov, Ukraine),
N.A.Belash, E.I.Polunovskij, O.A.Shishkin
(Kharkov State University, Faculty of Physics and Technology, Kharkov, Ukraine)

1.Introduction. Force Free Helical Reactor (FFHR) [1] is the subject of our study. The $l=3$ helical systems have the possibility to satisfy the "force-free" condition and the condition of the large plasma volume, simultaneously. FFHR has the potential to realize the high magnetic field device [1,2]. For the thermonuclear burning under the high magnetic field we do not need the high beta operation. The following law of the helical winding is applied as

$$\frac{m}{l}\phi = \theta - \theta_0 - \alpha_1 \frac{a_h}{R} sin\theta - \frac{1}{2}\alpha_2 \left(\frac{a_h}{R}\right)^2 sin2\theta,$$

where α_1 and α_2 are the first and second modulation coefficients: $\alpha_1 = -1$, $\alpha_2 = -0.5$. Here R and a_h are large and small radii of the helical winding. The parameter m is the magnetic field period number, l is the number of the helical windings, θ and ϕ are the angular variables along the minor and major toroidal circumference. The coil system is shown in Fig.1. The flexibility of $l=3$ helical system is similar to the flexibility of $l=2$ helical system (Large Helical Device) [3], when $l=3$ system has three pairs of vertical field coils.

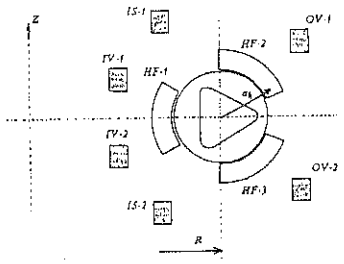

Fig.1 Coil system

Two cases of FFHR:

$l=3$, $m=18$, $R/a_h = 6$ (FFHR-18)

and

$l=3$, $m=12$, $R/a_h = 4$ (FFHR-12)

are considered. The confinement properties of FFHR-18 are studied in [2,4]. In this case the average radius of the last closed magnetic surface $a_p \approx 0.6 \cdot a_h$.

Now the case of more compact system (FFHR-12) is under study.

2.Magnetic configuration. We think that it is important that more compact magnetic configuration with the same average minor radius (under $l=3$, $m=12$ and $R/a_h = 4$) can be realized (Fig.2) .

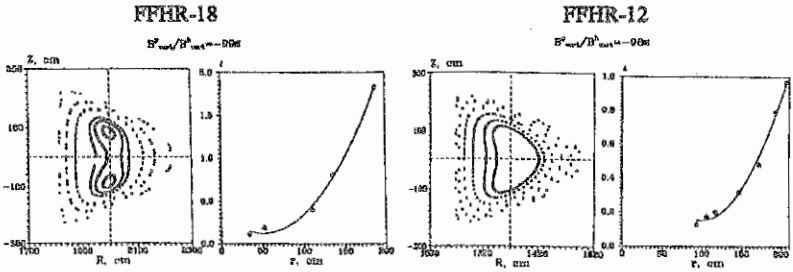

Fig.2 Magnetic surfaces and rotational transform.

The central magnetic surfaces are shifted by the vertical magnetic field outward ($B^v/B^h = -90\%$), inward ($B^v/B^h = -105\%$) [2,4] or may take the position near the geometrical axis of torus ($B^v/B^h = -99\%$) as it is demonstrated in Fig.2. Here B^v and B^h are the vertical magnetic field from VF and HF coils at the circular axis of torus. In the case of the reduced helical winding aspect ratio, the plasma aspect ratio $R/a_h = 6$ and the splitting of the magnetic axis is absent.

3.Loss cones and transport properties. Our previous study has shown [2,4] that the loss cones in the configurations of FFHR-12 are considerably larger, than those in the configuration of FFHR-18. For the particles with the starting point inside of torus loss cones can be seen in Fig.3.

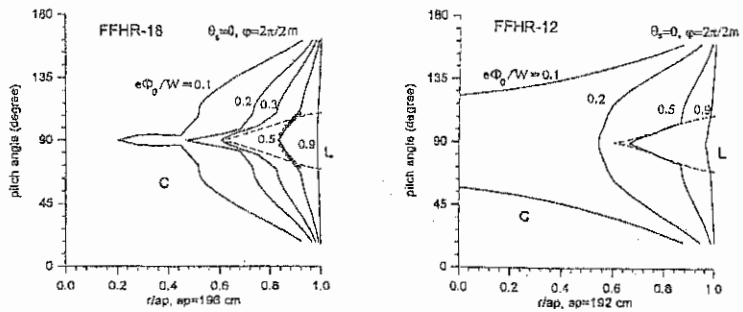

Fig.3. Loss cones in term of velocity pitch-angle versus magnetic surface radius.

One can see that at the small electric field regime $|e\Phi_0|/W < 0.9$ (where Φ_0 is the electric field potential at $r=0$ and W is the total particle energy) the confinement of both the trapped and passing particles is better in FFHR-18.

The analysis of transport properties particularly in $1/\nu$ regime with the use of analytical approach [2,4] has shown that the geometrical factor of neoclassical transport coefficient in FFHR-12 is three times larger than that in FFHR-18. That is why it is very important to find the way of toroidal effect compensation.

4.Alpha-particle orbits. In more compact system the more strong effects of toroidality are waited for. However, some sets of magnetic field parameters can decrease the effect of toroidality. Alpha-particles orbits in both configurations with $V_{II}/V = -0.9$ and $V_{II}/V = 0.9$ (Fig.4) do not coincide with the vacuum magnetic surface.

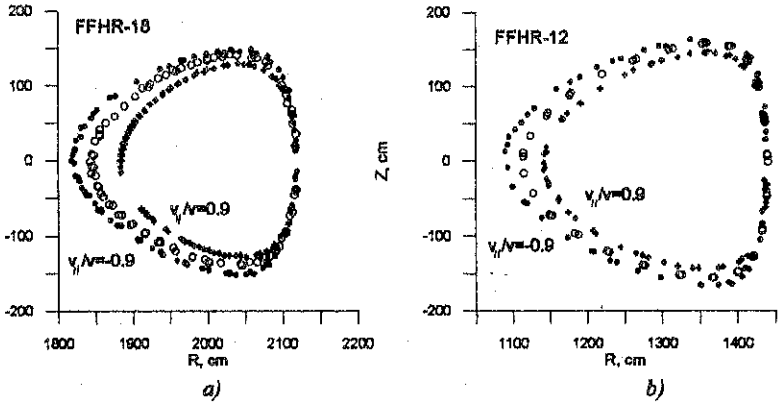

Fig.4. Alpha-particle orbits in meridional cross section relatively the magnetic surface.

Nevertheless, in both cases the displacement of the drift surfaces from the magnetic surface (marked by o) are almost the same. This is the consequence of the special choice of the magnetic field spectrum (the nearest satellite harmonics) in the case of more compact system. This set of parameters can be realized by the control of the vertical field coil currents. The optimization of the configuration is possible and should be continued. The effect of quadrupole magnetic field harmonics may be the strong positive one [5]. It is especially important for the high energy particles which do not feel the ambipolar electric field potential.

4. Conclusions.

1. l=3 helical system with the three pairs of vertical field coils provides the "force-free" helical winding (the high magnetic field, up to 12 T) and the average radius of the last closed magnetic surface equal to 0.6 that of the helical winding. It is possible to realize the magnetic configuration under the following set of parameters: l=3, m=18, R/a_h=6.

2. It is possible to make the magnetic configuration more compact with the same helical winding minor radius under l=3, m=12, R/a_h=4. The average radius of the last closed magnetic surface is approximately the same and the condition of "force-free" helical winding is conserved.

3. At the process of study at first we had the magnetic configurations where the loss cone ratio and neoclassical transport level were considerably larger in the case m=12, R/a_h=4 (compact system) in comparison with the case of m=18, R/a_h=6.

4. The principal new result obtained here is that in the more compact system (where toroidality is larger) the displacement of the drift surfaces of high energy passing particles relatively the vacuum magnetic surface is not larger. Such effect is possible due to the nearest satellite harmonic regulation with the control of the vertical field coil currents.

The further improvement of the confinement properties is necessary and possible. The process of the compact magnetic configuration optimization will be continued.

References.

1.O.Motojima, et al, in Plasma Physics and Controlled Nuclear Fusion Research (Proc.15th Int. Conf., Madrid, 1994), IAEA, Vienna (1994).
2. O.Motojima, et al, Transactions of Fusion Technology, April 1995, V.27,p.264-269.
3.A.A.Shishkin, K.Y.Watanabe, K.Yamazaki et al, National Institute for Fusion Science, Research Report NIFS-211,Mar.1993.
4.O.Motojima et al, Proc. 6th Workshop on Wendelstein 7-X and Helias Reactors, Max-Planck Institute of Plasma Physics Report, IPP 2/331, January 1996, p.227-236.5
5.O.Motojima, A.A.Shishkin, I.N.Sidorenko, E.I.Polunovskij, The 23rd EPS Conference on Controlled Fusion and Plasma Physics, June 1996, Kiev, Ukraine, b027.

Particle Orbits in Quadrupole Large Helical Device Configurations

O.Motojima
(National Institute for Fusion Science, Toki, Japan),
A.A.Shishkin, I.N.Sidorenko
(Institute of Plasma Physics, National Scientific Center "Kharkov Institute of Physics and Technology ,Kharkov, Ukraine),
E.I.Polunovskij
(Kharkov State University, Faculty of Physics and Technology, Kharkov, Ukraine)

1.Introduction. In recent years in connection with the construction of the Large Helical Device (LHD, Toki) [1], a new-generation thermonuclear device, considerable great attention has been focused on the features of plasma confinement in quadrupole magnetic configurations. Quadrupolarity of a magnetic configuration means elongation of the magnetic surface, on the average, along the length of a torus in the vertical direction (the *VE*-configuration) or in the horizontal direction (the *HE*-configuration). As it has been shown in experiments on the ATF-1 torsatron and in later experiments on the CHS heliotron/torsatron, the direction and magnitude of the bootstrap current change with changing quadrupolarity of the magnetic configuration. This is one of the most reliable and generally acknowledged confirmations of neoclassical ideas about plasma transport along the magnetic field. However, plasma transport across the magnetic surface [2-4] is in need of deeper study. In this report we examine the effect of quadrupolarity of magnetic configurations on the confinement of individual charged particles as a function of starting point of the test particle and the ratio between the longitudinal and total velocities. By numerically integrating the equations of motion in the drift approximation we have studied the characteristic trajectories of charged particles in quadrupole magnetic configurations. By characteristic trajectories we mean the particles which feel the effect of enhanced helical ripples (in the case of *VE*-configurations) and weakened helical ripples (in the case of *HE*-configurations) in the modulation of the magnetic field along a force line.

2.The main equations and the magnetic field model. Our study of the motion of charged particles is based on the system of equations of the drift approximation

$$\frac{d\vec{r}}{dt} = v_{II}\frac{\vec{B}}{B} + \frac{c}{B^2}\left[\vec{E}\times\vec{B}\right] + \frac{M_j c\left(2v_{II}^2 + v_{\perp}^2\right)}{2e_j B^3}\left[\vec{B}\times\nabla B\right],\quad \frac{dW}{dt} = 0,\quad \frac{d\mu}{dt} = 0,$$

where W and μ are the total energy and the magnetic moment of the particle. The remaining notation is standard.

The components of the magnetic field are given in the quasi-cylindrical coordinate system in the form of Fourier expansions over the harmonics of the angular variables θ and φ, $\vec{B} = \nabla\Phi$, and the scalar potential of the magnetic field has the form

$$\Phi = B_0\left\{R\varphi - R/m\left[\sum_N \varepsilon_N (r/a)^N \sin(N\theta - m\varphi) + \sum_{k=2}^{4} \varepsilon_k (r/a)^k \sin k\theta\right]\right\},$$

where $N = l, l \pm 1, l \pm 2$. Here a and R are the small and large radii of the plasma, l is the number of poles of the helical winding, m is the number of periods of the magnetic field along the length of the torus, r is the radial variable, θ and φ are the angular variables along the small and large circumference of the torus with θ accounted from the direction opposite to the main normal to the circular axis of the torus, ε_N and ε_k are the coefficients of the harmonics of the magnetic field. For the results presented here we choose the following values of the parameters: $l=2$, $m=10$, $B_0=3$ T, $R=390$ cm, $a=97.5cm$, the parameters ε_N and ε_k are taken in such way that the magnetic surfaces and magnetic field modulation coincide with the results of [2]. Such a magnetic field provides closed magnetic surfaces with noticeable indications of the quadrupolarity of the magnetic configuration: the magnetic surfaces are elongated along the vertical axis (Fig.1*a*) or along the horizontal axis (Fig.1*b*). In the modulation of the magnetic field along a force line, one observes an enhanced of the ripples in the space between the outer and inner regions of the torus in the case of vertical elongation (Fig.2*a*) or weakening of the ripples in the case of horizontal elongation of the magnetic surfaces (Fig.2*b*). For this model of the magnetic field we analysed the characteristic trajectories of particles which were launched from the outer and inner sides of the torus and which feel in their motion the effect of enhanced ripples of the magnetic field in the case of the *VE*-configuration and weakened ripples in the case of the *HE*-configuration.

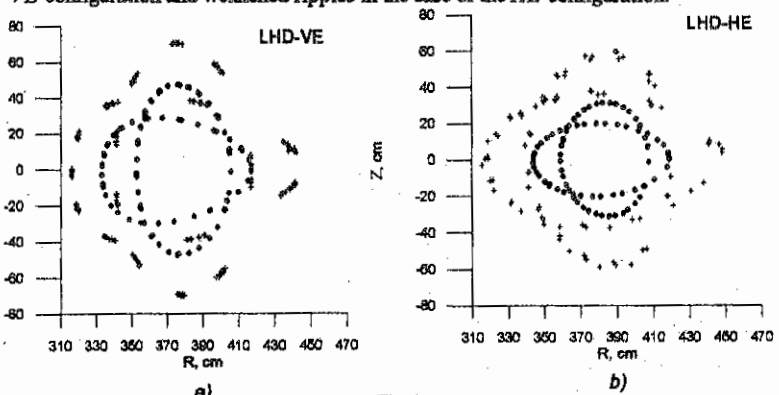

Fig.1

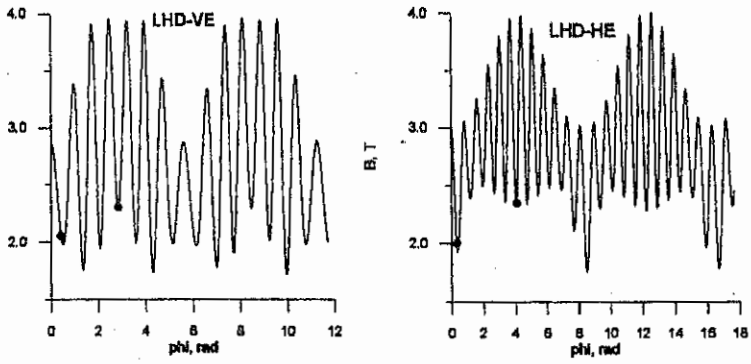
LHD-VE
LHD-HE
B, T
phi, rad
a)
b)

Fig.2

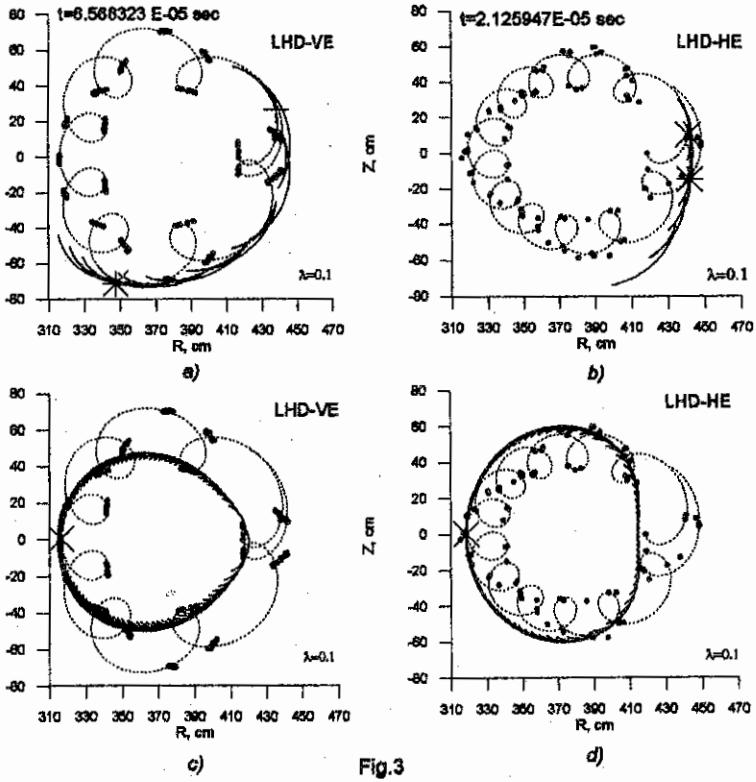
t=6.568323 E-05 sec
t=2.125947E-05 sec
LHD-VE
LHD-HE
Z, cm
R, cm
λ=0.1
a)
b)
c)
d)

Fig.3

3.Particles orbits features. The total energy of the particles is $W=10$ *keV*, the electric field is taken into account through the parameter $e\phi_0/W = 0.1$, where $\phi = \phi_0\left(r/a_p\right)^2$ is potential of the electric field. Variation of the parameter $\lambda = v_{II}/v$ let us study all classes of the particles: passing, transition, toroidally and helically trapped. The effect of the quadrupolarity on the particle motion and confinement is considerable for helically trapped particles. In Fig.3 one can see the characteristic trajectories for particles with $\lambda = v_{II}/v = 0.1$.

The trapped particles, started outside of the torus (Fig.3*a,b*) are lost in both configurations, but with different point of loss and "lifetime" of the particles in the confinement volume. In *VE*-configuration "lifetime" is an about half order magnitude longer than in the *HE*-configuration. In *HE*-configuration the point of loss (marked by ✳) lies in the outer side of the torus, as well as starting point (marked by X). In *VE*-configuration the trapped particles come from the outer to the inner region of the torus and point of loss lies in the inner side of the torus. The angular coordinates of particle point of loss in the real magnetic field geometry are under study.

The trapped particles, started inside of the torus (Fig.3*c,d*) in magnetic configurations with different quadrupolarity have quite different shape of the trajectories. In *VE*-configuration they lie inside the confinement volume, bounded by the last closed magnetic surface (dotted line) and such trapped particles are confined. In *HE*-configuration in the region with weakened helical ripples (between outer and inner sides of the torus) the trajectories of trapped particles cross the bounder of the confinement volume and has danger to leave the plasma.

4.Conclusions. Our treatment of the motion of particles in magnetic configurations, which differ in their quadrupolarity, shows that the confinement of the trapped particles is better in *VE*-configuration, than in *HE*-configuration. This means that *VE*-configuration is preferable both for the decreasing of the bootstrap-current [5] and particle losses across the magnetic surfaces.

References.

1.A.Iioshi, M.Fujiwara, O.Motojima et al., Fusion Technology 17, No. 1, 169 (1990).

2.A.A.Shishkin, K.Y.Watanabe, K.Yamazaki et al, National Institute for Fusion Science, Research Report NIFS-211,Mar.1993.

3.A.V.Zolotukhin, I.N.Sidorenko, A.A.Shishkin, O.Motojima, K.Matsuoka, H.Yamada, Tech. Phys. Lett. 21(6), June 1995, p.435-437.

4.I.N.Sidorenko, A.A.Shishkin, O.Motojima, K.Matsuoka, H.Yamada, Tech. Phys. Lett. 22(4), April 1996, p.315-317.

5.K.Watanabe, N.Nakajima, M.Okamoto et al., Nucl.Fusion 32, N 9, 1499 (1992).

Application of Mapping Techniques for the Kinetic Equation in the Weak Collisions Regime

S.V. Kasilov[1], V.E. Moiseenko[1], M.F. Heyn[2], W. Kernbichler[2]

[1] *Institute of Plasma Physics, National Science Center "Kharkov Institute of Physics and Technology", Akademicheskaya 1, 310108 Kharkov, Ukraine*

[2] *Institut für Theoretische Physik, Technische Universität Graz, Petersgasse 16, A-8010 Graz, Austria*

1. INTRODUCTION. In numerous studies of RF heating and particle transport a modeling of the particle distribution function in magnetic traps is needed. In the general case, the distribution function has to satisfy the five-dimensional (5D) quasi-linear drift kinetic equation and any numerical treatment becomes a formidable task. In the weak collisions regime and in the particular case of traps with axial symmetry, the method of bounce-averaging has been used successfully to reduce the dimensionality of the problem by isolating the unperturbed particle dynamics from the statistical problem when calculating the distribution function. In the present paper a method which allows for such a separation even for systems with broken symmetry is proposed. The efficiency of Monte-Carlo solvers for the kinetic equation based on this method is close to the efficiency of bounce-averaged Monte-Carlo methods [1,2].

2. STOCHASTIC MAPPING. The drift-kinetic quasilinear equation in covariant form is

$$\frac{\partial f}{\partial t} + V^\alpha \frac{\partial f}{\partial z^\alpha} = \frac{1}{J}\frac{\partial}{\partial z^\alpha} J \left(D^{\alpha\beta}\frac{\partial f}{\partial z^\beta} - F^\alpha f \right) - \nu_0 f + Q. \qquad (1)$$

Here, $\mathbf{z} = (\mathbf{x}, \mathbf{y})$ is a set of 5 guiding center variables where $(x^1, x^2, x^3 \equiv \vartheta)$ are general space coordinates of the guiding center, $\mathbf{y} = (y^1, y^2)$ are momentum space variables with the exception of the gyrophase ϕ, J is the Jacobian of the variables $(\mathbf{z}, \phi)$, $D^{\alpha\beta}$ and F^α account for diffusion and convection due to Coulomb collisions and quasilinear relaxation, Q and ν_0 represent generalized particle sources and sinks due to inelastic processes, and V^α is the 5D velocity of the unperturbed motion in the guiding center approximation

$$\dot{z}^\alpha = V^\alpha(\mathbf{z}). \qquad (2)$$

In this 5D phase space, Poincaré cuts are introduced as 4D hypersurfaces defined by

$$\vartheta - \vartheta_{(m)}(\mathbf{u}) = 0, \qquad (3)$$

where $\mathbf{z} = (\vartheta, \mathbf{u})$, $\mathbf{u} = (x^1, x^2, y^1, y^2)$. The set of functions $\vartheta_{(m)}(\mathbf{u})$ is chosen such that on one hand the velocity field V^α is never tangent to the hypersurfaces (3) and on the other hand the number of the cuts is sufficient to cover all particles, i.e., every unperturbed trajectory satisfying (2) intersects at least one of the cuts. For a negligible quasistationary parallel electric field, an obvious choice for the cuts (3) are surfaces where the magnetic field minimum is along the magnetic field line (m.f.l.) properly extended with respect to 2D momentum space. Subscript m in (3) numbers the cuts. For magnetic traps this number is periodic, i.e., the cut $m + M$ is the same as cut m where m has been defined to increase when stepping from one cut to the next in the direction of the magnetic field.

For a tokamak just one cut is sufficient if the equatorial plane outside the magnetic axis is chosen. In this particular case, $M = 1$, $\vartheta_{(m)}(\mathbf{u}) \equiv 0$, and $x^3 = \vartheta$ is the poloidal angle counted from the outer side of the torus.

With the help of these Poincaré cuts, the unperturbed particle motion can be described in terms of a particle coordinate map from cut (m) with starting values $\mathbf{u}_m$ to the next cut the particle strikes at $\mathbf{u}_{m'}$ when moving along its unperturbed trajectory defined by (2) as shown schematically in Figure 1. Obviously, just 3 types of transitions are possible characterized by $m' = m+1$, $m-1$, m, respectively. A "bounce" time $\tau_b(\mathbf{u}_m)$ is defined as the time required by the particle for one such a transition.

In the case of weak "collisions", such that $\tau_b \ll \tau_c$, where τ_c is the characteristic time of any stochastic "collisional" process described by the right-hand side of (1), the change of the distribution function along the unperturbed orbit between two adjacent Poincaré cuts is small. In first order with respect to τ_b/τ_c the kinetic equation (1) can be reduced to a stochastic mapping equation for the particle flux density $\Gamma_m(\mathbf{u}_m) = J_m(\mathbf{u}_m) f(t, \vartheta_{(m)}(\mathbf{u}_m), \mathbf{u}_m)$ per unit area d^4u_m of the Poincaré cut,

$$\Gamma_{m'}(t, \mathbf{u}_{m'}) \frac{\partial(\mathbf{u}_{m'})}{\partial(\mathbf{u}_m)} - \Gamma_m(t, \mathbf{u}_m) = \frac{\partial^2}{\partial u^i_m \partial u^j_m} \bar{D}^{ij}_m(\mathbf{u}_m) \Gamma_m(t, \mathbf{u}_m) \tag{4}$$

$$- \frac{\partial}{\partial u^i_m} \bar{\mathcal{F}}^i_m(\mathbf{u}_m) \Gamma_m(t, \mathbf{u}_m) - \tau_b(\mathbf{u}_m) \frac{\partial}{\partial t} \Gamma_m(t, \mathbf{u}_m) - \bar{\nu}_0(\mathbf{u}_m) \Gamma_m(t, \mathbf{u}_m) + J_m(\mathbf{u}_m) \bar{Q}(\mathbf{u}_m),$$

where

$$\mathcal{F}^i_m = \bar{F}^i_m + \frac{1}{J_m} \frac{\partial}{\partial u^j_m} J_m \bar{D}^{ij}_m, \qquad J_m = J V^\alpha \frac{\partial}{\partial z^\alpha} \left(\vartheta - \vartheta_{(m)}(\mathbf{u}) \right) \Big|_{\mathbf{z}=\mathbf{z}_m}, \tag{5}$$

and $\mathbf{z}_m = (\vartheta_{(m)}(\mathbf{u}_m), \mathbf{u}_m)$. The quantities with bar in (4) are time integrals of the respective local quantities along the unperturbed trajectory which emanates from cut m and ends at cut m'. Subscript m at the components of friction force and diffusion tensor indicate that the corresponding subintegrands are obtained from the local components by the tensor transform

$$F^i_m(\mathbf{z}) = c^i_{\ \alpha} F^\alpha(\mathbf{z}), \qquad D^{ij}_m(\mathbf{z}) = c^i_{\ \alpha} c^j_{\ \beta} D^{\alpha\beta}(\mathbf{z}). \tag{6}$$

The transformation matrix $c^i_{\ \alpha}$ where $i = u^1, \ldots, u^4$ is obtained by integrating

$$\dot{c}^i_{\ \alpha} = -c^i_{\ \beta} \frac{\partial V^\beta}{\partial z^\alpha} \tag{7}$$

along the unperturbed orbits with the initial conditions $c^i_{\ \vartheta} = -V^i J/J_m$ and $c^i_{\ j} = \delta^i_{\ j} + V^i(\partial\vartheta_{(m)}/\partial z^j) J/J_m$ for $j = u^1, \ldots, u^4$. Here, all functions of $\mathbf{z}$ have to be taken at $\mathbf{z} = \mathbf{z}_m$.

In this way, the problem of dynamic motion has been separated from modeling the stochastic processes described now by (4). The solution of the dynamic problem is obtained with usual ODE integration methods for a certain mesh of initial conditions. The resulting mapping functions, $\mathbf{u}_{m'}(\mathbf{u}_m)$, as well as all other quantities in (4) are then reconstructed by interpolation. This yields a considerable reduction in processor time.

The stochastic mapping equation (4) is finally solved with a simple Monte-Carlo algorithm, consisting of the following steps:

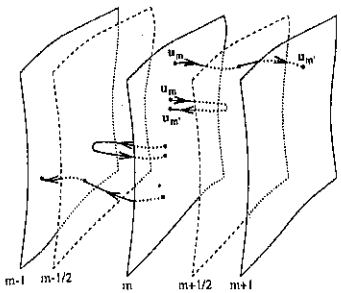

Figure 1: Different types of particle trajectories. On top pointing to the right a co-passing orbit, next two different trapped orbits, at the bottom pointing to the left a counter-passing orbit. The surfaces $m-1$, m, and $m+1$ are Poincaré cuts. The surfaces $m-1/2$ and $m+1/2$ indicate separatrix surfaces.

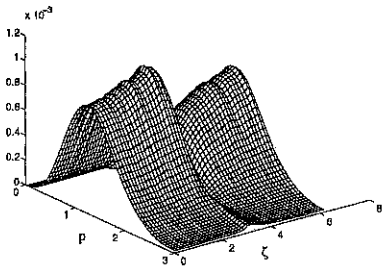

Figure 2: Pitch angle integrated particle flux as a function of toroidal angle ζ and momentum module p for the rational surface $q = 2$.

i) particles are removed and added to the cuts with event probabilities $\bar{\nu}_0(\mathbf{u}_m)$ and $J_m\bar{Q}(\mathbf{u}_m)$ respectively;

ii) particles remaining on the cuts are shifted in u^i_m by δu^i_m restricting the averages of the random shift δu^i_m to satisfy

$$\left\langle \delta u^i_m \right\rangle = \mathcal{F}^i_m(\mathbf{u}_m), \qquad \left\langle \delta u^i_m \delta u^j_m \right\rangle = 2\bar{D}^{ij}_m(\mathbf{u}_m); \tag{8}$$

iii) particles are exchanged between the cuts according to the unperturbed mapping function $\mathbf{u}_{m'} = \mathbf{u}_{m'}(\mathbf{u}_m)$ and $t' = t + \tau_b(\mathbf{u}_m)$.

For the systems with axial symmetry (tokamaks, axisymmetric mirrors) equation (4) reproduces the results of bounce-averaging. If the "collision" operator, as well as sources and sinks in (1) do not dependent on the corresponding cyclic angular variable ζ, the coefficients in (4) do not dependent on this variable neither. The unperturbed mapping over the remaining variables is trivial $\mathbf{u}_{m'} = \mathbf{u}_m$. Therefore, assuming the fluxes Γ_m to be independent on ζ, the difference on the left hand side of (4) is zero and the rest of the equation is identical to the bounce-averaged equation. Also, in cases with "collision" operators asymmetric in ζ, the bounce averaged equation is recovered, provided the inequality $\tau_r \ll \tau_c$ is satisfied where τ_r is the toroidal rotation period of the bananas in the tokamak (or orbit azimuthal rotation period in mirrors). But note that this condition is much more restrictive than the condition of weak collisions $\tau_b \ll \tau_c$.

3. SECOND HARMONIC ECRH WITH LOCALIZED PACKET. As an example, a tokamak with the condition $\tau_r \ll \tau_c$ violated is considered. For simplicity, the quasilinear diffusion operator in (1) is assumed in local form with the only nonzero component corresponding to diffusion over perpendicular momentum,

$$D_\perp = A(\zeta)\, p_\perp^2\, \delta\left(\omega - 2\omega_c(\mathbf{r})\right). \tag{9}$$

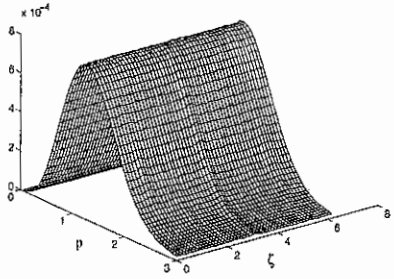

Figure 3: Same as Figure 2 but for the "most irrational" surface $q = 1.618$.

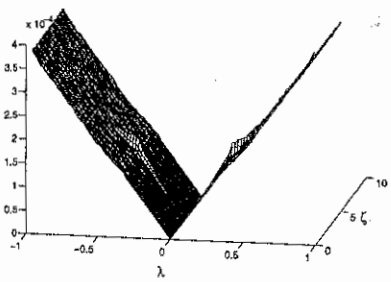

Figure 4: Momentum integrated particle flux as a function of toroidal angle ζ and pitch angle cosine λ for the irrational surface $q = 1.618$.

The amplitude $A(\zeta)$ is assumed to be Gaussian with toroidal width $\delta\zeta$. The Coulomb diffusion operator is taken for a Maxwellian background. The following parameters are used in the numerical computations: big radius - 150 cm, small radius - 15 cm, main magnetic field - 30 KG, plasma density and temperature - 1.5 10^{13} cm^{-3} and 1 KeV respectively, toroidal ECRH beam width $\delta\zeta = 0.1$, RF-power density averaged over the magnetic surface - 1 W/cm^{-3}.

In Figures 2 and 3 the flux $\Gamma_m \sim p_\| f$ integrated over pitch angle cosine in the magnetic field minimum $\lambda \equiv p_\|/p$ is presented as a function of toroidal angle ζ and momentum module p for two values of the safety factor, $q = 2$ and 1.618. The first case corresponds to a rational surface. A strong toroidal asymmetry of the electron distribution predicted earlier in [3] can be clearly distinguished. The second case corresponds to the "most irrational" surface. Even in this case, a toroidal distribution asymmetry is visible. Figure 4 presents Γ_m integrated over p as a function of ζ and λ for an irrational surface. Here, the asymmetry localized in the region of trapped particles, is more distinct. Even a small asymmetry of the trapped particle population results in a strong additional cross-field transport. This phenomenon has been described in [4].

REFERENCES

1. Kasilov S.V. and Moiseenko V.E., *International Conf. on Open Plasma Confinement Systems for Fusion.* Novosibirsk, Russia, 14-18 June, 1993, ed. A. Kabantsev, World Scientific, 1994, p. 341-347.
2. Eriksson L.-G. and Helander P., *Phys.Plasmas* V.1, 1994, p. 308.
3. Dendy R.O., *Plasma Phys. Control. Fusion* V.27, 1985, p. 1243.
4. Kasilov S.V., Pyatak A.I., and Stepanov K.N., *22-nd EPS Conference on Controlled Fusion and Plasma Physics,* Bournemouth, UK, 3-7 July 1995, Contributed Papers, Part III, p. 349-352.

Calculation of electron drift in a magnetic system of the DRAKON type

V.V.Kondakov, S.L.Lazarev, S.F.Perelygin, V.M.Smirnov, I.V.Tsvetkov
Moscow State Engineering Physic Institute (Technical University), MEPhI

This paper describes results of calculations of drift compensation stability in KREL and DRAKON relatively to shifts, turns and current perturbations in current rings. A simple analytical model of the drift in the curvilinear solenoid is proposed. This model allows to estimate the drift if the dependences of curvature and torsion along the solenoid axis are known.

The DRAKON magnetic system consists of two straight parts connected by two curvilinear elements (KRELs). The equilibrium of the whole system is determined by KREL's equilibrium quality. In the single particle mode, the equilibrium means the compensation of the electron vacuum drift, that is at the exit of a KREL an electron returns to the magnetic line, which it started from at the entrance of KREL (KREL consists of two periods of 5-periodical geodesic torus). It has been recently shown in experiments and calculations that the equilibrium part of the KREL is equal 1.5 periods. At the end of that part the drift is less than 0.1 of that in the center of KREL [1, 2, 3].

Computations of force lines and electron trajectories have shown that in the region close to an axis the electron driving along the force line from plane of one of initial coils drifts up to region of 20-th coils (i.e. centre of KREL) leaving from starting force line, and after that the electron approach it. On fig.1a dependence of the drift of 150 eV electrons on the number of coil is shown for different starting positions with 500 A winding current in solenoid. Dependence of electron drift D on the energy of electrones U_e and on the magnetic field strength B submitted on fig.1a confirm the dependence $D \sim \sqrt{U_e}/B$. Starting from region of 1-4-th of coils the electron have the drift which is compensated not less than on 90 % in the region of 35-38-th of coils.

On fig. 2a distribution of a magnetic field strength along force line leaving from the centre of 4-th coil is submitted. The undisturbed field (winding current 500 A) which is approximately constant from 4-th coil to 36-th one has a small magnetic hole in the central region of KREL, $\Delta B/B=0.35$, and sharply falls down on the ends of solenoid (the edge effect take place in the region of 4-th coil intervals from the ends of KREL). The perturbations of the magnetic field caused by the changes of current are local and it take place in the region of 4-th coil intervals from the centre in both directions.

Electrons drift has the local perturbations too (fig. 2b). The increase of the current in coils 20 and 21 two times reduces drift by 0.25 from the drift at the undisturbed magnetic field and the reduction it to 0 increases drift 1.5-fold. The similar picture is observed at perturbation of the current in other coils.

The perturbation of a magnetic field of the solenoid by shift of one coil perpendicular the axis of the solenoid or its turn on some angle is also local and it take place in the region of 2-3 coil intervals from the disturbing coil. 0.5 sm shift of the central current ring or 0.1 rad inclination of its axis has changed drift by 5-7 %.

In the case of statistical failure of orientation angles of coils from 10-th to 30-th with 0.1 rad amplitude the compensation of drift is similar to one in the undisturbed case. But force lines and trajectories of electrons starting from the plane of 4-th coil (U_e=100 eV, J=500 A) have significant and identical shifts. The displacement is accumulated up to 30-th coil and then it remains constant and equal to 0.8 sm (0.1 radius of the coil). In the case of statistical shifts of coils from 10-th to 30-th with 0.5 sm amplitude the displacement of a force line and electron trajectory is not accumulated and it has value less than 0.1 sm (0.01 radius of the coil) in the end of KREL.

Hence, the displacement of coils inevitably formed during building the experimental plant is not critical (for unclosed systems).

On fig. 3 curve 1 is the radius of curvature (R_k), curve 2 is the radius of torsion ($R_æ$), curve 3 is the angle of rotary transformation of magnetic field (α) along the axis of KREL. The number of coils, the positions of drift measurements and the boundary of equilibrium part are shown on fig. 3. In the region between position 3 and position 7 the radius of curvature is small, the drift velocity is large. The decrease of the drift velocity in the centre of KREL give the flat vertex on the plot D(N).

Assuming the curvature and the torsion of magnetic force line close to the axis are approximately equal to the curvature $k_0(s)$ and the torsion $æ_0(s)$ of the geometric axis it can be shown that

$$\partial \mathbf{d}/\partial t=-æ_0[\mathbf{d},\tau_0]+k_0R_B\mathbf{b}_0, \qquad (1)$$

where $\mathbf{d}(s)$ - vector of electron drift, s - distance along the axis, $R_B=mV_\parallel c/eB$. It is similar to the equation of velocity of effective positive charge in the crossed effective electric and magnetic fields:

$$\partial \mathbf{V}_e/\partial t=[\mathbf{V}_e,\mathbf{B}_e]+\mathbf{E}_e,\ \mathbf{B}_e=-æ_0\tau_0,\ \mathbf{E}_e=k_0R_B\mathbf{b}_0. \qquad (2)$$

In the case of $æ_0$=const, k_0R_B=const and initial speed $\mathbf{V}_e$=0 uniform movement of vector $\mathbf{V}_e$ in the plane (V_x,V_y) (it is the circle with centre $(-E_e/B_e,0)$, radius E_e/B_e, period $T_e=2\pi/B_e=2\pi/æ_0$ and maximum $V_e=2E_e/B_e$) corresponds to the equation (1) in the plane (x,y). Thus, the length of the axis of an equilibrum part L should be of the order of $2\pi/æ_0$ and maximum drift should be of the order of $2k_0R_B/æ_0$. In view of inhomogeneity of the B_e and E_e fields on the initial stage of the movement the particle is stronger accelerated by the field E_e in the weak field B_e, that gives stronger growth of drift. In the middle of KREL E_e falls and B_e is maximum that gives the fast turn of vector $\mathbf{V}_e$. At the end of equilibrum part the effective particle moves against increasing field $\mathbf{E}_e$ and it is strongly decelerated. At stage of decelerating speed $\mathbf{V}_e$ can have large fluctuations because the trajectory of the decclerated particle is more sensitive to initial conditions.

The stability of structure of a magnetic field of closed system DRAKON was investigated on the mathematical model of DRAKON with KRELs consisting of two semitorus connected with the straigth parts by two quarters of torus. Length of the straigth parts is approximately equal to the length of KRELs, step of coils is equal to half of radius of coils a. Undisturbed design of DRACON has a system of enclosed magnetic surfaces with axis deviating from geometrical axis. Destruction of magnetic surfaces (the appearance of a stochastic layer) begin at radius R_d=0.83a. Random and regular angular 0.2 rad deviations of coil axis cause the reduction R_d up to 0.64a-0.67a. External magnetic surfaces are stronger disturbed by the random deviations, however, the deviation of a magnetic axis from geometrical one is less than in the case of regular deviation. Thus, computations confirms the stability of the magnetic structure of the trap with space axis relative to the perturbations of current structure.

Summary.

The calculations carried out have shown a satisfactory stability of the magnetic structure of KREL and DRAKON as a whole relative to the various perturbations (shift of coils, change of their orientation and current in them), but also have revealed borders of this stability. Perturbations of coil orientation and local reductions of a magnetic field are more dangerous. The small residual drift in KRELs is nondangerous in closed plants from the point of view of confinement of single particles (i.e. at very small density of plasma). Dependence of the drift vector on the distance along the axis in the $(\mathbf{n},\mathbf{b})$ coordinates is similar to the dependence of the velocity of the effective charge on the effective time in crossed effective $\mathbf{E}\perp\mathbf{H}$ fields. In this case the effective electric field is proportional to the axis curvature, the effective magnetic field - to the axis torsion and the effective time - to the distance along the axis. Because of the general

magnetic structure with space axis the residual drift shifts are falled on the closed drift surfaces and the particles do not go away on the walls of the chamber. However, in the case of intermediate density (when Debay radius becomes comparable with the radius of plasma beam) the situation can change in connection with the appearance of the radial and azimuth electric fields because of the displacement of electron and ion drift surfaces. Therefore further researches are necessary.

The work is carried out at support of Russian fund of fundamental researches (project №94-02-05596-a).

References.

1.Shafranov V.D., Controlled Fusion and Plasma Physics (Proc. 10th Eur. Conf., Moscow,,1981), Vol.2, Europen Physical Society (1981), 77
2.Perelygin S.F., Smirnov V.M., Plasma Physics, 1991, Vol.17, №8, p.945
3.Perelygin S.F., Smirnov V.M., Nucl. Fus., 33, 2 (1993), p.354

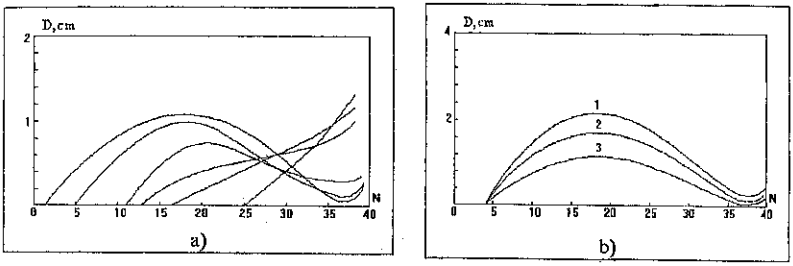

Fig. 1. Dependence of the electron drift in KREL: a) on the start position of electron; b) on the energy of electron and on the magnetic field strength: 1 — U_e= 100 eV, J = 300 A; 2 — U_e= 150 eV, J = 300 A; 3 — U_e= 150 eV, J = 500 A.

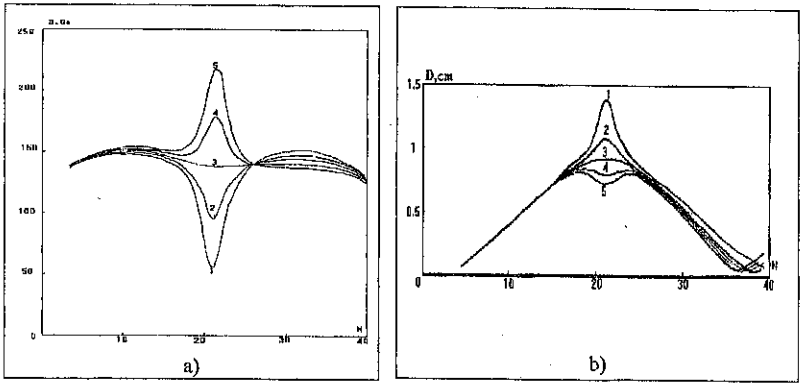

Fig. 2. Magnetic field strength (a) and electron drift (b) in KREL at the perturbation δJ in the central coils (20 and 21): 1 — δJ=-J; 2 — δJ=-0.5J; 3 — δJ=0; 4 — δJ=0.5J; 5 — δJ=J (J = 500 A).

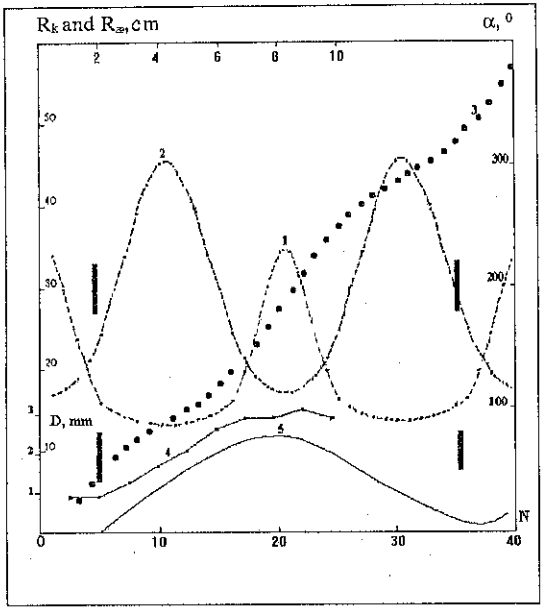

Fig. 3. Dependence of the radius of curvature (curve 1), the radius of torsion (curve 2), the angle of rotary transformation (curve 3) and calculated (curve 4) and experimental (curve 5) drift on the number of coil N in KREL.

Study of Magnetic Configuration of Heliotron Produced by Sectored Modular Coils

K.Y.Watanabe, K.Yamazaki and O.Motojima
National Institute for Fusion Science, Nagoya 464- 01, Japan

1. Introduction

Helical devices with continuous helical coils such as LHD provide rather large space for divertor pumping to control fusion ashes, impurities and neutral particles. However, amount of the technological development is required to construct and maintain large continuous coil system. On the other hand, the modular stellarator represented by W7-X is designed mainly to optimize the core magnetic confinement. In this system it is difficult to keep enough divertor space for heat load reduction and helium ash exhaust. Since to search for good confinement configurations compatible with the coil modularity and closed helical divertor is one of the most important issues for helical system, we are investigating the possible way to add a property of modularity to the continuous system[1].

The physics optimization of Modular Heliotron (MH) concepts with well-defined and efficient closed helical divertor has been carried out based on three criteria, modularity (gap between modular coils), closed divertor (thickness of separatrix region and localization of divertor legs) and plasma confinement (MHD equilibrium and stability, neoclassical flux and particle confinement). We find that heliotron device produced by sectored modular coils (Fig.1) has an efficient closed helical divertor and a good plasma confinement property.

In this paper, we show the physics property of the MH device.

2. Design of the magnetic field configuration

A variety of helical system configurations have been proposed so far by many researchers. Among these configurations, an l=2/m=10 continuous coil system is adopted for LHD to produce optimized plasmas[2] and to create a clean helical divertor, where l and m are the poloidal and toroidal multi-polarity numbers of the helical coil systems, respectively.

On the basis of the LHD configuration, we can produce the modular heliotron. In this paper, we focus on a helical coil system with a major radius 4m and a minor radius 1m. Figure 1 shows coil systems with a coil gap angle Δ_{gap} for the reference MH ($\alpha_{in}=-\alpha_{out}=0$, $\Delta_{gap}=8°$) and the modified MH ($\alpha_{in}=-\alpha_{out}=-0.3$, $\Delta_{gap}=8°$). Here the following helical winding law is adopted: $\theta=(m/l)\phi+\alpha\sin[(m/l)\phi]$, where $\alpha=\alpha_{in}$, at $0<(m/l)\phi<\pi/2-\Delta_{gap}/2$ or $3\pi/2+\Delta_{gap}/2<(m/l)\phi<2\pi$ and $\alpha=\alpha_{out}$, at $\pi/2+\Delta_{gap}/2<(m/l)\phi<3\pi/2-\Delta_{gap}/2$. This is the same definition of continuous coil winding law when $\alpha_{in}=-\alpha_{out}=0$, $\Delta_{gap}=0°$, where θ and ϕ are the poloidal and toroidal angles, respectively.

The coil system of the reference MH without one turn poloidal field coils (Fig.1(a)) was constructed based on the conventional heliotron by combining the sectored helical field coils with the sectored returning poloidal coils. Here, the connection current feeders were arranged to avoid the destruction of the divertor layer and to keep a large space for the divertor chamber. A modified MH with outside-plus/inside-minus modulated windings is shown in Fig.1(b). Here it is noted that these windings correspond to the optimized one from viewpoint of the good magnetic surface, clean divertor, high MHD equilibrium limit and tolerable neoclassical ripple transport as shown later.

Figure 2 shows the vacuum magnetic surfaces of four systems on the toroidal angle with vertically elongated magnetic surface. In the conventional heliotron like LHD (Fig.2(a)), the

position of the magnetic axis is adjusted to about a 15cm inward shift of the 4m system for the optimization of equilibrium/stability beta and particle orbit confinement. Unlike the magnetic surfaces of this conventional heliotron, the cross-sectional shape of the vacuum magnetic surfaces of the reference MH with α_{in}=-α_{out}=0, Δ_{gap}=8° are deformed to the rectangular shape and branching-off of divertor separatrix layers is induced. By other calculation, the reference MH systems with Δ_{gap}>2° are not tolerable for installing a divertor baffle plate. Even by applying the conventional pitch modulations (α_{in}=α_{out}≠0) or elliptical, triangular shaping of winding support structure, it is difficult to obtain the good magnetic surfaces and the good divertor structure. Here, the good divertor structure means that the divergence of divertor field-line Poincare plot is small, the position of divertor legs is localized in poloidal direction, and its separatrix field lines are easily extracted to the outside of the coil system.

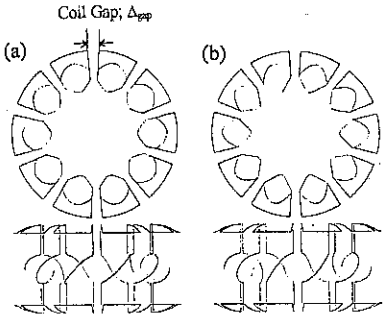

Fig.1 Top and side view of MH(Modular Heliotron) coil system (a) without pitch modulation and with plus/minus modulation.

On the other hand, a modified MH with outside-plus/inside-minus modulated windings (α_{in}=-α_{out}=-0.3, Δ_{gap}=8°) leads to reproduction of conventional heliotron configurations (Fig.2(c)), and gives rise to a better configuration with a larger plasma volume and a higher rotational transform. In this case, the divertor structure becomes clean and the stochastic region becomes thin. Figure 2(d) corresponds to the plus/minus modulation given by the continuity condition of the helical coil on gap. Here, the continuity condition of the helical coil

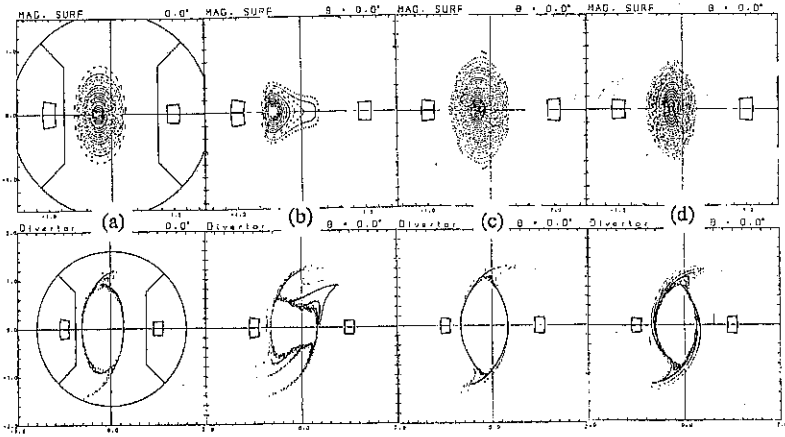

Fig.2 Vacuum magnetic surfaces and divertor layers for (a) the conventional heliotron, (b) the reference modular heliotron(α_{in}=-α_{out}=0, Δ_{gap}=8°), the improved modular heliotron ((c) α_{in}=-α_{out}=-0.3, Δ_{gap}=8° and (d) α_{in}=-α_{out}=-0.369, Δ_{gap}=8°).

on gap is defined as $(m/l)\phi_{out}+\alpha_{out}\sin[(m/l)\phi_{out}] = (m/l)\phi_{in}+\alpha_{in}\sin[(m/l)\phi_{in}]$ where $((m/l)\phi_{in}, (m/l)\phi_{out}) = (\pi/2+\Delta_{gap}/2, \pi/2-\Delta_{gap}/2)$ or $(3\pi/2-\Delta_{gap}/2, 3\pi/2+\Delta_{gap}/2)$. In this case, peripheral magnetic surface is destructed and the stochastic region becomes thick.

A modified MH system with outside-plus/inside-minus modulation is effective at reproducing the good magnetic surfaces by adopting optimum modulation as a function of gap ($\alpha_{in}=-\alpha_{out}=-0.1$ at $\Delta_{gap}=2°$, $\alpha_{in}=-\alpha_{out}=-0.15$ at $\Delta_{gap}=4°$ and $\alpha_{in}=-\alpha_{out}=-0.3$ at $\Delta_{gap}=8°$), and good magnetic divertor configurations are obtained even in the case of a large increase in gap angle Δ_{gap}.

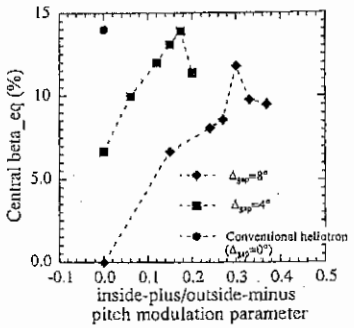

Fig.3 Dependence of equilibrium beta limit on the plus/minus pitch modulation parameters with $\Delta_{gap}=4°$ and $\Delta_{gap}=8°$.

3. MHD equilibrium and stability analysis

The configuration properties of the MH are analyzed by using the MHD equilibrium code VMEC[3]. In this paper, we adopted a fixed boundary assumption with pressure profile $P=P_0(1-\psi)^2$, where ψ is the normalized toroidal flux.

Figure 3 shows the equilibrium central beta limit versus the outside-plus/inside-minus pitch modulation parameter for three cases with gap angle 0°, 4° and 8°. Here equilibrium beta limits are determined by the criteria for the convergence of the VMEC calculation or large outward magnetic axis shift from the outermost magnetic surface center (beyond 0.7 of notarized plasma minor radius). As similar to the magnetic surface analysis, optimum modulation for MHD equilibrium is $\alpha_{in}=-\alpha_{out}=-0.15$ at $\Delta_{gap}=4°$ and $\alpha_{in}=-\alpha_{out}=-0.3$ at $\Delta_{gap}=8°$, which corresponds to that the modulation parameter is smaller than that given by the continuity condition of the helical coil on gap. The equilibrium central-beta limit of conventional heliotron is about 14%. The MH devices with the optimum modulation parameter have almost equal equilibrium performance to conventional heliotron. In the case of lower pitch modulation, the magnetic shear is not strong, the central rotational transform is small and the magnetic surface becomes horizontally elongated. Then shafranov shift is extremely large. On the contrary, in higher modulation case than optimum value, the degradation of calculation convergence determines beta limit.

As concerns stability analysis, we apply the mercier analysis. For $\beta_0 \geq 6\%$ in the conventional heliotron, $D_I>0.2$, which corresponds to existence of unstable global ideal interchange mode[4]. In the modified MH device with the optimum modulation parameter with $\Delta_{gap}=8°$, $D_I<0.2$ for $\beta_0<4\%$. The stability property is compatible to that of conventional heliotron.

4. Neoclassical ripple transport and particle orbit confinement

Even if the anomalous transport might be improved by the clean helical divertor and the plasma edge control, neoclassical ripple loss might not be negligible in heliotron type device. Figure 4 shows the geometric factor of helical ripple loss for three systems estimated by means of multi-helicity model of ripple transport. The level and radial profile in helical ripple and toroidal ripple are almost same in all systems. The reference MH system has extremely bad confinement property because it has strongly deformed plasma surface with horizontally elongated shape and large inward magnetic axis shift. The normalized geometric factor by

simple magnetic field model is 0.2 in conventional heliotron, which means that the effective helical ripple amplitude at the plasma edge is 0.08. On the other hand, for MH system with outside-plus/inside-minus modulated windings, the effective helical ripple amplitude at the plasma edge is 0.14. For the reactor we need the 2 times confinement improvement of the anomalous loss, and we should also reduce the ripple loss by about 1/5 for MH system with outside-plus/inside-minus modulated windings. The reduction of the neoclassical ripple transport by means of changing outside-plus/inside-minus modulation parameters independently is future subjects.

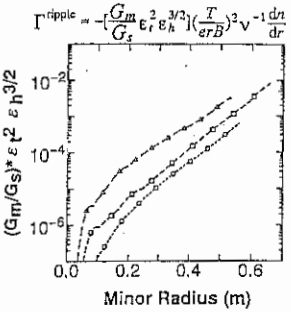

Fig.4 Geometric factor of helical ripple transport. (○; conventional heliotron, □; the improved modular heliotron with α_m= -$\alpha_{m'}$=-0.3 and △; the reference modular heliotron).

Particle orbit property is estimated from the minimum B contours. For $\Delta_{gap} \leq 4°$, in MH system with outside-plus/inside-minus modulated windings, the outer magnetic surface nearly agrees with the outer contour of minimum B. However, unlike the conventional heliotron, the central minimum B contour is deformed owing to the bumpy component of magnetic field (m=0/n=10). As Δ_{gap} becomes large, this effect becomes large. The outer magnetic surfaces do not coincide with the minimum B contour even if the magnetic axis coincides the center of minimum B contour.

5. Concluding Remarks

We have analyzed new modular helical system. We have clarified the following points;
(I) A new modular coil system with outside-plus/inside-minus modulation parameters is very effective at producing good magnetic surfaces equivalent to those of LHD.
(II) By means of this coil modularity, the closed helical divertor operations and the good plasma confinement (according to analysis of MHD equilibrium and stability, neoclassical ripple transport and particle confinement) is attained without additional poloidal coils.

In this analysis, we use the single filament coil model. According to recent reactor design of MH system[5], 4~6 degree of gaps between coil center is necessary to construct the super conductor coils. We can propose that MH system of $\Delta_{gap}>4°$ with sufficient divertor space, good plasma confinement and modularity. However, we need the effect of finite size coil on the divertor structure. That is one of future subjects.

Acknowledgment
The authors are grateful to Dr.S.P.Hirshman for permitting to use the VMEC code.

References

[1] Yamazaki K and Watanabe K.Y., Nuclear Fusion **35** (1995) 1289.
[2] Yamazaki K., et al, in Plasma Physics and Controlled Nuclear Fusion Research 1990 (Proc. 13th Int. Conf. Washington, DC, 1990), Vol.2, IAEA, Vienna (1991) 709.
[3] Hirshman S.P., Phys. Fluids **26** (1983) 3553.
[4] Nakamura Y., et al., J. Phys. Soc. Jpn. **58** (1989) 3157.
[5] Yamazaki K., et al., Trans. Fusin Tech., 27 (1995) 260.

RADIAL DISTRIBUTION OF ELECTRON TEMPERATURE IN RF DISCHARGE PLASMA IN TORSATRON MAGNETIC CONFIGURATION WITH ISLAND STRUCTURE.

E.D.Volkov, A.V.Arsen'ev, I.Yu.Adamov, A.E.Kulaga, I.M.Pankratov, T.E.Scherbinina.

Institute of Plasma Physics of the National Science Center "Kharkov Institute of Physics and Technlogy, 310108, Kharkov, UKRAINE

Results of the local measurements of electron temperature and the energy of superthermal electrons in RF discharge plasma of the URAGAN-3M torsatron are submitted. The measurements were carried out taking into account magnetic configuration pecularities. The data were obtained by the analysis of spectra of electron cyclotron emission (ECE) in the frequency range from the first to the second harmonics of the electron cyclotron resonance.

The measurements have been carried out during the URAGAN-3M torsatron (l=3, m=9, R=100 cm, a=12cm) experiments, when the confining magnetic field value on the axis was B=0.47 T. The plasma was created by RF waves in the ion cyclotron range of frequency $\omega<\omega_{ci}$ using the frame type antenna located at r=16 cm of minor radius from the low field side. The RF power input was not higher than 200 kW [1].

The ECE emission was measured by three heterodyne radiometers with spectral resolution $\Delta\omega/2\omega_{CE}$ ~0.038% and threshold sensitivity ~0.5 eV.

The module of Bo value in a space limited by the last closed magnetic surface changes in the range $0.84Bo\leq Bo\leq 1.12Bo$, which corresponds to the range of frequency 11.05-14.72 GHz for the first harmonics and 22.1-29.5 GHz for the second one, respectively. The used radiometers have a working range of frequencies 11.05-14.72 GHz, 22.1-29.5 GHz, 25.7-33 GHz. The radiometer's antennae have the direction diagram width ~7 degrees of the angle. These antennae were placed outside of the torus in two crossections, separated toroidally by the one helical field period. The ECE emission was detected as the O-mode for the fundamental harmonic and the X-mode for the second one.

To estimate the electron density profile the multichord microwave interferometer and single-antenna two-waves microwave reflectometer have been used.

The high reproducibility of plasma parameters in RF-discharges has allowed to measure ECE spectra during all the series of shots. In Fig. 1 the typical temporal evolution of the RF current in the antenna, ECE signal and the averaged chord plasma density are shown.

Fig. 2 shows the dependence of the radiation plasma temperature vs frequency obtained from the calibrated measurements of ECE signal intensity as a function of the emission frequency. The spectrum of emission at $\omega\approx 2\omega_{ce}$ is close to the thermal one, but it has peculiarities in the long-wavelength region $\omega/\omega_{ce}<1,85$ and in the short-wavelength region in

the vicinity of the frequencies $\omega/\omega_{ce}\approx 2.02$ and $\omega/\omega_{ce}\approx 2.1$, respectively. The form of a spectrum at $\omega\approx\omega_{ce}$, apparently, is determined by the emission of superthermal electrons on the periphery of a plasma.

For understanding of these peculiarities it is necessary to address to the analysis of the Uragan-3M magnetic configuration. The measurements made by the triode and luminescent techniques [2] have shown a complex structure of the magnetic surfaces in Uragan-3M. The numerical modeling of magnetic distortions has allowed to get a good agreement of calculated and measured magnetic configurations. In Fig. 3 calculated magnetic surfaces and B-module contours are shown in the cross-section, where measurements of ECE spectra were carried out. Configuration contains magnetic islands at $\iota=1/3$ and $\iota=1/4$. The shift of a magnetic axis from a geometrical axis of helical coils is equal to 5, 5 cm.

In the cylindrical geometry model, the region of a plasma, where ECE being measured, occupies the thin layer along the surface with $|B|=em_e/c\omega$. When antenna receives the ECE signal from the region of a plasma which is perpendicular to the magnetic field, the cross size of this region ΔS should be determined by non-uniformity of the magnetic field $L=B/|\nabla B|$ and the electron temperature Te:

$$\Delta S=3.8\,(T_e/mc^2)B/|\nabla B| \qquad (1)$$

where ΔS is determined in cm. Except the small zone near the singularity point in the Uragan-3M torsatron, where the values of L doesn't exceed 100 cm, and Te<500 eV. According to (1), in this case ΔS is less than 0,4 cm and, therefore, values of T_e and n_e in this zone should be considered as a constant. Near singularity point, where $L\approx 400$ cm and $\Delta S<2$ cm it is necessary to take into account spatial non-uniformity of plasma parameters along the resonance surface: $|B|=$const, the size of which in cross section of a plasma column could reach up to 30 cm.

The radiation temperature of a plasma is determined as

$$T_r(w)=\int \eta(l)T_e(l)\{1-\exp[-\tau(l)]\}dl \qquad (2),$$

where $\eta(l)$ takes into account the antenna direction diagram of along the integration line over the appropriate resonant surface $|B|=$const, and $\tau(l)$ is the optical depth of a plasma in the non-uniform magnetic field.

The maximum of the emission is observed at $|B/B_0|=0,96$, i.e. on the axis of a magnetic configuration. The peculiarity of the spectrum in the short-wavelength region corresponds to the localization of fast electrons with energy about of 1.2 keV on the plasma edge. This is caused by the peculiarities of RF power input into the plasma by the frame type antenna in described experiments [3]. The deviation of a measured spectrum from thermal one (shown in Fig.2 by a thin line in short-wavelength part) corresponds to a local maximum of the electron temperature in magnetic islands.

The calculated electron temperature Te using the Eqs.(1) and (2) is shown in Fig.3. Inside the magnetic surface (1) Te is ≈250 eV, in magnetic islands (2) Te≈290 eV. In the

region between the magnetic surface (3) and chain of islands (2) Te≈240 eV, and between surfaces (3) and (4) Te≈200 eV. In islands at ι=1/3 (marked in Fig.3 by (5)) Te is ≈210 eV. These distributions of Te were kept during all quasistationary state of the RF-discharge and were smoothed through 120-150 ms after RF pulse was switch off.

Acknowledgment. This work was supported in part by International Science Foundation by Grants No. UA 7200 and NSPU 062014.

REFERENCES

[1] E.D. Volkov et al. 14th Int. Conference, Wurzburg 1992, IAEA, Vienna (1993) vol.2, 679.
[2] G.G.Lesnyakov et al. Nuclear Fusion, 32 (1992) 2157
[3] A.I. Lysoivan et al. Fusion Engineering and Design 26 (1995) 185

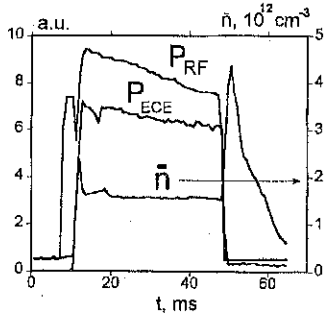

Fig. 1

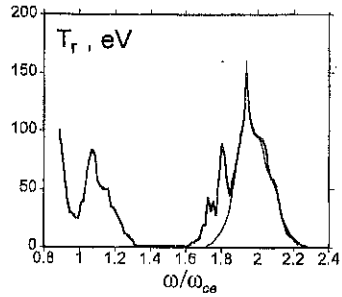

Fig. 2

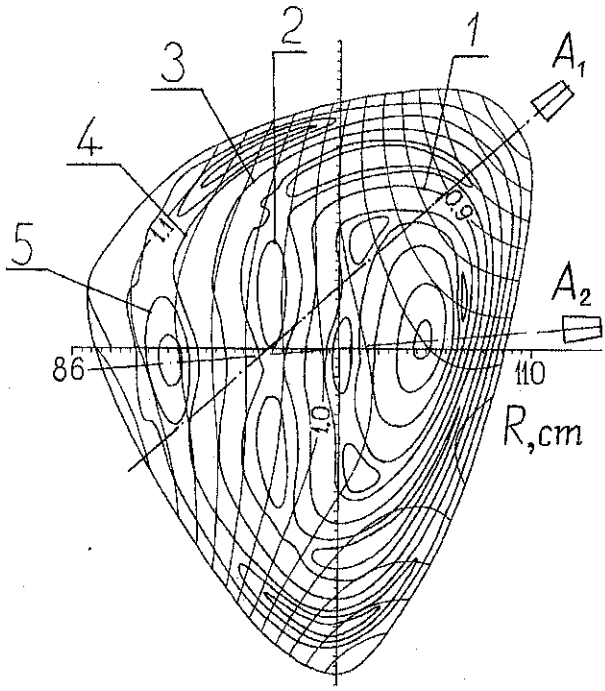

Fig. 3

Studies of Electron Confinement in Heliotron DR using Stellarator Tetrode Method

S.Morimoto, K.Matsushita, S.Iguchi, T.Hori, T.Yamamoto, T.Obiki*
Kanazawa Institute of Technology, Nonoichi, Ishikawa 921, Japan
*Plasma Physics Laboratory, Kyoto University, Uji, Kyoto 611, Japan

1. Introduction

Experimental studies of magnetic structures are very important for helical systems. The stellarator diode (or impedance) method (Fig.1a) has been successfully used for this purpose [1,2]. The stellarator triode method (Fig.1b) has also been used in which current into a transparent screen located in a poloidal plane is measured [3,4]. In both diode and triode methods, low energy (~several x 10eV) electrons are emitted from an electron gun along a magnetic field line and currents into vacuum vessel and screen are measured. Studies of single particle confinement in helical systems are also important because they have rather complicated loss cone structures. Particularly, in fusion reactors, confinement of α particles is crucial to achieve self ignition. From this viewpoint, we have studied behavior of energetic (E<3keV) electrons launched parallel to magnetic field in small helical devices by using the fluorescent target method [5-7].

A new method for studying particle motions in helical systems was developed through the US-Japan joint research between one of the authors (S.M.) and Auburn university torsatron group, and it (which we call "Stellarator tetrode method") was applied to the Compact Auburn Torsatron. In this method, a mesh anode (same potential as vacuum vessel) is set in front of the filament and higher bias voltages are applied between them (Fig. 1c). Thus, we can launch electrons with defined energy and can investigate not only magnetic structure but also particle motions. In the present study, we have applied this technique to the Heliotron DR and investigated dependence of electron confinement on the birth point (inboard or outboard side of the torus), energy and magnetic configuration (magnetic axis position).

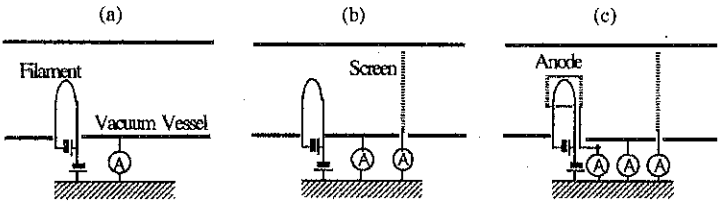

Fig. 1 Principles of stellarator (a) diode, (b) triode methods for magnetic field study and (c) tetrode method for studying electron confinement.

2. Experimental procedure

The Heliotron DR is a small heliotron/torsatron device with a high toroidal pitch number, M and a large aspect ratio (major and minor radii of the helical coil are 90cm and 13.5cm, M=15) [8]. The experiment was carried out at relatively low magnetic field (B=200~500 G), and the base pressure in the vacuum vessel was $p<5\times10^{-7}$torr. Figure 2 shows schematically the experimental arrangement and measuring circuit. The electron gun has a cylindrical mesh anode (stainless steel, 3.7mm in diameter, transparency~50%). We did not adopt usual single-hole anode because we could not determine actual pitch angle of electrons at the anode hole. The filament is tungsten wire (0.1mm in diameter) and negative bias voltages (E=50~800 V) are applied against to the anode. The electron gun is attached to a horizontal port and is movable by 24cm in the major radius direction. Thus, we can study dependence of electron confinement on its birth point. The transparent screen is made of tungsten mesh (transparency, T=93%) and its frame has an almost same shape as the calculated last closed flux surface (LCFS). It is placed in a poloidal cross section 72° apart toroidally from the electron gun and is movable in major radius direction to coincide with magnetic surface. Electrons are emitted in all directions from the filament (current I_T) and a part of them flows into the anode (current I_A). The remaining electrons (current $I_B=I_T-I_A$) pass through the mesh anode. Of which, unconfined electrons flow into the vacuum wall (current I_W). Confined electrons continue to circulate the torus, however, they are finally captured by the screen (current I_S). The relation between I_S/I_B and number of toroidal circulation of electrons, N is expressed by $I_S/I_B = 1-T^N$. For instance, I_S/I_B becomes 0.95 for N=40 and T=93% (present experiment). This means that the value of I_S/I_B should be close to 1 when the electrons are well confined.

3. Results and discussions

The emission current from the gun, I_B is typically 50μA and is equal to about a half of I_T. To examine effect of space charge on electron confinement, I_B was changed from 10μA to 180μA but no significant change was observed. Figure 3 shows dependences of I_S/I_B on electron birth point, R for different bias voltages, E. In case of E=50eV, the ratio I_S/I_B is ~1 when R is betwen 82cm and 97cm indicating a good confinement of electrons. However, it decreases for R<82cm and R>97cm although R is still inside of the

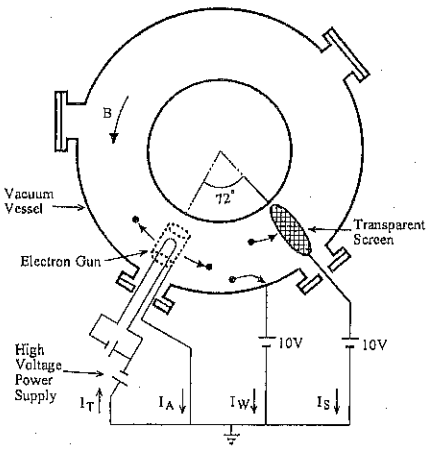

Fig. 2 Experimental set up and measuring circuit.

last closed flux surface (LCFS). This may imply that the flux surfaces are not perfect there. When the bias voltage is increased, confinement of electrons emitted from inner region is detereorated only at the outboard side of the torus.

To understand this result, we have calculated pitch angle distribution of electrons at the mesh anode of the gun assuming a straight filament wire located along the anode axis. Figure 4 shows pitch angle distributions for different bias voltages. When E is 50eV, electrons passing through the mesh anode have velocities almost parallel to the magnetic field. With increase of E, electrons with higher pitch angles are increased and at E=800eV, electrons with pitch angle~90° appear and the distribution becomes more uniform. Thus, observed deterioration of confinement with increase of bias voltage is attributed to increase of high pitch angle electrons which are not confined as predicted theoretically.

Effect of magnetic axis shift on the electron confinement has been studied and the result is shown in Fig.5. If we look at the data of E=800eV (electrons with high pitch angles are included), the radial point R_c where I_S/I_B starts to drop is moved outward when the magnetic axis is shifted inward. This result is consistent with the numerical caluculation [9] which shows that confinement of high pitch angle particles born at the outboard side of the torus is improved by inward shift of magnetic axis.

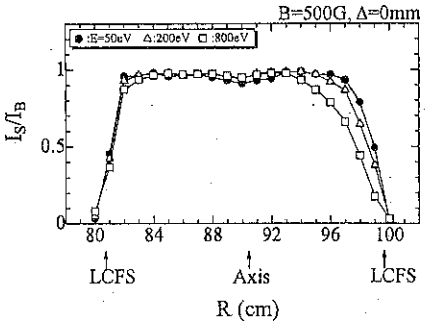

Fig. 3 Normalized screen current, I_S/I_B versus electron gun position, R. Electron confinement gets worse with increase of bias vlotage only at outboard side of the torus.

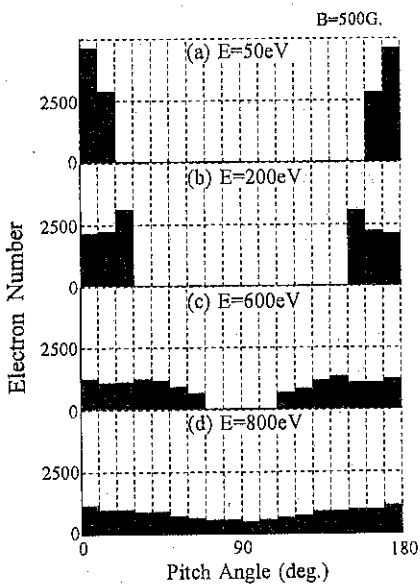

Fig. 4 Electron pitch angle disribution at the anode for different bias voltage, E

4. Conclusion

The stellarator "tetrode method" has been applied to Heliotron DR to study single particle confinement of electrons. With increase of the bias voltage, confinement deterioration has been observed for electrons launched only at the outboard side of the torus. This result can be attributed to increase of electrons which have higher pitch angles. Confinement of those electrons has been improved by inward shift of magnetic axis in consistent with numerical calculation.

Acknowledgments

One of the authors (S.M.) would like to expresss thank to R.F.Gandy, S.F.Knowlton, G.J.Hartwell, H.Lin, T.A.Schneider, D.Pritchard, E.Thomas Jr, M.Owens of Auburn University for fruitful discussions.

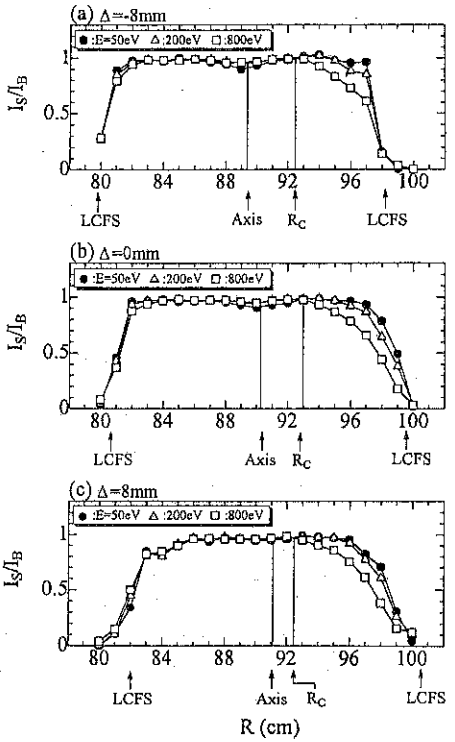

Fig. 5 Effect of magnetic axis shift on I_S/I_B - R dependence. Confinement of 800eV electrons is deteriorated outside $R=R_C$. B=500G.

References

[1] A.V.Georgievskij et al., Proc. of the 12th European Conference on Controlled Fusion and Plasma Physics **9F**, part 1, (1985).

[2] F.Sano et al., Transactions of Fusion Technology **27**, (1995) 206.

[3] A.G.Dikij et al., ORNL Report No. TR-86/29, (1986).

[4] G.J.Hartwell et al., Review of Scientific Instruments **59**, (1988) 460.

[5] S.Morimoto et al., Transactions of Fusion Technology **27**, (1995) 202.

[6] S.Morimoto et al., Japanese Journal of Applide Physics **34**, (1995) L256.

[7] R.F.Gandy et al., Physics of Plasmas **2**, (1995) 1270.

[8] S.Morimoto et al., Nucl. Fusion **29**, 1697 (1989).

[9] K.Hanatani, Proceedings of the 1st International Toki Conference on Plasma Physics and Controlled Nuclear Fusion, (1990) 45.

RESISTIVE STABILITY STUDIES IN THE TJ-II FLEXIBLE HELIAC

R.Sánchez, L. García, J.A.Jiménez[1]

Universidad Carlos III, 28911 Madrid, SPAIN
[1]Asociación EURATOM-CIEMAT, 28040 Madrid, SPAIN

ABSTRACT

Ballooning stability analysis is carried out on the standard TJ-II [1] configuration. Both ideal and resistive ballooning modes have been related to the deterioration of confinement at relatively modest value of ß in tokamaks [2], and should also be important in stellarators. The flexibility of TJ-II allows for variation of the key stability parameters (<ß>, magnetic well depth and ι) just by modifying the ratio of the current in the helical coil to that flowing in the circular coil, which makes this device specially suitable for this kind of analysis. Upper confined-<ß> limits to both ideal and resistive ballooning instabilities are numerically found for TJ-II equilibria with linear pressure profiles.

Main features of TJ-II: TJ-II is a four period flexible heliac device (R_o=1.5m, a=0.2m, B_o= 1T) now in an advaced state of construction and scheduled for operation in 1997 at CIEMAT. It has a built-in capacity of independently varying its configuration parameters, namely rotational transform (going from 0.96 to 2.5 at axis) and magnetic well depth (ranging from -1% to 6%)

Resistive ballooning equations: We derive the ballooning stability criterion following Ref. [3]. Boozer straight-line magnetic coordinates (s,θ,ζ) are used [4]. First, a two-scale perturbative analysis of the first order resistive MHD equations for a small departure from equilibrium is done, obtaining three equations for the perturbed parallel magnetic perturbation $\mathbf{B}\cdot\boldsymbol{\delta}\mathbf{B}$, and the potentials ϕ and a, from which the divergence-free first order terms of displacement vector $\boldsymbol{\xi}$ and magnetic field $\mathbf{B}$ are obtained.We apply then the ballooning transformation [5], which leads to a couple of second order ordinary differential equations along the magnetic line for F and D, the ballooning transforms of ϕ and $\mathbf{B}\cdot\boldsymbol{\delta}\mathbf{B}$-$\mu_o p'\partial_\alpha\phi$:

$$\frac{d^2D}{dy^2}=\left(\frac{g}{\psi'^2}\right)\left[\gamma^2\left(1+\frac{2B^2}{\Gamma p\beta_o}\right)+\gamma^{-1}\left(\frac{n^2}{S}\right)\left[\gamma^2\vec{C}^2+\beta_o p'\varepsilon^2\frac{B^2}{\psi'^2}\left(\kappa_s+\kappa_\alpha\iota'(y-y_o)\right)\right]\right]D+$$
$$+\left(\frac{gB^2}{\psi'^2}\right)\left[\frac{4\gamma^2}{\beta_o p'}+\gamma^{-1}\left(\frac{n^2}{S}\right)\beta_o p'\varepsilon^2\frac{1}{\psi'^2}\right]\left(\kappa_s+\kappa_\alpha\iota'(y-y_o)\right)F$$

$$\frac{d}{dy}\left(\frac{\bar{C}^2}{1+\gamma^{-1}\left(\frac{n^2}{S}\right)\bar{C}^2}\frac{dF}{dy}\right)=\left(\frac{gB^2}{\psi'^4}\right)\left[\gamma^2\frac{\psi'^2\bar{C}^2}{B^2}-\beta_o p'\varepsilon^2\left(\kappa_s+\kappa_\alpha \iota'(y-y_o)\right)\right]F-$$

$$-\left(\frac{gB^2}{\psi'^4}\right)\beta_o p'\varepsilon^2\left(\kappa_s+\kappa_\alpha \iota'(y-y_o)\right)D$$

Coordinate α is defined as $\theta-\iota\xi$. .The eigenvalue γ is normalized to the inverse Alfvèn time, κ_j are the normal ($j=s$) and geodesic ($j=\alpha$) components of curvature, $\varepsilon=R_O/a$, $n^2\bar{C}^2\approx k_\perp^2$, S is the quotient of resistive to Alfvèn time, and n is the poloidal number of the mode. B stands for the magnetic field, $\sqrt{g}$ for the jacobian, p for pressure, ψ for the toroidal flux and Γ for the compressibility factor. These equations must be solved separately on all magnetic surfaces subject to boundary conditions such that $F,D\in L^2(-\infty,+\infty)$, thus guaranteeing convergence. If any positive real γ exists on any surface, the system is ballooning unstable.

Incompressible limit: We will focus our study in the incompressible ($D\to 0$) limit:

$$\frac{d}{dy}\left(\frac{\bar{C}^2}{1+\gamma^{-1}\left(\frac{n^2}{S}\right)\bar{C}^2}\frac{dF}{dy}\right)+\beta_o p'\varepsilon^2\left(\frac{gB^2}{\psi'^4}\right)\left(\kappa_s+\kappa_\alpha \iota'(y-y_o)\right)F-\gamma^2\frac{g\bar{C}^2}{\psi'^2}F=0$$

The physical interpretation of the three competing terms is: the first one takes into account the stabilizing effect of magnetic line bending and is diminished by resistivity; the second term is the destabilizing unfavourable curvature-pressure gradient interaction term, which drives the instability and increases with <ß>; the last term is the inertia. The ideal ballooning equation ($S\to\infty$) can be posed as a Stürm-Liouville eigenvalue problem [6] defined on $[0,+\infty)$ for the eigenvalue $\lambda=-\gamma^2$, which has infinetely many real eigenvalues $\lambda_0<\lambda_1<\lambda_2<\cdots<\lambda_k<\cdots\infty$. Ideal stability is tested just by finding the sign of the lowest eigenvalue λ_0. If positive, γ must be imaginary and the system oscillatorily stable; if negative, γ must be real, and the system unstable. The resistive ballooning equation can be treated as a perturbation of the ideal problem for small resistivity, leading to a positive real contribution if γ_0 is real and a negative one if γ_0 is imaginary. Ideal ballooning instability is then enhanced by resistivity, whereas ideal oscillatory modes are damped away. Ideally stable equilibria may anyway be destabilized in the presence of resistivity by new purely resistive unstable modes, that will push the upper confined-<ß> limit further down. These modes have a characteristic time scale which lies between the Alfvèn and resistive times, whilst ideal time scale lies near Alfvèn time.

Shooting code: To numerically study ballooning stability we use a shooting code for the eigenvalue which integrates the two-point boundary-valued ballooning equations on any given surface. It works for both compressible or incompressible perturbations, and either ideal or

resistive solutions can be computed. Precalculated VMEC [7] 3D-equilibria must be supplied. The average confined ß is defined as the ratio of mean-pressure to magnetic energy at the axis.

TJ-II results: The standard vacuum TJ-II configuration main features are described in Table I. Different configurations can be achieved by modifying the ratio of the circular coil current (I_{cc}) to the helical coil current (I_{hc}), changing both rotational transform and magnetic well depth. For stability analysis we use different VMEC equilibrium profiles, corresponding to average-ß values ranging from 0% to 2.0%.

TABLE I. TJ-II *STANDARD* CONFIGURATION

ι/4	I_{cc}(kA)	I_{hc}(kA)	m.well	a(m)
0.365	233.8	96.2	2.2%	0.172

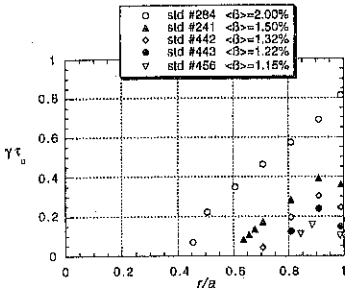

Fig. 1 Radial unstable ballooning modes location for equilibria with 1.1% ≤ <β> ≤ 2.0%

Eigenvalues obtained for ideal ballooning unstable equilibria are shown in Fig. 1,where it can be seen that unstable modes concentrate at *r/a* ≥0.5, where the curvature is most unfavourable. For equilibria with <ß>≤1.0%, all surfaces are stable to ideal modes. This limit is stricter than Mercier criterion [8,9], which gives ideal stability to perturbations localised along the line for <ß> <1.3%, as can be seen in Fig. 2.

In order to test the effect of resistivity we set $S=10^5$, and n=12. The ratio of the resistive to the corresponding ideal eigenvalue increases with S. As it was clear from perturbative analysis, non-zero resistivity makes these modes increasingly unstable. The ratio tends to unity as we approach the ideal limit. It can also be checked that stable modes are damped away in the presence of resistivity.

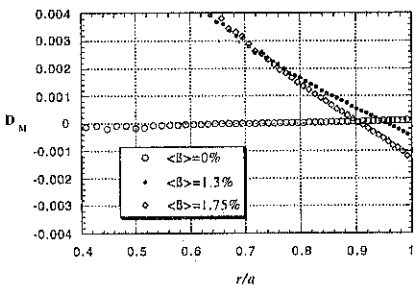

Fig.2 Mercier criterion predicts stability for <β> < 1.3% in TJ-II standard configuration.

Resistivity reduces further down the confined-<ß> limit imposed by ideal ballooning instabilities. In Fig.3 unstable purely resistive modes are plotted for the ideal ballooning stable TJ-II equilibrium with <ß>=1.0%. These modes destabilize all equilibria with <ß> ≥ 0.5% for TJ-II standard configuration.

Similar stability calculations are being done for other configurations of TJ-II (high-ι, deep and shallow magnetic well,etc.), and also for other devices such as TJ-IU, LHD, etc., and might also have some applications in future stellarator designs.

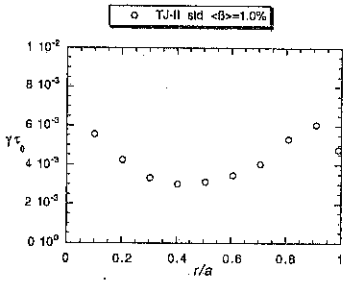

Fig.3 Purely resistive unstable ballooning modes in ideally stable TJ-II equilibria with <ß>=1.0%

CONCLUSIONS

We estimate the upper confined-<ß> limit stable to ballooning instabilities in TJ-II standard configuration. The result for ideal modes is instability for <ß> > 1.0% . This limit is stricter than the limit set by Mercier criterion, which is about 1.3%. Resistive ballooning modes reduce this limit further down, so that all equilibria with <ß> > 0.5% are unstable. Although these limits may be considered too severe, as incompressible perturbations are assumed, more realistic ones can be calculated using the compressible version of the code. Such a study is under way.

REFERENCES

[1] C.Alejaldre et al., *Fusion Technol.* **17** (1990) 131

[2] B.A.Carreras et al., *Phys. Rev. Lett.* **50** (1983) 503

[3] D. Correa-Restrepo, Z. *Naturforschung* **37a** (1982) 848

[4] A.H.Boozer, *Phys.Fluids* **23** (1980) 904

[5] J.W.Connor, R.J.Hastie and J.B.Taylor, *Proc. Roy. Soc. Lond. A.* **365** (1979) 1

[6] '*Boundary and eigenvalue problems in mathematical Physics*', H.Hagan, New York 1966

[7] S.P.Hirshman and O. Betancourt., *J. Comput. Phys.* **96** (1991) 99

[8] Mercier, C., *Nuclear Fusion* **1** (1960) 47

[9] Green J.M., Johnson J.L., Plasma Phys. **10** (1968) 729

Study of the power balance in the W7-AS stellarator by means of 2-dimensional limiter thermography and bolometry

R. C. Wolf, A. Herrmann, R. Brakel, Y. Feng, A. Elsner, L. Giannone, P. Grigull, D. Hildebrandt, F. Sardei, and the W7-AS team

Max-Planck-Institut für Plasmaphysik, EURATOM Association, Garching and Berlin; Germany

1. Introduction

Thermography is used in both tokamaks and stellarators to monitor the thermal load of first wall elements. At W7–AS a 2–dimensional infrared (IR) sensitive camera has been installed to observe the complete surface of one of the limiters.

Depending on the rotational transform ι, the plasma of W7–AS is limiter or, due to the formation of natural islands, separatrix bounded ($\iota < 0.4$ or $\iota > 0.5$, respectively). In the latter case the plasma edge island topology is of particular interest for future stellarators, which will utilize natural islands in divertor configurations [1]. The limiter temperature distribution shows a clear distinction between $\iota < 0.4$ and $\iota > 0.5$. For ι in the vicinity of 0.565 a ι–scan has been performed, where the strike point separation, inferred from the temperature distribution, is compared to code calculations of the magnetic field geometry.

By solving the heat conduction equation inside the limiter, the total power deposited on the limiters P_{lim} is derived, which, similarly to the calculation of the radiated power P_{rad}, assumes toroidal symmetry. For NBI and ECR heated discharges and ι ranging between 0.34 and 0.56 the total power loss $P_{rad}+P_{lim}+dW_{dia}/dt$ is compared to the input power.

2. Diagnostics

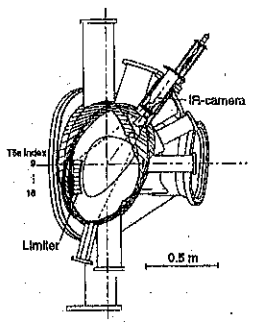

Fig. 1.: The toroidal view of W7–AS shows a cross-section of the IR-camera and the limiter observed. Viewing cone and the approximate plasma shape are also indicated. The spatial resolution of the camera is 4 mm, compared to the limiter dimensions of 120×231 mm².

The main component of the limiter thermography diagnostic is a 2-dimensional IR-camera, consisting of 120×160 InSb pixels. The IR-camera is calibrated allowing absolute surface temperatures to be derived. The temperature resolution achieved is of the order 1 K. The viewing geometry is illustrated in fig. 1. The limiter observed is one of nine inboard limiters (one is missing for technical reasons), symmetrically arranged according to the 5-fold toroidal symmetry of W7-AS. Corresponding to the 5 field periods, W7–AS consists of 5 modules. Each module contains two limiters toroidally displaced, but poloidally forming a continuous limiter. Each limiter is made of eight separate CFC tiles. Thus, the tile indices, running from 1 to 16 for a corresponding pair of limiters, denote different poloidal locations, while the modules denote

the toroidal locations. The limiter surface contour has been designed to achieve a constant power deposition for the standard configuration ($\iota = 0.34$) and a power flux decay length of 1 cm. The limiter tiles are only at the rear side thermally coupled. Thus, unless the heat has already propagated to the back of the limiter, the tiles can be treated independently in the heat conduction calculation.

Two bolometer arrays, each consisting of 30 sight lines, measure the radiation emitted by the plasma. The total radiated power P_{rad} is derived from the bolometer signals, taking the plasma shape and the relative position of the sight lines to the plasma into account.

3. Calculation of heat flux

The heat flux onto the limiter surface is calculated from the time evolution of the surface temperature, solving the heat conduction equation by means of the finite differences method [2] in a two dimensional slab geometry. This requires two simplifications: First, performing the calculations for each of the eight tiles independently, the problem is reduced to two spatial dimensions by averaging the temperature along the poloidal dimension of each tile. Consequently, the calculated heat flux is a function of the toroidal surface coordinate of the limiter only and the poloidal dependence is considered only in the change from tile to tile. Secondly, it is assumed that the depth, which the heat penetrates into the limiter, is small compared to the curvature radius of the limiter surface, thus allowing the curvature of each tile in toroidal direction to be neglected. By integrating the resulting heat flux over the tile surface, the power reaching the limiter tiles is calculated and subsequently, by integrating over the discharge duration, the energy.

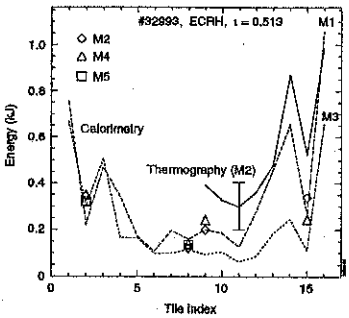

Fig. 2.: Comparison of thermography with calorimetry. The energy deposited on the limiters is plotted versus tile index for the different modules M1 to 5.

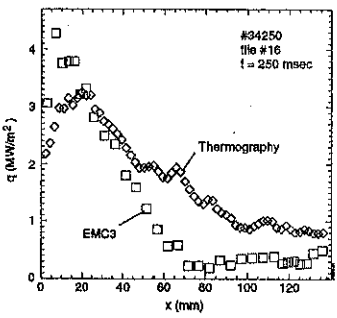

Fig. 3.: The heat flux as a function of the toroidal surface coordinate is illustrated for a ι=0.564 discharge, where the heat flux is strongly localized at tile #16.

To validate the heat flux calculation, the energy determined by thermography is compared with the results from the limiter calorimetry (fig. 2). Thermocouples, one in each limiter tile, measure the difference between the temperature before and 5 sec after the shot from which the energy is inferred. Two main conclusions can be drawn: (1) The calorimetry data show that at least the energy averaged over a whole discharge is approximately toroidally symmetric. (2) Generally, the thermography results are consistent with calorimetry. However, in particular at lower energies, thermography tends to give higher values. This could have several explanations:

On the part of calorimetry the finite heat resistance between limiter tile and thermocouple and, if after 5 sec because of the energy loss at the rear plate no temperature equilibrium is reached in the limiter, the method used by calorimetry to derive the energy could lead to lower energies. On the part of thermography a known problem is the reflection of IR-radiation from surrounding vessel components, which causes an apparent increase of the heat flux in form of a low level offset.

The 3D Monte Carlo code EMC3 (Edge Monte Carlo 3D [3] coupled to the transport code EIRENE), which has been developed to study transport in island divertors, is used to model the heat flux. It solves a simplified version of the 3D time independent plasma fluid equations with islands, private flux region and target plates (here limiters) modelled in their real 3D geometry. In fig. 3 a comparison between modelled and measured heat flux is shown. Although the toroidal distributions are to some extent different, the measurement confirms the modelled heat flux in so far as the same strong localization along the island fan with the largest connection length is observed, which collects a large power fraction crossing the last closed flux surface.

4. Results and discussion

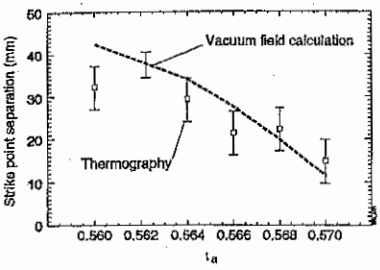

Fig. 4.: ι—dependence of strike point separation. The thermography results are compared with code calculations of the vacuum magnetic field.

As the spatial temperature distribution reflects the heat flux onto the target, the strike point locations should be related to the magnetic field topology of the island. In fig. 4 the dependence of the strike point separation on ι is shown. The results obtained by thermography are compared with the strike point separation derived from the vacuum magnetic field, which has been calculated by the GOURDON-code. Within the bounds of a pure vacuum field calculation, without considering diffusion processes and finite β effects, the thermography measurements agree with the vacuum field values. In particular, the decrease of the strike point separation with increasing ι is confirmed.

Two examples of the temporal evolution of the different power contributions are shown in fig. 5. In general, as in the examples, during the initial phase of the discharge the total power loss $P_{total}=P_{rad}+P_{lim}+dW_{dia}/dt$ is lower than the input power. Later the power is well balanced. Possible explanations could be: (1) At the beginning of a discharge, when the density is still low, the neutral pressure in the core plasma of W7–AS may be sufficient to cause energy losses by charge exchange, which in the power balance have not been considered. This effect could be enhanced by strong gas puffing, usually employed at the beginning of a discharge, which also could be responsible for toroidal asymmetries. (2) As the power decay length increases with decreasing density, the heat flux to first wall components other than the limiters is stronger at low densities. In case of NBI the power deposited has to be calculated, since depending on the density it deviates strongly from the power applied. The investigation of a wide range of discharges shows, that in general $P_{lim}+P_{rad}+dW_{dia}/dt$ underestimates P_{in}. Depending on ι and the type of heating, the mean deficiency from balanced power contributions ranges from 10 to 25%.

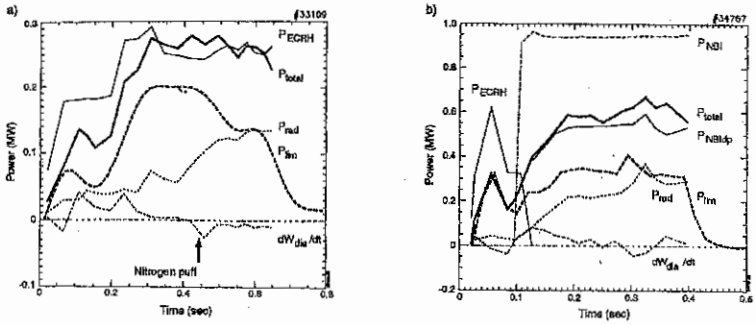

Fig. 5.: Temporal evolution of power. a) ECR heated, ι=0.344, n_e=4×10^{19}m^{-3} discharge with nitrogen puff [4]. b) NBI heated, ι=0.564, n_e=5×10^{19}m^{-3} discharge. P_{NBI} denotes the NBI power applied (U×I) and P_{NBIdp} the part deposited.

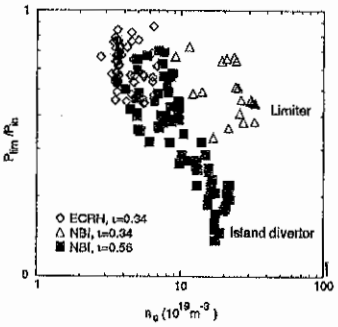

Fig. 6.: Proportion of input power which reaches the target (limiter) vs line averaged density for limiter (ι = 0.34) and separatrix (ι = 0.56) plasmas.

A relation between the power balance and plasma density or energy content has not been found, indicating that the assumption of toroidal symmetry is generally valid.

Fig. 6 shows the relation between the line averaged density and the proportion of the input power reaching the target (limiter). For densities above 1×10^{20} m^{-3} limiter and separatrix configurations show a clear distinction: For ι = 0.56 P_{lim}/P_{in} drops faster, i.e. the radiated power fraction rises faster, than for ι = 0.34. This observation is consistent with probe and H_α measurements, which for n_e=1.5×10^{20} m^{-3} show a reduced particle flux close to the target, indicating detachment [5].

5. References

[1] F. Sardei, et al., 12th International Conf. on Plasma Surface Interactions in Controlled Fusion Devices, Saint Raphael, France, (May 1996)*

[2] A. Herrmann, et al., Plasma Phys. Control. Fusion 37 (1995) 17

[3] Y. Feng, et al., 12th International Conf. on Plasma Surface Interactions in Controlled Fusion Devices, Saint Raphael, France, (May 1996)*

[4] R. Brakel, et al., "Radiative boundary studies in the Wendelstein 7–AS stellarator", this conference

[5] P. Grigull, et al., 12th International Conf. on Plasma Surface Interactions in Controlled Fusion Devices, Saint Raphael, France, (May 1996)*

* to be published in J. Nucl. Materials

GENERATION OF SEVERAL NON-THERMAL ELECTRON POPULATIONS IN TJ-IUpgrade TORSATRON

F. Medina, L. Rodríguez-Rodrigo, F. Castejón, M. A. Ochando and TJ-IU Team.
Asociación Euratom-Ciemat para Fusión
Av. Complutense 22, 28040 Madrid.

Introduction

Different behaviours of high energy electrons have been observed in TJ-I Upgrade torsatron (l =1, m=6, R=0.6 m, $\bar{a}$ ≈ 0.1 m, B = 0.5÷0.7 T) as a function of the magnetic configuration. In this device the standard magnetic configuration is characterised by a rotational transform, ι, of about 0.2, with almost negligible shear, and magnetic well depth of 6.9%. TJ-I U plasmas are produced by ECRH (X-mode, 2nd harmonic, P ≈ 90÷250 kW, pulse length ≈ 25 ms, 37.5 GHz [1]) and typical line average electron densities achieved, n_e, are about 0.2-0.5 x 10^{19} m^{-3} and electron temperature, T_e, ranges between 100-200 eV. For these parameters, ray tracing calculations predicted single pass power absorptions of the order of 20%, and therefore absorption by suprathermal electrons at high magnetic field was expected. To characterize the non-thermal electron populations, X-ray spectra have been recorded using Si(Li) (1-30 keV) and NaI(Tl) (over 20 keV) detectors. In the previous campaign, the high hard X ray fluxes, related to runaway electrons generated during magnetic field ramp-up and down, have been controlled using appropriate gas puffing rates [2]. Nevertheless, during ECR plasma production and heating, from moderated to high hard and soft X ray fluxes are also detected. It has been found a correlation between the detailed time evolution of the X ray signals and the average density and total plasma current which depends on the magnetic structure, namely the rotational transform and the magnetic ripple.

Experimental results and discussion

For the experiments presented here, the magnetic configuration and plasma shape were varied within the intervals: $0.136 < \iota(0) < 0.31$ and $0.10 < \bar{a} < 0.12$ m. The used Si(Li) detector views a plasma radial chord at a toroidal angle $\Phi = 90^{\circ}$ through a beryllium filter of 105 μm, while the NaI(Tl) detector looks at the plasma, either almost tangentially or near perpendicularly at $\Phi = 30^{\circ}$, through a glass window. Two additional NaI(Tl) detectors working in current mode are monitoring the average total hard X ray (HXR) flux. To obtain high energy electrons spectra we have accumulated data from series of repetitive discharges for each configuration. Special care has been taken to supress the runaway electrons generated during the field ramp-up, in order to try to investigate the characteristics of fast resonant electrons. For the discharges analysed here, electron densities and temperatures of the thermal population are of the order of 0.3 to 0.6 x 10^{19} m^{-3}, and around 100 eV, respectively. In figure 1 a typical energy spectrum of suprathermal electrons populations generated for the magnetic

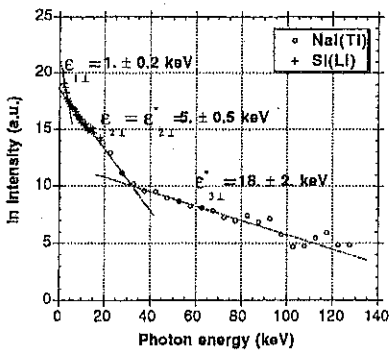

Figure 1. Full range perpendicular bremsstrahlung spectrum from plasmas with ι(0) ≈ 0.21. The characteristic energies for the suprathermal electrons are denoted by ε (obtained with the NaI) and ε (from the SiLi detector).*

configuration with ι(0) ≈ 0.21 is presented. It is remarkable the good agreement between the two detectors data for this configuration which lead to deduce the same characteristic electron energy from the photons lying in the overlaping detection region. But it must be mentioned that considerable toroidal asymmetries have been found for some of the configurations studied, in particular for the one with ι(0)= 0.136. Table I summarises the evaluated suprathermal electron energies for series of discharges with the indicated magnetic configuration. In the case of the highest rotational transform, to obtain spectra with the NaI detector was necessary to accumulate data from a high number of discharges due to their low intensity emission. For that magnetic configuration, thermal plasma confinement is the poorest achieved in this device, probably because the value of the rotational transform near the axis is close to 1/3.

energy (keV)	ι(0)= 0.31	ι(0)= 0.21	ι(0)= 0.16	ι(0)= 0.136
$\varepsilon_{1\perp}$	n.a.	1	1	1
$\varepsilon_{2\perp}$	n.a.	4	9	30
$\varepsilon^*_{2\parallel}/\varepsilon^*_{2\perp}$	n.a. / 6	5 / 4	5 / 4	8 / 6
$\varepsilon^*_{3\perp}$	100	20	16	200

Table I. Characteristic suprathermal electrons energies for several magnetic configurations. As in figure 1, (*) refers to slopes evaluated with the NaI detector. For those, the symbol ⊥ means near perpendicular detection at the gyrotron entrance port. (n.a.=non available)

As mentioned above, single pass absoption of the EC wave front by electrons at the location of the resonant field (0.67 T) is only about 20% of the input power and therefore notable non localised multipass absoption is expected [3]. Under these conditions, in the first pass, an important amount of microwave power is available for faster resonant electrons at the high field side of the machine, which might absorbe a certain fraction of this initial input power. Evaluations of the energy contained in the high energy tails from the bremsstrahlung intensity spectra would permit to estimate the relative density of these suprathermal electrons and their possible effect on the global plasma performance [4]. In figure 2 it can be seen that the second electron tail for shots with ι(0)= 0.14 may contain up to 15 times more energy than its equivalent in discharges with ι(0)= 0.21. Besides, we have compared the time evolution of

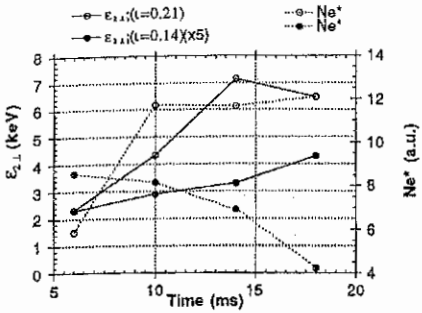

Figure 2. Time evolution of density and characteristic energy, $\varepsilon_{2,\perp}$, of the second suprathermal population for the two indicated configurations.

thermal parameters for representative discharges of the studied series with the behaviour of fast electrons. It has been found a tight correlation between the HXR flux and plasma density. Figure 3 (a and b) illustrates this fact: for a given configuration, the HXR flux increases as electron density does until the plasma transparency falls to cero, then a sudden drop in this signal is accompanied by drops in all of the signals from thermal monitors. This means that suprathermal electron population is built up almost at the same time as the thermal one by direct absorption at the high field side. When density cut-off is reached no longer absorption either by thermal or suprathermal electrons takes place. On the other hand, when from stable conditions the density is diminished, an increase in the flux of high energy photons can be detected while the signals of the rest of the monitors drastically fall. This fact resembles the standard "tokamak like" behaviour of high energy electrons related to the decrease of collisionality, but in present case the increase of the HXR flux is highly enhanced due to the absorption by fast resonant electrons as plasma transparency increases.

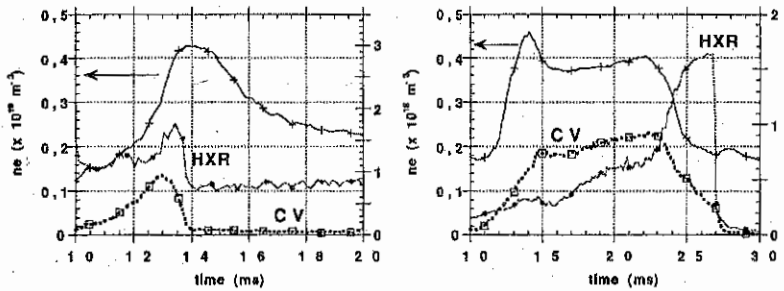

Figure 3. Time evolution of the hard X ray flux signal compared to the mean electron density evolution. a) cut-off density is reached at about 13.5 ms and b) gas puff is shut donwn at 21 ms. For comparison with thermal signals, the 227.1 nm C V line emission is also shown.

The Rogowski coil and all of the vertical flux loops signals reflect the presence of fast passing electrons and substantial changes with the magnetic configuration are observed in the measured total plasma current. There is a clear correlation between plasma current and HXR flux signals: the more intense the HXR flux, the less positive the plasma current. Identical

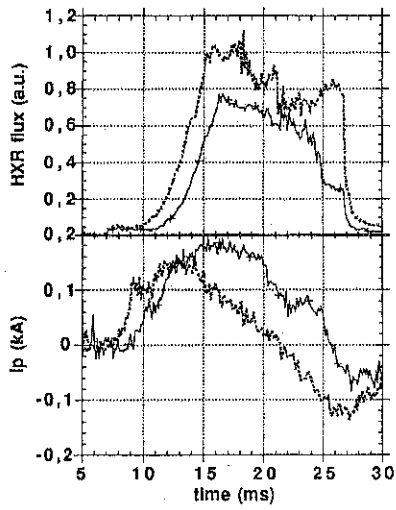

Figure 4. Hard X ray flux and plasma net current for two shots with the same magnetic configuration, ι(o)= 0.16, and different densities: ne (dotted lines) and 1.1 ne (solid lines).

relationship is observed when the hard X ray flux is modified as a result of minor changes in electron density for the same magnetic configuration (see figure 4).

A possible explanation for this observation could be related to the fraction of trapped particles corresponding to each magnetic configuration. In our device, the magnetic ripple near the plasma center decreases as plasma is moved inwards (as iota decreases) and therefore the fraction of trapped particles diminishes [5]. It is well known that the efficiency of the current generated by the EC wave front decreases with the number of trapped particles present in a plasma and that this ECCD could lead to a change in the net plasma current sign [6].

As will be discussed elsewhere [7], the present studies in TJ-I Upgrade torsatron are of relevance for TJ-II [8] when we will explore plasma properties in the low density region of its operational domain. In this sense, it is worthy to study the characteristics of the high energy tails as a function of electron density and input power and try to establish whether or not fast electrons can account for an important amount of the absorbed power. Also the possible occurrence of parallel/perpendicular asymmetries in the plasma energy content will be investigated.

References

1- Ascasíbar E. et al, Proceedings of the 15th IAEA Conf. on Plasma Physics and Controlled Nuclear Fusion Research in Seville (September 1994). **1**, 749, IAEA Vienna (1995).

2- Ascasíbar E. et al, Transactions of Fusion Technology **27**, 198, (1995).

3- Alejaldre C. et al, Proceedings of the 14th IAEA Conf. on Plasma Physics and Controlled Nuclear Fusion Research in Würzburg (September 1992) **2**, 665, IAEA Vienna (1993).

4 - Medina F. et al, to be published.

5 - Tribaldos V., private comm.

6 - Castejón F. et al, Physics of Fluids **4**, 3689 (1992).

7 - TJ-I U Team, submitted the 16th IAEA Conference on Plasma Physics and Controlled Nuclear Fusion Research in Montreal (September 1996)

8- C. Alejaldre et al, Fusion Technology **17**, 131, (1990).

ELECTRON CYCLOTRON EMISSION MEASUREMENTS IN THE TJ-I Upgrade TORSATRON

E. de la Luna, D.K. Akulina*, T. Estrada, J. Sánchez, V. Tribaldos, Yu.I. Nechaev*,
A. López-Fraguas and E. Ascasíbar
Asociación EURATOM-CIEMAT, 28040 Madrid, Spain
*General Physics Institute, Russian Academy of Sciences, Moscow, Russia

Introduction

A multichannel heterodyne radiometer has been used to measure the spectrum of the Electron Cyclotron Emission (ECE) in the TJ-I U Torsatron [1] (l = 1, m= 6, R= 0.6 m, a ≈ 0.1 m, B= 0.5 ÷ 0.7 T) during ECRH heating (37.5 GHz, 2nd Harmonic X-mode). In order to avoid the perturbation due to the ECH radiation, the radiometer was installed at a toroidal location where the magnetic field is higher than the resonant field for the heating position. The system operates with heterodyne detection and a 4 channel filter bank, which can be shifted along the frequency range of interest (40-44 GHz) by changing the Local Oscillator frequency.

The transmission line includes approximately 6 m of Ka band fundamental waveguide and a special filter to reject the residual 37.5 GHz gyrotron radiation. The antenna uses a parallel plate lens in order to provide a focused beam. A Macor viewing dump is installed to prevent signals from other parts of the optically thin plasma reaching the antenna.

Operating with a RF bandwidth of 250 MHz each channel and a video band of 20 kHz the sensitivity of the radiometer was 0.2 eV. Absolute calibration of the radiometer was achieved by using a hot-cold source (switching between room temperature and liquid Nitrogen). Also a 1.5 eV noise tube was used for on-line calibration of the front end and IF system.

Experiments:

Fig.1 shows the emission spectra (radiative electron temperatures) obtained for a typical TJ-IU discharge (200 kW heating power, iota (0)= 0.3, average electron density: 4×10^{12} cm^{-3}). According with multi-filament magnetic field calculations the thermal plasma emission for this configuration is expected to cover the range 42 - 44.7 GHz, the plasma centre corresponding to 43 GHz. In contrast, we see a profile which extends with high intensity to EC frequencies outside the plasma. Second harmonic X-mode ECRH at low density has been widely considered as a way to generate significant populations of suprathermal electrons whose EC emission appears downshifted to lower frequencies. As we will see in the following analysis, the spectrum on fig.1 includes two components, corresponding to the

thermal and the nonthermal emission, which exhibit different behavior with the changes of the plasma parameters (density, injected power).

A first test has been carried out by ECRH modulation. By modulating the power at 1 kHz a similar oscillation of the electron temperature is induced along the whole ECE spectrum (see fig.2). Even though the window between the energy confinement time on TJ-I U (0.3-0.5 ms) and the collision interval (50 μs due to the low densities) is not wide enough to allow clean interpretation of the experiments, a clear origin of the phase in the spectrum modulation is observed for 43 GHz, with moderate phase delays towards higher and lower frequencies. This result supports the idea of central heating, since the 43 GHz radius corresponds to the resonance (37.5 GHz) position at the toroidal plane were the ECH is being launched.

Power scan experiments (see fig.3) have shown a clear difference between the spectral region 42-45 GHz (assumed thermal emission) and 40-42 GHz (possible suprathermal emission). The thermal region shows a nearly linear increase of the radiative temperature with the increasing power. On the other hand, the nonthermal emission shows a much faster rise, mainly around 41 GHz (factor 1.7 when going from 130 to 160 kW and 2.2 from 130 to 200kW). Also clear differences are seen in the time evolution of both emissions during the initial density ramp-up: the nonthermal emission achieves the maximum intensity clearly earlier than the thermal one.

Analysis of the emission

As we have seen, there is a well defined different behavior between the 42-44.5 GHz frequency range and the emission bellow 42 GHz, which is assigned to downshifted non-thermal emission. An estimation of the resonant energy at the plasma edges and the axis is shown on fig.4, the maximum of the suprathermal emission appears around 41.5 GHz, which corresponds to an energy of the central electrons of about 20 keV. This value is in good agreement with the energies obtained from the X-ray measurements [2].

Once we are confident with the existence of the thermal and nonthermal emission, we can take the thermal part to derive the actual electron temperature in TJ-I U. When the plasma is optically thin, like in our device, the radiative temperature is no longer the electron temperature. We have used a method [3] to reconstruct the electron temperature profile from the ECE radiative temperature. The idea behind this method is very simple: if the detected emission, for a given frequency, comes from a *small* region $\Delta l = l_2 - l_1$ inside the plasma, we can make the assumption that the electron temperature is constant in this region $T_e(l) = \text{const.}\ (l_1 \le l \le l_2)$. So if we assume that the electron distribution function is Maxwellian then equation

$$T_{rad}^{exp}(\omega) - (2\pi)^3 \left(\frac{c}{\omega}\right)^2 \int_{l_1}^{l_2} dl\ \beta(\omega, n_e(l), T_e) \exp\left[-\int_{l_1}^{l} dl'\ \alpha(\omega, n_e(l'), T_e)\right] = 0\ ,$$

is an implicit equation for the electron temperature. Following this idea we have developed a numerical code, called RECCE, that for a given frequency ω calculates the position of the emitting electrons $l_1 < l < l_2$ and computes the electron temperature that makes the radiative temperature equal to the observed ECE temperature. The RECCE code solves this equation for each frequency, and thus gives an average value for the electron temperature over Δl.

The main limitations of this procedure are: (1) we have assumed that the electron distribution function is Maxwellian. This means that it is completely described by two parameters, namely: the density and the temperature. The procedure outlined before assumes that the density is known. If the deviation from thermal equilibrium is small, although relevant, the effect of this approximation is two-fold: on one hand the electron distribution function should be described by more than two parameters, and thus, from a mathematical point of view, it is impossible to obtain, unambiguously, more than one unknown; and on the other hand the existence of a number of high energy electrons broadens the region of emission thus making impossible the approximation T_e constant over Δl. (2), the observation must be along a direction with large magnetic field variation in order to satisfy the approximation that T_e is constant over Δl, but at the same time small enough to avoid harmonic overlapping.

The thermal part of the spectrum has been used for reconstructing the electron temperature profile with the RECCE code (see fig.5). The high electron temperature values obtained for negative effective radius can be explained remembering that the RECCE code gives the mean electron temperature and on this side of the plasma the electron temperature gradient is very high, so an overestimation is obtained.

Conclusions

Strong suprathermal emission has been observed on TJ-I U during 2nd harmonic X-mode ECRH with a multichannel heterodyne radiometer, the peak emission corresponding to 20 keV central electrons.

By using a specific reconstruction code the optically thin emission can be interpreted in terms of real electron temperatures. Central Te values of 200 eV are achieved.

References

[1] - Ascasíbar E. et al, Transactions of Fusion Technology 27, 198, (1995).

[2] - Medina F. et al, these proceedings

[3] - Tribaldos V. et al. Submitted to Plasma Phys. and Control. Fusion.

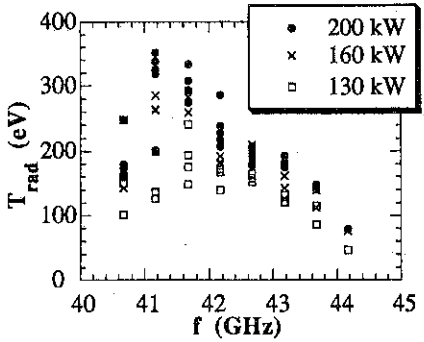

Fig. 1. Emission spectra (radiative electron temperatures) obtained for a typical TJ-I U discharge.

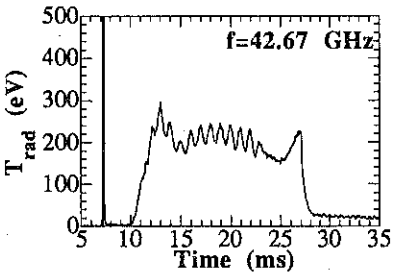

Fig. 2. Temporal evolution of the radiative electron temperature during ECRH modulation experiments.

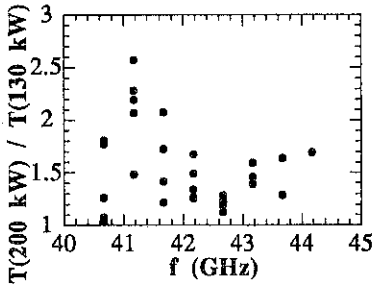

Fig. 3. Ratio between radiative electron temperature for different ECRH power for the emission spectra shown in fig. 1

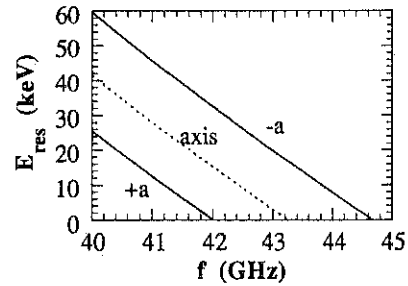

Fig.4 Resonant energies for the plasma edges and the axis versus frequency.

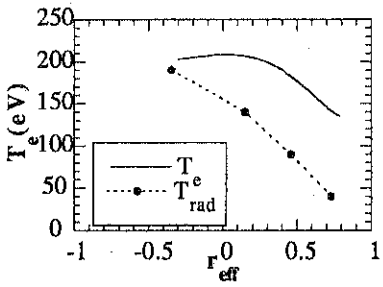

Fig. 5. Reconstruction of the electron temperature profile (solid) with the experimental data (dots).

Energy Distribution of Charge Exchange Neutral Particles and Vertical Asymmetries in the TJ-IU Torsatron

I. Sbitnikova*, R. Balbín, S. Grebenshchikov*, C. Hidalgo, N. Kharchev*, A. López-Fraguas, A. Meshcheryakov*, M.A. Pedrosa, V.N. Sukhodol'skii*, V. Tribaldos and the TJ-IU Team.

Asociación Euratom-Ciemat, 28040-Madrid, Spain
*General Physics Institute, Moscow, Russia

Charge exchange neutral particle energy spectra have been measured in the TJ-IU torsatron[1] ($l = 1$, $m = 6$, major radius $R = 0.6$ m, average plasma radius $a = 0.11$ m, average magnetic field at axis $B = 0.52$ - 0.67 T and rotational transform in the range $\iota(0) = 0.1$ - 0.41 with negligible shear). For the present investigation plasmas have been achieved using a 28 - 37.5 GHz (2nd harmonic, X-mode) ECRH system with $P_{ECRH} = 100$ - 200 kW and integrated line electron densities $\bar{n}_e \approx (0.2 - 0.5) \times 10^{19}$ m^{-3}. Measurements were done near to the perpendicular velocity distribution to investigate trapped particle effects on charge exchange spectra for different magnetic configurations with different $\iota(0)$. To increase the neutral flux in front of the spectrometer collimator, gas was puffed in the same port of the vacuum chamber during the plasma discharge. The slope in the spectrum in the range of energies 100 - 200 eV provides an ion temperature, T_i, of 20 - 40 eV, whereas the same analysis for fast atoms with energies above 250 eV provides a temperature of 60 - 80 eV. A dependence of ion temperature on heating power has been observed.

Measurements were carried out with a five channel charge exchange neutral atoms spectrometer[2]. Analyzer scans a poloidal cross section along a vertical line and was placed in the cross section with the highest magnetic ripple. In that cross section and in the magnetic configuration with $\iota(0) = 0.26$ the magnetic ripple is 14% at $r/a \approx 0$ and about 35 % at $r/a \approx 0.4$. In that position charge exchange analyzer measures ion energy distribution of trapped particles.

Figure 1 shows ion energy distribution measured at the plasma center in different plasma regimes. For plasmas with integrated line plasma densities ($\bar{n}_e$) below 0.2×10^{19} m^{-3} and magnetic field $B = 0.52$ T the ion energy spectra were not maxwellian (curve 1). The T_i value deduced from the slope of the energy spectrum in the energy range 100 -200 eV is in the range 20 - 25 eV. At higher magnetic field ($B = 0.67$ T) a different behavior was observed for the ion energy spectra: in many cases it is maxwellian for a wide range of energies (curve 2) while in other discharges some non-maxwellian tail (curve 3) was observed. In plasma regimes with the same plasma density, $\bar{n}_e \approx 0.4 \times 10^{19}$ m^{-3}, $T_i(0)$ varied by a factor of 1.5 depending on the breakdown phase. In certain discharges, we observed an anomalous

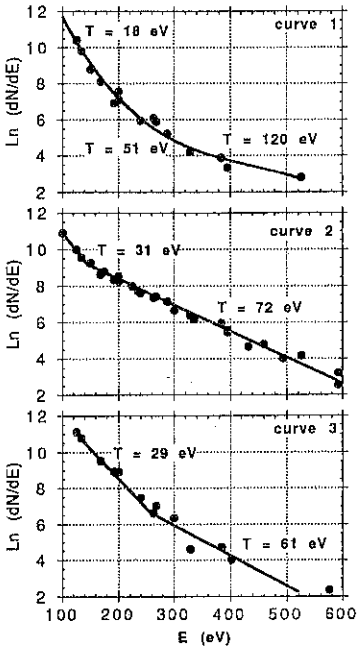

Figure 1: Curve 1 corresponds to a non Maxwellian distribution at B = 0.52 T and $\bar{n}_e \approx 0.2 \times 10^{19}$ m^{-3}. Curve 2 and 3 show the case of a Maxwellian distribution and a distribution with tail respectively at B = 0.65 T and $\bar{n}_e \approx 0.4 \times 10^{19}$ m^{-3}.

dependence of the ion temperature on the plasma density; in plasma discharges with the lowest density, $\bar{n}_e \approx 0.2 \times 10^{19}$ m^{-3}, $T_i(0) \approx 56$ eV, while, in discharges with higher density, $\bar{n}_e \approx 0.4 \times 10^{19}$ m^{-3}, $T_i(0) \approx 32$ eV. In general, T_i (0) varied within the range 30 - 70 eV. It should be noted that in some discharges non maxwellian tails in the energy spectra were observed (curve 3) which could appear and disappeared during the discharge. The spread in the measured temperature together with the deviation of the ion energy distribution from a Maxwellian may be attributed to an additional mechanism for the ion heating (not due to electron to ion collisions). At present, we have not sufficient information to identify the physics underlying this effect.

To obtain the radial T_i (r) profiles across the plasma, measurements were done in a conventional way, i.e., by changing the direction of the magnetic field to avoid the effect of drifted trapped ions. The $T_i(r)$ profile measured in the opposite direction of the ion drift velocity is show in figure 2. This profile is approximately parabolic: $T_i = T_i(0)\left[1-(r/a)^2\right]^{\alpha}$, where α = 1 - 1.5, for $r/a < 0.6$. It should be noted that the shape of radial distribution of T_i is independent on central ion temperature or average electron density. In figure 2, the open points correspond to observation in the direction of the drift of trapped ions. In this case the shape depends on central ion temperature. When $T_i(0)$ = 20 eV, curves coincide for $r/a < 0.4$ but they do not coincide if $T_i > 40$ eV. When $r/a > 0.4$, T_i increases with the radius. This behavior allows us to assume that these deviations are caused, mostly, by trapped ions drifting from the radius $r/a > 0.4$. The estimates for the bounce frequency, ν_b (where the electric field is not taken into account) and $\nu^* = \nu_{ii}/\varepsilon_t$ (where $\varepsilon_t = 0.5\left[(B_{max} - B_{min})/(B_{max} + B_{min})/2\right]$ are consistent with the observed drift of trapped

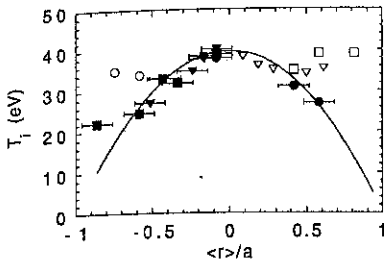

Figure 2: Radial profile of ion temperature at ι(0)= 0.26 at different densities. Closed points correspond to measurements in direction opposite to the drift of trapped particles while open points correspond to measurements in the direction of the drift. Triangular points correspond to measurements at B = 0.52 T. In this case $T_i(0)$ = 20 eV and temperature has been normalized to compare with the case of B = 0.65 T.

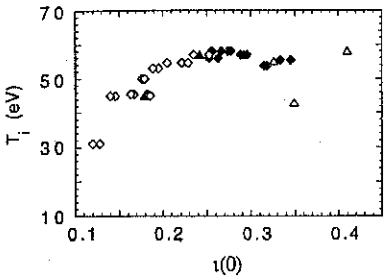

Figure 3: Central ion temperature, $T_i(0)$ dependence on central iota. Triangular points correspond to a case with smaller ion temperature; the values have been normalized to $T_i(0)$ at the standard configuration.

ions, i.e., when T_i = 40 eV, for r/a = 0, then $\nu_b \approx 2 \times 10^5$ s^{-1} and $\nu^* \approx 2 \times 10^5$ s^{-1} and for r/a = 0.4 then $\nu_b \approx 3 \times 10^5$ s^{-1} and $\nu^* \approx 9 \times 10^4$ s^{-1}.

Making use of the $T_i(r)$ measured profiles, we can estimate the minimum ion energy confinement time $\tau_{Ei}^{min} = W_i/P_{ei}$. Since, presently, the profiles $T_e(r)$ and $n_e(r)$ are not measured, for a preliminary estimate of the τ_{Ei}^{min}, we assumed $n_e(r) = n_e(0)\left[1-(r/a)^8\right]$, $T_e(r)/T_i(r) = 3$ over the whole plasma radius. For $T_i(0)$ = 40 eV, $\bar{n}_e = 4 \times 10^{18}$ m^{-3} and $n_e = n_i$, we obtain τ_{Ei}^{min} = 1.7 ms and for $n_i = 0.6 n_e$, then τ_{Ei}^{min} = 1.2 ms. For this calculation only P_{ei} was taken into account.

In the TJ-IU torsatron, the shape of the magnetic surfaces, ripple of the magnetic field, and plasma parameters are dependent on the rotational transform which can be varied significantly. In particular, the magnetic ripple increases as the rotational transform increases. Figure 3 shows the central ion temperature as a function of ι(0); $T_i(0)$ is approximately constant for ι(0)> 0.24 and monotonically decreases as the rotational transform decreases to ι(0) ≈ 0.15. Such behavior was observed in a wide range of plasma parameters (high and low ion temperature). Figure 4 shows the radial profiles $T_i(r)$ corresponding to ι(0) ≈ 0.18 (circular points) and ι(0) ≈ 0.36 (square points). For the case ι(0) ≈ 0.36 (square points) the radial profile shows a behavior similar to that shown in figure 2 for ι(0) ≈ 0.26. For ι(0) ≈ 0.18

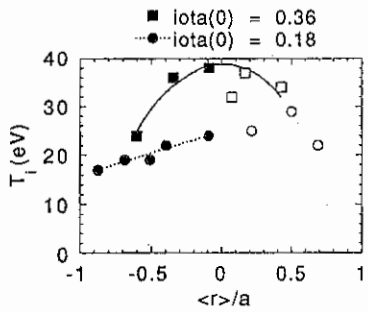

Figure 4: Radial profile of ion temperature for different configurations. Closed points correspond to measurements in the direction opposite to the drift of trapped particles and open points correspond to measurements in the direction of the drift.

(circular points), in the low iota range, the ion temperature does not vary significantly over the radius and remains almost equal to T_i (0). This practically flat profile points to an increase in the ion heat transport in the plasma core region.

In summary the radial profiles of the ion temperature have been measured in low density ECRH plasmas in the TJ-IU torsatron. The central ion temperature was found to be in the range 20 - 70 eV. Deviations of the ion energy spectra from a Maxwellian were observed. In the magnetic configuration with $\iota(0) = 0.24$ - 0.4, both the central ion temperature and radial profiles depend weakly on the rotational transform. Decreasing $\iota(0)$ below 0.24 the ion temperature decreases and the radial profile flattens, which points to an increase in the ion heat transport. Effects of the drift of trapped ions causing distortion of the radial profiles appear to be less strong than one would expect taking into account the large value of magnetic ripple.

---

[1] E. Ascasíbar et al. plasma Physics and Controlled Nuclear Fusion Research. IAEA **1**, 749 (1995)

[2] V.V Afrosimov, E.L. Berezovskii, I.P. Gladkovskii, et al. Zh. Tekh. Fiz. **45**, 56 (1975) [Sov.Phys. Tech. Phys. **20**, 33 (1975)]

Polarization effects on ECRH in TJ-II Stellarator

V. Tribaldos, F. Castejón and B. Ph. van Milligen
Asociación EURATOM-CIEMAT para Fusión
Av. Complutense 22, E-28040 Madrid, Spain.

Introduction

Ray tracing Electron Cyclotron Resonance Heating (ECRH) calculations have been performed for the flexible heliac TJ-II. This device is a four period mid-size helical axis stellarator[1], under assembly at CIEMAT, Madrid, with a nominal toroidal field of 1 T, a mayor radius of 1.5 m and a bean-shaped plasma cross section with average minor radius between 0.1 and 0.25 m. From a geometrical point of view, the main difference between other fusion devices and TJ-II is the possibility of TJ-II to change, within certain limits, the magnetic field structure and the plasma position, shape and size to a significant degree. On the other hand these large variations from configuration to configuration imply some constrains in the design of the ECRH injection system.

Moreover, the calculation of ECRH in TJ-II must take into account another effect, not usually of importance in other devices: the rotation of the wave polarization due to Faraday rotation and the rotation of the device's magnetic field along the wave's path. These effects can be non-negligible in TJ-II, since that the poloidal component of the magnetic field is of the same order as the toroidal one.

In this work we present a method for calculating the evolution of the polarization in a sheared magnetic field valid in the electron cyclotron frequency range, and the results, based on the 3D ray tracing code TRECE[2], for the ECRH efficiency in TJ-II Stellarator.

Evolution of the State of Polarization

To compute the evolution of the state of polarization of an electromagnetic wave with frequency near, or equal, to the electron cyclotron frequency or its harmonics in a magnetically confined plasma we have developed a formalism similar to the one used in ref. [3], which is only valid for conditions where $\omega^2 >> \omega_p^2$. In this theory the state of polarization is uniquely represented by a point

$$s = \{s_1, s_2, s_3\} = \{\cos 2\chi \cos 2\psi, \cos 2\chi \sin 2\psi, \sin 2\chi\} \qquad (1)$$

with $(-\pi/4 \le \chi \le \pi/4,\ 0 \le \psi \le \pi)$, in the *Poincare sphere*[4], and its evolution as it traverses the plasma is described, in the WKB approximation, by a rotation about an axis, defined by the fast characteristic polarization s_f, of an angle Ω, equal to the phase difference between the two characteristic polarizations:

$$\frac{d\mathbf{s}(l)}{dl} = \boldsymbol{\Omega}(l) \times \mathbf{s}(l) \quad , \tag{2}$$

where

$$\boldsymbol{\Omega}(l) = \frac{\omega}{c}\left[N_O(l) - N_X(l)\right] \mathbf{s}_f(l) \quad ,$$

and N_O and N_X are the refractive indexes corresponding to the O and X modes. Equation (2) gives the propagation of the state of polarization from an initial polarization $\mathbf{s}_0$ and the local polarization of the fast wave $\mathbf{s}_f(l)$. The extension of the theory presented in ref. [3] for conditions where the frequency is of the order of the plasma frequency is done calculating $\mathbf{s}_f(l)$ in the cold plasma approximation. Since the coordinates of the point $\mathbf{s}$ in the *Poincare sphere* are the *Stokes parameters* these can be obtained from the dispersion equation for the electric field of the wave. Using the coordinate system shown in figure 1 and after a tedious calculation they are found to be:

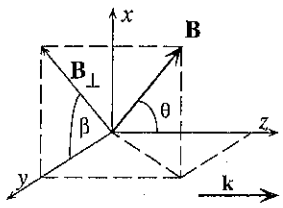

Figure 1: Coordinate system used for calculations

$$\mathbf{s}_f(l) = \frac{1}{\sqrt{1+F^2(l)}}\left\{\cos 2\beta(l),\ \sin 2\beta(l),\ F(l)\right\} \tag{3}$$

where according to eq. (1) means that

$$\chi = \tfrac{1}{2}\arctan F, \quad \psi = \beta, \quad \text{with} \quad F(l) = \frac{2\left(1-\frac{\omega_p^2(l)}{\omega^2}\right)\cos\theta(l)}{\frac{\omega_c(l)}{\omega}\sin^2\theta(l)}$$

being ω_p and ω_c the plasma and electron cyclotron frequencies. The expression for $\mathbf{s}_f$ is identical to eq. (11) of ref. [3] except for the factor $1-\omega_p^2/\omega^2$ in the definition of F. The absorption of ECRH waves, in a given mode of polarization, have been computed using a 3D ray tracing code taking into account that the calculated local absorption must be multiplied by the fraction of the injected power in this mode. For a wave, of intensity P_0, launched in a polarization state $\mathbf{s}_0$, the state of polarization, at a given point l along the ray path, $\mathbf{s}(l)$ is computed integrating eq. (2) with a Runge-Kutta method and the fraction of the intensity in the local polarization state $\mathbf{s}_X(l)$, or $\mathbf{s}_O(l)$, at this point, is[4]:

$$P_{X,O} = \frac{P_0}{2}\left[1 + \sin 2\chi_s \sin 2\chi_{X,O} + \cos 2\chi_s \cos 2\chi_{X,O} \cos(2\psi_s - 2\psi_{X,O})\right] \tag{3}$$

Effects of Polarization on ECRH for TJ-II Stellarator

The ECRH system planned for TJ-II consist of two subsystems injecting Gaussian beams of $f = 53.2$ GHz (2nd harmonic on axis). One is bottom launching at φ

= 25.47° directed towards the plasma, and the other is side launching at $\varphi = 64.52°$, and through a movable mirror, located inside the vacuum vessel, directs the microwaves to the plasma. The complicated design[5] of the second system is caused by the flexibility of TJ-II, and allows the microwaves to be launched at different angles with respect to the static magnetic field, and thus makes it possible to use it for ECCD. However, due to the local magnetic field shear, induced by the circular and helical central coils of this device, and the existence of a component of the magnetic field in the direction of launching, a rotation of the polarization of the waves, as they traverse the plasma, is expected.

To analyze the possible effects of the polarization rotation a new module that solves the equation (2), and computes equation (3), has been added to the TRECE ray tracing code. Using this code the effects of polarization rotation on the ECRH performance has been extensively studied for different configurations in TJ-II Stellarator although here only an example of the standard configuration for typical plasma parameters and the first injection system is presented.

Since we are interested in maximizing the heating efficiency we have first simulated the polarization of the waves at the mirror by launching a pure X-mode on axis and tracking its polarization, assuming straight line propagation, up to the mirror. In figures 2a and 2b the evolution of the polarization s and the fraction of power in the X-mode (eq. 3) is shown, for zero density (dash) and for the following density profile (solid)

$$n_e(\mathbf{r}) = 1.5 \times 10^{19} \left(1 - \psi_n(\mathbf{r})^{1.375}\right)^{1.5} \text{ m}^{-3}$$

where ψ_n is the normalized magnetic flux. Notice that the effect of density once the proper polarization has been chosen is negligible, and the main concern is the rotation of the magnetic field. This also means that the effect of the polarization can be ignored in the plasma startup.

Then we have computed the power deposition profile for a bunch of rays launched from the mirror with the polarization deduced above. In figures 3 the absorption coefficient is shown with (solid) and without (dash) taking into account the effect of the polarization.

Conclusions

A method for computing the evolution of polarization at frequencies in the range of the electron cyclotron frequency has been presented. It has been shown that the effect of polarization on the ECRH efficiency is negligible in TJ-II once the proper polarization is chosen, and moreover does not depend strongly on the density.

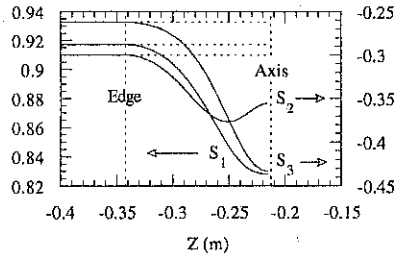

Figure 2a: evolution of the polarization $s = (s_1, s_2, s_3)$.

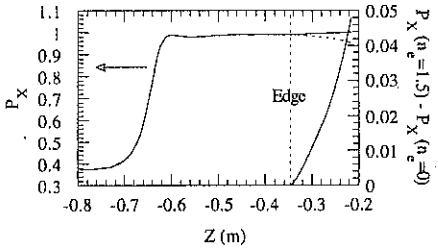

Figure 2b: Power in the X mode

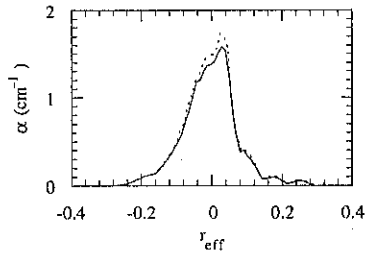

Figure 3: Absorption coefficient with and without polarization effects

References

[1] C. Alejaldre et al., Fusion Technology, **17** 131 (1990).

[2] V. Tribaldos and B. Ph. van Milligen, Nuclear Fusion **36** 283 (1996).

[3] F. de Marco and S.E. Segre, Plasma Phys. **14** 245 (1971).

[4] G.N. Ramachandran and S. Ramaseshan, *Crystal Optics*, Encyclopaedia of Physics, **25/1**, Springer, Berlin, (1961).

[5] K.L. Likin et al., Proc 10th Conf. on Stellarators, Madrid, 212 (1995).

OBSERVATION OF TOPOLOGICAL STRUCTURES AND ASYMMETRIES IN IMPURITY RADIATION PROFILES IN A TORSATRON

B. Zurro, E. Ascasibar, K. J. McCarthy, F. Aragón, C. Burgos, A. López, A. Salas, E. Sánchez, V. Tribaldos and B. P. Van Milligen

Asociación EURATOM/CIEMAT para Fusión. Avd. Complutense 22. E-28040 Madrid.

Introduction. The fact that the electron energy transport is anomalous in stellarators and tokamaks, that similar scaling laws can be applied to both, and that in both cases confinement degradation with increasing power is observed, would suggest that similar anomalous transport mechanisms may be in operation in both configurations. A common hypothesis that can be used to explain this anomaly is that deterioration of the confinement may be caused by chains of islands which enhance the energy transport. This idea has been the driving motivation in the search for topological structure in radiation profiles in the TJ-I U torsatron.

The observation of flattenings and humps on tokamak radiation profiles has already been correlated with the position of rational surfaces (1) and (2). To our knowledge, similar studies have not been performed on stellarator plasmas, although other observations using reflectometry (3), in the plasma interior, and Langmuir probes (4), at the edge, have shown that magnetic islands produce observable effects on these diagnostics.

In this paper, we report the observation of topological features in high resolution profiles of impurity line emissions in the TJ-I U torsatron and we discuss their possible correlation with the position of resonant iota values. We describe the experimental system used to obtain these profiles, we report the results and discuss them in relation to the context above, before finally drawing some conclusions and making some suggestions for future work in this field.

Experimental. The measurements reported here were made on the TJ-I U machine. In this l/m = 1/6 torsatron (R=60 cm, a = 10 cm), the plasma is created and heated by injecting 200 kW of ECRH power at 37.5 GHz through a quartz window. The magnetic field coils are powered by capacitor banks and the discharge lasts about 30 ms. Plasmas with maximum line-averaged electron densities of 5×10^{12} cm^{-3} and with central electron temperatures between 150 and 250 eV were used for this experiment. Chord-integrated radiation profiles of line emissions from CV (2271 Å) and O V (2781 Å) are routinely obtained with a 1 m monochromator. In order to maximise the spatial resolution the

plasma is imaged onto the monochromator vertical entrance slit by a set of three mirrors which rotates the image 90°. A fast rotating polygonal mirror close to the plasma allows us to obtain an impurity radiation profile in about .4 ms once every 2 ms. The plasma is viewed from its outer equatorial plane and profiles scan are made from the bottom to the top with a resolution of about 8 mm. Signals were digitised every 3.2 μs by the data acquisition system. Independent checks were performed, with a faster and more accurate system, for a few cases to ensure that the observed effect was not due to the digitizer.

Observation of spatial structure. Significant maxima and minima have been clearly observed in chord-integrated line radiation profiles obtained on the TJ-I U torsatron. Fig. 1 shows such features for a profile of C V (2271 Å). We can show that these features are not random by plotting the location of such features, with respect to the profile centre, for 4 successive profiles for the same discharge, see Fig. 2. We also show the number of occurrences of each feature, which is between 4 and 8, as this is difficult to discern from the figure due to the scale and the bunching of points with respect to h(ms). Note: h(ms) is related to h(cm) of Fig. 1 by the scan rate (1 cm = 12 μs). It is obvious that, if these features were due to statistical fluctuations or to superimposed light fluctuations, they would not appear as being accumulated around well defined positions. Instead these points would be smeared out when considering data from several profiles. Therefore, we can base our argument that these structures are of topological nature on the following criteria: a) The main features appear at the same positions in successive scans for a single discharge, and for similar discharges within a sequence; b) The features are approximately symmetric about the plasma centre. Thus we can eliminate any artefact caused by statistic or plasma fluctuations.

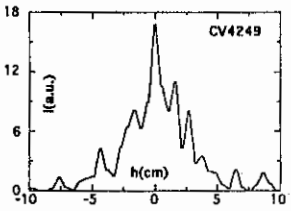

Fig. 1. A typical profile showing topological features. The minima and small flattenings are associated with structure.

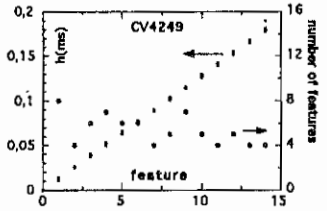

Fig. 2. The positions of features for four sequential profiles. The repeatability of the points indicate topological features. ß

We have checked, by examining the absolute periodicity, that the order displayed by the points in this figure is not introduced by the analysis method as a small artificial sliding when choosing the profile centre. However, we have been unable to check the

observations as a function of the scan speed of the system due to limitations in the scan mode used. In addition, we have observed good overlapping in the positions of these features when data from C V and O V profiles are combined. In such cases, C V profiles are best when observing core features while O V profiles are best for peripheral ones.

We believe that there are several reasons why a local and symmetric structure can produce a systematic signature in a line integrated measurement. These are, 1) That the line integral is dominated by emission from the hotter and denser parts of the plasma along the chord; 2) that the diagnostic only sees a decrease or flattening in its signal when the observational chord perpendicularly traverses a radius containing structure, while at any other radius, the chain of islands on the near and far side of the plasma would produce a smoothed effect on the profile. It should also be mentioned that the finite spatial and temporal resolution of the system does not allow observation of very fine structure that may be present since features with separation less than the system resolution cannot be distinguished. However, our emphasis is on proving that our observation are not experimental artefacts.

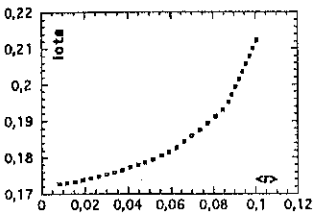

Fig. 3. Iota profile calculated for beta equal to zero.

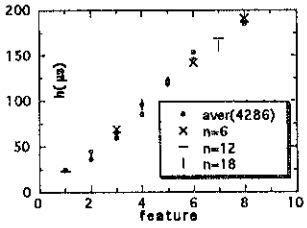

Fig. 4. Correlation between radiation features and resonant iota positions.

The possible correlation of the position of these features with resonant iota values deduced from calculated profiles, see Fig. 3, has been studied. For this purpose we have used experimental averaged values of the positions of these features obtained in several profiles within the same discharges, these points are the circles plotted in Fig. 4, a different point has been determined for the lower and upper part of the scan. In the same figure we plot the expected positions of resonant iota values corresponding to toroidal numbers n= 6, 12 and 18. In these cases, we have used profiles that are smoother than those used for generating Figs. 1 and 2. This was done to make the comparison clearer. This could explain the absence of experimental points for two of the expected resonances in this figure. Thus, for finer features, higher resonances would be needed.

Several arguments could be used against our approach: 1) The comparison is meaningless because of the richness of rationals some of which can always match the experimental data; 2) The magnetic structure of the TJ-I U device is somehow distorted thereby explaining the observations. Our reply to the first of these is that only the most important resonances would be observed in smoother data or profiles with poorer spatial resolution whereas we observe finer details in our more detailed profiles. With regard to the second point we can highlight that a standard method to measure vacuum magnetic surfaces revealed good TJ-I U magnetic surfaces (5). However, even if small defects in the magnetic structure could enhance our observations, it would not imply that these features are not present in more perfect devices, only that they would be more difficult to observe. Therefore, similar high resolution measurements should be performed on other devices in order to rule out or to confirm that these effects are confined only to small and low temperature stellarator devices like TJ-I U. These features have been observed in some tokamaks and they have relevant implications for transport. The approach of obtaining radiation profiles with a set of discrete channels, even if numerous, is not equivalent to our method because they do not provide a continuous profile and the uncertainty in the relative response of channels can make this observation difficult. Furthermore, selected impurity emission is better than global radiation because of its sensitivity to steps in local density and temperature profiles within the radial range of the emission. In addition, by choosing different ions we can focus on either the central core or on the periphery of the plasma.

We have observed up/down asymmetries mainly in O V(2781 Å) radiation profiles, in most of the discharges the emission tends to be higher in the downward part of the plasma. However, we have found up to now difficulties to establish any systematic correlation between these asymmetries and the global discharge parameters.

Conclusions. We have reported the observation of topological structure in line impurity radiation profiles. We believe that any physical mechanism, such as chains of small islands, which are capable of producing small steps at specific radii in either the local electron temperature, the density or the impurity concentration profiles, could account for these observations.

References

(1) V. A. Vershkov et al., Sov. J. Plas. Phys. **10**, 515 (1984).
(2) B. Zurro et al., Rev. Sci. Instrum. **65**, 2580 (1994).
(3) J. Sánchez et al., Nucl. Fusion **30**, 2383 (1990).
(4) M. A. Pedrosa et al., Plasma Phys. Control. Fusion **38**, 365 (1996).
(5) E. Ascasibar et al., Trans. Fusion Tech. **27**, 198 (1995).

Equilibrium Beta and Diamagnetic Beta in Stellarators

J. Qin, E. Ascasíbar, J.A. Jiménez, A. López-Fraguas, O. Fedyanin* and TJ-IU Term
Asociación EURATOM-CIEMAT Fusión, Av. Complutense 22, 28040 Madrid, Spain
**General Physics Institute, Russian Academy of Science, Moscow, Russia*

Introduction

Stellarators are usually operated in a net-current-free mode. From plasma equilibrium, it is known that the perpendicular plasma current $J_\perp$ (diamagnetic current) is accompanied by a parallel current $J_\parallel$ (Pfirsch-Schlüter current). The diamagnetic measurement, which measures the magnetic flux produced by the current $J_\perp$, is a conventional diagnostic to obtain plasma $\langle\beta\rangle$ (the so-called diamagnetic beta $\langle\beta\rangle_{dia}$). In this method, however, the relative-signal-ratio, the signal due to plasma beta over the background signal, is usually very low.

Plasma $\langle\beta\rangle$ can also be derived from measurements of the magnetic flux produced by the parallel current $J_\parallel$. Since the current $J_\parallel$ produces mainly a vertical field and the vacuum vertical field is much lower than the toroidal field, a higher relative-signal-ratio could be expected in this measurement. These two methods have been applied to the ECRH plasmas in TJ-IU [1]; experimental results are presented.

Cylindrical and 3-dimensional Models

Diamagnetic beta is given by a simple formula:

$$\langle\beta\rangle_{dia} = \frac{2\phi_{dia}}{\phi_0} \qquad (1)$$

where ϕ_{dia} is the diamagnetic flux, $\phi_0=\pi\langle a\rangle^2 B_0$ is the toroidal flux inside the plasma, $\langle a\rangle$ and B_0 are the average minor plasma radius and the toroidal field. Plasma beta given by equation (1) is independent of the pressure profiles. Its relative-signal-ratio ($=\langle\beta\rangle\langle a\rangle^2/2b^2$, b is the loop radius), however, is very low ($\sim 10^{-4}$ for $\langle\beta\rangle=0.1\%$ plasmas), which could cause some difficulties in low-beta measurements. In a stellarator configuration, there are also the toroidal and helical effects in ϕ_{dia} measurements [2, 3].

The density of Pfirsch-Schlüter current is approximately given by:

$$j_{ps} = \frac{2P'(r)}{\iota(r)\, B_0}\cos\theta \qquad (2)$$

where $P'(r)$ is the pressure gradient and $\iota(r)$ is the rotational transform. If $P(r)$ and $\iota(r)$ profiles are known, integrating j_{ps} over a half plasma cross-section, from $\theta=-90^0$ to $\theta=+90^0$, gives out the Pfirsch-Schlüter current I_{ps} flowing in one direction, and the total net current is zero. For example, with the pressure profile $P(r)=P_0(1-r^2/<a>^2)^2$ in a shearless configuration we have: $I_{ps}=\pm(16<a>B_0<\beta>/5\mu_0\iota)$, where $\pm$ signs indicate the currents I_{ps} flow in two opposite directions. The magnetic field produced by the currents I_{ps} is like: $B_r\sim\sin\theta$, $B_\theta\sim\cos\theta$. To measure this field, the vertical-flux loops located around $\theta=\pm90^0$ near the plasma column could be used. The vertical-flux signals due to plasma beta may be expressed by: $\phi_V=k<\beta>$, where the coefficient k, depending on the loop's size and position, the magnetic configuration and the pressure profile, can be obtained from the numerical simulations or experiments. In the case that the net plasma current I_p is not zero, the total vertical-flux signal is: $\phi_V=k<\beta>+mI_p$, where m is another coefficient like the coefficient k. In this case, if there is a pair of vertical-flux loops at different positions, plasma $<\beta>$ could be obtained independent of I_p by: $<\beta>=(\phi_{V1}-\phi_{V2}m_1/m_2)/(k_1-k_2m_1/m_2)$. The beta obtained from the vertical-flux loops is referred to as the equilibrium beta $<\beta>_{eq}$, to distinguish from $<\beta>_{dia}$.

To simulate the magnetic field produced by the currents I_{ps}, filament models could be used approximately. In a simple 2-filament model, two filaments carry the same amount of current equal to I_{ps}, flowing in two opposite toroidal directions, at positions of equivalent current-centre. In a multi-filament model, some 360 filaments distributed poloidally and uniformly ($\Delta\theta=1^0$) at the current-peak radius may be used, with each filament-current proportional to the $\cos\theta$--function. If an element-filament model is used, in which the element-filament current at the position (r, θ) is given by $j_{ps}r\delta\theta\delta r$ (e.g., $r\delta\theta=\delta r=1\%$ of $<a>$), it would be easy to deal with the different pressure and $\iota(r)$ profiles.

To obtain more accurate values of $<\beta>$ from measurements of either diamagnetic-flux or vertical-flux in a stellarator, a complete 3-dimensional equilibrium simulation is needed. In this work, we have used the VMEC code[4], in which a total of 13x25 modes (poloidal and toroidal mode-number: m=0, ..., 12 and n=0, ..., ±12) and a radial grid of 99 flux surfaces are chosen. The relative difference of magnetic pressure across the plasma boundary is $\sim1\times10^{-5}$.

Experimental Results

TJ-IU is $\ell=1/m=6$ torsatron with $R_0=60$cm, $<a>=10$-13cm. The magnetic configuration is controlled by the ratios between the helical, external and internal vertical fields, with the rotational transform in a range of $\iota(0)=0.11$-0.52. Plasmas are produced by ECRH (37.5GHz, 2nd harmonic, 200kW).

Several vertical-flux loops (13-13.5cm in radius) designed to measure the magnetic field of the Pfirsch-Schlüter current are located around the top ports of device as shown in Fig.1a. There are also two diamagnetic loops (b=17.2cm), together with their compensation loops, installed inside the vacuum vessel at equivalent $\varphi=20^0$ and 30^0 cross-sections (see Fig.1b).

For the vertical-flux loops, the simulation results obtained from the different models are shown in Fig.2a, with the pressure profile $P(r)=P_0(1-r^2/<a>^2)$ in a reference configuration $\iota(0)/\iota(<a>)=0.23/0.27$. If the profile $P(r)=P_0(1-r^2/<a>^2)^2$ is used instead, a result of about 3% larger is obtained for a given $<\beta>$. This means the value of $<\beta>_{eq}$ is insensitive to the pressure profiles, due to the fact that the configuration has a low magnetic shear. Fig.2b shows the diamagnetic flux versus $<\beta>$, given by the cylindrical model and 3-D simulations. Here, 3-D simulations show an interesting result that the diamagnetic flux is dependent of the loop's toroidal position, with a difference of up to ±30% from the cylindrical value. This toroidal asymmetry of diamagnetic flux is probably due to the helicity of plasma (helical shape and axis). It is also seen in Fig.2 that, for a given $<\beta>$ in TJ-IU, the vertical-flux signal due to plasma beta is as large as the diamagnetic signal. However, the background vertical flux through the loop is less than 4% of the toroidal flux. Thus, the relative-signal-ratio in $<\beta>_{eq}$ measurements is about two orders of magnitude higher than in $<\beta>_{dia}$ measurements.

Measured $<\beta>_{eq}$ and $<\beta>_{dia}$ in TJ-IU discharges are shown in Fig.3. Here we have $<\beta>_{eq} \approx <\beta>_{dia}$. If the plasma pressure is anisotropic, it would be possible to have $<\beta>_{eq} \neq <\beta>_{dia}$. Fig.4 compares all the $<\beta>$ values obtained from the different methods and loops. $<\beta>_{dia1}$ and $<\beta>_{dia2}$ are given by two diamagnetic loops at $\varphi=20^0$ and 30^0 using the cylindrical model, $<\beta>_{loop1}$ and $<\beta>_{loop2}$ are given by two vertical-flux loops at the same toroidal position but separated vertically 2cm, and $<\beta>_2$ is obtained from these two vertical-flux loops independent of I_p measurement. It is clear that all the beta values obtained agree with one another. However, the data shown in Fig.4 does not show clearly the toroidal asymmetry of diamagnetic flux.

Discussion and Conclusion

Two methods of measuring plasma $<\beta>$ in a stellarator have been compared. They are complementary to each other, in the sense of relative-signal-ratio, influences of pressure profiles and magnetic configurations, etc. Although 3-D simulations indicate that the diamagnetic flux may depend on the toroidal position of loop, the experimental results obtained in TJ-IU do not show clearly this toroidal asymmetry. One reason for this is that the two diamagnetic loops (at $\varphi=20^0$ & 30^0) are too close, the biggest difference in ϕ_{dia} is between $\varphi=0^0$ & 30^0. Another reason is that the plasma beta investigated in TJ-IU is too low.

References

[1] E. Ascasíbar et al., Transactions of Fusion Technology, Vol.27 (1995) 198-201.

[2] S. Besshou et al., Nucl. Fusion 26 (1986) 1339-1348.

[3] V.D. Pustovitov, Some theoretical problems of magnetic diagnostics in tokamaks and stellarators, National Institute for Fusion Science Report, NIFS-262, December 1993.

[4] S.P. Hirshman et al., Comput. Phys. Commun. 43 (1986) 143-155.

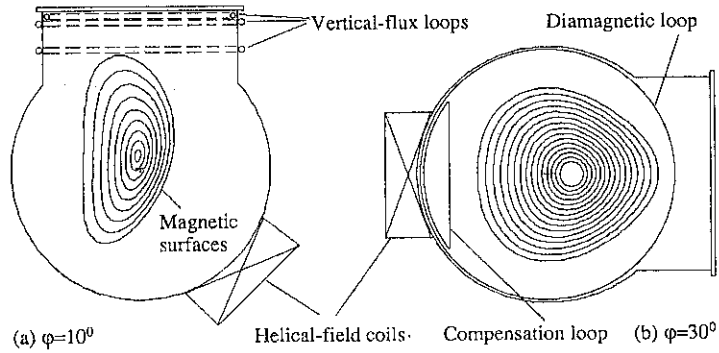

Fig.1 Vertical-flux loops(a) & a diamagnetic loop(b) at $\varphi=10^0$ & 30^0 cross-sections in TJ-IU.

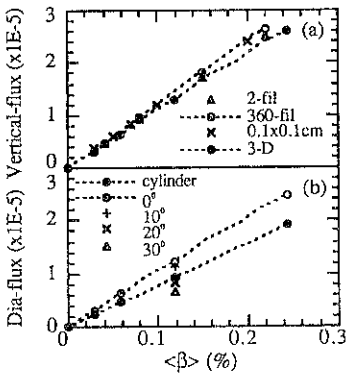

Fig.2 Vertical-flux (a) and diamagnetic-flux (b) vs <β> obtained from the simulations.

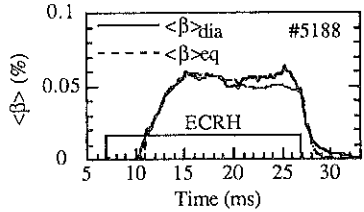

Fig.3 Measured $<\beta>_{dia}$ and $<\beta>_{eq}$ in TJ-IU.

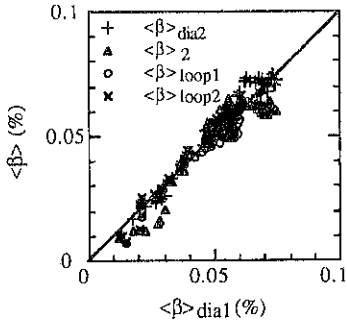

Fig.4 Plasma <β> obtained from the different methods and loops in TJ-IU.

Plasma collapsing mechanisms in stellarators

F. Castejón and M. A. Ochando
Asociación EURATOM/CIEMAT para Fusión.
Av. Complutense 22, E-28040 Madrid, Spain

Introduction

Radiative collapses in the Advanced Toroidal Facility (ATF) [1] have been already studied using the predictive transport code Proctr [2]. A local rather than a global breaking of the power balance has been suggested as the possible origin of the thermal collapse and the search for the spatial localization of this breakdown and for possible precursors could help to develop methods to control these catastrophic phenomena. [3]. The dynamics of plasma parameters were simulated with the Proctr code for selected discharges [4]. It was found that in collapsing discharges there is an efficient energy transfer from electrons to ions at about 0.5a; radiation presents a local maximum at about 0.8a which slowly propagates inwards; cool neutrals enter deeper into the plasma favouring an enhancement of the CX losses mostly by collisions with non thermalized ions, and also a more extense ionisation region is established. For those radial locations, the electron temperature does not surpass 100 eV and radiative thermal instabilities can easily develop when light impurities, such as carbon and oxygen, are present. As a result, the enhanced heat conduction from plasma core established is not enough to sustain the local energy balance and the collapse appears.

Density scan

In order to investigate the role of the density in the dynamic plasma response to a possible collapse, we have analysed a series of simulated shots with increasing average density, starting from that of a non collapsing ATF discharge (shot # 15990, see ref. 1), n_o, until the collapse appears because the density limit for the considered heating power has been reached [4], in this case $n = 1.5\ n_o$. For the considered discharges, the electron power density is governed by the following equation:

$$\frac{3}{2}\frac{\partial}{\partial t}(n_e T_e) = q_{NBI}(\rho) + q_{ECRH}(\rho) + q_{rad}(\rho) + q_{ion}(\rho)$$
$$-3\frac{m_e}{m_i}\frac{n_e}{\tau_e}[Z](T_e - T_i) - \frac{1}{V'_\rho}\frac{\partial}{\partial \rho}\left(V'_\rho q_e\right) \qquad (1)$$

where n_e, T_e and m_e are the electron density, temperature and mass, m_i and T_i are the bulk ion mass and temperature, τ_e is the electron collision time, [Z] is the mass-weighted ion charge, ρ the effective radius and V'_ρ is the derivative of the volume contained by the magnetic surface of radius ρ. q_{NBI} and q_{ECRH} are the power densities transferred to electrons

by neutrals and EC waves; q_{rad} and q_{ion} are the radiation and ionization losses. The fifth term corresponds to the heat transferred to electrons by collisions with ions, $q_{e\text{-}i}$, and the sixth one is the power density transferred by radial heat transport. The radial heat flux, q_e, is given by the heat and ripple conductions plus the convection:

$$q_e = -\left\langle (\nabla\rho)^2 \right\rangle n_e \chi_e \frac{\partial T_e}{\partial \rho} + q_e^{na}(\rho) + \frac{3}{2}\Gamma_e T_e \qquad (2)$$

being χ_e the heat conductivity and Γ_e the radial electron flux.

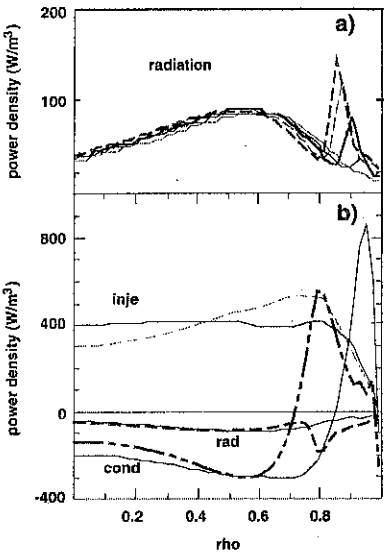

Figure 1. A) Radial profile of the total radiated power for a density scan series starting from the parameters of shot # 15990, n = no, until the collapse appears , for n=1.4 no. As the density is increased, the radiation peak is more pronounced and moves inwards. b) Injected, radiated and conducted power densities for the initial (continuos lines) and final discharges of the series (dashed lines).

As the same injected power has been supposed for all of the discharges of the series, the average power per particle is monotonically decreasing. Simulations indicate that, as density is increased, the total radiation peak increases and goes deeper into the plasma as the edge temperature diminishes (see figure 1a) and that plasma core reacts to cure the increasing loss of energy at the boundary by conducting power from the center to those cold regions. As density increases, the radial profiles of the main terms of the power balance appearing in equation 1 evolve from the shapes shown in figure 1b, in continuos lines, to their corresponding in dashed lines. In plasmas with the considered impurities (carbon and oxygen), it is seen that a radiative mantel is established whose radial extent is growing towards the confinement region, even though the relative impurity concentration is diminishing.

Influence of the impurity species

The role of carbon and oxygen in the occurrence of collapse has been also checked separately. Increasing amounts of those impurities have been added to the mentioned non collapsing discharge until reaching the collapse. It has been found that oxygen seems to be the most active species responsible for

the energy extraction and that the local slope of the total radiation profile is much more pronounced just before the collapse takes place (see figure 2a). This is a result consistent with the well known fact that among low Z impurities, oxygen is especially negative for confinement. Like in the mixed impurity case [4], the collapse is originated at the plasma edge even when the total radiated power is well bellow the input power. It has been seen again that a high amount of energy is supplied from the plasma core to the radiative region, whose spatial location depends on the detailed electron temperature and impurity cooling rate profiles.

For comparison, titanium impurities, easily introduced by the interaction of plasma with the limiter or with the chamber wall when titanium gettering is applied, have been considered as the main plasma contaminants. It has been observed that titanium is an efficient radiator at the plasma center and that the plasma collapse induced by high concentration of this impurity has a pure radiative nature, that is, it is the usual radiative collapse (Prad/Pin =100%) originated mainly at the plasma core (see figure 2b). Once radiation from the center equals the input power, the central electron temperature goes to about 10 eV. It has been also seen that when initial titanium concentration is slightly reduced, plasma may decay to another power balance state with a lower temperature (partial collapse), and still stable. However, it must be emphasised that there is not a monotonic improvement of plasma performance when small further reductions of the Ti concentration are done. From the outputs of Proctr, it could be concluded that for a given radial profile of electron temperature there exists an optimum titanium concentration for which some of the energy sink channels, such as fast energy ion losses, are minimized.

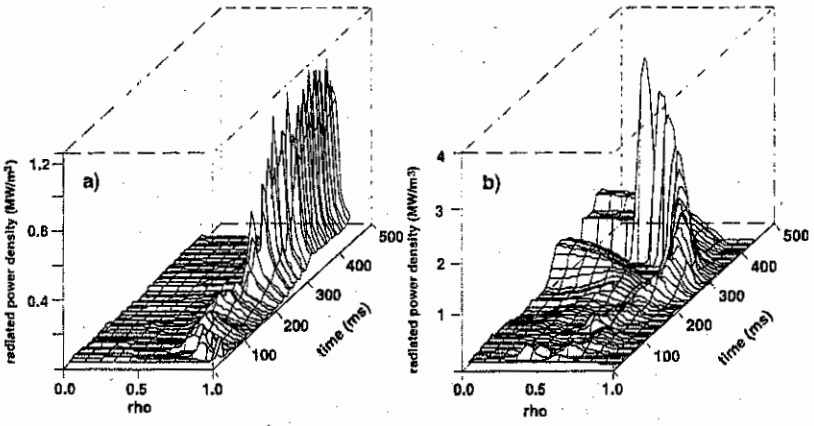

Figure 2. Time evolution of the radial profile of the radiated power density for a) oxygen and b) titanium contaminated plasmas close to collapse conditions.

Conclusions

Thermal collapses in ATF plasmas have been simulated using the Proctr code. The role of impurity radiation has been analysed and it is found than it can be considered as the main driving agent of collapse for the plasmas studied here. Depending on the impurity species, it has been observed that collapsing plasmas behave in different ways.

If the plasma contaminant is a low Z species, such as oxygen, thermal instabilities seem to be the trigger mechanism of collapse. Collapse develops when the rate of conducted power demanded by the plasma edge exceeds the maximum value that would allow the radial profile of the plasma thermal conductivity. As discussed elsewhere [6] the time evolution of local radiated power can be understood as a collapse indicator and could be used as a feed-back monitor.

On the contrary, as heavy impurities accumulate in the plasma core, the main radiative losses region is already localized where the absorbed power is maximum. In this case there is no need to transfer energy to any other plasma region and therefore the detailed radial dependence of the transport coefficients does not play an important role.

The simulations made with increasing density seem to confirm that there is a minimum power density per particle necessary to sustain a stationary plasma for given radial profiles of density, temperature and transport coefficients.

From the cases analysed here, it can be concluded that additional heating of plasmas might delay the occurrence of thermal collapse, but preferently in the case of high Z impurities. For low Z impurities, as much power must be transferred to the outer region of plasma, a local increase of absorbed power would be more useful to prevent collapses. In this sense, a heating method being able to deposit the power locally would be preferable: ECRH can be a suitable method or even a small amount of ohmic power, because of the expected local increase of the plasma resistivity at the impurity accumulation region.

These different behaviours suggest that stellarators may also present a limited operational domain, as tokamaks do. Further studies to try to establish the existence of possible boundaries, similarly to those appearing in the so called Greenwald [7] and Murakami [8] operation limits for tokamaks, are in progress.

References

[1] Lyon J.F. et al., Fusion Technol. **17** (1990) 33.

[2] Howe H.C., Oak Ridge National Laboratory Report ORNL/TM-11521 (1990).

[3] Hiroe S. et al. Nucl. Fusion **32** (1992) 1107.

[4] Ochando M.A. et al. 22nd EPS Conf. Controll. Fusion Plasma Phys. **19C-III** (1995) 225.

[5] Sudo S. et al., Nucl. Fusion **30** (1990) 11.

[6] Navarro A.P. et al., Rev. Sci. Instrum. **66** (1995) 552.

[7] Greenwald M. et al., Nucl. Fusion **28** (1988) 2199.

[8] Murakami M., Nucl. Fusion **16** (1976) 347.

"The peculiarities of breakdown and plasma heating in the stellarator L-2M by EM waves on the second harmonic of electron cyclotron resonance frequency (ECRH)."

Akulina D.K., Batanov G.M., Fedyanin O.I., Gladkov G.A., Grebenshchikov S.E.

The General Physics Institute RAN.

117942 Moscow, Vavilova 38, Russia

Introduction.

The breakdown and plasma heating experiments on L-2M stellarator with l=2, M=14, R=100 cm, a_p=11.5 cm using gyrotron complex (P≤350 kW, f=75 GHz, t~14 msec) have been carried out. The power was fed in the extraordinary mode from the low-field side (LFS) in the equatorial plane of stellarator by quasi-optical system. Power density in the center of beam was up to 1 watt/cm^3. The magnetic field strength, corresponding to second harmonic resonance was 13.4 kG. The diagnostics set permits us to determine the temporal evolution of: plasma density (n_e), plasma energy (W) by diamagnetic signals, electron and radiation temperatures ($T_{e,r}$) measured by ECE on f=77 GHz and f=71 GHz frequency (coming from opposite sides of the heating zone, f_{heat}=75 GHz), radiation losess, Pfirsh-Shlutter field. It was shown earlier [1] that as a result of ECRH in the L-2M the plasma parameters with $n_e \approx (1+2)10^{13}$ cm^{-3}, $T_e \leq 1$ keV, $W_{dia} \approx 0.4$ kJ was obtained. In addition to thermal plasma component some suprathermal groupe of electron was found having a radiation temperature strongly depending on input power and plasma density and exceeding thermal temperature (see f≈71 GHz) [2].

The view of closed magnetic surfaces and |B|=const lines are shown on Fig.1. The lines of |B|=const had a complicated form and differs essentially from tokamak type one having straight form and |B|=const value proportional to 1/R. Nonuniformity of stellarator |B|=const lines leads to complicated dependence of the plasma optical thiknees along the ray trace and plasma radius because of the variation of B/gradB determaining the absorption rigion.

Experimental results.

In the Fig.2 the typical experimental discharge parameters are shown. During the gas breakdown time high intensity ECE signals are observed reflecting the appearance of suprathermal electron group. The value of plasma density in the begining of discharge depends upon the pressure of neutral gas but during a pulse duration density increases because of a strong interaction of hot plasma with the vacuum chamber that partially restricted by graphite limiter. The different breakdown time delay depending upon magnetic field B(0) at R=100 cm was observed for n_e, T_e, W and shown in Fig.3. This dependence has resonat type with the minimum time delay equal to 1.5 msec at the magnetic field B(0)=13.2 kG that correspond to resonance condition for gyrotron frequency on the magnetic axis (B=13.4 kG). One can suppose that the breakdown process is performed by suprathermal component of electrons and time delay conditions depends on its confinement.

In the Fig.4 electron temperature (T_1) and radiative temperature (T_2) measured by ECE on the frequencies $f_1^{T_1}$=77 GHz and $f_2^{T_2}$=71 GHz as a function of B(0) are shown. One can see essential difference of curves in Fig.3 and Fig.4. Let us remind that with variation of B(0) from 1) B(0)=12.6 kG till B(0)=13.2 kG and from 2) B(0)=13.2 kG till B(0)=14 kG the noncentral heating process take place in the L-2M. For 1 heating case

the absorption region shifted to inner chamber wall. The power beam absorption occurs along $|B|$=const line marked 1.04 (see Fig.1) for B(0)=12.6 kG in the vicinity of equatorial plane. For 2 heating case and B(0) up to 14 kG the absorption occurs along $|B|$=const line marked 0.95. In spite of essential shift of heating zone (2 case) the electron temperature measured near with this zone do not decrease noticably. The explanation of this effect can be done by exemining the Pfirsh-Shlutter current signals that depends on the angle of rotational transform $I_{PS} \sim 1/\iota$. For L-2M $\iota = 0{,}185 + 0{,}2(r^2/a_p)^2 + 0{,}42(r/a_p)^4$. In Fig.5 the dI_{PS}/dt vs time for different B(0) are shown. The presence of peak-shaped form in dI_{PS}/dt in the time when gyrotron power is switched off characterize the process of central zone heating.

One can see that when the magnetic field decrease (1 case) the hot plasma region shifted from heating zone because of "β" increase but for 2 case heating when magnetic field is increased upper then B(0)=13.2 kG the hot plasma zone is shifted to heating zone, resulting in increase of temperature and lead to a shape-form variation dI_{PS}/dt after the gyrotron pulse is switched off.

References.

[1] V.V.Abrakov, D.K.Akulina et al. Proc. of 10-th International conference on stellarators, Madrid, 1995 pp.10-16.

[2] D.K.Akulina, G.A.Gladkov et al. ibld pp.136- 139.

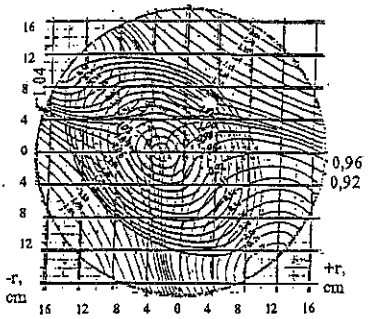

Rig.1Schematic of the L-2M chamber cross-section. /B/=const lines and magnetic surfaces.

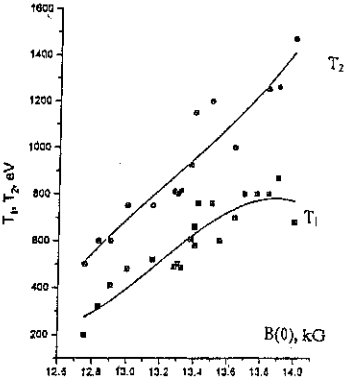

Fig4 Electron temperatures vs B(o), measured at f=77GHz(T_1) and f=71GHz(T_2).

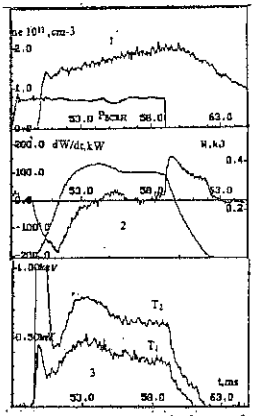

Fig.2 Typical discharge curves: 1.plasma density; HF power 2.The derivative of diamagnetic signal(dW/dt) diamagnetic signal(W) 3.The temperature curves vs time.

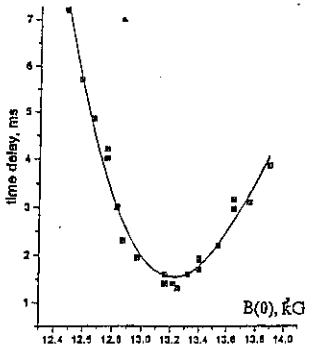

Fig.3The time delay breakdown curve vs magnetic field.

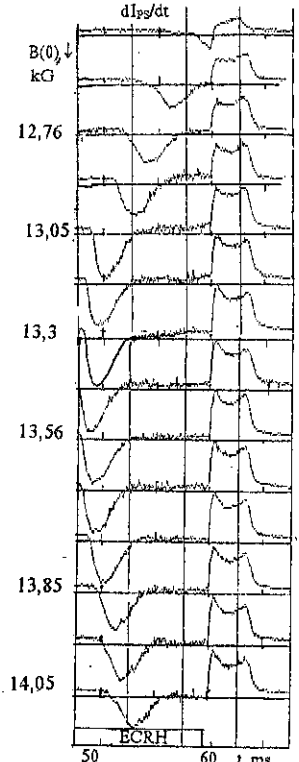

Fig.5 Time variations of derivatives of Pfirsh-Shlutter current at different B(O).

PLASMA CONFINEMENT IN L-2M STELLARATOR

D.K.Akulina, E.D.Andryukhina, G.M.Batanov, M.S.Berezhetskii, I.S.Danilkin, N.P.Donskaya, O.I.Fedyanin, G.A.Gladkov, S.E.Grebenshchikov, N.K.Kharchev, Yu.V.Kholnov, L.V.Kolik; L.M.Kovrizhnykh, N.P.Larionova, A.A.Letunov, K.M.Likin, N.I.Malykh, A.I.Meshcheryakov, Yu.I.Nechaev, A.E.Petrov, K.A.Sarksyan, I.S.Sbitnikova, V.A.Tsygankov

General Physics Institute of the Russian Academy of Sciences, Moscow, Russia

This paper presents the results of recent ECRH experiments in the L-2M stellarator , which is the modernized L-2 device [1]. The major radius of the magnetic system is 1 m; the l=2 helical magnetic field has 14 periods along the torus; the mean separatrix radius is 11.5 cm. The main goal of the experiments is to investigate the physics of ECR heating and plasma confinement at high values of the volume heating power density. A currentless plasma was produced and heated by an extraordinary wave at the second harmonic of the gyrofrequency. For this purpose, a gyrotron with a frequency f = 75 GHz (the resonance magnetic field B = 1.34 T) was used; the input power reached P = 0.4 MW. High-frequency power was transmitted from the gyrotron to stellarator through a quasioptical transmission line consisting of four copper mirrors. A well-focused microwave Gaussian beam was launched into the stellarator chamber through an outer horizontal port. In these experiments, the mean plasma density was in the range (1-2)x10^{19} m^{-3} ; the central electron temperature, in the range 0.7--1.1 keV, depending on plasma density. A growth of the electron temperature during the discharge was constrained by an increase in the plasma density and radiation, and the electron temperature fell to the pulse end. The ion temperature was about 100-120 eV.

The results of first experiments on an ECH plasma heating on L-2M were published elsewhere [2,3]. As follows from these experiments, the observed energy confinement time τ_E ~ 2--2.5 ms agrees rather well with both the widely known empirical LHD scaling and times that were calculated using the hybrid neoclassical code. Another finding is that the efficiency of plasma heating (the ratio between the power absorbed by a plasma bulk and input power) is about 0.5--0.7, i.e., noticeably less than unity although, according to the 3-D ray tracing calculations and microwave measurements, the single-path absorption coefficient is close to

unity. To date, the nature of effects that are responsible for this discrepancy is not clear.

At present, we have a more representative data base including about 1500 discharges obtained after the L-2 device has been modernized. In particular, novel data are concerned with a detailed study of the plasma heating and confinement depending on the plasma radius. Although, in L-2M, the separatrix is located inside the vacuum chamber,

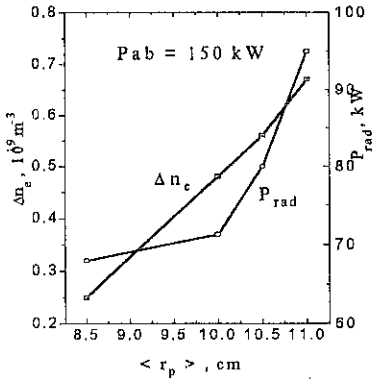

Fig. 1

an interaction between a plasma and wall causes both the plasma density and radiation losses to grow with time. A movable rail-type limiter made it possible to depress these effects. The carbon limiter was introduced into a plasma through the outer horizontal port. A vertical dimension of the limiter plate was 70 mm; a thickness (the dimension along the torus axis) was 14 mm. In the azimuthal plane, a shape of the working edge of this limiter coincided with the separatrix. The limiter, introduced into the chamber, restricted the plasma radius noticeably. When its displacement from an initial position (in which it touches the separatrix) was as large as 3 cm, the corresponding plasma radius decreased from 11.5 cm to 8.5 cm according to the vacuum configuration of the magnetic surfaces. Figure 1 shows a build-up of the plasma density at the end of the heating pulse in its dependence on the mean plasma radius given by the limiter. These measurements were conducted under the same conditions in which absorbed power was P=150 kW, and the initial plasma density was 1×10^{19} m^{-3}. In this figure, the radiation losses are also shown as a function of the limiter position. Note, when the limiter is removed from the plasma, and the plasma is bounded by the separatrix, nearly 2/3 of the

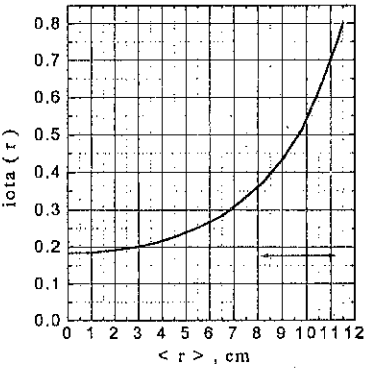

Fig. 2

microwave power absorbed in the plasma center is lost with radiation.

On the other hand, in the presence of the limiter, the rotational transform at the plasma edge changes considerably. Figure 2 shows the rotational transform as a function of the mean plasma radius corresponding to the vacuum configuration. A decrease in the plasma radius by 3 cm causes the rotational transform at the plasma boundary to change from 0.78 to 0.39, in which case, the quantity $\Delta\iota = \iota_p - \iota_0$ characterizing the average shear decreases, respectively, by a factor of 3. In the figure, the arrows indicate a range over which the plasma radius was varied. As is seen, the region in which the shear is most pronounced becomes cut off if the limiter is introduced into the plasma.

Figure 3 shows the dependence of the energy confinement time on the minor plasma radius. The average plasma density is $n_e = (1.5 \pm 0.25)\times10^{19}$ m^{-3}; the absorbed power according the diamagnetic measurements is 150 ± 10 kW (Fig. 3a) and 200 ± 10 kW (Fig. 3b). In the figure, we present also the well-known empirical LHD scaling [4] and the numerical dependence calculated using the TRANSZ code [5] based on the hybrid neoclassical model. In simulation of the plasma confinement and heating, a full matrix of the neoclassical transport coefficients is used [6]. The pure neoclassical model is hardly compatible with actual boundary conditions because large neoclassical fluxes outward the plasma through the boundary are impossible since the transport coefficients are small near the boundary. Therefore, we included additional anomalous transport coefficients in the model; these coefficients are inversely proportional to the product n_eT_e and important only for the edge plasma. As is seen in the figure, for the given plasma parameters and heating power, numerical results, obtained with the TRANSZ code, differ from the LHD scaling by not more than 25 %. In general, the experimental values are close to both dependences; for the International Stellarator Scaling (ISS95), a discrepancy is somewhat greater (see Fig. 3a).

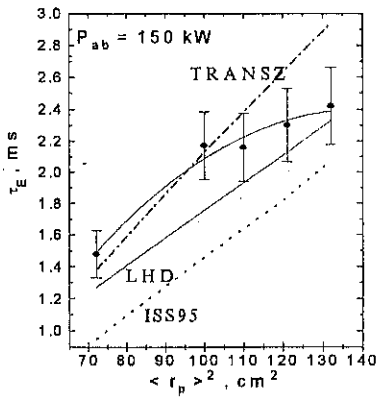

Fig. 3a

The experimental energy confinement time firstly increases as $\sim r_p^2$ and, then, somewhat slowly when the limiter approaches the separatrix. This occurs in spite of the shear increases near the boundary. It is likely that the large shear occurring near the boundary does not affect strongly the plasma confinement. Probably, τ_E increases more slowly with increasing r_p because the plasma-wall interaction becomes more strong, resulting in an increase in radiation losses. In general, the results of the recent limiter experiments confirm our previous conclusion that, under conditions of an ECR plasma heating, the current-free plasma confinement in L-2M is described rather well by both the LHD scaling and the TRANSZ hybrid neoclassical code.

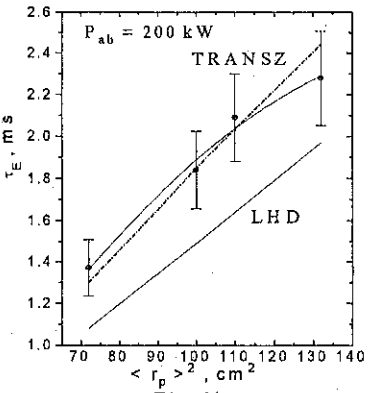

Fig. 3b

Although the plasma energy and confinement time diminishes with a decrease in the plasma radius, the electron temperature in the plasma center does not vary noticeably. The value of $<\beta>$ is about 0.15-0.2 and also depends weakly on plasma radius.

The present work is partly supported by the International Science Foundation, grants 4T000 and M6L300.

REFERENCES

1. S.E. Grebenshchikov, V.V. Abrakov, D.K. Akulina, et al., Plasma Phys. and Contr. Nucl. Fusion Res. 1994, IAEA, Vienna, V.2, p.327, 1995
2. S.E.Grebenshchikov, G.M. Batanov, O.I. Fedyanin, et al., Trans. Fusion Technology, 1995, V.27, p.270
3. V.V. Abrakov, D.K. Akulina, E.D.Andryukhina, et al., Proc. of the Int. Conf. on Stellarator, Madrid, Spain, p.10, 1995
4. S. Sudo, Y. Takeiri, H. Zushi, et al., Nucl. Fusion, V.30, No.1, p.11, 1990
5. S.E. Grebenshchikov, I.S. Danilkin, A.B. Mineev, Plasma Phys. Reports, V.22, No.7, p.551, 1966
6. L.M. Kovrizhnykh, Nucl. Fusion, V.24, p.851, 1984
7. V. Stroth, M. Murakami, R.A.. Dory, et al., NIFS-375, 1995

C

ALTERNATIVE MAGNETIC CONFINEMENT

Reversed-Field Pinch Operation with a Resistive Shell and Graphite Wall in Extrap T2

S. Hokin, H. Bergsåker†, P. Brunsell, J.H. Brzozowski, J. Drake, T. Fall*, G. Hedin, A. Hedqvist*, G. Hellblom, P. Hörling*, D. Larsson‡, A. Möller, E. Rachlew-Källne*, J. Sallander*, M. Tendler, E. Tennfors and A. Welander

Division of Fusion Plasma Physics (Association EURATOM-NFR), Alfvén Laboratory
*Department of Physics I
†Department of Physics-Frescati
Royal Institute of Technology, 100 44 Stockholm, Sweden

Abstract

The Extrap T2 reversed-field pinch ($R = 1.24$ m, $a = 0.18$ m) has exhibited improved performance resulting from continued RFP operation, periodic He glow discharge cleaning (GDC), baking at 130 °C and solid-target boronization. Solid-target boronization results in reduced oxygen influx from the graphite first wall, and, along with He GDC, provides a full range of density control ($1.5 < I/N < 30 \times 10^{-14}$ Am). Every discharge contains a quasi-stationary $m = 1$ radial magnetic field perturbation of around 60° toroidal extent located at arbitrary positions around the torus. At the same time, toroidal flux perturbations are observed to rotate in the electron diamagnetic drift direction at 20–40 km/s. A high-frequency (200–700 kHz) mode with $\tilde{\mathbf{B}} \perp \mathbf{B}$ has been observed at the edge which may be associated with an Alfvén eigenmode. The frequency increases with V_A and falls in the range $V_A/2a < \omega < V_A/a$. Signals exhibit weak coherence, suggesting that the mode is strongly driven and damped. Experiments in the near future will include plasma biasing using an electrode to study the connection between plasma flow, mode rotation and locked mode growth. In 1997 T2 will be rebuilt with a new toroidal field system, shell and plasma-facing wall.

1. Introduction

The present goals of the T2 research program are to: (1) develop wall conditioning methods to allow density control with low impurity influx at high current density with a graphite wall; (2) investigate MHD phenomena arising from a shell penetration time (1.5 ms) much shorter than the discharge duration (over 13 ms); (3) study the effects of active profile control such as electrode biasing MHD behavior and confinement; and (4) investigate anomalous heating and confinement issues. This paper focuses on the first two points; a companion paper [1] at this meeting presents results from topic (4). Electrode biasing experiments have just begun and will be reported in the future.

Extrap T2 is a high aspect ratio ($R/a = 6.8$) reversed-field pinch (RFP) with a resistive shell ($\tau \simeq 1.5$ ms) and full graphite coverage of the first wall. It was previously run as OHTE at General Atomics (GA) [2]. It is capable of very high current density (3 MA/m^2 at 300 kA toroidal current), input power density (40 MW/m^3) and wall loading power (3 MW/m^2).

2. T2 Operation and Wall Conditioning

Over the past year, plasma performance in the Extrap T2 reversed-field pinch has steadily improved as a result of continued RFP operation, inductive baking at 130 °C, He glow discharge cleaning (GDC) to remove hydrogen and carbon monoxide which build up on the first wall as

a result of RFP operation, and boronization using a B_4C target inserted into the edge of RFP discharges [3]. As a result, T2 is nearing the goal of sustained discharges at 300 kA.

Boronization increased the maximum density achieved at a given current, with $I/N \equiv I/\pi a^2 \bar{n}_e$ as low as 1.5×10^{-14} Am in sustained discharges. CO release following RFP discharges of a given input power dropped by a factor of two.

Ramped mode startup, where the toroidal flux is ramped during the current rise due to the dynamo effect, has been used almost exclusively because it does not exhibit density 'pump-out' and an associated increase of plasma resistance that occurs with matched-mode startup, in which the initial toroidal flux matches the steady-state value.

T2 performance is similar to that obtained at GA [2] at peak current up to 240 kA. However, as at GA, hard terminations, in which the discharge rapidly terminates at $t \simeq 4$ ms with a huge impurity influx and density rise, hamper present operation above 240 kA. Further wall conditioning is expected to extend the hard termination limit above 300 kA.

3. Resistive Shell Physics

Most RFPs make use of close-fitting conducting shells to stabilize a number of modes which have nonzero B_r at the plasma surface, known collectively as 'resistive shell' modes. A thick conducting shell has the drawback, however, of preventing active control of the plasma equilibrium, such as with a vertical field, on a rapid time scale.

A focus of T2 research is on the effects of plasma flow, mode rotation and shell penetration time on MHD mode stability and growth. This area is not only vital for future RFPs with pulses much longer than the shell penetration time, but also bears on advanced tokamak modes where shell stabilization is employed. T2 is currently the only major resistive-shell RFP in the world program, with a shell time constant of 1.5 ms, much shorter than the pulse duration of 5–15 ms, and is in a unique position to evaluate resistive shell physics.

T2 is equipped with a large array of pickup coils sensitive to the radial component of the magnetic field B_r at the outer surface of the shell. Sets of four coils, equally spaced poloidally and located at 32 equally-spaced positions around the torus, were connected to provide an $m = 1$ component of B_r with toroidal resolution up to $n = 16$. In addition, a partial array of toroidal flux loops measures $m = 0$ dynamo activity on a fast time scale.

All T2 discharges exhibit a localized $m = 1$ radial field structure with toroidal extent $\Delta\phi < 60°$ that grows after $t = 3$ ms. Spatial Fourier analysis indicates the expected $n \sim 2R/a$ internally-resonant modes; in addition, particularly in discharges lasting longer than 8 ms, modes of opposite helicity with $2 \leq -n \leq 6$ are observed to grow. These modes are the DC version of the 'slinky' observed previously in OHTE [4]. In well-centered discharges the localized structure appears at an arbitrary toroidal location, and can appear at different locations in a single shot. However, if the externally-applied vertical field is altered to move the discharge inward or outward, the localized mode locks to the shell gap.

The toroidal flux coils display a stationary toroidal asymmetry of $\langle B_\phi \rangle$. However, the unintegrated signals, high-pass filtered in the 5–100 kHz range for enhanced sensitivity, show rotation of $|n| > 2$ modes with $v_\phi \simeq 20$–40 km/s in the electron diamagnetic direction in most discharges (Fig. 1). It is intriguing that this rotating 'dynamo' activity exists in the presence of the stationary $m = 1$ B_r and $(m = 0)$ $\langle B_\phi \rangle$ structure.

There is no clear indication that the growth of the radial perturbation *per se* terminates the discharge (rather than the impurity influx which it causes); as wall conditions have improved, shots of longer duration are more common, including many that consume the available 2.5 Wb capacity of the unbiased iron core. (The flux capacity will soon be extended to 5 Wb in order to extend the shot duration, which, at up to 13 ms, already exceeds the shell penetration time by a factor of 9.)

4. Alfvén Eigenmode Observations

A high-frequency magnetic probe placed near the plasma edge reveals a mode with frequencies 200-700 kHz (Fig. 2). The fluctuations are highly polarized, with $\tilde{B}_\phi \sim 10\tilde{B}_\theta$, and are weakly coherent with autocorrelation time $\tau_{auto} \simeq 1$ μs, indicating that it is both strongly driven and strongly damped.

The hypothesis that it is an Alfvén eigenmode is supported by the observed increase in peak frequency with Alfvén speed. In fact, the mode frequency falls between the on-axis and edge expressions for the TAE eigenfrequency [5] for $|m_1 - m_2| = 1$:

$$\begin{aligned} \omega &= \frac{V_A B_\theta}{2rB}|m_1 - m_2| \\ \omega(0) &\simeq \frac{V_A}{a} \quad (r = 0 : B = B_\phi, q \simeq \frac{a}{2R}) \\ \omega(a) &\simeq \frac{V_A}{2a} \quad (r = a : B \simeq B_\theta) \end{aligned}$$

It is not clear what the driving mechanism is; it is possible that the mode draws power from the ambient dynamo activity at $f \sim 20$ kHz of much greater amplitude.

5. Future Work

Plasma biasing experiments using an inserted electrode have begun. These are aimed at two areas: (1) the relation between plasma flow, mode rotation and mode locking; and (2) measurement of cross-field conductivity in a stochastic magnetic field [6], an important quantity in ambipolar potential formation and confinement.

Transformer core biasing will be installed in the near future to allow full 5 Wb flux swing. This, combined with further conditioning, should allow 300 kA operation and discharge duration of 15-20 ms.

The unintegrated $m = 1$ $\dot{B}_r$ spectrum will be measured to determine whether a rotating $m = 1$ mode accompanies the observed $m = 0$ rotation, as was seen previously in T1 [7].

Multiple probes will be employed to measure $\mathbf{k}(\omega)$ for the high-frequency mode to clarify whether it is an Alfvèn eigenmode.

6. T2 Rebuild

Design work is underway on a rebuild of T2 scheduled for 1997. Modifications include: (1) replacement of the helical TF coil set with a conventional solenoidal TF coil set; (2) replacement of the resistive shell with a conducting shell ($\tau \leq 25$ ms); (3) installation of a new liner with molybdenum or tungsten armor; (4) installation of additional coil systems for pulsed vertical field at plasma startup, AC helical rotation drive and shell gap field error control.

References

[1] Hörling, P. *et al.*, this conference.

[2] Goforth, R.R. *et al.*, Nucl. Fusion **26**, 515 (1986)

[3] Den Hartog, D.J. *et al.*, J. Nucl. Mat. **200**, 177 (1993)

[4] La Haye, R.J. *et al.*, Nucl. Fusion **28**, 918 (1988).

[5] Turnbull, A.D., Strait, E.J. and Heidbrink, W.W., Phys. Fluids B **5**, 2546 (1993)

[6] Tendler, M. *et al.*, this conference.

[7] Mazur, S., Phys. Plasmas 1, 3356 (1994).

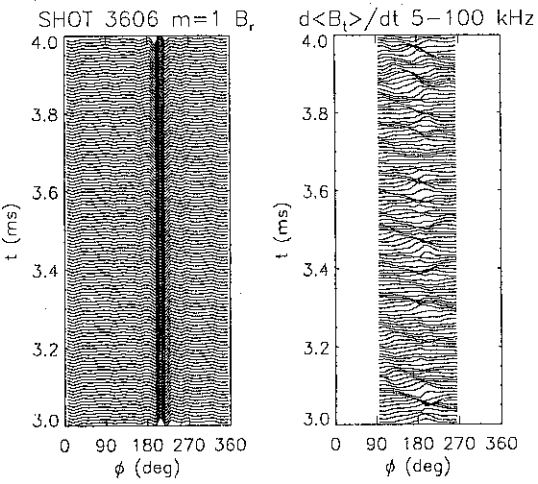

Figure 1. A full toroidal array of $m = 1$ B_r coils indicates a structure locked at $\phi = 210°$ while a partial array of toroidal flux loops displays a rotating $m = 0$ disturbance with $v \simeq 20$ kHz.

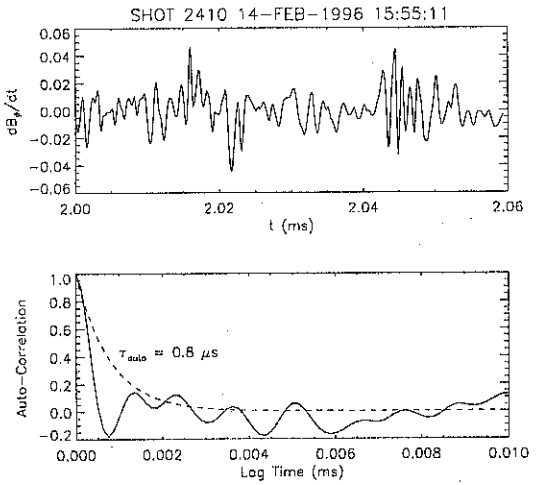

Figure 2. The signal from a high-frequency dB_ϕ/dt probe placed at the plasma edge displays weakly coherent oscillations in the 200–500 kHz range, thought to be a signature of an Alfvèn eigenmode.

Recent Results of RFX

A. Buffa and the RFX Team
Gruppo di Padova per Ricerche sulla Fusione
Associazioni EURATOM-ENEA-CNR-Università di Padova
Corso Stati Uniti, 4 - 35127 Padova (Italy)

1. Introduction

The RFP experiment RFX [1] has been operated during almost all '93 and '94 with experimental campaigns mainly dedicated to the performance optimization in the current range of 0.5÷0.9 MA. The different optimizations have lead to progressive improvement of plasma behaviour. The most significant results have been obtained by improving the magnetic field quality by accurate equilibrium and error field control and by reducing the impurity content (Z_{eff}) by frequent wall conditioning and boronization with Trimethylboron [2,3].

All RFX pulses always exhibit large stationary magnetic disturbances, not controllable in amplitude from the outside, interpreted as the effect of MHD modes which lock in phase and to the wall at the reversal time and remain saturated for the whole discharge [4].

Nevertheless at 0.5 MA the previously mentioned optimizations allowed the achievement of discharges with $Z_{eff} \sim 1.2 \div 1.5$ which, at the highest density $n_e \sim 4 \div 5\ 10^{19}\ m^{-3}$, reached $\beta_\theta \sim 10\%$ and energy confinement time $\tau_E \sim 1.5$ ms for a long and completely stationary period (flat top ~ 80÷100 ms), in substantial agreement with the most optimistic RFP global scaling projection [3]. At the highest explored current the improvement in confinement was lower than expected due to enhanced losses attributed to the effect of field lines interception with the graphite first wall consequent to a still insufficient control of field errors, plasma shift and shape, and to an enhanced effect of MHD mode locking at the wall [2, 3]. The analysis of the spectroscopic data [5] shows that the loop voltage is constituted by two additive terms: the first related to the on-axis electron temperature and Z_{eff} (measured outside the locking region) proportional to the Spitzer resistivity, the second being an anomalous term (~15 V), likely to be connected to the losses associated to field lines interception at the wall [6].

During 1995, the RFX machine was modified. The changes include the installation of 112 specially shaped graphite tiles on the first wall to prevent damages to the vacuum vessel in the poloidal gap zones, the closure of the outer equatorial gap and the partial closure of one of the two poloidal gaps of the shell. Furthermore an 8 pellet injector, a Diborane boronization system, a SXR/bolometry tomographic diagnostic and an Electron Energy Analyser (EEA) were installed.

This paper describes the new results and the advances made during the first months of 1996 operating mainly at 0.6 MA.

2. Effect of machine modifications on plasma performances

As a consequence of the outer equatorial gap short-circuit [7], the fluctuating radial fields measured through the 12 equatorial pumping ports have been reduced by a factor 2-3, particularly during the fast reversal phase, but also during flat-top, where they remain below 1% of the main poloidal field. The most important global effect has been the reduction of the dependence of the loop voltage on the horizontal plasma position which now permits the attainment of good performances at 0.6 MA operating with shift as high as 2 cm, reducing in this

way the breakdown problems imposed by the bias centering vertical field.

The closure of one poloidal gap, togheter with an improvement of the field shaping coil feedback control system on the other gap, reduced the maximum radial field through the vertical gaps to less than 4% of the main field.

The effect of shell gaps closure resulted, at 0.6 MA, in a better pulse reproducibility, with reduced scattering of data and a more reliable density behaviour under the same experimental conditions, and in a global decrease of ~ 10% of loop voltage and a consequent increase of the energy confinement time, β_θ remaining completely unchanged, as shown in fig. 1.

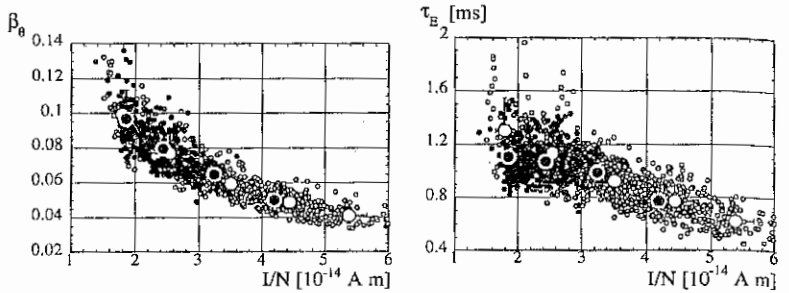

Fig.1 Poloidal beta ($\beta_\theta=2\beta_{\theta e}$) and energy confinement time versus I/N for old (black circles) and new (open circles) data. Big symbols represent averaged data. Plasma current is between 500 and 600 kA.

From measurements of the central temperature there is evidence that the voltage reduction corresponds to a decrease of the anomalous voltage from ~15V to~12V, obtained by improving the magnetic profile quality and reducing field line interception to the wall. Field errors and shift are now kept within a range where their influence on loop voltage is negligible. The remaining portion of anomalous voltage can probably be attributed to the magnetic field distortion due to the MHD locked modes.

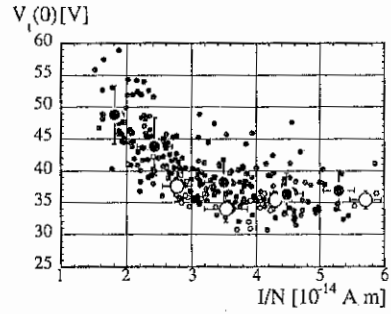

Fig. 2: VLoop vs I/N for old (black circles) and new (open circles) data at I=0.8÷1MA

Only few preliminary tests have been performed at higher currents (up to 1 MA). The results obtained confirm a global improvement on loop voltage, consequent to the gaps closure, of the same order of ~ 10% as shown in fig. 2.

It must be mentioned that the performances at higher current have not yet been well optimized from the point of view of shift and shape of plasma column, due to breakdown problems and to a bad reproducibility of the discharges because of mode locking effects.

3. Locked modes

Stationary magnetic disturbances consequent to the phase locking of unstable MHD modes to the wall are observed in each RFX discharge. These modes develop during the formation of the RFP configuration and lock in phase at the wall as soon as the reversal is reached. The modes have a spectrum of m=1, n=7÷15 and are resonant internally to the toroidal field reversal surface (r/a

$\simeq$0.9). The locking causes a global helical deformation of the plasma which decays by more than 50% in half its typical toroidal period of 30°÷40°.

Parallel power fluxes of the order of 100÷200 MW/m^2, which are mostly accounted by the superthermal electrons flowing along the field lines [8], heat the tiles up to 2000°C in the region where the graphite wall is intersected by the distorted magnetic surfaces. This lead to an enhancement of the influx of carbon by a factor of $\simeq$ 100, of oxygen by a factor of $\simeq$ 40 and of hydrogen by a factor of $\simeq$ 30. The emission spectrum measured by a survey spectrometer, wavelength integrated from 100 to 1100 Å (and therefore representing only a portion of the radiation), increases more than one hundred times. This indicates, with the uncertainty connected to the evaluation of the spatial extension of the phenomena, that the power locally radiated may be a relevant fraction of the total one (up to 50% when the radiated power measured by bolometry in the unperturbed region is ~20% of the ohmic input power) [9].

In high current discharges (0.8÷1 MA) the carbon tile temperature may reach values close to that of carbon sublimation (3350 °C), resulting in frequent carbon blooming phenomena, with the consequent global increase in Z_{eff} (from ~1.2÷1.5 up to ~2) and density which causes a decrease of the temperature and an increase of the loop voltage.

Damage observed on the graphite tiles and the vacuum vessel [10] have been ascribed to the effect of halo currents consequent to the short-circuiting by the tiles and the vessel of the distorted field lines. The current density at the edge carried by the superthermal electrons can reach 500 kA/m^2. A rough evaluation of the total halo current taking into account the current density at the edge and the total surface intercepted by the field lines, gives a value of about 10% of the toroidal plasma current. Considering the contact resistance between tile and vessel, a power dissipation greater than 1.5 MW is estimated [10], which is of the order of 5-10% of the input power.

Summarizing, one may estimate that locked modes induce losses that amount to ≈25÷30% of the total power input due to radiation and to halo currents through the vessel. These losses correspond to a portion of 7.5÷10.5 V of the typical 30÷35 V loop voltage, to be compared with the additive anomalous loop voltage of ~12 V. This estimate does not include possible losses due to parallel particle fluxes.

4. Measurements on the unperturbed region

4.1 Hot electrons

Measurements with the EEA confirm the presence of a high energy tail in the electron distribution function [11]. The temperature T_h of these electrons is comparable to the electron on axis temperature T_0 at low plasma density and decreases at higher density. This behaviour has been related to the non-dimensional parameter E/E_c, where $E=V_{loop}/(2\pi R)$ while E_c is the on-axis critical field for runaway generation. The dependence of T_h on E/E_c and the fact that T_h is comparable to T_0 indicate that these superthermal electrons are probably generated in the centre of the plasma, and then transported to the outer region, flowing along stochastic magnetic field lines.

4.2 Radiation losses

The high density best confinement regime is characterized by an higher level of plasma radiation Prad. The measured total radiation emissivity profiles [12] appear to be sharply peaked in the plasma outer region ($0.6 \leq r/a \leq 0.9$), where the emissivity can be comparable to the local deposition of ohmic input power per unit volume. As I/N approaches 1.6×10^{-14} Am, PRAD sharply

increases and the ratio γ=Prad/Pohm reaches values as high as 0.4. No evidence of disruptions at high density is found. These values of γ can possibly be underestimated because of the presence of locked modes, which, as previously described, may cause a local enhancement of radiation in the region of their maximum amplitude.

4.3 Pellet injection

The first results on pellet injection are encouraging [13]. The pellets can be completely ablated in the plasma core and relatively peaked electron density profiles are obtained, which last for several milliseconds. Global density increases up to a factor 3 with a single pellet are achieved without disruptive processes, confirming the robustness of the RFP. Preliminary analyses of pellet trajectory and ablation rate are consistent with the presence of superthermal electrons in the plasma core and can complement the EEA measurements.

5. Summary and future plans

Preliminary results after the recent machine modifications and diagnostics implementations have evidenced the importance of the locked mode phenomena: by their removal a strong reduction of power losses can be expected. More detailed and space resolved studies are in progress to better quantify the different contributions to the losses and to identify ways to remove the locking. Further work has to be dedicated to the density profile control by pellet injection and operation with boronized (Diborane) and/or hot wall (up to 280 °C). Tests are under way on current profile control by pulsed poloidal current drive.

References

[1] Fusion Engineering and Design, Special Issue, (1995) Vol. 25 N. 4, 301
[2] V. Antoni et al., 15th IAEA Conf. ,Seville, Spain (1994) Vol. 2, 405
[3] A. Buffa, F. Gnesotto, 16th SOFE, Champaign, Illinois-USA, (1995) to be published
[4] A. Buffa et al., 21st EPS Conf. Montpellier (1994) Vol. 1, 458
[5] L. Carraro et al., 22nd EPS Conf. Bournemouth UK, (1995) Vol. 19C, Part. III, 161
[6] B. Alper et al, Plasma Physics and Controlled Fusion, (1988) Vol. 30, N. 7, 843
[7] T. Bolzonella et al., this Conf. paper n. c002
[8] V. Antoni et al. Nuclear Fusion, 36 (1996), 435
[9] M. Valisa et al 12th PSI Conf. Saint-Raphael, France (1996), to be published
[10] P. Sonato et al, M. Valisa et al 12th PSI Conf. ,Saint-Raphael, France (1996), to be published
[11] Y. Yagi et al., this Conf. paper n. d001
[12] L. Marrelli et al., this Conf. paper n. c005
[13] L. Garzotti et al., this Conf. paper n. c003

The RFX Team:

ANTONI V., APOLLONI L., BAGATIN M., BAKER W., BASSAN M., BELLINA F., BETTINI P., BILATO R., BOLZONELLA T., BUFFA A., CAMPOSTRINI P., CAPPELLO S., CARRARO L., CASAROTTO E., CAVAZZANA R., CHINO F., CHITARIN G., COSTA S., DE LORENZI A., DESIDERI D., GAIO E., GARZOTTI L., GIUDICOTTI L., GNESOTTO F., GUARNIERI M., HEMMING O., INNOCENTE P., KUSSTATSCHER P., LUCHETTA A., MALESANI G., MANDUCHI G., MARCHIORI G., MARRELLI L., MARTIN P., MARTINES E., MARTINI S., MASCHIO A., MASIELLO A., MORESCO M., MURARI A., O'LEARY P., PACCAGNELLA R., PASQUALOTTO R., PERUZZO S. PIOVAN R., POMARO N., PUGNO R., PUIATTI M.E., ROSTAGNI G., SARDELLA A., SATTIN F., SCARIN P., SERIANNI G., SONATO P., SPADA E., STELLA A., TOIGO V., TRAMONTIN L., TREVISAN F., VALISA M., VITTURI S., ZACCARIA P., ZILLI E., ZOLLINO G.

Effects of Shell Gap Modifications on RFX Plasma Behaviour

T.Bolzonella, G. Chitarin, F. Gnesotto, E.Martines, S.Martini, N. Pomaro, F. Trevisan, Y.Yagi*, G. Zollino

Gruppo di Padova per Ricerche sulla Fusione
Associazioni EURATOM-ENEA-CNR-Università di Padova
Corso Stati Uniti, 4 - 35127 Padova (Italy)
*Electrotechnical Laboratory, Tsukuba (Japan)

1. Introduction

All pulses of RFX evidence wall locking of MHD modes [1]. Rotation of phase locked modes has been obtained in MST by reducing the field errors at the shell vertical gap [2]; significant confinement benefits derived from these actions. In RFX, the influence of field errors at the shell vertical gap on confinement is clear since they can be varied by acting on the equilibrium control, whereas no information is available on effects of equatorial gap and port errors, since they depend only on plasma behaviour and cannot be varied on purpose. Since the vertical ports on the shell give a little contribution to field errors [3], it has been decided to act on both the vertical and the equatorial gap errors. The feedback control of currents in the field shaping coils has been improved [4] and one of the two vertical gaps and the outer equatorial gap of the shell have been short-circuited.

Since the error reductions did not succeed in unlocking modes (with some exceptions that will be discussed in the last section), the paper presents the effects of gap modifications mainly in terms of loop voltage variations. In the first section, the relationships between loop voltage and magnetic perturbations are given; then the field quality improvements after closing the gaps are shown and their effects on loop voltage are discussed. Finally, some evidences of temporary, low-speed mode rotations are shown, whose enhanced rate can be also related to shell modifications.

2. Sensitivity of loop voltage to magnetic perturbations

Owing to several improvements on the gap field error compensation system (introduction of feedback control, shorter response time of the amplifiers), the correction of field errors at the vertical gaps is now very effective. In the present range of field errors (B_r at the shell surface is always less than 6-8% of the poloidal field B_θ and on the plasma surface it is typically less than 2-3%) no clear correlation with the loop voltage is found. The significant dependence presented before [5] is overcome, since errors are kept within the range where their influence on loop voltage is negligible.

The sensitivity of the loop voltage to the amplitude of the stationary field perturbation (mode locking to the wall) has also been analysed. Two parameters have been chosen to quantitatively characterise the perturbation: the peak-to-peak amplitude of the toroidal field undulation along the toroidal coordinate ΔB_ϕ and the energy of the modes m=1, n=7 to 15. Both parameters show a very weak correlation to the loop voltage; the loop voltage is slightly lower (1.5 V on average) in the case of locking located far from the gaps. It is worth noticing that ΔB_ϕ ranges between 20 and 45 mT in all the pulses and thus no data are available for the case of small perturbations.

These results suggest that the locked magnetic perturbation is "saturated"; its amplitude mainly depends on machine parameters like the distance between plasma column and stabilising shell.

3. Reduction of magnetic perturbations

Field error correction at the equatorial gap. The outer equatorial gap of the shell has been short-circuited by means of 96 copper bars, bolted to the shell halves as near as possible to the insulating gap. The radial field through the equatorial gap is measured by means of probe

coils, located around the 12 pumping ports, which also link the flux due to eddy currents in the stabilising shell, in the vacuum vessel and in the pumping port itself. A numerical model of all these conductors has been developed to calculate the radial field at the plasma boundary as a function of the flux measured by the probes; the short-circuiting bar effect can be also taken into account. The experimental results show that the short-circuit produced a clear reduction of the fast (>500 Hz) radial field fluctuations: the peak-to-peak amplitude, calculated at the plasma edge and averaged on a number of comparable pulses, has been reduced from 6.3 mT to 2.3 mT during the start-up phase. A similar reduction applies to the fast fluctuations during flat-top, but in this phase the radial field is mainly composed by low frequency (<50 Hz) harmonics, and marked differences between signals from adjacent probes are always measured close to the toroidal position of the locking [3]. Since the electromagnetic time constant of the short-circuiting system is around 5 ms for the horizontal field, frequency components below 200 Hz are not attenuated; in fact, no variation of the low frequency radial field components during flat-top has been observed after modifying the equatorial gap.

Field error correction at the vertical gaps. To reduce the stray field through the vertical gaps, in particular during the setting-up phase when the feedback efficiency is lower due to the limited bandwidth of the control amplifiers, one of the two vertical gaps has been short-circuited by means of metallic plates [6] and the currents through them are routinely measured. Their distribution in the poloidal direction gives a useful information on the actual distribution of the currents induced in the stabilising shell. Both gaps are equipped with two saddle coils which give a measurement of the vertical field component on the inner surface of the shell. The open vertical gap is also equipped with 16 radial field probes located at the outer surface of the shell.

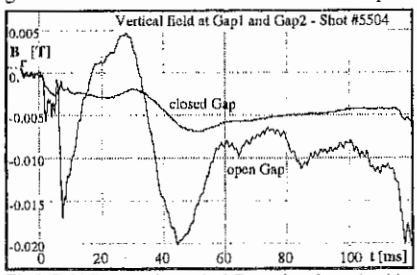

Fig.1 Field Error at the vertical Gaps after short-circuiting Gap1. Locking is far from both the Gaps

Fig. 1 shows the effect of the short-circuit in a pulse where the locking is far from both gaps. Before gap closure, the two signals were approximately the same; presently the maximum amplitude of the radial field on the closed gap is reduced by a factor of three and a very effective filtering action is evidenced on fast fluctuations. With locking far from both gaps, the cosθ (horizontal) component of the radial field at the open gap is negligible and the sinθ (vertical) component is the predominant one. Its temporal evolution is very similar to the cosθ component of the current distribution in the short-circuit.

Locking still occurs sometimes near the closed gap, in spite of the field error reduction, but now the region near the open gap exhibits a higher number of locking events. When the locking is near to the open gap, the cosθ component of the radial field at this gap becomes significant and can be even larger than the sinθ component, reaching 10% of the poloidal field. Since the RFX feedback system is not able to produce horizontal field, such component is due to the locking and not to a lack of equilibrium control.

"Matched Reversal" mode. The "matched reversal" mode is a particular setting up of the RFP configuration, in which the poloidal voltage around the plasma boundary is kept near to zero during the whole phase of toroidal current rise. Compared to the "aided reversal" mode, where the toroidal field at the edge is quickly reversed when the plasma current has already reached a level close to the final one, the "matched reversal" gives the advantages of lowering the eddy currents (and consequent field ripple) induced on passive elements and of reducing the plasma-wall interaction during the reversal phase, where losses are relatively large due to the poor confinement. On the other hand, the "matched reversal" mode precludes operation with

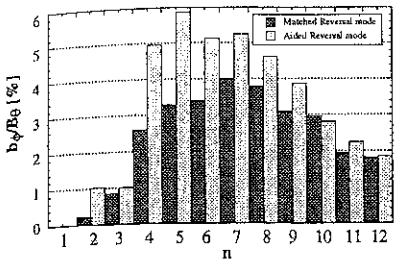

Fig.2 Amplitude of toroidal field modes with aided and matched reversal.

large vertical bias field, so reducing the possibility of centring the plasma column with respect to the first wall.

During the startup phase, before reversal, modes with increasing n become resonant in sequence, and show a growth followed by a decay [3]. The matched programming has produced a beneficial effect on the maximum amplitude reached by these modes, both in absolute and relative terms. Fig.2 shows the toroidal field modes amplitude, normalised to the poloidal field, with aided and matched reversal. A reduction of 30% in matched discharges is clearly observed for the strongest modes (n=4-9). Furthermore, the same modes are excited at a much lower level of plasma current than in aided discharges, so that in absolute terms a reduction of more than 50% is achieved. Nevertheless, after reversal no reduction is observed on the amplitude of the locked pertubation.

4. Effects on confinement

An improvement has been observed in the average dependence of loop voltage on the I/N parameter (ratio between toroidal plasma current I and average line density N) after the machine modifications: the most recent data show an average decrease of 3-5 V on the loop voltage (fig.3). Fig.4 shows the dependence of loop voltage on the magnetic shift; after the short circuit of the two gaps it is possible to operate with a larger horizontal displacement of the plasma column without significantly increasing the loop voltage. Since in RFX the plasma horizontal position is only controlled by a bias vertical field, a lower bias could be used, allowing gas breakdown at a lower toroidal field. This improvement opened the possibility of operating with the above mentioned "matched reversal mode". As discussed in Sect. 3, the short-circuit of the outer equatorial gap significantly decreased the high frequency magnetic fluctuations in the outer equatorial region; this can partially justify the reduction in loop voltage and can explain why the minimum in loop voltage is now obtained for a larger horizontal displacement, i.e. when plasma is shifted towards the short-circuited gap.

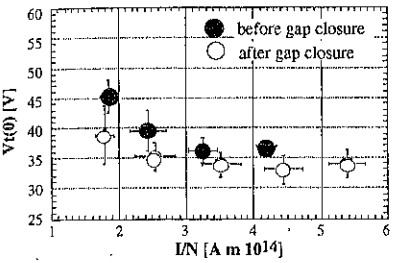

Fig.3 Loop voltage Vs. I/N for well centred discharges in the range (500 kA>I>600 kA).

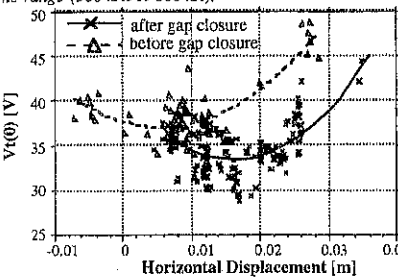

Fig.4 Loop voltage Vs. Horizontal displacement for discharges in the range (500 kA>I>600 kA) and I/N=3 10^{14} A m. A parabolic fit of data is also shown.

5. Mode locking and rotation

Despite the presence in every discharge of RFX of modes locked both in phase and to the wall, some mode rotation events have been observed by high-pass filtering the magnetic field signals with a 100 Hz numerical filter. Measurements of the toroidal component are made by two toroidal arrays of 72 probes each, which allow to

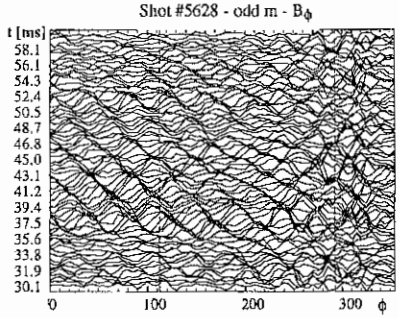

Fig.5 Example of mode rotation. Toroidal magnetic field for odd m modes is plotted as a function of the toroidal angle ϕ and of time.

obtain the odd m perturbation. The frequency range of the signals is DC-5 kHz. An example of rotation is shown in fig.5, where the toroidal magnetic field for odd m modes is plotted as a function of the toroidal angle ϕ and of time, after high-pass filtering. In this discharge the locked perturbation was at ϕ=310 degrees, and in fact a region of enhanced fluctuation is observed around this location. It is also possible to observe a rotation which appears at t=36 ms and lasts for 15 ms. Fourier analysis shows that in this case the rotating mode is n=9. In general, rotation events are observed to last from a few ms up to 10-15 ms. Often only one mode is seen to rotate, with a toroidal mode number n in the range 8-16, n=9 being the most frequently observed one. In some other cases more than one mode rotates.

By assuming rigid plasma rotation, it has been possible to compute the rotation frequencies in the toroidal and poloidal directions, f_ϕ and f_θ, through the formula $f = f_\theta + n f_\phi$, where m has been taken equal to 1 and f represents the rotation frequency of the mode with the specified n. In typical 600 kA discharges, f_ϕ is in the range 50-200 Hz while f_θ is in the range 0.5-2.5 kHz.

It is important to observe that, although the dominant mode of the locked perturbation (n=8) is sometimes seen to rotate in the 0.1-5 kHz range, a stationary n=8 is also present as a part of the perturbation. This is also true for higher n modes, although in some cases these are seen to rotate also in the DC-5 kHz range.

The magnetic measurements referred to above are taken outside the vacuum vessel, which behaves like a low-pass filter. Its transfer function relative to the toroidal component of the magnetic field has been computed. By approximating the vessel with a first order system, it exhibits the cut-off frequency at approximately 420 Hz. For several pulses, the signals of the toroidal arrays have been numerically reconstructed, applying the transfer function, but no clear change in the mode structure and no mode rotation at higher frequency (>200 Hz) have been observed.

Rotation events are more frequently observed after the closure of the gaps, but no visible effect on the main plasma parameters, such as loop voltage or confinement time, is observed as a consequence of them.

6. Conclusions

The short-circuit of the shell equatorial and vertical gap allowed to reduce loop voltage by more than 10 %, probably owing to the relevant reduction of magnetic fluctuations. Mode locking to the wall is still present, but temporary rotations of single modes are evidenced in selected pulses. Work is in progress to relate these events to operational conditions.

References

[1] A. Buffa et al., 21st EPS Conference (Montpellier, 1994), part I, p. 458.
[2] A. F. Almagri et al., Phys. Fluids B 4, 4080 (1992).
[3] V. Antoni et al., 22th EPS Conference (Bournemouth, 1995), part IV, p. 181.
[4] P. Fiorentin et al., Proceedings of the16th IEEE/NPSS S.O.F.E. (Urbana-Champaign, 1995)
[5] S. Martini et al., 20th EPS Conference (Lisboa, 1993), part II, p.459
[6] P. Sonato et al., Proceedings of the16th IEEE/NPSS S.O.F.E. (Urbana-Champaign, 1995)

First Results of Hydrogen Pellet Injection in the RFX Experiment

L. Garzotti, P. Innocente, S. Martini, T. **Bolzonella**, L. Carraro, E. Casarotto
R. Pasqualotto, B. Pégourié*, R. Pugno, P. Scarin, M. Valisa

Gruppo di Padova per Ricerche sulla Fusione Associazioni Euratom-ENEA-CNR-Università di Padova
Corso Stati Uniti, 4 - 35127 Padova, Italy

*Association Euratom-CEA sur la Fusion Contrôlée, C.E.Cadarache,13108 Saint-Paul-lez-Durance, France

ABSTRACT

The results of the first experiments of solid H pellet injection in the RFX reverse field pinch (R=2 m, a=0.46 m, I=1-2 MA) are presented. Pellets with masses of $1.5 \div 5 \cdot 10^{20}$ atoms and speed of 0.5÷1 km/s have been injected in pulses with plasma current of 0.5 ÷1 MA and density of $2 \div 6 \cdot 10^{19}$ m^{-3}. The ablation cloud emission and the increase of the plasma density are measured by a CCD camera, an H_α detector and a multichord interferometer. Significant ablation beyond plasma axis indicates that the ablation process is not adiabatic. Experimental profiles are compared with simulation by a NGPS model. Global density increase factors ≥ 3 with a single pellet are achieved, without causing the plasma to disrupt. With optimised parameters, the pellets are ablated in the plasma core and density profile peaking factors of ≈ 2 are obtained, which decay in a few milliseconds. Small effects are caused on the loop voltage and T_e drops 70÷100 eV, so that ≤50% enhancements of β_Θ and ≤30% of τ_E are estimated after injection. For low velocity pellets, trajectory deflections along the electron drift direction are seen, which are discussed in terms of asymmetric ablation by supra-thermal electrons.

INTRODUCTION Pellet injection has been extensively used in tokamaks and proved effective in achieving improved confinement regimes such as the PEP [1]. In RFP's, some pellet injection experiments were also performed on ZT40 and ETA-BETA II [2,3] albeit in plasmas with particle confinement time, τ_p , smaller than the pellet ablation time, hence strong density profile peaking was never obtained; moreover in ZT40 large poloidal deflections of the pellet trajectories hampered on-axis deposition. In RFX for the first time it is possible to inject pellets in an RFP plasma with $\tau_p \geq$ ablation time, although, due to the systematic presence of large MHD locked modes, RFX has not yet reached its target performance at 2 MA.

EXPERIMENTAL SET-UP The RFX 8-barrel injector [4] produces by in-situ condensation 8 pellets of $1.5 \div 5 \cdot 10^{20}$ atoms and pneumatically accelerates them at velocities of 0.5÷1.5 km/s. Adjusting the poloidal angle of injection, the pellets can be aimed at plasma center or up to 16 cm off-axis, to counter the poloidal deflection of the trajectory. Velocity and mass of each pellet are measured by optical detectors and a microwave cavity respectively. The pellet ablation rates and trajectories are monitored by an integrated diagnostic system. A position sensitive detector equipped with H_α light interferential filter (band pass 652÷666 nm) views the pellets looking at their trajectories from behind and a digital CCD camera also with H_α filter views the injection poloidal section from a tangential viewport. The two systems allow the reconstruction of the time-resolved 3-D trajectory of each pellet. The total H_α emission rate is measured by the H_α detector. An 8-chord two-color MIR interferometer [5] measures the electron density at a toroidal port 120° far from the injection one. The interferometer main wavelength (10.6 μm) is short enough and its bandwidth (1 MHz) is large enough to follow the evolution of the density profile during the ablation of each pellet without loosing fringes.

PELLET DATABASE Due to the higher priority of other experimental studies [6], pellet experiments have been performed on RFX only as an ancillary test program in ≈50 pulses at currents of ≈0.6 MA and in ≈20 pulses at currents of 0.7÷1 MA. Generally one or two pellets of small ($1.5 \cdot 10^{20}$ atoms) or intermediate ($3 \cdot 10^{20}$ atoms) size were launched during the current flat-top phase at velocities of 500÷900 m/s. In a few cases, very low velocity (≈100 m/s) pellets were injected, without timing control, by 'self-firing' (obtained by heating the gun barrel until the pressure build up in the breech due to pellet evaporation causes its self-propulsion). Due to

the relatively low current, only the small pellets fired at low velocity (500÷600 m/s) were completely ablated in the plasma. Intermediate size pellets were generally ablated less than 50% with a few exceptions at ≈80%. The self-firing cases were always ablated with shallow radial penetration and large trajectory deflections. In many cases, large global density increases (typically $\Delta n/n \approx 2$) were obtained with a single pellet causing relatively small effects on plasma current and loop voltage (see fig.1). Even in the most perturbing cases, when $\Delta n/n \approx 3$ and the post pellet plasma was in a high radiation, no disruptive process was excited, confirming the apparent immunity of the RFP to thermal instability,

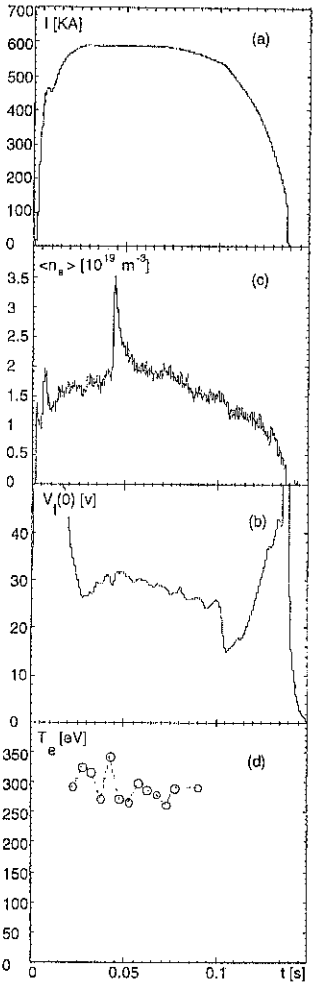

Fig.1 General behaviour in a pulse with pellet injection: a) plasma current, b) Loop voltage, c) global electron density, d) electron temperature.

ABLATION MEASUREMENTS AND MODELLING

The time behaviour of the pellet ablation rate estimated from the H_α emission is generally in good agreement with the time behaviour of the global n_e computed from the multichord interferometer measurements, particularly for completely ablated pellets, as shown in fig.2. In the case of incomplete ablation, the H_α emission increases again after the pellet strikes the wall and vaporises, but in this case little further density increase is seen by the interferometer, confirming the higher fuelling efficiency of pellets compared to gas puff. Generally, the ablation rate is not affected when the pellet crosses plasma center and continues until the pellet is completely consumed. This indicates that the ablation process is not adiabatic, consistently with the energy confinement time for all of the pulses in the present database being ≤ 2 ms. Therefore significant plasma heating occurs during the ablation time. Both the CCD camera and the H_α detector measure deflections of the pellet trajectories (see fig. 3). The deflections for pellets with speed of 500÷700 m/s are of the order of 10÷15 cm on axis both poloidally and toroidally. Self-fired pellets at 100 m/s suffer dramatic deflections, similar to those reported on ZT40 [3].

The measured ablation rates and trajectory deflections have been simulated with a NGPS ablation code [7]. An asymmetric ablation due to a suprathermal population has been included, which results in an asymmetric expansion of the ablation cloud. Since the ablation process has been shown to be non adiabatic, the calculated ablation rate has been adapted to match the experimental penetration. A reasonable agreement with experiments (see fig.3) have been obtained using a T_e profiles proportional to $1-r^3$ with the central value measured by Si(Li) PHA system prior to injection and a suprathermal population

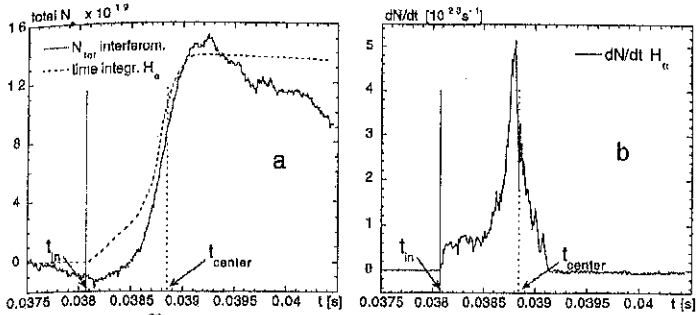

Fig.2 Example of a 1.5·10^{20} atoms pellet completely ablated in the plasma: the evolution of the global n_e from the multichord interferometer (fig.a solid line) agrees well with the time integral of the H_α emission (fig.a dotted line). The raw data of the latter signal (fig.b) show that the pellet continues to ablate beyond plasma axis until is consumed.

increasing from 0.3% n_{e0} at the edge to 1% n_{e0} on axis and with T_{supra}=2T_{e0}. Actually, while poloidal and toroidal deflections are in good agreement with experiments, the ablation profile does not match the H_α emission. The latter feature cannot be reproduced with the present status of the NGPS model unless the T_e profile is much more peaked than presently estimated.

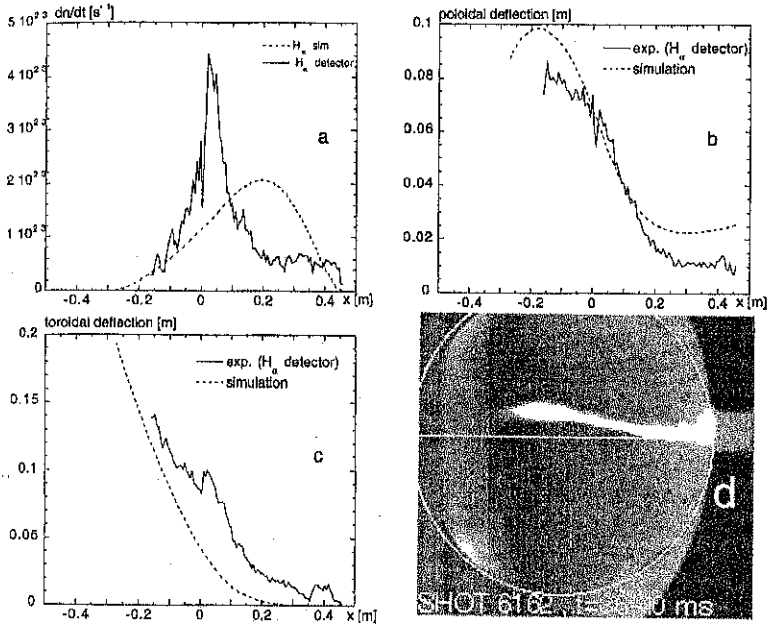

Fig.3 Experimental (solid lines) vs. simulated (dotted lines) ablation rate (a) and deflections (b poloidal, c toroidal and d from CCD camera).

BEHAVIOUR OF DENSITY PROFILES The evolution of the density profile during pellet ablation is shown in fig. 4 for the same pellet as that of fig.2. As expected from the progressive pellet penetration in the plasma, the density profile, nearly flat before injection, first peaks at the edge and then at the center.

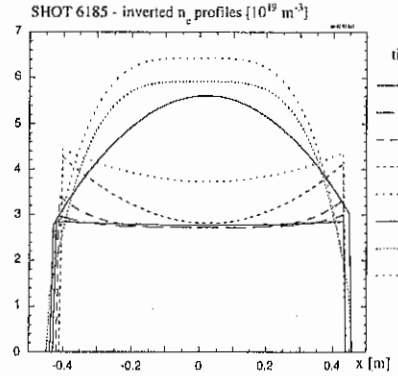

Fig.4 Inverted density profiles (inverted form the multichord interferometer measurements) during pellet ablation for shot 6185. First profiles is pre-pellet and last profile corresponds to ablation end.

At the maximum peaking the density is well fitted by a parabolic profile on top of a constant pedestal. The density peaking factor achieved is $\lesssim 2$.

During the following density decay phase the profile flattens again in a few milliseconds. This profile evolution has been simulated by means of a 1-D code [8] modelling transport across the stochastic magnetic field with a coefficient

$$D = \left(\frac{\delta B}{B}\right)^2 L_c \, v_{th}$$

where $\delta B/B$ is the fluctuation level, $L_c \approx 0.5$ m is the fluctuation correlation length and v_{th} is the ion thermal velocity. The best agreement has been obtained with $\delta B/B \approx 2 \div 3\%$, so that $D \approx 20 \div 40$ m^2 s^{-1}, which is consistent with a particle confinement time of ≥ 5 ms.

EFFECTS ON GLOBAL CONFINEMENT For the limited pellet database available, the only direct measurement of electron temperature is that of the Si(Li) PHA, which generally cannot provide a measurement immediately after injection, since the photon flux is too low to build-up a spectrum. Some estimates of T_e post injection could be obtained by modelling the time behaviour of the emission of OVII measured by an MLM monitor [9], which generally indicates a T_e drop of the order of 70÷100 eV. A similar value (≈70 eV) is also found in a few pulses where the number of count of the Si(Li) system was sufficient to attempt a measurement post injection. Assuming that the T_e profile is unchanged, the value of the central $\beta_{\Theta e}$ should be higher by 30÷50 % post-injection. This increase is consistent with the empirical RFX scaling of $\beta_{\Theta e}$ with density [6]. On the other hand, the actual $\beta_{\Theta e}$ increase should be larger by 10÷20% due to both the flatter T_e profile and the more peaked n_e profile in the post-injection phase. The toroidal loop voltage generally increases by 2÷3 v, which is consistent with the expected change of the classical resistivity due to the T_e drop, hence the confinement time, at least for the electron part, is also increased by ≤30 %.

References

[1] Smeulders,P., et al., Nuclear Fusion **35** (1995) 225.
[2] Wurden,G.A., Weber,P.G. et al., Nuclear Fusion **27** (1987) 857.
[3] P.Innocente, S.Martini, in *"Physics of Mirrors, Reversed Field Pinches and Compact Tori"*, Int.School of Plasma Phys., Varenna 1987, vol. III 1043.
[4] W.Baker, L.Garzotti, et al.*"Multishot Pellet Injection System for RFX"*, proc. 16th Symposium on Fusion Engineering SOFE, Champaign-Urbana 1995, to be printed.
[5] P.Innocente and S.Martini, Review of Scientific Instruments **63** (10) 1992, p. 4996.
[6] A.Buffa et al., *"Recent Results from RFX"*, this Conference paper 001.
[7] B. Pégourié, et al., Nuclear Fusion **33** (1993) 591.
[8] S..Martini, et al. , 21th EPS Conf. on Controlled Fusion and Plasma Physics, Montpellier 1994, Vol. I, p. 454.
[9] L.Carraro, et al. ,"An Ultra Soft X-Ray Multilayer Duochromator for the RFX Experiment", submitted to Reviews of Scientific Instruments

Study of the dependence on density control of the RFP setting-up phase in RFX

L.Garzotti, S.Martini, **T.Bolzonella**, E.Casarotto, P.Innocente, M.E.Puiatti

Gruppo di Padova per Ricerche sulla Fusione
Associazioni EURATOM-ENEA-CNR-Università di Padova
Corso Stati Uniti, 4 - 35127 Padova (Italy)

Abstract

The RFP setting up phase on the RFX experiment is analysed to try to explain the different behaviour observed as function of the electron density. In particular at high density, the setting-up is characterised by lower plasma resistivity, impurity influx and MHD activity whereas, during the following RFP phase, higher densities plasmas correspond to lower temperatures and higher resistivities. Moreover higher electron density should be associated to higher values of the Lundquist number and increased MHD activity. A possible interpretation is presented which links the enhanced impurity influxes in a low density start-up to the influence of stronger production of runaway electrons caused by large values of the E/E_C parameter (applied electric filed / Dreicer field). Increased radiation cooling and current density profile modification would follow, leading to increased MHD activity and RFP magnetic profiles farther form the BFM state.

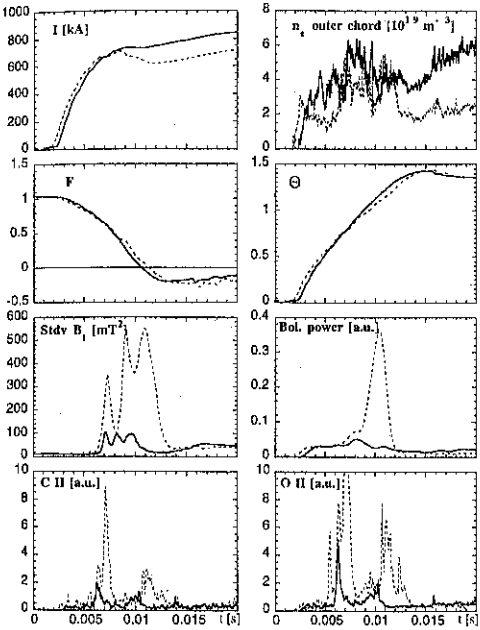

Fig.1 Comparison between a 'good' (# 4663, solid line) and a 'poor' (# 4665, dashed line) setting-up discharge. Plasma current, electron density, F, Θ, magnetic mode energy, radiated power from bolometer measurement and CII and OII impurity emission are plotted vs time for the initial 20 ms of the pulse.

1. Introduction

The setting-up of the Reversed Field Pinch magnetic field configuration is a highly turbulent phase during which the safety factor q(a) assumes rational values critical for resonance of MHD modes and, hence, strong magnetic activity is observed. Several different setting-up techniques can be adopted to reach the RFP configuration [1,2], whose effectiveness is often found to be critically dependent on the fine tuning of the magnetic circuits timing [3]. On the other hand the control of the density also plays a crucial roles during this phase: very different setting-up behaviours are obtained, due to different density control, in pulses with the same magnetic circuit programming.

In RFX in particular the setting-up in the 'aided reversal' mode [2] is better when the density is kept as high as possible by gas puffing or by high influx of gas from the vessel first wall. The high n_e setting-up is accompanied to a lower level of MHD activity and to a lower loop voltage. Conversely, in the low density cases, the unstable phase can be so bad that the increase in loop voltage terminates the discharge preventing the achievement of

the RFP configuration. A clear marker of the quality of the setting up is the behaviour of the plasma current which, during the unstable phase of before field reversal, shows a decrease which ranges from 0÷10 kA in the best cases to more than 100 kA in the worst ones .

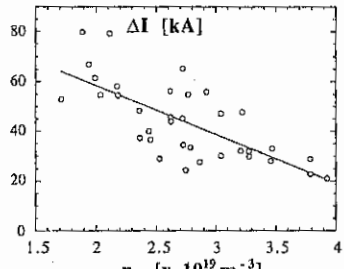

Fig.2 ΔI vs line averaged electron density at t=20ms.

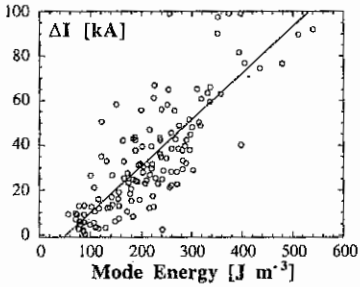

Fig.3 ΔI vs energy of magnetic modes at reversal time for high current (I=800 kA) discharges.

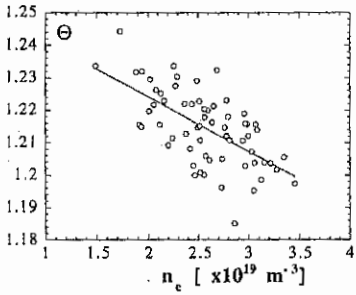

Fig.4 Θ parameter vs.electron density at reversal time.

This behaviour seems to be in contrast with that observed during the RFP phase, when higher densities plasmas are characterised by lower temperatures and higher resistivities. Moreover higher densities regimes should be associated to higher values of the Lundquist number and, consequently, to an increased MHD activity.

The paper presents a study of the RFX setting-up which analyses the behaviour of the plasma density, the amplitude of the MHD modes, the current drop during the unstable phase and other quantities representative of the magnetic field profiles and of the impurity influxes in order to find an explanation to this apparent paradox.

2. Experimental data analysis

To start with, a rough survey of the main characteristics of the high and low density setting-up has first been done by comparing the time evolution of several couples of discharges with the same magnetic circuits programming, but different density control, as shown e.g. in Fig.1. As already mentioned, the plasma current, I, shows a drop, ΔI, that reaches a values of ≈100 kA in the low n_e case. A radiation peak measured by bolometer and a peak in the magnetic energy of MHD modes are also seen during the unstable phase and are enhanced in the low n_e case. Similar differences between good and poor setting-up are found in the spectroscopic measurements of impurity ion emissions (CII and OII), although their time evolution are not always well related with those of the total radiation or of the plasma current. From the point of view of the magnetic configuration, relatively small effects are seen: the initial rate of current increase is the same, which indicates the plasma inductance is the same, and the magnetic configuration is also unaffected, at least in terms of the pinch parameters $\Theta = \langle B_\theta(a)\rangle/\langle B_\phi\rangle$ and $F=\langle B_\phi(a)\rangle/\langle B_\phi\rangle$. Actually some differences in the F-Θ trajectory appears during the unstable phase prior to field reversal.

The above behaviours have then been studied statistically on a large database of discharges at low (500 kA) and medium (800 kA) plasma current, all with 'aided reversal" setting-up [2]. The parameters in the databases were plasma current I, ΔI, I/N parameter (N=line density), central and edge density from the multichord interferometer, Θ,

toroidal magnetic shift, energy and position of the wall-locked MHD modes. Each quantity is sampled at the first maximum of plasma current (i.e. immediately before the most turbulent phase), at the B_ϕ reversal time, t_{RFP}, (which is close to the most perturbed phase) and at 20 ms (which is a time early enough in the RFP to get good quasi stationary estimates of all the quantities still saving some reminiscence of the pre-RFP phase). The favourable dependence of the start-up phase on density is confirmed both in terms of higher maximum plasma current, lower magnetic mode energy, lower impurity content and lower radiation.

We find a good correlation between the current drop, ΔI ,and density related quantities such as central chord density, I/N parameter and a form factor of the density profile defined as the ratio between the average densities measured by central and external interferometer chords. In Fig.2 is shown that ΔI decreases with an increasing average density; on the other hand ΔI is well correlated also with the energy of the magnetic MHD modes (Fig.3).

To investigate the possible dependence of the MHD mode energy at t_{RFP} on magnetic field profiles, we have correlated the value of Θ at t_{RFP} with ΔI: discharges with lower values of Θ at t_{RFP} are indicative of current profiles closer to the flat, fully relaxed one, as expected from the Bessel Function Model (BFM) [5]. From Fig.1 and Fig.4 it is indeed possible to see that the RFP is reached earlier and at lower Θ values under the 'good' set-up conditions; no over-relaxation phenomena [3] have been observed up to now in RFX.

3. Discussion

The most obvious effect of a different gas influx from the first wall or from the gas puffing valves should be on the density both in terms of mean value and profiles. Indeed high n_e discharges show hollow profiles (with the maximum in the external region), whereas low n_e ones have peaked or nearly flat profiles, as shown in Fig.5. Consequently, differences in electron temperature, T_e, values and profiles could be expected. In particular, based simply on a pressure balance effect, the electron temperature should be lower and more peaked at high density. A different power deposition and differences in content (global Z_{eff}) and in spatial distribution of the impurity ions might also be expected. All the above factors should induce different current density and magnetic field profiles, thus providing a link with the observed behaviour of MHD modes.

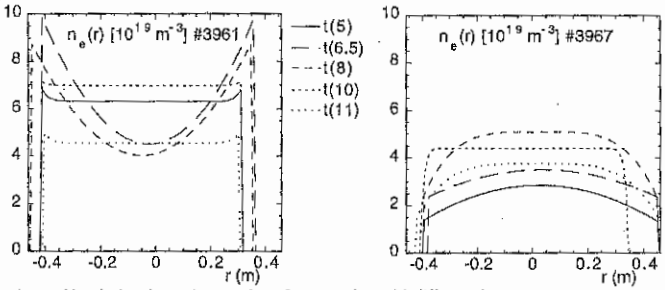

Fig.5 Density profiles during the setting-up phase for two pulses with different density.

As said in the introduction, from the point of view of the T_e and associated classical resitivity profile, one would predict the lower n_e case to correspond to the more stable situation. On the other hand, no difference in terms of magnetic quantities is seen to precur the unstable phase. Hence, a different mechanism linked to lower density and, presumably, higher T_e must be identified, which could efficiently and quickly lead to an unstable situation.

A possible interpretation may be found observing that when the density is lower, the plasma is less collisional, allowing a larger production of suprathermal electrons. This effect is illustrated in Fig. 6 where the values of the parameter E/E_C (electric field/Dreicer critical field) and of the runaway fraction generation per collision time have been estimated for the same discharges of Fig.5 following the formulae valid for an ideal plasma [5] and using for T_e (which is not measured during setting-up) a value derived from the n_e measurement according to an empirical scaling

valid for the RFP phase. From Fig. 6 it can be seen that at low n_e the E/E_C increases quickly, exceeding 10% during the unstable phase before field reversal. Moreover, while in the high n_e case a dense edge layer may cause a less efficient diffusion of the suprathermal electrons towards the wall, in the low n_e case this does not happen. During that phase the large destabilized MHD modes can cause both the stochasticization of the central region of the plasma, which helps the diffusion of fast electrons and, by deforming the external magnetic surfaces, the creation of zones of localised interaction with the first wall. All the above mechanisms conjure up in causing a stronger localised energy loading on the graphite first wall and a consequent increased impurity emission. An experimental evidence of such an effect, besides the differences in impurity line emissions seen in Fig.1, is given in Fig.7 where the sum density of CV and CVI ions measured by means of a Schwob spectrometer during the start up phase is compared for several couples of neighbouring discharges with the same field programming but different n_e.

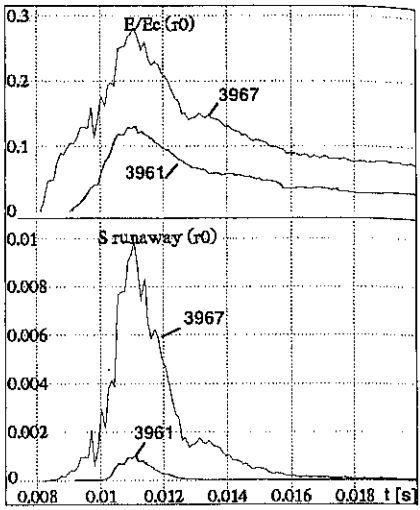

Fig.6 Estimateds of tte time behaviour of the E/E_C parameter and of the runaway fraction generation per collision time for two pulses at high (# 3961) and low (# 3967) n_e.

The larger impurity content would be responsible for enhancing the plasma resistivity, especially in the external region, due to both higher Z_{eff} and edge cooling caused by enhanced radiation losses (as confirmed by the bolometer measurements in Fig.1). In fact this could compensate for the lower edge electron temperatures otherwise expected at high density. Faster processes of resistive diffusion, moreover in a region close to that of magnetic field reversal, would then lead the current profile towards not fully relaxed, unstable magnetic configurations, explaining the high peak in the m=1 magnetic mode energy and the achievement of the RFP at later times and higher Θ.

References

[1] S.Martini et al., 20th EPS Conference (Lisboa, 1993), part II, p.459.

[2] V.Antoni et al., 15th IAEA Conference (Seville,1994) vol. II p. 405.

[3] S. Mazur and P. Nordlund, Phys. Plasmas **2**, 3734 (1995).

[4] J.B.Taylor, Phys. Rev. Letters **33**, 139 (1974).

[5] H.Knoepfel and D.A.Spong, Nuc. Fus. **19**, 785 (1979).

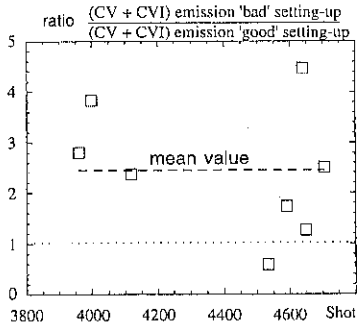

Fig.7 Ratio between carbon density (CV e CVI ions) from integrated (10<t<30 ms) spectroscopic measurements for pairs of neighbouring 'good' and 'poor' setting-up discharges.

Total Radiation Emissivity Distributions in RFX

L.Marrelli, P.Martin, A.Murari.

Padova Fusion Research Group
(Euratom-Enea-CNR-Università di Padova)
Corso Stati Uniti 4, Padova, Italy

1 Introduction.

This paper contains the results of a detailed survey of the total radiation emitted by hydrogen plasmas in the Reversed Field Pinch (RFP) configuration. The measurements have been taken with a 8 chords bolometric camera [1], housing miniaturised metal foil bolometers [2] and installed on RFX [3], the highest current RFP experiment nowadays in operation (major radius = 2 m, minor radius = 0.5 m, target plasma current = 2 MA). The steady state profiles of the total radiation emissivity have been characterised in various operative conditions, during all the essential phases of the 1994/1995 RFX experimental campaign [4], which was dedicated to the investigation of two different current ranges: one between 0.5 and 0.7 MA and one between 0.8 and 0.95 MA. The plasma density was varied in the range between $2x10^{19}$ and $1.2x10^{20}$ m^{-3}.

The 8 chords bolometric camera was installed on a central porthole located at the bottom of the RFX vacuum vessel; the lines of sight were arranged in a fan-like geometry covering 2/3 of the equatorial diameter. The outputs of the absolutely calibrated sensors are processed by 50 kHz carrier frequency amplifiers with a bandwidth of 1 kHz. The signals have been then averaged over an interval of 10 ms. The various sources of experimental error are estimated to give an uncertainty in the measurements of about ±10%.

From the experimental values of the brightness $f(p_i,\phi_i)$, emissivity profiles of the form $g(r,\theta) = g_0(r) + g_1(r)\cos\theta$ have been reconstructed by means of a generalised inversion algorithm, since the geometrical lay-out of the chords allows to resolve only the m = 0 and m = 1 (cosinusoidal) poloidal harmonics. For $g_0(r)$ and $g_1(r)$, linear piecewise functions (see fig.1) have been chosen, which depend on 4 parameters (the maximum of the cosinusoidal component g_{1max}, the maximum of the m = 0 component g_{0max}, the value at the centre of the m = 0 component g_{0cent} and the radial coordinate α of the knee). These parameters are determined by a least-squares fit to the difference between the experimental measurements and the values analytically computed on the basis of the model. The shape of this function was suggested by preliminary indications that the total radiation in RFX usually comes from the outer region of the plasma cross-section; this hypothesis has then been confirmed by the results of the fit, as shown in fig.1, where a comparison of the reconstructed profiles with the experimental brightness measurements is reported.

2 Phenomenology of the emissivity profiles and total radiation losses.

The adopted technique turns out to be quite effective in reproducing the experimental data over the all range of RFX plasma horizontal shift. From the computed emissivity $g(r,\theta)$, the radial position, x_G, of the total radiation barycentre, defined as $x_G = \int_0^a r^2\, g_1(r)\, dr/2 \int_0^a r\, g_0(r)\, dr$, can be determined. As shown in fig.2, this quantity proves to be well correlated with the plasma shift, not only contributing to reinforce the confidence in the model chosen for the inversion algorithm, but also confirming that appreciable outward displacements of the plasma column and the ensuing enhanced plasma-wall interactions correspond to higher edge radiation.

Irrespective of the detailed shape of the emissivity profiles, the total emitted power increases sharply with the plasma density. This fact is evident from fig.3, which is a plot of P_{RAD} versus I/N, where P_{RAD} is calculated integrating the reconstructed emissivity $g(r,\theta)$ over the entire volume (in the hypothesis that this quantity does not depend on the toroidal coordinate) and I/N is defined as the total current divided by the linear electron density ($N = \int_0^a 2\pi r\, n_e(r)\, dr$). In the high density regime (low I/N), the ohmic input power P_{ohm} rises as well, but the relative importance of the radiative loss channel continues to grow. This tendency is confirmed in RFX as can be seen in fig.4, where the ratio $\gamma = P_{RAD}/P_{ohm}$ is plotted versus I/N. As I/N decreases toward its lower limit ($I/N \approx 1.8\ 10^{-14}$ A m for this set of RFX data), the spread of the values of γ becomes wider but on average the fraction of the input power which is radiated is larger (up to 40 %).

The dependence of the total emitted radiation on plasma purity has also been confirmed by bolometric measurements, comparing the γ ratio for reproducible discharges at various densities before and after boronization of the graphite first wall. After wall conditioning, the γ values are lower for similar levels of I/N (see fig.5; each point is an ensemble average to better show the trend) and therefore higher density regimes are accessible.

3 Discussion and conclusions.

Approaching high density regimes, the total radiation emitted from RFX plasmas increases decidedly in a barrier-like fashion, as shown in fig.3. It is still an open question whether this trend of P_{RAD} can be associated with a radiation dominated density limit of the type described in [5]. In fact, as it is evident in fig. 4, even at the lower I/N values the γ ratio does not exceed 0.4. This regime, where the best confinement performances are obtained [4], is not strictly the one typical of radiation dominated discharges. Indeed it must be kept in mind that these low levels of the γ ratio cannot be ascribed to systematic errors in the measurements, whose reliability is fairly good, since the bolometers have been calibrated absolutely and P_{RAD} has been calculated, unlike on other RFP machines, on the basis of the measured emissivity profiles.

A possible explanation for the obtained results can be related to the presence of strong local disturbances of the equilibrium magnetic field, normally interpreted as "locked modes"

[6], which affect the RFX plasmas. These distortions have a typical toroidal extension ranging between 20 and 40 degrees, where strong interactions with the first wall are observed. It is also worth mentioning that these locked modes have been considered one of the main sources of the anomalous component of the plasma resistance, which adds to the Spitzer-like term and causes an increase in the input power required to sustain the discharge. As a result, the P_{RAD} values previously discussed, which refer to discharges where the disturbance was not located in front of the bolometric camera and which are calculated under the hypothesis of toroidal symmetry, may constitute an underestimate, since a significant fraction of input power could be locally radiated in the region where the locked mode is present [7].

A different estimate of γ can be obtained by comparing the "toroidally symmetric" P_{RAD} with the input ohmic power calculated from the helicity balance $P_k = I/\phi \int \eta J \cdot B \, dV$ [8], where I is the plasma current, ϕ the toroidal flux and η the resistivity. In this relation a Spitzer-like resistivity is assumed, experimental values of Z_{eff} are used and the profiles of J and B are calculated with the PFM model. P_k is normally interpreted as the power needed to sustain a toroidally symmetric RFP configuration, including the contribution of the dynamo, and is the value with respect to which the anomalous input power, due to locked modes and other local effects, is calculated as $P_{an} = P_{ohm} - P_k$. The ratio $\gamma_k = P_{RAD}/P_k$ versus I/N is reported in fig.6, emphasising how, in the high density regimes, almost all of P_k is lost by radiation (the plot of fig.6 includes shots of a reduced set, for which reliable values of Z_{eff} are available; for this data set, the values of γ are less than 30 %). This confirms the robustness of the configuration with respect to these losses since, even at relatively high levels of radiated power, no evidence of disruptions, as those associated with the density limit in tokamaks, is observed.

Acknowledgements

The authors would like to acknowledge the contribution of Gianluca Spizzo to the development of the reconstruction algorithm and to the data analysis.

References

[1] A.Murari et al, Rev.Sci.Instrum. **66**, 665, (1995).

[2] K.F.Mast et al, Rev.Sci.Instrum. **62**, 744, (1991).

[3] R.Fellin et al., Fusion Engineering and Design, **25**, (1995).

[4] V. Antoni et al, in Proc. 15th conf. on Plasma Phys. and Controll. Fus. Res. **2**, 405 (1994).

[5] S.Ortolani and G.Rostagni,Nuclear Instruments and Methods, **207**, 35 (1983).

[6] F.Gnesotto et al. in Proc. 22nd EPS Conference on Contr. Fus. and Pl. Phys., **19C-part IV**, 181 (1995).

[7] M.Valisa et al., "Locked Modes Induced Plasma-Wall Interactions in RFX" submitted to Journ. of Nucl. Materials.

[8] S.Ortolani, in Proc.7th Int.Conf. Plasma Phys., 802, (1987).

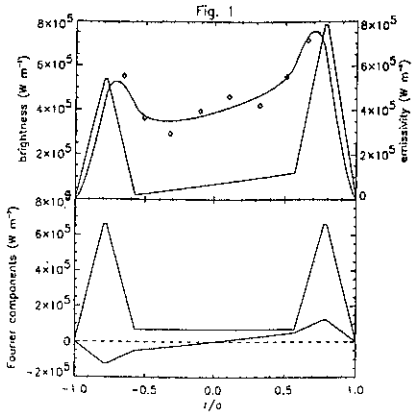
Fig. 1
brightness (W m⁻²)
emissivity (W m⁻³)
Fourier components (W m⁻²)
r/a

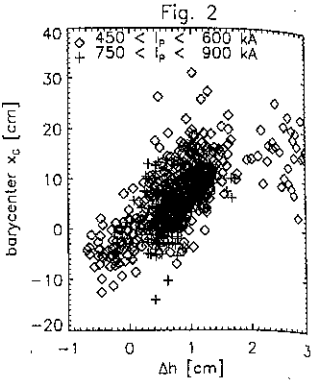
Fig. 2
◇ 450 < Ip < 600 kA
+ 750 < Ip < 900 kA
barycenter xG [cm]
Δh [cm]

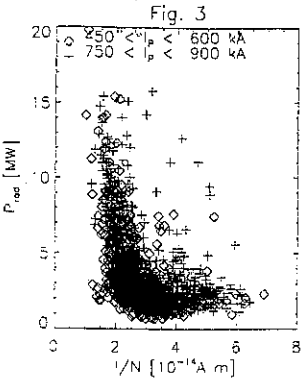
Fig. 3
◇ 450 < Ip < 600 kA
+ 750 < Ip < 900 kA
Prad [MW]
I/N [10⁻¹⁴A m]

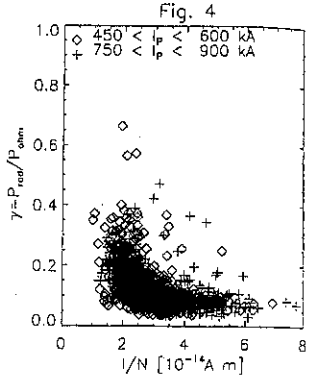
Fig. 4
◇ 450 < Ip < 600 kA
+ 750 < Ip < 900 kA
γ=Prad/Pohm
I/N [10⁻¹⁴A m]

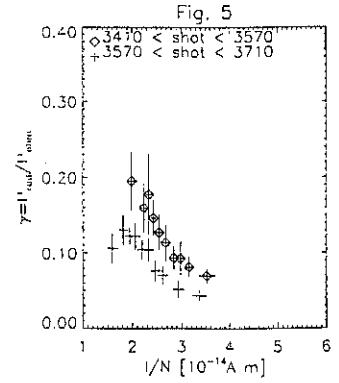
Fig. 5
◇ 3410 < shot < 3570
+ 3570 < shot < 3710
I/N [10⁻¹⁴A m]

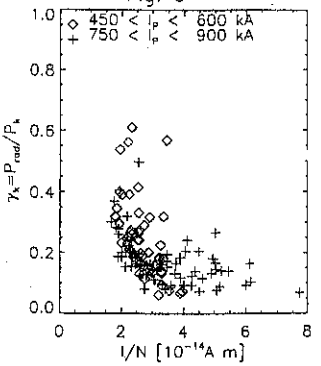
Fig. 6
◇ 450 < Ip < 600 kA
+ 750 < Ip < 900 kA
γx=Prad/Px
I/N [10⁻¹⁴A m]

Studies of the Ion Heating in RFX

L. Carraro, S. Costa, R. Paccagnella, M.E. Puiatti, P. Scarin, M. Valisa

Gruppo di Padova per Ricerche sulla Fusione
Euratom-ENEA-CNR-Università di Padova Association - Padova, Italy

Introduction - This paper summarises the ion temperature measurements recently carried out on RFX in 600 kA discharges ($1<n_e<7$ (10^{19}) m^{-3}, $180 < Te < 350$ eV and $\Theta = 1.45$) aiming in particular at the evaluation of the ion pressure, its contribution to the total β - the kinetic to magnetic pressure ratio - and its anomaly level . In fact the assumption Te=Ti is not met in Reversed Field Pinches (RFP) and Ti is often found anomalously high in various ohmically heated experiments [1..10]. Generally Ti results to be sensitive to the pinch parameter $\Theta = B\theta(a)/\langle B_Z \rangle$. However, for a given Θ value, variations in Ti have been associated also to changes in the wall conditions [5] or in the shell resistivity [9]. Moreover Te and Ti often display the tendency to counterbalance, though uncoupled, in such a way that the total β, for given current to density ratios, remains fairly constant [5,9]. An attempt to explain such a varied phenomenology was made in [9] where by means of a dimensional analysis it was shown that Te and Ti have an opposite dependence on the velocity fluctuations.

The study of the ion temperature behaviour in RFX is based on the proton temperature data collected by means of a 4 m long Time Of Flight (TOF) neutral particle analyser [11] and on the impurity ion temperatures measured by a 1.33 Czerny-Turner spectrometer equipped with a 2400 g/mm grating. The instruments observed the plasma along a diameter on the equatorial plane in two different toroidal locations.

Results - The Doppler broadening of several chord integrated lines emitted by various ionisation states of different impurities have been measured (See **Table I**).

Table I

ion	λ(Å)	Ti (eV)
O VII	1623	175
N VI	1896	142
C V	2271	122
B IV	1823	83
O V	2781	75
C IV	1548	60
C III	2297	46
C I	1931	12

In order to recover information on the impurity ion temperature profile a 1-D impurity diffusion code has first been used that, assuming a temperature profile of the type $T_e=T(0)(1-(r/a)^4)$, by simulating the experimental emissivities of the oxygen, carbon and boron lines, reconstructs their radial distribution. Finally, the average of the impurity ion temperature, weighted on the calculated emission profiles, has been computed, varying test ion temperature profiles until a good agreement with the experimental data has been found. Since the spectrometer can typically observe one ionisation state at a time, ensembles of shots with comparable Θ and I/N (I= plasma current, $N=\langle n_e \rangle \pi a^2$) have been considered. It has been found that a temperature profile of the type $T_i=T(0)(1-(r/a)^4)$ is adequate to fit the spectroscopic

experimental data within 20 %. In Table I the impurity temperature data are summarised for the shots with I/N comprised between 4 and 5 10^{-14} Am and Θ =1.45. In such situation, the central ion temperature results to be ≈ 190 eV. **Fig. 1** shows the temperatures of the helium-like states as a function of I/N. The temperatures increase with I/N but their estimated profile, within the uncertainties of the method, does not change .

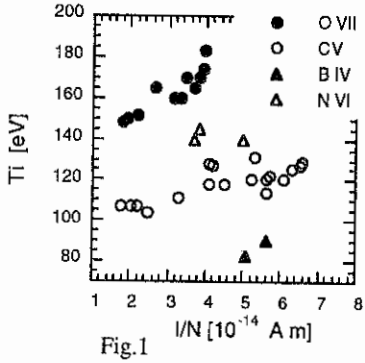

Fig.1

The hydrogen temperatures measured by the TOF system are shown in **Fig. 2** versus I/N. Each triangle corresponds to an ensemble average over "raw" data, result of a direct fit of a neutrals spectrum built by overlapping 40 time windows of 1.5 μs taken in 20 ms during the current flat-top. The error bars show the standard deviation. In order to deconvolve the effects of possible opacity of the plasma on the escaping neutrals a number of discharges have been simulated by means of a Monte Carlo code that under a number of assumptions (electron temperature and density profiles as well as the neutral density at the edge are input to the code) simulates the emitted neutral spectra.

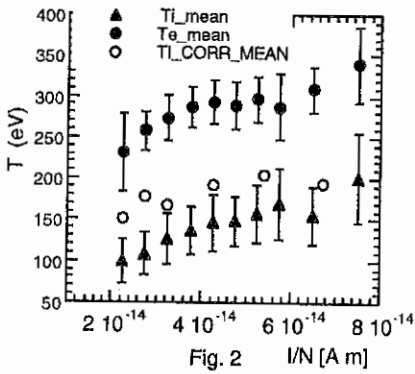

Fig. 2

The simulation has been performed for a number of shots at different I/N and the ensemble averages are shown as open circles in **Fig. 2**: the central ion temperature is statistically higher than indicated by the "raw" data. In many discharges, in particular at low I/N , the shape of the neutral spectra is characterised by the presence of a non Maxwellian tail whose origin will be matter of future investigations but that anyway hampers the determination of the spectrum slope and therefore of the ion temperature. As to the radial profiles, the ones deduced by the Monte Carlo code analysis at low I/N agree fairly well with the fourth power profile recovered by the impurity data, though sometimes a flatter profile, up to the eighth power, appears more suitable. For comparison, Fig. 2 shows also the electron temperature measured by the Si(Li) detector . The ion temperatures are typically lower than the electron ones by a factor 2/3. The data have been used to evaluate the plasma $\beta\theta$, shown in **Fig. 3** as a function of I/N. The points may be fitted by a curve proportional to $(I/N)^{-0.7}$.

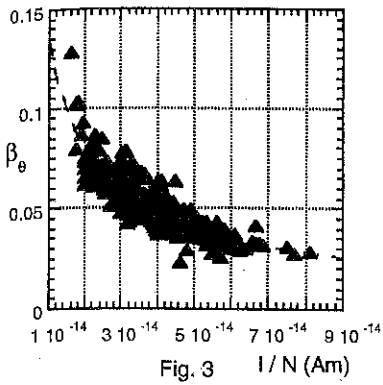

Fig. 3

Discussion Impurity and hydrogen temperatures are found to be comparable in RFX. The temperatures of the various impurities are a clear function the ion charge i.e. of the ionisation potential and therefore of the impurity radial distribution, that depends on the electron temperature and on the transport processes. This confirms that the ion temperature does not depend on the ion mass, as expected by the fast energy equipartition rate between ions and impurities, according to which the latter reach almost instantaneously a temperature equal to the local ion temperature in the RFX situation.

The resulting $\beta\theta$ values exceed 10% in the high density regime where the best confinement is obtained and decays approximately with $I/N^{-0.7}$. Within the relatively narrow I/N range explored and the experimental uncertainties electron and ion temperatures seem to have the same dependence with I/N. We just mention the presence of energetic ion tails especially at high densities: a careful analysis of the spectra as well of the experimental technique is to be performed in order to understand the mechanism that originates the fast ions and to evaluate the contribution of these particles to the energy content.

The ion temperature is only slightly lower than the electron one, in contrast with the fact that in ohmically heated RFP's only electrons absorb directly energy through Coulomb collisions. Ions are energetically uncoupled from electrons, due to an energy equipartition time (several ms) long in comparison with the ion energy confinement time, that is of the order of the global energy confinement time (1-1.5 ms in RFX). To explain this phenomenon of anomalous ion heating, we compare our experimental findings with two different theoretically derived ion heating terms. The first was proposed in [12] and is based on viscous ion heating, while the second one [13] results from the model of a plasma in a stochastic magnetic field.

The time evolution of ion temperature can be written in a simple way as:

$$\frac{dT_i}{dt} = \nu_{i/e}\,(T_e(t) - T_i(t)) - \frac{T_i(t)}{\tau_i^E} + P_{ion} \qquad (1)$$

where $\nu_{i/e}$ is the electron-ion equipartition rate, τ^E_i is the ion confinement time and P_{ion} is the input heating power. Following [12]: $P_{ion} = A\,\tau_{ii}\,T_i\,(\tau_\eta\,b\,f)^{-2}$

where A is an arbitrary enhancement factor, τ_{ii} is the ion-ion collision time, τ_η is the classical resistive-diffusion time, b the normalised magnetic fluctuation level and f the so called "dynamo efficiency". Instead using the results of [13]: $P_{ion} = -\,Ze\,E_r\,J_i$ where

$$J_i = D_{st}\left(\frac{d}{dr}\left[n_i\left(\frac{2T_i}{m_i}\right)^{1/2}\right] - n_i\left(\frac{2T_i}{m_i}\right)^{1/2}\frac{ZeE_r}{T_i}\right) \quad \text{and} \quad E_r = \frac{1}{e}\frac{dn}{dr}\frac{1}{n}T_e - \frac{1}{2}\frac{dT_e}{dr}$$

D_{st} being the stochastic magnetic diffusivity and E_r the ambipolar electric-field. Note that the total work of this field on the plasma (electrons and ions) is zero. The various gradients are approximated in our O-D approach by typical decay lengths. The electron temperature is assumed to be a given function of time in accordance with experimental measurements. The result of the integration of **Eq.(1)** is given in **Fig. 4(a,b)** for the two ion heating terms.

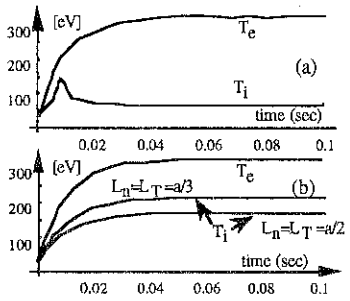

Fig. 4

We note that the viscous term, considered in the present simulation 50 times the classical value (A=50), is not able to sustain the ion temperature at later times, while it gives a non negligible contribution initially. The ambipolar term instead can efficiently heat the ion. The rate is obviously largely influenced by density and temperature gradients. The temperature evolution of **Fig. 4** is not influenced if the ion temperature is evolved in time coupled to an analogous energy equation for an impurity species.

Conclusions - Ion temperatures in 600 kA RFX discharges are typically 2/3 of the electron one. $\beta\theta$ is confirmed to be of the order of 10 % at low I/N ($\leq 2\ 10^{-14}$ Am) and decays proportionally to $(I/N)^{-0.7}$. The ion heating does not depend on the ion masses: the various (light) impurities and the hydrogen ions have approximately the same temperature. Ti is anyway anomalous , i.e. higher than expected from equipartition between ions and the ohmically heated electrons. A simple preliminary 0-D approach suggests that an ambipolar electric field in the plasma could be effective in heating the ions. This mechanism would also qualitatively explain the apparent balance between Ti and Te mentioned in the introduction. A viscous term could contribute to the ion heating mainly in the initial phase of the discharge with minor effects during the sustainment phase.

References

[1] R.B.Howell, Y. Nagayama, Nuclear Fusion, 28, (1985) 734
[2] P.G. Carolan et al, Proc of the 14th EPS Conf on Contr. Fus. Plasma Phys., Madrid 1987, Vol II, 469
[3] G.A. Wurden et al, Proc of the 15th EPS Conf on Contr. Fus. Plasma Phys., Dubrovnik 1988, Vol II, 533
[4] T. Fujita et al., Nuclear Fusion, 31, (1991) 3
[5] L.Carraro et al, Proc of the 18th EPS Conf on Contr. Fus. Plasma Phys., Berlin 1991, Vol II, 309
[6] A. Fujisawa et al , Nuclear Fusion, 31,(1991) 1443
[7] T. Shimada et al,. Plasma Physics and Controlled Fusion 36,(1994)561
[8] E Scime et al., Phys. Fluids B4 (1992) 4062
[9] A.Lazaros , Plasma Physics and Controlled Fusion 31,(1989)1995
[10]G.Hedin et al. Plasma Phys. and Controlled Fusion, 38 (1996) 657
[11] S. Costa et al . Rev. Sci. Instrum. 66(1995) 330
[12] C. Gimblett, Europhysics Letters, 11, 541 (1990)
[13] A.V. Gurevich, A.V. Lukyanov, K.P. Zybin, Sov. Phys. JETP 70, 259 (1990).

SOME FEATURES OF NEUTRON RADIATION AND DEUTERON BEAMS GENERATION IN A PLASMA FOCUS WITH THE FLAT ELECTRODE GEOMETRY

N.V.Filippov, T.I.Filippova, M.A.Karakin, **V.I.Krauz**
INF, RRC "Kurchatov Institute", 123182, Moscow, Russia

J.R.Brzosko, J.S.Brzosko
Compton R&D Laboratories, 1500 Hudson St., Hoboken, NJ 07030, USA

Abstract. When Filippov-type plasma focus is fired in the "current sheath run-away mode" (CSRAM) in pure Ar (low pressure gas filling) and with Ta anode insert, significant neutron yield is observed. Experimental tests lead to conclusion that D(d,n)^{3}He reaction is the neutron origin. D^+ from anode (deuterium occluded Ta) are accelerated and impinge the limiter above the anode that is covered with Ta (also D - occluded) deposited during previous discharges.

Introduction. Presented work has been carried in the frame of a broad study program of the plasma focus (PF) physics and technology. This research is related to low-pressure discharges, which differ in physical phenomena when compared to the high-pressure discharges leading to dense plasma focus regime [1, 2]. At the low pressure of the filling gas, discharges lead to the so-called "current sheath run-away mode" [3]. The contraction of the current at the electrode axis is not accompanied by compression of the plasma, and the current sheath slides along the electrode surface at low angles. PF with Filippov type electrodes, operating in this regime emits hard X-Rays, HXR [4] as well as intense, MeV's ion beams of gas and anode material origin [5, 6].

It was found that for anode with a central tantalum (Ta) insert, discharges in pure argon (Ar) following those in deuterium (D) are accompanied by the emission of relatively strong neutron pulses. The paper presents a set of experiments aiming to extract the information used in finding the origin of this neutron production phenomenon.

Experiment and Results. Experimental set-up is shown in Fig. 1. PFE-machine used for this experiment is plasma focus with Filippov-type electrodes operating in the CSRAM regime, at capacitor bank energy W=50 kJ (14 kV, 0.3 Torr of Ar). The experiments in pure argon were performed after saturation of the discharge chamber elements with deuterium by means of the deuterium puffing into the preliminarily - evacuated (down to ~10^{-3}Torr) chamber for a long time. The preparatory series of discharges were also done in pure deuterium.

Typical neutron yield (Ar gas filling only) is $Y_n \cong 3 \cdot 10^7$. Identification of the neutron source position is based on tests done with: (a) "silver counter" (Ag-GM) and (b) fast plastic scintillator (NE102) working in "current mode" as time-of-flight (ToF) sensor. Comparison of Ag-GM readings for detector in different axial positions is in conformity with the assumption that the neutron source is located at the surface of the limiter which seals the flat and/or extended chamber. This test also excludes near-anode zone as potential emitter. Test with NE102 was done with detector at L = 2.5 m base (normal to PFE symmetry axis). Different segments of chamber were shielded with a

20 cm thick moderator $(CH_2)_n$ attached onto the chamber. For this particular arrangement it was found that the neutron signal is reduced more than by the order of magnitude, when NE102 can not "see" a volume limited by R ≤ 30cm and $(Z_1 - 4cm) \le Z \le Z_1$.

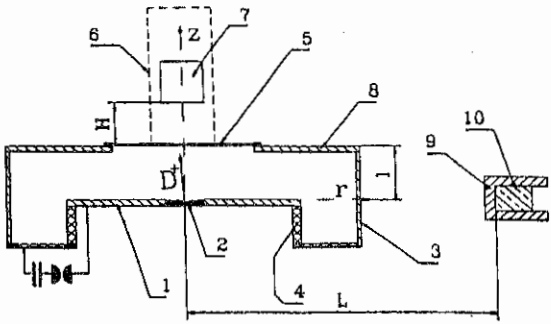

Fig. 1. Experimental set-up. #1 is the anode with Ta insert (#2); #3 & #8 are the cathode and chamber walls with Al limiter (#5); #4 is the insulator; #6 is the cylindrical extension on the chamber (closed by Al limiter at the end) mounted for some of discharge series; #7 is the calibrated Ag-GM neutron counter (Geiger-Muller counter wrapped in thin Ag foil and surrounded by $(CH_2)_n$ moderating medium and covered with Cd), mounted outside the chamber at distance H from the limiter; #10 is the NE102 neutron detector shielded by 3 cm of Pb (#9); l is the anode-limiter distance (variable in this experiment).

The following neutron production scenario has been verified:

(a) Neutrons are produced in D(d, n)^{3}He reaction;

(b) The source of deuterium is Ta, well known occludant that can absorb hydrogen up to hydrogen tantalum atomic ratio of ca. 0.75 [7]. In fact it was observed that till saturation of the Ta-anode-insert and the Ta deposited on limiters (by previous discharges), D_2 is rapidly absorbed in the chamber, with the rate exceeding 100 cm^3/min (D_2 at STP);

(c) The mechanism of ion acceleration is related with surface processes in the contact zone of a plasma current sheath with the anode. As a result of explosive anode surface evaporation, the discharge current disconnection by a vapour interlayer takes place. In strong electric field emerging in this case the acceleration of charged particles occurs, reproducing the current conductivity. In this case, both the ions of an anode material (Ta [6]) and those of the deuterium absorbed in it are involved into the acceleration process;

(d) Condition for acceleration of relativistic electrons and fast ions occurs at the same instant;

(e) Accelerated D^+ ions bombard the limiter (containing Ta with occluded D_2) inducing D(d, n)^{3}He reaction.

Some results are shown in Fig. 2-4. Traces of ToF experiment (see Fig. 2) reveal two pronounce signals. The origin of those signals was defined by setting alternatively Pb (15 cm) and/or $(CH_2)_n$ (20 cm) slabs in front of NE102. Pb shielding eliminated the first signal (indication of HXR), while $(CH_2)_n$ discarded the second one (indication of fast neutrons). D^+ ion energy, E_d, has been calculated from the equation for the measured delay time between maxima of HXR and neutron pulses, ΔT:

$$\Delta T = ToF(n) + ToF(D^+) - ToF(HXR) = \frac{L}{1.38 \cdot 10^9 \cdot E_n^{1/2}} + \frac{l}{9.76 \cdot 10^8 \cdot E_d^{1/2}} - \frac{L}{c} \qquad (1)$$

where: $[E_n] = [E_d]$ = MeV, $[\Delta T]$ = s, L and l are the flight paths of neutrons and ions, respectively; [L] = [l] = cm,
Eq. 1 relies on special feature of D(d, n)^{3}He reaction i.e. energy of neutrons emitted at 90^0 to the D^+ beam direction does not depend on D^+ energy.

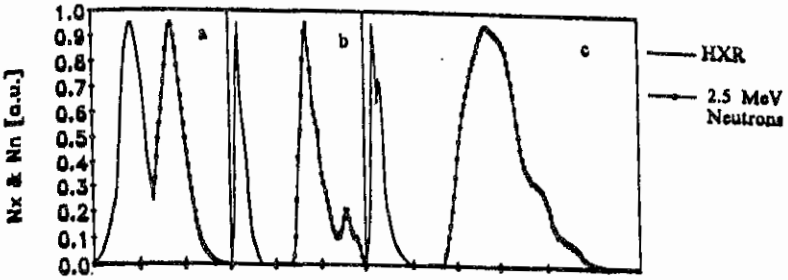

Fig. 2. Characteristic signal structures from the NE102 readings for different PF - detector arrangements: (a) L = 0.28 m, l = 0.22 m; (b) L = 2.5 m, l = 0.22 m; (c) L = 2.5 m, 0.45 ≤ l ≤ 0.73 m. For presentation purposes maxima of HXR and neutron components were normalized to the same values. Time scale is 100 ns per division.

Analysis of a broad series of shots (see Fig. 3) reveal while D^+ effective energy alters in the range of 0.1 MeV ≤ E_d ≤ 0.6 MeV, width of HXR and neutron signals remain close to their average values, i.e. $FWHM_x^{av}$ = 32 ns and $FWHM_n^{av}$ = 43 ns. For experiment with the chamber extension, $FWHM_n$ is about 100 ns and decreases gradually (when extending tube is covered with moderator) to about 45 ns when only the tube limiter remains in view of NE102.

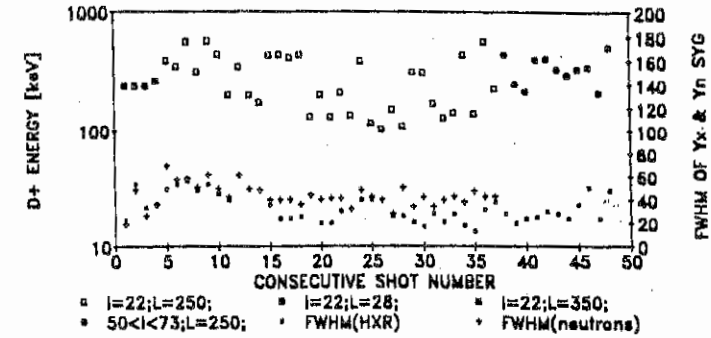

Fig. 3. D^+ ion energy estimated from the time difference of HXR and neutron maxima as measured by NE102 scintillator (see Eq. 1). The uncertainty of the estimates is caused by subjectivity of maxima definition and is within 20% error bar. Additionally, the FWHM of signals are shown.

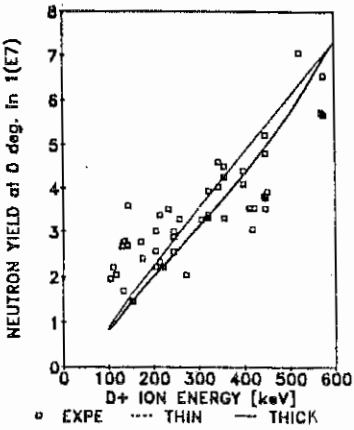

Fig. 4. Dependence of neutron yield measured on the axis by Ag-GM counter and energy of ions inducing D(d, n)^{3}He reaction. The curves represent variants of thin target (dashed line) as well as thick target with conserved overall beam energy (solid lines).

Relation between E_d, estimated from the delay time between HXR and neutron pulses, and the neutron yield in axial direction (0^0), measured by Ag-GM counter, Y_n, is shown in Fig. 4. These data are compared with two limits of deuterium target thickness, both in the maximal occlusion state. The first model assumes that a layer of Ta (D_2 occluded) is so thin that D^+ energy loses are negligible and Y_n is proportional to the reaction cross-section. The second model considers thick Ta (D_2 occluded) target and requires thick-target-yield calculations. $Y_n(E_d)$ estimate is too steep to fit the experiment. However, if one assume conservation of the total energy of all D^+ ions in the beam ($W = E_d \cdot Y_d = \text{const}$) the experimental data well represented for W ~ 30 J.

Summary. At this early stage of the study the following observation can be made:

(a) Timing of D^+ signal is in conformity to previously observed Ta and relativistic electron signals; **(b)** Energy of D^+ ions remains quasi constant during the signal as $FWHM_n$ does not depends on I; **(c)** The light ions (deuterons) as well as heavy ions(Al, Ta) lifted from the anode during the explosive evaporation are efficiently accelerated, and what is very important for the further model considerations, all kind earn the same energy per nucleon (about 0.2-0.5 MeV).

The authors express their gratitude to A.N.Filippov, V.P.Tykshaev and J.V.Vinogradova for the assistance in realization of the experiments and for the paper design.

References.

1.N.V.Filippov, et al., Nucl. Fusion Suppl., Part 2, p.577 (1962).
2.J.W.Mather, Physics Fluids, 8(1965) 1645.
3.K.G.Gureev, N.V.Filippov, T.I.Filippova Sov. J. Plasma Phys., 1(1975), 120.
4.N.V.Filippov, et al., IEEE Trans. PS, to be publ. August 1996.
5.N.V.Filippov, Sov. J. JETP 76(1979) 1547.
6.N.V.Filippov, A.N.Filippov, J.R.Brzosko, XXII-ICPIG V.4, p.9 (1995).
7.D.P.Smoth, "Hydrogen in Metals", The Univ. Chicago Press, 1958.

Work was supported in part by Russian Foundation of Basic Research grant #95-02-04422-a.
Participation of J.R.Brzosko in experiments at Moscow was financed by Neutronics/Photonics R&D.

RESONANT DIOCOTRON INSTABILITY OF A WIDE ELECTRON LAYER IN MAGNETIC GAPS OF MAGNETOELECTROSTATIC TRAPS

I. Ya. Gordienko, **V. D. Yegorenkov**

Kharkov State University, Svobody sq. 4, 310077, Kharkov, Ukraine

In magnetic gaps of a magnetoelectrostatic trap (MET) the noncompensated electron layer consists of travelling and trapped electrons (Gordienko I. Ya. et al. (1992)). The space electron charge in magnetic gaps causes the development of the diocotron instability (DI) observed in single-slot and multi-slot MET. Levy R. H. (1965) has constructed the DI theory for the oscillations propagating across the magnetic field. The low frequency long wavelength DI has been shown to develop if the vacuum gap width exceeds the electron layer halfwidth (the electron layer is located symmetrically between ideally conducting walls), whereas in the opposite case the electron layer is stable with respect to the excitation of these oscillations. Gordienko I. Ya. et al. (1988) have pointed out the importance of travelling electrons in the development of the instability for the oscillations propagating at an angle to the magnetic field. Davidson R. C. (1985) has shown that in the domain where the nonresonant instability for waves propagating across the magnetic field is absent a resonant DI can develop and he has constructed the quasilinear theory for the electron layer with one of the edges touching the conducting wall.

This report gives the growth rate of the resonant low frequency DI for a wide electron layer symmetrically located with respect to conducting walls (the nonresonant low frequency long wavelength DI is absent in the parameter region considered). The waves propagating across the magnetic field as well as oblique to it participate in the instability development.

We will consider the oscillations propagating strictly across the steady magnetic field $(k_z = 0)$. This case corresponds to the maximum of the DI growth rate and therefore it is the most interesting one. The electron layer of the halfwidth Δ consisting of travelling and trapped electrons occupies the region $x_1 < x < x_2$ and is located symmetrically with respect to the conducting walls. In this case the dispersion equation for low frequency oscillations $(\omega << \omega_c, \omega_c = |e|B/mc)$ coincides with the dispersion equation obtained in [2]

$$\omega_{1,2}^2 = \frac{\omega_p^2 q^2}{\mathrm{sh}\left[2k_y\Delta(1+\delta)\right]}\{k_y^2\Delta^2\mathrm{sh}\left[2k_y\Delta(1+\delta)\right] -$$

$$-2k_y\Delta\mathrm{sh}\left[k_y\Delta(2+\delta)\right]\mathrm{sh}\left(k_y\Delta\delta\right) + \mathrm{sh}\left(2k_y\Delta\right)\mathrm{sh}^2\left(k_y\Delta\delta\right)\}, \qquad (1)$$

where k_y is the wave vector projection on the drift direction, $\omega_p = \left(4\pi e^2 n/m\right)^{1/2}$, $q = \omega_p/\omega_c$, $\delta = x_1/\Delta$.

It has been shown that in the long wavelength limit $k_y\Delta << 1$ the nonresonant DI occurs if
$\delta > 1$ with

$$\omega_{1,2}^2 = \frac{\left(k_y\Delta\right)^2(1-\delta)}{1+\delta}\omega_p^2 q^2. \qquad (2)$$

We will consider the case of a wide electron layer when $\delta \le 1$ and the nonresonant DI does not occur. However, as it has been shown in [4], the excitation of a weaker resonant DI is possible then. In our case the expression for the growth rate has the form

$$\gamma^{(i)} = \frac{\pi \left|\delta\varphi^b(x_{si})\right|^2 \left|\frac{\partial n}{\partial x}\right|_{x=x_s}}{\left|k_y\Delta\right|\omega_p q n \left[\frac{\left|\delta\varphi^b(x_2)\right|^2}{\left(\omega - k_y\Delta\omega_p q\right)^2} - \frac{\left|\delta\varphi^b(x_1)\right|^2}{\left(\omega + k_y\Delta\omega_p q\right)^2}\right]}, \qquad (3)$$

where n is the density profile, the letter i denotes the dispersion equation root number, $\left|\delta\varphi^b(x)\right|$ is the Fourier component modulus of the electrostatic potential, x_{si} is the resonance layer coordinate determined from the equation

$$\omega - k_y v_D(x_s) = 0, \qquad (4)$$

here $v_D(x_s) = q^2\omega_c(x_s - x_0)$, x_0 is the electron layer centre coordinate. It follows from (4) that

$$x_{s1,2} = x_0 \pm \Delta \times \qquad (5)$$

$$\left\{\frac{\left(k_y\Delta\right)^2 \mathrm{sh}\left[2k_y\Delta(1+\delta)\right] - 2k_y\Delta\,\mathrm{sh}\left[k_y\Delta(2+\delta)\right]\mathrm{sh}\left(k_y\Delta\delta\right) + \mathrm{sh}\left(2k_y\Delta\right)\mathrm{sh}^2\left(k_y\Delta\delta\right)\right\}}{\left(k_y\Delta\right)^2 \mathrm{sh}\left[2k_y\Delta(1+\delta)\right]}\Bigg\}^{1/2}$$

In the long wavelength limit $k_y\Delta << 1$ for $\delta \le 1$ we have

$$x_{s1,2} = x_0 \pm \Delta\left(\frac{1-\delta}{1+\delta}\right)^{1/2}. \qquad (6)$$

In the short wavelength limit $k_y\Delta >> 1$ and $\delta <<$ we obtain

$$x_{s1,2} = x_0 \pm \left(1 - \frac{1}{2k_y\Delta}\right). \qquad (7)$$

The plus and minus signs correspond to different oscillation branches. Thus the resonant layers occupy the regions

$$x_0 + \Delta\left(\frac{1-\delta}{1+\delta}\right)^{1/2} \le x_{s1} < x_2,$$

$$x_1 < x_{s2} \le x_0 - \Delta\left(\frac{1-\delta}{1+\delta}\right)^{1/2}. \qquad (8)$$

For an example, we take the plasma profile in the region $x_2 - \Delta_b < x < x_2$ (Δ_b is the density nonuniformity width) in the form

$$n(x) = n_0 + \frac{\Delta n_b}{\Delta_b}\left[x - \left(x_2 - \frac{\Delta_b}{2}\right)\right], \qquad (9)$$

where n_0 is the average value of the electron layer density, Δn_b is the density nonuniformity value. We obtain then from (3) that

$$\gamma^{(1)} = \frac{\pi}{\left|k_y\Delta\right|\omega_p q n_0} \frac{\left|\delta\varphi^b(x_{s1})\right|^2 \frac{\Delta n_b}{\Delta_b}}{\frac{\left|\delta\varphi^b(x_2)\right|^2}{\left(\omega - k_y\Delta\omega_p q\right)^2} - \frac{\left|\delta\varphi^b(x_1)\right|^2}{\left(\omega + k_y\Delta\omega_p q\right)^2}}; \gamma^{(2)} = 0. \quad (10)$$

For example, for long wavelength oscillations with $k_y\Delta << 1$ and $\delta \le 1$ we get

$$\gamma^{(1)} = \pi \frac{\Delta n_b}{n_0} \frac{\Delta}{\Delta_b} \left|k_y\right| \Delta \frac{\delta^2 \omega_p q}{(1-\delta)^{1/2}(1+\delta)^{3/2}}, \quad (11)$$

and the applicability condition of the linear approximation $(\omega >> \gamma)$ has the form

$$1 - \delta >> \frac{4\pi\delta^2}{1+\delta} \frac{\Delta n_b}{n_0} \frac{\Delta}{\Delta_b}. \quad (12)$$

For characteristic MET parameters B=1.7T, $n_0 = 5 \cdot 10^{11}\,\mathrm{cm}^{-3}$ the development time of the resonant DI comprises $\tau \sim 200$ ns whereas for the plasma production with electron injection $\tau_{inj} \approx 4$ms. Therefore the resonant DI has enough time to develop already at the initial stage and it can influence the process of plasma accumulation in MET. For the oscillations propagating oblique to the steady magnetic field for a wide electron layer there is possible the excitation of the two-stream and slipping instabilities [5].

References.

1. Gordienko I. Ya., Yegorenkov V. D., Stepanov K. N. Fizika plazmy. 1992. V. 18. n. 1. P. 9 (In Russian).
2. Levy R. H. Phys. Fluids. 1965. V. 8. P. 1288.
3. Gordienko I. Ya., Yegorenkov V. D., Pokroev A. G., Stepanov K. N. Fizika plazmy. 1988. V. 14. n. 12. P. 1451 (In Russian).
4. Davidson R. C. Phys. Fluids. 1985. V. 28. P. 1937.
5. Gordienko I. Ya., Yegorenkov V. D., Stepanov K. N. Ukrainian Physical Journal. 1990. V. 35. N 8. P. 1187 (In Russian).

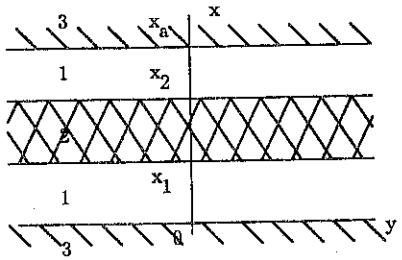

Fig. 1. Mutual location of the electron layer and conducting walls: 1 is vacuum gap, 2 is the electron layer, 3 is the conducting wall.

Principles of D-3He fusion.

V.I.Khvesyuk, D.V. Semenov, A.N.Lyakhov
Moscow Bauman State Technical University, Power Engineering Institute

I. INTRODUCTION.

Nowadays, the fusion community is facing the problem of reducing research and development studies. The key is that from the last results one can see, that "classical" D-T fusion cycle has no real advantages over fission, neither in fuel capability (lithium resourses are estimated for 20000-30000 years, the same as pure uranium for fast breeders), nor in radiation safety [1].The only one way to us is to revise our views, and center ourselves on developing environmentally safety, non-radioactive fusion, based on a D-3He fuel with no neutrons and radioactive nucleuses.

$$D_1^2 + He_2^3 \rightarrow He_2^4 + p_1^1 + 17.6 МэВ \quad (1)$$

In this work we present our results on kinetic/power balances investigation for this reaction and formulate physical principles of obtaining the highest available power efficiency in cycle (1) together with environmentally safety.

II. MATHEMATICAL MODEL.

Early estimations [1] have shown that postive power output from the magnetized D-3He plasma could be run under the fullfilment of the following requirements:

$$T_{fuel} = T_D = T_{He} = 60..90 \text{ keV} \quad (2)$$

$$_{pl} = \frac{P_{fus}}{P_{req}}, \quad Q_{pl} > 10 \quad (3)$$

$$P_{fus} > 2 \text{ MW/м}^3 \quad (4)$$

Here P_{fus}, [W/м^3] is fusion power.P_{req} - extra heating power, necessary to obtain the given T_{fuel} value. The β_E values must be large enough ($\beta_\Sigma \sim 0.4 \ldots 0.9$) to reduce cyclotrone radiation losses. The last condition reduce our choice of a confinement system to tandem mirrors and FRCs.

We use kinetic equations in form [2,3]:

$$\frac{\partial f}{\partial t} = \left(\frac{\delta f_a}{\delta t}\right)_{FP} + \left(\frac{\delta f_a}{\delta t}\right)_{B} + S_a - L_a \qquad (5)$$

where: $f_a(v, r, t)$ - distribution fucntion of protons, α-particles, T, ^{3}He ; S_a - sourse term, L_a-losses term. $\left(\frac{\delta f_a}{\delta t}\right)_{FP}$ - Fokker-Plank collisional operator, desribing Coulomb scaterring and $\left(\frac{\delta f_a}{\delta t}\right)_{B}$ - Boltsman collisional operator, describing nuclear elastic scaterring. We complete the system of equations with balance equations:

$$\frac{d(1.5 n_a T_a)}{dt} = -\frac{n_a}{\tau_e}(T_e - e\Delta\varphi_e) - \frac{1.5 n_e T_e}{(\tau_R)_e} + \sum_i Q^{i-e} - Q^{rad} \qquad (6)$$

T_a - electron temparature, Q^{a-b} - power transfered from "b" to "a", Q^{rad} - radiation losses, $\tau_{i,e}$ - mirror confinement time, τ_R - radial confinement time.

We consider fuel and electrons as equilirium species with Maxwell distribution, thus complete the system with particle balance equation and quasineitrality condition:

$$\frac{dn_a}{dt} = -n_a\left(\frac{1}{\tau_a} + \frac{1}{\tau_R}\right) + S_a \qquad (7)$$

$$\frac{dn_e}{dt} = \sum_i z_i \frac{dn_i}{dt} \qquad (8)$$

III.RESULTS.

At first we calculated power efficiency with no radial transport ($\tau_R \to \infty$) (Fig.1). It is clear that Q_{pl} does not exceed 1.3 and, so, condition (3) did not fulfilled. Then we carefully studied the influence of radial transport on $_{pl}$ and P_{fus}, under the assumption that τ_R is the same for all plasma species. On Fig.2 results are presented, where τ_R=20 sec, β_Σ=0.7, B_0=5T. There exists the optimum value of τ_R, delivering maximum of Q_{pl} [2].

But condition (3) is still not completed. The reason is that in the whole β_Σ value fusion products take nearly the half, thus decreasing fuel beta and fusion power. This allow us to formulate strictly another criteria: D-3He fusion can not produce enough power without ash pumping [1,2].

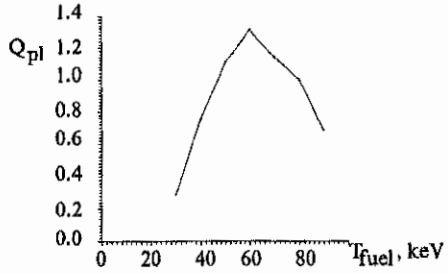

Fig.1. Depemdence of Q on plasma temperature.

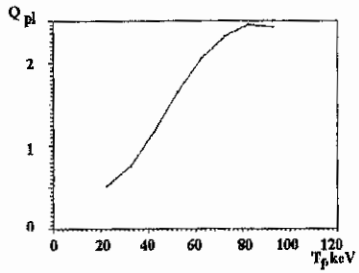

Fig.2. The power efficiency dependence of fuel temperature at a fixed radial confinement time

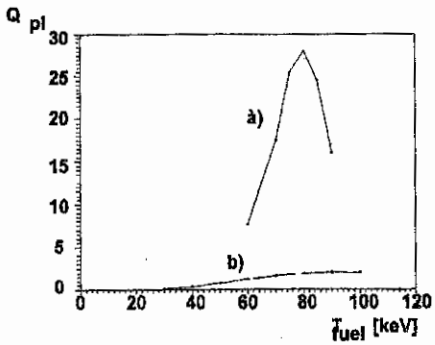

Fig.3 The influence of ash pumping on power efficiency. Ash pumping in region 300..400 keV (a).

The method has been developed for the selective ions pumping from an axisymmetric magnetic field [4] based on the using of weak external magnetic fields, varying in time with drift frequencies. The pumping process takes place in a selected energy regions different for alpha-particles and protons. We have found out pumping parameters, that allow to obtain very high values for Q_{pl} (Fig.3). They are: pumping region: 300-400 keV, width of region: 5-100 keV, pumping time - 0.02 sec. This time can be achieved within the magnitude of perturbation field 1..2% from the main one. Ash pumping strongly modifies power balance, with reducing radiation losses, transport of fuel ions into the loss-cone and extra heating requirements.

Also the precense of fusion products with non-equilibrium distribution functions might cause the excitation of kinetic electromagnetic instabilities, thus leading to increasing losses of heating. This problem also has been studied. It was found out, that both Alfven and Fast waves would be excited. The growth rates here are in order larger than in D-T cycle, namely $\gamma \approx 0.025...0.035\Omega_{Di}$ (here Ω_{Di} -deiterium gyrofrequency). The realistic ways of supression are: (a) reducing plasma radius; (b) increasing plasma beta up to $\beta_E=0.95$. The last way is much more attractive, because of the increasing of Q_{pl} with β_E.

REFERENCES.

1.Golovin I. N., Khvesyuk V. I., et al., in *Proc of the Cource and Workshop held at Villa Monastero.* - Varenna (Italy), 1989. - pp. 673 - 692.

2. Semionov D. V., Khvesyuk V. I., Poletaev D. L.. in *Proc. of Int. Conf. on Open Plasma Confinement Systems for Fusion.* - Novosibirsk, 1993. - pp. 249 - 256.

3. Golovin I. N., Khvesyuk V. I., Semionov D. V. Transactions of Fusion Technology, **27** 150 (1995).

4. V.I. Khvesyuk, N.V.Shabrov, A.N.Lyakhov, Transactions of Fusion Technology, **27** 427(1995).

Kinetic Stability of D-3He plasma in the central cell of tandem mirror

A.N.Lyakhov, V.I.Khvesyuk

Moscow Bauman State Technical University, Power Engineering Institute

I. MATHEMATICAL MODEL.

Before it was pointed out, that the only one way for controlled fusion to outperform future fission technology (namely fast breeders), is to use D-3He fuel cycle. In this reaction there is no radioactive waste, so it is environmentally safety and it does not impose heavy demands to the material of the first wall [1]. But the requirements to the plasma parameters [2] restrict our choice of confinement system to tandem mirrors and FRCs. The first one is well developed now. MHD stability is obtained and high plasma parameters have been obtained in last years [3], very close to these on 10-years before tokamaks. So to formulate necessary condition to D-3He fusion in tandem mirror we are to study not only the classical balances [2], but also the question of plasma stability in reactor regime with consideration for high β values and finite size.

We restrict our attention to electromagnetic microinstabilities, driven in the tandem mirror central cell (where fusion itself occurs) by the hot fusion products: alpha-particles and protons. These ashes have non-equilibrium distribution functions in velocity space, due to the precence of loss-cone and slight influence of plasma potential on their confinement. We concern low-frequency limit $\omega \leq \Omega_D$, where Ω_D - deiterium gyrofrequency. In this limit there are three wave branches - Alfven wave, Fast magnetosonic wave and Hybrid wave, with $\Omega_D < \omega < \Omega_{He}$.

Mathematical model used is in general the same as in [5]. The differences are: the inclusion of plasma potential, the taking into account of all components of dielectric tenzor K in all harmonics, the replacement of analytical expressions for K with Bessel functions expantion by strictly numerical evaluation.

The following assumptions have been accepted. The central cell is conceived as a longless sharp-boundary plasma cylinder of radius r_p, surrounded by a conductive wall at radius r_2. Vacuum magnetic field B_v=4.7T. Diamagnetic depression is taken into account: $B_z = B_v \sqrt{1-\beta}$. To obtain the growth rate of a given wave branch one must at first calculate the radial profiles of an eigenmode with given azimuthal m and radial n

wavenumbers, and then calculate the growth rate through the coupling coeffisients of plasma-wave interaction [4]. In eigenmode calculation we consider cold plasma consists of only fuel ions and electrons. Then the dielectric tenzor of hot plasma was calculated, with non-equlibrium distribution functions of fusion products obtained from well-known solution of Fokker-Plank equation through expantion in Legandre series. The modification of the loss-cone by plasma potential was also taken into acoount. At least the growth rate was calculated using the following expression [4]:

$$\gamma = \int_0^{r_p} rdr\mathbf{E}^* \cdot K^A \cdot \mathbf{E} \Big/ \int_0^{r_p} rdr\mathbf{E}^* \cdot \frac{\partial K^H}{\partial \omega} \cdot \mathbf{E} \qquad (1)$$

Here superscripts A and H notes anti-Hermitian and Hermitian parts of dielectric tenzor K respectively, where summation over all plasma species is taken place. The distribution functions of fuel ions and electrons were assumed Maxwellian.

II. RESULTS.

From the first series of calculations it was obtained. that in the central cell of D-3He tandem mirror reactor Alfven and Fast wave branches would be unstable. The most unstable are modes with m=-1 (asimuthal mode number) and n=0 (radial mode number). Typical growth rates are in order greater than in D-T plasma (Fig.1). So the operation of such a reactor is under question, because of strong instability, which in turn will cause losses of fusion products and so reducing of plasma heating by alpha-particles and protons thus increasing requirements to extra heating system.

We tried to find how to suppress such instabilities. There are the following ways:

(a) reduce ash's partial beta; (b) reduce vacuum magnetic field; (c) reduce plasma radius; (d) increase plasma beta. Our calculations show, that instabilities disappear only when ash's partial beta tends to zero. This is no way, because we practically artficially create conditions of pure heating in the same way as it results from the precense of unstable waves. Then, we can not reduce magnetic field, because of the properties of D-3He reaction [1]. Only (c) and (d) methods are noteworthy. The reducing of plasma radius causes the suppression of instabilities (Fig.2). Though this leads to sufficient decreasing of the whole power output, it could be compensate by the increasing of reactor length. The most appreciable way is to increase plasma beta up to the level of

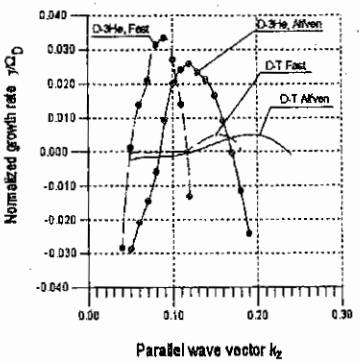

Fig.1 Typical dependence of the growth rates from k_z for D-3He reactor and D-T plasma (MARS project).

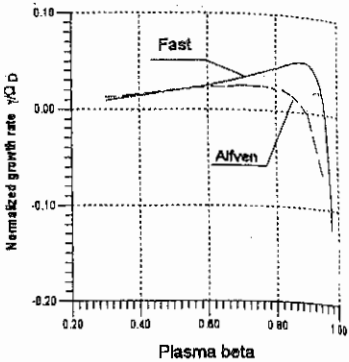

Fig.3 Suppression of instabilities at high beta values.

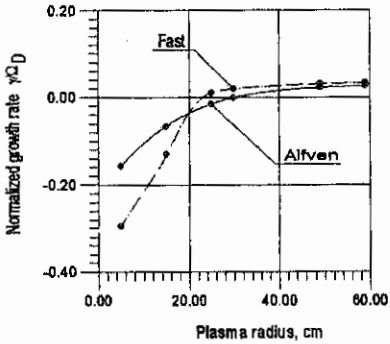

Fig.2 Dependence on the plasma radius for the modes $A_{-1,0}$,$F_{-1,0}$.

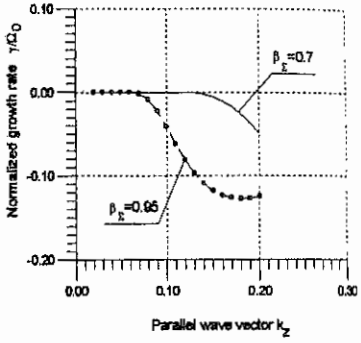

Fig.4. Cyclotrone damping on deiterium.

0.95 or more. Here all unstable modes are heavily damped (Fig. 3.4), and power efficiency of D-3He reaction does not reduce.

III. CONCLUSION

We add another one criteria to the conception of D-3He fusion. In order to avoid the excitation of electromagnetic plasma microinstabilities in the tandem mirror central cell, and respectively anomalous losses of fusion products and so pure plasma heating, we must either reduce plasma radius or increase plasma beta. To our mind the last way is the most acceptable for the future low-radioactive D-3He fusion reactor.

REFERENCES

1. I.N.Golovin, V.I.Khvesuyk . in Proc. of Intern. Conf. on Open Plasma Confinement Systems for Fusion, Novosibirsk, Russia, 14-18 June 1993.World Scientific, Singapore. 1993. P. 245-261.

2. Golovin I.N., Khvesyuk V.I., Semenov D.V. Transactions of Fusion Technology. 1995. V.27. P. 402-406.

3. Tamano T. Transactions of Fusion Technology. 1995. V. 27. P. 111-117.

4. Kaufman A.N. Phys.Fluids. 1971. V. 14. P. 387-397.

5. Ho S.K., Nevins W., Smith G., Miley G. // Phys.Fluids. 1988. V.31. P.1656-1672.

Characteristics and Mechanisms of Hot Initial Plasma Creation in the End System of AMBAL-M

T.D. Akhmetov, E.D. Bender, **V.I. Davydenko**, G.I. Dimov, V.G. Igoshin, A.A. Kabantsev, V.B. Reva, V.G. Sokolov, S.Yu. Taskaev

Budker Institute of Nuclear Physics, 630090, Novosibirsk, Russia

Experiments on MHD stabilization by high pressure plasma in a conducting shell have been planned at the end system of the completely axisymmetric ambipolar trap AMBAL-M [1]. The possibility exists of creating a hot ion population in the end mirror by neutral beam injection and a hot electron population by double-frequency ECR heating [2]. The performance of the proposed experiments demands high electron temperature of the initial plasma to eliminate significant energy transfer from hot particles to plasma electrons. At the present time the initial plasma with high electron temperature is obtained. The plasma in the end system has the electron temperature ~50 eV, ion temperature ~200 eV and density ~$6 \cdot 10^{12}$ cm^{-3} [3].

For creation of hot initial plasma, a plasma stream with the developed low-frequency turbulence is used. The paper considers the main mechanisms providing creation of the hot initial plasma.

Fig. 1 shows the scheme of the experiment. The plasma stream is generated by an annular gas-discharge source, placed in the region before the entrance throat. Duration of the discharge current

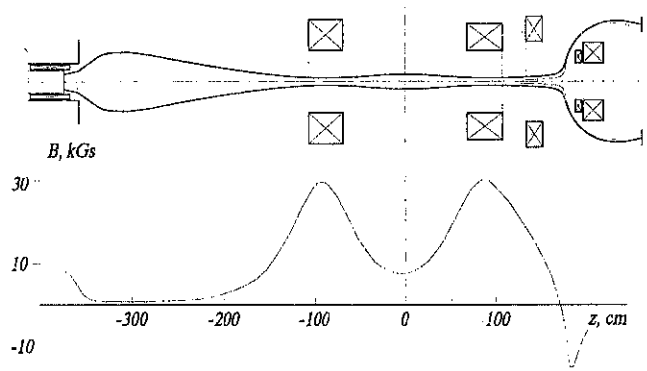

Figure 1. Scheme of initial plasma creation in the end system.

pulse is 1.8 ms. The presence of the transverse electric field is an essential feature of the plasma stream generated by the source. This electric field is responsible for development of Kelvin-Helmholtz instability with a broadband frequency spectrum of electrostatic oscillations which lead to stochastic anisotropic ion heating. The plasma flowing from the plasma source with the density ~$2 \cdot 10^{14}$ cm^{-3} and temperature of 10 eV, is substantially heated downstream.

The most crucial factor providing hot initial plasma creation in the end system, is thermal insulation which suppresses high electron thermal conductivity between the mirror and the transporting region. With the purpose to elucidate the reasons of thermal insulation, we measured radial profiles of the plasma potential using probes in different cross-sections of the plasma. Fig. 2 shows distribution of the plasma potential along different force lines of the magnetic field. From the presented distributions it follows that for the periphery plasma, thermal insulation is provided by the minimum of the potential located in the entrance throat, which is a barrier for cold electrons from the transporting region. The minimum of the potential is caused by a density decrease arising as a result of reflection of anisotropically heated ions from the increasing magnetic field in the region of the entrance throat. However, in the near-axis plasma, the minimum of the potential is absent in the region of the entrance throat despite the drop in density.

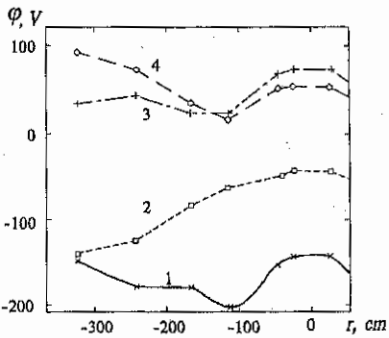

Figure 2. Longitudinal distributions of plasma potential. 1— on the axis, 2— on the field line of radius equal to 0.5 of the gas-discharge channel radius, 3— on the field line of the gas-discharge channel, 4— at the periphery.

The reason of thermal insulation at the near-axis force lines is the presence of the longitudinal electron current of 1—2 kA, due to the escape of a part of the discharge current along the magnetic field into the plasma of the end system and because of transverse ion losses in the transporting region. With a magnetic probe made in the form of a small coil located in an insulating boron nitride shroud, the azimuthal magnetic field has been measured in different cross-sections. Current density radial profiles determined from these measurements and mapped along magnetic field lines to the plane of the plasma gun, are presented in Fig. 3. In the beginning of the transporting region the longitudinal current has an annular structure, then compresses to the axis, and in the entrance throat the inner cavity becomes filled. The interpolated current density in the entrance throat is $j_e \approx 100$ A/cm^2, the measured plasma density $n \approx 2 \cdot 10^{12}$ cm^{-3}, and therefore, the stream velocity of the electrons is of order of $v_e \approx 3 \cdot 10^8$ cm/s which corresponds to the energy of 25 eV. The stream velocity of the electrons in the throat is larger than the

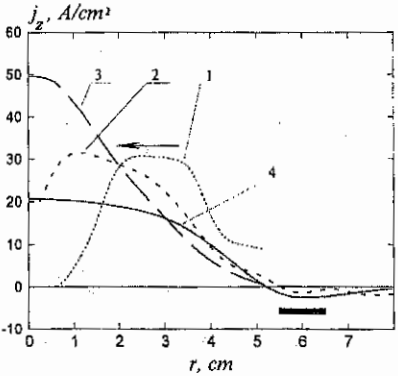

Figure 3. Radial profiles of longitudinal electron current density. Curve 1 corresponds to z= -243 cm, 2 — z=-168 cm, 3 — z= +25 cm, and 4 — z= +168 cm. Black rectangle denotes gas-discharge channel of the plasma gun.

thermal velocity, and this eliminates heat transfer from the mirror to the transporting region due to thermal conductivity.

With a set of probes we have studied electrostatic oscillations originating in the plasma of the end system during operation of the plasma source. These oscillations with a broad spectrum lead to stochastic transverse ion heating. Fig. 4 shows the measured power spectrum of oscillations. One can see that the spectrum consists of two parts — the low-frequency, below 200 kHz and the high-

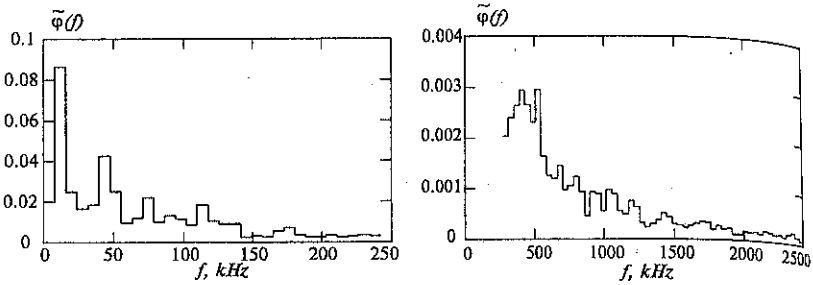

Figure 4. Power spectra of electrostatic oscillations.

frequency one. The source of oscillations in the low-frequency region is Kelvin-Helmholtz instability, and the peaks on the presented spectrum correspond to separate azimuthal modes. An interesting peculiarity of development of the instability in the plasma of the end system is that the odd azimuthal modes with m=1, 3, 5 are predominating which amplitudes are an order of magnitude larger than the amplitudes of the even modes with m=2, 4. The origin of oscillations in the high-frequency portion of the spectrum is related with the noise of current loops in the plasma source. The discharge current is divided into the separate current loops corresponding to separate cathode spots having a finite lifetime. Collapse of a separate spot causes an increase of a voltage drop across the other loops, and since a portion of the loops are completed through the plasma of the end system, its potential fluctuates. Thus, the plasma source is a "white noise" generator in the frequency band up to ω_{ci} and, although the power in the high-frequency region of the spectrum is moderate, its presence is important for providing stochasticity of heating, because it ensures effective phase mixing.

Development of oscillations in the plasma causes enhanced diffusion. An integral diffusion coefficient of the plasma in the transporting region determined from the rate of change of the radial plasma density profile, $D \approx 2 \cdot 10^5$ cm^2/s. Local measurements of the radial flux associated with the electrostatic transport, based on probe measurements of the azimuthal electric field and density fluctuations, provide the mentioned value of the diffusion coefficient. At the same time, the presence of the longitudinal electron current is accompanied by fluctuations of the radial magnetic field with the amplitude up to 5 Gs and the spectrum correlating with the low-frequency portion of the spectrum of electrostatic oscillations. Simultaneous local measurements of fluctuations of the radial magnetic field and density showed that the magnetic transport occurs in the frequency range from 8 to 12 kHz and

the value of the corresponding diffusion coefficient is $D_M \approx 1.5 \cdot 10^4$ cm^2/s. It should be noted that the use of the turbulent plasma stream for creation of the initial plasma in the end system does not cause considerable transverse energy losses. At a power of longitudinal heat losses to the end plasma receiver of the semicusp of order 100 kW, the measured power of transverse losses to the limiting diaphragm in the mirror is less than 1 kW.

As the plasma stream flows, populations of trapped ions and electrons are created in the mirror. Creation of the populations is provided by the capture of particles from the streams flowing through the mirror. Measurements at the end plasma receiver of the semicusp show that an ion current of ~140 A flows through the mirror. Transition from the passing ions into the trapped ones occurs because of the increase of the pitch-angle as a result of Coulomb scattering and because the transverse energy rises during stochastic heating by electrostatic oscillations. Considerations show that the influence of these factors is roughly the same and ~30 A must be trapped into the mirror. The estimated value of the trapping agrees with the amount of losses from the mirror measured from the rate of plasma decay, which is close to the classical one. Electrons in the mirror are confined in a potential well of depth $\Delta\varphi \sim 2T_e/e \sim 100$ eV. According to the Pastukhov formulas [4], the losses of the trapped electrons from the mirror are estimated at ~300 A, and the power carried by the electrons is ~35 kW. Trapping of electrons into the mirror, compensating the losses, is provided by scattering and deceleration of electrons from the stream flowing along the mirror and can be easily explained by classical processes. Estimates show that while passing through the mirror, the current-carrying electrons from the stream scatter through the angle ~0.3, lose their energy of ~30 eV and as a result of reflection from the potential barrier of the exit throat, a part of the flowing stream is captured into the mirror. The power that is transferred to the electrons trapped in the mirror from the hot ion population is about ~4 kW, and the power transfer to the trapped electrons from the passing electron stream is ~30 kW. Thus, the presence of the longitudinal current maintains high electron temperature. As a whole, the classical behavior of the mirror trapped particle populations, is significant for successful accomplishment of the planned experiments on injection of powerful neutral beams and RF heating.

The work was carried out at the AMBAL-M facility with financial support from the Russia Ministry of Science.

References

1. G.I. Dimov, *Program of AMBAL-M experiments*, In: Proc. Int. Conf. on Open Plasma Confinement Systems for Fusion, 1993, Novosibirsk, Russia, p.23—35.
2. V.S. Belkin, E.D. Bender, E.A. Gilev et al., *First phase of AMBAL-M experiment*, In: Proc. Int. Conf. on Open Plasma Confinement Systems for Fusion, 1993, Novosibirsk, Russia, p.37—49.
3. T.D. Akhmetov, V.S. Belkin, E.D. Bender, E.A. Gilev, V.I. Davydenko et al., *First stage experiments at the end system of the axisymmetric tandem mirror AMBAL-M*, In: Proc. 21st Eur. Conf. on Controlled Fusion and Plasma Physics, Montpellier, 1994, v.1, p. 446—449.
4. V.P. Pastukhov, Nuclear Fusion, **14**, 3 (1974).

Impurity ion temperature and flow velocity measurements at the Extrap-T2 reversed-field pinch

P. Hörling[1], T. Fall[1], J. H. Brzozowski[2], K. Sasaki[3],
Z. Yoshida[3], P. Brunsell[2], E. Tennfors[2], and J. Morikawa[3]
[1]*Department of Physics I,*
[2]*Division of Fusion Plasma Physics (association EURATOM-NFR), Alfvén Laboratory Royal Institute of Technology, S-10044 Stockholm, Sweden*
[3]*Inoue lab., Dept. of QUEST, Faculty of engineering, Univ. of Tokyo, Japan*

Introduction

The Extrap-T2 (former OHTE) toroidal reversed-field pinch in Stockholm started operation in spring -94. It is equipped with a resistive shell, and pulse lengths of up to 13 ms are now achieved. The main aim is to study pulses with lengths many times longer than the shell field penetration time. The vacuum vessel wall is covered by carbon tiles and lack limiters. The major radius is 1.24 m, minor radius is 0.18 m [1, 2].

The still not completely understood high ion energies, and the origin of ion heating in reversed-field pinches and related confinement schemes (e.g. spheromaks) are under investigation both experimentally[3], and theoretically [4, 5]. Yoshida points out [6, 7] that several heating schemes can give anisotropic ion temperatures ($T_{i,\|} \neq T_{i,\perp}$ (anisotropic energy transfer faster than heat isotropization time scales). This has been investigated in Extrap-T2 by probing O^{4+}Doppler line broadening perpendicular and tangential to the magnetic field lines.

Another effect seen in many RFP's is toroidal and poloidal rotation of the plasma[8, 9]. Toroidal rotation is thought to contribute to stability, especially against wall-locking of MHD modes. It has been seen in other RFP's, for instance at MST, that a continuously increasing rotation could get interrupted, or even reverse direction, during sudden bursts of MHD activity during this event. The ion temperature also increased [8]. By examining the momentum-balance equation one can see that a net flow (poloidal/toroidal rotation in a toroidal device) can be caused by, for instance, ion diamagnetic drift due to density gradients and by a radial electric field via the $E \times B$ force. Viscosity dependence appears in the pressure tensor, which implies that sheared flow is important. Velocity fluctuations contribute to the "MHD dynamo" via the component $\langle \tilde{v} \times \tilde{B} \rangle$ in the time averaged local Ohm's law[8, 9]. The MHD dynamo is important in RFP's because it sustains the reversed field configuration against resistive diffusion by continuously generating toroidal field. Also the dynamo magnetic fluctuations are thought to preferentially heat ions.

Experimental

Two ports, one perpendicular, and one tangential to the torus main axis have been used for measurements of Doppler shifted and broadened spectral lines in the visible and quartz-UV wavelength region. The toroidal angle between the intercept points of the line-of-sights (LOS's) through these ports with the plasma center is 102 degrees (2.2 meters). Fibers guide light to two high-resolution spectrometers (focal lengths 1.0, 1.5 m, gratings 2400, 1180 l/mm). Two spectral line detection systems at the exit slits have been used at two different periods: Arrays of 8 PM tubes positioned after magnifying cylindrical lenses, or an optical multichannel analyzer (OMA). Time resolution is 15 μs for the PM arrays, and down to 1.2 ms for the OMA. The PM arrays were used for determining T_i anisotropy and rotation change during one and the same shot. When using the OMA, the fibers from the tangential ($\|$) and perpendicular ($\perp$) LOS's were swapped for every second shot, giving $T_{i,\|}$ and rotation, and $T_{i,\perp}$ for every second shot. Determination of zero rotation was made from the $\perp$ LOS. Doppler shifts and widths are computed by least-square linefitting (for the OMA described in ref. [10]) and by extracting the

first and second moment of the spectral line [11].

Measurements of ion temperature anisotropy

O^{4+}Doppler broadening was recorded along the $\perp$ and $\parallel$ LOS's. The emissivity profile of this species is supposed to be quite flat. The features showed by both channels were large broadening, corresponding to 100-300 eV, in the early phase of the discharge, i.e. during the set-up of the reversed-field configuration. The lineshape were sometimes non-Gaussian, reflecting non-Maxwellian velocity distributions or turbulence especially along the $\parallel$ LOS. This is known to be a strongly turbulent phase with extensive magnetic reconnection processes. During the central several milliseconds long phase of the discharges, T_i stays fairly constant without any strong fluctuations. The plasma current during this phase was slowly decaying or constant. T_i is around 40-80 eV. No clear time correlations of $T_{i,\parallel}$ and $T_{i,\perp}$ are seen. However, an inverse scaling (see below) of T_i with the electron density n_e is seen, and n_e seems not to be toroidally symmetric. Spectroscopic signals of oxygen and carbon are very different depending on toroidal location, which shows strong toroidal variations of impurity influx and/or electron density. Also, magnetic fluctuation levels and the amplitude of MHD modes change with toroidal angle[1]. Hence, it is plausible that ion heating, which seems to be related to the magnetic fluctuation level in RFP's, is also toroidally asymmetric.

Ion temperature scalings

A trend for T_i vs. I/N is seen in fig 1. The data are taken at the plasma current maximum. The electron density is strongly dependent on wall loading history, and nearly independent of fill gas pressure. The way to control n_e is via baking, helium glow discharges and boronization which allows operations with higher n_e[1]. There is a clear effect on the ion temperature which is increased directly after glow discharges which reduces the density for the next two-three shots. The corresponding scaling for the perpendicular ion temperatures is certainly not as clear, mainly depending on the toroidal asymmetries of the electron density, making the ratio I/N toroidally dependent. $T_{i,\parallel}$ is measured at approximately the same toroidal angle as is n_e. Magnetic fluctuations and T_i are normally seen to increase with the pinch parameter Θ in RFP's[3], but such a scaling has been difficult to obtain on Extrap-T2 because of the limited variation interval of Θ. The electron temperature T_e deduced from Thomson scattering and VUV line ratios, is normally larger than the T_i: $60 < T_e < 150$ eV during the central parts of the discharge.

The heliumlike impurity C^{4+}which is abundant in a wider and slightly higher T_e interval than O^{4+}, and is expected to be most common in the central parts of the plasma, shows about the same temperatures as O^{4+}. It must be pointed out that even though $O^{4+}$and C^{4+}temperatures seem to be the same, the majority (hydrogen) ion temperature does not need to be the same. Collisional equilibration time between the hydrogen and carbon/oxygen can be appreciable compared to the (not yet measured) particle confinement time. The energy confinement time has been estimated from Thomson scattering to be of the order of 50 μs.

Measurements of toroidal rotation

The toroidal rotation of the impurities $O^{4+}$and C^{1+}has been measured from Doppler shifts of spectral lines along the tangential direction. When probing in the tangential and cotangential direction at the same time (viewing the same plasma volume along two opposite LOS's), the two ion temperatures deduced are the same, and velocities are anticorrelated, as expected. From O^{4+}, a constant rotational velocity of around 5 km/s is seen for most shots (in the direction of the plasma current) and for long shots, the plasma often tends to accelerate to velocities up to 30 km/s during 2-3 ms, see fig 2. This means that around half of the stored ion energy can reside in this collective motion. No strong fluid velocity fluctuations are seen, and there is no clear correlation with magnetic mode rotation/locking[1]. On MST[8], fast interrupts (on a

100 μs timescale) of rotation followed by slow acceleration (on particle confinement timescale) were seen. In the Extrap-T2 case however, the particle confinement time is supposed to be much shorter, but the acceleration timescale is about the same, several milliseconds.

For some discharges, the broadening and shift of two spectral lines from ions with differing ionization potential have been measured. This can give information on the velocity shear in the plasma, if the spatial locations of the emissivity are known. Shear will via the fluid viscosity give an effect in the momentum balance. The main investigation here has been performed by probing the O^{4+}line and a neighbouring C^{1+}line at 2836 Å. The results indicate that in the beginning of the discharge, the low ionization stage C^{1+}rotates against the plasma current with decaying speed during the discharge. O^{4+}, as mentioned above, starts at a low velocity in the direction of the plasma current, and often accelerates. That is, there seems to be a sheared rotation of the impurity ions. However, in the most extreme case, the C^{1+}ions can accelerate 40 km/s during around 1 ms, see fig 3 (but for this shot O^{4+}does not move). Rise of T_i correlates with acceleration, but a velocity shear along a LOS where a the ion line emissivity is flat, can give rise both to a Doppler shift as well as a broadening additional to the thermal one. This means that parts of the broadening cannot be interpreted as a temperature. To estimate this contribution would require radially more localized measurements.

Future plans

Future plans aim to investigate the velocity shear more in detail by probing Doppler shifts of a larger set of ions with different ionization potentials. This together with information on the radial emissivities will give a picture of the impurity ion velocity shear in the Extrap-T2 plasma. Also, measurements of $T_{i,\parallel}$ and $T_{i,\perp}$ at both the same and different toroidal angle will improve the understanding of the ion heating process.

Acknowledgements This work has been supported by the European Communities under an association contract between EURATOM and the Swedish Natural Science Research Council. Anders Welander is acknowledged for estimating τ_E.

References

[1] S. Hokin *et al.*, this conference.

[2] P. Brunsell *et al.*, in *22:nd EPS Conf. Control. Fusion and Plasma Physics, Bournemouth, United Kingdom*, III-157 (1995).

[3] P. Hörling *et al.*, Plasma Phys. Control. Fusion, in press (1996).

[4] N. Mattor, P. Terry, and S. Prager, Comm. Plasma Phys. Control. Fusion **15**, 65 (1992).

[5] E. Tennfors, Physica Scripta **T60**, 65 (1995).

[6] Z. Yoshida and A. Hasegawa, Phys. Fluids B **4**, 3013 (1992).

[7] Z. Yoshida, A. Hasegawa, and M. Wakatani, Phys. Fluids B **5**, 3261 (1993).

[8] D. Den Hartog *et al.*, Phys. Plasmas **2**, 2281 (1995).

[9] A. Ejiri *et al.*, Phys. Plasmas **1**, 1177 (1994).

[10] P. Hörling and K.-D. Zastrow, J. Quant. Spectrosc. Radiat. Transfer **53**, 585 (1995).

[11] D. Den Hartog, A. Almagri, S. Prager, and R. Fonck, Rev. Sci. Instrum. **66**, 444 (1995).

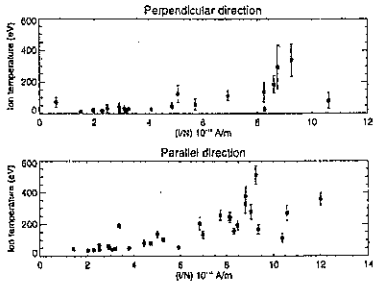

Figure 1: Scaling of T_i vs. I/N, the plasma current divided by the line averaged electron density. Data are taken at max I_p. Gaussian linefits are used.

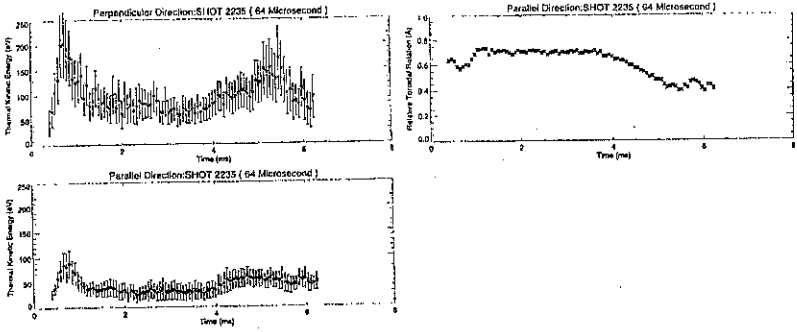

Figure 2: Perpendicular (upper left), parallel T_i (lower left) together with the toroidal rotation (right) for shot# 2235. Velocity increase is 30 km/s (0.3 Å shift) in the direction of I_p during 2 ms. All parameters deduced from Doppler effects on the O^{4+}2781 Å line, using the moment method which gives average thermal energy [11].

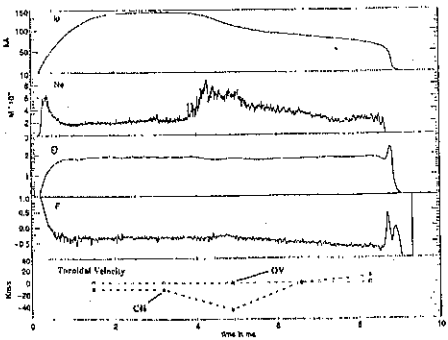

Figure 3: Some plasma parameters for shot# 3578 where there appears a strong shear in the velocity for C^{1+} and O^{4+}. From the top: Plasma current, electron density, pinch parameter, reversal ratio and velocities of the impurities. This effect is correlated with impurity influx which increases n_e and causes a decay of the plasma current.

Investigation of the Fundamental Processes of Plasma Accumulation, Heating and Confinement in the Multislit Electromagnetic Traps*

O.A.Lavrent'ev, V.A.Maslov, S.V.Germanova, M.G.Nozdrachev, V.P.Oboznyi, B.A.Shevchuk.

Institute of Plasma Physics National Scientific Center Kharkiv Institute of Physics and Technology, 310108, Kharkiv, Ukraine.

In multislit electromagnetic trap the casing character of plasma confinement is realized: that is electrons are kept by multipole magnetic field and electrostatic field in magnetic slit, and ions - by the field of electrons volume charge. Such system of combined plasma confinement by electrical and magnetic fields has unique properties, enabling successfully struggle with plasma instabilities of a various type. Multipole magnetic field of a sharp-angle geometry with a gradient directed outside and with convex force lines provides absolute hydrodynamic stability. Large volume of plasma, situating in powerless and thermoequilibrium state, provides the kinetic stability of plasma, executing a role of buffer capacity for attenuation of oscillations, developing in surface plasma layer and magnetic slits of trap. Deep magnetic well leads to the fast chaotization of electrons injected to the slit on the directions of velocities and to the suppression of beam instabilities. Stationary mode of operation, constructive simplicity and opportunity of obtaining of a high-temperature plasma without additional sources of heating puts multislit electromagnetic traps in a number of the most perspective systems for creation economical thermonuclear reactor.

The experiments were conducted on " Jupiter 2M" device [1]. A magnetic field of device has axlesymmetric sharp-angle structure with seven ring magnetic slit in a central part and axial holes on the ends. The length of magnetic system between axial holes is 1.3 m, diameter of a ring slit - 0.43 m, diameter of axial holes - 0.025 m. Maximum value of magnetic field in the ring slit B_A=9 kgs. The value of magnetic field in axial holes $B_{A0} = 2\ B_A$. The space distribution of magnetic field in the region of plasma confinement is characterized by deep magnetic well, so that with $r \le 0.1$ m, $|z| \le 0.25$ m $B/B_A < 5\%$ take place. All magnetic slits are closed by the system of electrodes with high negative potential. The plasma in a trap is created with the help of injection of electrons through the axial holes.

Unlike the other systems with magnetic plasma confinement in the electromagnetic trap the width of diffusional layer is limited by magnetic flow through the anode diaphragm of magnetic slit, which can't be wide because of condition of ions confinement in the potential well of negative volume charge. Really in electromagnetic traps the width of diffusional layer is 20-60 Larmor radii of electrons and the question about character of the electron transfer the meaning of principle for evaluation of perspectives for creation the thermonuclear reactor based on the electromagnetic trap.

In the report influence of a neutral gas on process of the electron transfer through magnetic field in multislit electromagnetic trap is considered. Experimental investigation on "Jupiter 2M" proved the high efficiency of plasma creation by electron injection; absence highfrequency plasma activity and close to classical the coefficients of transfer. It was found experimentally that plasma accumulation is accompanied by escaping ~ 10^{18} particles of neutral gas. At first it was predicted that gas escapes during plasma disintegration in consequence of its interaction with chamber walls. Later it was determined that gas escaping takes place at the initial stage of plasma accumulation. Gas fills in internal cavity of magnetic system with volume 100 l., then through the slit it spreads about whole volume of vacuum chamber. For evaluation of the time dependence of neutral gas density in plasma we shall find the velocity of ionization of neutral gas in the trap. From the equation of material balance for ions:

$$f_1(n_a,T_{e0}) = \langle\sigma_e v_e\rangle n_a = (dN_i/dt + I_i)/N_i \qquad (1)$$

where: n_a - neutral gas density; T_{e0} - temperature of electrons in the central part of plasma; $\langle\sigma_e v_e\rangle$ - ionization rate; N_i - total number of ions in the trap; I_i - the flow of ions, leaving the trap through the magnetic slits.

Equation (1) gives the connection between neutral gas density in plasma and temperature of electrons, which allows, having know the dependence $T_{e0}(t)$, to determine the dependence $n_a(t)$. However the temperature of electrons was measured in the trap with the help of Lengmur probe in the limited amount of points, that why that doesn't give the complete imagination about the time

dependence of electron temperature. That is why we shall use the equation of transfer of electrons through the magnetic field [2]:

$$f_2(n_a,T_{e0}) = I^{\Sigma}_{e\perp}=[D_{ea}(1 + \Phi_p/2T_{e0}) + D_{ei}]F\ n_{e0}R^2 \qquad (2)$$

where: D_{ea} and D_{ei} - diffusion coefficients of electrons on neutral gas and ions; n_{e0} - electron density in the central part of the trap; Φ_p - plasma potential; F - factor, taking into account the geometry of magnetic field; R - trap radius on the ring magnetic slit. Substituting to the equations (1) and (2) the experimentally found dependences $n_{e0}(t)$, $N_i \cong N_e(t)$, $I_i(t)$, $I^{\Sigma}_{e\perp}(t)$ and $\Phi_p(t)$ we shall obtain the system of two equation with two unknown values. The results of its solving are given in the table:

t, msec	$<\sigma_e v_e>n_a$, 1/sec	T_e, eV	$n_a 10^{-12}$, sm^{-3}	$n_e 10^{-11}$, sm^{-3}	Φ_p, V
0.5	593	2.97	3.86	0.70	200
1.0	1100	2.82	9.27	0.98	108
1.5	1627	2.89	12.2	1.39	108
2.0	2294	3.25	9.58	1.97	212
2.5	2295	3.54	6.58	2.78	196
3.0	1805	3.77	3.98	3.76	176
3.5	1568	4.07	2.56	4.92	160
4.0	1275	4.52	1.42	6.31	150
4.5	1173	6.15	0.52	7.97	136
5.0	1485	27.5	0.07	12.3	124
5.1	866	34.6	0.03	13.1	122
5.2	623	39.7	0.02	13.6	120
5.3	498	42.7	0.02	13.8	118

The density of neutral gas, knocked out from the chamber walls, increases, reaching the maximum 10^{13} sm^{-3} on the second msec. plasma accumulation. Then decrease of density till 5 10^{11} sm^{-3} occurs in consequence of neutral gas spread about whole vacuum chamber volume. And finally the process of "burning doun" occurs till the density 2 10^{10} sm^{-3} in consequence of ionization processes. Neutral gas "burning down" is accompanied by sharp increase of electron temperature.

The evaluations of time dependences of neutral gad density in plasma allow to express a conclusion about the classical character of plasma accumulation in the multislit electromagnetic trap "Jupiter 2M": at the initial stage of plasma accumulation' when plasma density still low, throwing off the waste electrons is realized through the channel of classical diffusion on the neutral gas with taking into account mobility of electrons in electrical field of plasma volume charge. At the final stage the waste electrons are removed from the trap in consequence of classical diffusion on the plasma ions.

* The research described in this publication was made possible in part by Grant N. UA 2000 from International Science Foundation.

Literature:

1. Vdovin S.A., Lavrent'ev O.A., Maslov B.A., Nozdrachov M.G., Oboznyi V.P., Sappa N.N. Plasma storage in the multislit electromagnetic trap "Jupiter 2M". Voprosy Atomnoj Nauki I Tekhniki, seriya Termouadernyi Sintez 3, Moskow, 1989, pp. 40 - 45.

2. Germanova S.V., Lavrent'ev O.A., Petrenko V.I. Crossfield transport of electrons in a multicusp electromagnetic trap across the end magnetic surfaces. Voprosy Atomnoj Nauki I Tekhniki, seriya Termoyadernyi Sintez 2,Moscow, 1991, pp. 74 - 76.

Modeling of Processes of Plasma Accumulation, Heating and Confinement in the Multislit Electromagnetic Trap*.

O.A. Lavrent'ev, V.A. Maslov, S.V.Germanova, B.A. Schevchuk.
Institute of Plasma Physics National Scientific Center Kharkiv Institute of Physics and Technology, 310108, Kharkiv, Ukraine.

Modeling of the plasma accumulation, heating and confinement in multislit electromagnetic trap was conducted with the use of equations of material and energetic balance. A model of 3-component plasma has been applied. This plasma consist of the fast electron of injection, thermal electrons and ions. Equations:

$$dN^f_e/dt = I_e/e - N^f_e/\tau^f_e \qquad (1)$$

$$dN_e/dt = I_e/e + \Gamma - N_e/\tau_e \qquad (2)$$

$$dN_i/dt = \Gamma - N_i/\tau_i \qquad (3)$$

$$dW_e/dt = P_e - \Sigma_k P_{ek} \qquad (4)$$

$$dW_i/dt = P_i - \Sigma_k P_{ik} \qquad (5)$$

describe time dependencies of total quantities of rapid electrons N^f_e, thermal electrons N_e, thermal ions N_i accumulated in consequence of injection and ionization. Also they describe time dependencies of total energymaintenance in electrons $W_e=1.5\ T_eN_e$ and ions $W_i=1.5\ T_iN_i$ components of plasma. Such description is convenient for traps with large volume of unmagnetized plasma, were plasma parameters remain space contancy. Features peculiar to plasma systems in electromagnetic traps are taken into consideration in the equations. These features are: collisionless transference of energy from electrons to ions by means of potential well of volume plasma charge; recuperation of energy; influence of strong electrical field on transfer of electrons through magnetic field; charged particle diffusion in the space of velocities.

The fist equation from this system realizes a material balance of rapid electrons injected in the trap. Since their lifetime in the trap is essentially more than time of energy transference for heating the plasma electrons, ionization and excitement of neutral atoms, then we shall consider the loss of rapid electron as it energetic "cooling" with the transition to the group of thermal electrons and:

$$1/\tau^f_e = 3\sqrt{2}\ \pi e^4\lambda n_e/\sqrt{m_e}\,\Phi^{3/2}_A + (\varepsilon/\Phi_A)\langle\sigma_e v_e\rangle_f\, n_a \qquad (6)$$

where: n_e - density of electrons; n_a - density of neutral gas; Φ_A - potential of electron acceleration (in energetic units); ε - energy of one act ionization, taking into account

energy losses on excitement, for hydrogen $\varepsilon \cong 70$ ev; $\langle\sigma_e v_e\rangle_f$ - ionization rate by rapid electrons.

The second equation takes into consideration the material balance of thermal plasma electrons. At initial period of accumulation, when plasma density is low, the ionization of neutral gas occurs in the volume and depends on density of already accumulated electrons and their energy. The total number of ionization act:

$$\Gamma = \langle\sigma_e v_e\rangle_f n_a N^f_e + \langle\sigma_e v_e\rangle_T n_a N_e \qquad (7)$$

where $\langle\sigma_e v_e\rangle_T$ - ionization rate by thermal electrons..

The lifetime of electrons τ_e is defined by crossfield (in the space of co-ordinates) and longitudinal (in the space of velocities) electron losses from the trap, so that:

$$1/\tau_e = 1/\tau_{e\perp} + 1/\tau^{(1)}_{e||} + 1/\tau^{(2)}_{e||} \qquad (8)$$

The flow of crossfield transfer of electrons in multislit electromagnetic trap with axialsymmetric geometry of magnetic field have been calculated in the article [1] :

$$I^{\Sigma}_{e\perp} = N_e/\tau_{e\perp} = [D_{ea}(1 + \Phi_p/2T_{e0}) + D_{ei}]\, F n_{e0} R^2 \qquad (9)$$

where: D_{ea} and D_{ei} - coefficients of electrons diffusion on neutral gas and plasma; T_{e0} and n_{e0} - temperature of electrons and plasma density in the central part of the trap; F - factor, which takes into account the geometry of magnetic field; R - radius of the trap on ring slit.

The longitudinal losses from the trap are made up of two parts: electrons, leaving the central part of unmagnetized plasma and electrons, leaving the diffusional layer surrounding the central part. Both of them leave the trap through magnetic slits getting over external electrostatic barrier. The difference is that in the first case the adiabatic invariability of charged particles isn't executed and calculations were being conducted with taking into account the theory of slit leaving of charged particles Kaye [2]. In the second case the adiabatic invariability is executed and Pastukhov [3] was used.

The value and functional dependence of parallel electrons transfer flow from the volume of unmagnetized plasma depends on plasma density. For low densities the value of flow is limited by the speed of particles Maxvellization in the plasma volume and:

$$N_e/\tau^{(1)}_{e||} = 4\sqrt{2\pi}\, e^4 \lambda n_{e0} V_p \exp(-\Phi_e/T_{e0})/m_e^{1/2} T_{e0}^{1/2} \qquad (10)$$

where: V_p - unmagnetized plasma volume; Φ_e - the height of electrostatic barrier, confining electrons in magnetic slit of the trap (in energetic units).For high plasma densities the value of flow is limited by the ability to handle of magnetic slits:

$$N_e/\tau^{1}_{e||} = 4\,\pi^{1/2} M r_p c n_{e0} T_{e0} B_0^{1/2} \exp(-\Phi_e/T_{e0})/e B_A^{3/2} \qquad (11)$$

where: M - number of magnetic slits; r_p - plasma radius; $B_0 = [8\pi(T_e + T_i)n_{e0}]^{1/2}$ - magnetic field on the boundary surface, dividing plasma and vacuum magnetic field.

The flow of longitudinal electrons transfer from diffusional layer:

$$N_e/\tau^2_{el} = [(2\pi)e^4\lambda n^2_e V_d \exp(-\Phi_e/T_{e0})]/\{m_e^{1/2} Te03^{/2}[(\Phi_e+T_{e0})/T_{e0}]\ln(4B_A/B_c+2)\} \quad (12)$$

where: V_d-volume of diffusional zone; B_c- magnetic field in the center of diffusional zone.

The third equation takes into account the material balance of ions. Ions come to the trap only in consequence of neutral gas ionization. Ion losses from the trap are accomplished through the magnetic slits by means of getting over the electrostatic barrier for ions $\Phi_i = \Phi_p - \Delta\Phi$, $\Delta\Phi$ - drop of volume charge potential in magnetic slit. For low plasma densities, the same as for electrons, the flow is limited by the speed of particle Maxvellization in the plasma volume, and:

$$N_i/\tau_i = \{4(2\pi)^{1/2}e^4\lambda n_{e0}^2 V_p \exp(-\Phi_i/T_{i0})\}/m_i^{1/2}T_{i0}^{3/2} \quad (13)$$

where: T_{i0} - ion temperature in the central region of the trap. For high plasma densities the flow of longitudinal ion transfer is limited by the ability to handle of magnetic slits and

$$N_i/\tau_i = \pi M a^* R v_{it} n_{i0} \exp(-\Phi_i/T_{i0}) \quad (14)$$

where: a^* - the effective width of slit for ions leaving the trap; v_{it} - thermal ions velocity

The drop of potential:

$$\Delta\Phi = 2\pi k e n_a a^2 \quad (15)$$

is defined by density of uncompensated electron volume charge in magnetic slit, k - takes into account the profile of electron density in slit and rate of their compensation by ions. The electron density in magnetic slit:

$$n_A = \{ 4(B_0/B_A)^{1/2} (T_{e0}/\Phi_i)^{1/2} (r_p/R) a^2 n_{e0} \}/3\pi^{1/2} \quad (16)$$

is about one order less than electron density in the central part of the trap.

Forth and fifth equation take into account energetic balance on electron and ion channels. The capacity $P_e = I_e\Phi_A$ is brought into the plasma by electron injection. This capacity wastes: ionization and excitement of neutral gas; on heating of electrons and ions; on energetic losses, connected with charged particles' leaving the trap; on charge exchange ; on braking and betatron radiation.

Collisions transference of energy from electrons to ions occurs on the slopes of the potential well of volume charge. Ions, formed in consequence of neutral gas ionization, are accelerated by electrostatic field to the center of potential well. The analysis of ion trajectories Showed that under the conditions of deep magnetic well ion, started from any

point of volume, reaches the center, acquiring the energy $\Phi(x_{st}) - \Phi_p$. Averaging on plasma volume gives expression for the capacity of energy given to ions:

$$P_i = \Gamma \alpha \Phi_p \qquad (17)$$

where α takes into account profiles of potential and neutral gas in the trap.

The system of equations (1 - 5) is calculated by numerical method in real time scale for experimental parameters on "Jupiter 2M".

Parameters	Jupiter2Mexp	Jupier2Mmod	Jupiter2	JupiterT	Elemag
Ring cysp diameter, m	0.43	0.43	1.34	2.8	6
Length between end, m	1.4	1.4	3.9	6.4	40
Ring slit magnetic field, kgs	5	5	25	40	70
Point hole magnetic field,kds	10	10	50	80	140
Applied voltage, kV	2.5	2	25	100	300
Electron injection current, A	0.2	0.2	5	30	-314
Electron injection energy,kev	2	2	25	100	300
Plasma density, sm^{-3}	$0.8\ 10^{12}$	$1.04\ 10^{12}$	$3\ 10^{13}$	10^{14}	$8\ 10^{13}$
Electron temperature, kev	0.015	0.0146	2	10	40
Ion temperature, kev	0.03	0.0297	1	10	40
Plasma volume, m^3	0.05	0.05	0.5	4	1130
Electron diffusion current,A	1.6	1.39	13.7	116	149
Electron lifetime, sec	$2\ 10^{-3}$	$1.92\ 10^{-3}$	0.36	1.3	36

* The research described in this publication was made possible in part by Grant N. UA 2200 from the Joint Fund of the Government of Ukraine and International Science Foundation.

Literature:

1. Germanova S.V., Lavrent'ev O.A., Petrenko V.I. Crossfield transport of electrons in a multislit electromagnetic trap across the end magnetic surfaces. Voprosy Atomnoj Nauki I Tekhniki, seriya Termoyadernyi Sintez 2, Moscow< 1991, pp. 74 - 76.

2. A.S. Kaye, Adiabatic cusp losses, 1969, CLM - P 193.

3. V.P. Pastukhov, Collisional losses of electrons from an adiabatic trap in a plasma with a positive potential, Nucl. Fusion, 1974, 14, 1, 3 - 6.

The plasma neutron source simulations in the GDT experiment.

A.V.Anikeev, P.A.Bagryansky, P.P.Deichuli, A.A.Ivanov, A.N.Karpushov, V.V.Maximov, I.V.Shikhovtsev, N.V.Stupishin, Yu.A.Tsidulko, S.G. Voropaev, S.V. Murakhtin
Budker Institute of Nuclear Physics, 630090, Novosibirsk, Russia
K.Noack, H.Kumpf, St.Krahl, and G.Otto
Forschungszentrum Rossendorf e.V., 01314 Dresden, Germany

1. Introduction

A neutron source based on the gas-dynamic trap concept has been first proposed in [1,2]. The gas-dynamic trap is a high mirror ratio magnetic mirror with a length substantially exceeding the ion mean free path of scattering into loss cone. To generate neutrons, 80-100keV D-T neutral beams are to be obliquely injected at the midplane of the device into relatively cold (0.8-1.1keV) collisional target plasma. For the given plasma parameters, the trapped fast tritons and deuterons are slowed down much faster than they scattered over pitch angles. Therefore, their angular spread keeps rather small during their relaxation in the plasma which results in strong ion density increase in the vicinity of the turning points located near the mirrors. Correspodingly, the neutron flux is then peaked in these regions housing the test zones. Recent pre-conceptual design study [3] provided the following parameters of the source:power consumption-60MW, neutron flux-2MW/m^2, tritium consumption-0.16kg yearly.

To test basic physical ideas underlying the source operation the studies of plasma stability and contaiment are being undertaken on the GDT facility. In this paper, the recent experimental results obtained in the studies of the fast ions produced by neutral beam injection, are presented. The parameters of the fast ions are compared with those obtained by Monte-Carlo simulations in order to reveal possible anomalies in their angular scattering or slowing down which might be caused by instabilities.

2. Experimental Apparatus

The GDT facility is axially symmetrical. It consists of a 7m central cell bounded from each ends by min-B anchor cells of an expander or/and cusp configuration. Magnetic field at the midplane is 0.22T, mirror ratio is variable in the range 12.5 - 75. Initial plasma is produced by plasma guns located in the end tanks. In order to heat the gun-produced plasma and to provide energetic ions, six neutral beams are injected at the midplane at 45^0 to the axis. Total injected power of 15-16 keV neutral beams was up to 3.5MW in 1.2ms pulses. The inner walls of the central cell vacuum chamber were covered by titanium between the shots. That significantly reduced outgassing of the first wall, accompanied in GDT with access to higher plasma parameters [4].

3. Experimental results

Fig. 1 shows the temporal behavior of the fast ion energy content in typical plasma shots. Target plasma density was varied in the range $4 \div 20 \cdot 10^{13} cm^{-3}$ whereas sloshing ion density (mean

energy of 3-6 keV) reached $5 \cdot 10^{12} cm^{-3}$. The central cell electron temperatures approaching 70eV have been observed. With the Ti-covered first wall, the charge-exchange lifetime of the sloshing ions approached 10ms, so that these losses became negligible in the plasma energy balance.

3.1 Longitudinal heat conduction on the end wall

Generally, from measurements of the plasma energy balance no evidence has been found of an additional cooling of the central cell plasma due to electron heat conduction onto the end walls. In separate experiments, near axis segment of the end wall was substituted by a plate which can be moved along the axis. When heated, the plate served to deliver cold electrons into the plasma. Their current density was comparable with that of the plasma electrons. Then, it was expected that these electrons would reduce near wall potential drop allowing thermal electron freely striking the wall, that is, perfect thermal contact with the wall would be thus established. The plasma parameters in the near-axis region in the central cell were measured for different positions of the plate in expander and for different current densities emitted by the plate. It was observed that when the distance between the plate and the mirror exceeded certain value corresponding to the reduction of the magnetic field 20-40 times, the plasma parameters in the central cell were unchanged. If it was positioned closer, significant reduction of the temperature occurred, thus indicating the heat conduction to the plate. Then, it can be concluded that in accordance with the theoretical consideration [5], the electron heat conductivity is to be suppressed when the magnetic field reduces towards the end wall approximately by a factor of $\sqrt{m_e/M_i}$.

3.2 Characterization of fast ions

Behavior of the neutral beam injected fast ions is the issue of primary concern in the studies of plasma containment in the GDT. If these ions scatter or loss their energy faster than via Coulomb collisons it deteriorates parameters of the GDT-based neutron source. Whenever it occurs, fast ion density in the peaks diminishes and the ion energies reduce. These result in lower efficiency of neutron production. To characterize the sloshing ions in GDT, the experimentally measured parameters of the ions were compared with those obtained by Monte-Carlo simulations. It was presupposed that the relaxation rates of the fast ions in given plasma background are defined by Coulomb scattering solely. The charge-exchange processes were also included through effective density of neutrals which was taken from the experimental data and from neutral transport modelling as well. As it seen from Fig.1, simulated behavior of the sloshing ions energy content agrees rather well with the experimental observation. However, it is worthwhile to note the local parameters of fast ions are expected to be more sensitive to presence of non-classical mechanisms

of plasma-fast ions interaction. Our previous measurements indicate that angular spread of the fast ions, averaged over volume, is quite close to that theoretically calculated [6]. Additionally, we have measured the local distribution function of the ions by making use of „artificial charge-exchange target" method. This involved injection of a diagnostic neutral beam at the center of the device. Then, the fast ions experince charge-exchange collisions with the beam particles thereby producing secondary neutrals. It is important that their parameters are essentially identical to those of fast ions. Spatial resolution of the method is determined by transverse size of the diagnostic beam which was about 4cm. These measurements were done at the center of the device where the injection of the main neutral beam was carried out. Therefore, we have been forced to employ the diagnostic beam with high current density (equivalently, 0.7-1A/cm^2 at 15keV energy) in order to ensure reasonable signal-to-background ratio in the presence of the neutral atoms from the main six injectors that totaling 0.2-0.3 A/cm^2 of neutrals in the plasma. The grids of the diagnostic beam injector were concave so that to focus the particles at the machine axis at the distance of 1.2m from the injector outlet. The injector provided 15-18A of hydrogen atoms with energy of 15keV in 100 μsec pulses. As an example of the row data, Fig.2. shows signals in the energetic channel of a charge-exchange analyzer when the diagnostic beam was turned on. The fast ion distribution at the center of the device measured at an angle of 45^o to the axis is shown on Fig.3 together with the distribution obtained from the simulations. Note, these data are in reasonable agreement with results of calculations taking into account the accuracy of the measurements ($\pm$15%) Further comparision of the the measured energy and angular distributions of the sloshing ions with the simulations did not provide us with any singificant evidence of anomalies.

4. Conclusions

The plasma parameters in GDT experiments have been significantly improved with Ti-gettering . In the regimes with the cusp end cell and mirror ratio of 12.5 confinement is almost completely determined by collisional losses through the mirrors as expected. No anomalies in sloshing ions relaxation in the target plasma have been observed as yet.

Acknowledgments

This work was supported in part by the Russian Fund for Fundamental Researches through Research Grant #96-02-19297a.

References

[1] Kotelnikov IA, Mirnov VV, Nagornyj VP, Ryutov DD, Proc. of XVI IAEA Conf. **2** 309 Vienna, IAEA (1985)

[2] Ryutov D.D., Plasma Phys. and Controlled Fusion **32** 999 (1990)

[3] Ivanov A.A., Kruglyakov E.P., Tsidulko Yu.A., Krasnoperov V.G., Korshakov V.V., Proc. of Symp. on Fusion Energy (SOFE'95), Urbana, IL, USA (1995) (to be published)

[4] A.V. Anikeev, P.A. Bagryansky, E.D. Bender, A.A. Ivanov, A.N. Karpushov, I.V. Shikhovtsev, Proc. of SOFT Symposium, Karlsruhe, 1994

[5] Konkashbaev I.K., Landman I.S., Ulinich F.R., Sov. JETP, **74**, 3 (1978), p.956 (in Russian)

[6] Anikeev A.V., Bagryansky P.A., Bender E.D., Contr. paper, 22nd EPS Conf. on Contr. Fusion and Plasma Phys., Bournemouth, UK (1995), V.19C, part IV, p.193

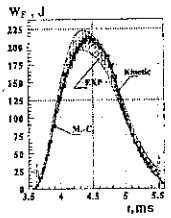

Fig.1 Fast ion energy content.

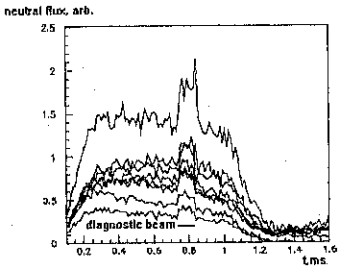

Fig.2 Flux of the charge-exchange neutrals with different energies

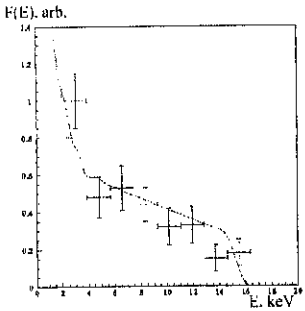

Fig.3 Distribution of the fast ions over energies

Studies of plasma axial confinement and transverse transport in the GDT experiment.

A.V.Anikeev, **P.A.Bagryansky**, P.P.Deichuli,A.A,Ivanov, A.N.Karpushov,
G.I.Kuznetsov, A.Lizunov, V.V.Maximov, S.V.Murachtin, K.Saunichev,
N.V.Stupishin, K.Noack†.
Budker Institute of Nuclear Physics, Novosibirsk 630090, Russia
† Research Center Rossendorf, Inc., PF 510119, D-01314 Dresden, Germany

1 Introduction

The general feature of Open Confinement Systems for Fusion is the direct contact of the confined plasma with end absorbers. Therefore, the longitudinal energy transport is a critical issue for investigations of plasma confinement in Open Systems.

The report summarizes the results of detailed investigations of the longitudinal particle and energy transport in the Gas Dynamic Trap (GDT). The experiments for studying transverse energy transport are now in progress on the GDT. The recent results of these experiments are also presented.

The GDT is a magnetic mirror device which has a completely axisymmetric configuration. A two component plasma is confined in a long solenoidal central cell with mirror plugs at both ends [1, 2]. Plasma start-up is carried out by injecting a plasma along the field lines from one end. Then the injected target plasma is heated up by neutral beam injection which also provides fast ions.

2 Investigations of the axial confinement.

Under conditions of the experiment, the ion mean free path exceeded the length of the mirror region and as well as the length of expanders (regions behind the mirrors). Since the plasma in the central cell of the GDT was a collisional one, the electron and ion distribution functions were isotropic Maxwellian. At the same time the regime of the plasma outflow through mirrors was collisionless. Such regimes being rather common for the GDT have been studied theoretically [3] in detail.

To study axial confinement of energy and particles in GDT we used the following diagnostics:

1) tripple Langmuir probe to measure the density and electron temperature of the central cell plasma. The reliability of the tripple probe data has been verified by comparing with Tomson scattering and the neutral beam attenuation data;

2) a movable single probe was used to measure the longitudinal profile of the mean energy of electrons and the potentials in the expander;

3) an emitting probe for monitoring the potentials in the central cell;

4) a bolometer for detection of energy end-losses in the expander;

5) a gridded collector for measuring the ion-flux density in the expander;

6) a multi-grid electrostatic analyzer for studying the ion distribution function over energies near the end wall in the expander.

The tripple probe, emitting probe, collector and bolometer were installed in the expander alternately on the movable support, which allowed different positioning along the expander axis. We monitored the

plasma density and electron temperature simultaneously on the axis of the central cell. Measurements of the plasma parameters in the expander were also carried out near the axis.

According to the theoretical predictions based on the model described in [3], the ion flux density at the mirror throat is described by the following expression:

$$q_i = 1.53 \cdot n \cdot \sqrt{T/2\pi m_i},$$

where n is density, $T = T_i = T_e$ is temperature of the plasma in the central cell, m_i is ion mass. Density of the total energy flux through mirror is calculated as

$$Q = 7.89 \cdot q_i \cdot T,$$

According to the results of our experiments, the ion flux density was:

$$q_i = (1.13 \pm 0.25) \cdot n \cdot \sqrt{T/2\pi m_i},$$

By comparing the experimental values of q_i and Q we derived the following relation:

$$Q = (8.7 \pm 1.8) \cdot q_i \cdot T,$$

Note that q_i and Q have been measured when the local magnetic field in expander was in the range of $22 < B_{max}/B < 54$, where B_{max} - magnetic field in the mirror. The ion distribution function over the longitudinal energies in the expander using the model proposed in [3] can be written as:

$$f(\varepsilon_{\|}) = n \left(\frac{m_i}{2\pi T}\right)^{1/2} \exp\left(-\frac{\varepsilon_{\|} - eU}{T}\right) \left(1 - \exp(-\frac{\varepsilon_{\|} - eU}{T(R^{-1} - 1)})\right) \quad (1)$$

where U is the drop of the ambipolar potential between the center and the end wall, $R = B_w/B_{max}$, B_w is the magnetic field near the expander wall (plasma dump). We determined the mean ion energy at the end wall in the expander from the measured ion distribution function. The mean ion energy was obtained to $\varepsilon_{\|} = (6.3 \pm 0.1) \cdot T$. The ambipolar potential drop between the center and the end wall has been obtained as the result of comparison of the measured ion distribution function with that predicted by Eq.1. It was $U = (4.6 \pm 0.1) \cdot T$.

3 Experiments with emitting plasma dump.

Theoretical predictions concerning axial energy confinement in the Gas Dynamic Trap are based on the assumption that electron emission on the plasma dump is negligible. In the presence of emission the substitution of the hot electrons from magnetic trap and emitted electrons becomes possible. This phenomena results in a decrease the ambipolar potential in the trap, and therefore, in an to elevation of the longitudinal thermal conduction [4].

As it was shown in [5] ambipolar potential and axial confinement are independent of the electron emission from plasma absorber under condition $k > 40$, where $k = 1/R = B_{max}/B_w$ is expansion ratio. Under such conditions the ambipolar potential is predicted to be $4.6 \cdot T_e$ independently of emission.

We carried out a special experiment to verify this hypothesis. A heatable disk (plasma dump) was installed in expander region of the GDT. Before installation the disk was coated by BaO. A movable support allowed us to change the location of the dump as well as the expansion ratio. We measured the current density of the electron emission by special electrode installed on dump. Typical value of the current density of the thermoemission was $7 - 10\ A/cm^2$. By emitting probe, installed in central cell, we monitored the variations of the ambipolar potential which is caused by electron emission. Fig.1 shows the measured ambipolar potential vs expander ratio. In case of $k > 40$ the saturation of the measured ambipolar potential takes place. The saturated value is equal to the ambipolar potential without emission.

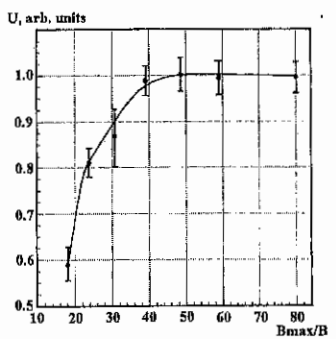

Figure 1: Ambipolar potential vs expansion ratio.

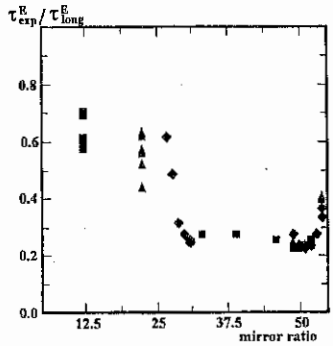

Figure 2: Energy confinement time of the target plasma vs mirror ratio.

4 Behavior of the fast ions.

Confinement study of the fast ions based on comparison between its measured and simulated parameters. Diagnostics to study energy and particle transport for target plasma and fast ions is described in detail in [6]. The main parameters for such comparison are the following:

1. Neutral Beam (NB) power trapped by target plasma;
2. total energy content of the fast ions;
3. energy and angular distribution functions of the fast ions, obtained in recent experiments using scanning energy analyzer of the fast charge-exchange neutrals and artificial neutral target.

Computer codes, based on classical theory of binary Coulomb collisions, was used to simulate the behavior of fast ions. Input data for simulations were the following:

-configuration of the magnetic field;

-time evolution of the temperature and density radial profiles of target plasma;

-time evolution of NB parameters.

The comparison between measured and calculated energy content of the fast ions shows, that within the accuracy of measurement the experimental and simulated data are identical. The measurements of energy and angular distributions of the sloshing ions compared with the simulations also did not give us any evidence of anomalies. This permits us to conclude that binary Coulomb collisions determine the behavior of the fast ions. Microinstabilities which could cause the additional scattering of ions and anomalous transport was not observed in the GDT experiments.

5 Confinement of the target plasma.

Investigations of the transverse energy transport for target plasma is based on local analyzes of energy balance. To carry out the analyzes computer codes were used to simulate the radial profile of electron drag power in the target plasma. Using the radial distributions of plasma temperature and density the longitudinal energy losses were calculated. Results of the local considerations were then used in calculations of the global energy balance of the target plasma. The dependences of energy confinement time on the mirror

ratio is shown in Fig.2. This energy confinement time is presented in terms of corresponding longitudinal lifetimes. Axial power loss ammounts to at least 60-70% of the total drag power for a mirror ratio in the range of 12.5-20. 30-40% of the drag power are passed to transverse losses and possible anomalous longitudinal heat flux, which might be caused by direct contact of the central cell plasma with cold and dense flowing plasma near by plasma gun. Separation of the transverse losses and possible anomalous heat flux is the purpose of futere investigations.

6 Conclusions.

I. Axial confinement of energy and particles have been experimentally studied in detail in regime of collisionless plasma flow through mirror region:

1. the measured energy dependence of the ions in the expander reasonably agrees with the model of the collisionless flow [3];

2. the energy flux into the expander is carried mostly by the ions, while the electron heat flux is small;

3. the mean energy carried out by an ion is 6.3 ± 0.1 of the electron temperature inside the trap, and the total drop of the ambipolar potential is equal to $(4.6 \pm 0.1) \cdot T$;

4. it was shown experimentally that expanding magnetic field behind mirrors reduces thermal conduction of electrons. By expansion ratio larger than 40 ambipolar potential and axial energy losses are independent on electron emission from plasma dump.

II. Experiments to study tranverse energy transport in a two-component plasma are now in progress. The resent results are the following:

1. binary Coulomb collisions determine the behavior of the fast ions. Microinstabilities which could cause additional scattering of ions and anomalous transport was not observed in the GDT experiments;

2. axial power loss amounts to at least 60-70% of the total heat power of the target plasma for mirror ratio of 12.5-20. 30-40% pass to transverse losses and possible anomalous longitudinal heat flux, which could be caused by direct contact of the central cell plasma with cold and dense flowing plasma near by the plasma gun. Separation of the transverse losses and possible anomalous heat flux is the purpose of the future studies.

References

[1] Mirnov V.V, Ryutov D.D., Sov. Tech. Phys. Lett., v.5,p.279(1979)

[2] Ivanov A.A., Anikeev A.V., Bagryansky P.A., et al., Phys. of Plasmas, 1(5-II),p.1529 (1994).

[3] Mirnov V.V, Tkachenko O.A., Report 85-32, Inctitute of Nuclear Physics, Novosibirsk 1985 (in Russian).

[4] Hobbs G.D., Wesson J.A.,Plasma Physics, vol.9,pp.85-87, Pergamon Press 1967.

[5] Konkashbayev I.K., Landman I.S., Ulinich F.R., Sov. JETP, v.74(1978),3,pp.956-964 (in Russian).

[6] Anikeev A.V., Bagryansky P.A., Bocharov V.N. et al., Fizika Plazmy, v.20(1994), p.192.

Steady-State Electrodischarge Magnetic Trap - GALATEYA

A.I.Bugrova*, V.V.Chebotarev, I.E.Garkusha, D.K.Kharchevnikov*,
M.V.Kozintseva*, F.I.Lipatov*, A.I.Morozov**, A.A.Pushkin*, **D.G.Solyakov**, V.I.Tereshin
Institute of Plasma Physics of the National Science Center KFTI, 310108 Kharkov, Ukraine
**) Moscow Institute of Radioelectronics & Automatics, Moscow, Russia*
***) Russia National Center "Kurchatov Institute", Russia, Moscow*

The history of development of work on Nuclear Fusion is complete of paradoxes. In particular, now practically all efforts were concentrated on huge systems (tokamaks and stellarators) with small values of β = 2-5 %, whereas the traps with β = 1 which are very interesting in physical and in the applied plans, including in connection with problems Nuclear Fusion, are really outside of fields of sight. It is explained by the fact that for creation of such effective traps it is necessary to use magnetic systems, containing conductors, shipped in a plasma. However this circumstance causes literally mystical fear. At the same time already the first magnetic trap proposed by A.D.Sakharov [1], traps constructed by S.Yoshikawa and other [2], as well as general analysis of this problem, made by A.I.Morozov and other [3,4,5], have shown, that serious problems here are not present.

The transition to traps with β = 1 essentially reduces size of installation (especially on the physical stage, when there is no necessity to use neutron protection and protection against γ-radiation), values of the magnetic fields, as well as decides a problem of stability in relation to hydrodynamic instability and, probably provides transport coefficient to be close to their classical limit. Following the reference [3], we shall use the terms for traps with conductors (magnetic coils) shipped in plasma and for such conductors as GALATEYA and MIKSINA respectively.

In the present paper we describe results of experiments with steady-state quadrupol toroidal GALATEYA, working in electrodischarge mode of operation [6-8]. The experiments were carried out in MIREA and IPP NSC KFTI on, in principal, identical installations. Schematically the trap is shown in fig. 1. The magnetic field was created by two identical coils. Diameter of coils is 30 cm, distance between them is 10 cm. Separatrix of magnetic field is shown in fig.1 In its center there is an area with zero (or small) magnetic field, surrounded by a magnetic barrier.

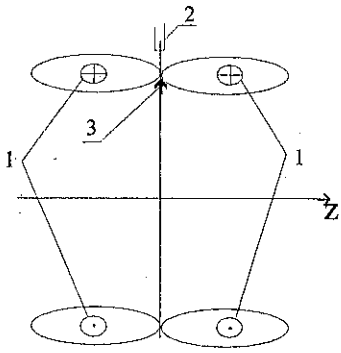

Figure 1. Schematic of quadrupol magnetic trap: 1) current windings (magnetic coils); 2) pipe of gas filling; 3) cathode

In the area between coils was filled an inert gas (xenon - in MIREA or argon - in IPP). Hot cathode was inserted in to region with minimum magnetic field value. Distance between a cathode and gas filling port was 5 cm. The vacuum chamber and screen of the magnetic coils was used as anode. The experiments were carried out in vacuum chambers with gas pressure varied from 4.10^{-4} torr (with xenon) till 8.10^{-5} torr (for argon). Switching on gas discharge between an anode and cathode in magnetic field, a plasma ring (so called Plasmida) with average diameter 1.5-2.5 cm (in dependence on conditions of experiments), located between coils in the region with minimum value of magnetic field. During experiment another mode of the discharge was found, when luminescence plasma surrounded the magnetic coils. We shall name this discharge as a mode with MANTIYA.

Dynamic of the charge particles of a formed plasma are represent as follows. More movable electrons are magnetized and move along lines of a magnetic field and magnetic field lines are eqvipotential. The cathode was placed in area with minimum magnetic field value, formed potential well in which ions of a plasma are kept. We shall note, that at energy of ions xenon 100 eV in a magnetic field of an order 20 Oe, Larmor radius is about 10^3 cm, that essentially more than diameter of PLASMIDA. It obviously specifies electrostatic character of confinement of ions.

Measurements of plasma parameters were carried out by electrostatic probes and spectroscopic methods. The region of a superseded magnetic field was measured by magnetic probes. In fig. 2 radial distributions of plasma density, electron temperature and plasma potential for one mode of operation (discharge voltage 180 V, discharge current 160 mA, magnetic barrier 20 Oe) are shown. It follows from these measurements that mode of operation with $\beta = 1$ was realized in electrodischarge trap. It is important to note, that the measured volume of a superseded magnetic field good coincided with its calculation value on the base of measured plasma parameters.

When we used argon as working gas at voltage 300 V, current 180 mA and size of

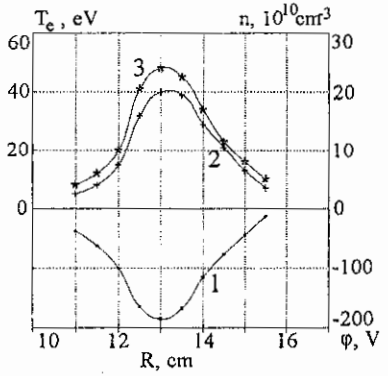

Fig. 2. Radial distributions of the plasma potential (1), plasma density (2) and electron temperature (3) at U_d = 300 V, I_d = 180 mA, H = 40 Oe. Working gas is argon.

barrier of magnetic field 40 Oe the plasma density in the center of PLASMIDA reached 2.4.10^{11} cm^{-3}, electron temperature 50 eV, plasma potential 140 V. Plasma parameters in MANTIYA, measured in this mode of operation has appeared essentially lower than in PLASMIDA. The maximum values of density and electron temperature were in the vicinity of separatrix and achieved 10^9 cm^{-3} and 10 eV, accordingly. Plasma potential in MANTIYA was of an order 4-5 V and practically didn't depend on radius. Close to coils screen the plasma density did not exceed 10^7 cm^{-3}, and electron temperature was less than 1 eV. It is necessary to note, that the change of a kind of a working gas has not resulted in change of qualitative dependencies of main plasma parameters on radius, magnetic field and discharge voltage.

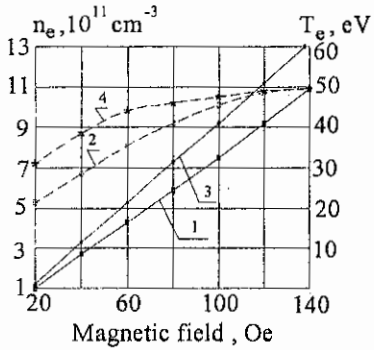

Fig 3. Dependencies of plasma density and electron temperature on value of the magnetic field barrier (working gas is xenon).

To increase the plasma parameters the value of a magnetic barrier was increased up to 140 Oe. Measurements have shown that thus the character of radial distributions of plasma parameters (density, electron temperature and plasma potential) has not been changed. The value of potential well increased up to 140 V, dependencies of plasma density and electron temperature in a center of PLASMIDA on a magnetic barrier value for various modes of operations are shown in fig. 3. One can see that plasma density and electron temperature are increasing with the magnetic field value. The saturation of curves $T_e = f(H_0)$ can be explained by

decreasing of region occupied by plasma and decreasing the negative plasma potential which suppresses the emission of electron current.

For confirmation of results of probes' measurements there were carried out spectroscopic measurements of radiation from a plasma at value of a magnetic barrier 20 Oe in ultraviolet (2000-4000 Å) and visible (4000-6700 Å). It was indicated the radiation of both neutrals and single and double charged ions of xenon. Some of spectrum lines identified are as follows: for XeI - λ = 6141.40 Å: 5d [3/2]^0 (9.96 eV) - 9f [5/2] (11.96 eV), λ = 6333.97 Å: 5d [3/2]^0 (9.96 eV) - 8f [5/2] (11.92 eV); for XeII - λ = 4965.00 Å: 6p$'$ ^{2}P^0 (16.08 eV) - 7s$'$ ^{2}D (18.57 eV), λ = 2441.60 Å: 6s$'$ ^{2}D (13.39 eV) - 33^0 (18.47 eV), λ = 4340.37 Å: 6p ^{2}P^0 (15.44 eV) - 6d ^{2}P (18.00 eV); for XeIII - λ = 3377.09 Å: 6p$'$ ^{3}D (20.63 eV) - 31^0 (24.30 eV), λ = 2811.67 Å: 6p ^{5}P (18.20 eV) - 7s ^{5}S^0 (22.61 eV), λ = 2992.91 Å: 6p ^{5}P (18.48 eV) - 6d ^{5}D^0 (22.62 eV).

The availability in a spectrum of radiation of single and double ionized atom's of xenon (with excitation and ionization potential up to 24 eV) testifies that electrons with high energy are present in plasma.

Concluding, measured parameters of a plasma demonstrated that β close to 1 is achievable in such simplified magnetic trap. Energy confinement time calculated as $\tau_E = W_{pl}/P_{dis}$, (here W_{pl} is energy containment in PLASMIDA, P_{dis} - power of discharge) is not less than 50-60 μs. Taking into account the plasma confinement in MANTIYA, the τ_E value has to be increased by several times.

References

[1] Sakharov A D 1958 in "*Plasma Physics and Problems of Controlled Fusion Reactions*" (Moscow: Academia Nauk USSR) **1** 20-30

[2] Yoshikawa S 1973 *Nuclear Fusion* **13** 433

[3] Morozov A I 1990 *Letter Sov. Phys. Tech. Phys.* **16**(15) 86

[4] Morozov A I 1992 *Sov. J. Plasma Phys.* **18**(3) 159-65

[5] Morozov A I and Khripunov V I 1992 *Sov. J. Plasma Phys.* **18** 838-49

[6] Bugrova A I, Lipatov A S, Morozov A I and Kharchevnikov V K 1991 *Letter Sov. Phys. Tech. Phys.* **17**(19) 29-31

[7] Bugrova A I, Lipatov A S, Morozov A I and Kharchevnikov V K 1992 *Letter Sov. Phys. Tech. Phys.* **18** 1-4; 1992 *Letter Sov. Phys.Tech. Phys.* **18**(24) 54-7

[8] Bugrova A I, Lipatov A S, Morozov A I and Kharchevnikov V K 1993 *Sov. J. Plasma Phys.* **19**(8) 972-6; 1993 *Sov. J. Plasma Phys.* **19**(12) 1411-7

D

PLASMA EDGE PHYSICS

Divertor Characterization Experiments and Modeling in DIII-D*

G.D. Porter, S. Allen, M. Fenstermacher, D. Hill, M. Brown, R.A. Jong, T. Rognlien, M. Rensink, G. Smith
Lawrence Livermore National Laboratory
P.O. Box 808, Livermore, CA 94550
R. Stambaugh, M.A. Mahdavi, A. Leonard, P. West, T. Evans,
and the DIII-D team
General Atomics
P.O. Box 85608, San Diego, CA 92186-9784

1. Abstract

Recent DIII-D experiments with enhanced Scrape-off Layer (SOL) diagnostics permit detailed characterization of the SOL and divertor plasma under a variety of operating conditions. We observe two distinct plasma modes; attached and detached divertor plasmas. Detached plasmas are characterized by plate temperatures of only 1 to 2 eV. Simulation of detached plasmas using the UEDGE code indicate that volume recombination and charge exchange play an important role in achieving detachment. When the power delivered to the plate is reduced by enhanced radiation to the point that recycled neutrals can no longer be efficiently ionized, the plate temperature drops from ≥ 10 eV to 1–2 eV. The low temperature region extends further off the plate as the power continues to be reduced, and charge exchange processes remove momentum, reducing the plasma flow. Volume recombination becomes important at high density and low temperature when the plasma flow time to the plate is comparable to the recombination time.

2. Introduction

The design of a viable means of removing the plasma particle and energy exhaust continues to be one of the most challenging efforts in the design of the ITER device. Detailed plasma models which have been validated against extensive experimental data are an important component in that design effort. Diagnosis of the Scrape-off Layer (SOL) and divertor plasmas in the DIII-D tokamak has recently been enhanced with new measurements of the plasma density and temperature in the divertor region[1], and an extension of the measurements of impurity behavior.

* Work supported by U.S.DoE under LLNL contract W-7405-ENG-48 and GA contract DE-AC03-89ER51114

A recent extensive experimental campaign has fully characterized the behavior of the SOL and divertor plasmas under a variety of operating conditions, including operation with additional Deuterium and/or impurity gas injection to induce divertor plasma detachment. The interpretation of the data obtained from this experimental campaign is the subject of this report. We briefly describe the overall experimental results in Section 3, focusing on the qualitative behavior we have observed. We describe the application of our 2-D plasma model to the experimental data, focusing on simulation of detached plasma operation, in Section 4.

3. Experimental Results

Initial experimental results from recent DIII-D experiments using the enhanced set of SOL diagnostics have been described previously [2]. Additional results are described in papers presented at this conference (see P. West, R. Woods, and M. Wade). We give a broad overview of the observed behavior to provide background for understanding the detailed modeling results discussed in the next section. The experiments were done over a broad range of plasma operating conditions. We obtained two distinctly different states of the divertor plasma for all operating conditions--an attached and detached plasma. The attached plasma state is characterized by high ion currents to the plate, and plate electron temperatures above 10 eV. The detached state, described in detail earlier [3], is characterized by low plate ion currents, and low electron temperatures. One of the principal observations made with the new divertor Thomson system in DIII-D is that the electron temperature of the detached state is only 1 to 2 eV. Such low temperatures raise the possibility that volume recombination processes may play a role in determining the physics of the divertor plasma, and hence the power and particle load on the divertor. Since the physics of the detached plasma is of particular interest in the divertor design of future devices, we describe our modeling of the detached state in the next section.

4. Results of modeling detached plasmas

We attempt to better understand the physical processes which lead to the detached plasma state by simulating experimental results with the UEDGE code [4], a 2-D fluid plasma code with classical parallel physics and anomalous perpendicular transport. We consider a DIII-D discharge which obtained detachment with deuterium injection and use a simple fixed fraction model to simulate the effect of impurity radiation. The simulation begins by determining the anomalous perpendicular transport coefficients consistent with the measured upstream radial profiles of density and temperature. We obtain the best match for the discharge discussed here (87506) with $D_\perp = 0.2$ m^2 /s, $\chi_e = \chi_i = 0.28$ m^2 /s. In general, we find the electron thermal

diffusivity increases with heating power.

Having used the experimental measurements of the upstream density and temperature to determine the perpendicular transport coefficients, we compare the simulated electron temperature near the divertor with that measured on the divertor Thomson system in Figure 1. The parameter ΔZ is the distance off the divertor floor at a major radius of 1.94 m. The measurement is entirely within the SOL for this particular discharge, i.e. no data are taken in the private flux region. As can be seen in Figure 1, the temperature measured near the floor is only 1 eV, consistent with the simulation. The measured temperature remains between 1 and 2 eV until approximately ΔZ=8 cm. The X-point is only 15 cm off the floor, so the low temperature region is measured to extend over a large portion of the plasma below the X-point. Although the simulation obtains similar temperatures at the floor, the spatial extent of the low temperature region is somewhat smaller than measured. This discrepancy probably arises from the simple treatment of impurity radiation which is used for the simulation. The simulation obtains temperatures between 1 and 2 eV over a much larger spatial extent on the inner divertor leg because of the higher density and larger radiation occurring on that region. This discrepancy probably arises from the crude treatment of impurities. If we included the effect of impurity transport, the steep poloidal temperature gradient would force impurities farther from the plate, increasing the radiation power there and extending the low temperature region.

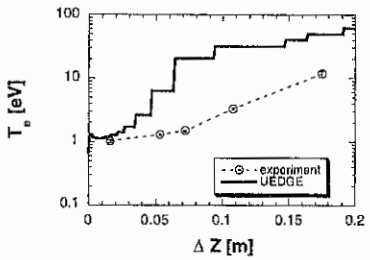

Figure 1 Variation in the electron temperature along a vertical line at R=1.94 m.

We examine the simulation in detail to determine the physical processes which are important in this detached plasma. The dominant processes can be deduced from the data shown in Figure 2. The upper portion of this figure shows the poloidal variation of the particle source rates due to volume recombination and ionization along the separatrix on the inner leg. The lower portion of the figure shows the poloidal variation of the Mach number of the plasma flow, and the ratio of the time scale for recombination ($1/\nu_{recomb}$) to the time constant for flow to the plate. The ionization rate peaks about 10 cm off the plate, corresponding to the location of the region where the electron temperature drops below that needed for efficient ionization (about 5 eV). Since the

electron temperature is in the range of 1 to 2 eV below this ionization front, charge-exchange reactions dominate over ionization. These collisions between neutrals and plasma ions are an effective way of transferring momentum from the plasma to the neutrals, and thus to the walls. This momentum removal then results in a decrease in the parallel flow velocity, as seen in the lower curve of Figure 2. When the flow velocity slows sufficiently to permit volume recombination to compete with flow to the plate, the recombination rate increases, and the plasma ions are converted very effectively to neutrals, reducing the ion flow to the plate. As shown in Figure 1, the simulated temperature at the outer strike point has also dropped to only 1 eV, sufficiently low to permit volume recombination.

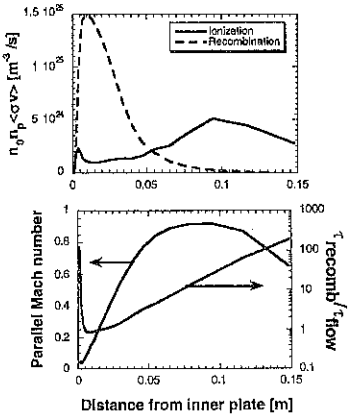

Figure 2 Poloidal variation of plasma parameters near the separatrix on the inner leg.

However, the ionization front is only about 4 cm off the plate, rather than 10 cm for the inner divertor, and there is little momentum loss from charge exchange. Hence the ion current to the outer plate remains high, as seen experimentally. The simulated divertor heat load is also much higher at the outer plate than the inner, consistent with experiment.

5. References

[1]T. N. Carlstrom, G. L. Campbell, J. C. DeBoo *et al.*, "Design and Operation of the Multipulse Thomson Scattering Diagnostic on DIII–D," Review of Scientific Instruments **63**, 4901 (1992).

[2]G.D. Porter and et al., "Analysis of SOL and Divertor Behavior in DIII–D," Phys. Plasmas **3**, 5 (1996).

[3]G. F. Matthews, "Plasma Detachment from Divertors and Limiters," Journal of Nuclear Materials **220-222** (1995).

[4]T. Rognlien, J. Milovich, M. Rensink *et al.*, "A fully implicit, time dependent 2-D fluid code for modeling tokamak edge plasmas," J. Nucl. Mater. **196-198**, 347-351 (1992).

Physical Prospects of the Dynamic Ergodic Divertor

K.H. Finken[1], G. Mank[1], M. Baelmans[1*], T. Evans[4], D. Faulconer[2], G. Fuchs[1], B. Giesen[1], M. Haßler[1], T.H. Jensen[4], A. Kaleck[1], R. Koch[2], A. Montvai[3], D. Reiter[1], A. Rogister[1], M.Z. Tokar'[1], G. Van Oost[2], G.H. Wolf[1]

[1]Institut für Plasmaphysik, KFA Jülich, Association "EURATOM-KFA", Germany
[2]Laboratoire de Physique des Plasmas - Laboratorium voor Plasmafysica, Association "EURATOM - Belgian State", ERM - KMS, B-1000 Brussels, Belgium
[3]FOM Instituut voor Plasmaphysica 'Rijnhuizen', Association "EURATOM -FOM", Netherlands
[4]General Atomics, San Diego, USA
*Supported by EURATOM in frame of its fellowship scheme

1. Introduction

In recent years considerable progress in fusion devices has been made e.g. on the improvement of the energy confinement, on the reduction of the impurity content in the plasma and on controlling long pulse discharges. There is still a need for improvements in controlling power and particle exhaust and in the avoidance of locked modes [1]. For the power and particle exhaust, a need for a high recycling divertor combined with a radiative mantle - requiring seed impurities - is foreseen; for avoiding locked modes, the extrapolation of present day devices to reactor-like devices predicts a maximum error field amplitude as low as a few times 10^{-5} of B_T field if no plasma rotation is induced [2].

2. Characteristic parameters of the DED

For TEXTOR-94 a Dynamic Ergodic Divertor (DED) is proposed which addresses those critical questions. It consists basically of a set of perturbation coils located at the high field side, which produce a propagating magnetic field pattern. The fundamental physics, which may be extrapolated to large devices, are the main motivation for the DED.

The set-up proposed for TEXTOR-94 is shown in Fig. 1: The perturbation currents are brought through four quartets of feeders (four flanges) at the bottom of the machine. Each feeder is connected to one perturbation coil. Neighbouring coils have a phase difference of 90° such that the net current of a quartet is zero. The perturbation coils (16) are wound helically once around the torus in such a way that they are parallel to the field lines at the q=3 surface (optimized for $\beta_{pol} = 1$). On top, the perturbation coils are connected to quartet star points (similar to electrical motors) and the "common" connector is fed out of the

machine. The power supplies of the perturbation coils can be operated such that they either provide DC-current or AC-current at frequencies of 50 Hz, 1 kHz or 10 kHz. The current amplitude is limited to 15 kA for DC, 50 Hz and 1 kHz and to 7.5 kA for 10 kHz. For each of these frequencies, different sets of capacitors are used to compensate for the reactive power. For the proposed set-up, two additional compensation coils (current: $+-(1/\sqrt{2})\cdot I_{pert}$; 45^0 phasing relative to top coil current) above and below the perturbation coil are needed to avoid an m = 0, n = 0 pertubation of the equilibrium.

In the "standard" mode of operation, predominantly the m=12, n=4 mode is excited by the perturbation current. If the AC-current is applied, the perturbation pattern is swept with velocities of 12 m/s (50 Hz), 240 m/s (1 kHz) and 2400 m/s (10 kHz) in the poloidal direction. At 10 kHz, the inertia of the current feeders is so large, that the currents in each feeder quartet do not need to be compensated any longer. This allows connecting the conductors of each quartet in parallel and excite the m=3,n=1 mode in the plasma. In the "vacuum" approximation, the low m mode reaches deeper into the plasma than the high m mode.

The perturbation current is resonant to the magnetic field near the q=3 surface. The degree of ergodization depends significantly on the perturbation current amplitude and the plasma position (distance to perturbation coils). The characteristic Chirikov parameter [3] (island width/island separation) at full current is about 1 for central plasma positioning and can be increased by shifting the plasma to the high field side. Thus operation either in an island dominated regime or in an ergodic regime is possible. Figs. 2 a) and 2 b) show examples of an island dominated magnetic pattern and of an ergodized pattern. A detailed analysis shows that the ergodization starts with the overlapping of high m mode islands. By moving the plasma radially it is possible to guide the power and particle exhaust predominently towards the ALT-II pumplimiter or towards the divertor target plates. Particle removal questions both in island dominated regimes and in ergodized regimes can be addressed in pump limiter experiments [4].

3. Application of a rotating pertubation field

The local field near the perturbation coils creates a "helical near field divertor" (not to be confused with a helical island divertor). Insight into the structure is gained from field line tracing: At full perturbation current about half of the magnetic field lines entering the near field area are "swept" to the walls while the other half is "pushed" into the plasma. For the

case of cylindrical symmetry, this is shown in fig. 3. The "loss area" represents the part where the field lines (and particles) are swept to the divertor target plate in one toroidal pass. The model also predicts helical stripes where a high power load may be expected (at TORE SUPRA called laminar zone) [5]. The *dynamic feature* of the proposed DED allows a smearing of the heat load to those zones. For this sweeping a low rotation frequency is sufficient; because of technical convenience 50 Hz has been chosen for this.

There are more reasons for applying a rotating perturbation field. The time scale for the recycling cycle of particles near a limiter or at the divertor is about 1 ms. When a frequency of 1 kHz is applied for driving the perturbation field, it may be expected that the recycling process changes and that a "dynamic shielding" may occur. The option of 10 kHz has been chosen, because the resulting rotation velocity of the perturbation field is of the order of the diamagnetic drift velocity. A heuristic model, based on data from DIII-D, has been developed which allows the calculation of the force - resulting from the perturbation field - acting at the singular surface. At the nominal perturbation amplitude, the relevant toroidal component of this force exceeds 1 N, which is about the same as the force due to Co-NBI. From experiments on TEXTOR-94 it is known that this force is sufficient for unlocking modes. In addition it has been speculated that an imposed (differential) rotation of the plasma enhances the confinement.

Modelling activities using the EB2-EIRENE code, RITM-code and a drift orbit code have been started. The EB2-EIRENE code predicts a flattening of the profiles in the edge due to the ergodization and enhanced removal rate by the pump limiter. The peak power load is predicted to decrease by a factor of 2 - 4 and the surface erosion by sputtering should also be reduced. The RITM code has been applied to experimental findings of TORE SUPRA. It explained how the level of intrinsic carbon impurities is reduced due to enhanced transport coefficients when the ergodic divertor was applied and that under these conditions, impurities radiate more effectively. This opens a route for TEXTOR-94 to further optimize the radiative blanket concept.

References

[1] A.W. Morris, et al., Phys. Rev. Letters **64** (1990) 1254.
[2] R.J. La Haye, et al., Phys. Fluids B **4** (1992) 2098.
[3] B.V. Chirikov, Phys. Reports **52** (1979) 265.
[4] S. Takamura, H. Yamada, T. Okuda, Nucl. Fusion **28** (1988) 183.
[5] C. DeMichelis, et al., Nucl. Fusion **35** (1995) 1133.

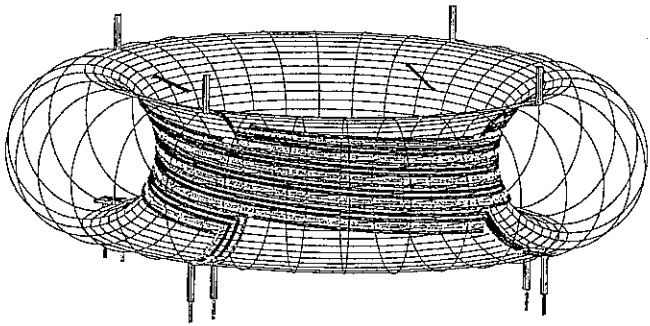

Figure 1: Schematic view of the DED coil system for TEXTOR-94. Four coils of one system are bundled to a quartet. Two compensation coils are added to keep the plasma equilibrium.

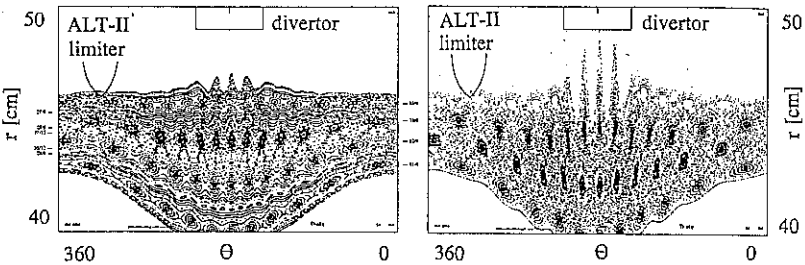

Figure 2 a,b: Poincaré plot for a) moderate (I_{eff}=3.2 kA) and b) maximum perturbation current (I_{eff}=10.6 kA). The abscissa is the poloidal angle and the ordinate is the minor radius.

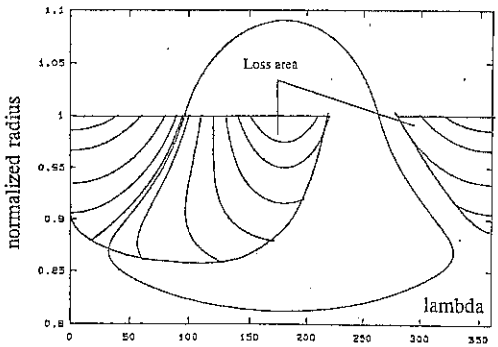

Figure 3: Contour plot for magnetic field lines in a cylindrical near field solution with a length of 2πR starting at r/a=1. The abscissa is the poloidal angle binormal to the radial direction and the direction of the perturbation current.

FIRST MEASUREMENTS OF ELECTRON ENERGY DISTRIBUTION IN RFX EDGE PLASMA

Y. Yagi*, V. Antoni, M. Bagatin, **D. Desideri**, E. Martines, G. Serianni, F. Vallone

Gruppo di Padova per Ricerche sulla Fusione
Associazioni EURATOM-ENEA-CNR-Università di Padova
Corso Stati Uniti, 4 - 35127 Padova (Italy)
*Electrotechnical Laboratory, Tsukuba (Japan)

1. Introduction

In the outer region of plasmas confined in reversed field pinch (RFP) experiments a high energy tail is commonly observed in the electron distribution function [1]. These superthermal electrons flow along the magnetic field lines, which in the outer region are nearly poloidal, carrying a substantial fraction of the edge current density. Their existence in the reversed field pinch experiment RFX has already been inferred from soft X-rays detected by a Target Emission Probe (TEP) [2] and from the up/downstream asymmetry in shot-integrated energy flux measurements with calorimetric probes [3]. The TEP measurements have also shown the presence of a small backflow.

In order to measure the time resolved flux and energy spectrum of superthermal electrons, an electrostatic Electron Energy Analyzer (EEA), developed at the Electrotechnical Laboratory of Tsukuba, has been employed in RFX.

2. EEA equipment and experimental setting up

The structure of the EEA is identical to that used on TPE-1RM20 [4] except for the outermost molybdenum jacket, which has been replaced with a graphite one to be compatible with the full graphite first wall of RFX. Because of the thicker jacket, the distance of the entrance hole for the electrons from the tip of the EEA is one millimeter greater on RFX (8.5 mm) than on TPE-1RM20 (7.5 mm). On RFX, the jacket has been kept electrically floating, whereas in TPE-1RM20 it was electrically connected to the vacuum vessel.

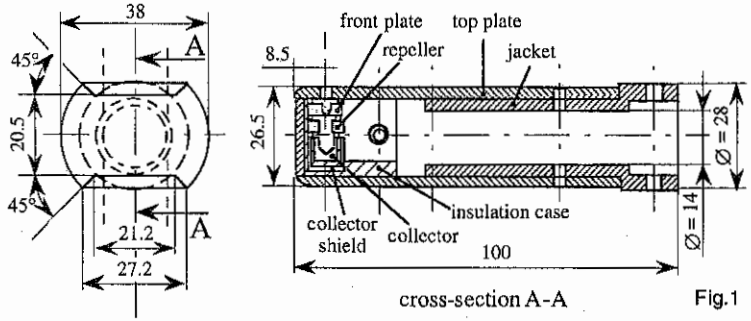

Fig.1

A schematic cross section of the EEA is shown in fig.1. The core of the device consists of a front plate, a repeller and a collector. The electron energy distribution is derived measuring the collector current as a function of the repeller voltage, which is varied in order to discriminate the energy of the electrons passing through a narrow pinhole in the front plate. The front plate is made of molybdenum, while the repeller and the collector are made of a W 65% and Cu 35% alloy. The front plate has a 2.5 mm Ø channel with a 0.1 mm Ø pinhole (0.05 mm thick) to reduce the current of superthermal electrons without distorting their energy distribution. Note that typical Larmor radii of

bulk edge electrons and hydrogen ions in the edge of RFX for 600 kA discharges are 0.07 mm and 3 mm respectively. The Laplace equation has been numerically solved to simulate the potential profile in the repeller surroundings. The on-axis potential in the repeller hole (3 mm ∅) is found to be ~ 95% of the applied voltage. The collector is kept to a voltage of +70 V (referred to the vacuum vessel, as all the voltages reported in the following) in order to avoid the loss of secondary electrons. No breakdown is observed up to a repeller potential, V_{rep}, of -600 V, even though the inner volume of the EEA is not differentially pumped. The tip of the graphite jacket has been radially inserted up to 19 mm beyond the graphite tiles. The system can be rotated of ±180 degrees around its axis to ensure alignment with the local magnetic field.

A specific linear power supply has been developed in order to apply a variable voltage waveform to the repeller up to 1 kV, with a rise and fall time of a few milliseconds. The measured signals are: the voltage applied to the repeller, the collector current, the floating potential of the graphite outermost jacket and the front plate voltage. Ground loops have been avoided using isolation amplifiers.

The measuring circuits give a resulting bandwidth of 5 kHz for the floating potential signals, of 10 kHz for the collected current and of 35 kHz for the repeller voltage. The floating potential signals have been digitized by a 16 channels INCAA Model CADF transient recorder at a sampling rate of 10 kHz; the current and the repeller voltage by a 4 channels INCAA Model CADH transient recorder at a sampling rate of 80 kHz.

3. EEA operation

The repeller voltage V_{rep} has been linearly swept in 10-20 ms up to -600 V, several times per discharge. Figure 2 shows an example of V_{rep} and I_{col} (collector current) waveforms, along with the plasma current and the toroidal magnetic field at the wall. It is worth noting that the I_{col} signal starts when the toroidal field at the wall changes sign, as a consequence of the EEA becoming aligned with the local magnetic field. I_{col} vs. V_{rep} characteristics measured during each ramp have been used to obtain information about the electron distribution function.

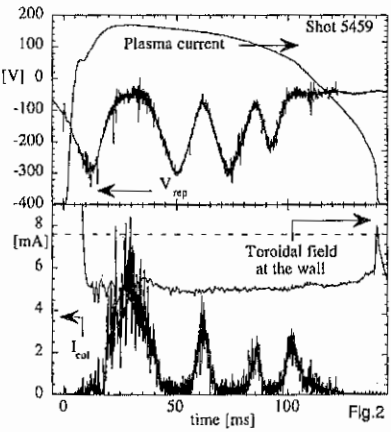

Fig.2

Two experimental campaigns were performed, both of them on 600 kA discharges. In the first one the front plate was electrically floating. The analysis of the data from this campaign showed that, due to the superthermal electron flux, the front plate reached a floating potential of ~ -200 V depending on the insertion depth. Only repulsive voltages lower than the front plate voltage are useful for the I_{col}-V_{rep} characteristic, since for higher ones the I_{col} signal becomes almost constant. In fact the Debye sheath thickness is comparable to the pinhole diameter, causing the front plate to act as an effective repeller. Therefore, during the second campaign the front plate was connected to the vacuum vessel through a 2.3 Ω, 50 W resistor. Such a connection led to typical front plate voltages of -20 V, allowing also the low energy part of the distribution function to be explored.

The front plate heating due to the superthermal electron energy flux has been estimated. The rise in

temperature of the region around the pinhole during a typical RFX discharge turns out to be much less than the evaporation temperature of the molybdenum. The inspection of the pinhole after the experimental campaigns has confirmed that its diameter was unchanged even after many discharges.

4. Measurements

Applying a time changing voltage to the repeller, I_{col}-V_{rep} characteristics have been deduced with the EEA exposed to the electron drift side. On the ion drift side the current signal turned out to be too small to provide reliable characteristics. An example of characteristic obtained on the electron drift side is shown in fig.3. The characteristic changes slope at $V_{rep} \sim -150V$ so that two portions can be identified. In this context the lower energy portion, which could be distorted by space charge effects, is not discussed. It is worth noting that if this portion is fitted by a half-Maxwellian distribution function, the resulting temperature is $T_e \sim 50$ eV which is at least twice the bulk electron temperature expected in this region of plasma [3]. On the other hand, the higher energy portion of the characteristic confirms the presence of a superthermal tail. This high energy tail has been assumed to be a distinguishing feature of the electron drift side, in the hypothesis of negligible backflow.

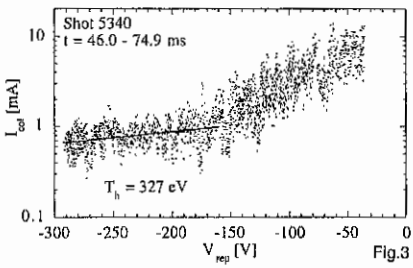

Fig.3

Following reference [5], the high energy tail has been fitted with a half-Maxwellian distribution. The result of the fit, also shown in fig.3, gives a temperature $T_h = 327$ eV, much larger than the edge electron temperature.

Generally speaking, the temperature T_h of the high energy tail turns out to be of the order of the on-axis bulk electron temperature T_0, which in these discharges was 250-350 eV. It is worth noting that the values found for T_h are comparable to those found in TPE-1RM20 with the same EEA. The intercept I_0 of the fitting curve with the I_{col} axis yields the population density n_h, according to the equations

$$I_0 = \frac{e n_h v_h}{\sqrt{\pi}} A, \qquad v_h = \sqrt{\frac{2T_h}{m}}$$

where A is the pinhole area and all perpendicular velocities are assumed to be collected. Such a procedure assumes the plasma to be at the same potential of the vacuum vessel, which is taken as the reference potential. Data collected in the past have shown that plasma potential in this region is in the range 0-30 V [3], so that, in consideration of the relatively high values of T_h, the error introduced by this assumption is negligible. The deduced values of n_h are between 10^{17} and $5 \cdot 10^{18}$ m^{-3}. The ratio between n_h and the line averaged electron density <n> is for most discharges of a few percent.

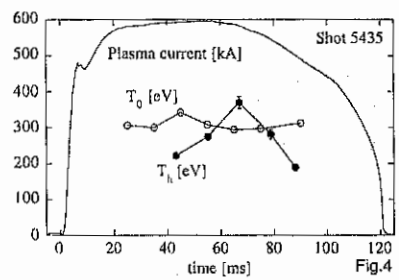

Fig.4

Under the assumption made above that the high energy electrons are present only on the electron drift side, the edge current density carried by them has been evaluated as $j_h = I_0/A$. Typical values are in the range 100-500 kA/m^2, consistent with the estimated current density in the

RFX edge region, although in some cases values exceeding 1 MA/m^2 are obtained.

The unique possibility of applying many voltage ramps to the repeller in a single discharge has led to the measurement of the time dependence of the superthermal electron temperature. An example of T_h as a function of time is shown in fig.4, superimposed to the plasma current waveform and to the on-axis bulk electron temperature T_0 as measured with a SiLi detector. T_h is observed to be comparable to T_0 and the time behaviour can be interpreted as a rise during the slow ramping phase of the plasma current followed by a decrease during the current decay. Different behaviours have also been observed.

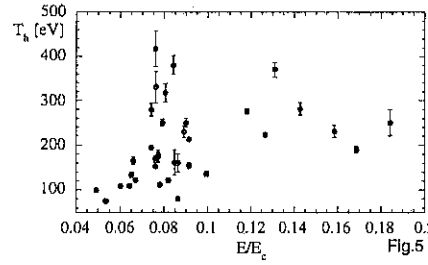

Fig.5

The data collected about T_h have been related to the non-dimensional parameter E/E_c, where $E = V_{loop}/(2\pi R)$ is the on-axis inductively applied electric field, while E_c is the on-axis critical field for runaway generation as defined in [6], assuming the on-axis density comparable to the line averaged one. This comparison has been made using data collected over a radial range of 7 mm, implicitly assuming the changes in T_h to be negligible over this range. Figure 5 shows T_h as a function of E/E_c. If the hypothesis of independence on radial position is confirmed, it may be concluded that there is a tendency of T_h to grow as E/E_c becomes greater. A similar tendency is observed also for the ratio T_h/T_0. The dependence of T_h on E/E_c shown in fig.5 and the fact that T_h is comparable to T_0 indicate that superthermal electrons are probably generated in the centre of the plasma, and then transported to the outer region, possibly flowing along stochastic magnetic field lines.

5. Conclusions

For the first time the electron distribution function in the outer region has been measured on RFX by means of an electrostatic EEA. The high energy portion of the data collected on the electron drift side shows the presence of a superthermal tail in the electron distribution function. Such tail has been interpreted assuming a half-Maxwellian shape. The EEA power supplies have made it possible to measure the time evolution of the superthermal electron temperature T_h. It has been found that T_h is comparable to the on-axis electron temperature and the superthermal current density j_h is in most cases of the order of the estimated RFP equilibrium current density in the edge region. The superthermal electron density n_h is a few percent of the line average electron density. A correlation between T_h and the E/E_c ratio has been found, in the hypothesis of independence of T_h from the radial coordinate on a 7 mm distance. This correlation, together with the fact that $T_h \approx T_0$, supports the idea that superthermal electrons found at the edge are produced in the central plasma.

References

[1] S. Ortolani, Plasma Phys. Controlled Fusion **34**, 1903 (1992).

[2] P. Martin, V. Antoni, A. Murari, S. Peruzzo, G. Serianni, Rev. Sci. Instrum. **66**, 431 (1995).

[3] V. Antoni, E. Martines, M. Bagatin, D. Desideri, G. Serianni, Nucl. Fusion **36**, 435 (1996).

[4] Y. Yagi, Y. Hirano, Y. Maejima, T. Shimada, to appear in Japanese J. of Applied Phys. **35** (1996).

[5] J. C. Ingraham et al., Phys. Fluids B **2**, 143 (1990).

[6] H. Knoepfel, D. A. Spong, Nucl. Fusion **19**, 785 (1979).

Analysis of VUV Ne radiation in the JET divertor during Ne injections

R. Guirlet*, R. Giannella, L. Horton, K. Lawson†, A. Maas, C. Maggi, M. O'Mullane†
JET Joint Undertaking, Abingdon, Oxfordshire, OX14 3EA, UK
*Permanent address: DRFC/SPPF, Association EURATOM-CEA sur la Fusion, CE CADARACHE, St-Paul-lez-Durance, France
†UKAEA Government Division, Fusion, Culham, Abingdon OX14 3DB, UK

To enhance the radiated power fraction at the edge of a tokamak plasma without degrading the confinement parameters of the bulk, impurity seeding is a classical method. Although neon is one of the most often used impurities, its ability to radiate at the edge without contaminating the plasma itself is still under discussion. This paper presents a detailed estimate of the neon radiated power in the JET Mark I divertor together with an aspect of the Ne behaviour as a function of the Ne density in the bulk using the data provided by a VUV spectrometer viewing the divertor region.

The main diagnostic for this study is an absolutely calibrated double VUV spectrometer (SPRED) directed to the inner part of the divertor horizontal target (fig.1). It is equipped with 2 gratings (450 g/mm and 2105 g/mm) giving a wavelength range of 150Å ≤ λ ≤ 1450Å. The time resolution is 11 ms - 50 ms per spectrum. To extract the various line intensities of D, He, C and Ne, a multigaussian fitting code is used in order to deal with the severe blending of most of the Ne lines. The Ne II resonance line (461Å) intensity is not estimated because of the blending with a C III line in a particularly complex part of the spectrum. The main Ne IX and Ne X lines lie outside the wavelength range of the detector but they radiate in the bulk rather than in the divertor. For each of the other ionisation stages the most important lines are measured. To cross-check the results a bolometer line of sight (BLOS) viewing approximately the same region of the inner target plate is used. The divertor contribution is estimated by subtracting the signal measured by a line of sight viewing only the bulk.

ESTIMATE OF THE POWER RADIATED IN THE DIVERTOR: To estimate the power radiated in the inner strike point region, a low-Ne content, L-mode discharge ($<n_e> = 4.4\times10^{19}m^3$, fig.2) with a small Ne puff is chosen. The X point position is swept. The estimate is made from the D I, He II, CII to IV and Ne III to VIII line intensities. One of the largest uncertainty comes from C IV because the resonance line (1549Å 2p-2s) lies outside the wavelength range of the spectrometer. The ratio of 2 other C IV lines (312Å 3p-2s and 384Å 3d-2p) is used to determine (with ADAS [1]) a value of T_e and subsequently the resonance line intensity. As far as Ne is concerned the largest error is due to the lack of information about the Ne VII triplet configuration. However the maximum contribution of the triplet resonance line to the radiated power is estimated by ADAS to be 16% of the singlet resonance line. It is observed that the Ne III to V line intensities are strongly modulated by the sweeping, indicating a peaked distribution along the target direction, whereas the Ne VI and VIII intensities are not or weakly modulated (the Ne VII line used in fig.2d is thought to be blended, thus giving an overestimate of its intensity and a fake correlation with the sweeping). This is thought to be due to the location of the higher ionisation stages farther from the divertor target or even above the X point. The radiated power is more or less evenly distributed between the lower (III to V) and the higher (VI to VIII) ionisation stages of Ne. This is in agreement with the bolometer measurements showing that half of the additional radiated power is radiated above the X point. The electron temperatures measured from the line ratios available give Te(C III) =6±4eV, Te(C IV) = 9±4eV, Te(Ne V) = 11±4eV, Te(Ne VI) = 12±6eV. The similarity of the latter two is surprising since only Ne V is modulated by the sweeping. It might be due to the weak sensitivity to T_e of the Ne VI line ratio we

use here (I(2s2p^2 ^{2}S-gs)/I(2s2p^2 ^{2}P-gs)). The total radiated flux (fig.2c) estimated from the SPRED measurements, and in particular the extra flux after the Ne puff, due almost entirely to Ne (75%) and deuterium (25%), are in good agreement with the power flux measured by the BLOS. In all the pulses analysed here, the ratio of the BLOS signal to the radiated power in the X point region (calculated by an Abel inversion of the bolometer array signals) is constant as a function of time, due to the fact that the emission comes mainly from the region seen by the BLOS. The agreement between the SPRED and the BLOS being good, this ratio can be used to convert the flux measured by the SPRED to a radiated power, keeping in mind that the obtained value is likely to be an underestimate of the power radiated in the divertor. The same estimate was made for an ELMy H-mode discharge at lower density ($<n_e> = 3\times10^{19}$ m^{-3}), with P(NBI) = 15MW (fig.3). This time the Ne injection (7.8×10^{20} atoms) is aimed at maximising the radiation. It results in a saturation of a number of spectral lines on the double SPRED. These line intensities were estimated using line ratios during the non-saturated phases of the signals, giving a factor 2 on the global uncertainty of the power radiated by neon. Only the C III and Ne VII contributions could not be measured because of the saturation of all the corresponding lines. In this case it is clear that however large the error is, the strongest radiator among the neon ions is Ne IV which radiates about 70% of the total neon radiated power, indicating an ionisation equilibrium very different from the L-mode case. Another evidence is the Ne VI modulation as a function of the sweeping, indicating that the Ne VI radiates closer to the target than in the preceding case. Since C III, as in the previous case, is the strongest radiating carbon ion, these results are in qualitative agreement with the bolometer array measurements showing that the radiation balance is slightly in favour of the X-point radiation (60% of the total radiated power). More experiments are needed to compare these results to the analysis of the bolometer measurements described in [2]. Because of the CIII saturation, it is not possible to say which species, either C or Ne, is the strongest radiator, but from a comparison with the BLOS it can be said that the deuterium radiates about 20% of the total 3.5MW.

EFFECT OF A FORCED D_2 FLOW ON THE NEON RADIATION: The first pulse shown in the preceding part is one of a series of L-mode, moderate density ($<n_e> = 3\text{-}4.4\times10^{19}$ m^{-3}), moderate NBI power (3.5MW), X point-swept, divertor D_2-fuelled ($2.3\text{-}5.5\times10^{21}$ atoms/s) discharges. The aim of this series was to study the effect of a forced D_2 flow on the impurity radiation. Ne is puffed as a tracer rather than as a radiator. Both the neon and the deuterium could be injected either from the top of the machine or directly into the divertor, and all combinations were performed. For a given electron density, no effect of the D_2 or Ne injection location was observed regarding the maximum radiation, either on the neon radiation or on the other species (C, O), confirming the results found in [3]. The only difference is the radiation due to the deuterium: it is stronger when the D_2 is injected in the divertor because of the higher deuterium flow necessary to maintain the bulk density.

EFFECT OF INCREASING THE NEON DENSITY IN L-MODE: A recurrent question about impurity seeding experiments is whether or not it is possible to enhance the edge radiation without contaminating the core. From the series described in the last paragraph, two pairs of shots have been chosen to study the effect of increasing the amount of injected Ne in the plasma at two different densities (fig.4a, $<n_{Ne}> = 0.66\times10^{17}$m^{-3} (solid line), 1.5×10^{17}m^{-3} (dashed line); fig.4b, 1.9×10^{17}m^{-3} (solid line), 3.3×10^{17}m^{-3} (dashed line)). The gain in radiated power when increasing the amount of Ne is considered. However, since the Ne density is different for every shot, we normalise this gain to the Ne density increase in the bulk (estimated from the Z_{eff} measurement):

$$g = \frac{P_{rad2} - P_{rad1}}{n_{Ne2} - n_{Ne1}}$$

g = gain in radiated power / increase in Ne density					
$<n_e>$	Ne III	Ne IV	Ne V	Ne VI	Ne VIII
3×10^{19} m^{-3}	1.6	1.6	1.4	saturated	1.3
4.4×10^{19} m^{-3}	0.8				

At moderate density and for the lower ionisation stages (Ne III to V) the gain in radiated power is significantly higher than the increase of injected neon (see table). For the higher ionisation stages, the gain in radiated power is less favourable, but at least 30% higher than the Ne density increase in the bulk. The difference in the lower and higher ionisation stages indicates a modification of the ionisation equilibrium, even with this small amount of Ne. The decay times of the Ne signals (4.9s for Ne III-V, 4.4s for Ne VI-VIII) significantly decrease when doubling the amount of injected Ne. At higher density, the gain is lower than the increase in the amount of Ne. All the ionisation stages behave in the same way as far as the gain in radiated power is concerned. This is thought to be due to the smaller amount of Ne injected. The decay times (3s for Ne III to V, 3.4s for Ne VI to VIII) do not depend on the amount of injected Ne.

CONCLUSION: The SPRED has proven to be a useful tool for precise estimates of the radiated flux and even, with few assumptions, the radiated power in the divertor. However, more work is needed to ascertain the C IV resonance line intensity due to its strong dependence upon T_e. The measured Ne VII contribution to the radiation seems fairly small (less than 10% in the L-mode case). Hence if the neon atomic data are revised with more sophisticated calculations, we suggest to put the emphasis on Ne IV which is the strongest radiator of the Ne ions in the pulses presented here. The Ne ionisation equilibrium appears very different in L- and H-mode discharges, more favourable to the edge radiation in H-mode, mainly due to the strong Ne IV radiation. Another Ne-seeding experiment this year will allow us to precise the first results presented here, in particular the relative importance of the various impurities in the radiated power fraction.

In L-mode, for small Ne puffs (compared to the Ne injections aimed at maximising the radiation), the higher density pulses presented here show that the Ne bulk density increases faster than the power radiated at the edge when increasing the amount of injected Ne. At lower density (corresponding here to larger Ne puffs), there is a change in the ionisation equilibrium, suggesting that the T_e and n_e profiles are modified significantly in the divertor region. This is thought to be due to the larger amount of neon in the discharge rather than to an effect of the density.

Simulations with an impurity transport code such as DIVIMP[4] are necessary to confirm the assertions made in this paper, in particular in providing a consistent overview of the T_e, n_e profiles and of the Ne ionisation equilibrium.

[1] H.P. Summers, ADAS, JET-IR(94) 06 (1994)
[2] H.J. Jäckel et al., 37th APS Conference on Plasma Physics, Louisville, USA (1995)
[3] P.J. Harbour et al., 22d EPS Conference on Controlled Fusion, Bournemouth, UK (1995)
[4] P.C. Stangeby and J.D. Elder, J. Nucl. Mater. 196-198 (1992) 258.

Fig.1: SPRED line of sight and BLOS in the divertor region. The extreme X point positions are indicated for #35042.

Fig.2: #35402: a) volume average density; b) radiated power measured by the bolometer array; c) radiated flux measured by the BLOS (solid) and the SPRED (dashed: total, dotted: D, broad-dashed: C, dashed-dotted: Ne); d) Flux radiated by Ne as measured by the SPRED.

Fig.3: #32767: volume average density, neutral beam injection power, Ne atoms injected into the vessel and radiated flux measured by the SPRED.

Fig.4: Neon radiated flux at $<n_e> = 4.4\times10^{19} m^{-3}$ (left) and $3\times10^{19} m^{-3}$ (right). From top to bottom: Ne III, IV, V, VI and VIII.

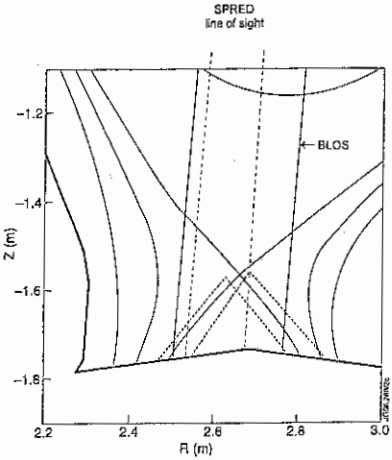

Fig.1

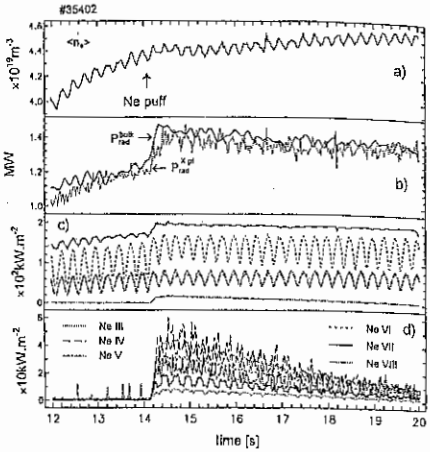

Fig.2

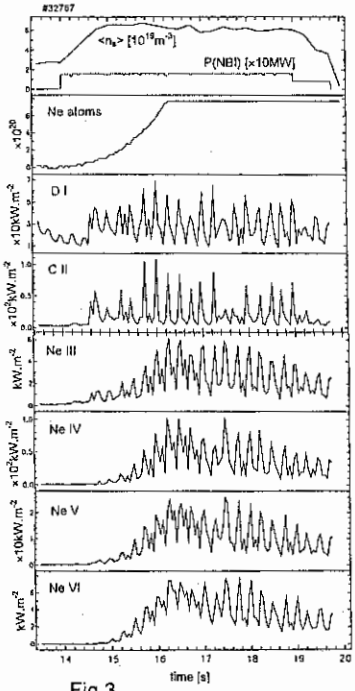

Fig.3

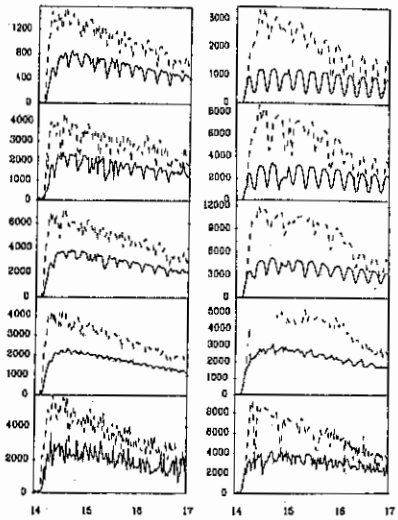

Fig.4

Electron temperature in front of the target plates in various divertor scenarios in ASDEX Upgrade

M. Weinlich, A. Carlson, R. Chodura, C.S. Pitcher[2], V. Rohde[1], U. Wenzel[1] and the ASDEX Upgrade and NBI Teams

Max-Planck-Institut für Plasmaphysik, EURATOM Association, D-85748 Garching

[1] *IPP, Bereich Berlin* [2] *CFFTP, Toronto, Canada*

1 introduction

The magnitude of the potential drop across the Debye sheath between a plasma and its surrounding wall takes on a value proportional to the electron temperature ensuring equal ion and electron fluxes to the wall. Most of the plasma wall interaction processes are determined by this sheath. In addition most of the atomic and molecular processes including ionization, radiation and recombination are also determined by the same temperature. For these reasons the electron temperature is one key parameter for understanding divertor behavior.

From the logarithmic slope of a I-V-characteristic measured with Langmuir probes a temperature can be derived. The main part of the slope is determined by the electron temperature, but the ion temperature (mostly taken to be equal to T_e) must also be known to derive the sound speed, used to determine the density. The characteristic is usually fitted with an exponential, which assumes a Maxwellian distribution function. Both limitations are well known and have been extensively studied in various cases. Additional questions have arisen in recent years concerning the plasma at the target plates in fusion devices, namely the influence of parallel resistivity and temperature gradients. We will focus on the last items and discuss their effects in the ASDEX Upgrade tokamak.

2 temperature gradients

The effect of temperature gradients has been discussed by several authors [1][2] and can be summarized as follows: The floating potential at the wall is determined by the electrons which can overcome the retarding sheath potential ($E_\parallel \simeq 3k_BT_e$, hydrogen plasma) . The parallel heat flow is dominated by the same tail electrons, whose mean free path (assuming $Z_{\text{eff}} = 1$) can be estimated by

$$\lambda_{\text{mfp}} = (1.07 \times 10^{18}\ \text{m}^{-2}\,\text{eV}^{-2})\ \frac{T_e^2}{n_e \ln \Lambda} \qquad (1)$$

If this characteristic length is small compared with the distance from the midplane (the source region) a temperature gradient will be established which is tied up with a heat flux to the target. The parallel sheath condition at the target ($q = \delta n_e c_s k_B T_e$) and the free streaming energy limit of the electrons ($\simeq 0.2 v_{e,th} k_B T_e$) result in a typical temperature gradient length at the target of the same order as the above mean free path length. Probes usually scan only the high energy tail of the electron distribution function. The temperature derived form the I-V-characteristic is therefore close to the temperature one gradient length upstream and not

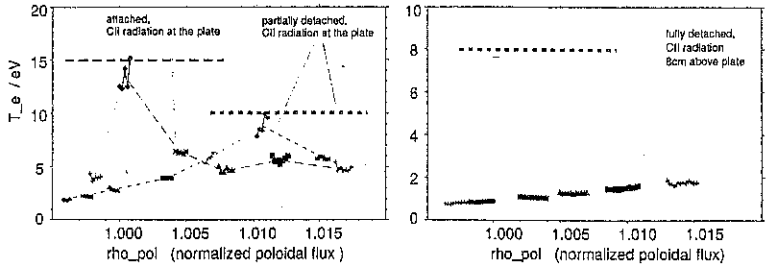

Figure 1: *Comparison of electron temperature profiles at the outer target plate derived from probe data (filled symbols) with CII temperature (dashed lines). The CII temperature originates from the region of maximum CII emission.*

the temperature of the electrons at the Debye sheath edge. This situation can be modeled self-consistently in a 1D-pic code including coulomb collisions [1]: The temperature gradient and the Debye potential in front of the plate can be clearly reproduced, resulting in a non-Maxwellian distribution function at the target plate. Trying to match the electron current at the target (which should vary exponentially with the potential drop across the sheath) with the local plasma parameters at the sheath edge leads to higher temperatures and locates the edge about one mean free path upstream.

Using two probe systems, a reciprocating probe upstream and fixed (flush mounted) probes at the target plate, it can be shown that temperature gradients inside the divertor can only be measured if the mean free path is small compared to the connection length of the probes.

Secondary electron emission at the plate is determined by the (hot) electrons reaching the target plate. Sputtering is due to the ions being accelerated across the sheath, whose potential drop is once again established by the upstream electrons. The ionization of neutrals released by the walls as well as the radiation from impurity ions in front of the plate are mainly induced by high energy electrons. So even in the case that a steep temperature gradient may exist inside the last mean free path of the "upstream" electrons, the derived temperature is the one describing the physics dominating this region.

The probe temperature can be compared with the temperature derived from line ratios of CII emission [3]. In a fully attached case (Fig. 1 left) the measured radiation originates from the target plate close to the strike point and is in good agreement with the probes' temperature at the separatrix. In a partially detached case (Fig. 1 left) the radiating zone moves with the temperature maximum away from the strike point, but both temperatures are still in good agreement. If the divertor plasma is fully detached (Fig. 1 right), the maximum of CII emission lies somewhat upstream, indicating a temperature gradient towards the target plate. The mean free paths in the attached and partially detached cases are close to 0.15 m, whereas it drops in the fully detached case below 1 mm. The good agreement of probe and CII temperature in the first cases show that both temperatures are determined by the same electron population.

3 plasma resistivity

The influence of the parallel plasma resistivity can be understood as an additional resistor being in series with the sheaths resistance. As reported earlier [4] this will flatten the slope of the measured I-V-characteristic and lead to an overestimated temperature. If single probes are used to determine the temperature we expect that the curvature of the characteristic, which can not be affected by the parallel resistivity, allows for a better estimate fitting the whole characteristic then deriving the temperature from the slope near the floating potential. Using a double probe model, as we do at ASDEX Upgrade, the size of the return electrode also influences the fitted temperature. A scan of various normalized resistances shows the fitted temperature closer to the original one for small current ratios which are frequently observed with flush mounted probes.

For a simple estimate the parallel resistance $R_\parallel = 2l/(2A_{\mathrm{probe}}\sigma_{\parallel,\mathrm{Spitzer}})$ can be calculated for a constant temperature along the path, using an averaged cross section of $2A_{\mathrm{probe}}$ according to experimental data. Taking the temperature equal to that of the electrons which overcome the sheath the apparent temperature including resistive effects can be related to the mean free path length (Eqn. (1)):

$$T_{\mathrm{apparent}} = T_e\,(1 + 0.12\,l/\lambda_{\mathrm{mfp}}) \tag{2}$$

If there are temperature gradients in the plasma, they will reduce the influence of the resistivity even further. The resistive effects will therefore be important only if the current flows much further than several mean free paths along the field lines.

The temperature comparison (Fig. 1) in the foregoing section shows that the resistive effects are negligible in the attached and partially detached case ($l \simeq \mathcal{O}(\lambda_{\mathrm{mfp}}) \ll L_\parallel$). If the very low temperature in the detached case would be accounted for as a pure resistive effect, the length of the current path can be estimated using different input temperatures for the Spitzer resistivity. If one takes the 1 eV apparently measured at the target plate, the resistive length would be below 3 cm. As an upper limit for the effect of temperature gradients the same calculation with the spectroscopically determined temperature of 8 eV (3 m upstream along field lines) yields a maximum length of 1.9 m which is still below the connection length. These results show as well as earlier measurements of return currents at the target plate [5] the existence of high cross field currents, allowing the probe circuit to be closed near the probe with a short current path inside the plasma, minimizing the total resistance.

4 return currents

To study the effect and the magnitude of cross field currents, we set up a special probe head for the mid plane manipulator at ASDEX Upgrade (Fig. 2). It consists of a fixed housing around a rotable probe array, which is build of 15 tips of different sizes. This allows for the separation of angular and size effects on the I-V-characteristic as well as for the detailed observation of the return current. The probe is inserted in between two ICRH antennas and has therefore a short connection length (3 m) to the next limiter. The plasma density and temperature measured with a conventional small probe tip and with the big checkerboard probe head are similar, indicating only a small disturbance of the plasma. The ratio of the calculated mean free path length (Eqn. (1)) and the connection length is about 1:20. Operating one small tip

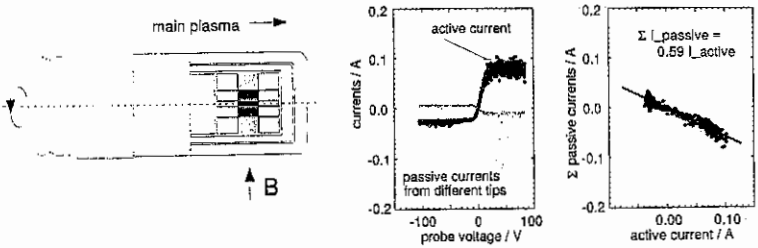

Figure 2: *The checkerboard probe used to measure the return currents from one small active probe tip (black) on several surrounding tips (grey). The sum of the measured return currents balances the active current to 59%, the extrapolation to the total probe surface yields 100%.*

in the center of the probe head as an active single probe and measuring the return currents on the neighboring tips allows for the calculation of a current balance extrapolated to the total surface (Fig. 2). Even in that case of short connection length to the next limiter there are cross field currents (indicated by $I_{sat,right} > I_{sat,left}$) and they flow close enough to the probe, that the electrical circuit is completely closed by return currents instead of currents to the limiter ($l_{current} \lesssim 10\,\lambda_{mfp} = L_{\parallel}/2$).

The existence of strong cross field currents has implications reaching far outside probe theory. Thermoelectric currents in the scrape off layer can, for example, only flow if the cross field currents and the plasma resistivity directly at the plate are not too high. It has been experimentally observed, that they vanish completely after the detachment of one divertor leg.

5 summary

The experimentally derived temperature from the probe diagnostic and from CII radiation is in good agreement in attached cases. This temperature describes most of the relevant processes in front of the target plates even if there exist strong temperature gradients across the last mean free path. The probe temperature in detached cases gives an upper limit to the real temperature, but is small enough that physical conclusions will not be significantly modified even if resistivity effects occur. This observation leads immediately to the question of cross field currents. The existence of strong cross field currents could be directly demonstrated with a dedicated experiment. The existence and magnitude of currents in the scrape off layer has to be studied further on in the light of these results.

References

[1] CHODURA, R., Contributions to Plasma Physics 36/*S* (1996) 61.

[2] WESSON, J., Plasma Physics and Controlled Fusion 37 (1995) 1459.

[3] WENZEL, U. et al., this conference.

[4] GÜNTHER, K., europhysics conference abstracts 19C/part I (1995) I/433.

[5] WEINLICH, M., PhD Thesis, IPP Report 5/64 (1995).

Scaling of edge parameters for high confinement, high density ASDEX Upgrade discharges

J. Schweinzer, O. Gehre, G. Haas, H. Murmann, J. Neuhauser, H. Salzmann, W. Sandmann, W. Schneider, W. Suttrop, M. Weinlich, ASDEX-Upgrade-Team, NBI-Group
Max-Planck-Institut für Plasmaphysik, EURATOM Association, W-85748 Garching

INTRODUCTION

The purpose of this paper is to describe general dependencies of parameters in the SOL (Scrape-Off-Layer). These dependencies are gained by analysing diagnostic data of various discharges making use of regression analysis. Used diagnostic tools and some general considerations how the data was compiled will be presented first.

Radial profiles $n_e(r)$ and $T_e(r)$ in the SOL (Scrape-Off-Layer) are measured routinely by means of a lithium beam probe and an ECE radiometer. Radial ranges $R-R_{sep}$ = -15 to 5 cm and $R-R_{sep}$ = -5 to 9 cm are covered by the ECE and lithium beam diagnostics, respectively. The position of the separatrix R_{sep} is determined magnetically within an uncertainty of ± 5 mm. From the radial $n_e(r)$ profile three edge parameters are derived, the line-averaged SOL (Scrape-Off-Layer) density n_e^{SOL}, the separatrix density n_e^{sep} and the fall-off-length λ_{ne}. The parameter n_e^{SOL} was introduced to gain a direct measure both for the transparency of the SOL plasma for neutral atoms and for the SOL thickness. Fall-off-lengths are determined by fitting an exponential function to the profiles in a radial range of $R-R_{sep}$ = -1 to 2 cm. In addition information about n_e and T_e near and inside R_{sep} is also gained from a Thomson scattering system. The neutral gas flux density Φ_0 in the divertor is measured by Haas-type pressure gauges. T_e^{div} and n_e^{div} in the outer divertor was determined by searching for the respectively highest values in signals of various Langmuir probes mounted on different locations on the target plate neglecting all spatial information. Total plasma radiation is measured with bolometers.

Only data of deuterium single-null discharges in quasi-stationary phases are used in this study. All discharges are fuelled by gas puffing. The ratio P_{rad}/P_{tot} (P_{rad} = total radiated power, P_{tot}=total heating power) was kept between 0.2 and 0.65 in order to stay outside the marfe regime. No discharges with additional impurity gas puffing have been included in the database. A rather uniform occupation in parameter space spawned by n_e, I_p, B_T, P_{tot} was achieved by the choice of the included discharges. Two data sets for ohmic (OH) and H mode (H) deuterium discharges are considered: (OH): $n_e = 2 - 9 \times 10^{19}$ m^{-3} I_p = 0.6 - 1 MA, B_T = 1.5 - 2.5 T, q_{95} = 3 - 6; (H): n_e = 3.5 - 10.0 x 10^{19} m^{-3}, I_p = 0.6 - 1.2 MA, B_T = 1.5 - 3 T, q_{95} = 3 - 5; All parameters are time-averaged over 10 ms, thus smoothing over ELMs of all types.

RESULTS for OHMIC DATASET

The dependency of n_e^{sep} with neutral gas flux density Φ_0 in the divertor has been investigated [1]. In fig. 1 n_e^{sep} and n_e^{div} is plotted vs. Φ_0 in an double logarithmic scale. A clear change of the n_e^{sep} slope can be seen at $\Phi_0 = 6 \times 10^{21}$ m^{-2} s^{-1} corresponding to $n_e^{sep} = 1.4 \times 10^{19}$ cm^{-3}. For lower n_e^{sep} values a pure linear relation $n_e^{sep} \sim \Phi_0$ is found (regression coefficient R=0.9), whereas for higher values $n_e^{sep} \sim \Phi_0^{0.4}$ results from regression analysis (R=0.9). The change in the n_e^{sep} behaviour seems to be caused by a strong increase of the divertor density n_e^{div} (cf. fig. 1). An estimate ($\lambda_0 = 1 / (\sigma^{CX} n_e^{div})$; $\sigma^{CX} = 5 \times 10^{-15}$ cm^2) of the neutral mean free path λ_0 in the divertor plasma leads to values of about 10 cm, thus being in the order of the radial extend of the divertor plasma. Therefore, the permeability to recycling particles in the divertor plasma is considerable decreased breaking the linear relationship between n_e^{sep} and Φ_0.

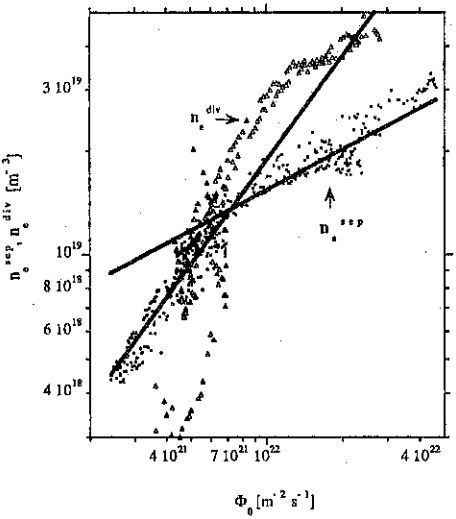

Fig. 1: Electron densities n_e^{sep} and n_e^{div} depended on neutral gas flux density Φ_0 (cf. text). Only a subset of data used for regression analysis is shown.

Results of regression analysis for dataset OH is summarised in table 1. Decisive parameters in the fits of the dependent quantities n_e^{sep}, n_e^{SOL}, λ_n are the neutral flux density in the divertor Φ_0, the safety factor q_{95} and the total radiated power Prad (A high percentage of Prad is radiated outside closed flux surfaces.) Inclusion of further independent parameters improves scaling only to a rather small extend. The ratio (range: 2 - 4) of line averaged central density ne and n_e^{sep} is mainly a function of the separatrix density. Central, edge density and Φ_0 are strongly coupled in ohmic phases.

An ordering of λ_n by T_e^{sep} pointing to different regimes for high and low T_e^{sep} values like in the case of ASDEX [2] has not been found. However, an almost uniform increase of λ_n with decreasing T_e^{sep} is detected over the complete operational range (cf. fig. 2).

	C	Φ_0	Prad	Ptar	I_p	q_{95}	n_e^{sep}	R
n_e^{scp}	21.74	0.416	0.13	-	-	-0.26	-	0.97
n_e^{SOL}	14.037	0.481	0.336	-	-	0.326	-	0.97
λ_n	-11.21	0.254	-	-0.344	0.188	0.645	-	0.92
n_e / n_e^{sep}	26.675	-	0.3	0.07	-	0.14	-0.69	0.96

Table 1: Fits $F = e^C A^\alpha B^\beta ...$ and corresponding regression coefficient R for experimental parameters of dataset OH. n_e denotes line averaged density and $P_{tar} = P_{heat}$-Prad.

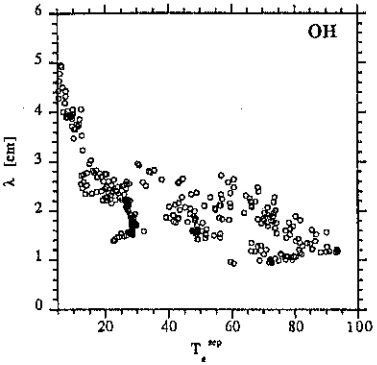

Fig. 2: SOL density fall-off length λ vs. midplane separatrix temperature T_e^{sep} for ohmic discharges.

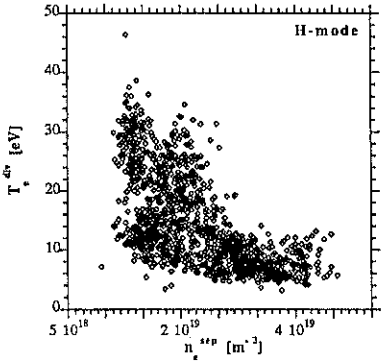

Fig.3: Divertor temperature T_e^{div} vs. midplane separatrix density n_e^{sep} for H-mode discharges.

RESULTS for ELMy H-MODE DATASET

Recently, the invariance of divertor impurity retention on the external gas puff rate has been demonstrated [3]. In a series of discharges the pumping speed (by activating different number of turbomolecular pumps) was varied while keeping the neutral gas flux Φ_0 in the divertor constant by an appropriate feedback control of the gas puff rate. In this discharges (I_p=1MA, B_T=-2.5T, n_e=7.4 10^{19} m^{-3}, Φ_0 = 2.8 10^{22} m^{-2} s^{-1}, P=5.4 MW) the gas puff rate was varied by a factor of 3. Within error bars all SOL density parameters were constant, no influence of the different gas puff rate was detected.

As mentioned earlier all quantities are averaged over 10 ms. All direct measurements of T_e^{sep} were not suited for regression fits because of too high scatter. Therefore, an edge temperature T_e^{ed} measured by Thomson scattering a few cm inside the separatrix was used

instead. Although the regression fit is not of high quality (cf. table 2), it is interesting to note, that the power dependence of T_e^{ed} is rather close to an exponent of 4/9 what is expected from a conduction limited model for the SOL energy flow [4]. A convection limited model would predict a linear dependence of T_e^{ed} with P [4].

The divertor temperature T_e^{div} (range: 5 - 40 eV) was found to be independent of P and increased with decreasing separatrix density n_e^{sep} (cf. fig. 3). In addition the maximal attainable line averaged density is independent of the total heating power P.

The behaviour of the SOL thickness turned out to be very similar in H and OH mode (compare table 1 and 2 for regression exponents). No direct dependency on P is found, but of course Prad is strongly connected with P (table 2).

Only poor fits for n_e^{sep} ($= n_e^{0.5} \times \Phi_0^{0.24}$, $R < 0.85$) could be produced. No strong relation with other parameters could be recognised. Although ELMs cause energy and particle transport from the main plasma, the SOL seems to be much more disconnected from the core plasma as compared to the ohmic phases.

	C	Φ_0	Prad	P	I_p	q_{95} / BT	n_e^{sep}	R
T_e^{ed}	6.844	-0.21	-	0.48	0.164	0.563 *	-	0.89
n_e^{SOL}	13.459	0.51	0.236	-	-	0.4	-	0.95
λ_n	-2.747	0.412	0.34	-	-	0.855	-0.534	0.93
Prad	-7.33	-		0.818	-	-0.15	0.21	0.95

Table 2: Regression fits $F = e^C A^\alpha B^\beta$... and corresponding regression coefficient R for experimental parameters of dataset H (P = total heating power). The star indicates the fit for T_e^{ed} is with BT instead of q_{95}.

CONCLUSION

We have shown that parameters derived from SOL density profiles scale rather nicely with global parameters and with Φ_0 for ohmic and H-mode discharges. These global parameters have been chosen mainly in order to derive regressions of good quality, but might, however, represent a fit to a 'hidden' parameter like e.g. T_e^{sep}.

A clear transition from low to high recycling divertor operation was found in the relation of separatrix density n_e^{sep} with neutral gas flux density Φ_0.

External gas puff rate has no influence on SOL density profiles as long as Φ_0 stays constant, thus demonstrating the importance of the latter.

The ELM-averaged SOL thickness (n_e^{SOL}) in H-mode discharges behaves similar to the ohmic one. Edge temperatures depend only weakly on the heating power.

REFERENCES

[1] J. Schweinzer et al. 1995, contr. p. to 22nd EPS Conf. on Contr. Fusion & Plasma Phys.
[2] K. McCormick et al. J. Nuc. Mat. 196-198, (1992), 264-270
[3] H. S. Bosch et al. Phys. Rev. Lett. 76 (1996), 2499-2502
[4] M. Keilhacker et al. Phys. Scr. T2/2, (1982), 443-453

Mutual Influence between the ICRF Antennas and the Edge Density on ASDEX Upgrade

J.-M. Noterdaeme, J. Schweinzer, Ph. Verplancke,
M. Brambilla, F. Hofmeister, W. Schneider, ICRF Group and ASDEX Upgrade Group

Max-Planck-Institut für Plasmaphysik
Euratom Association
D-85748 Garching, Germany

ABSTRACT - Significant changes of the density in the shadow of the antenna limiters can be seen on field lines connected to an active ICRF antenna. The changes are sudden at turn-on and turn-off of the antenna, indicating that this is a direct effect due to the RF. For experiments where densities in the shadow of the antenna limiter were in the 2x 10^{18} m^{-3} range, the density decreases. At lower density values, the effect is less pronounced. Under completely detached H-mode (CDH) conditions, where the density in the shadow of the antenna was above 1x 10^{19} m^{-3}, the density increased slightly.

INTRODUCTION

In ASDEX Upgrade, the distance between the separatrix and the vacuum chamber is large (≈ 35 cm in the equatorial plane). Two main regions can be identified : 1) from the separatrix to the first limiting surface (this is on the low field side, under most conditions, the antennas) and 2) beyond the antennas. The plasma density *between separatrix and antennas* plays an important role in the coupling resistance of the ICRF antennas. We have measured this density to investigate whether the ICRF affects its own coupling resistance. In the region *beyond the ICRF antennas*, plasma is still present. The plasma density there (near and in the antenna) influences its voltage stand-off. Changes of the density in this region due to the RF can also be indicative of edge plasma/RF and edge plasma/antena interactions.

METHOD

The edge/SOL density is measured in ASDEX Upgrade using a fast Li beam diagnostic [1]. The radial distance between plasma separatrix and the Ion Cyclotron Resonance Frequency (ICRF) antennas [2] is 3 to 5 cm in the equatorial plane. The Li beam allows a space and time resolved (0.6 cm, 1 ms) measurement in a range $R-R_{sep}$ = -5 to +9 cm relative to the separatrix position R_{sep}. Thus, radial locations up to 6 cm behind the front face of the ICRF antennas are covered by the Li beam measurement.

The "shadow" of a particular antenna, as obtained by following the contours of that antenna along field lines, can map (or not) to the location of the Li beam (horizontal axis 30 cm below the midplane) density measurement, depending on the pitch of the magnetic field lines (the magnetic field direction and the q value). Different values of the plasma density is the edge/SOL were obtained by operating at different plasma currents (resulting in different SOL density gradient length at the separatrix), and different operating conditions (gas puffing, CDH mode). By activating the antenna, the influence of the RF on the density in the region between the separatrix and the antenna and in the region beyond the antenna limiter can be determined. The ICRF power was in the range of 500 kW to 1 MW per antenna.

For different combinations of B_t and I_p (Table 1), using the actual magnetic configuration, as reconstructed from the magnetic measurements, the antennas were mapped along field lines to the location of the Li beam. Two examples are shown schematically in Fig1 a,b. Which antennas map to the location of the Li beam for the other combinations is shown in the table.

shot nr	B_t (T)	Ip (MA)	q	antennas mapping to Li beam location	frequencies
8116	-2.5	1	3.9	1,2,4	38 MHz (1)
6167	+2.1	1	3.2	3,4	30 MHz (1,4) 31.6MHz (2,3)
6501	-2.1	0.6	5	1,2,4	id.
6499	-2.5	1	3.9	1,2,4	id.
6492	-2.1	1	3.2	1,4	id.
6504	-2.1	1.2	2.6	1	id.

Table 1. Conditions for the different discharges.

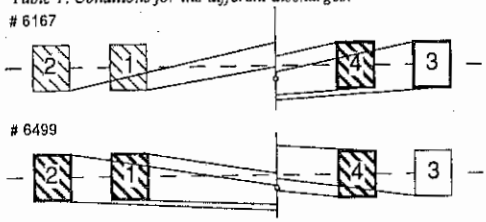

Fig. 1. Schematic view of how the antennas map along field lines to the location of the Li beam measurement (indicated by the small circle). The antennas in bold are connected, the others not. Antennas 1,2,4 have a Faraday screen (pitch w.r.to B indicated, value 15°).

RESULTS

Fig 2. shows the edge/SOL density at the location of the Li beam for the discharges of Table 1. The high density discharge, the low density discharge and the discharges in the middle range of densities behave differently. The discharges in the middle range of the densities (# 6167, 6592, 6499, 6501) have 3 x 10^{18} m^{-3} at the antenna, and 1 x 10^{18} m^{-3} at 1 cm behind the antenna. The time traces for #6167 in Fig. 3 (see the emission of the Li resonance line at R = 2.075 m) show clearly that the density changes suddenly at turn-on and turn-off of *those* antennas (3, 4) that map to the location of the Li beam measurement. The density at 2 cm behind the antenna decreases strongly. The density profiles (plotted in Fig. 4a for specific times) indicate that the decrease of the plasma density is essentially in the region beyond the antenna limiters and only for those antennas that are connected to the location of the Li beam density measurement along field lines. All other parameters are constant. Note that the difference in resonance position between antennas 3 (center + 2 cm) and 4 (+11 cm) does not play a role, nor the fact that antenna 4 has a Faraday screen and antenna 3 none.

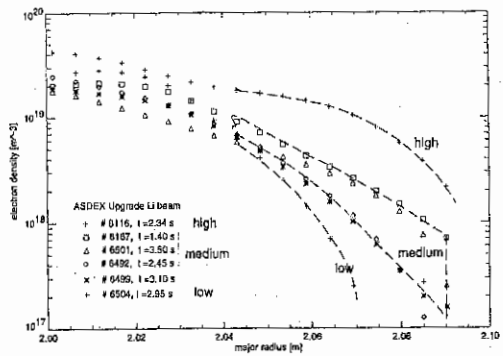

Fig.2 Density profile at the location of the Li beam density measurement

At - 2.5 T (#6499), the resonance position for both frequencies are off-axis (1,4 at +33 cm and 2,3 at +44 cm). The density in the shadow of the antenna limiter decreases for antenna 1 and 4, and increases for antenna 2. Those antennas all map to the Li beam measurement. The density is not affected, at the location of the measurement, by antenna 3 which does not map to this location (Fig. 4b). Similar results are obtained for the other combinations at the average densities. The distinct behaviour of antenna 2 for this series is probably related to a difference in the electrical connection of the antenna limiters (see discussion), rather than to the variation in resonance position.

At the higher current and lower q value of # 6504, the steeper density gradient results in a lower density in the shadow of the antenna limiter. Under this conditions the density still decreases, but is less affected as shown in Fig 4c.

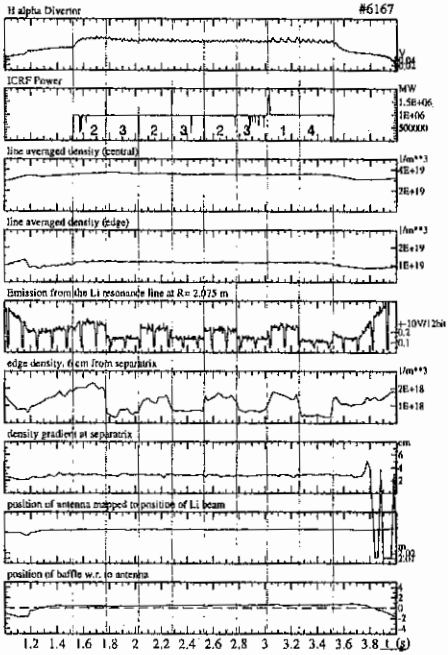

Fig. 3. Time traces of the discharge # 6167.

In the completely detached H-mode (#8816), the density near the antenna is a factor 10 higher (Fig. 4d) than for the cases above (and is much higher than one would estimate from a simple exponential decay of the density at the separatrix). The effect of the RF is a slight increase of the density in the shadow of the antenna.

DISCUSSION

The effect of the RF on the SOL/edge density profile is essentially restricted to the region beyond the antenna limiters on field lines connected to an active antenna.

Between separatrix and front of the antenna, the changes are small so that the RF itself does not change the normal coupling resistance of the antenna (this is in contrast to Lower Hybrid which produces its own plasma in front of the coupler).

The change of the density in the region beyond the antenna limiters, along field lines connected an active antenna, is a direct indication of edge plasma/antenna interaction due to the RF. With the FELICE code, we calculated that the RF fields due to ICRF are *not* restriced (toroidally nor poloidally) to field lines connected to the antenna. However, where those field lines intersect the antenna, sheaths will develop. The density on the field lines can then decrease, either if the

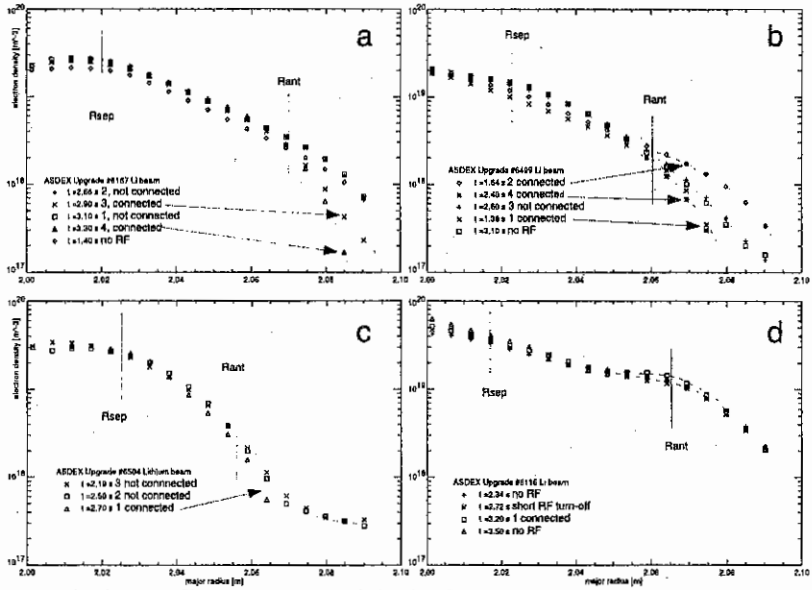

Fig 4. Edge density profiles, and their changes during the RF.

parallel transport is increased or if the perpendicular transport is decreased. The *parallel transport* can be increased if heating of the ions increases their sound velocity. The *perpendicular transport* in the edge is due to turbulent diffusion in convective cells which extend along field lines. Radial electric fields (a consequence of the sheaths) at the ICRF limiter can affect those convective cells [3]. The radial electric fields depend on electrical properties and connections of the antenna limiters. This was different for antenna 2 and could be the reason for its peculiar behaviour.

Note that what happens on field lines connected to the antenna can partly be seen as a model of what happens, for an antenna without Faraday screen, to a possible plasma density inside the antenna. Because of the different connection lengths (shorter in the antenna) and different strength of the RF fields (stronger inside) a decrease of density outside the antenna is sufficient to conclude that a decrease will also occur in the antenna. On the other hand, when no decrease occurs in the shadow, no immediate conclusion is possible for the effect in the antenna. For medium to low density, the density decreases. This is consistent with a decrease of the parasitic loading observed at low power on other machines, when high power (> 100 kW) is applied. The inferred reduction of the density is also favourable for the voltage stand-off of the antenna. It remains to be investigated to what extent the conditions of much higher density lead to parasitic loading and reduced voltage stand-off.

REFERENCES

[1] J. Schweinzer et al., this conference
[2] J.-M. Noterdaeme et al., Fus. Eng. Des. 24 (1994), 65
[3] Bora D. et al., Nucl Fus. (1991), 2383

The Edge Turbulence in the W7-AS Stellarator: 2 d Characterization by Probe Measurements

J. Bleuel, G. Theimer, M. Endler, L. Giannone, H. Niedermeyer,
ASDEX and W7-AS Teams
Max-Planck-Institut für Plasmaphysik, EURATOM Association, Garching, Germany

Introduction

In the edge region of the W7-AS stellarator spatially and temporally resolved measurements of turbulent electrostatic fluctuations are performed using Langmuir probe arrays. They are intended to explore the limits of our physical model based on former investigations of the scrape-off layer of ASDEX [1]. A very high correlation of the ion saturation current fluctuations $\parallel \mathbf{B}$ was observed implying that the interaction between plasma and target plates must be taken into account. The sheath conditions are added to a 2d fluid model which includes magnetic curvature, $\mathbf{E} \times \mathbf{B}$, and diamagnetic drifts. In linear order its predictions agree with the experiment in a wide range of discharge parameters [1].

Another interesting subject is the investigation of the nonlinear dynamics of the saturated turbulent state. The latter is characterized by an unpredictable formation and decay of structures. Observing the evolution of structures should therefore offer insights into the nonlinear dynamics. Simple global properties, as average velocities, can be determined from the spatial-temporal correlation function. More detailed information, e. g. concerning the question whether typical structures exist, may be obtained by studying individual structures. Our starting point of a quantitative classification of structures is the decomposition of fluctuation data in a sum of simple "events" (pulse-shaped in space and time) with individually determined spatial and temporal position, velocity, size, lifetime, and amplitude. A search for statistically significant deviations from the spatially and temporally uniform distribution of the events follows. An analysis of that kind was applied to spatially 1d plus time dependent data taken from measurements with a poloidal probe array: In the environment of events with a high magnitude/size ratio the floating potential exhibits a dipole-like conditional average which is oriented such that in its center the $\mathbf{E} \times \mathbf{B}$ drift is directed radially outwards. Because the conditional average of the ion saturation current has a maximum there a very high local particle flux must be associated with these structures [2].

Of course, without a minimum knowledge about the radial behaviour it would remain uncertain to what extent the 1d poloidal properties describe the fluctuations. Especially the possibility of radially moving structures must be considered. New measurements at W7-AS with a right-angled probe array consisting of 20 tips in poloidal and 8 tips in radial direction are addressed to these questions.

Correlations

Basic space-time characteristics of the fluctuations are contained in the correlation function

$$\rho(\mathbf{d},\tau) = \frac{\left\langle \tilde{s}(\mathbf{d},t)\,\tilde{s}(\mathbf{x}+\mathbf{d},t+\tau)\right\rangle}{\sqrt{\left\langle \tilde{s}^2(\mathbf{x},t)\right\rangle\left\langle \tilde{s}^2(\mathbf{x}+\mathbf{d},t+\tau)\right\rangle}} \qquad (1)$$

where $\mathbf{x}$, $\mathbf{x}+\mathbf{d}$ are the spatial positions of two probes and $\tilde{s}$ denotes the fluctuating part of a random process $s := \tilde{s} + \bar{s}$ as given by the measured quantities (e. g. floating potential). For the present analysis time intervals with constant discharge conditions and negligible probe movement were chosen. Thus, $\bar{s}$ may be regarded as stationary. Estimates of (1) are based on temporal averaging.

Correlation $\parallel$ B

To study the behavior of the fluctuations along the field lines simultaneous measurements of the floating potential with a radially movable Langmuir probe array of 19 tips extending in poloidal direction and a static Langmuir probe at a distant toroidal position were carried out. Because the poloidal positions of the probes are fixed the rotational transform of the magnetic field ι had to be adjusted such that the field line bundle crossing the fixed probe passed the accessible poloidal-radial range of the movable probe array. (By numerical field line tracing it was estimated that this constraint requires a rotational transforms near $\iota = 0.253$ which is somewhat smaller than typical values for W7-AS.) The corresponding connection length between the 19 tips array and the distant probe is about 6 m. Other plasma conditions relevant to these measurements are: B = 1.25 T, gas H_2, line averaged central density 1×10^{19} m^{-3}, ECR heating: 170 kW.

Between the 19 tips array and the distant probe a correlation of 0.92 was found representing a lower limit for the actual maximum correlation parallel B. It might be even higher, if the field line was not hit precisely. Within the temporal resolution (0.5 μs) the peak of the correlation function with the highest peak value is centered around $\tau = 0$. Apart from that the poloidal-temporal correlation function between the 19 tips array and the distant probe looks very similar to the correlation function obtained from the 19 tips array itself. Correlation lengths, correlation times and propagation velocities are the same. A comparison of such correlation lengths $\parallel$ B to the correlations lengths $\perp$ B in the order of 1 cm suggests an essentially 2-dimensional structure of the fluctuations. Obviously the physical process responsible for the fast balancing along the field lines has only very little tendency to spread $\perp$ B.

Correlation in the radial-poloidal plane

Measurements concerning the radial-poloidal structure of the fluctuations are performed with a right-angled probe array consisting of 20 tips in poloidal and 8 tips in radial direc-

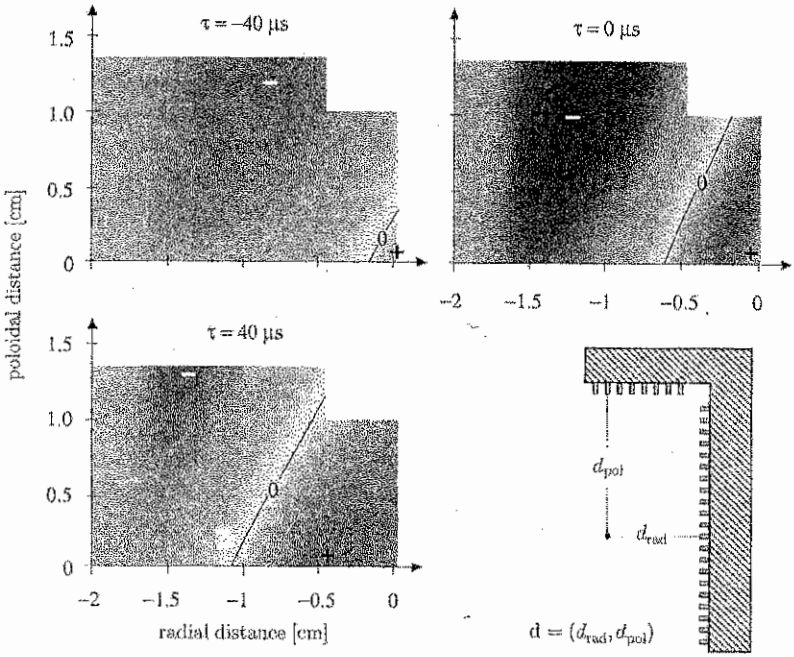

Figure 1: *Cuts through the spatially 2-dimensional correlation function of the floating potential for constant τ.*

tion. The distance between adjacent tips is 0.25 cm; the diameter of the tips is 0.09 cm. From such time series discrete estimates of the 2-point-correlation function $\rho(\mathbf{d}_{ij}, \tau)$ can be calculated where $\mathbf{d}_{ij} = \mathbf{x}_j - \mathbf{x}_i$ denotes the radial-poloidal distance vector between the i-th and j-th probe. Due to poloidal homogeneity $\rho(\mathbf{d}_{ij}, \tau)$ is only a function of the poloidal probe distance whereas inhomogeneity in radial direction implies that $\rho(\mathbf{d}_{ij}, \tau)$ depends not only on the radial distance but also on the radial position. For the right-angled array the $\mathbf{d}_{ij}$ form a rectangular grid. Figure 1 shows cuts through the discrete 2-point-correlation function of the floating potential for constant values of τ. Discharge parameters were: B = 2.53 T, gas: D_2, line averaged central density 1×10^{19} m^{-3}, ECR heating: 300 kW. Smoothness was obtained by interpolation between the spatial grid points. The 2d spatial cut through the correlation function at $\tau = 0$ exhibits an oblique structure which may be attributed to an oblique orientation of the fluctuations. Movies, i. e. τ-sequences, of such 2d spatial cuts indicate further that the fluctuations propagate as well in radial as in poloidal direction. In figure 1 a propagation to the left, i. e. radially

inwards, can be seen. These findings have important consequences for the interpretation of spatially 1d resolved measurements: Radial velocity components of oblique structures appear as poloidal motion, if only the poloidal direction is observed which explains the similarity between the radial-temporal and poloidal-temporal correlation functions. Velocity components perpendicular to the direction of observation lead to apparently smaller correlation times or lifetimes of individual structures.

It should be noted that figure 1 reflects the situation at one certain radial probe position a few centimeters outside the confinement region. Radial profiles of parameters associated with the poloidal correlation function show the well known velocity shear layer where the sign of the poloidal velocity changes and the correlation lengths and times exhibit minima. Accordingly at other radial positions different spatially 2d correlation functions are observed.

Conclusion

In the edge region of the W7-AS stellarator fluctuations of the floating potential show a very high correlation along the field lines over distances in the order of 10 m with zero time delay similar to former results for the ion saturation current in the scrape-off layer of ASDEX. This confirms the idea that in the shadow of a limiter the turbulence is essentially a 2-dimensional process under the far-reaching control of the sheath conditions. A poloidal *and* radial propagation of the fluctuations seen in the 2d spatial correlation function sheds light on the limits of spatially 1d resolved measurements.

References

[1] M. Endler et. al., Nuclear Fusion **35**, (1995) 1307–1339.

[2] G. Theimer et. al., Proc. 22nd EPS Conference on Controlled Fusion and Plasma Physics, Bournemouth 1995, volume 19C, part I, pp. 301–304

Edge Ion Temperature Profiles in L- and H-Mode Discharges of ASDEX

O. P. Heinrich, R. Schneider, H. Verbeek, D. Reiter* and the ASDEX-Team

Max-Planck-Institut für Plasmaphysik, EURATOM Association, D-85748 Garching, Germany
Institut für Plasmaphysik, Forschungszentrum Jülich, EURATOM-KFA Association, D-52425 Jülich, Germany

Introduction

A common, and widely believed unalterable, feature of the H-mode is the formation of a steep gradient region of the radial electric field E_r at the transport barrier of the plasma edge. E_r in turn is connected with the ion pressure gradient ∇p_i and the rotation velocity through the radial force balance equation. Although it is not yet clear what the triggering mechanism for the L-H transition is, the ion temperature respectively its gradient is seen to play a crucial role in the feedback loop of the radial force balance. On ASDEX edge ion temperature profiles have been made accessible with the help of low energy neutral fluxes in an analysis after shutdown. Therefore these profiles are now available for ASDEX L- and H-mode plasmas.

Experimental

Neutral deuterium fluxes in the energy range 15 to 700 eV/amu were measured with the LENA diagnostic [1] at ASDEX with a time resolution of 50 to 100 ms. This neutral (CX) spectrum, which originated mainly from the plasma edge, is simulated with the help of the Monte-Carlo neutral particle code EIRENE, including all available data about the plasma and the geometry near the line of sight. From the fit of the simulated to the experimental spectrum an edge ion temperature (T_i) profile of the main plasma species from the separatrix to about 10 cm inside (in the case of ASDEX) can be deduced [2]. This method has been further developed and is now also used on ASDEX-Upgrade [3].

It is known from spectroscopic measurements on ASDEX and other experiments, that the edge T_i increases at the L-H transition. A look at the LENA CX spectra during a H-mode discharge also shows a significant change of shape in different phases. This can be clearly seen in the upper picture of Fig. 1.1: starting from the ohmic phase over the L- to the ELM-free H*-phase the slope of the high energy part increases indicating already a higher T_i. At the same time a sharp bend at low energies (100 eV) occurs. The lower picture compares the corresponding ion and electron temperature (T_e) profiles and the T_i profile of a comparable L-mode discharge, i.e. where no L-H transition took place. A significant difference between L- and H-phases is found: in the H-Mode, the absolute T_i value and the gradient is much higher than in the L-Mode. The temperature in the H-mode increases from around 50 eV at the separatrix to more than 400 eV within 1-2 cm inside the separatrix, which is even much higher than the electron temperature. The radial range of the steep T_i gradient becomes clearer in Fig. 1.2, where the gradient at the separatrix and some cm inside are compared during the H-mode discharge. From this the transport barrier can be located in a narrow

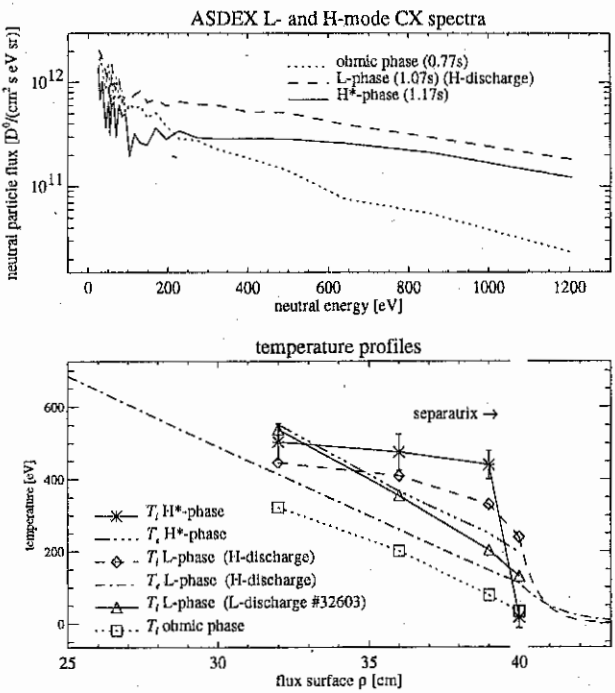

Fig. 1.1: *Low energy neutral spectra and corresponding T_i and T_e profiles in L- and H-phases. If not indicated, the data refer to discharge #33308.*

range of 1-2 cm at the separatrix, which is in agreement with similar observations on ∇T_i and E_r in other machines.

These T_i profiles correct earlier interpretations of the L-H transition at ASDEX [4], where, due to the lack of appropriate edge T_i measurements, the main influence on the transition has been attributed to the edge electron temperature. The T_i profiles in Fig. 1.1 also reveal that already the L-phase prior to the H-transition has a higher edge T_i than in a pure L-Mode discharge. This supports the major role of the ion temperature or its gradient in the L-H transition.

Discussion

One possible interpretation of the L-H transition follows from the obviously different LENA T_i edge profiles: a minimal T_i at the edge seems to be a prerequisite of the H-mode. Therefore

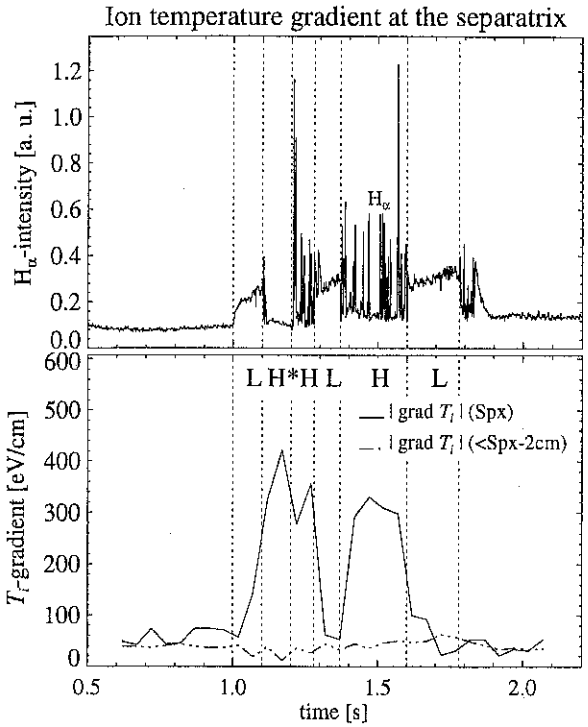

Fig. 1.2: *Ion temperature gradient at and inside the separatrix (Spx) with the H_α-intensity for the identification of the phases in the H-mode discharge #33308.*

we have used the T_i edge profiles as an input parameter of the ion orbit loss model of Shaing and Crume [5]. This assumes the loss of collisionless ions across the separatrix as the trigger, which in turn induce the radial electric field. The critical parameter is the ion collisionality ν_{*i}, which forces the L-H transition at values $\nu_{*i} \lesssim 1$. Table 1.1 lists the effective collisionality

$$\nu_{*i}^{eff} = \nu_{*i} \left(\frac{Z_{eff}\, n_e}{Z_i^2\, n_i} \right) , \tag{1.1}$$

where the impurities are taken into account by a Z_{eff} [6], about one poloidal gyroradius inside the separatrix for the L-and H-phases. A typical value of $Z_{eff} = 4$ with an impurity charge of 7 has been assumed. The phenomenological explanation for the pure L-mode discharge is found probably in the double null (DN) configuration (vertical shift $z = 0$), which has a higher power threshold than the single null (SN). It is clearly seen, that in the L-mode #32603 the high value of $\nu_{*i}^{eff} \approx 4$ prevents the L-H transition, whereas in #33308 the

discharge	time [s]	mode	P_{NI} [MW]	$\bar{n}_e$ [cm^{-3}]	$T_{i,39}$ [eV]	$\rho_{\Theta,i}$ [cm]	ν_{*i}^{eff}
#32603	1,46	L	2,5	$3 \cdot 10^{13}$	180	1,2	3,9
(DN $z = 0$ cm)							$\pm 1,2$
#33308	1,07	L	2	$2,8 \cdot 10^{13}$	350	1,9	0,7
(SN $z = 1$ cm)							$\pm 0,2$
	1,17	H*			450	2,1	0,8
							$\pm 0,25$
	1,47	H			380	2,0	0,8
							$\pm 0,25$
#33301	1,07	H	2	$3 \cdot 10^{13}$	540	2,0	0,2
(SN $z = 2$ cm)							$\pm 0,05$

Table 1.1: *Effective collisionality ν_{*i}^{eff} and poloidal gyroradius $\rho_{\Theta,i}$ of the ions for different L- and H-phases. ν_{*i}^{eff} and $\rho_{\Theta,i}$ are calculated 1 cm inside ($\rho = 39$ cm) the separatrix. The errors in ν_{*i}^{eff} follow from the $\pm 30\%$ uncertainty in electron density at the edge.*

$\nu_{*i}^{eff} = 0.7$ is sufficient for the transition and consequently no change in the H-mode is seen. The long H-phase in #33301 with regular ELMs has due to the low edge density an even smaller ν_{*i}^{eff}. Therefore the L-H transition with respect to our T_i observations is in good agreement with the prediction by the ion orbit loss modell.

Conclusions

With the help of the low energy neutral fluxes it has been possible to obtain T_i edge profiles in L- and H-mode plasmas for the first time in ASDEX, the machine, which first discovered the H-mode. High T_i with a large gradient at the separatrix are found in the H-mode, in concurrence with T_i measurements on other experiments. The comparison with the ion orbit loss model of Shaing is in good agreement, however it offers no direct evidence for this explanation.

References

[1] H. Verbeek (1986), Journal of Physics E: Scientific Instruments, 19, 964-970
[2] O. Heinrich (1995), report of MPI für Plasmaphysik, IPP III/207
[3] J. Stober et al., this conference
[4] ASDEX Team (1989), Nuclear Fusion, 29 (11), 1959-2040
[5] Shaing and Crume (1989), Phys. Rev. Lett., 63 (21), 2369-2372
[6] M. Mori et al. (1994), Plasma Phys. Contr. Fus., **36**, A39-A49

OBSERVATION OF ELM-INDUCED NEUTRAL PARTICLE CHARGE EXCHANGE FLUXES IN TCV

W. van Toledo, B.P. Duval, R.A. Pitts and H. Weisen

Centre de Recherches en Physique des Plasmas
Association EURATOM-Confédération Suisse
Ecole Polytechnique Fédérale de Lausanne, Switzerland

ABSTRACT

During Ohmic H-mode discharges in TCV, ELM-induced neutral particle bursts have been recorded by a Neutral Particle Analyzer for several plasma configurations. These bursts occurred simultaneously with the characteristic Dα pulses. In this paper it is shown that prompt desorption and recycling of the particles, expelled during an ELM, at the divertor strike zones can account for the magnitude of the ELM-induced neutral particle fluxes.

INTRODUCTION

Ohmic H-modes with regular Edge Localized Modes (ELMs) have been obtained in the TCV tokamak ($R = 0.88$ m, $a \leq 0.25$ m, $B_T \leq 1.5$ T) in a variety of configurations [1], mostly Single-Null and Double-Null discharges in the parameter range $1.05 < \kappa < 1.7, 0.3 < \delta < 0.7, 200 < I_p < 500$ kA, $4\times10^{19} < n_e < 10^{20}$ m^{-3}, $T_e(0)$~800 eV, $200 < T_i(0) < 400$ eV. Bursts of charge exchange (CX) neutrals are observed in all five channels of the Neutral Particle Analyzer (NPA) at TCV during ELMy H-modes. They occur simultaneously with the characteristic pulses of Dα emission from the edge and divertor regions. During an ELM the measured neutral flux can exceed the pre-ELM value by up to a factor of 5. The contribution of noise, photons and ions to the signal during ELMs was found to contribute to less than 1% of the signal. Other types of CX neutral fluxes modulated by MHD activity have been observed at the PBX tokamak (sawteeth) [2], and at ASDEX-Upgrade, where an ELM induced drop of the CX signal from energetic trapped particles was measured [3].

EXPERIMENT AND OBSERVATIONS

Fig. 1 shows the Dα signal, the signal from the low energy NPA channel, the electron temperature deduced from soft x-ray emission, and the ion temperature of an ELMy plasma (shot #8001) in SNU configuration (see Fig. 2). During this shot the NPA integration time was 1 ms. It is seen that the Dα pulses coincide precisely with those in the NPA signal. In general, T_i was observed to decrease slightly during the ELMy periods. The particle and power flux during an ELM was estimated by integrating over energy the energy-resolved flux recorded by the four low-energy channels (E=600, 800,1200,1650 eV;ΔE=40,60,150,200 eV, respectively), at each time instant. In Fig. 3 the fluxes averaged over the ELMs in one ELMy period are shown together with the fluxes normalized to the flux value at the time immediately before the ELM starts. After correction for the background, integration of the fluxes over time, area and solid angle gives the total average CX particle and power loss for an ELM. For shot #8001 CX the particle loss (~10^{16}) and the corresponding energy loss of the order 1-10 J per ELM represent a few percent of the direct ELM losses, which are about 2 % for the small type III ELMs considered here [1].

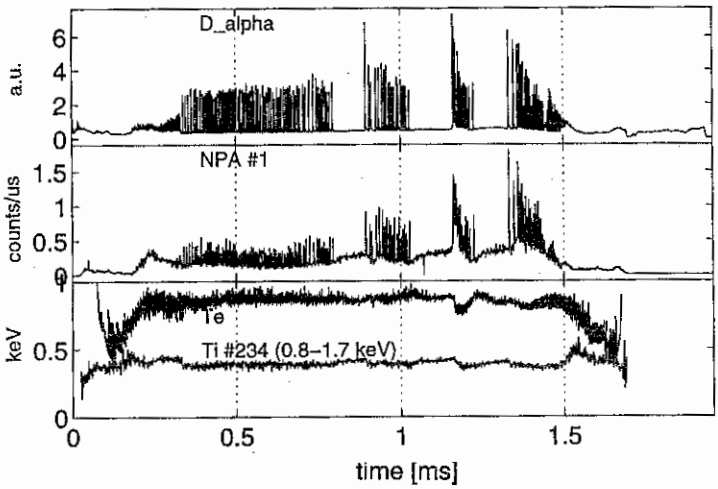

Fig. 1. D_α, NPA signal, T_e and T_i during shot #8001.

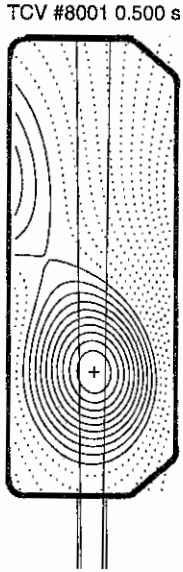

Fig. 2. Magnetic configuratios of shot #8001 (Ip=319 kA, q(o)=2.2, κ=1.5, δ=0.3) at 0.5 s discharge time. The NPA viewing area is shown.

In contrast to the CX particle and power fluxes, the ion temperature is observed to remain unaltered within the experimental accuracy during an ELM. This is to be expected, since only a minor part of the particle content (up to 5%) is affected by a single ELM .

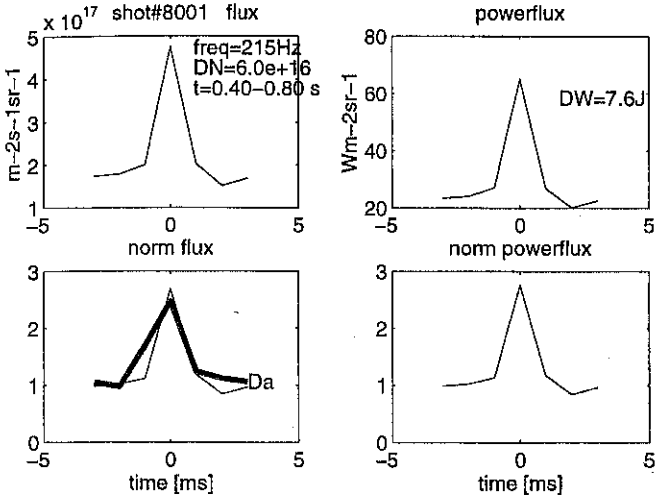

Fig. 3. Averaged and normalized particle and power flux during an ELM of shot #8001. The D_α signal has been resampled to the NPA time base.

ANALYSIS AND INTERPRETATION

From Fig. 1 it is deduced that, since T_i does not change much during ELMs, the energy spectrum of the neutrals does not change either, which implies that the bursts of neutrals, like the normal CX background, originate from the main plasma. The enhanced CX neutral flux is modelled by assuming a transient increase of the neutral density in the main plasma with an unchanged radial profile. Two possible mechanisms are examined which may provide the neutral source. In the first one, the arrival of the particle and heat pulse expelled by the ELM leads to prompt recycling and desorption at the divertor strike areas. In the second one, recombination of expelled particles in the divertor zone is responsible for the additional neutral source.

In order to assess the importance of these mechanisms, the energy resolved neutral particle flux is calculated from the count rate of each of the n NPA channels as

$$\frac{d\Gamma_{E(n)}}{d\varepsilon} = \frac{N_n}{\alpha_n(E_n)\,\Delta E_n\,A d\Omega} \qquad \left(m^{-2}s^{-1}eV^{-1}sr^{-1}\right), \quad (1)$$

where E(n) is the energy of the particles transmitted into the n-th channel, N_n is the count rate, α_n represents the detection efficiency (~ 10^{-3}), ΔE_n is the width of the energy window and $Ad\Omega$ is the etendue (1.2×10^{-8} m^2sr). From the example in Fig. 1 (shot #8001), it was found that between 0.4 and 0.8 s discharge time an averaged 6×10^{16} particles were expelled in the energy range 600-1650 eV in one ELM (see Fig. 3), which

yields a total flux towards the TCV wall of 6×10^{19} s^{-1} for an ELM with a duration of 1 ms. For this type of ELM (type III), the particle exhaust is in the order of 2% of the total particle inventory in the volume V_{ELM} [4]. Starting with the desorption and recycling model, the source can thus be written as

$$S_{des} = \frac{0.02\,\overline{n_e}V_{ELM}R}{\tau_{ELM}} \quad (s^{-1}) \qquad (2)$$

Taking $\overline{n_e} \sim 10^{20}$ m^{-3}, $V_{ELM} \sim 1.6$ m^3 and the ELM duration $\tau_{ELM} \sim 1$ ms, this leads to a source of about 4×10^{21} R s^{-1}, where R is the recycling coefficient. The source from recombination at the divertor, may be written as

$$S_{rec}=\left(0.05\overline{n_e}\frac{V_{ELM}}{V_{DIV}}\right)^2\langle\sigma_{rec}v\rangle V_{DIV} \quad (s^{-1}) \qquad (3)$$

leading to a source of about 10^{16} s^{-1} for a divertor volume of $V_{DIV} \sim 0.2$ m^3 and for a recombination rate in the order of 10^{-20} s^{-1}.

In order to predict the neutral particle flux which follows from these sources, attenuation of the cold neutral particle flux between divertor and the plasma centre by electron impact ionisation, A_{01}, the charge exchange probability in the plasma centre, P_{CX}, and attenuation of the neutral CX particle flux towards the NPA, by electron impact ionisation and renewed charge exchange, A_{10}, are included in the estimate. Using calculated values of A_{01}=0.9, P_{CX} = 0.1 and A_{10} = 0.5, the magnitude of the CX neutral flux observed in the NPA can be accounted for by the desorption source (Eq. 2), with a recycling coefficient of ~ 1.

CONCLUSIONS

Analysis of ELM-induced neutral particle CX flux bursts measured with an NPA during ELMy H-modes in TCV, allowed us to assume that desorption and recycling of expelled particles in the divertor zone is the responsible mechanism to provide the neutral particle source. An additional estimate shows that the effect of recombination alone is insufficient to explain the magnitude of the observed bursts of CX neutrals. The effect of these CX flux bursts on the energy balance is small, since the CX losses make out a few percent of the direct ELM losses.

ACKNOWLEDGMENTS

This work was partly supported by the Fonds National Suisse de la Recherche Scientifique. The contribution of the TCV team is gratefully acknowledged.

REFERENCES

[1] H. Weisen, F. Hofmann, M.J. Dutch et al., Proceedings of the IAEA meeting on H-mode physics, Princeton University, 1995
[2] R.J. Goldston, R.Kaita, P. Beiersdorfer et al., Nuclear Fusion 27 (1987), 921-929
[3] W. Hermann et al., 1995, report IPP 1/288

Ion Behavior and Electron Energy Distribution Function Observed by Electrostatic Probes in Tokamak Boundary Plasma

K. Uehara, H. Amemiya*, A. Tsushima**, S. Sengoku and JFT-2M Group
Tokai Annex, Naka Fusion Establishment, JAERI, Ibaraki, Japan
*Institute of Physical and Chemical Research, Wako-shi, Saitama, Japan
**Yokohama National University, Yokohama, Kanagawa, Japan

Abstract

In this report, we want to describe the ion behavior observed by the toothbrush probe as well as Katsumata probe and the information on the energy distribution function observed by a single probe in the tokamak boundary plasma in JFT-2M. The plasma profile has been measured and the existence of non-Maxwellian energy distribution has been confirmed from the first derivative of the single probe characterictics near the divertor plate.

1. Introduction

The diagnostics in the boundary plasma is performed by using many methods. Among them, the diagnostics by using electrostatic probes is very useful compared with indirect diagnostics such as spectroscopic method since the electrostatic probe can catch many information of plasma with a good spatial resolution by gathering the direct current from plasma particles. Plasma diagnostics using electrostatic probes is applied to a large extent in tokamaks, however, there are few data on ions. Much remains to be done to study the transport of the boundary plasma to include also the contribution of the ions. The instantaneous measurement of plasma profile is useful to study the transport physics and the formation of electric field is open question to solve the transport physics.

We will show the detail data on the toothbrush probe [1] as well as Katsumata probe [2] for the information of ions in SOL plasma. As for the Katsumata probe the direct measurement of $T_i > T_e$ in the scrape-off layer (SOL) of tokamak for ohmic heated (OH) lower single null (LSN) plasma is given and the ion behavior corresponding to the signal of H_α responsible for the formation of improved confinement mode in JFT-2M [3], where T_e and T_i are electron and ion temperature. As for the formation of the electric field we will show an observation of an electron energy distribution of a plasma on a divertor plate in JFT-2M using an electrostatic probe. Since the divertor was chosen as the counter electrode for the probe measurement the probe current-voltage characteristics were taken up to the plasma potential. From the inspection of the returding part, the electron energy distribution has been founds to be non-Maxwellian.

2. Ion behavior observed by toothbrush probe and Katsumata probe

2.1 Ion behavior observed by toothbrush probe

We equipped the fixed asymmetric double probe (named by the divertor ion probe, the probe tip radius a= 1.5 mm and the length L = 6, 12 mm) developed by Amemiya at the divertor plate and the toothbrush probe, which is a multi-asymmetric probe for the purpose of the instantaneous measurement of plasma profile, is inserted at the vertical port, which can be scanned in the radial direction. We can estimate the ion temperature by only detecting the ratio of the ion saturation current of the asymmetric double probe. The value of T_i is calculated in Fig. 1 against the ion saturation current ratio I_1/I_2 of the asymmetric double probe with the magnetic field B ($= [B_t^2 + B_p^2]^{1/2}$) as a parameter for the toothbrush probe (a= 2 mm and L= 6, 12 mm), where B_t is toroidal field and B_p is poloidal field. The typical model characteristics of the probe current I_p against the probe voltage V_p are also shown in the left top of the figure. Since in the divertor ion

probe the value of I_1/I_2 is 1.13 the following data are obtained in the ohmic heated (OH) D_2 plasma at $B_t = 1.65$ T and the toroidal current $I_t = 200$ kA : $T_i = 100$ eV, $T_e = 40$ eV and $n_e = 5 \times 10^{11}$ cm^{-3} at $t = 600$ msec. The data of the toothbrush probe are obtained for OH plasma at $B_t = 1.3$ T, $I_t = 200$ kA at $t = 600$ msec and the raw data of the toothbrush probe are shown in Fig.2, in which radial distance increases from P1 to P5. These data indicate that the ion saturation current ratio decreases from P1 to P5, which corresponds the decrease of ion temperature in the radial direction and the saturation current also decreases along this direction, which corresponds to the decrease of plasma density in the radial direction. The values of I_1/I_2 are from 1.21 to 1.49, which corresponds to be $T_i = 80$ - 230 eV from Fig. 1. The obtained profile of SOL plasma is shown in Fig.3. The obtained T_i is larger than T_e and the e-folding length of them are almost same to that obtained by rotating double probe.

2.2 Ion behavior observed by Katsumata probe

The Katsumata probe has been often used in a linear chamber as the case of $T_i << T_e$. However, many data are reported indicating $T_i > T_e$ in tokamak boundary plasma. The Katsumata probe can determine T_i by setting the electron barrier inside the electrode by using the large difference of Larmor radius between ion and electrons [2]. In JFT-2M, the Katsumata probe is installed and the barrier height h of the ion collector interrupting the electron orbit can be controlled shot by shot without breaking the vacuum condition. When h is reduced from zero to about the ion Larmor radius the electron current I_e flowing into the ion collector decreases and the ion current I_i flowing into this collector becomes measurable. We directly observed the fact of $T_i > T_e$ by Katsumata probe as shown in Fig.4, where the time behaviors of probe voltage V_p (top), Langmuir probe characteristics using the electron barrier as an electrode (middle) I_e and I_i (down) are shown. The form of V_p is triangle with 200 Hz. As seen in this figure, the current of the ion collector rise gradually against V_p, whereas the current of the Langmuir characteristics rise rapidly against V_p, which indicates that T_i is larger than T_e. The semi-log plot of the ion current and Langmuir characteristics well ride on the Maxwellian curve and we get $T_e = 8$ eV and $T_i = 24$ eV for OH plasma in this case.

The time behavior of the ion current of the ion collector in the Katsumata probe are observed simultaneously to the measurement of H_α as shown in Fig. 5. The channel 7 sees near the plasma center and the channel 19 does near upper single null (USN) point. The experiment is performed at the experiment of divertor bias experiment [3] and the negative bias voltage is applied to the outer divertor plate against the wall. The experimental result shows that for the negative divertor bias the particle loss is reduced and this is confirmed by the decrease of these two channel H_α signals. The signal of the Katsumata probe well corresponds to this signal which indicates both ion and electron current decrease by divertor biasing.

3. Electron Energy Distribution Observed by Electrostatic Probe

One of the difficulties in using an electrostatic probe in a tokamak boundary plasma is that the electron-to-ion saturation current ratio is much less than a square of the ion-to-electron mass ratio. The situation that the return sheath resistance is much larger than the probe sheath resistance is the possible explanation, according to Stangeby [4]. We can thus evaluate only an electron temperature of high-energy tail, from the voltage-current characteristics below a floating potential. In order to overcome this problem, i.e., lack of information on low-energy electrons, we used an electrostatic probe on a divertor plate. The divertor plasma flows out through a ring without

poloidal magnetic field, where a plasma is toroidally connected to a field line, and a cross-section of the return current against the probe should be large enough to decrease the return current resistance compared to the probe sheath resistance. In fact, the measurements in JFT-2M showed that the electron-to-ion saturation current ratio of the divertor probe was a value expected from the probe theory, say about 20. Electron energy distribution functions were then taken by introducing probe current, I_p into a differential circuit with sweep in bias voltage, V_p (300 V, 200 Hz). This is because we have the relation of

$$dI_p / dV_p = (e^2 n_0 S_p / m_e) f(v),$$

where n_0 is the electron density, e is the electron charge, m_e is the electron mass, S_p is the cross-section of the probe surface and $v = [2 e (V_s - V_p)/m_e]^{1/2}$ using a space potential, V_s. Figure 6 shows the results observed in a period of a typical OH shot of JFT-2M, specifically, between 520 and 530 msec of the shot #80759 (D_2 plasma $B_t = 1.3$ T, $I_t = 195$ kA). Since the space potential is about 50 V, we see an energy hump exists at about 30 eV or $V_p = 20$ V and the gradient of the curve, dI_p/dV_p vs. V_p, increases with electron kinetic energy or decreasing V_p, indicating that the electron distribution is non-Maxwellian with multi-component.

4. Summary

We observe the ion temperature by the fixed asymmetric double probe at the divertor plate to be T_i= 100 eV for OH LSN plasma at B=1.65 T and we can get a simultaneous measurement of plasma profile and the ion temperature of T_i = 80 - 230 eV in OH LSN plasma at B=1.3 T by the toothbrush probe. We observe the direct measurement indicating $T_i > T_e$ in tokamak boundary plasma by Katsumata probe. The time behavior of the ion current of Katsumata probe well corresponds to the signal of H_α responsible to the formation of improved confinement mode.

We were able to observe electron energy distributions including low-energy electrons using the electrostatic probe faced to the diverted plasma. The results show that a hump appeared in an electron distribution function at a period in a typical OH shot. We expect that the observation of non-Maxwellian electron energy distributions is important to understand plasma-wall interactions, while we need further investigation before we clarify the mechanisms. The electron distribution function without magnetic field in hydrogen plasma has been obtained by the second derivative of the probe current I_p [5]. However, due to the strong anisotropy in velocity space the first derivative of the probe current is taken here since the tokamak is in the strong magnetic field and the probe current forms one dimensional electron flow along the magnetic field line.

In future, we want to develop this measurement to the density dependence of ion temperature, the effect of impurity to check the charge state and the ion temperature measurement during electron cyclotron heating. It is interested with the ion behavior observed the Katsumata probe and with the observation of electric field estimated by the electron distribution function during L/H transition in order to clarify the mechanism of H mode formation.

References

[1] K. Uehara and H. Amemiya, Proc. 22th EPS Conf. on Contr. Fusion & Plasma Phys., Bournemouth, 1995, part I, I-397
[2] I. Katsumata and M. Okazaki Jpn. J. Appl. Phys. **6**, 123 (1967)
[3] T. Shoji, et al.,in Proc. 14th Int. Conf. on Plasma Phys. & Contr. Fusion Res. IAEA-CN-56/C-3-5, Würzburg, 1992, IAEA-CN-56/A-5-5
[4] P. C. Stangeby, Plasma Phys. Control. Fusion **37**, 1337-1347(1995)
[5] H. Amemiya, Jpn. J. Apple Phys. **25**, 595 (1986)

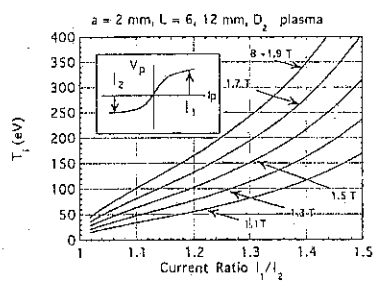

Fig. 1 The estimated ion temperature against the current ratio of ion saturation current of toothbrush probe.

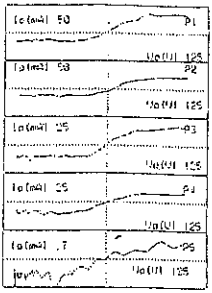

Fig.2 Raw data of toothbrush probe, where the radial distance increases from P1 to P5.

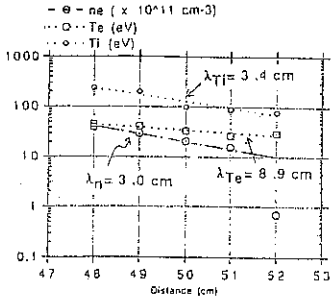

Fig.3 The plasma profile obtained by the toothbrush probe

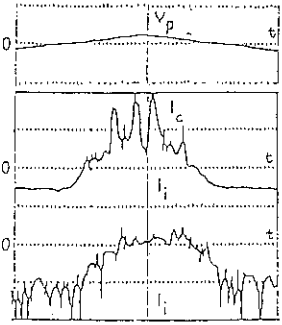

Fig.4 Time behavior of Katsumata probe. Probe voltage(top), Langmuir characteristics using electron guard (middle) and ion current (down), where the scale of I_i is expanded.

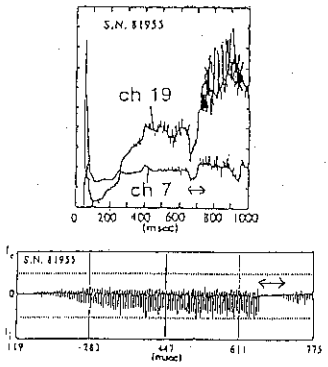

Fig.4 Time behavior of H_α signal (top) and ion current (down). Arrows are time of divertor biasing.

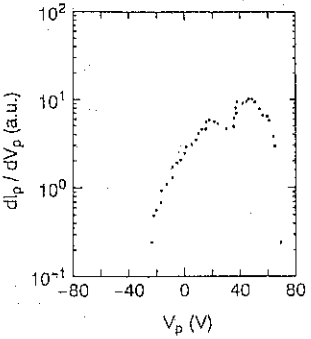

Fig.6 First derivative of the probe current against the probe voltage V_p.

THERMAL RADIATION OF SEMIBOUNDED PLASMA WITH TRANSITION LAYER

A.S.Usenko

Bogolyubov Institute for Theoretical Physics, Kiev, Ukraine

Many papers are devoted to investigation of the thermal radiation of plasma and plasma-like systems of different geometry (see, for example, [1,2]). However, up to now, the thermal radiation spectra of bounded systems obtained by conventional approaches [1,2] were calculated without regard to the proper thermal fields of the external medium. At the same time, as is shown in [3] for the case of semibounded system, the proper thermal fields of the external medium can significantly affect the thermal radiation spectra of one-sided flux. In the present paper, we found the thermal radiation spectra of a plasma half-space into the external medium in the presence of a homogeneous transition layer between the plasma and external medium.

General Relations for the Thermal Radiation Spectra of Semibounded Plasma with a Homogeneous Transition Layer. We consider a piecewise homogeneous system that consists of two homogeneous media, namely: a quasineutral plasma half-space (the third medium) that occupies the region $z<0$ and dielectric layer (the second medium) of thickness L with the dielectric permittivity ε_2 which separates the plasma from the external transparent medium (the first medium) with the dielectric permittivity ε_1. The first ($z>L$), second ($0<z<L$), and third media are defined by temperatures T_1, T_2, T_3, respectively (the more general case of a nonisothermal plasma is considered in [4]). We take into account the spatial dispersion of the plasma and use the model of specular reflection of charged plasma particles from the boundary $z=0$.

The spectral energy density of one-sided thermal radiation flux $P(\omega,T_1,T_2,T_3)$ into the external medium through a unit surface area oriented parallel to the plane $z=L$ can be written as

$$P(\omega,T_1,T_2,T_3) = \int_{\theta \le \pi/2} d\Omega \cos\theta \cdot I(\omega,\theta,T_1,T_2,T_3), \qquad (1)$$

where the thermal radiation intensity $I(\omega,\theta,T_1,T_2,T_3)$ in the unit solid angle $d\Omega = \sin\theta \cdot d\theta \cdot d\varphi$ (θ and φ are the polar and azimuth angles that define the direction of the axis of the solid angle $d\Omega$) is presented as follows:

$$I(\omega,\theta,T_1,T_2,T_3) = \sum_{n=2}^{3} I(\omega,\theta,T_n) + I_0(\omega,T_1)\cdot\mathcal{R}(\theta,\omega). \qquad (2)$$

The quantities $I(\omega,\theta,T_2)$ and $I(\omega,\theta,T_3)$ are the thermal radiation intensity of the second and third media into the external region, moreover, they are defined by the classical Kirchhoff law

$$I(\omega,\theta,T_n) = I_0(\omega,T_n)\cdot\Gamma_n(\theta,\omega), \qquad n = 2,\ 3, \qquad (3)$$

and the term $I_0(\omega,T_1)\cdot\mathcal{R}(\theta,\omega)$ in relation (2) describes a contribution of the proper thermal radiation to the one-sided thermal radiation flux from the boundary z=L.

Here, $\Gamma_n(\theta,\omega)$ is the absorption coefficient of a plane unpolarized electromagnetic wave by the layer (for n=2) or semibounded plasma (for n=3) that is incident at the angle θ upon the piecewise homogeneous system (z<L); $\mathcal{R}(\theta,\omega)$ is the energy reflection coefficient of this wave from the piecewise system, and

$$I_0(\omega,T_n) = \frac{\omega^2\varepsilon_1}{4\pi^3c^2}\cdot\frac{\hbar\omega}{e^{\frac{\hbar\omega}{T_n}}-1} \qquad (4)$$

is the radiation intensity of a black body with the temperature T_n in a transparent medium with the dielectric permittivity ε_1.

The relation for the thermal radiation intensity of one-sided flux in the form (2) can be regarded as the generalization of the classical Kirchhoff law to the case of the piecewise homogeneous system, different temperatures of media of the system, and account of the proper thermal fields of the external medium.

Note that the thermal radiation spectra of a semibounded plasma without a transition layer were obtained in [5] for the case of the cold external medium. However, the expressions for the radiation spectra given in this paper are so complicated that one fails in presenting them in the form similar to the Kirchhoff law.

With the thermal radiation intensity of the one-sided flux for the case of semibounded plasma with a homogeneous transition layer being presented in the form of the generalized Kirchhoff law (2), we may assume that in a more general case, when the transition layer between the plasma and external medium is inhomogeneous and can be simulated by an arbitrary number N of homogeneous layers determined by temperatures T_n and dielectric permittivities ε_n, the expression for the thermal radiation intensity $I(\omega,\theta,T_1,T_2,\ldots,T_{N+1},T_{N+2})$ has the form similar to (2)

$$I(\omega,\theta,T_1,T_2,\ldots,T_{N+1},T_{N+2}) = \sum_{n=2}^{N+2} I(\omega,\theta,T_n) + I_0(\omega,T_1)\cdot\mathcal{R}(\theta,\omega), \qquad (5)$$

where the summation in (5) is performed over all media of the

transition region (n=2,3,...,N+1) and plasma (n=N+2); the quantities $I(\omega,\theta,T_n)$ are defined by the classical Kirchhoff law (3) in which $\Gamma_n(\theta,\omega)$ are the absorption coefficients of a plane unpolarized electromagnetic wave by the n-th medium of the inhomogeneous system ($z<L$) and $\mathcal{R}(\theta,\omega)$ is the energy reflection coefficient of the wave from the system under consideration.

Homogeneously Heated System. For homogeneously heated radiative system ($T_2=T_3\equiv T$), expression (2) is reduced to the form

$$I(\omega,\theta,T_1,T) = I_0(\omega,T)\cdot\Gamma(\theta,\omega) + I_0(\omega,T_1)\cdot\mathcal{R}(\theta,\omega), \qquad (6)$$

where $\Gamma(\theta,\omega) = \Gamma_1(\theta,\omega) + \Gamma_2(\theta,\omega) = 1 - \mathcal{R}(\theta,\omega)$ is the absorption coefficient of a plane unpolarized electromagnetic wave by the inhomogeneous system at hand. The first term in Eq.(6) corresponds to the thermal radiation intensity of the piecewise homogeneous system with the temperature T into the external region.

In the quasiclassical approximation ($\hbar\omega\ll T,T_1$), relation (6) can be presented as follows:

$$I(\omega,\theta,T_1,T) = I_0(\omega,T)\cdot\left\{\Gamma(\theta,\omega) + \frac{T_1}{T}\cdot\mathcal{R}(\theta,\omega)\right\}, \qquad (7)$$

The temperature of a radiative system is usually much greater than the temperature of the external medium. However, in spite of a small value of the ratio T_1/T, one cannot neglect the second term of relation (7) (this term defines a contribution of the proper thermal fields of the external medium into the thermal radiation intensity of one-sided flux) in the case of a slightly absorbing medium. Moreover, if the condition

$$T_1/T \gg \Gamma(\theta,\omega)/\mathcal{R}(\theta,\omega) \qquad (8)$$

is satisfied, then the thermal intensity radiation of one-sided flux is defined, mainly, by the radiation of the external medium, i.e., $I(\omega,\theta,T_1,T)\approx I_0(\omega,T_1)$.

Thus, Eq.(8) is the criterion of the dominant contribution of thermal radiation of the external medium to the one-sided thermal radiation flux. Let us estimate the criterion in the simplest case of semibounded plasma without a transition layer between the plasma and external medium. If the spatial dispersion of plasma is not take into account, then we obtain the following simple criterion for temperatures in the frequency range $\nu_e\ll\omega<\omega_{pe}$ (ω_{pe} is the electron plasma frequency and ν_e is the effective collision frequency of electrons with neutrals) for the radiation angle θ smaller than the critical angle of total reflection:

$$\frac{T_1}{T} \gg \left(\cos\theta + \frac{1}{\cos\theta}\right) \cdot \frac{\nu_e}{\omega_{pe}} \cdot \sqrt{\varepsilon_1}. \qquad (9)$$

To estimate this criterion, we consider, as an example, the radiation of the semibounded gaseous plasma with the temperature $T=10^4$ K into vacuum ($\varepsilon_1=1$) at room temperature $T_1=300$ K. In this case, criterion (9) holds at $\nu_e/\omega_{pe} \ll 0.015$. For the typical value of the ratio $\nu_e/\omega_{pe} = 10^{-3}$, the plasma radiation along the normal to the boundary surface ($\theta=0$) accounts for only about 6% of the total thermal radiation intensity of measured one-sided flux.

In the low-frequency range $\omega \ll \nu_e$, the temperature criterion is proved to be weaker then (9). Therefore, as the frequency decreases, the contribution of the plasma radiation to the one-sided flux reduces (for the case at hand, it is less than 1%).

Transparent Transition Layer. In the case of a transparent transition layer, $\Gamma_2(\theta,\omega) = 0$ ($\Gamma(\theta,\omega) = \Gamma_1(\theta,\omega)$) for any width of the layer. It yields $I(\omega,\theta,T_2) = 0$ and the thermal radiation intensity $I(\omega,\theta,T_1,T_2,T_3) \equiv I(\omega,\theta,T_1,T_3)$ is independent of the temperature of the layer and has the same form as that for the case of plasma without a transition layer [4]

$$I(\omega,\theta,T_1,T_3) = I_0(\omega,T_3)\cdot\Gamma(\theta,\omega) + I_0(\omega,T_1)\cdot\mathcal{R}(\theta,\omega). \qquad (10)$$

Thus, the role of the transparent transition layer is only reduced to a change in absorption properties of the system due to multiple reflections of electromagnetic waves from the layer boundaries z=0 and z=L.

The detailed numerical analysis of frequency and angular dependencies of the thermal radiation spectrum of semibounded plasma with the transparent transition layer is given in [4].

REFERENCES:

1. S.M. Rytov, Theory of Electric Fluctuations and Thermal Radiation [in Russian], Izv.Akad. Nauk, Moscow (1967).
2. M.L.Levin and S.M.Rytov, Theory of Equilibrium Thermal Fluctuations in Electrodynamics [in Russian], Nauka, Moscow (1967).
3. A.S.Usenko, A.G.Zagorodny, and I.P.Yakimenko, Izv.Vyssh.Uchebn. Zaved., Radiofizika, 37, No. 10, 1237-1261 (1994).
4. A.S.Usenko, Preprint Inst.Theor.Phys., Acad.Sci. Ukraine, No. 94-12P, Kiev (1994).
5. A.G.Zagorodny, I.V.Krivtsun, and I.P.Yakimenko, Ukr.Fiz.Zh., 31, No. 12, 1830-1836 (1986).

WALL CONDITIONING IN T-15
INVESTIGATION OF WALL SURFACE STATE BY WASA II

S.Zvonkov, G.Igonkina, A.Stefanovskij
NFI RRC, Moscow,Russia
A.Herrmann
IPP BB, Berlin, FRG

The carbon is practically the unavoidable plasma impurity in tokomak with graphite limiters like T-15. To diminish a carbon flux into plasma different methods are used such as boronisation, usage of composites and so on. A decrease of the influx of another light impurity - oxygen - can be reached by long term backing of vacuum vessel and discharge cleaning (DC). The temperature of T-15 vacuum chamber walls at backing is not homogeneous - it can be 200-230^0 C in toroidal part of vessel (total area equals 75 m^2) and only 40-50^0 C in far parts of ports (total area of ports equals 75 m^2 also). Therefore optimization of discharge cleaning procedure is rather important to reduce T-15 plasma contamination by oxygen. Three types of discharges are used in T-15 for this aim: inductive discharge in hydrogen (IDCH2) and glow discharges in hydrogen (GDCH2) and helium (GDCHe). These methods are widely used for wall conditioning in other tokomaks and usually RGA gives some information about wall purity. Because of the big temperature differences in the T-15 vessel, the RGA spectra didn't represent the condition of the first wall. The diagnostic station WASA II (Wall Analysis with SIMS and Auger) on T-15 was used for in situ measuring of the impurity content on probe surface (PS) exposed to cleaning and tokomak discharges (TD). Description of this diagnostic was given in [1] and first results were published in [2,3]. In this work different cylindrical probes made from copper and stainless steel with a tantalum foil on the lateral surface of probe were used for measurements. In special experiments with Faraday cylinders it was shown that ion current densities on analyzed lateral and plasma facing surfaces are equal each other and therefore processes of deposition and desorption of impurity atoms and molecules are the same on both surfaces. Measurements with biased and floating probes had shown that chemical composition of PS was almost the same in both cases though the desorption of main impurity - carbon - is a little lower at floating potential. The usual position of probe in all experiments was on the minor radius 76 cm what is larger than inner radius of unmovable limiters (70 cm). Extraction of probe from the discharge chamber into analysis chamber of WASA II and measurements of AES and SIMS on PS were made every 1,5-2 hours in discharge cleaning or after a number of TD.

During the DC the content of oxygen on the wall surface is probably the result of the deposition of oxygen escaping weakly backed and poorly outgassed parts of the vessel (ports) and desorption of oxygen from the wall surface due to generation of volatile molecules and impact sputtering. The same processes have to be observed on the PS. In fig.1 one can see that more rapid desorption of carbides leads to appearance of foil material line in AES which afterwards disappears due to deposition of oxygen and iron. Using this figure data one can calculate initial values of carbon desorption rate (~ 10^{15} at cm^{-2} s^{-1}) and deposition rate of oxygen (~ 6 10^{14} at cm^{-2} s^{-1}), equilibrium concentrations of these impurities at which deposition and desorption are equal each other (~.8 10^{15} at cm^{-2}) and rather roughly a characteristic time of deposition-desorption balance (~ 2-3 10^{3} s). Assuming that a total concentration of impurities on PS is about of one monolayer (a short term appearance of Ta line shows that we have a rather like case) we can use a simple equation for some impurity concentration neglecting overlapping with other impurities. According to solution of this equation the characteristic time gives an estimation of an effective cross-section of desorption process (σ ~.7-1 $10^{-17}cm^{2}$).

Practically the same value of desorption cross-section can be obtained using the initial desorption rate of carbon and a balance condition for oxygen. Then the total desorption rate of some impurity "m" is σCI where I - current of glow discharge and C - average concentration of impurity "m" on the wall surface. A pumping speed must be high enough to remove this flux of impurities at their pressure much lower then a pressure of working gas.

The highest concentration of oxygen on PS (up to 50%) was measured in GDCH2 at low wall temperature (T =40-100^{0} C). It is seen in fig.2 that it did not practically changed in almost 40 hours discharge. The partial pressure of water was constant during this time also. In GDCHe the oxygen content fell down to less than 20% at the same wall temperature. The change in chemical composition of PS at transition from GDCH2 to GDCHe can be seen in fig.2 where two last hours of cleaning were performed with helium discharge. Another example of impurity contents on PS is shown in fig.3. The special feature of this case is the very high concentration of nitrogen on PS what may be due to a nitrogen contamination of the helium used. It is worth to notice that after this event traces of nitrogen were observed in AES during the month of intense tokomak operation though part of nitrogen was released from PS as ammonia in the first following IDCH2. This means that during GDC impurity atoms (in this case nitrogen) were implanted in near surface layer of PS where they had a wide spectrum of binding energy with surface. Therefore the usage of GDC at high level of impurities on chamber walls is undesirable. The lowest oxygen content (<10%) was observed in IDCH2 (T =40-230^{0} C) what can be seen in fig.4. So the

measurements don't contradict to assumption that contamination of chamber walls by oxygen is the consequence of port wall cleaning. Glow diacharges penetrate deeper into ports than inductive one and produce the higher flux of oxygen into toroidal part of chamber (GDCH2 higher than GDCHe). According to these results one can expect that contamination of T-15 plasma by oxygen will be lowest in TD after IDCH2.

In contrast to oxygen the carbon content on PS was almost the same in all three types of discharges - 40-60% but the state of carbon films was quite different. The tokomak discharges (TD) with low current (~.25 MA) performed after IDCH2 were accompanied by continuous density increase and disrupted at the density limit (see fig.5). SIMS analysis showed that after IDCH2 a great part of carbon is bonded on PS as methan or its radicals which could be easily desorbed during TD. Practically the same spectra of secondary ions were observed in intensively deposited carbon after such TD. A content of methan radicals is not constant in these spectra and two examples of them with maximal and minimal population of radicals are shown in fig.6. For both cases (after IDCH2 and after TD) we could not find any correlation between shape of secondary ions spectrum and a type of a foregoing discharge. On the contrary the plasma density of TD with much higher current after GDCHe and foregoing IDCH2 was well controlled by gas puff and the carbon deposition on PS after TD was low (appropriate traces are drown in fig 5).

Summary. For T-15 it was shown that conditioning of ports walls can be made most effectively by GDCH2. When cleaning the rate of impurity desorption is about 5 10^{-3} at/ion. Some of impurities are implanted in near surface layer in GD and can be partly released in IDCH2. The wall surface is saturated by hydrocarbons after long term IDCH2. Therefore the optimal cleaning procedure for T-15 is the following.

1.Removal of oxygen from ports by GDCH2.

2.Release of implanted impurities by IDCH2.

3.Desorption of hydrocarbons and CO by GDCHe.

References

/1/ M.Behnke et al., Vacuum, 37 (1987) 145-147

/2/ A.Herrmann et al., Proc. 18th Europ. Conf. on Contr. Fus. and Plasma Phys., Berlin 1991, Vol. 3, p. 53

/3/ V.A.Alkhimovich et al. Plasma Devices and Operations, Vol., 2, pp 27-46

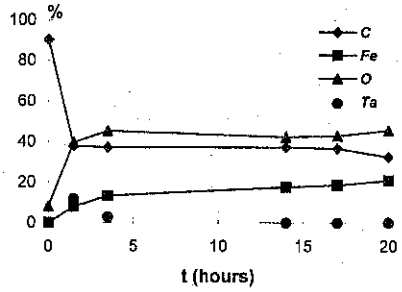

Fig.1 Surface concentration of elements on the Ta foil during GDCH2

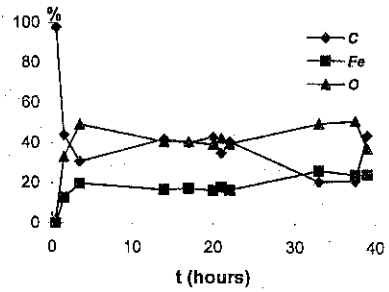

Fig.2 Impurities content on SS PS during GDCH2 and GDCHe (last points)

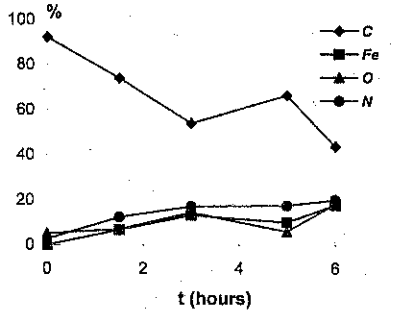

Fig.3 Chemical composition of PS in GDCHe

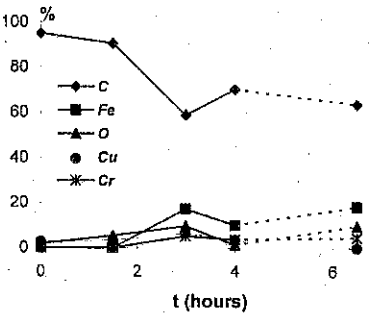

Fig.4 Concentration of impurities on Cu PS during IDCH2

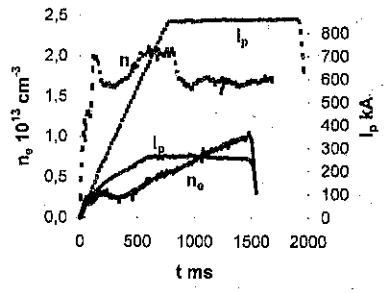

Fig.5 Plasma current and electron density in TD followed after IDCH2 (——) and GDCHe (- - -).

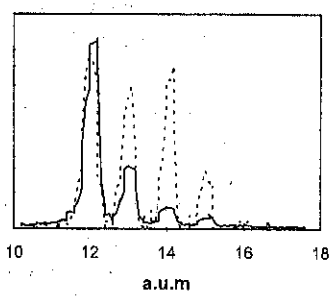

Fig.6 Mass spectra of secondary ions after IDCH2 or following TD

Spectroscopy of molecular hydrogen in TEXTOR edge plasmas

G.Sergienko[1], A.Pospieszczyk, D.Rusbüldt

[1]Institute for High temperatures RAS, Assotiation "IVTAN", 127412 Moscow, Russia
Institut für Plasmaphysik, Forschungszentrum Jülich GmbH, Association EURATOM-KFA, D-52425 Jülich, Germany

1. Introduction

Molecular species can play an important role in the edge plasma of tokamaks [1]. For an investigation of the particle balance the contribution of molecular hydrogen to the total hydrogen flux must be known [2]. The measurement of the emission of light by the molecules entering into the high temperature plasma permits to measure the flux as in the case of atoms and ions. However, the molecule exhibits a complex spectrum of groups of bands, each band of which is composed of large numbers of discrete line transition. The interval between molecular lines are rather small and the lines appear as a continuum at a low resolution spectrum [3]. Therefore, high resolution spectroscopy must be used to measure a molecular spectrum. To evaluate H_2 molecular flux from the spectrum a collisional-radiative model like in [4] must be used. The goal of the investigation is the determination of the population distributions of the vibrational levels and rotational sublevels of molecular hydrogen injected into the TEXTOR edge plasma.

2. Measurement

The H_2 gas was puffed through a 1mm diameter hole near the top of a graphite test limiter moved into the plasma from the bottom of the torus. The test limiter was positioned at the same plasma radius as the toroidal belt limiter ALT-II (r_{lim}=46cm). The emission of the gas jet, polarized parallel to the toroidal magnetic field, was collected along the chord in the poloidal direction, tangentially to the test limiter surface. The viewing chord had the rectangular cross-section about 3mm in radial and 21mm in toroidal direction. The molecular hydrogen spectra have been measured by a grating spectrometer equipped with a cooled CCD camera. The spectrometer had a spectral resolution of about 0.2 Å in the 11th diffraction order and a spectral interval of about 100Å. The wavelength range of 5900Å-6500Å was selected by an appropriate glass and interference filter. The spectrometer with the CCD camera had been calibrated with help of a standard tungsten ribbon lamp. The spectrum exposure time was equal to the 1-2 s in the flap top of the discharge.

3. Results

Spectra of the Fulcher-band (transition $3p^3\Pi_u \rightarrow 2s\Sigma_g^+$) emission were measured in the range 6000Å-6500Å during the injection of H_2 into the TEXTOR edge plasma, see Fig.1 (wavelength in vacuum). Always five spectra were measured during reproducible discharges.

The lines of the R-, Q- and P-branches of the (0,0), (1,1), (2,2), (3,3), (4,4) bands of the $H_2(3p^3\Pi_u \rightarrow 2s\Sigma_g^+)$ transition can be observed in the measured spectral range. The Q-branch lines shown in fig.1 were used to evaluate the populations of the rotational sublevels and the vibrational levels of the $3p^3\Pi_u^-$ electronic state. In order to evaluate the relative level populations the integral line intensities were used. As shown in fig.2 the populations of the rotational sublevels conform to a Boltzmann distribution. The measured rotational temperature is reduced with increasing vibrational quantum number of the level. The population distributions evaluated from the R- and P-branches are practically identical with those evaluated from the Q-branch. The rotational temperatures were used to determine the populations of the vibrational levels. In contrast to the population of the rotational levels the population of the vibrational levels do not obey a Boltzmann distribution. As seen in fig.3 there is no effect of a variation of the plasma density and the gas influx on the population of the vibrational levels.

The line intensities in the Fulcher-band spectrum were redistributed with increasing of the molecular hydrogen flux. Fig.4 shows that this is due to the rotational temperature variation. The rotational temperature for vibrational level $\nu=0$ rises from 480K to 750K when the hydrogen flux increases from 3.9 mbar·dm^3/s to 12 mbar·dm^3/s. The rotational temperature also grows with the increase of the line-averaged plasma density from 449 ± 22K for $n_e=1.3\cdot10^{13}$cm^{-3} to 544 ± 25K for $n_e=3.1\cdot10^{13}$cm^{-3}. The spectra have been measured also without gas injection, but were not very intense. Only few bright lines of the Q-branch for the (0,0), (1,1) and (2,2) transition could be observed for $n_e=3.4\cdot10^{13}$cm^{-3}.

The spectra measured in TEXTOR exhibit also changes in line profiles. The Q(1) lines of the $H_2(3p^3\Pi_u \rightarrow 2s\Sigma_g^+)$ transition are essentially broadening (fig.1). In the same spectral range the bands of the $3d^3\Sigma \rightarrow 2p^3\Pi$ transition could be observed. The π-components of the Q-branch lines are strongly split. The splitting increases with growing rotational quantum number (fig.5).

3. Discurssion

The rotational temperature follows to the translational temperature of the gas under appropriate conditions [5]. The gas temperature can increase due to a gas expansion (heating owing to Joule-Tomson effect for hydrogen) and an increased flux of charge-exchange particles inside of the gas channel. However, the rise of the temperature due to Joule-Tomson is very small (less 1K) for used pressure drop. Therefor, the observed increase of the temperature may be explained by an increased flux of charge-exchange particles during the

gas blow. The energy of the charge-exchange particles is transfered to the hydrogen molecules inside the gas channel. The weak dependence of the temperature versus the plasma density confirms this assumption. The charge-exchange flux increases with growing plasma density when also the plasma temperature is reduced. For this reason, the heat flux to the surface changes only weakly with the plasma density.

The populations of the vibrational levels of the $3p^3\Pi_u$ state are $1:1.15\pm0.05:0.960\pm0.04:0.685\pm0.082:0.242\pm0.009$ for the data shown in fig.3 and $1:1.15\pm0.31:1.01\pm0.27$ without gas injection. Almost identical populations were observed for electron impact excitation from the $X^1\Sigma_g^+(v=0)$ state [6]. Therefor, there is not substantial vibrational excitation of the ground state of H_2 molecules under TEXTOR condition.

The estimation shows that the Zeeman splitting is the dominant effect for the line broadening of the π-component of the Q(1) line of the $3p^3\Pi_u^-\rightarrow 2s\Sigma_g^+$ transition. The upper and lower state of this transition obeys the Hund's case (b) coupling scheme. The splitting of the Q line is reduced with growing rotational quantum number. Also the π-component of the $3d^3\Sigma^+\rightarrow 2p^3\Pi$ Q-branch lines are split due to Zeeman splitting. But the latter splitting differs from the splitting of the $3p^3\Pi_u^-\rightarrow 2s\Sigma_g^+$ lines because the upper and lower electronic states belong to different coupling cases: $3d^3\Sigma_g^+$ - Hund's case (d) and $2p^3\Pi_u$ - Hund's case (b). The Zeeman splitting calculated with help of g-factors of the $3d^3\Sigma^+$ state from [7] is in agreement with the measured value.

4. Conclusion

- The rotational temperature of the $3p^3\Pi_u^-$ state of H_2 depends on the molecular hydrogen flux.
- There is no effect of a variation of the plasma density and the gas influx on the population of the population of the vibrational levels of this state.
- The observed line profiles is the result of Zeeman splitting in toroidal magnetic feild.

References

[1] D.E. Post, J. Nucl. Mater. **196-198** (1995) 143
[2] D.H. McNeill, J. Nucl. Mater. **162-164** (1989) 476
[3] D.H. McNeill, Rev. Sci. Instrum. **56**(11) (1986) 2724
[4] K. Sawada, T. Fujimoto, J.Appl.Phys. **78**(5) (1995) 2913
[5] B.P. Lavrov, Opt. Spectrosc. **48**(4) (1980) 680
[6] B.P. Lavrov, V.P. Prosikhin, Opt. Spectrosc. **64**(3) (1988) 498
[7] R. Jost, at al., Mol.Phys. **37**(5) (1979) 1605

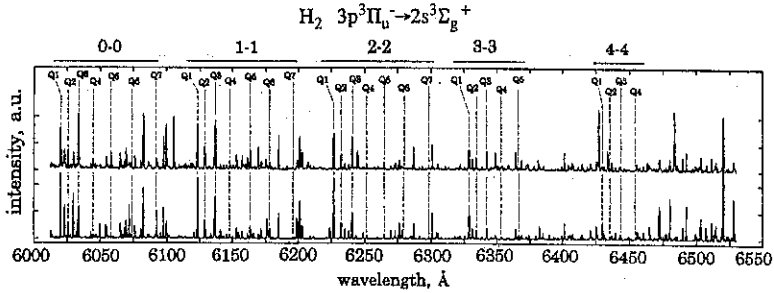

Fig.1 Fulcher-band spectrum of H_2 injected in TEXTOR with a comparison spectrum from a gas discharge tube (lower trace).

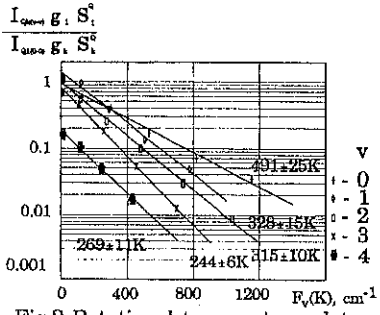

Fig.2 Rotational temperature plots for the vibrational levels of the 3p state, H_2 flux 2 mbar·dm^3/s, $\bar{n}_e = 1.3 \cdot 10^{13}$cm^{-3}, OH.

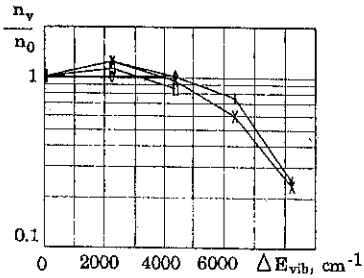

Fig.3 Populations of the H_2 $3p^3\Pi_u^-$ vibrational levels:

+ - OH, $\bar{n}_e = 1.3 \cdot 10^{13}$cm^{-3}, $\Gamma_{H_2} = 2$ mbar·dm^3/s
X - OH, $3.1 \cdot 10^{13}$, 2
□ - OH, $3.1 \cdot 10^{13}$, 3.3
◊ - NBI, $1.9 \cdot 10^{13}$, 12

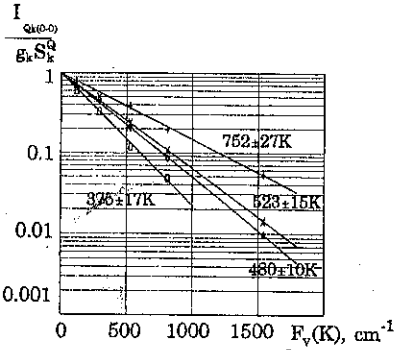

Fig.4 Populations of the $3p^3\Pi_u^-$ (0) rotational sublevels for different H_2 fluxes, $n_e = 1.9 \cdot 10^{13}$cm^{-3} :
□ - 0.5 mbar·dm^3/s, ◊ - 3.9, X - 4.9, + - 12.

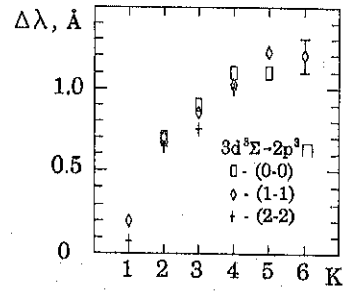

Fig.5 Line splitting versus rotational quantum number.

On application of plasma chemical reaction for particle removal by cryopumped divertor of thermonuclear device

G. G. Lesnyakov

Institute of Plasma Physics,
National Science Center "Kharkov Institute of Physics and Technology", Kharkov, Ukraine

1. Introduction

It is becoming evident that power and particle control will play a pivotal role in next step controlled fusion devices. Now this control includes gas target divertors, impurity-seeded radiating divertors [1], and cryopumped divertors [2,3]. Up to now nitrogen seeding was most frequently used as a recycling impurities to achieve high power radiative divertor operation [4,5]. However, for progress in developing such techniques it is necessary to replay on the question of whether low pressure gas target divertor solution exist. The divertor geometry clearly plays a role in it performance.

2. Principle of proposal

It is proposed one more variant of the divertor operation in what the functions of the baffle or the divertor chamber, the gas target at the divertor plate for the radiative divertor operation and cryopumping can be combined in a new quality for active particle removal during plasma discharge. At the required conditions (optimized divertor geometry, baffle elements, divertor plate and cryopumping) the plasma chemical reaction between the diverted plasma of hydrogen isotopes and the filling nitrogen (the gas target) in divertor volume must be performed to form of the ND_3 (NH_3, NT_3) product that is easily condensed on the LN_2 cooled surface surrounding the LHe cooled surface. Usually, in a cryopump the LN_2 cooled surface (shield) is several times more than the LHe cooled surface. Now, the LHe cooled surface can be only used for selective pumping of the ash (He exhaustion) - the cryosorption of helium on argon frost [6]. Additionally, one can used the cryosorption of hydrogen on NH_3 layers [7].

The previous studies of the plasma synthesis of ammonia in the low-pressure discharges [8,9] give us a chance to support the proposal above described.

To discuss such possibility it was carried out the experimental modeling of the plasma synthesis of ammonia in the mirror trap with the steady-state plasma stream from duoplasmatron source (the model of the device is similar to a bandle-divertor) and with the LN_2 cooled surfaces surrounding the plasma stream.

3. Experimental setup

A schematic of the experiment is shown in Fig. 1. The device was divided on two vacuum volumes: V_1=0.86 m^{-3} and V_2=1.415 m^{-3}. The axial magnetic field of a mirror trap (mirror ratio 1.2) about B=3 kG is produced by two LN_2 cooled coils (Position 1). The

duoplasmatron source (Pos. 3) installed in the V_2 volume generates the 0.7-1.2 cm diameter plasma stream that is injected into a non-uniform magnetic field (see the magnetic field lines, Pos. 2). The electron density (n_e=10^{17}-10^{19} m^{-3}) and the electron temperature (T_e=2-40 eV) is controlled in the plasma source by the arc current (I_d=1-4 A) and the gas flow ($\bar{f}$=5.5×10^{-2} - 8×10^{-2} torr·l/s). The two volumes are connected by a long tube (Pos. 4) which has a well-determined conductivity (F_{H2}=5.325 l/s). The length of the tube is l=0.27 m. The inside diameter is 1.5 cm. The plasma, after passing through the long tube inserted in magnetic field, enters into the V_1 volume and interacts with a target plate (Pos. 5). The V_1 volume is pumped both with a LN_2 cooled surface (Pos. 10) and with a diffusion pump (Pos. 13). The pumping of gases in the V_2 volume is fulfilled both with a LN_2 cooled surface of the magnetic coils (Pos. 11) and with a diffusion pump (Pos. 13). Analyses of input gases and the plasma synthesis products condensed on the cooled surfaces in the device are performed with ROMS-2 mass-spectrometer (Pos. 12). At the end of a run the condensate from the V_1 volume can be warmed to room temperature in individual volume with valves (Pos. 10). The working gases are hydrogen (H_2), deuterium (D_2) and nitrogen (N_2).

The device was designed such that we could determine differences in ammonia formation when the plasma source is filled gas mixtures (H_2+N_2, D_2+N_2) and when the hydrogen (deuterium) plasma is injected into magnetic field but the nitrogen is filled in the V_2 volume.

4. Results

The recording of gas pressure variations in the volumes is one of the main procedure to confirm the plasma synthesis of ammonia and deuteroammonia during transport of plasma along magnetic field. The signals of ionization gages (Pos. 8) in two volumes is shown in Fig. 2(a) in case when a gas mixture (H_2+N_2) is filled in the plasma source. Dashed curves draw the pressure variations in the volumes when the arc current in the plasma source is I_d=1 A (n_e=8×10^{17} m^{-3}, T_e=15 eV, duration of the discharge is t_d=13.5 min). Solid curves draw the pressure variations in the volumes when the arc current in the plasma source is I_d=2 A (n_e=1.0×10^{18} m^{-3}, T_e=12 eV, duration of the discharge is t_d=8.7 min). The input rate of the gas mixture is about 5.5×10^{-2} torr·l/s, Mass-spectrum of gases for similar series of experiments show the formation of NH_3 (Fig. 3).

The input of gas mixture in the V2 volume does not produce any variations in the pressures without discharge in the plasma source. Before discharges, in two volumes are kept usual deference in the pressures that are determined by the conductivity of the long tube. The injection of deuterium (hydrogen) plasma in the magnetic trap does not produce noticeable variations in the pressures also (see in Fig. 2(b) the parts of curves between t=0.5 min and t=5.5 min).

The plasma synthesis of deuteroammonia is performed in discharge that is described in Fig. 2(b). The curves draw the pressure variations in the volumes when the arc current in the plasma source is I_d=4 A (n_e=6×10^{18} m^{-3}). The input rates of D_2 and N_2 are about 8×10^{-2}

torr·l/s. When the nitrogen flow rate is decreased (since t=15 min) then the composition of the gas mixture is approached to optimum and the pressure in the V_2 volume is decreased sharply.

5. Conclusions

Experimentally it was demonstrated that ammonia and deuteroammonia are mostly formed when the LN2 cooled surfaces are in the device and when the lasts are located apart from the plasma flow. The deuteroammonia formation is independent of the production method of the gas mixture. The decrease of neutral gas pressure about two orders of the magnitude during discharge was measured in the device at the initiating of the plasma synthesis both ammonia and deuteroammonia.

The deuteroammonia plasma synthesis for the particle removal of plasma flux in the cryopumped divertor systems can be tested in the large toroidal controlled fusion devices as JET and LHD.

References

1. Vlases G.C., Pl. Phys. and Contr. Fusion **35** B67 (1993)
2. Schaffer M.J., IAEA Techn. Comm. Meet. On Stellarators and other Helical Confinement Systems, Garching, Germany, 1993, IAEA, Vienna, 504 (1993)
3. Papastergion S., et al, JET report JET-**P(94)37** (1994)
4. Allen S.L., et al., J. Nucl. Mater. **196-198** 804 (1990)
5. Reichle R., et al., 22nd EPS Conf. On Controlled Fusion and Plasma Physics, Bournemouth, UK, Vol. 19C, Part III, III-085 (1995)
6. Kamperschroer J.H., et al, Report **PPPL-2658** (1989)
7. Schonherr W.D. Absorptiongleichgewichte von H_2 an kondensierten NH_3-schichten und H_2-dampfdrucke von NH_3-H_2-mischkondensaten. Dr. der Naturwissenschaften (Dipl. Chem.). Technischen Universitat Berlin. Berlin, 1970, D83.
8. Schechter A.B. *Chemical reactions in electrical discharge.* ONTI, Leningrad-Moscow, (1935) (in Russian)
9. Touvelle M., et al., Plasma Chemistry and Plasma Processing 7 101 (1987)

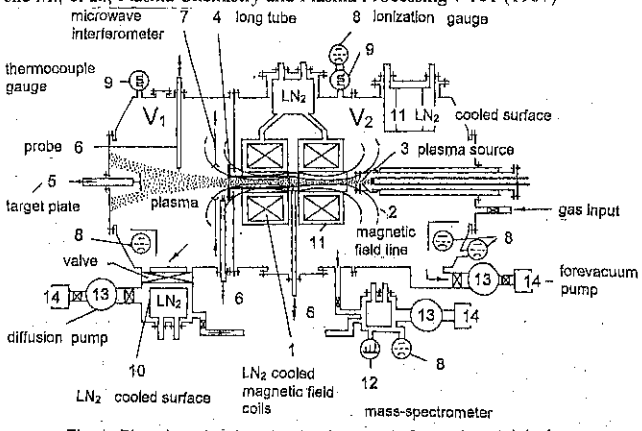

Fig. 1. *Plan view showing structural concept of experimental device.*

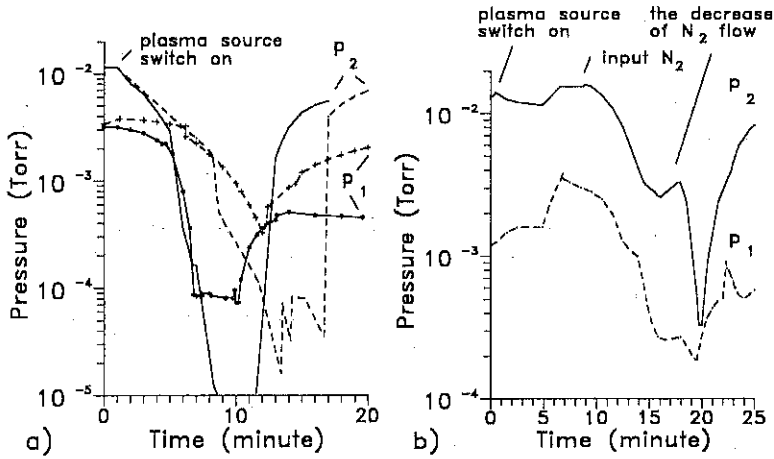

Fig. 2. *The temporary variations of p_1 (in the V_1 volume) and p_2 (in the V_2 volume) gas pressures during discharges: (a) the plasma flow is generated in the source by the H_2+N_2 gas mixture, the parameter is the arc current; (b) the deuterium plasma is generated in the source and then, after any time, the input of the nitrogen in the V_2 volume initiates the deuteroammonia plasma synthesis.*

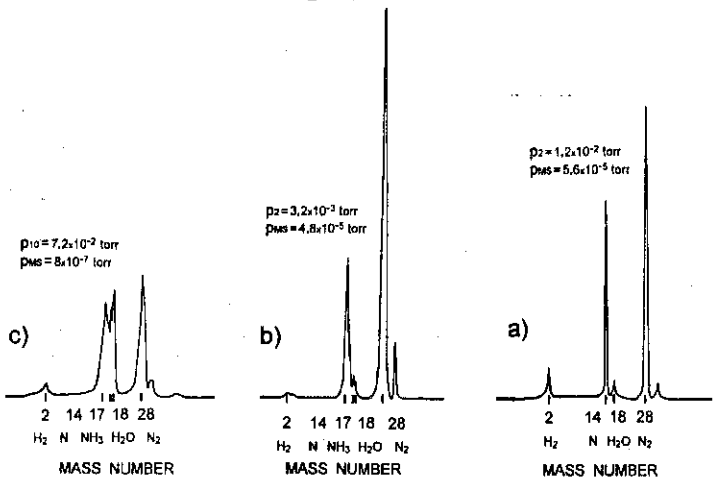

Fig. 3. *Mass spectra of gases: (a) before the beginning of discharge, when N_2+H_2 gases are filled in the V_2 volume; (b) in the V_2 volume during the plasma source discharge; (c) in the V_1 volume, after experimental day, following bakeout at 23°C of the LN_2 cooled surface (Fig.1, Pos. 10). p_{MS} is pressure in the mass-spectrometer (Fig.1, Pos. 12).*

EXPERIMENTS WITH EDGE-PLASMA AND A BIASED MOVABLE B_4C-LIMITER INTERACTION : POSSIBLE USE FOR BORONIZATION AND PUMPING DURING DISCHARGE CLEANING IN URAGAN-3M TORSATRON

G.P.Glazunov [a], E.D.Volkov [a], V.G.Kotenko [a], A.V.Shtan' [a], Yu.K.Mironov [a]
N.I.Nasarov [a], O.S.Pavlichenko [a], A.Sagara [b], N.Ohyabu [b], O.Motojima [b]

[a] Institute of Plasma Physics of National Science Center
"Kharkov Institute of Physics & Technology", 310108 Kharkov, Ukraine
[b] National Institute for Fusion Science, Nagoya, 464-01, Japan

Abstract

The new method for Uragan-3M starting procedure with using of movable limiter, the head plate of which is made of vacuum hot-pressed boron carbide, is suggested. It is shown that at negative limiter bias up to -200V during work and pulsed cleaning discharges the boron spectral signal from plasma increases with the head limiter ion current increase. Also the relationship between oxygen concentration in plasma and negative bias was observed by carrying out BII and OII line spectroscopy studies. The estimations of the limiter application for impurity pumping and solid target boronization shows that the negatively biased movable B_4C-limiter can be used to improve pulsed discharge cleaning and boronization in Uragan-3M torsatron.

1. Introduction

Previously [1] the Uragan-3M torsatron movable boron carbide limiter was studied for solid target boronization possibility and limiter head material erosion behavior in the biased limiter experiments during plasma work discharges. Also the the effect of suppression of the ohmic discharge at the stages of magnetic field increase and decrease was observed when the negative power (>40V) was transferred to the limiter. Recently the Local Island Divertor (some functions of which is similar to pump limiter) with hot carbon head plate has been proposed as a method drastically shorting the discharge cleaning time required in wall conditioning to remove main impurities on the surface of plasma facing components [1]. As the Uragan-3M torsatron (U-3M) design did not provide the baking of the metallic plasma facing surfaces, water is the main impurity and it needs usually a few weeks to obtain controllable work discharges. The similar situation can be arised in the Uragan-2M torsatron [3], the baking temperature of which is 100-150°C. Therefore it was of a great interest to use the above idea in reference to the U-3M movable B_4C-limiter. Here we report the first results of an experimental study of B_4C-limiter use for H_2O and O_2 pumping during pulsed discharge cleaning (PDC) in U-3M

2. Experiment

To perform experiments, a new version of a movable limiter was designed and installed in the U-3M vacuum chamber. It included a 90mm•90mm•8mm head plate, which was made by the method of vacuum hot pressing of boron carbide powder (B - 78.2%, C-21.5%). The technology and equipment for making of B_4C bulk tiles intended to protect plasma facing surfaces and movable (unmovable) limiters was developed in NSC KIPT. The limiter plate material has the following characteristics: density - 2.46 g/cm^3, heat conductivity ~ 30 W/m·K, electrical resistivity ~ 10^{-2} Ohm·m. Estimation of erosion rates was made by material irradiation with the high power pulsed hydrogen plasma flows during 3 μs. It gave the values from $8•10^{-2}$ at/ion to 10at/ion with energy density varying from 5 J/cm^2·pulse to 30 J/cm^2·pulse and the H^+ energy varying from 200eV to 2 keV. The specific rate of outgassing carried out in a special test after 24-hour heating at 200°C in vacuum $4•10^{-9}$ Torr was ~ 10^{-11} Torr l/s.cm^2. This limiter was installed at the U-3M vacuum chamber bottom bellows inlet in such a way that the limiter plate edge could be located at distances from 22 cm to 12 cm from the plasma column axis. Possibilities were provided to switch on/off negative or positive bias pulses with an amplitude of up to 200 V and duration 1-50 ms.

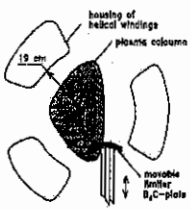

Fig. 1. Schematic drawing of the experiment

The layout of the experiment is shown on Fig.1. It should be noted that in this configuration the U-3M movable limiter fulfills the functions of an open pump limiter. There were two channels for boron and oxygen spectral line intensity measurements to provide boron observation on the opposite to B_4C-plate side of the plasma column. For mass-spectrorometry of residual gases on omegatron mass-spectrometer was used. Measurements of current - voltage characteristics, BII and OII spectral line intensities , and residual gas mass-spectrometry in the U-3M vacuum chamber have been made in the PDC with typical parameters: hydrogen pressure $p \approx 1•10^{-4}$ Torr, $n_e \approx 2•10^{-12}$ cm^3, $T_e \approx$10-15 eV, B ≈

0.035 T, plasma pulse duration τ=50 ms, pulse frequency f=0.2 Hz, total discharge power W ≈ 80 kW.

3. Results and discussion

As it is seen in Fig.2 the highest ion current of the limiter plate in the PDC was only 0.2 A even at the nearest distance r=12cm of B_4C-plate from the plasma column axis and a bias up to -90 V. But with a further negative bias increase the arc regime with currents up to 2-10 A developed and controllable BII signals from the plasma in two spectroscopy channels were observed (Fig.3a). At the same time the oxygen spectral line intensity decreases (Fig.3d).

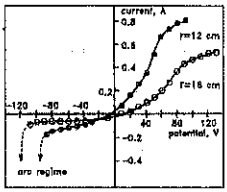

Fig.2. The limiter current as function of the limiter potential.

And this probably points to H_2O and O_2 effective trapping by the B_4C-plate, because the main plasma characteristics (e.g. the CIV line intensity, from which we estimate the plasma temperature), show no changes in this moment. It should be noted that there was no such effect when positive bias up to 200 V was switched on in the limiter.

There may be a few reasons for oxygen decrease in plasma during negative bias. One of them is that the water, which is the main impurity at the start stage of PDC, can be dissociated and ionized at the plasma edge, and positive ions (O^+ , O^{++}) can be trapped by boron carbide tile. The efficiency of this method of impurity pumping one can be essentially increased by using the island configuration and high magnetic fields as indicated in [1]. If it is assumed that the oxygen saturation concentration in B_4C is ~$1.6 \cdot 10^{17}$ cm^{-2} [4] and the plate area is ~100 cm^2 then the total amount of trapped oxygen could be ~10^{19}. The water content of the monolayer on the stainless steel protective housing of helical windings is about $3 \cdot 10^{19}$, thus a few B_4C-plates will be sufficient for pumping several adsorbed impurity monolayers.

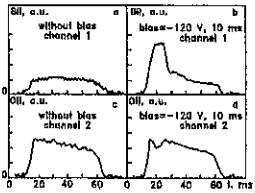

Fig.3. Time evolution of BII and OII spectral lines intensity: BII intensity without bias (a) and with -120 V bias during10ms(b), OII intensity without bias ©, OII intensity with 10ms -120 V bias (d)

The B_4C sputtering during negative limiter bias might be the second reason of oxygen decrease as the result of boronization. Really, if the B_4C erosion coefficient is ~$2 \cdot 10^{-2}$ at/ion [5] and the negative pulsed bias duration is 10 ms then the sputtered particles make up about 10^{17} per pulse. We assume that most of sputtered boron deposits on the plasma facing surfaces because no boron signs in the U-3M vacuum chamber were observed in mass-spectrometry measurements. The fresh boron layer partially coating the protective housings effectively absorbs oxygen and prevents it from coming to the plasma from oxides. Also, it should be noted that it is necessary about 10^{20} particles to form the monolayer coating on the plasma facing surfaces of the U-3M protective housing of helical windings. So, a few days of PDC regime would be sufficient to produce several boron monolayer coating i.e. for the U-3M boronization.

The preliminary analysis of the limiter application for impurity pumping and U-3M boronization shows that the negatively biased movable B_4C- limiter can be used to improve pulsed discharge cleaning and solid target boronization in the Uragan-3M torsatron. In the nearest future we are going to measure the boron distribution along helical windings and the efficiency of this method in reducing actually the time of the pulsed discharge cleaning procedure.

References

[1] G.P.Glazunov et.al., Lett. J. Tech. Phys., vol.29(11), p.78-83, 1995.
[2] A.Sagara et.al., Trans. of Fus. Technology, vol.27, p.532-535, 1995.
[3] V.E.Bykov et.al., Fus. Technology, vol.17, p.140-147, 1990.
[4] N.Noda et.al., J. Nucl. Mater., vol.220-222, p.623-626, 1995.
[5] C.Garcia-Rosales et al., J. Nucl. Mater.,vol.189, p.1-8, 1992.

MEASUREMENTS OF DIVERTOR IMPURITY CONCENTRATIONS ON DIII-D*

R.D. Wood,† R.C. Isler,‡ S.L. Allen,† M.E. Fenstermacher,† C.J. Lasnier,†
A.W. Leonard, and W.P. West

General Atomics, P.O. Box 85608, San Diego, California 92186-9784 U.S.A.

INTRODUCTION

One promising method of reducing the target plate heat load is to enhance the divertor radiation with deuterium and gaseous impurity injection.[1] On DIII-D, during discharges with heavy deuterium (D_2) gas injection, we have observed divertor peak heat flux reductions (~3-5x) at the target plate with a corresponding increase in radiative losses.[2] Reconstructed bolometer data show increased radiation in the outboard divertor extending from the X-point to the outer strikepoint (OSP).[3] Furthermore, the electron pressure near the OSP decreases significantly, but only modest changes are observed farther out in the scrape off layer (SOL); i.e., these divertor plasmas are detached near the separatrix, but remain attached farther out in the SOL and are referred to as a Partially Detached Divertor (PDD).[2]

To characterize the constituents of the radiation in a PDD, emissions in the 100–1100 Å spectral region are measured with an absolutely calibrated SPRED[4] spectrograph. The spectrograph has a vertical view of the lower divertor along the same line of sight as the eight-channel Divertor Thomson Scattering (DTS) system.[5] One channel of the bolometer array has a similar line of sight as the SPRED and provides a line-integrated measurement of the total radiated power. The extent of the radiation zones of selected visible lines along the line of sight of the SPRED are determined from a tangentially-viewing TV camera[6] with filters. This diagnostic set enables us to evaluate the power radiated from individual ions and to determine impurity densities in the divertor region.

During PDD operations, the divertor plasma was swept so that the field of view of the vertically viewing diagnostics (R=1.48 m) sampled the divertor region from the X-point to outside the OSP. Figure 1 shows a time trace of discharge parameters with D_2 puffing and a sweep of the divertor plasma. At 2500 ms D_2 gas is puffed into the vessel at the midplane, and increases in the core electron density and total radiated power are observed. The PDD begins to form at 3100 ms and from visible TV data (not shown) the carbon emissions shift from the inner scrape off layer near the X-point to a distributed region from the X-point to partially down the outer leg. The divertor plasma is slowly swept inward from 3200 ms to 4300 ms. During the sweep an abrupt increase in CIV emissions occur when the highly radiating zone enters the SPRED line-of-sight (3600 ms). As the divertor plasma is swept inward, CIV emissions decrease while the Ly-β emissions increase showing that carbon radiation dominates near the X-point and deuterium radiation dominates near the OSP.

DETERMINING ION DENSITIES AND TOTAL RADIATED POWER FROM SPECTROSCOPY

At divertor-relevant electron densities (n_e) and temperatures (T_e) on DIII-D, the bulk of the radiated power comes from the 400–1600 Å spectral region. In principle, the total radiated power can be determined by summing the absolute intensities from all significant transitions. However, some of the strong lines of deuterium (Ly-α, 1216 Å) and carbon (CIII, 1175 Å and CIV, 1550 Å) are outside the spectral region of the divertor SPRED instrument. For deuterium, the measured intensity of the Ly-β (1025 Å) transition is used to

*Work supported by the U.S. Department of Energy under Contract Nos. DE-AC03-89ER51114, W-7405-ENG-48, and DE-AC05-96OR22464.
†Lawrence Livermore National Laboratory.
‡Oak Ridge National Laboratory.

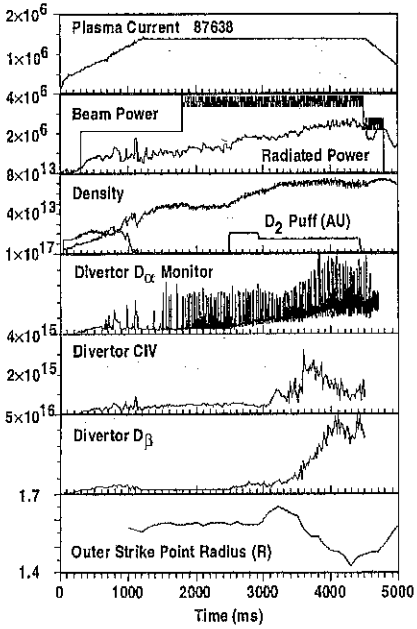

Fig. 1. Time traces of selected experimental parameters for a discharge with partially detached divertor and a sweep of the divertor plasma. At 2500 ms D_2 gas is puffed near the vessel midplane, and increases in the core n_e and total radiated power are observed. The PDD begins to form at 3100 ms and the divertor plasma is slowly swept inward from 3200 ms to 4300 ms. During the sweep an abrupt increase in CIV emissions occur when the highly radiating zone enters the SPRED line-of-sight (3600 ms). As the divertor plasma is swept inward, CIV emissions decrease while the Ly-β emissions increase.

predict the Ly-α (1216 Å) contribution and to obtain the total deuterium radiated power using the Johnson and Hinnov[7] results. For carbon it is necessary to employ collisional-radiative modeling to evaluate the total radiated power from measured transitions of ions. The effective T_e at the site of each ion is first determined from a spectral line ratio; the emitted power is then deduced from the emission of a single line using the inferred T_e.[8] The effective T_e, derived from line ratios measured along the line of sight of the SPRED spectrograph, represents an average T_e over the radiating volume. This analysis is also used to provide line-integrated ion densities.

Over the temperature and density range of interest (2–20 eV, 1.0×10^{20}), the carbon radiation is due principally to emission by CIV at 1550 Å; the total contributions from CII and CIII are small (~20%). Determination of CIV power loss is complicated by the fact the measured line emission used to predict the total radiation is sensitive to both n_e and T_e; transitions with a change in the principal quantum number ($\Delta n\neq0$ transition) are generally sensitive to n_e and T_e. Furthermore, the temperature at which the measured CIV lines radiate is slightly higher than for the strong $\Delta n=0$ transitions (CIV 1550 Å). As a result, the effective T_e, calculated from the measured line ratios is slightly elevated, which results in an underestimate of the total CIV radiated power. Thus, a simple one-dimensional transport code (STRAHL[9]) along with DTS measured n_e and T_e are used to predict the measured line ratios.

The transport coefficients are adjusted until the calculated and measured line ratios are in good agreement. The total radiative losses are then compared to obtain correction factors for using the measured line ratios mentioned above. The transport code is used as a tool to predict line-of-sight profiles from the measured emissions and is not intended to model impurity transport in the divertor. In general, the spectroscopic determinations of power losses agree well with those from bolometry; during beam heated discharges, differences in the two results are less than 25%.[8]

CHARACTERIZATION OF INTRINSIC EMISSIONS

The effective electron temperatures from line ratios are found to vary little during a discharge, which indicates that a given ion tends to exist over a rather limited temperature range. Using this fact, the vertical

locations of the carbon ions and the n_e at these locations are established by correlating the effective electron temperatures with spatially resolved DTS data. The vertical location of the radiation zone determined from inversions of two-dimensional bolometer and visible TV data are in good agreement with those established from line radiation measured with the SPRED. For example, in PDD operation the CIII and CIV radiation is located in a region near the X–point.

A representative two-dimensional distribution of the radiated power density, and the carbon and deuterium fractional power during the OSP sweep is shown in Fig. 2. When the PDD forms, the carbon radiation zone at the X–point is in the field of view of the SPRED spectrograph and the bulk of the radiation comes from CIV. As the OSP is swept inward, the radiated power from deuterium increases until it dominates when the OSP is near the spectrograph line of sight. The carbon power fraction from the X–point along the outer leg of the divertor is ~80% of the total with the balance coming from deuterium. Near the OSP the deuterium power fraction is 60% of the total. These power fractions are similar to those reported on JT-60U where carbon has been reported as the major contributor to divertor radiation losses;[10] the plasma-facing surfaces of both DIII–D and JT-60U are constructed with carbon materials.

The carbon ion concentrations during the OSP sweep are also determined. They are obtained from the line-integrated ion densities by employing the images from the tangentially viewing TV camera equipped with a CIII filter to determine the extent of the radiation zone. During the sweep of the divertor plasma shown in Fig. 2, the estimated carbon concentrations range from 1% to 2% of the electron density.

CONCLUSIONS

Carbon emissions in the DIII–D divertor during partial detachment have been measured, and the deduced radiated power and the temporal behavior of the impurity emissions from spectroscopy are in good agreement with bolometer measurements. Effective electron temperatures from line ratios for CIV (9–11 eV) and CIII (6–8 eV) are correlated with DTS measured electron temperatures to determine the spatial location of the carbon radiation zone. During PDD operation, the bulk of the divertor radiation is emitted from CIV near the X–point while deuterium radiation is strongest near the outer strikepoint. The carbon ion concentrations are in the range of 1%–4% of the electron density.

REFERENCES

[1]S.L. Allen, *et al.*, J. Nucl. Mater., **220–222**, (1995) 336.

[2]T.W. Petrie, *et al.*, J. Nucl. Maer., **196–198**, (1992) 848.

[3]A.W. Leonard, *et al.*, 22nd European Conf. on Controlled Fusion and Plasma Physics, Bournemouth, United Kingdom, Vol. 19C, Part III (1995) 105.

[4]R.J. Fonk, A.T. Ramsey, and R.V. Yelle, Appl. Optics **21**, 2115 (1982).

[5]S.L. Allen, et al., "First Measurements of Electron Temperature and Density with Divertor Thomson Scattering in Radiative Divertor Discharges on DIII–D," Proc. of 12th Conf. Plasma Surface Interactions, St. Raphael, France 1996.

[6]M.E. Fenstermacher, *et al.*,"A Tangentially Viewing Visible TV System for the DIII–D Divertor," Proc. of 11th High Temperature Plasma Diagnostics, Monterey, California, to be published in Rev. Sci Instrum. 1996.

[7]L.C. Johnson and E. Hinnov, J. Quant. Spectros. Rad. Transfer **13**, 333 (1973).

[8]R.C. Isler, *et al.*, "Spectroscpic Characterization of the DIII–D Divertor," to be submitted to Physics of Plasmas, 1996.

[9]K. Behringer, JET Report JET-R(87)08, 1987.

[10]H. Kubo, *et al.*, Nucl. Fusion **33**, 1427 (1993).

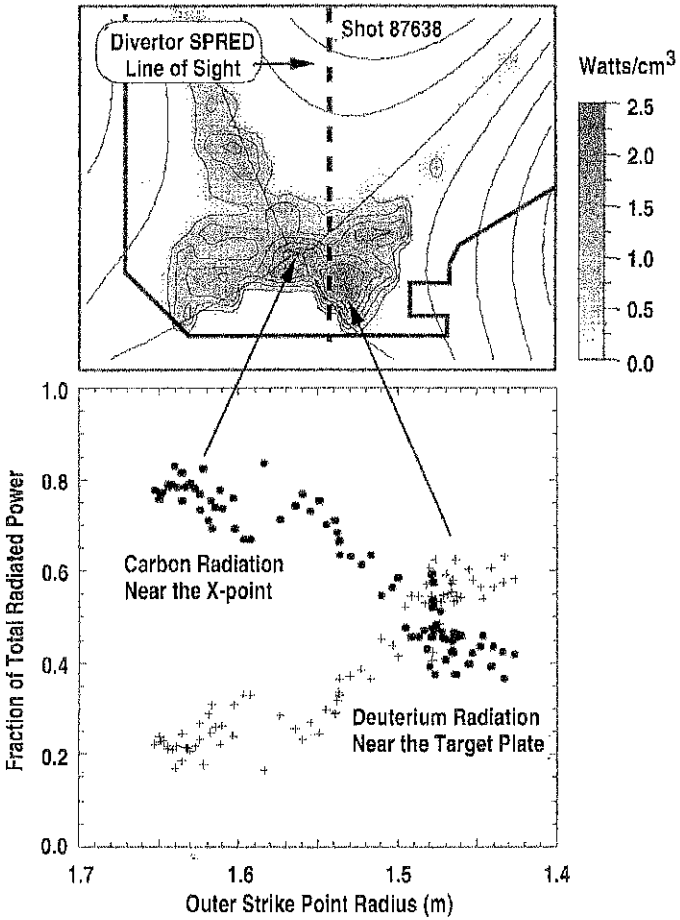

Fig. 2. (Top) Two-dimensional radiated power density distribution from reconstructed bolometer data obtained at 3800 ms during a sweep of the divertor plasma. (Bottom) Reconstructed spatial variation of SPRED data showing carbon (circles) and deuterium (+'s) power fraction as a function of outer strike point location. The divertor plasma was swept across the divertor floor such that the axis of the vertically viewing diagnostics intercept the divertor region from the X–point, then along the outer leg to the outer strikepoint. Near the X–point most of the radiation is emitted from carbon (80%) with the balance from deuterium; near the target plate deuterium radiation dominates (60%).

MODELING OF IMPURITY SPECTROSCOPY IN THE DIVERTOR AND SOL OF DIII-D USING THE 1D MULTIFLUID MODEL NEWT1D*

W.P. West, T.E. Evans, N.H. Brooks, M.E. Fenstermacher,† S. Hirshman,‡ R.C. Isler,‡
A.W. Leonard, G.D. Porter,† M.R. Wade,‡ D.G. Whyte,Δ R.D. Wood†

General Atomics, P.O. Box 85608, San Diego, California 92186-9784 U.S.A.

NEWT1D, a one dimensional multifluid model of the scrape-off layer and divertor plasma, has been used to model the plasma including the distribution of carbon ionization states in the SOL and divertor of ELMing H–mode at two injected power levels in DIII–D. Comparison of the code predictions to the measured divertor and scrape-off layer (SOL) plasma density and temperature shows good agreement. Comparison of the predicted line emissions to the spectroscopic data suggests that physically sputtered carbon from the strike point is not transported up the flux tube; a distributed source of carbon a few centemeters up the flux tube is required to achieve reasonable agreement.

Introduction

A basic understanding of the tokamak divertor, including impurity transport, is required in order to develop predictive capability for future high power tokamak divertors. However the strong spatial gradients in the divertor and SOL plasmas make detailed understanding difficult, both theoretically and experimentally. Benchmarking the complex codes used to model the divertor plasma against data from present day diverted tokamaks is key to assuring a detailed understanding of the plasma transport and to providing predictive capability. To date, 2D modeling codes that include impurities require long run times on even the fastest workstations, and therefore are not easily used for analysis of experimental results. The relatively simplistic approach of a 1D model has obvious shortcomings, failing to address rigorously radial plasma transport and the inherently 2D (or even 3D) problem of neutral transport. However the NEWT1D multifluid code handles impurities implicitly, and converges quickly. Here we have used the 1D modeling of impurity spectroscopy to yield some insight into the distribution of carbon ions in the divertor. The model provides detailed information on both the plasma parameters and impurity ionization state distribution along the flux tube just outside the seperatrix, where the plasma temperature and density is highest in the divertor. The plasma parameters and calculated impurity line emissions can be compared directly to DIII–D data.

The discharges used in this work are a part of recent experiments on DIII–D focusing on characterizing the divertor and SOL plasma in great detail using divertor and midplane Thomson scattering, fixed and plunging Langmuir probes, bolometry, IR cameras, and visible and VUV spectroscopy.[1] Here, the data from a set of attached ELMing H–mode discharges at two injected beam power levels, 3.1 MW, and 8.4 MW, are compared to the output of the NEWT1D model. Matching the poloidal distributions of plasma electron density and temperature and the midplane values of electron density and temperature and ion temperature gives confidence that the parallel impurity transport (dominated by flow friction, ion temperature gradient force, and pressure gradients) simulated in the code is representative of the transport expected in these plasmas.

The NEWT1D Model

The NEWT1D code is a multifluid model of a single open field line flux tube from the midplane to strike plate of a diverted tokamak. The model includes the momentum and energy balance between the electron fluid and the ion fluids; impurity and neutral radiation is treated as a loss term for the electron energy balance. Particle and momentum balance are treated independently for the primary ion and each impurity ionization state, however all ion fluids are assumed to be at the same temperature. The code is capable of modeling up to three impurity species simultaneously; in this work only carbon has been studied. A choice of parallel transport models is available, either a Braginskii model[2] or the Hirshman-Sigmar formulation.[3] In this study, only the Hirshman-Sigmar model has been used. The magnetic geometry of the flux tubes are obtained from the EFIT magnetic equilibrium reconstruction code.

*Work supported by U.S. Department of Energy under Contract Nos. DE-AC03-89ER51114, DE-AC05-90OR22464, and W-7405-ENG-48.
†Lawrence Livermore National Laboratory.
‡Oak Ridge National Laboratory.
ΔINRS—Energie et Materiaux.

The primary inputs to the code are: (1) power (ion and electron) and particle fluxes from the core plasma into the flux tube, (2) primary ion recycling coefficent, (3) impurity recycling coefficient (= zero), (4) a multiplier for impurity sputtering temperature dependence (the impurity sputtering rate is adjusted according to the electron temperature at the plate) was kept fixed at 0.01, (5) impurity gas puffing along the flux tube as described below. Perpendicular transport is included as an ad hoc loss term, and is specified in the input by transport coefficients and a radial scale length. The midplane end of the flux tube is a stagnation point. At the strike plate, all ion fluid velocities are assumed equal to the primary ion sonic velocity. The ionization, recombination, and total radiation rates are obtained from the ADPAK data base.[4]

Modeling the spectroscopic data is done in a post-processing mode. The impurity ion density and excitation rate distributions along the flux tube are mapped onto the geometry of the spectrometer viewing chords on DIII–D and line integrated emissivities are calculated. The excitation rates at the electron densities and temperatures along the flux tube are obtained from a collisional-radiative model of the CII, CIII, and CIV ions.[5] In these discharges the dominant impurity is carbon, being the order of 2% of the electron density. In the model, the carbon sources, sputtering at the strike plate and neutral injection at selected locations along the flux tube, are adjusted until reasonable agreement is obtained with the visible and VUV spectroscopic data.

The Experimental Data

The DIII–D tokamak, with an extenisve set of divertor diagnostics and a flexible and dynamic plasma shape control system, is suited to detailed characterization of the 2D structure of the divertor plasma.[1] Diagnostic chords of divertor Thomson scattering and visible and VUV spectrometers pass through a central region of the divertor floor, and the X–point and strike points are swept past these chords as a function of time during the discharge. This sweep also provides a detailed picture of the electron density and temperature at the strike points as they are swept past fixed position domed probes. At the midplane detailed measurements of the electron density and temperature are obtained with the core Thomson scattering system and ion temperatures with the Charge Exchange Recombination Spectrscopy (CER) system. All of these data are mapped onto the flux tube geometry using the EFIT magnetic reconstruction code.

The VUV emissivity data from 100 to 1100 Å is obtained with an absolutely calibrated vertically viewing SPRED spectrometer, having a viewing width of 8 cm at the floor of DIII–D.[7] An integration time of 50 ms was used. In all of the data shown, the variation due to the ELM's has been included in the averaging.

Comparison of the Model to the Data

The measured and calculated electron density and temperature as a function of normalized poloidal length from the strike plate, over the region of the outer divertor leg, is shown (Fig. 1) for both the high and low injected power cases. Some of the important discharge characteristics and the model input parameters are in Table 1.

Table 1 Plasma Parameters	High Power	Low Power
Injected Beam, Total Radiated, Dvertor Radiated Power (MW)	8.4, 4.2, 2.8	3.1, 1.6, 1.0
I_p (MA), q_{95}	1.4, 4.8	1.4, 4.5
$\langle n_e \rangle$ (m^{-3})	6.2×10^{19}	7.0×10^{19}
Code Inputs:		
Electron Ion Input Power (MW)	1.96, 2.94	0.25, 1.60
D^+ Particle Input (s^{-1}), Recycling Coefficient	1.1×10^{22}, 0.987	8.0×10^{21} 0.987
Carbon Sputtering Coefficient (multiplier)	0.003 (0.01)	0.002 (0.01)
Neutral Carbon Injection Rate (s^{-1})	1.2×10^{20}	7.5×10^{19}

To compare the calculated electron densities and temperatures along the outer divertor leg, the Thomson scattering points are mapped onto ($\psi_{norm} = \psi - \psi_0 / \psi_{sep} - \psi_0$) and L_{norm}=poloidal length from plate/X–point to the strike point length. The data within a ψ_{norm} range of 1.003 to 1.007 are bin averaged over L_{norm} = 0.125. To obtain better statistics data from three repeat discharges have been averaged together. Langmuir probe data at the strike plate and core Thomson scattering and CER data at the midplane at a ψ_{norm}= 1.005 have been chosen for comparison to the model. The error bars shown in the Thomson scattering data are representative of the scatter in the data over which the averaging was done, and are much larger than

the error in each Thomson scattering data point. This scatter is typical of divertor and SOL data during ELMing discharges.[6]

As can be seen, the modeling code does a reasonably good job of matching the data. Notable is that the rapid drop in the electron density away from the plate predicted by the code, due to the recycling neutral source, matches reasonably well with the Langmuir probe measurements at the plate and the Thomson scattering points just above the plate. Table 2 compares the plasma data at Ψ_{norm}= 1.005 at the midplane with the code predictions. Ion temperatures significantly higher than the electron temperatures are routinely seen in the model and in the data. To match the CER data a distribution of power flux favoring the ion channel was required in the code (Table 1). In the low power case, it was not possible to increase the midplane ion temperature up to the measured value while keeping the total power flux at a reasonable level and maintaining agreement with the divertor plasma density.

Figure 2 shows a comparison of the measured line emissivities to simulated emissivities for both the high and low power beam injection cases and for two neutral carbon source models: 1) sputtering only, dashed line, and 2) sputtering plus carbon neutral injection along a 5 cm length of the divertor leg above the strike plate, solid line. The data is plotted as the measured line emissivities versus ΔR_{sep}, the distance between the radial location of the outer strike point and the position of the viewing chord on the divertor floor, and similarly for the model. The agreement for line emission intensities of CII, III and IV and the spatial distributions of CIV is reasonable. The model indicates that the dominate source for CII and CIII line emission is the sputtered carbon. However for CIV, line emission from carbon that exists well above the strike plate contributes strongly to the modeled signals, resulting in a significant difference between the two cases with and without neutral carbon injection.

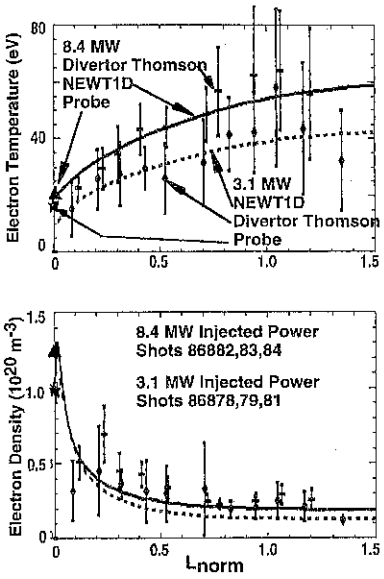

Fig. 1. Comparison of the NEWT1D simulations to the measured plasma electron temperature and density along the divertor leg from the strike plate to near the X-point. The data are plotted as a function of the normalized poloidal distance, defined in the text. The crosses (8.4 MW) and diamonds (3.1 MW) with error bars are the Thomson scattering data, as describe in the text. Langmuir probe data are plotted at L_{norm}=0.

Table 2	8.4 MW			3.1 MW		
	n_e 10^{19} m^{-3}	T_e eV	T_i eV	n_e 10^{19} m^{-3}	T_e eV	T_i eV
Simulation	1.9	66	233	1.3	47	180
Plasma Data	1.7(0.16)	65(6)	230(50)	1.0(0.1)	40(4)	240(50)

Discussion

NEWT1D code gives remarkably good agreement with the measured divertor plasma parameters in two ELMing H-mode plasmas at two different heating powers using input parameters consistant with the operating conditions. The measured electron density and temperature near the strike plate, and their poloidal gradients, as well as the ion temperature at the midplane, are in good agreement with the simulations.

The measured CII and CIII spatial distributions are broader than the model predictions, which is not surprising since the these ionization states should be dominant in the colder, less dense outer regions of the divertor and SOL which are not modeled. To accurately model these regions requires a 2D code. The spatial

distribution of the CIV emission predicted by the code, which is likely to come predominately from the hot, dense part of the SOL nearest the sepratrix, matches the data reasonably well.

In both the high and low power simulations, considerable sputtering from the divertor strike plate results in very little carbon transported to the midplane. To achieve a level of CIV line emission observed in the experiment, neutral carbon must be injected into the flux tube well above the recycling zone. Similar conclusions were drawn by Matthews et. al.[8] and Krieger et. al.[9] using Monte Carlo techniques for modeling carbon spectroscopy on JET and ASDEX-Upgrade. Stangeby and Elder[10] provide an in-depth discussion of the transport physics in the recyling zone that leads to the entrainment of sputtered impurities. Near the plate in the strong recycling zone, the strong flow of the primary ion fluid toward the plate provides a strong frictional push on the impurity ions. If the sputtered neutrals are ionized before escaping the recycling zone, they are trapped at the plate. However, just above the plate the frictional force is significantly reduced and the ion temperature gradient force pushes the impurity ions toward the midplane. Stangeby and Elder refer to processes that lead to such neutrals as "deep injection" These results indicate the importance of neutral transport. More complete simulation of carbon in a tokamak plasma will require a more physically realistic model of neutral carbon (or hydrocarbon) generation.

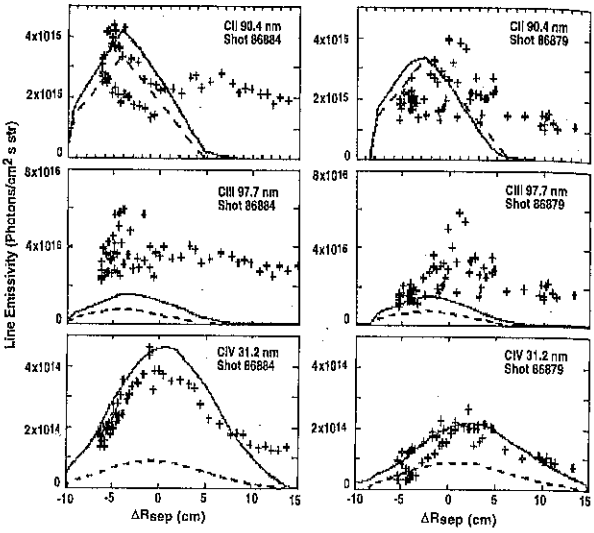

Fig. 2. Comparison of the simulated and measured line emissivities for CII, III, and IV VUV lines for the 8.4 MW and 3.1 MW ELMing H–modes. Crosses are the measured values. The solid (dashed) lines are for the simulation with (without) neutral carbon injection along a 5 cm poloidal length of the flux tube just above the strike plate. Both simulation cases include sputtering.

[1]M.E. Fenstermacher, *et al.*,"Comprehensive 2D Measurements of Radiative Divertor Plasmas in DIII–D," Proc. of 12th Conf. Plasma Surface Interactions, St. Raphael, France 1996.
[2]S.I. Braginskii, Revof Plasma Physics, Vol 1. Ed. M.A. Leontovich, New York (1965).
[3]S. P. Hirshman, Phys Fluids **20**, 589 (1997).
[4]R. A. Hulse, Nucl Techn/Fusion **3**, 259 (1983).
[5]R.C. Isler, *et al.*, "Spectroscpic Characterization of the DIII–D Divertor," to be submitted to Physics of Plasmas, 1996.
[6]R. Moyer, *et. al.*, "The Role of Turbulent Transport in DIII–D Scrape-off Layer and Divertor Plamsas," Proc. of 12th Conf. Plasma Surface Interactions, St. Raphael, France 1996.
[7]R. W. Wood, this conference.
[8]G.F. Matthews *et. al.*, Nucl Mater **196–198**, 374 (1992).
[9]K. Krieger, *et. al.*, Nucl Mater **220–222**, 548 (1995).
[10]P. C. Stangeby and J.D. Elder, Nucl Fusion **35**, 1391 (1995).

CONTROL OF PLASMA EDGE VIA BIASING IN TOKAMAK TF-2

V.P. Budaev

Institute for High Temperatures of the Russian Academy of Sciences,

Scientific Station. 720049, IVTAN, Bishkek, Kyrghyzstan, CIS

INTRODUCTION

To control confinement in tokamak , the mechanisms that induce turbulent transport in edge should be identified. There are conceptions [see, f.e., 1] that consider the tokamak turbulence to consist of a few types of turbulences having got different physical nature, frequency and wave number spectra. The types react differently on dynamic changes of the discharge condition, impurity and working gas puff, the intensity of every type depends on small radius. It was observed on tokamaks the suppression of edge turbulence causes by setting up a radial electric field at plasma edge [2]. The aim of this study is to analyze the experimental data of small-scale tokamak TF-2 edge turbulence with respect to identifying the types of the edge plasma fluctuations observed and how these types of fluctuations change trough setting up the biasing in edge plasma.

EXPERIMENTAL RESULTS AND DISCUSSION

The experiments were performed with ohmically heated limiter discharges in small-scale tokamak TF-2, R=0.23 m, r=0.04 m , $B(_{r=0})$=1T (corresponding to the safety factor q=3.6), I_{pl}=6 kA, n_e=2-3 10^{19} m^{-3} T_{e0}=0.2-0.3 keV [3]. A radial electric field was driven by cross-field current from an insulated molybdenum electrode positioned 1 cm inside to the Last Closed Flux Surface (LCFS) at the outer side of tokamak vessel that was earthed and connected with ring limiter. Electrode (normally floating) has got 0.12 cm^2 surface perpendicular to the magnetic field. Negative biasing of electrode (-500 V with respect to the vessel) was performed in steady state of tokamak discharge. Changes in edge plasma parameters (ion saturation current, poloidal electric field, turbulence driven flux) into outerboard Scrape-Off-Layer (SOL) and inside LCFS were measured making use movable probe array that allows measure the edge plasma time-averaged parameters and fluctuations (with bandwidth 1<f<500 kHz) of density n (determined from the probe ion saturation current I_{sat}), floating potentials φ_n, electron temperature T_e. Two poloidal spaced probes allow poloidal electric field E_p to be estimated from difference in φ_n (assuming T_e is time invariant). The poloidal phase velocity of the fluctuations has been obtained from the phase difference between I_{sat} signals measured in the same poloidal section and 4.5 mm apart

Fluctuation level n_{rms}/n is reduced by 20-30% with the biasing in shear region (fig. 1b). Fluctuation-induced particle flux Γ_r~<nv> is also reduced by ~2 times in the shear region and SOL (fig. 1c). Frequency spectra of fluctuation in the shear region and SOL are less broader with biasing (fig.2). In the

SOL fluctuations propagate in the ion diamagnetic direction and inside LCFS they propagate as a whole in the electron one (fig. 1d). The inversion of the poloidal velocity of the fluctuations is observed near LCFS (shear region). Setting up the biasing -500 V affected the location of the shear layer and, in turn, the edge fluctuation characteristics. Poloidal wave numbers change significantly as in SOL also inside LCFS in biasing phase (fig. 3a,b,c).

At the SOL in floating phase as a whole two different parts of the dispersion relation can be distinguished in the two point estimation of the conditional spectrum S(k,w) (fig. 4a) : (1) with frequency below ~30 kHz the fluctuations propagate in the ion drift direction, correlation length of their fluctuations is about 15-20 mm (denoted as "i"-mode); (2) turbulence of higher frequency (~100 kHz) propagates in the electron drift direction with poloidal correlation length ~10 mm (denoted as "e"-mode). Like this bimodal structure was observed in different tokamaks and stellarator [4-7]. We observed also "i"-mode fluctuations with ~4 mm correlation length in bandwidth 100-200 kHz. The biasing resulted in broader "e"-mode and no significant changes in "i"-modes in the SOL, density is decreased over float phase values by ~20% (fig 1a).

In the shear region near LCFS the mentioned above bimodal structure is also observed in floating phase with higher intensity of "e"-mode shifted in the frequency bandwidth 50-100 kHz (fig. 4b). The biasing leads to the dumping of "i"-mode with high frequency 200-300 kHz and enhancement of "e"-mode. Change in k-spectra is observed in biasing phase. Both in floating and in biasing phase poloidal propagation velocity of the fluctuations reverses over a layer extended radially ~0.3 cm (fig. 1d). The scale ~0.3 cm of shear region was also found on the large-scale tokamak (PBX-M [8] as in L- also in H-modes) indicating the scale of shear region is not appear to depend on the tokamak scale. Fractal dimensionality in the shear region TF-2 in biasing phase is decreased from ~7 to >10 indicating the higher disorder of turbulence [3]. The higher decorrelation leads to the reduction in the turbulence induced transport in biasing phase.

Inside the LCFS, r/a=0.88, "e"-modes are mainly present with poloidal correlation length ~4 mm and ~20 mm The "i"-mode intensity is low in this region in floating phase, this mode is suppressed by the biasing. Meanwhile small-scale ion modes in the frequency region <30 kHz do not suppress by biasing (fig. 4c, 6). High coherent mode at 150-250 kHz, that was observed in float phase inside LCFS at r/a=0.88, was destroyed by biasing (fig. 5,6). This mode has $k_\theta \leq 0.4$ cm^{-1} indicating that oscillations have poloidal mode number $m \leq 10$, it propagates in electron drift direction and its velocity the order of magnitude as local E×B drift velocity.

In conclusions, in edge of TF-2 the crucial processes in turbulence multi-modal structure were observed through the setting up the negative (-500 V) biasing experiment.The biasing affects the location of the shear layer. Inside LCFS the modes, that propagate in to ion diamagnetic drift direction and have

large correlation scale ~2 cm, are suppressed significantly by the biasing, meanwhile small-scale (<0.5 cm) ion modes do not suppress.

Author is grateful for TF-2 staff in making the experiment possible. The research was supported by RF Ministry of Science and Technical Policy and by Grant N51000 from the ISF.

References

1. V A Vershkov. 22nd EPS Conf Contr Fusion Plasma Phys. Bournemouth,1995,19C,IY,005. Fonk R. Report at APS Meeting, St. Lois (1993).
2. R.R. Weinants et a. 17th EPS Conf., Amsterdam, 14B,p.287 (1990); R.J. Taylor et.a. Phys.Rev. Letter, 63, p.2365 (1989).
3. V Budaev et al.21st EPS Conf Contr Fus Plasma Phys, Montpellier,V18B,I, 170 (1994)
4. V Vershkov e a.21st EPS Conf Contr Fus PlasmaPhys, Montpellier,V18B,II,998(1994)
5. M.A. Pedrosa et al. 22nd EPS Conf Contr Fus PlasmaPhys,V19C,I,305(1995)
6. R.D. Durst et. al. Phys.Rev. Letter, 71 p.33135(1993).
7. T.P. Crowley et.al. Nucl. Fus. 32,1295 (1992).
8. G.R. Tynan et.al. Phys. Plasmas. 1,(10), p.3301(1994).

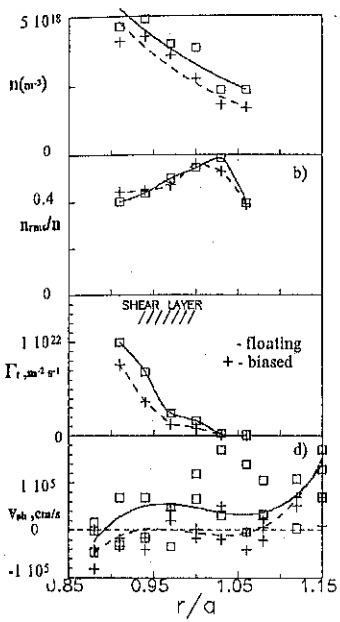

Fig. 1 Radial profiles of density n (a), n_{rms}/n (b), turbulence induced flux $\Gamma_r=<nv>$ (c) and poloidal phase velocity of fluctuations (d) in floating (boxes) and biased (crosses) phases.

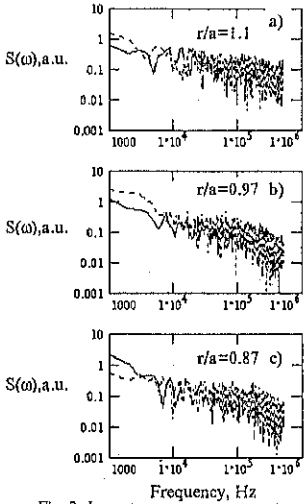

Fig. 2. Ion saturation current spectra for radial probe position in SOL (a), in shear region (b), inside LCFS (c) for floating (solid) and biasing (dashed) phases.

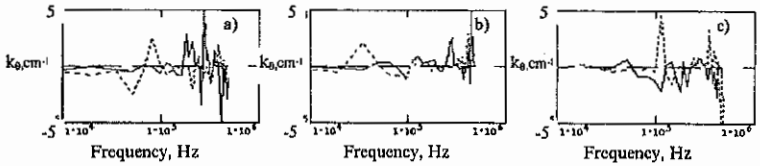

Fig. 3. Poloidal wave number k_θ for SOL (a), shear region (b) and inside LCFS (c) , floating (solid) and biasing (dashed) phases.

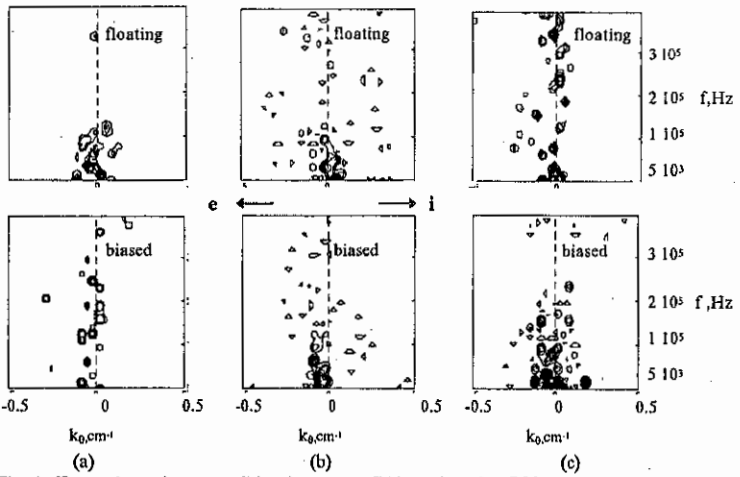

Fig. 4. Two-point estimate conditional spectrum $S(k_\theta, w)$ at the SOL (a), shear region (b) and inside LCFS (c) for floating and biasing phases.

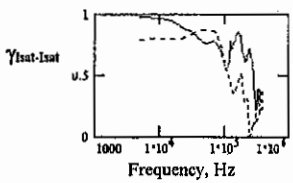

Fig. 5. Coherencies for I_{sat}-I_{sat} signals of probes separated poloidallyby 4.5 mm at r/a=0.88. Solid-floating, dashed - biased phase.

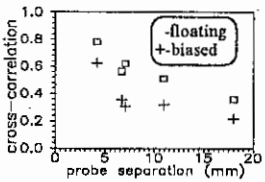

Fig. 6. Maximal cross-correlaton coefficient I_{sat}-I_{sat} fluctuations vs. probe poloidal separation. Inside LCFS, r/a=0.88, boxes-float, crosses - biased leads to the suppression of long-scale correlations > 5 mm.

Classic-like I-V Characteristics of swept Langmuir probe and measuring edge plasma electron temperature

L.M. Bogomolov

Institute for High Temperatures of Russian Academy of Sciences
Scientific Station in Bishkek, 720049, IVTAN, Bishkek, Kyrgyzstan, CIS.

1. Introduction.

Langmuir probes are widely used in tokamaks to monitor the electron density and the temperature of edge plasmas. Some methods of Te measurements (for example, double harmonic method [1], swept probe method [2]...) give rather reasonable results that, at least, do not contradict to other data about edge temperature. However, the traditional interpretation of Current-Voltage Characteristics (I-V Ch) of probe operating in tokamak conditions has a little chance to be correct. Present studying has been aimed to explain why the probes can give reasonable results about edge plasma parameters at all. The question is related to the problem of mechanism driving radial electric current that must close the circuit of positively biased probe.

Recent [3,4] and present studies have demonstrated that dynamical I-V Ch are similar to well-known I-V Ch of Langmuir probe in unmagnetized plasma provided the rate of voltage ramping is high enough and the impedance of the generator used for biasing is low enough. Like to classical I-V Ch dynamical I-V Ch observed appears to have explicit electron branch, the ratio of electron-to-ion saturation currents reaches 20÷35, meanwhile usual quasystationary I-V Ch resulting from slow voltage ramping gives the value of this ratio less than 10 [5,6]. The comparative analysis of dynamical and quasystationary I-V Ch obtained on TF-2 tokamak allows to generalize the methods of Te determination from I-V-Ch and to remove some doubts concerning their inaccuracy. Besides that the new method of Te computation has been proposed.

2. Experiment

Experimental investigation of dynamical I-V Ch has been held on TF-2 tokamak (R= 23,5 cm; a= 3,5 cm; $B_T \cong 1$ T; I_{pl} = 6÷ 10 kA), typical density and electron temperature of edge plasma being respectively $n \cong 3 \div 7\ 10^{12}$ cm^{-3}, Te = 10÷ 20 eV. Radially moveable Langmuir probe (Ø1 mm tungsten wire, collecting area S_p =3mm^2) is installed on the outside midplane 0,4 mm away from the limiter ion side. The plate electrode (10×2 mm^2) can be located near probe (the distance along magnetic line is about 6mm) or can be shifted out of plasma. The plate and the wire form Pin-Plate Probe system that, according to [5], allows to verify Te measurements made by single probe. TF-2 tokamak is equipped by the ring poloidal limiter, which may be electrically connected to the wall of vacuum vessel or be isolated. During experiments the limiter and the vessel wall have been earthed independently via measuring transformers, the currents flowing to the limiter and to the wall have been recorded as well as the probe current. The capacitor system forming powerful pulse of unipolar ramping voltage (0÷200 V) or bipolar ramping voltage (-150÷70 V) is used for biasing. The duration of ramping varies from 20 to 1000 μs. Sinusoidal AC generator is used also to supply thin probe by 200 kHz AC voltage, the amplitude being 50 V. The signals have been recorded by conventional ADC with time-discretization 25 ns (in the case of fast ramping) or 1μs (in the case of slow ramping).

Fig.1 represents the plots of dynamical I-V Ch of probe located in SOL at the depth r/a=1.05 and outside SOL at r/a=0.95. The plots are similar, they have intervals of quasyexponential current growth. Unlike to quasystationary case the point of inflection, where $d^2I_p/dU^2=0$, can be localized. To the right from inflection point on I-V Ch the current continues to growth. This is related to density growth, i.e. density profile

modernization (biasing effect). To the left of this point the probe operates in measuring mode: electron temperature may be extracted from any local part of dynamical I-V Ch provided polarization current effects are taken into account (see below).

Measurements of currents closing the probe current I_p have shown that I_p is devided to longitudinal current I_L flowing to poloidal limiter along magnetic lines and radial current I_W flowing to vacuum vessel wall across magnetic field, $I_p = I_W + I_L$ (fig.2). The proportion between I_L and I_W depends on the voltage biased rather than probe radial position. The maximum correlation between I_p closing via wall current I_W ($C(I_p, I_W) \approx 0{,}9$) is found to take place at the beginning of positive voltage ramping, when $U < 20{+}40$ V. The maximum correlation between I_p and limiter current I_L corresponds to relatively large voltage biased, $U \geq 60$ V. In terms of correlation Fourier spectra this reads as follows- I_p , I_W cross-correlation reaches its maximum at higher frequency than I_p, I_L cross-correlation. The response in I_W compensating fast growth of probe current occurs due to polarization current [3].

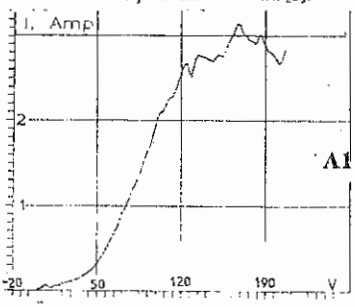

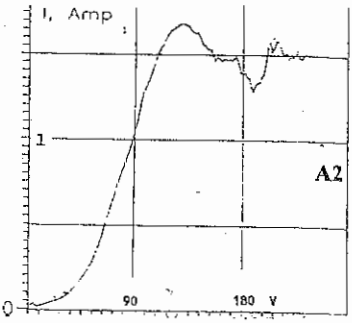

Fig.1 Examples of I-V Ch : A1 - Dynamical I-V Ch of pin probe in main plasma (r/a = 0.95 ; $\dot{U} \cong 2\ 10^6$ V/s ; $S_p \cong 3$ mm^2), A2 - Dynamical I-V Ch of the same probe in SOL plasma, r/a = 1.05 ; B - I-V Ch of Plate Electrode, $\dot{U} \cong 2\ 10^5$ V/s ; $S_p \cong 40$ mm^2 r/a = 0.95

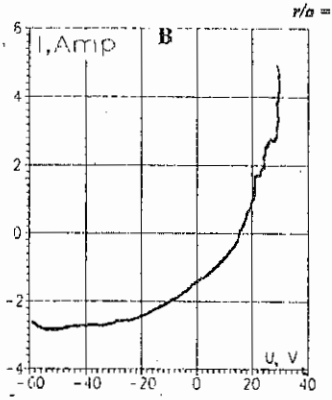

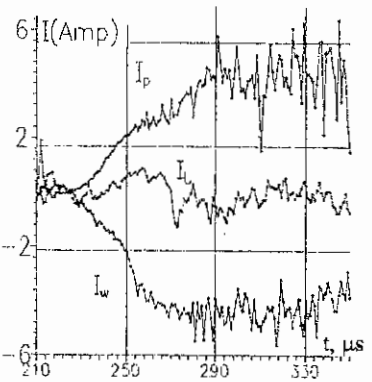

Fig. 2 Responses of currents I_W , I_L closing the circuit of I_p during probe current growth. Response of I_L has a delay

3. On the T_e determination.

The measuring part of I-V Ch is proved to be similar to I-V Ch of equivalent layout (fig3) modeling the division of voltage biased by sheath/presheath drop (the voltage on nonlinear Cunkel-Guillary resistance) and plasma layer drop driving radial current. In the case of fast voltage ramping the capacitance describing polarization currents plays the main role, in the case of slow ramping $R_\perp$ is the main. The capacitance C is related to polarization frequency ω_p introduced in [3] as follows

$$C = I_s / (T_e \omega_p) = I_s / (T_e \omega_{ci}) \rho_i L_\parallel / S_p , \qquad (1)$$

(I_s - ion saturation cufrent , ρ_i - ion gyroradius, S_p - probe area). No relation for $R_\perp$ exists, thus we try to evaluate $R_\perp$ as well as T_e from experimental data. Following expressions are valid, when the rate of voltage ramping is high

$$T_e = (\dot{U} \dot{I} / I - \ddot{U}) [(2 + I_s /I) \dot{I}^2 / (I + I_s)^2 - \ddot{I} / (I + I_s)]^{-1} , \qquad (2)$$

$$\omega_p = (I_s /I) [\dot{U} / T_e - \ddot{I} / (I + I_s)] \qquad (3)$$

(index p denoting probe current and voltage is omitted). In other case, when the ramping is slow, T_e and $R_\perp$ may be evaluated as follows

$$T_e = (U \dot{I} / I - \dot{U}) [\ln (1 + I / I_s) - \dot{I} / (I + I_s)]^{-1} , \qquad (4)$$

$$R_\perp = U / I - (T_e / I) \ln (1+ I/ I_s). \qquad (5)$$

(Expressions (2-5) result from consideration of layout shown on fig.3) A nondesirable factor, namely the small difference between big quantities, stands in above formulas near floating point. But in the limit $I \to 0$ they become to known expression $T_e = \dot{U} I_s / \dot{I}$ or, in the form coinciding with detector effect analysis result [4]

$$T_e = (dI / dU) / (d^2I / dU^2) = \dot{U} (\ddot{I} / \dot{I} - \ddot{U} / \dot{U})^{-1}, \qquad I_s = \dot{I} (\ddot{I} / \dot{I} - \ddot{U} / \dot{U})^{-1} \qquad (6)$$

The results given by (2-6) have been compared with reference measurements of T_e made with the help of Pin-Plate system recording sheath drop directly. At any point of I-V Ch reference T_e is determined by the expression $T_e = (\dot{U}_{plate} - \dot{U}_{pin})(I+ I_s) / \dot{I}$. Fig.4 represents the example of T_e time dependence determined by Pin-Plate system. The comparison has pointed to intervals where (2-6) actually give correct results. In the case of slow voltage ramping the accuracy of (4) is satisfactory at moderate negative probe voltage. U≅-30 + -10 V. Meanwhile the evaluation of T_e by single probe signals $T_e = (dI / dU)^{-1} (I + I_s)$ is proved to correspond the measurements by Pin-Plate probe as long as the probe voltage is negative or small positive, U< 10 V.In the case of fast voltage ramping formula (2) has inaccuracy less than 20 %, when the probe current is not small (apart from floating point on I-V Ch). But the best accuracy of T_e determination is reached by using formula (6) near floating point of dynamical I-V Ch. Fig 5 shows how the frequency ω_p determined by (3) depends on U. The evaluation $\omega_p \sim 2 \cdot 10^5$ 1/c obtained at U≥ 20 V corresponds the theory [3]. The enhanced value of ω_p given by (3) at low voltage biased speaks in a favour that $L_\parallel$ (the toroidal length of region around probe where radial currents flow to the wall) is less significantly than toroidal circumference length.

References

[1] Ivanov R.S,Chemilevsky A.V. et. al., *Physics Letters*, A173, 288 (1993)

[2] Hidalgo C, Balbin R et.al.,*19 th EPS Conf.on Contr. Fusion and Plasma Phys., Innsbruck*. pt.II, 783 (1992).

[3] Bogomolov L.M.,Nedospasov A.V. et.al., *Proc. of 21st Int. Conf. on Phenomena in Ionized Gases*, pt.II, 353 (1993), Bochum.

[4] Bogomolov L.M. et.al.,22 *nd EPS Conf.on Contr. Fusion and Plasma Phys., Bournemouth*, pt.III, 329 (1995).

[5] Stangeby P.S. Preprint JET-P(95) 21 (1995).

[6] Guenther K., Herrman A. et. al., *J. Nucl. Mater.*, 176 &177, 236 (1990).

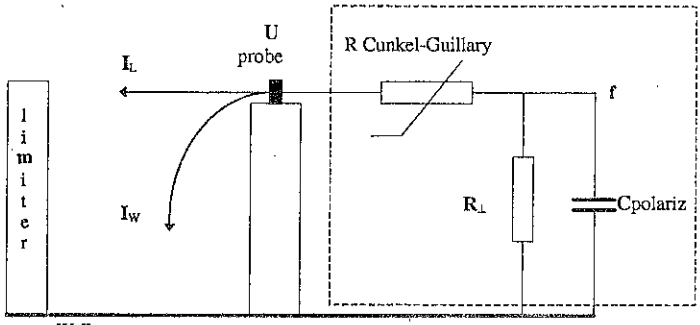

Fig. 3. Equivalent layout of Langmuir probe current, Usheath=U-f.

Fig.4 Example of T_e fluctuations in TF-2 discharge measured by Pin-Plate probe system, r/a =0.95 . The dependence of T_e on time has been obtained by using expression $T_e = (U_{plate} - U_{pin}) / (I_{r,\,plate} - I_{plate}) / I_{plate}$ in all points of measuring part of I - V Ch. The spike of T_e at 200 μs corresponds the minor disruption.

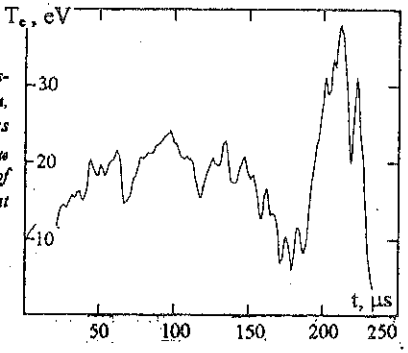

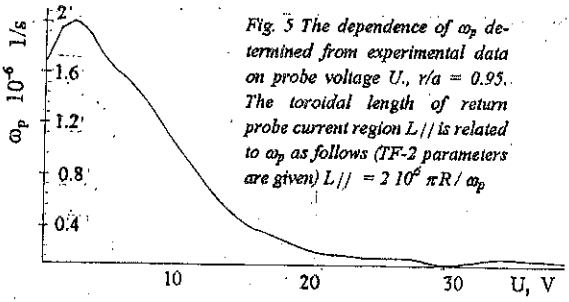

Fig. 5 The dependence of ω_p determined from experimental data on probe voltage U., r/a = 0.95. The toroidal length of return probe current region L// is related to ω_p as follows (TF-2 parameters are given) $L// = 2\,10^6\,\pi R / \omega_p$

Scrape off Layer Plasma Measurements in Lower Hybrid Heating Experiments on FT -- 2 Tokamak

Budnikov V.N., Chechik E.O., Dyachenko V.V., Esipov L.A., Its E.R., **Lashkul S.I.**, Lebedev A.D., Podushnikova K.A., Sakharov I.E., Shatalin S.V., Shcherbinin O.N., Shorikov V.Yu., Stepanov A. Yu.

A.F. Ioffe Physical-Technical Institute, 194021, St.-Petersburg, Russia.

In the lower hybrid heating experiments on FT-2 tokamak (a = 8 cm, R = 55 cm, B_T = 2.2 T, I_p = 22 - 40 kA, P_{LH} < 150 kW, f = 920 MHz) the effective heating of ions and electrons associated with the parametric absorption of LH wave, the mechanism of current drive switch off and the origin of the improved energy confinement mode in the post heating phase have been studied [1]. This paper concerns the generalization of the scrape-off layer (SOL) plasma parameter data and their correlation with central plasma behavior in the above mentioned experiments, particularly during L - H transition. Plasma parameters have been studied by visible, UV and VUV spectroscopy; Langmuir and magnetic probes; charge exchange analyzer and bolometer. Besides, the cross-correlation analysis of magnetic probes, microwave reflectometry and enhanced-scattering signals, as well as ASTRA transport code have been used.

The transition in the improved confinement has been observed in the FT-2 experiments after RF pulse switch off [2]. When the RF pulse is turned off, the emission in the H_β line falls down with an increase in the average density and diamagnetic signal; a sharp decrease in the MHD activity and slight decrease in the voltage U_p are also seen. The energy lifetime, equal to 0.8 ms in the ohmic regime (I_p = 22 kA), in the post-heating stage (PLH) increases up to 2 ms and agrees with Kaye-Goldstone and the DIII-JET scaling. The plasma microturbulent analysis in the range of frequency 0 - 500 kHz has been carried out by the enhanced scattering technique and the reflectometery [3]. The enhanced scattering measurements shown the oscillation at the outside torus edge, whereas the reflectometer inspected the inner side. In both cases the maximum fluctuations were observed at the periphery of the plasma. It was found, that already in LHH pulse the essential suppression of plasma oscillations (up to 50%) was observed. The spatial maximum of such suppression was at a discharge periphery at r = 7 cm.. The low oscillation level of the reflectometer signal remained after P_{rf} pulse when transition to improve confined mode happened. Taking into account the lifetime particle rise and

suppressing of the fluctuations, one can suppose that the transport body plasma losses are reduced already during of the LHH. It was found, that the poloidal rotation shear at the plasma periphery can be responsible for the appearance of the improved confinement regime [1]. In the recent experiments with the higher plasma current I_p = 40 kA and P_{LH} = 100 kW the abrupt fall down of H_β line emission has been observed during of HF pulse already. In this case the role of neutral hydrogen influx (from the wall) during the HF pulse diminishes.

The small dimensions of the tokamak and the absence of a feedback system maintaining the plasma equilibrium makes it difficult to achieve a stable state for more than 10 ms in the post LH phase. However, in these cases when it was possible, we observed the ELMs that reveal themselves as outbursts on the H_β line intensity. The Mirnov probes and reflectometer data for H-mode transition and ELMs are shown in Fig. 1. One can see the coherent magnetic precursor oscillation of frequency ν_{prec} ~ (24-32) kHz. Cross-correlation analysis of magnetic probe signals gives poloidal mode m ~ 9 at the resonance magnetic surface q ~ 4,5. Simultaneously with the precursor we observed the growth of the highly turbulent coherent structure by the reflectometer at frequency ν_{prec} ~ (44-62) kHz and m = 9.. It was located mainly near the plasma outside boundary. In the Fig.1 the integral reflectometry signals over (0 - 500) kHz are shown. The oscillations at resonance surface q = 4,5 (r = 6 cm) are registered at the probing o-mode frequency of f_{ref} = 27 GHz. At the experiments on other large tokamaks the same coherent magnetic precursor (with somewhat higher frequency) was observed and characterized as III ELMs type [4]. Their exhibition were explained by the resistive ballooning mode development at the outside plasma toroidal boundary. The energy flux through the plasma boundary in the ohmic heating case was P_{oh} - P_{rad} ~ (30 - 40)kW, where P_{rad} ~ 40% P_{oh}. This value was somewhat lower than the threshold power for a transition to H-mode, calculated by ASDEX's scaling [4, 5]: $P_{thr} = 0.04 \cdot \bar{n}_e \cdot S \cdot B_t$ [MW, m^{-3}, 10^{20}, m^{-2}, T] = 50 kW at $\bar{n}_e = 3\ 10^{19}\ m^{-3}$. So, one can also suppose, that improved confinement begins during RF pulse and then remains after the pulse because of a plasma state hysteresis. The plasma can be in H-state between $P_{thr}^{L\text{-}H} > P_{thr}^{H\text{-}L}$. For the opposite transition from H to L-mode the threshold power is smaller due to broadening of the current-density profile and due to slowing of the hydrogen recycling at the discharge periphery. We have experimental evidence (e.g., the inductive changes in the loop voltage) supported by the calculations carried out with the

"ASTRA" code that the current channel is modified during and after the LH pulse [2].

As was mentioned above, the L - H transition at additional RF heating occurs when the flux through the plasma separatrix achieves the threshold value. Recently the same transition (at I_{pl} = 22 kA) has been obtained in the OH regime only. For this purpose the plasma was leaned to the outside of the torus. The pre-controlled plasma shift of that kind (1 cm range), as Fig. 2 shows, causes the decrease of both H_β line emission and MHD activity, while the average density and ion temperature $T_i(0)$ increase. Plasma temperature T_{eL} and density n_{eL} in the outside limiter shadow measured by Langmuire probe at r = 8.5 cm were higher as compared with the cases when plasma core was in the center (I) or was leaned to the inner side (III). One can notice, that such heating of the outside SOL due to the outside plasma shift leads to longer (without ELM) plasma stage in H-mode. Fig. 3 shows the plasma limiter shadow parameters for both OH and LHH regimes. One can see, that the RF power influences upon SOL plasma parameters differently. In the cases (I) and (III) the outside edge density rise is considerably higher with respect of the outside (II) plasma deposition. One can suppose that the limiter shadow density rise depends upon the additional hydrogen ionization in RF electrical field. Besides the additional RF power losses at ionization in the (I) and (III) cases the density rise near the grill causes the modification of the real spectrum (N_{II}) of the grill launched mode [6]. We have experimental evidence of such processes that are shown in Fig. 3 and Fig. 4. Fig. 3 shows the central ion temperature rise for different plasma core position for P_{RF} = 100 kW. One can see that plasma leaning on the outside wall (where the grill is installed) causes the higher ion temperature increase. The data for two experiments are shown here. In this case the ion energy lifetime is higher by factor 2 also. In Fig 4 the charge-exchange atom energy spectrum for both cases (I) and (II) are shown. When the plasma core is leaned to outside wall, besides the increase of the bulk ion temperature to higher value, the supertermal "tail" region begins from the higher energy values.

The research has been supported by ISF Grant #23000 and RFBR Grant #95-02-04072.

[1] Budnikov V.N., et al, 22 EPS. Conf. on CF and Pl. Phys., V. 19C, p.II, , 085, (1995).

[2] V.N. Budnikov, et al, JETP lett., Vol. 59, No.10, 685 - 689, 25 may 1994.

[3] V.N. Budnikov, et al, Fizika Plasmy, vol. 21, No. 10, 865 - 871, 1995

[4] H. Zohm, et al, Nuclear Fusion, vol. 32, No.3, 481 - 489, 1992.

[5] H. Zohm, et al, Plasma Phys. Control. Fusion, 37, 437 - 446, 1995

[6] V.V. Dyachenko, O.N. Scherbinin, Preprint of IFT Inst., No 755, 1982

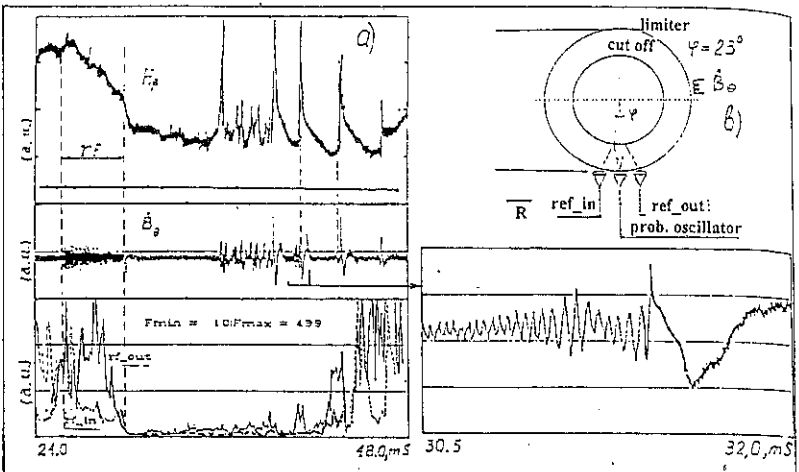

Fig. 1 *Data for H-mode transition and ELM outbursts on the H_θ spectral line. $\dot{B}_\theta$ is Mirnov probe signal; inner chord (rf_in) reflectometer signal is shown by dashed curve. Out chord reflectometer signal (rf_out) is shown by solid curve. The scheme of measuremets is shown in (b).*

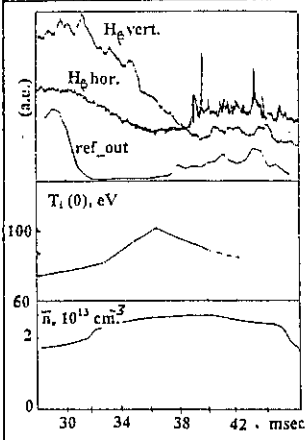

Fig. 2 *Data for the L - H mode transition in the OH regime alone. $H_\theta$vert - along the vertical central chord signal; $H_\theta$hor - the horizontal central chord signal;* ref_out *- out chord reflectometer integ. over (0-500)kHz signal.*

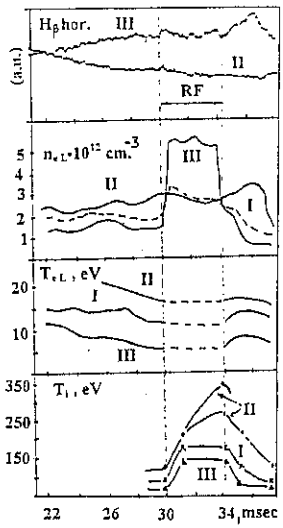

Fig. 3 *Oscilloscope traces and data for different plasma core deposition. I -central, II -outside and III -inner side leaning of the plasma. n_{eL} and T_{eL} -limiter shadow data.*

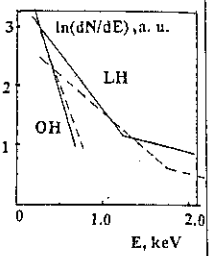

Fig. 4 *Charge - exchange atom spectra along the horizontal chord for different plasma deposi - tions. Here the OH and LHH data are shown. T_i^{OH} = 90eV and T_i^{LH}= 350el' in case* II *-dashed line. T_i^{LH}=250el' in case* I *-solid line*

Acceleration of electrons in the near field of lower hybrid frequency grills

M.Goniche[1], J.Mailloux*, Y.Demers*, D.Guilhem, J.H.Harris**, J.T.Hogan**,
P.Jacquet*, P.Bibet, P.Froissard, G.Rey, F.Surle, M.Tareb

Centre d' études de Cadarache
Association Euratom-CEA
F-13108 Saint Paul-lez-Durance, France
*Centre canadien de fusion magnétique
1804 Boul.Lionel-Boulet, Varennes, Québec, Canada, J3X 1S1
**Oak Ridge National laboratory, Oak Ridge, Tennessee, USA

[1] *Present adress : JET Joint Undertaking, Abingdon, Oxfordshire, OX14 3EA, UK*

1. Introduction

On Tore Supra, during lower hybrid (LH) current drive experiments, localized heat flux deposition is observed on plasma facing components such as the guard limiters of the LH grills [1] or any object which is magnetically connected to the LH launching waveguides : modular low-field side limiters, ion cyclotron heating antennas, inner first wall. Similar observations have been made on the divertor plates and limiters of TdeV [2]. In particular, by alternating the rf power of the 2 grills of Tore Supra, it was shown that the heat flux on the tiles of the guard limiters is related to the local rf electric field but not to the convective power [3]. The following model shows that Landau damping on the thermal electrons occurs in the region near the grill. Results of this model are compared to experimental results.

2. Model

We will consider the trajectory of the guiding center along the field lines, in a 1D model. Electrons are supposed to be driven only by the oscillating electric field and any electrostatic fields are neglected. In the near-field approximation, waves of amplitude E_n and phase φ_n excited by each individual waveguide n do not interfer and the particle responds successively to the discrete values of the electric field when travelling along the array of waveguides. This assumption is valid only for a very thin layer (few mm) at the antenna aperture. In such

conditions, the equation of motion of an electron traveling from one side of a waveguide to the opposite side is simply $\frac{d^2z}{dt^2} = \frac{(-e)}{m} E_n \cdot \sin(\omega t + \varphi_n)$, where E_n and φ_n are the amplitude and the phase of the electric field excited by the waveguide n. If only the fundamental TE01 mode is considered, E_n and φ_n are constant in front of a waveguide and integrating twice the equation of motion leads to a set of non-linear equations which can be easily numerically solved to obain the final speed and the phase of the electron with respect to the wave. Starting from an initial random phase and a Maxwellian velocity distribution (E=25eV), the final energy distribution is obtained by a nw-step iterative method, where nw is the number of waveguides in a row.

3. Results of computation

Let us consider first the ideal case where the phasing $\Delta\Phi$ between adjacent waveguides is constant ($\Delta\Phi$=90deg.) and the amplitude is the same for the n=32 waveguides (E=1.3 and 4.5 10^5 V/m). This corresponds to a perfect antenna with no reflection from the plasma. It is convenient to use the normalized velocity $v^*=2v/(b$ ($\omega/2\pi$ is the rf frequency and b the waveguide width). The velocity distribution function $f(v^*)$ is the superposition of the initial distribution (corresponding to the non-accelerated electrons) and a much wider distribution function (Figure 1). For the low electric field case, electrons are accelerated up to 600 eV (v^*=0.11), but for the high electric field case, the distribution function is even wider and the final energy can reach 4.2 keV (v^*=0.30). For the 2 cases, the mean energy of the accelerated electrons is repectively 120 and 620 eV. The latter case can be compared to a plasma-loaded antenna case : for a Tore Supra shot, for which 3.2 MW was launched with 1 of the 2 antennas, the electric field distribution is calculated from the rf measurements achieved at the input of the antenna and the coupling code SWAN. For one of the waveguide rows, the mean electric field is 4.5 10^5V/m (standard deviation 1.1 10^5 V/m) and the mean phasing is 93 deg. (standard deviation 36 deg.). It can be seen that the velocity distribution is modified with respect to the ideal case : mean and maximum energies of the accelerated electrons are reduced to, respectively, 435 and 2200 eV (v^*=0.22).

The near-field approximation is strictly valid only at the antenna/plasma interface. Further in the plasma some smoothing of the electric field occurs. In order to evaluate the effect of the sharpness of the electric field function on the acceleration process, the discrete values of the electric field E_n were linearly linked up on a length d. For d >1mm, the mean acceleration of the electrons falls off rapidly. Accordingly, the high N content (23<N <100), which is related to small scale features, decays (Figure 2).

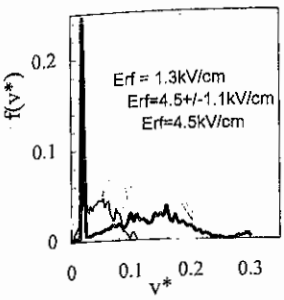

Figure 1. Velocity distribution function for different electric fields

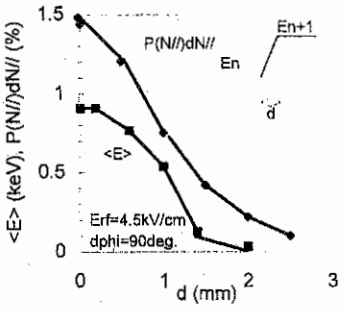

Figure 2. Effect of Erf gradiant on mean energy and high N content)

3 Experimental results

On Tore Supra, the heat flux on plasma facing components connected to the array of waveguides was evaluated in a wide range of RF powers (2-5 MW). In these experiments, the 2 LH antennas were 4 cm from the LCFS and a vertical limiter at the bottom of the vessel was set 2.5cm behind the LCFS in order to intercept low convected flux from the plasma. For qa=6, both antennas are connected to this limiter (ion-drift direction, L =15m). The heat flux on the grill 2 guard limiter and the vertical limiter was calculated in the semi-infinite wall approximation. For one of the 4 rows of waveguides, the electric field Erf, then the mean energy of the accelerated electrons <E> were calculated. Using the BBQ impurity SOL transport code and the CASTEM 2000 finite element thermal analysis code, a self-consistent computation, including the local sheath potential, allows to calculate the enhancement of the heat flux F/Fth when the fast electrons distribution is taken into account. Figure 3 shows the experimental flux, <E> and F/Fth as a function of the mean electric field <Erf>. The measured heat flux on the vertical limiter, up to 1.5 MW/m^2 is lower because the grazing angle (~5 deg.) of the field lines with the surface of this limiter is smaller than for the guard limiter (15-45 deg).

Effect of plasma and SOL densities on the total power lost by this mechanism has been studied in details on TdeV. For a given plasma configuration (single-nul diverted plasma, qa=3.9), the plama density was varied between 2 and 6 10^{19}m^{-3}. In this configuration, with a fixed distance of 1.5cm between the antenna and the separatrix, the antenna is connected to specific divertor plates. A good correlation is found between the edge density and the total losses on the

connected plates (Figure 4). This correlation is weaker when considering the plasma line average density. On Tore Supra, total losses have been measured by thermographic and calorimetric measurements : when the plasma density ranges between 1.5 and 3.5 $10^{19}m^{-3}$, losses are in the 1-2 % range. No edge density measurements were available for these shots but for similar plasma conditions, density in the 0.5-1.0 $10^{18}m^{-3}$ range have been measured.

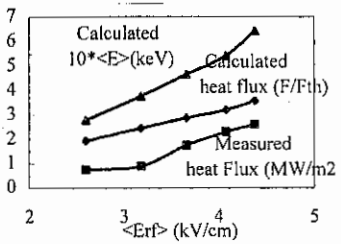

Figure 3. Measured heat flux and calculated acceleration and heat flux

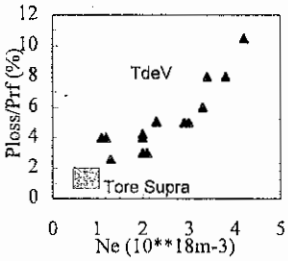

Figure 4. Effect of the density at the antenna on the total ion-drift side losses

4. Conclusion

Acceleration of thermal electrons occurs in the near field of LH antennas up to a few keV. This acceleration arises from small scale variation of the electric field or, equivalently, high N// content of the launched spectrum. A semi-analytical model shows that the acceleration vanishes when no power with N >23 is available. These accelerated electrons provide a heat flux on connected components : for typical electric field strength (4 10^5 V/m), the normal heat flux in the flux tube is estimated to be 4 MW/m^2 from thermographic measurements. Self consistant calculations lead to slightly lower fluxes (F/Fth~~3). The fraction of power coupled to the thermal electrons increases with the electronic density at the antennna aperture and losses below 3% are measured when this density is lower than 1 $10^{18}m^{-3}$.

References

[1] M.Goniche et al., IAEA conference, Seville, 1994

[2] J.Mailloux et al., to be published in Proc.on the 12th Int.Conf.on PSI, May 20-24, 1996

[3] J.H.Harris et al., Controlled Fusion and Plasma Physics, Part IV, p.397, 1995

IMPURITY PRODUCTION & RADIATION PROPERTIES OF THE TORE SUPRA ERGODIC DIVERTOR CONFIGURATION WITH RF-HEATING

W.R.Hess, L.Chérigier, J.T. Hogan*, W.Mandl, C.DeMichelis, M.Mattioli
C.C. Klepper*, M.Druetta+ and M.Z.Tokar‡

Association EURATOM-CEA sur la Fusion ContrôléeCEN-Cadarache, 13108 Saint-Paul-lez-Durance Cedex, France
*Fusion Energy Division, Oak Ridge Nat. Lab., Oak Ridge, TN 37831-8072, USA
+Lab. TSI, URA CNRS 842, Univ. J. Monnet, 42023 St. Etienne Cedex 2, France
‡ Institut für Plasmaphysik, Forschungszentrum Jülich, Ass. EUR-KFA, Germany

Introduction : Power and particle exhaust is a leitmotiv in fusion research. Both are addressed by the ergodic divertor (ED) configuration of Tore Supra (TS). The ED increases the perpendicular heat flow by ergodising the edge magnetic field. The ergodised zone, with its characteristic n = 6, m = 18 structure, occupies about 20% of the small plasma radius (a = 75cm). It matches the ionisation region of the main impurities C and O, i.e. the highest line emitting ionisation states, CVI or OVIII, are already in the confined plasma, whereas low ionisation states are either in the stochastic zone (e.g. CIV) or in the laminar region (LR), which corresponds to the SOL. A first set of neutraliser plates was of a closed configuration, i.e., the neutralised particles are reflected into a pump duct. Presently, a new type of neutraliser plates, which can be qualified as "open" (i.e. the active surface faces the plasma), are installed within the divertor modules. In this paper the recycling properties of Carbon are measured via visible spectroscopy, and the 3-D Monte Carlo code "BBQ" [1] is used for the simulation of local ion fluxes within the LR. A 1-D impurity transport code (CNET) is used for the stochastic zone and the main plasma .

Experiment : The plasma parameters are : R = 2.385 m, a = 0.78 m, B = 3.5 T, gas = D_2, I_p = 1.58 MA, P_{ICRH} = 2 MW, $\langle n_e \rangle_{vol} = 2.75\ 10^{19}\ m^{-2}$, no ED: $\langle Z_{eff} \rangle = 1.65$, with ED: $\langle Z_{eff} \rangle = 1.3$, with ED and ICRH: $\langle Z_{eff} \rangle = 1.45$ (see fig. a, b, c). Because of the use of a horizontal, external limiter slightly ahead of the divertor modules, this configuration is qualified as "mixed". The incoming fluxes are monitored by a number of in vessel (in situ) fibers looking at the new "open" actively cooled neutraliser plate (proto n°4) (CII brilliance see fig.d), the nearby horizontal limiter (n°5) which protrudes about 25 mm above the divertor armour (R_{div} = 3.18 m), the inner carbon wall (n°1), a vertical limiter (n°2) and a free plasma surface (n°3) close to the vertical limiter. Another in situ fiber looks at a "closed" neutraliser plate. The bakable 'in situ' fibers, connected to normal fibers through a vacuum feed-through, are linked to three Czerny-Turner spectrometers with CCD cameras. There are one open and 29 closed neutralisers. The open neutraliser consists of four B_4C coated 30 cm long bars which are separated by three 10 mm wide pumping slots. A fixed Langmuir probe, flush to the active surface, is located within a pumping slot and measures n_e and T_e at r/a = 1.03. A reciprocating Langmuir probe at the top of the plasma chamber shows typically flat n_e and T_e profiles when the ED is activated. The absolute brilliance of CII (6578 Å) for three typical shots I) no ED, II)

with ED and III) ED plus 2MW additional ICRH-heating between 5 and 9 s are analysed. These brilliances (b), which are mean values at the specified locations, are converted in the usual way via the S/XB factor (ionisations per photon) into ion fluxes $\Gamma_{part} = 4\pi$ b (S/XB) [1,2]. Table I summarises these data for Carbon.

Results and Discussion : The impurity content is monitored with a measurement of visible bremsstrahlung, soft X-ray emission and visible spectroscopy [3]. Under the assumption of Carbon being the main impurity, these measurements yield consistent values of Z_{eff}. Furthermore, it is observed that the CVI Lyα emission drops by a factor of two during the ED resonance, due to the ED induced change of edge T_e profile.

Simulations of the ED shots in accordance with the input values (Z_{eff}, total radiated power, soft X-rays and VUV-spectrometry), require a flat T_e profile between r/a = 1 and 0.85. For these medium density discharges, the neutral deuterium density is low, so that CX reactions are neglected in the simulations. The major part of the total radiated power originates from (Li-like) CIV ions. Comparing the shots without and with ED, the total radiated power remains constant whereas the Z_{eff} diminishes from 1.6 to 1.3. This is explained by the ED induced flat T_e profile and the concomitant increased transport at the plasma edge, which produce the same total Carbon radiation for a lower impurity content. For the heated case, only 70% of the measured radiated power can be justified by the simulation. The bolometer is probably perturbed by the presence of a RF-antenna in its field of view.

Table I : CII fluxes [part/s]

Viewing line Surf (cm^2)	inner wall n°1 2.5 10^5	vert. lim n°2 3000	proto n°4 1x150	normal neutr 29x30	hor.lim. n°5 3000
no ED Σ = 1.9e20	1.6 10^{19} 8.4%	1.2 10^{19} 6.3%	6.2 10^{17} 0.3%	1.4 10^{18} 0.7%	1.6 10^{20} 84%
ED Σ = 1.9e20	6.3 10^{18} 3%	3.0 10^{19} 16%	8.2 10^{17} 0.5%	1.1 10^{19} 6.5%	1.4 10^{20} 74%
ED+ICH Σ = 8.4e20	7.8 10^{18} 1%	1. 10^{20} 12%	1.2 10^{19} 2%	8.6 10^{19} 10%	6.3 10^{20} 75%

The measured mean fluxes have been multiplied by the actual emitting surfaces (Surf). The total Carbon source (Σ) is then divided by the plasma surface (75 m^2) in order to compare this mean flux to the corresponding value necessary as a boundary condition in the 1-D simulation to match the central Carbon content (i.e., the Z_{eff} value) given by the simulation :

I. no ED	measured 2.5 10^{18}	simulation 5 10^{18}	[part/m^2 s]
II. ED	measured 2.5 10^{18}	simulation 5 10^{18}	[part/m^2 s]
III.ED+ICRH	measured 1.1 10^{19}	simulation 7 10^{18}	[part/m^2 s]

The measured values are within a factor of two in agreement with the simulation.

It is noticeable that in this 'mixed' configuration, i.e. limiter plus ED, the major recycling

surface is still the limiter. Another striking fact is that recycling on the new prototype neutraliser is quite important compared to the old one. In fact, with all neutralisers of the new type the recycling fraction would amount to about 30% in this configuration.

3-D Modelling : A preliminary evaluation of impurity generation and plasma penetration has been undertaken for the conditions of these experiments. The three cases have been simulated with the MASTOC, CASTEM-2000 and BBQ codes. The MASTOC code [4] calculates the magnetic field structure near the neutraliser plates. CASTEM-2000 [5] is used to calculate the resulting generation of impurities from physical and chemical sputtering sources (either C^0 or CD_4). For the graphite surfaces of the old (closed) neutralisers this depends on the surface temperature distribution. BBQ [6] follows the subsequent impurity evolution in the SOL as the produced C^0 or CD_4 ionise/dissociate to spectroscopically observable stages.

The main purpose of the modelling study is to compare impurity generation and penetration processes for the closed and prototype neutraliser geometries, under assumed identical plasma conditions. For this preliminary study a 'typical' MASTOC neutraliser plate field distribution is used for the prototype geometry. Incident plasma conditions for the series are taken from the fixed Langmuir probe at the prototype neutraliser and these values are used for both geometry cases.

Impurity generation and penetration : Both chemical and physical sputtering increase by a factor of 4-5 for the closed neutraliser plates during ED activation. For the open neutraliser the calculation yields only an increase of 2-3. However, calculating the total particle flux from the B_4C surface (which would result in negligible C chemical sputtering) of the open neutraliser leads to an unrealisticly low estimate compared to the measurements. Indeed, the neutraliser is likely to be covered by Carbon deposits from the neighbouring graphite armour. A striking difference between the open and closed neutraliser is found in the penetration probability of released Carbon. Only 25% of the particles generated by physical sputtering at the closed neutraliser, because of its closed structure, penetrate into the confined plasma, whereas 90% penetration is found for the open one. Due to the increased surface temperature of the closed neutraliser plates, enhanced chemical sputtering is observed during ED activation; the penetration probability, however, is reduced from 9 to 2%.

References :

[1] S.J.Tobin et al Plasma Phys. Control. Fusion 38 (1996) 251-263

[2] K.Behringer et al Plasma Phys. Control. Fusion 31 (1996) 2059

[3] C.DeMichelis et al Nucl.Fusion 35 (1995) 1133

[4] F.Nguyen, Ph.Ghendrih and A.Samain. DRFC/CAD Report EUR-CEA-FC-1539. "Calculation of magnetic field line topology of the ergodized edge zone in real tokamak geometry. Application to the tokamak Tore Supra through the MASTOC code., Feb. 1995

[5] L.Bohar et al, " CASTEM-2000 - Notice, Version 1994"

[6] J.Hogan, ORNL EPPC Memo 7/94, "BBQ-impurity scrape-off layer transport code for Tore Supra", Dec. 1994.

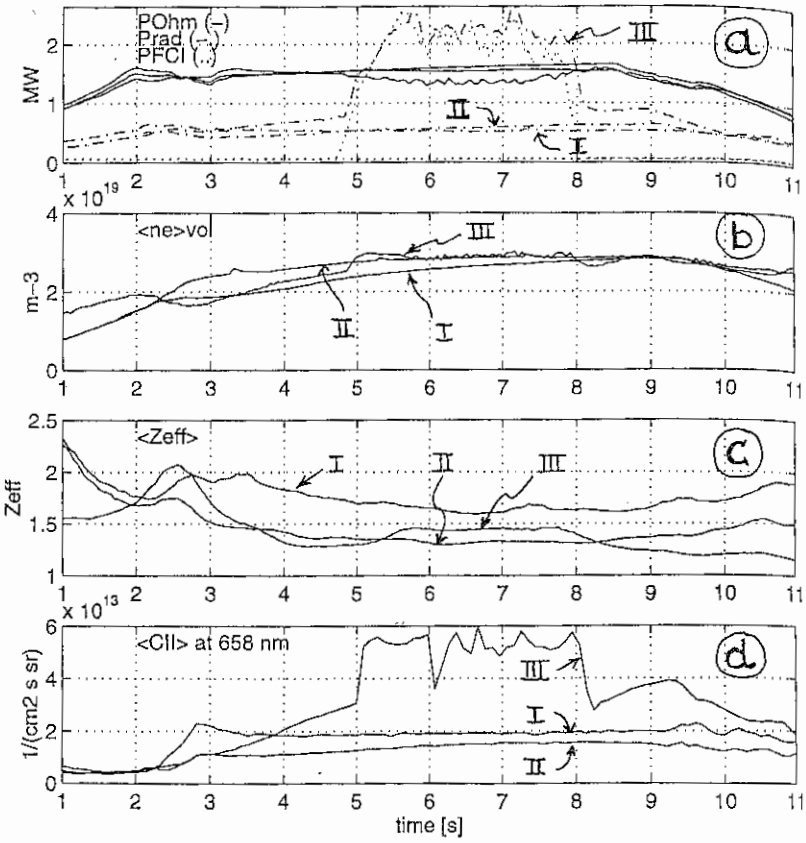

Figure captions : Time traces of three discharges I) no ED, II) ED, III) ED and ICR-heating
a) ohmic heating power (P_{ohm} -), radiated power measured by bolometry (P_{rad} -.), ICR-heating power (P_{FCI} ...)
b) <ne> mean volume density measured by interferometer
c) $\langle Z_{eff} \rangle$ mean effective charge number measured by bremsstrahlung
d) brilliance of CII 6580 Å measured by an in-vessel fiber looking at the prototype neutraliser. Although the brilliance decreases during ED activation, it yields higher CII particle fluxes due to the change in the S/XB factor with T_e.

Ion Surface Cyclotron Waves in Edge Plasma of the Fusion Devices

Girka V.O., Pavlenko I.V., Sporov A.E.

Kharkiv State University, Svobody sq.4, Kharkiv, 310077, Ukraine,

e-mail: azarenkov@pem.kharkov.ua

The paper presents the results of theoretical investigations of the new type of surface waves propagating on the harmonics of ion cyclotron frequency (SCW). We consider two possible orientations of external magnetic field relatively interface of metal chamber. Under the considered conditions the SCW can propagate across magnetic field along metal wall with (or without) dielectric coating. The problem is solved using Vlasov-Boltzman kinetic equation for the description of plasma particles and Maxwell equations for the SCW field. The SCW dispersion equation is obtained by Fourier analysis method using linear boundary conditions for the wave field and supposition that spatial plasma dispersion is weak along the direction of external magnetic field. We suppose that nonperturbed distribution function of plasma particles is Maxwellian one and particles reflection from the plasma interface is simulated by diffuse and mirror models. Plasma nonuniformity is simulated by a collection of an uniform plasma layers with different values of particle concentration.

Simple analytical expressions for the SCW eigenfrequency are obtained in the case of uniform plasma. In the case of nonuniform plasma the SCW frequency spectrum is examined numerically. Increments of the SCW parametric excitation are found in the case of small amplitude pump wave.

Let consider a semi-bounded nonuniform plasma occupying the half-space $X > 0$ and bounded at the plane $X = 0$ by a dielectric layer with dielectric coefficient ε_d and thickness a_d which in his turn is bounded by metal wall at the plane $x = -a_d$. The $\vec{B}_0$ is directed along Y-axis. Plasma nonuniformity is

simulated by a transient plasma layer with density value n_1 (it is placed between planes $X = 0$ and $X = a_1$) and semibounded plasma with density value $n_0 > n_1$ (it is placed in a region $X \geq a_1$). We consider the SCW field in the form $E, H \propto f(x)\exp(ik_2 y - i\omega t)$, here ω and k_2 are frequency and wave number respectively. We obtain the dispersion equation for the arbitrary number of cyclotron harmonic (because of it's cumbersome form we don't cite it here), but we represent the results of the SCW dispersion equation investigation only in the case of second ion cyclotron harmonic because of it importance for practical applications. Simple analytical solutions of the dispersion equation can be obtained only in the case of uniform plasma for the longwave limit $(\omega - 2\omega_{Ci} = h \propto (k_2\rho_{Li})^2)$,here ρ_{Li} is Larmor radius of ions, ω_{Ci} is cyclotron frequency of ions. Numerical analysis shows that in the case of nonuniform plasma with dielectrical coating dispersion equation has five solutions. One of them (with the higher frequency for the fixed value of wave number) may be defined as the main SCW mode, which propagate along dielectric-metal interface and depends mainly by conditions on it. The rest four are the additional modes which appear due to the considered model of the plasma inhomogeneity. So increasing of the transient plasma layers number should lead to the expansion of the SCW frequency spectrum. The skin depth of the SCW field in to the plasma, in our geometry, is approximately equal to their wavelength. The existence of dielectric layer strongly change the dispersion characteristics of wave guide system. Unlike the case of plasma-metal structure the SCW in the considered waveguide can propagate in the both directions across external magnetic field along plasma-metal interface. The frequencies of the SCW, which propagate in the mutually opposite directions with equal wavelength values, are different. We must emphasize that SCW slightly depends upon variation of dielectric parameters. Essential effect on the SCW dispersion is exerted by the magnetic field $\vec{B}_0$ value. It is normal one (it means that phase and group velocities of the SCW have identical direction) for a small $\vec{B}_0$ value,

when there is inequality $\beta_i = \Omega_i^2 \cdot \omega_{Ci}^{-2} >> 1$ takes place. Increasing of the $\vec{B}_0$ value leads to the SCW dispersion exchanging. Under the condition, when inequality $\beta_i < 1$ is valid, the SCW dispersion becomes an anomal one (the SCW phase and group velocities have mutual opposite directions).The parametrical instability of the SCW under the influence of the electrical pump wave $E_0 \sin(\omega_o t)$ is studied as well. We use nonlinear boundary condition for tangential magnetic field, taking into account nonlinear surface electric current, on the plasma interface. In the framework of the uniform, small amplitude pump wave we obtained the expressions for the SCW parametric instability increments. In the case of the SCW on the second ion cyclotron harmonic the increment value is: $\mathrm{Im}(\omega) \propto \omega_{Ci} E_0 (k_2 \rho_{Li})^2$.

In the region of divertor plasma the external steady magnetic field is directed perpendicularly to the plasma interface and the SCW dispersion is essentially depended on dielectric coating of a reactor wall characteristics. Let consider semibounded nonuniform plasma occupying the half- space $z > 0$ and restricted at the plane $z = 0$ by a dielectric slab with dielectric constant ε_d and thickness a_d, an ideally conducting metal is situated in the region $z < -a_d$, $\vec{B}_0$ is directed along z- axis. We consider the SCW field in the form $E, H \propto f(z) \cdot \exp(ik_1 x - i\omega t)$, here k_1 is wave number. The obtained dispersion equation describes the SCW propagating on arbitrary number of cyclotron harmonic. Plasma inhomogeneity is modeled by a set of several plasma layers with different densities. Simple analytical solution of the dispersion equation can be obtained only in the case of uniform plasma. For the SCW on the second ion cyclotron harmonic $h \propto -(k_1 \rho_{Li})^2$ in the limit of long wavelengths $(k_1 \rho_{Li} << 1)$ and $h \propto (k_1 \rho_{Li})^{-2}$ in the limit of short wavelengths $(k_1 \rho_{Li} >> 1)$. Under considered conditions the SCW frequency is not depend on the direction of their propagation. Due to the used plasma nonuniformity model the SCW spectrum consists of some modes. One of them exists in the metal- dielectric- uniform plasma structure. Shape of the

dispersion curves is determined mainly by the properties of the dielectric slab. Increasing of the ε_d/a_d and decreasing of the β_i parameters lead to the flatting of the SCW dispersion curves to the resonance line $\omega = 2\omega_{Ci}$. It means strong dissipation of the SCW energy. The SCW skin depth is greater than their wavelength. In the frame work of the uniform, small amplitude pump wave we obtained the expressions for the SCW parametric instability increments: $\mathrm{Im}(\omega) \propto E_0^{2/5}(k_1\rho_{Li})^2$ for $(k_1\rho_{Li} << 1)$ and $\mathrm{Im}(\omega) \propto E_0^{2/5}(k_1\rho_{Li})^{-1/2}$ for $(k_1\rho_{Li} >> 1)$. In the case of a plasma layer with transverse dimension a_p the $\mathrm{Im}(\omega)$ value is proportional to $a_p^{-1/2}$.

The knowledge about SCW properties can be useful for the analysis of experimental data concerned plasma edge heating. At present there are some experimental data (see e.g.[1,2]) which testify that the surface modes are the most possible cause of the plasma edge heating and it contamination by admixture ions during all regimes of ion cyclotron resonance heating (ICR) which is often used for additional heating. It is observed in the ICR experiments that significant fraction of the input power is dissipated in the plasma edge. This effect is still not well understood because there are very little data available concerning the wave fields in the plasma edge.

Summarizing the data, presented here one can state, that

- the SCW can be parametrically excited in thermonuclear devices,
- the existence of dielectric layer strongly change the SCW dispersion,
- plasma nonuniformity expands the frequency spectrum of the SCW, enhances the SCW damping.

[1] Ballico M.J., Cross R.C. Fusion Engineering and Design 197 (1990) 12

[2] Weison H. et. al. 22-nd Europ. Phys. Soc. Conf. on Control. Fus. and Pl. Phys., Abstr. of Invited and Contrib. Papers, UK, July, 1995, p.312

Finite element modelling of TdeV edge plasma and beyond

R. Marchand, M. Simard, C. Boucher, J. Gunn, J. Mailloux, B. Stansfield and TdeV team.

Centre Canadien de Fusion Magnétique*
1804 boul. Lionel Boulet, Varennes Qc J3X 1S1 Canada
* Supported by AECL, Hydro-Québec, and the Institut National de la Recherche Scientifique

1. Introduction

Results from finite element modelling of TdeV edge and divertor plasma are presented, with particular emphasis on geometry and electric fields. Much of the recent experimental programme on TdeV was concerned with edge physics. This is the case, for example, with biasing experiments, and experiments in which the parallel plasma velocity has been measured. In this, it is recognized that electric fields and the resulting drifts play a critical role. Yet, most numerical models presently available do not account for electric fields and particle drift effects in the edge. Moreover, because most of these models are based on a finite volume discretisation of the transport equations on a structured quasi-orthogonal mesh, they present some intrinsic and, sometimes, very serious difficulties when modelling domains with multiple connectivity and/or complicated boundaries. For these reasons, we have developed a new computer model for the edge plasma, based on a finite element discretisation of the transport equations on an unstructured triangular mesh. This approach allows a straightforward representation of simulation domains, of arbitrary complexity. Our model also accounts for particle drifts associated with the presence of electric fields in the edge; an effect essential in modelling certain measurements such as the plasma flow in the direction parallel to the magnetic field, and the reverse flow observed in the divertor region in the vicinity of the separatrix.

2. Model description

Transport is described with standard macroscopic (fluid) conservation equations for particles, parallel ion momentum, electron and ion energy, and electric charge. These equations can be found in a number of references and are not repeated here for brevity. Their general form can be found, for example in Refs. [1, 2]. The main difference with previous analyses is the inclusion here of the **E×B** drift velocity in all transport equations. For example, the ion continuity equation reads

$$\frac{\partial n_i}{\partial t}+\nabla\cdot[\Gamma_{i//}\vec{b}+\vec{v}_{Di}n_i-D_{ni}(\mathbf{I}-\vec{b}\vec{b})\cdot\nabla n_i]=n_e(\alpha n_0-Rn_i)$$

where $\Gamma_{i//}$ is the ion parallel flux, **b** is a unit vector in the direction parallel to the magnetic field, D_{ni} is the anomalous particle diffusivity, n_e is the electron density, α and R are the ionisation and recombination coefficients for neutrals and ions respectively. In general, v_{Di} should be the sum of both the **E×B** and the diamagnetic drift velocities. In this study, we limit our attention to the **E×B** drift velocity only. The electric field used in the calculation is obtained selfconsistently, as suggested in [3], by solving for $\nabla\cdot\mathbf{J}=0$, where **J** is expressed in terms of the local gradients in ϕ, p_e and T_e . For simplicity, recycling and neutral transport is also described in the fluid approximation. Specifically, a diffusion equation is solved for both the neutral density and thermal energy:

$$\frac{\partial n_0}{\partial t} - \nabla\cdot(D_{n0}\nabla n_0) = n_e(-\alpha_0 n_0 + R_i n_i)$$

$$\frac{3}{2}\frac{\partial p_0}{\partial t} - \nabla\cdot(n_0 D_{T0}\nabla T_0 + \frac{3}{2}D_{n0}\nabla n_0) = \frac{3}{2}p_i(R_i n_e + X n_0) - \frac{3}{2}p_0(\alpha_0 n_e + X n_i)$$

where p_i is the ion pressure, D_{n0} and D_{T0} are diffusion coefficients for the neutral density and thermal energy respectively, and X is the coefficient of charge exchange. In this approximation, only atomic neutrals are considered. The particle and energy fluxes at any given boundary are calculated by assuming a Maxwellian distribution function for neutrals. Exchange of energy between neutrals and ions (the r.h.s. in the last equation) is also accounted for in the ion energy equation. In the ion parallel momentum equation, however, neutrals are assumed to have zero momentum. In all transport equations, diffusion coefficients are limited so as to prevent flow velocities from exceeding the thermal velocities times a flux limiter (all limiters are set to 0.2). The ion parallel viscosity is also limited so as to prevent the ion stress from exceeding the ion pressure times 0.2. Standard sheath boundary conditions are imposed at the divertor plates, for the plasma flow velocity, and the electrostatic potential. 100% recycling is assumed at all material boundaries (divertor plates, limiters and baffles), where atomic neutrals are assumed to be generated at a temperature of 3eV. For simplicity, all flow is assumed to be ambipolar.

3. Simulation results

Simulations have been made for two configurations of TdeV illustrated in Fig. 1.

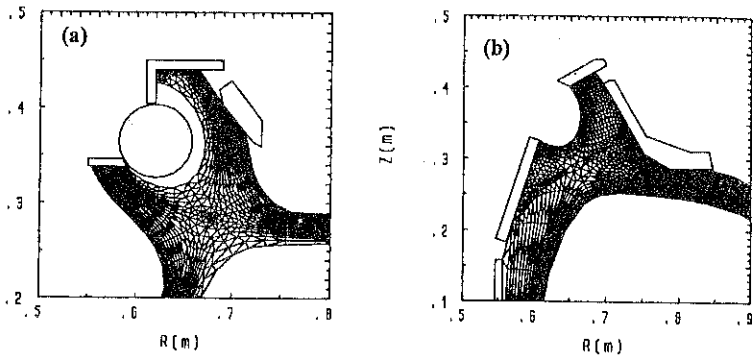

Figure 1. Simulation domains for the TdeV95 (a) and TdeV96 (b) configurations.

The first configuration corresponds to TdeV, for which measurements of edge radial electric fields and parallel flow velocities are available. The other configuration, TdeV96, is for the new upgrade, scheduled for operation in August. In both geometries, the "normal" field configuration corresponds to a toroidal magnetic field coming out of the page and a clockwise poloidal field in the central region (corresponding to an ohmic current into the page). In the calculations, the sign of the parallel velocities refers to the direction of the local magnetic field. Thus, for example in the normal configuration, a parallel flow velocity directed toward the outer plate has a negative sign. The plasma parameters considered here are those of a low density (line average density between

2 and 3×10^{19} m^{-3}) ohmic detached plasma.

For the TdeV configuration, the effect of toroidal field reversal is considered for the parallel flow velocity. For reference, a simulation is also made while ignoring **E×B** drifts. A comparison of the parallel flow velocities calculated along two vertical positions is shown in Fig. 2.

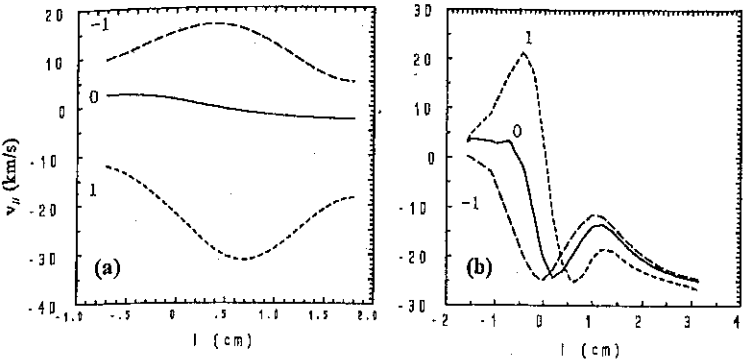

Figure 2. Parallel velocity profiles across a horizontal cut in the outer SOL, in the midplane (a), and in the deflector region at z=0.35m above the midplane (b). The solid line (0) is obtained without **E×B** drifts. Dashed curves (1) and (-1) correspond to a normal and to an inverted toroidal magnetic field respectively. The position of the separatrix corresponds to l=0.

In the midplane, the parallel velocity is small when **E×B** drifts are neglected. It is strongly negative for the normal toroidal field, and positive for a reversed B_T. In the outer divertor, the picture is more complex. The parallel velocity is mostly negative (toward the plate) when **E×B** is ignored. For a normal B_T it is negative outside the separatrix and it changes sign inside the separatrix. For a reversed B_T, the parallel velocity doesn't change sign. It is always negative, toward the plate. These results are in good agreement with Mach probe measurements of the parallel flow velocity in TdeV [4]. The profiles described above for the parallel velocities can be explained by the facts that 1) the electrostatic potential is nearly proportional to the local electron temperature in the SOL, and 2) whether **E×B** drifts are included or not, the net poloidal flux (the summation of the projections in the poloidal plane of the of the parallel and **E×B** fluxes) does not change significantly. For example, in the outer midplane, the **E×B** drift is downward for a normal B_T. This implies a compensation by a negative (upward) value of the parallel flux. In the inner private region, the **E×B** drift is toward the plate. In order to maintain approximately the same poloidal flow there, the parallel particle flow must be positive; i.e.; *away* from the plate.

Simulations have also been made for the TdeV96 geometry shown in Fig. 1b. In this case, the simulation domain includes the usual SOL as well as a region which extends beyond the baffles and nearest limiters. The inclusion of these structures is important because it allows simulations which are much less sensitive to the boundary conditions imposed on the outer flux surfaces. Indeed, in a machine with a narrow divertor throat, significant plasma density and fluxes may remain on the outer flux surfaces entering the divertor region. The effect of the baffles and limiters just beyond these surfaces could, in principle, be taken into account by some judicious boundary condition. A proper analysis, however, requires that they be taken into account in detail. The inclusions of such structures in the simulation domain is achieved in a natural way with the present

discretisation on an unstuctured triangular mesh. Their inclusion in a structured quadrilateral mesh can be made in principle, but at the cost of a greatly increased complexity. An example result is given in Fig. 3, which shows the plasma density and electron temperature across the SOL at one poloidal location. The cut across which these profiles are calculated is located approximately 5cm to the right of the outer baffle in Fig. 1b. Both profiles show a double structure. In the "conventional" SOL; that is, the region which extend from the separatrix to the last flux surface which does not intersect a baffle or a limiter, there is a relatively rapid decay. In the outer region, the decay is slower.

4. Summary and conclusion

The edge and divertor plasma of TdeV and TdeV96 have been modelled with a finite element code in which transport equations are discretised on an unstructured triangular mesh. This approach offers some important advantages compared to more familiar models, which rely on a finite volume discretisation on structured quasi-orthogonal quadrilateral meshes. The principal advantage is the ability to readily represent computational domains of arbitrary shapes and connectivity. The model also accounts for **E×B** drifts; an effect which has long eluded development efforts with conventional approaches. This model has been used to calculate parallel flow velocities in TdeV under various magnetic field configurations. The net poloidal flow is found to be relatively insensitive to these drifts. In practice, a good approximation of that flux can be obtained while neglecting **E×B** drifts altogether. In order to calculate the correct parallel velocity, however, it is essential to account for drifts; as the parallel velocity adjusts itself so as to nearly compensate any **E×B** drift. Drifts are also responsible for the parallel flow reversal in the private region, near the divertor plate towards which **E×B** is pointing. The strong velocity shear which results could impact microinstabilities in that region.

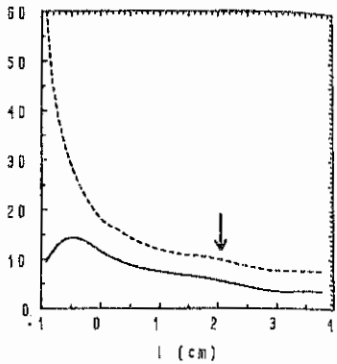

Figure 3. Electron density (solid) and electron temperature (dashed) profiles across the SOL calculated for TdeV96. The density and temperatures are in units of 10^{19} m^{-3} and eV respectively. The arrow indicates the extent of the "conventional" SOL.

References

1. S.I. Braginskii, in Review of Plasma Physics, Vol. 1 (M.A. Leontovich, Ed.), Consultant Bureau, New York, (1965), 205.
2. B.J. Braams, Ph.D. Dissertation, Rijksuniversiteit Utrecht (1986).
3. M.E. Rensink, J. Molvich and T. Rognlien, IAEA Technical Committee Meeting on Tokamak Plasma Biasing, Montreal, 8-10 September, 1992.
4. B.L. Stansfield, C. Boucher, J.P. Gunn, H. Guo, et al. J. Nucl. Matt. 220-222, 1121 (1995).

Interpretation of the Carbon Line Emission in the ASDEX-Upgrade Divertor

U. Wenzel, B. Napiontek, G. Fussmann,
H. Kastelewicz, M. Laux, A. Thoma

Max-Planck-Institut für Plasmaphysik, Berlin and Garching
EURATOM Association, Mohrenstr. 40-41, D-10117 Berlin, Germany

1 Introduction

Spectroscopic observation of plasma facing structures in a fusion device allows the estimation of the released particle flux. In ASDEX Upgrade the visible emission of CII at 658 nm was previously used for a quantitative determination of the carbon influx from the outer divertor target [1].
For a homogeneous plasma (constant T_e) the particle influx is given by

$$\Gamma = 4\pi \frac{S}{XB} I$$

where S and X are ionization and excitation rate coefficients, B is the branching ratio and I is the measured intensity (in $photons/m^{-2}sr^{-1}s^{-1}$). In general, the quantity S/X is a strong function of the electron temperature typical for divertor plasmas (below 20eV) and has to be known to evaluate the fluxes [2]. Moreover, if there are temperature gradients in the divertor the above equation only holds for an average but unknown temperature T_{eff}.
In [1] the plasma parameters determined by an in-vessel probe in the outer divertor at fixed position were used for the evaluation of the flux. Here, we apply a line ratio method for an estimation of the electron temperature at the position of the radiating species and discuss the limitations of the method due to temperature gradients.

2 Carbon emission in the divertor

A scanning spectrometer for the VUV and visible range was used for spectroscopic studies of the divertor radiation [3]. Its schematic arrangement on ASDEX Upgrade is shown in Fig. 1. Because the targets are observed nearly in normal direction the measured intensity is proportional to the particle flux.
Carbon line emission profiles are given in Fig. 2. For CII the emission of the resonance line at 135.5 nm is compared to the visible line at 658.3 nm (ohmic discharge with ion grad B drift toward the X-point). CIII emission at 465 nm and 97.7 nm is also shown for a neutral beam heated discharge. The emission profiles of both species in the visible differ from the VUV emission. Typically, the line ratio I_{vis}/I_{vuv} is much greater in the outer divertor which can only be explained by an in-out temperature asymmetry. In the inner divertor the temperature must be so low that the high lying initial level of the visible line is not as efficiently populated as the lower lying level of the VUV line. For an evaluation of the particle flux this asymmetry must

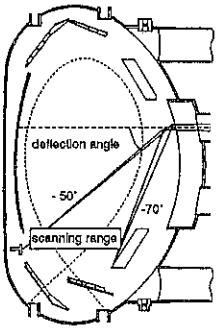

Figure 1: Schematic arrangement of the scanning spectrometer for the VUV and visible range used for divertor studies. Carbon emission will be plotted over the deflection angle.

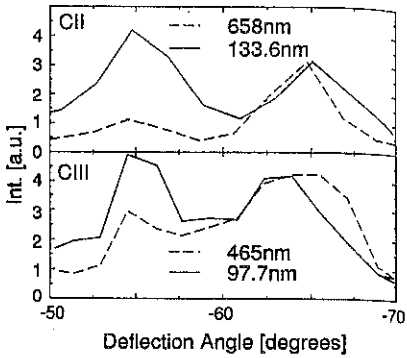

Figure 2: Carbon emission in an ohmic (CII) and neutral beam heated discharge (CIII) in the visible and VUV spectral range. Emission of the VUV resonance lines is nearly symmetric whereas the emission in the visible dominates in the outer divertor.

be taken into account. Without knowledge of the temperature one can only say that the visible emission profile is a better representation of the relative carbon influx than that in the VUV. In Fig. 3 the CII and CIV emission in an ohmic discharge is shown. At 2.0 s the gas valve was closed leading to a reduction of the plasma flux to the targets. The divertor density decreases, followed by an increase of the temperature. In the outer divertor both intensities decrease as expected. In the inner one, however, the CII emission decreases whereas the CIV emission rises. Here the temperature dependence of the ratio S/X is essential for a correct interpretation.

3 Electron temperatures determined by the line ratio method

The line ratio method was already applied to determine the electron temperature in the divertor of the DIII-D tokamak [4]. The chosen carbon lines at distant wavelengths in the VUV, however, require an absolute calibration of the spectrometer. We use instead closely neighbouring lines of CII at 80.7 nm (quartet system) and 85.8 nm (doublet system) which can be quantitatively analyzed without a calibration. The line ratio was calculated with a collisional-radiative model [5]. In this model all metastable levels of carbon were taken into account. The temperature dependence shown in Fig. 4 results mainly from the energy separation of 5.3 eV of the metastable and ground term of CII which are the initial states to populate the upper levels of the transitions at 80.7 nm and 85.8 nm, respectively. Temperatures determined in this way characterize the region where CII emission is maximal along the line of sight (T_{emis}).

The investigation of the ohmic discharge described above showed clearly the assumed asymmetry. A value of $T_e = 5\,eV$ in the inner divertor and 12 eV in the outer divertor is found. After closure of the gas valve this asymmetry is reduced. Now the inner divertor temperature rises to 9 eV which is the reason for the observed increase of the CIV signal (see Fig. 3).

A lower temperature with subsequent detachment in the inner divertor is also found in other divertor tokamaks (DIII-D, ALCATOR C-Mod) and can be explained by a preferential energy input into the outer part of the sol [6]. Symmetry returns when both divertors (inner and outer) are detached. As an example we consider a neutral beam heated discharge (#7743) with two density plateaus. At a density of $5 \cdot 10^{19} m^{-3}$ we find $T_{in} = 5\,eV$ and $T_{out} = 10\,eV$. When the density is increased up to $8 \cdot 10^{19} m^{-3}$ the outer divertor detaches too and T_{emis} is 8 eV in both divertors. CII radiates now in a greater distance from the plates.
Such an asymmetrically detached divertor was found in the 2D-modeling with the B2-Eirene code. Fig. 5 shows the isolines of the electron temperature in steps of 1 eV together with the isolines of the total CII emission for a 3.5 MW neutral beam heated discharge. In the inner divertor CII emission peaks at 4 eV and in the outer at 8 eV which is near to the temperatures found by the line ratio method.

4 Carbon flux ratios

We consider the symmetrical emission profiles in the VUV. When taking into account the temperature dependence of S/X we arrive at a flux ratio (inside - outside) in the detached phase of 1 : 60 and after closing the valve of 1 : 1 for the ohmic discharge discussed above. Visible emission shows an asymmetrical influx already directly. A quantitative evaluation with the proper ratio of S/X results in the same ratio as above.
With the strong temperature gradient and the low temperatures in the inner divertor a problem arises. If the ionization length is comparable to the temperature gradient length we have $T_{eff} > T_{emis}$. A higher value of the temperature value results in a greater S/X and therefore reduces the flux asymmetry. A quantitative evaluation is then impossible without modeling the temperature gradient. The flux asymmetry, however, remains in any case. One can state that the electron temperature has a great influence on the carbon erosion indicating the role of physical sputtering.

5 Summary

Electron temperatures in the divertor have been estimated using the line ratio method. Asymmetries were found with temperatures as low as 5 eV in the inner divertor resulting in an asymmetrical carbon influx from the target plates. B2 - Eirene modeling of the divertor confirms the temperatures found as well as the observed inside - outside asymmetry.

References

[1] Field, A.R., Garcia-Rosales, C., Lieder G. et al., Nucl. Fusion 36(1996), 119.

[2] Behringer, K., Summers, H. P., Denne, B. et al., Plasma Phys. Control. Fusion 31(1989), 2059.

[3] Field, A.R., Fink, J., Dux, R. et al., Rev. Sci. Instrum. 66(1995), 5433.

[4] Isler, R., to be published in Fusion Eng. and Design

[5] Napiontek, B., degree thesis, submitted to Humboldt University, Berlin, 1996

[6] Harbour, P.J., Contrib. Plasma Phys. 28(1988), 417.

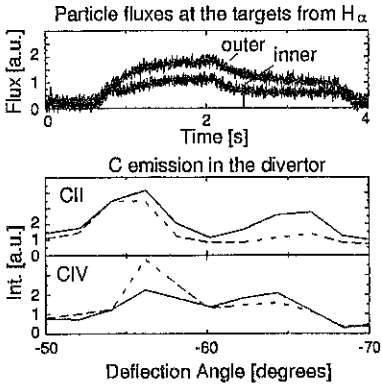

Figure 3: Comparison of the CII and CIV emission in two phases of the standard discharge: solid line - before closure, and dashed line - after closure of the gas valve. Note the opposite behaviour of CII and CIV emission in the inner divertor.

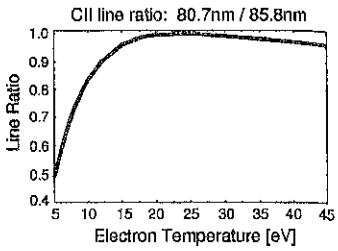

Figure 4: CII line ratio of 80.7 nm (quartet system) and 85.8 nm (doublet system) as a function of the electron temperature. The energy of the initial levels is 20.6 and 14.4 eV, respectively.

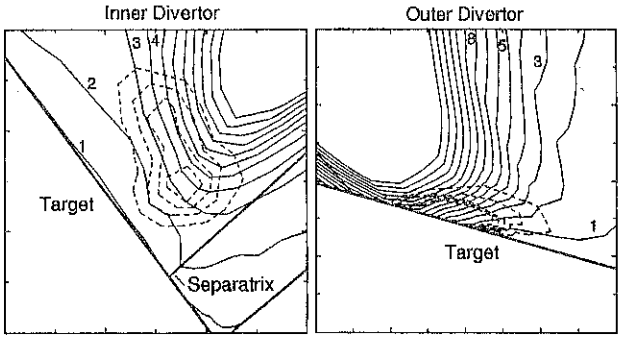

Figure 5: Typical asymmetrical divertor detachment obtained from B2 Eirene code calculations for 3.5 MW input power and $n_e = 4 \cdot 10^{19}\, m^{-3}$. In the inner divertor (left) the CII radiation zone (broken contour lines) is well separated from the plates. The maximum appears at 4 eV (full lines). In the outer divertor (right) this zone is attached to the plate. Higher temperature regions where the T_e contours are less inclined with respect to the lines of sight of the spectrometer contribute preferentially to the measured intensity (8 eV).

B2 - Eirene Simulations for a Deuterium Plasma at PSI-1

H. Kastelewicz, D. Reiter(*), R. Schneider, D. Coster, H. Meyer
Max-Planck-Institut für Plasmaphysik, EURATOM Association, Germany
(*) IPP, Forschungszentrum Jülich GmbH, EURATOM Association, Germany

1. Introduction

PSI-1 is a linear, axisymmetric device (Fig.1) which generates a plasma column of about 1.8m length and 5 to 10 cm diameter by means of a high current arc confined by an axial magnetic field ($0.05 \leq B/T \leq 0.1$). It is primarily designed to study outstanding problems of plasma-surface interactions at high ion flux densities relevant for fusion devices. The plasma column (outside of the anode) is axially limited by a target plate (carbon) and radially bound by diaphragms (carbon) for differential pumping ($10^{-2} \leq p/Pa \leq 1$) or by walls (stainless steel) of different radii ($10 \leq r/cm \leq 20$). Plasma density and temperature are in the ranges $10^{11} \leq n_e/cm^{-3} \leq 10^{14}$, $T_e \leq 10eV$ / 1 /.

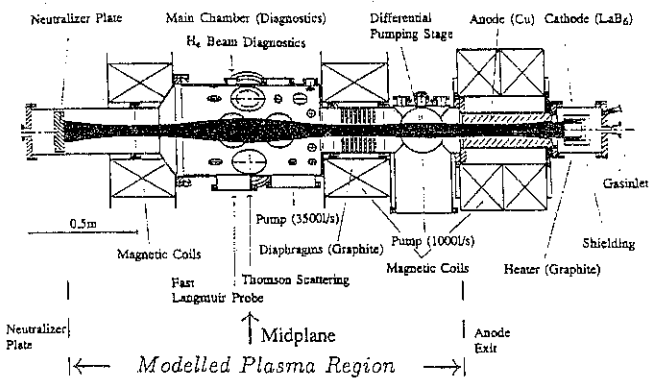

Fig. 1: Plasmagenerator PSI-1 (experimental arrangement)

2. Model System

The plasma is numerically modelled in the region between the anode exit and the target plate limiting axially the column using the coupled package of the B2 2D hydrodynamic plasma code and the Eirene 3D neutral Monte-Carlo-code / 2,3 /. Eirene provides a correct kinetic description of the neutrals recycling from the surfaces or streaming in from the anode (partially ionized plasma) and the gas pumping; the essential interaction processes with the surfaces and the plasma are taken into account.

The B2 calculational grid is defined by the magnetic flux surfaces. The ion motion in the axial direction (parallel to the field lines) is described by hydrodynamic equations and in the

radial direction (orthogonal to field lines) by an anomalous diffusion with a diffusion coefficient in the range $D_i \approx (0.1 \div 1)m^2/s$. For the radial heat conductivities $\kappa_{e,i}/n_{e,i} = 1m^2/s$ and the viscosity $\eta_i/m_i n_i = 0.2m^2/s$ are assumed. Boundary conditions must be specified for the ion density, the ion and electron temperatures (or the corresponding particle and energy fluxes) and the ion velocity parallel to field lines.

The boundary conditions at the anode exit defined by the arc are the driving parameters of the model. Up to now, they have not been derived yet from experiments (or theoretical simulations of the arc) and, therefore, will be considered as adjustable parameters. In order to simulate a particular experiment in PSI-1 they must iteratively be calculated by comparing code results with measured profiles in the diagnostic plane (midplane).
For the boundary conditions at the wall side of the grid a decay length of 1cm for all plasma profiles is assumed and at the target plate and the outer anode surface Bohm conditions are used.

We calculate steady states for a deuterium plasma. In steady state, the "external" D^+ ion (and D atom) source at the anode exit is balanced by the loss of deuterium neutrals through the two pumps; the energy influx from the anode equals the energy deposited onto the different surfaces by electron and ion thermal conduction and convection and by the neutrals.

3. Results

Plasma state

In the present model, the essential parameters controlling the plasma are the boundary conditions (radial plasma profiles) at the anode exit. Calculations have been done assuming radially constant profiles for the plasma density, temperature and axial velocity to study the general properties of the system as well as hollow n_e, T_e profiles which are more appropriate to simulate the actual experimental situation in PSI-1 where, at present, concentric ring-shaped structures are used for both the anode and cathode.

Figs.2a) and 2b) show the radial density and temperature profiles in the midplane for various (radially constant) anode temperatures T_e, T_i but the same density $n_e = 5 \cdot 10^{18} m^{-3}$ ("soft" B2 boundary condition) and Mach number $M = 0.1$ of the parallel velocity assuming two different radial diffusion coefficients $D_i = 1m^2/s$ and $D_i = 0.2m^2/s$.

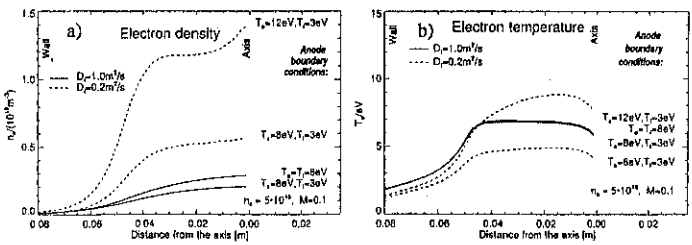

Fig. 2: Radial plasma profiles (midplane) for various anode parameters and diffusion coefficients

The sensitive dependence of the plasma density on the anode temperature T_e shows that plasma recycling basically determines the plasma state. The arc provides an energy source and an initial particle influx from the anode exit, but obviously, the plasma column is actually produced afterwards by the interaction with the neutral background. Better confinement and, as a consequence, enhanced plasma recycling is also the reason for the strong increase of the plasma density with decreasing radial diffusion coefficient D_i.

The (constant) radial temperature profile prescribed at the anode exit is hardly changed along the column because of the high parallel heat conductivity. It is remarkably modified only in the high-recycling regime where a slight hollow profile is formed due to enhanced ionization cooling near the axis of the column.

Because of the long mean free path of the neutrals ($\approx 0.5m$) under the typical conditions of PSI-1, practically the whole plasma is involved in the recycling process. Figs.3 show the density contour plot and some axial profiles for the low temperature case ($T_e = T_i = 8eV$ at the anode exit, $D_i = 1m^2/s$). The electron density has axial maxima which do not coincide with the places of maximum plasma compression due to the inhomogeneous magnetic field. This is a consequence of the strong recycling zones (plasma sources) which arise in these regions, although they are far away from the main neutral sources at the target plate and the outer anode surface. The ionization and electron energy loss rates per cm column length (radially integrated rates, Fig.3b) are maximum in the regions of greatest plasma radius. This also causes a steep axial T_e drop near the diaphragm.
Local recycling at the target plate, however, increases nonlinearly with T_e and would dominate for boundary anode temperatures above $\approx 12eV$. In this case an additional density maximum develops in front of the target plate.

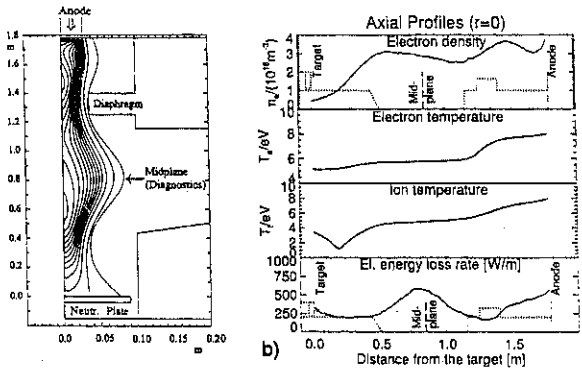

Figs. 3:
a) Electron density contour plot
b) Axial plasma profiles

Neutrals

The deuterium atomic and molecular densities and temperatures are obtained from the Eirene code which takes into account the essential surface processes (reflection, absorption and re-emission of molecules) as well as the collision processes with the plasma (dissociation, ionization, charge exchange, elastic collisions).
The D_2 density has clear maxima in front of the target plate and near the walls where the molecules are produced with wall temperature by thermal re-emission. D atoms originate from surface reflection of ions or atoms or from the dissociation of molecules (Franck-Condon atoms) and posses a much higher mean energy (about 3eV). Their mean free path ($\approx 0.5m$) is larger than the radial dimension of the plasma ($5 \div 10cm$), so they experience many wall reflections and tend to form an almost uniform neutral background in the axial direction.
In the radial direction one obtaines complementary density profiles for D and D_2 (Figs.4a) which show that the radial dependence is caused by D sources and D_2 sinks, respectively, which arise from the dissociation of molecules. Similar profiles are found experimentally (Fig.4b).

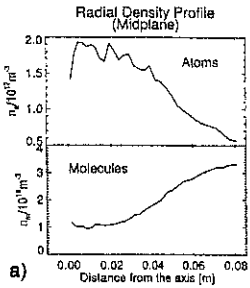

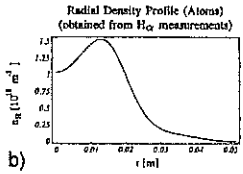

Figs. 4:
a) Calculated density profiles (midplane) for $T_e = T_i = 8eV$ at the anode exit and $D_i = 1m^2/s$
b) Density profile of H atoms derived from H_α diagnostics

Fitted code solution

The various diagnostics in PSI-1 yield hollow density and temperature profiles due to the special configuration of the cathode-anode system which cannot be modelled satisfactorily with radially constant anode boundary conditions. Fig.5b shows a set of anode n_e, T_e profiles (dashed curves) chosen to fit the measured profiles in the midplane (Figs.5a). $T_i = 3eV$ is assumed. Good agreement can be achieved for the T_e profile which is transformed from the anode to the midplane almost without distortion because of the high parallel heat conductivity.

The density profile , however, is largely smoothed out. For $D_i = 0.2m^2/s$ assumed in this case a good fit can be obtained for the plasma region inside the geometric projection (along field lines) of the anode exit (although for an extremely hollow profile at the anode), but in the outer region the density decreases too fast (compared with the experimental results) and a higher value for D_i would be required. ($D_i = 1m^2/s$ yields already a monotoneously decreasing profile in the midplane.) This discrepancy needs still to be clarified (variable D_i , check of the experimental data for larger radii).

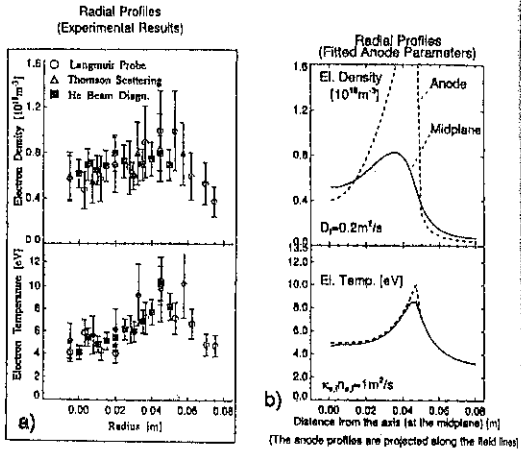

Figs. 5
Measured plasma profiles (a) and code solution for fitted parameters (b)

References

/ 1 / Behrendt, H. et al., 1994 Proc. 21th EPS Conf. on Contr. Fusion and Plasma Physics (Montpellier) p III-1328
/ 2 / Reiter, D., J. Nucl. Mat. 196-198 (1992) 80
/ 3 / Schneider et al., J. Nucl. Mat. 196-198 (1992) 810

Characterization of the Power Deposition Profiles in the Divertor of ASDEX Upgrade

A. Herrmann, M. Laux, O. Kardaun, G. Fussmann, V. Rohde, ASDEX Upgrade Team, NI Team

Max-Planck-Institut für Plasmaphysik, EURATOM Association, Garching and Berlin; Germany

1. Introduction

Handling the high energy flux passing through the plasma boundary into the scrape-off-layer (SOL) of a tokamak is an important problem for reactor-size fusion devices. Especially the maximum heat flux onto the target plates of a divertor tokamak has to be kept below a critical value, which depends on the divertor material. The investigation of the energy transport in the SOL and the control of the dissipated energy is a main topic in the working schedule of ASDEX Upgrade. In this paper we present a scaling of characteristic parameters of the heat flux profile with SOL and plasma parameters. In addition to the scaling, which represents the pragmatic way to derive predictive formulae, we compare a 1D model for energy transport in the SOL with a specially conducted experiment, keeping the experimental conditions as defined as possible.

2. Diagnostics

The parameters of the core plasma and the SOL as well as the heat load to the target plates are routinely measured at ASDEX Upgrade by different diagnostics. In this paper we use the line averaged electron density, $\bar{n}_e$, measured by a DCN interferometer, the electron density at the separatrix, $n_{e,sep}$, from the deconvolution of the interferometer signal, the electron temperature, $T_{e,sep}$, from Thomson scattering, the neutral gas flux, Γ_N, from ionization gauges, the safety factor at 95% of the normalized poloidal magnetic flux, q_{95}, from function parametrization, and the heat load from thermography [1].

3. Experiments

The data used for the scaling are time averaged between 2.3 and 2.8 s, a time interval in which the discharge is normally stable and the heating power is constant. Only plasma shots with a complete set of data were selected. The discharges are routinely characterized by an off-line regime identification procedure discriminating the following regimes: ohmic, low confinement (L), high confinement (H), high radiative L-regime, and completely detached H-regime [2]. The last two regimes, however, were not considered for the scaling described below because the investigation of single shots has shown that for these regimes the target load is very small [3], which makes a peak characterization difficult.

The variation of discharge parameters was as follows: q_{95} = (2.7...4.8), $\bar{n}_e = (3...10)\times 10^{19} m^{-3}$, P_{sep} = (0.8...5.7) MW, $\Gamma_N = (8.4\times 10^{21}...1.5\times 10^{23})$ $cm^{-2}s^{-1}$.

For the comparison of the 1-D energy transport model with the experiment, data from a current ramp down experiment starting at 1.2 MA were used.

4. Results and Discussion

Scaling of profile parameters

Heat load profiles, routinely measured by thermography, are characterized by the total power, P_{plate}, the height of the peak, q_{max}, and the power decay length, λ_p, in the scrape off layer for each

target plate separately. Considering that the radial decay of the heat flux follows an exponential law close to the maximum, but shows a broader shoulder further away, only the region near the peak is used to fit a decay length (Fig. 1).

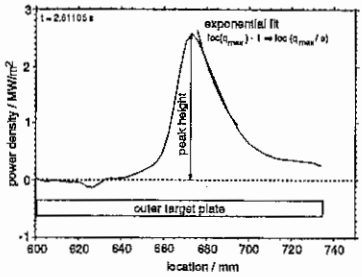

Fig. 1: Heat flux profile across the outer target plate. The characteristic parameters are indicated.

Only global plasma and SOL parameters are used to find a scaling of characteristic parameters of the heat flux profile. At first, the maximum heat flux and the power decay length were fitted against the power flowing into the SOL, P_{sep}, the safety factor, q_{95}, the line averaged density, $\bar{n}_e$, and the neutral particle flux in the outer divertor, Γ_N. The contribution of the plasma current and the magnetic field strength is included via the safety factor only. This scaling shows that both the decay length and the maximum heat flux are only weekly dependent on the neutral particle flux. Furthermore, because only low radiating scenarios are considered, the power to the target plate varies linearly with the power crossing the separatrix. For these reasons, in the scaling presented below, the maximum heat flux and the power decay length were fitted against a reduced parameter set (P_{plate}, q_{95}, $\bar{n}_e$).

The SAS® system for statistical data analysis was used to derive the scaling [4].

Using a simple power law ansatz we obtained the following scalings of the maximum heat flux and the decay length, respectively:

$$q_{max}(Wm^{-2}) = 8.837 \times 10^3 P_{plate}^{0.5\pm0.05}(W)\, q_{95}^{-0.27\pm0.3}\, \bar{n}_e^{-0.77\pm0.16}(10^{19}m^{-3}) \quad (1)$$

$$\lambda_p(mm) = 6.56 \times 10^{-3} P_{plate}^{0.52\pm0.05}(W)\, q_{95}^{0.7\pm0.3}\, \bar{n}_e^{0.09\pm0.17}(10^{19}m^{-3}) \quad (2)$$

The indicated errors denote one standard deviation. Figs. 2 and 3 show the observed versus predicted values for these two scalings.

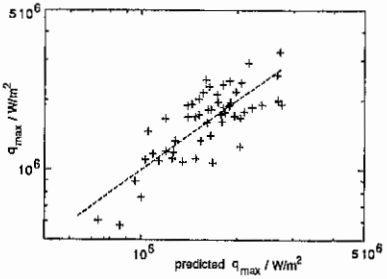

Fig. 2: Measured maximum heat flux to the outer plate versus the predicted value, equ. (1)

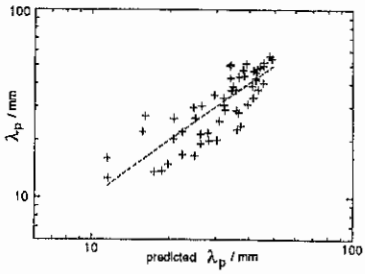

Fig. 3: Measured decay length across the outer plate versus the predicted value, equ. (2)

The above scaling may be interpreted qualitatively in the following manner: Both the maximum heat flux and the decay length increase with the square root of the total power, so that their product, which is proportional to the peak area, is nearly linear to the total power. The line averaged density affects the maximum heat flux, whereas the decay length behavior is influenced by the safety factor. An increase of the line averaged density tends to increase the separatrix density too and causes a decrease of the temperature [5]. As a result, the parallel heat flux to the plates is reduced because electron heat conduction dominates. The safety factor is proportional to the connection length between midplane and target plate. An increasing connection length increases the time for perpendicular transport, resulting in a larger decay length. Additionally, an increase of q_{95} reduces the target load at a given parallel heat flux due to the decreasing pitch angle.

Despite the fact that the scatter of the data is high (the residuals are lower than ± 0.5) the qualitative conclusions of the scaling are stable with respect to modifications of the data set. In detail, however, the exponents may vary slightly. Therefor it proves difficult to compare the results with analytical models. The fact that the scatter of the fit is larger than the experimental errors, indicates that not all relevant parameters are included in the scaling. Because the data were drawn from shots distributed over an extended experimental campaign, hidden parameters might be parameters depending on the first wall conditioning such as for instance the impurity flux.

Divertor detachment: experiment and modeling

In order to keep the experimental conditions as defined as possible, a discharge with a current ramp down from 1.2 MA to about 600 kA with a constant input power of 3.5 MW and a controlled line average density was performed. The variation of the current affects mainly three parameters: the connection length, the temperature and the density at the separatrix. In the following, a 1-D single fluid model for the heat transport parallel to the field through the SOL as proposed by P. J. Harbour [6] is used to correlate the measured target load with plasma parameters at the separatrix. The model allows non-ambipolar boundary conditions at the target plates resulting in an electrical current in the SOL. This current may be one of the reasons for the asymmetric target load found experimentally [7]. In the model, the connection lengths between the midplane and each target are allowed to be unequal. Radiation, ionization and charge exchange are ignored. The target load is described in terms of the Knudsen number, defined as $Kn = \frac{\lambda_{ee,m}}{L_{\parallel,o}}$, where $\lambda_{ee,m}$ is the mean free path for electron-electron collisions in the midplane, and $L_{\parallel,o}$ the connection length between the midplane and the outer target. Note, that the shorter of the two connection lengths is used to define K_n. The model predicts a decreasing target load with inverse Knudsen number, either on account of increasing electron-electron collisions or by increasing connection lengths, see Fig. 4. A strong decrease of the target load is expected if the mean free path of the electrons is only a fraction of the connection length, $Kn < 0.1$. To calculate the Knudsen number from experimental data we used the relations

$$\lambda_{ee,m} \simeq 1.7 \times 10^{16} (m^{-2} eV^{-2}) \frac{T^2_{e,sep}(eV)}{n_{e,sep}(m^{-3})} \quad , \tag{3}$$

and

$$L_{\parallel,o}(m) = 3.07\, q_{95} \quad , \tag{4}$$

resulting in the following expression for the Knudsen number:

$$Kn \simeq 5.5 \times 10^{15} \frac{T^2_{e,sep}}{n_{e,sep}\, q_{95}} \tag{5}$$

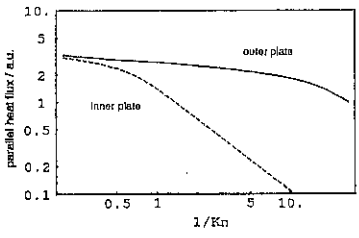

Fig. 4: Parallel heat flux to the outer and inner plate as a function of the inverse Knudsen number according to a 1-D model [6].

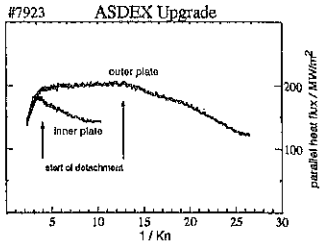

Fig. 5: Parallel heat flux to the outer and inner plate as a function of the inverse Knudsen number derived from experimental data.

The parallel heat flux was calculated from the measured maximum heat flux at the target plate, using the field line pitch derived from the ASDEX Upgrade function parametrization. The power crossing the separatrix is nearly constant in this experiment. Fig. 5 shows the variation of the parallel heat flux versus the inverse Knudsen number. The inner plate starts to detach at an inverse Knudsen number of about 4, the outer plate at about 13. The connection length from the midplane to the inner plate is more than 3 time as long than that to the outer one. Hence one would expect that the inner target starts to detach first, as it is actually found in the experiments. The ratio of the Knudsen numbers at the beginning of detachment is 3.25 and reflects the ratio of the connection lengths, $\frac{L_{\parallel,i}}{L_{\parallel,o}} = 3.4$.

In principle this is predicted by the model , but has to be corrected using the ratio of the associated midplane temperatures. Experimentally this correction factor was found to be close to one, whereas the model predicts a larger factor.

5. Summary

The maximum heat flux and the decay length were scaled with the total power, the electron density, and the safety factor. Both parameters increase with power. An increase of the electron density mainly reduces the maximum heat load. On the other hand, the decay length becomes larger with increasing safety factor.

The simple 1D fluid model is able to describe the beginning of the divertor detachment separately for the inner and outer divertor in terms of midplane parameters and the connection length. The model cannot cover the detached case properly because radiation is not included.

6. References

[1] A. Herrmann, et al., *Plasma Phys. Contr. Fusion* 37 (1) 17 (1995)
[2] P. Franzen, et al., 'Online Confinement Regime Identification for the Discharge Control System at ASDEX Upgrade', *this conference*
[3] M. Kaufmann, et al., *Plasma Phys. Contr. Nucl. Fusion Research* V1 491 (1995)
[4] SAS Institute Inc., SAS User's Guides, Version 6 (1990)
[5] V. Rohde, et al., 'Scrape-off layer behavior in ASDEX Upgrade ohmic L-mode density scan' *this conference*
[6] P.J. Harbour, *Contrib. Plasma Phys.* 28 (1988) 4/5 417-419
[7] M. Laux, et al., *22nd EPS conference on Contr. Fusion and Plasma Phys.* III-097 (1995)

Scrape-off layer behavior in ASDEX Upgrade ohmic L-mode density scan

V. Rohde, A. Herrmann, M.Laux, D.Hildebrandt,
B. Napiontek, M. Weinlich and ASDEX-Upgrade-Team

Max-Planck-Institut für Plasmaphysik, EURATOM Ass.,
Garching and Berlin, Germany

1 Introduction

The transport of particles and energy along the scrape-off layer (SOL) into the divertor and the influence of the divertor conditions on the edge region of the tokamak are crucial issues for the physical understanding of the interaction of SOL and divertor, which in turn is a key problem for the design and operation of ITER. Here we present profiles of plasma parameters in the divertor and at the midplane, respectively, for three regimes of divertor operation.

2 Diagnostics

Radial profiles of electron density n_e, electron temperature T_e, streaming velocity, and plasma potential are routinely observed using the fast reciprocating Langmuir probe (MLP) carried by the manipulator in the outer midplane of ASDEX-Upgrade. The characteristics obtained have been analyzed using a nonlinear fit to an asymmetric double probe characteristic [3]. The divertor plasma conditions are measured by the divertor probe system and the power deposited to the plates by thermography.

3 Profiles

Comparing upstream and divertor temperatures (T_e^{up}/T_e^{div}) and upstream with divertor pressure ($p^{up}/p^{div} = (n_e^{up} * T_e^{up})/(n_e^{div} * T_e^{div})$) different regimes of divertor operation can be characterized. According to LaBombard [1] we classify the following regimes: high-recycling ($T_e^{up}/T_e^{div} > 2$), low-recycling ($T_e^{up}/T_e^{div} < 1.2$) and detached ($p^{up}/p^{div} > 5$).

A typical ohmic discharge ($\#7737, I_p = 0.8MA, B_t = -2.1T$) with a slow density ramp ($2.0 * 10^{19}\ m^{-3} \ldots 5.4 * 10^{19}\ m^{-3}$ in 2 s) was used to study those different regimes including the onset of detachment in ASDEX-Upgrade. To compare radial profiles originating from different poloidal locations we map onto the magnetic flux coordinate ρ.

Radial profiles of T_e, n_e and the derived pressure p taken at the outer midplane are shown in Fig. 1 for three different densities during the ramp. Unfortunately, most of the fixed Langmuir probes in the divertor plates are located in the private flux region, so that only plasma parameters close to the power deposition maximum slightly outside the strike point are available (full symbols in Fig. 1).

Using the saturation current I_e^{sat} and T_e from the MLP the profile of the power load to the probe in the midplane $P = I_{sat} * (\gamma T_e + W_e)$ is constructed, where $\gamma = 7$ is the transmission factor and $W_r = 13.6$ eV the hydrogen ionisation energy. To compare this load with the power flux density measured by thermography we scale the flux density by a factor of 3 (Fig. 2).

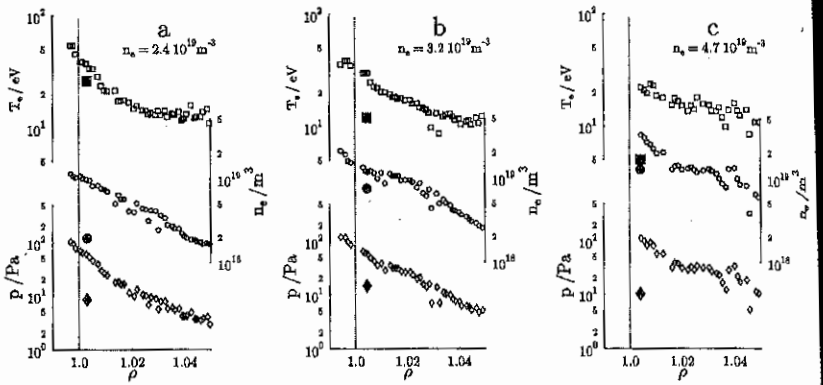

Figure 1: Radial profiles of T_e (squares), n_e (circles), and pressure (diamonds) at the midplane. The three regimes are marked as a, b and c. Mapped data of the divertor probes are indicated by full symbols.

At low densities we find high T_e and a very steep radial gradient of T_e near the separatrix. The radial T_e profile shows two distinct regions with different decay lengths. Comparing with the divertor probes we find almost the same temperature and, therefore, we identify this regime as **low recycling**. But in contrast to LaBombard [1] we also find an unexpectedly large parallel density gradient, causing a pressure difference. On the other hand the SOL-plasma is only weakly collisonal connected to the divertor plate ($\lambda_{cc} = 1.7 * 10^{16}(m^{-2}ev^{-2})T_e^2(eV)/n_e(m^{-3}) = 3m$), so that $\lambda_{ei}/L_c \approx 5$. Consequently, the radial profiles of the power flux density in the midplane and the divertor are equal (Fig. 2 a).

At medium densities (Fig. 1b) the steep T_e gradient near the separatrix vanishes. The pressure drops from the midplane to the divertor by a factor of two as expected. The temperature decreases in the parallel direction by a factor of 2.5 and, therefore, this state of the divertor plasma is called the **high recycling** regime. Comparing probes with plate thermography (Fig. 2 b) we find similar profiles close to the separatrix, but a wider midplane profile at larger distances, although the radially integrated power is nearly the

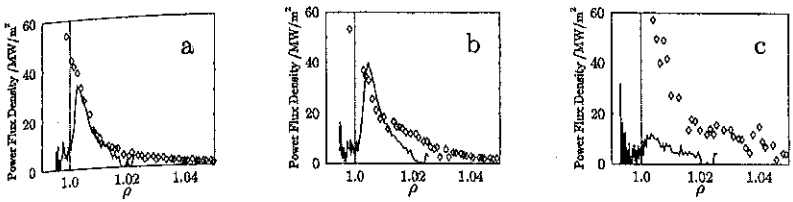

Figure 2: Power flux density profiles from the Langmuir probe at midplane (diamonds) and data measured by thermography to the midplane mapped (solid line).

same.

At high densities very low and flat T_e profiles were measured in the midplane. Close to the separatrix the density rises and shows a steep gradient. Thermography detects much less power at the divertor plates. We find a parallel T_e drop by a factor of 5 and pressure loss by a factor of 10. Therefore we identify this to be the **detached regime.**

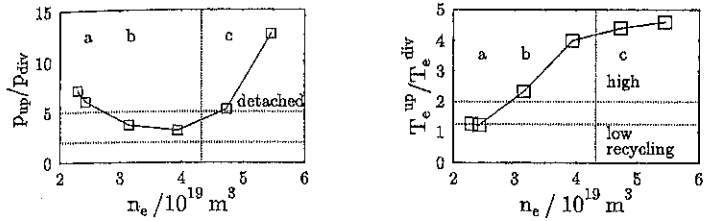

Figure 3: Temperature and pressure losses towards the divertor plasma. Possible criteria for the different divertor regimes are indicated by dashed lines.

The detachment is independently monitored by a divertor spectrometer and found to set on at $n_e \approx 4.3 * 10^{19} m^{-3}$ (indicated in Figs. 3, 4 and 5 by a dashed line). This observation is in close agreement with the classification above.

If we restrict ourselfs to parallel heat conduction only [2], neglecting radiative losses, we can estimate the electron heat conductivity κ_o using $\kappa_o^m \approx \frac{7}{2}(q_{up}L_c)/(T_{up}^{7/2} - T_{div}^{7/2})$. Fig. 4 a shows the derived κ_o^m normalized to the theoretical value $\kappa_o = 4.05 * 10^4(9 - 8 * Z_{eff}^{-1/7})/(Z_{eff}\ ln\Lambda)$ with $Z_{eff} = 2$ and $ln\Lambda$ the coulomb loarithm. Until the onset of detachment κ_o^m is constantly 8 times the theoretical value for heat conduction (an error of 20 % for T_e may explain this decrepancy). With the onset of detachment the ratio rises to 30 because of additional power losses, essentially indicating that the simple model brakes

down.

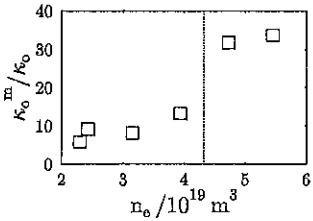

Figure 4: Ratio of Electron heat conductivity κ_o^m/κ_o

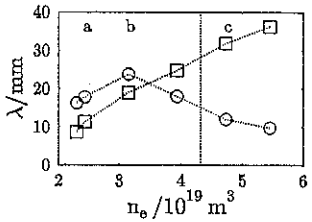

Figure 5: Decay lengths near the separatrix (T_e squares, n_e circles).

The decay lengths of T_e and n_e show different dependences on central density close the separatrix compared to 20 mm inside the SOL. Further out we find a linear rise according to $\lambda_{n_e} = (-8. + 10. * n_e/10^{19}m^{-3})mm$, and the decay length of T_e is 20% bigger than the one for n_e. Near the separatrix a more complicated behavior is observed (Fig. 5). The decay length for T_e rises with central density and for low density plasmas λ_{T_e} it is smaller than λ_{n_e}. The decay length of n_e shows a maximum for medium dense plasmas and reaches again low values for high central density.

4 Summary

Using temperature and pressure gradients we can identify low and high recycling as well as detached regimes of divertor operation. The identified onset of detachment is in close agreement with spectroscopic observations. The decay lengths near the separatrix show a complicated behavior as a function of the bulk density.

5 References

[1] LaBombard, B. et al. , PSI-96, St.Raphael, France

[2] Neuhauser, J. et al. ,Plas. Phys. Contr. Fusion, **31**,p1551,(1989)

[3] Weinlich, M. and Carlson, A. *Proceedings of the second Workshop on electrical probes in magnetized plasmas*, Akademie Verlag, Berlin. (1996).

Investigation of the removal efficiency for D_2, He, and Ne in the ALT-II limiter throat

G. Mank, M.Z. Tokar', K.H. Finken, J.A. Boedo*, T. Denner, J. Hobirk, R. Jaspers, U. Samm
Institut für Plasmaphysik, Forschungszentrum Jülich, Ass. Euratom-KFA, Germany
**FERP, University of California, San Diego, USA*

1. Introduction

The flow pattern in the exhaust channel of a pump limiter is a critical issue for density and impurity control, because it determines the removal of the hydrogen isotopes and helium ash, as well as the removal of seed impurities as proposed for edge radiation cooling. In order to get an extended understanding of the transport of intrinsic gases (D_2,H_2) and seed impurities (e.g. Ne, He) after the collection and neutralization of the ions, either on divertor plates or on a limiter, the removal efficiency has been studied independently from the transport in the plasma confine region and compared with theoretical calculations.

2. Experimental investigation

The Alt-II toroidal belt limiter at TEXTOR-94 is used to investigate the particle exhaust. The experiment discribed here uses the same experimental set-up as in [1], therefore it will be discribed only briefly (figure 1). Particles of a selected test gas are injected into the throat of the Alt-II pump limiter close to the neutralizer plate. Both the amount of injected gas (Φ) and their density in the plenum (n^{Pl}) are measured (resolved for the considered gas species). For the removal of this test gas a removal efficiency $\varepsilon^*_{rem} = S_{eff} \cdot n^{Pl}/\Phi$ is defined, with S_{eff} being the effective pumping speed of the different species. ε^*_{rem} contains not only the "standard" vacuum removal efficiency $\varepsilon_{0,rem}$ but also the influence of the background plasma due to ionization (and subsequent sticking to field lines), due to viscous forces (due to a streaming background plasma), due to thermal forces, and due to pressure gradiant forces in the scoop. The removal efficiency is the ratio of the number of pumped particles to the one of injected particles. The density of the test particles in the throat depends on the plasma background condition (n_{th},T_{th}). Since the time constant of the particle removal in the throat is relatively short ($\tau \sim V/S_{eff} \sim 100$ ms) the flow of the test gas (D_2, He, Ne) is kept constant at changing plasma parameters. The electron-density inside the throat varies between $5 \cdot 10^{11}$ cm^{-3} and $6 \cdot 10^{12}$ cm^{-3} and the electron temperature between 8 and 18 eV. Figure 2 shows the

experimental results for the removal efficiency ε^*_{rem} versus the electron density in the throat. Without background plasma the measured removal efficiency ε_0 agrees with the value obtained from vacuum conductance consideration. For helium (filled squares) ε^*_{rem} clearly exceeds the value of the plasma free case at low densities. Values from a previous experiment [1] (open squares) are included, where the removal efficiency decreases for increasing density. For neon (filled diamonds) ε^*_{rem} is somewhat lower than for He and for deuterium (stars) ε^*_{rem} is increasing to about 0.6. The results for deuterium agree within the error (about 20 % for these measurements) with previous measurements done at the ALT-II limiter [2]. The experiment reflects the influence of the plasma parameters as it can be described by an analytical model of the transport [3] taking a hydrodynamic approximation.

3. Discussion

The removal efficiency ε_{rem} of deuterium, helium, and neon relative to the throat electron density for different throat electron temperatures has been calculated with the analytical model. The removal efficiency, $\varepsilon_{rem}=1-J_n^{th}/J_i^{th}$ (where J_i^{th} is the influx of ions from the SOL into the limiter throat and J_i^{th} is outflow of neutrals into the SOL) is determined by the neutral transport in the limiter throat. We assume that diffuse collisions of neutrals with the side walls lead to randomization of their velocities and as a result the motion alongside the throat is diffusion like. The effective diffusivity D_n is estimated as $v_n\delta$, where v_n is the thermal velocity of particles and δ is the throat width. The dependence of ε_{rem} on D_n, pumping speed S_{eff}, throat length L_{th} and the width L_o of the plenum opening in the direction perpendicular to the magnetic field is expressed as follows: $\varepsilon_{rem}\approx S_{eff}\cdot L_{th}/(S_{eff}\cdot L_{th}+\zeta_i\cdot D_n\cdot\delta\cdot L_o)$. Here the factor $\zeta_i=\alpha/sh\alpha$ (with α being the ratio between L_{th} and the ionization length $\lambda_i=(D_n/k_i/n_{th})_{1/4}$) describes the increase of the removal efficiency with ionization of neutrals in the throat.

Figure 3 shows the results for the removal efficiency of deuterium. With increasing electron density and increasing electron temperature the removal efficiency increases, which has been found in the experiment as well. Taking a reduction factor of 1.5 as in [1] for the electron temperature into account, T_{th} has to be taken between 5 and 8 eV . Thus the resulting removal efficiency ε_{rem} increases to about 0.6 qualitatively in agreement with the experiment. The calculations for helium and neon agree also qualitatively with the measurement. However, if we assume that the plasma temperature changes with n_{sc} in such

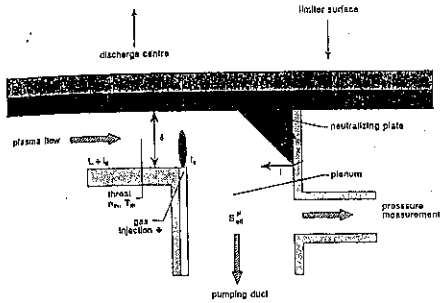

Fig. 1: Schematic description of the throat of one of the limiter blades. Deuterium, helium, or neon is injected into the throat close to the neutralizer plate.

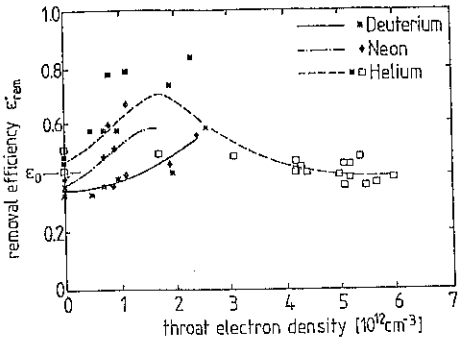

Fig. 2: Experimental results for the removal efficiency for D_2, He, and Ne as determined by the measurement of the influx of the gases relative to the neutral density in the pumping duct. (The lines are drawn to guide the eye.)

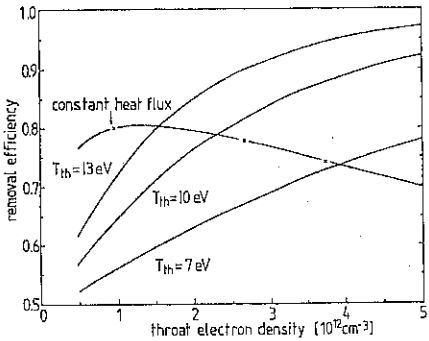

Fig. 3: Calculation of the removal efficiency for deuterium for different electron temperatures.

a way that the heat flux into the throat, being proportional to $n_{th}T_{th}^{3/2}$, remains unchanged, the removal efficiency should decrease with increasing electron density as shown in figure 3. At high electron densities the approximation of the model used here becomes invalid. In figure 4 the removal efficiencies of D_2, He, and Ne for constant heat flux relative to the throat electron density are shown. The result emphasizes the relative behaviour of the different gases. However, at the different experimental points the heat flux was not constant as assumed and therefore the calculated data do not agree qualitatively with the measured ones. For helium at higher electron densities (open squares) the results of the calculations predict - in agreement with the measurements - a decrease of the removal efficiency with increasing density. It should be noted, that for similar conditions the removal efficiency for neon is about 50 % higher than for helium. This may explain results in [4] where it was found, that the effective particle confinement time $\tau^*_p = \tau_p/\varepsilon_{col}\cdot\varepsilon_{rem}$ (with ε_{col} being the collection efficiency) is much lower for neon as for helium.

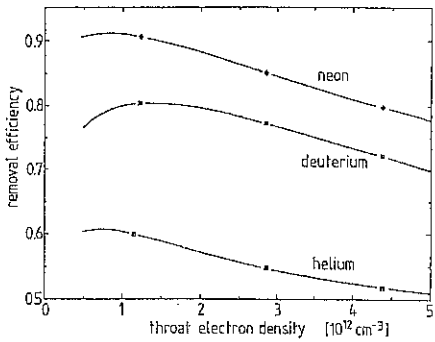

Fig. 4: Calculation of the depence of the removal efficiency on the plasma density in the throat under the assumption of a constant heat flux proportional to $n_{th}T^{3/2}$.

References

[1] G. Mank, et al., Nucl. Fusion **34** (1994) 1641.
[2] D.S. Gray, et al., J. Nucl. Mater., **196 - 198** (1992) 1096.
[3] M.Z. Tokar', D. Reiter, Proc. 19th EPS, Innsbruck, Europhys. Conf. Abstracts, Vol.16C (1992) 741.
[4] G. Mank, et al., Proc. 22nd EPS, Bournemouth, Europhys. Conf. Abstracts, Vol. 19C (1995) I-57.

CHARACTERISTICS OF THE IMPURITIES MO AND W IN DISCHARGES WITH NEON EDGE RADIATION COOLING IN TEXTOR-94

J. Rapp, G. Bertschinger, L. Könen, H.R. Koslowski, A. Krämer-Flecken, K. Ohya*, V. Philipps, A. Pospieszczyk, M. Rubel**, U. Samm, B. Schweer, T. Tanabe***, M.Z. Tokar, B. Unterberg and G. Van Oost****

Institut für Plasmaphysik ASS-Euratom, Forschungszentrum Jülich GmbH

* University of Tokushima, Japan

** Royal Institute of Technology Physics Department-Frescati, ASS-Euratom-NFR, Stockholm, Sweden

*** Center for Integrated Research, Nagoya University, Japan

****Laboratoire de Physique des Plasmas - Laboratorium voor Plasmafysica - ERM/KMS - ASS–Euratom-Belgian State, B-1040 Brussels, Belgium

1. Introduction

High-Z materials as tungsten are intended to be used as a divertor material in future fusion reactors due to their low sputtering rates and high melting points. One of the questions is, whether the use of high-Z materials is compatible with the concept of a cold radiative boundary. To investigate the local release and transport behaviour of the impurities, Mo and W test limiters were used in auxiliary heated discharges under different radiation scenarios with neon seeding. In order to extend the description of the general accumulation behaviour, given already by Fussmann [1], ohmic discharges with several impurities were investigated in more detail.

2. Experimental set-up

In the limiter tokamak TEXTOR-94 ($R_0 = 175cm$, $a = 46cm$ determined by the toroidal belt limiter ALT-II) we used W and Mo test limiters usually placed at $r = 45cm$. Additionally we performed gas puff experiments with Xe and some laser ablation experiments with W and Mo. As main diagnostics for the core plasma a 26-channel bolometry system, a 9-channel HCN-interferometer/polarimeter and a 11-channel ECE-system were used. With VUV-spectroscopy we obtained measurements of Ne VIII (77nm), Mo XXVII (56.9nm), Xe XXVI (17.4nm) and W (quasi-continuum, 5nm). The impurity source information we determined from Mo I (390.3nm, 414.3nm) and W I (400.8nm).

3. Ohmic discharges

In ohmic discharges ($I_p = 350kA$) accumulation of Mo and W above a critical density of $\overline{n_e} \approx 2.5 - 3.0 \cdot 10^{13} cm^{-3}$ [2,3] was observed already, which led to instabilities with periodically repeat (fig.1). The concentration profiles of W, derived from bolometric measurements by using the data of Post [4] for coronal equilibrium, showed prior to the internal disruption peaked profiles with central values of $1.6 \cdot 10^{-4}$ (fig.3), which remain almost unchanged after the internal disruption. Similar to the experiments with high-Z limiters we observed accumulation in gas puff experiments with xenon (fig.2). To investigate the accumulation scenario in more detail, q-profiles (fig.4) are evaluated before and during the

accumulation as well as before and after the internal disruption. In general the scenario can be explained in the following way:

Phase 1: The sawtooth amplitude decreases and $T_e(0)$ is reduced up to the point, when q_0 exceeds 1.

Phase 2: The central concentration of the high-Z impurity increases on a much faster time scale, $T_e(0)$ is further reduced and $Z_{eff}(0)$ increases. The measured q-profile (t=2.34s) shows a reversed shear in the central region, consistent with the observations on $T_e(0)$ and $Z_{eff}(0)$.

Phase 3: The current displacement, due to the strong cooling of the plasma center, drives a $m/n = 2/1$ MHD instability, which leads to an internal disruption. After the internal disruption the T_e-profile recovers slightly while keeping $q_0 > 1$ (t=2.42s).
Already in other tokamaks it was observed, that the reversed magnetic shear can lead to improved confinement [5]. A transport barrier is developed, so that the transport coefficients in the region of negative magnetic shear are reduced to neoclassical values. This might be the reason for the good central confinement even after the disruption, which was already observed in the W-test limiter experiments, and furthermore enhances the accumulation procedure in phase 2.

4. Auxiliary heated discharges

In additionally heated plasmas ($P_{heat} = 1.6MW, I_p = 350kA, \overline{n_e} = 2.5 \cdot 10^{13}cm^{-3}$), with the test limiter at $r = 45cm$ absorbing 5% of the convective energy, for radiation levels $\gamma_{rad} = P_{rad}/P_{heat} > 0.65$ accumulation of tungsten took place. Again we observed quite similar phenomena as in ohmically heated plasmas (fig.5):

Phase 1: With Ne-puffing the sawtooth amplitude of T_e decreases while the density profile peaks and impurity concentration in the center is increasing slowly.

Phase 2: The central concentration of the high-Z impurity increases dramatically, $T_e(0)$ is further reduced and finally reaches a stationary condition with central W-concentrations of $\approx 10^{-3}$.
Under the same discharge conditions no accumulation of neither Mo nor Xe was found, although τ_p is increasing with higher density and higher γ_{rad}. In addition in a few experiments laser ablation of W and Mo were performed. Only W was found to accumulate ($P_{heat} = 1.6MW$, $\overline{n_e} = 4.0 \cdot 10^{13}cm^{-3}$, $\gamma_{rad} = 0.75$). Polarimetric measurements confirmed recently in laser ablation experiments with W the development of a reversed magnetic shear during the accumulation. For the test limiter experiments in figs.7 and 8 a comparison of the intensities of the local W I and Mo I line radiation with the corresponding central line brightness shows the influence of the radiation level γ_{rad} on the impurity confinement. The source varies only weak with γ_{rad}, while the central values of W and Mo are clearly increasing. In contrast to the results in the laser ablation experiments with the W test limiter for $\gamma_{rad} = 0.75$ and $\overline{n_e} = 4.0 \cdot 10^{13}cm^{-3}$ no accumulation occurred. This is mostly

due to a reduced impurity source. $T_e(r = 45cm)$ drops from $45eV$ to $32eV$ and the line intensity W I decreases absolutely by a factor of 2.5 and the ratio of the fluxes W I/H_γ by a factor of 3.

5. Impurity transport

To investigate the transport behaviour during the accumulation period in more detail the neoclassical inward pinch velocity is determined from measured T_e and n_e profiles. The collision frequency of Mo, Xe and W is larger than their bounce frequency, thus they are in the PS-regime, while the background ions are in the BP–regime. In fig.6 the normalized pinch velocity (calculated from $v_z/(zD_{neo}) = 1/n_i \cdot \partial n_i/\partial r - 1/2T_i \cdot \partial T_i/\partial r$, $n_i = n_e$, $T_i = T_e$) is shown for several times with respect to fig.5. During phase 1 sawteething and temperature screening is still present, while the impurity concentration is increasing slowly. In phase 2 with $q_0 > 1$ sawteething disappears, and no temperature screening is present anymore, so that the neoclassical inward flow gives rise to the central impurity concentration. The cooling of the plasma center then further decreases $T_e(0)$ and consequently increases v_z again.

6. Summary

We found a general explanation of the accumulation behaviour, which can be divided in 3 phases: A sawtoothing period with temperature screening and $q_0 < 1$; a non-sawteething period with a dramatic accumulation of impurities in the center which leads to a reversed magnetic shear and improved confinement; and a period (for ohmic discharges), where the current displacement drives an MHD-instability, which leads to a internal disruption. The accumulation behaviour in ohmic discharges for Mo, Xe and W is quite similar. In NBI-heated discharges with radiation cooling an increasing confinement with increasing radiation level and density was observed. But accumulation just occurred with W and $\gamma_{rad} > 0.65$ for test limiter experiments with $\overline{n_e} = 2.5 - 3.0 \cdot 10^{13} cm^{-3}$. Accumulation in test limiter experiments can be avoided by increasing the density. This is due to synergetic effects: 1.) lower T_e at the edge and consequently lower sputtering yield, 2.) less low-Z impurities (neon) and consequently lower sputtering yield, 3.) less impurity-impurity driven fluxes, which result in a smaller inward pinch velocity.

7. References

[1] G. Fussmann et al., J. Nucl. Mater., **162-164** (1989)
[2] V. Philipps et al., Nuclear Fusion, **34** (1994)
[3] V. Philipps et al., Europh.Conf.Abstr. Vol.19, Part II, 321 (1995)
[4] D.E. Post et al., Atomic Data and Nuclear Data Tables, **20** (1977)
[5] E. Joffrin et al., Europh.Conf.Abstr. Vol.17C, Part I, 321 (1993)

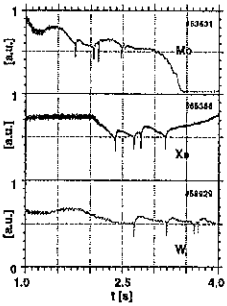

Fig.1: Accumulation scenario in W and Mo test limiter and Xe gas puff experiments with internal disruptions

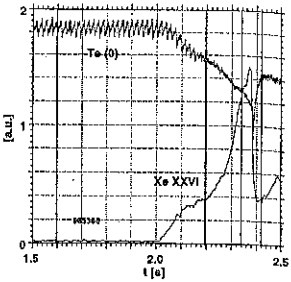

Fig.2: Accumulation scenario in xenon gas puff experiment, comparison of central Te and Xe XXVI

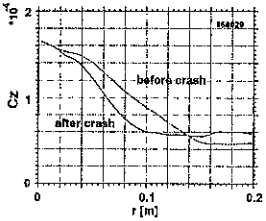

Fig.3: Tungsten concentration profiles before and after the internal disruption

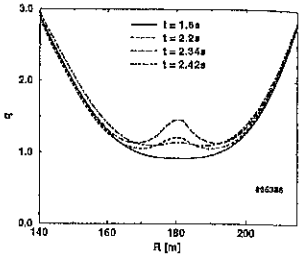

Fig.4: q-profiles during accumulation of xenon in ohmic discharge (Ip=350kA)

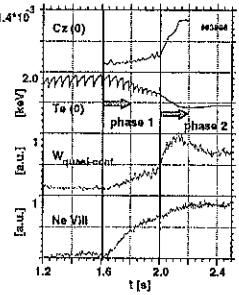

Fig.5: Tungsten test limiter: Accumulation scenario in auxiliary heated discharge with radiation cooling (75%)

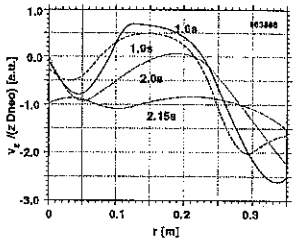

Fig.6: Neoclassical pinch velocity Vz / (z Dneo)

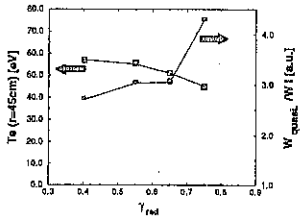

Fig.7: Tungsten test limiter (r=45cm), Fraction of Ag-and Pd-likes W-ions to neutral W and Te as function of γ_{rad}

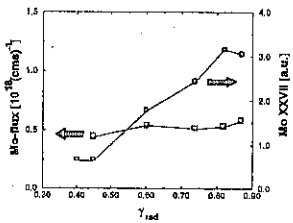

Fig.8: Molybdenum test limiter (r=45cm), comparison of Mo XXVII with Mo-flux at the edge as function of γ_{rad}

A Predictive Study of the JET Mark II Gas Box Divertor

R Simonini, G Corrigan, G Radford, J Spence, A Taroni, G Vlases
JET Joint Undertaking, Abingdon, Oxon, OX14 3EA, United Kingdom

INTRODUCTION

A principal aim of divertor studies at JET is to develop and verify solutions that are relevant for ITER power exhaust and particle control. The Mark II GB divertor was designed specifically to test the ITER Gas Box concept, and is due to begin operation in mid 1997.

The Mark II GB divertor incorporates a flexible design which allows several configurations to be tested. These include horizontal and vertical targets, and an optional septum of as yet unspecified conductance to neutrals. A third possible variant is one which uses a broad, opaque septum to form a double slot divertor.

The EDGE2D/NIMBUS [1] modelling reported in this paper was undertaken to compare the various configurations from an overall performance standpoint.

The perpendicular transport model used is $D_\perp$=0.5 m^2/s, v_{pinch}=7.5 m/s, $\chi_i = \chi_e = 1$ m^2/s, constant in space, which has been shown to give reasonable simulations of attached L-mode JET plasmas. The Monte Carlo package contains a detailed model of the divertor volume, and includes pumping and by-pass leakage.

EFFECT OF SEPTUM ON A RECYCLABLE IMPURITY

We consider first the case of a deuterium plasma seeded with nitrogen, assumed to be fully recycling. The results are obtained for an equilibrium configuration (I_p=4.5MA), with vertical targets. Fig. 1 shows parts of the computational mesh adopted, with details of the divertor region. In the model, the vessel and the divertor are made of carbon, while the sub-divertor region is made of iron. Sputtering of wall material is inhibited for the runs with nitrogen. We have performed scans of the density at the separatrix mid-plane, n_s, and impurity radiated power, P_{rad}. The required level of P_{rad} is achieved by changing the content of nitrogen through gas puffing. The pumping efficiency of the cryopumps is taken to be 20% for both deuterium and nitrogen. The conductance of the divertor wall to neutrals has been estimated by Monte Carlo calculations [2]. Neutrals entering the by-pass leaks are re-injected at the bottom of the main chamber, while the pumped deuterium is fed back into the SOL from the top of the vessel. Ions diffusing outside the computational mesh toward the vessel are assumed to be transported along field lines and recycled near the divertor shoulders. Boundary conditions at the edge of the computational domain toward the walls are $\nabla_\perp T$=0 and decay length of λ_n=2.5 cm for temperature and density, respectively.

Table I shows relevant parameters for comparing the effects of the presence and shape of the septum for separatrix density $n_s=2\times10^{19}$ m^{-3}, input power $P_i=P_e$=5 MW uniformly into the edge, and impurity radiated power P_{rad}=6 MW.

None of the three configurations seems to have a clear advantage over the others. The small differences listed in Table 1 tend to disappear or even change direction at lower density such as $n_s=1\times10^{19}$ m^{-3} or at lower radiation power. Note that the distribution of the radiated power, as expressed by the fraction $P_{rad,sol}$, does not mirror the impurity density distribution (N^z_{sol}/N^z_{tot}) because of the limited temperature range where radiation is effective.

Table 1. $n_s=2\times10^{19}m^{-3}$, $P_i=P_e=5MW$, $P_{rad}=6MW$, recycling Nitrogen

Symmetry indicators (SOL averages)

Septum	p_{up} (Pa)	$T_{e,up}$ (eV)	p_{out} (Pa)	$T_{e,out}$ (eV)	p_{in} (Pa)	$T_{e,in}$ (eV)
none	292.8	40.5	87.3	5.9	12.5	1.0
opaque	291.2	40.1	85.2	5.7	16.6	1.2
deep V	297.1	40.7	77.2	4.4	39.8	2.1

Particle and power balance

Septum	N^z_{sol}/N^z_{tot} (%)	S^z_{sol}/S^z_{tot} (%)	$P_{rad,sol}$ %	$Z_{eff,max}$ (sol)	N_z/N_i (%)	$\Gamma^{0,i}_{pump}$ ($10^{21}s^{-1}$)	$\Gamma^{0,z}_{pump}$ ($10^{19}s^{-1}$)
none	66.1	12.1	22.3	1.8	0.92	4.0	7.6
opaque	67.2	7.7	17.3	1.7	0.86	4.0	7.6
deep V	74.1	6.1	17.0	1.8	1.19	4.0	15.4

EFFECT OF SEPTUM ON THE INTRINSIC IMPURITY CARBON

In this case, carbon is produced by sputtering. The dominant process is chemical sputtering, for which we have used the model of Ref.[3]. Fig. 2 shows Z_{eff} along the separatrix for the three cases of septum out, septum in, deep V, for $n_s=2\times10^{19}m^{-3}$ and $P_i=P_e=5MW$.

The difference in Z_{eff}, due to additional material sputtered from the carbon structure in the private region, influences the approach to detachment, as illustrated in Table 2. While the mid-plane temperature is nearly the same for the three configurations (about 40 eV), the carbon concentration N_z/N_i increases from 3.7% to 8.8% to 19%, and radiation from 6 MW to 8 MW to 9 MW. In the deep V case, the plasma is fully detached. Note that even though the content of C is much higher, the radiated power is not much higher, again a consequence of the narrow range of temperatures effective for radiation. A fully detached plasma may not be useful since the SOL becomes more and more transparent to neutrals.

Table 2. Approach to detachment induced by carbon, $n_s=2\times10^{19}m^{-3}$, $P_i=P_e=5MW$

Septum	Γ^i_{target} (10^{23} s^{-1})	$P_{e,target}$ (MW)	$P_{H,rad}$ (MW)	$P_{H,cx}$ (MW)	P_{rad} (MW)	N_z/N_i (%)
none	3.1	2.4	0.3	0.8	6.3	3.7
opaque	1.7	0.8	0.3	0.5	8.0	8.8
deep V	0.9	0.4	0.2	0.4	8.8	19.4

However, these results depend drastically on the model assumed for chemical sputtering, which is subject to large uncertainties. We have assessed the effect of reducing chemical sputtering by a constant factor. In particular, for the sake of comparison with nitrogen, we have reduced the sputtering yield for carbon to 57% of that given in Ref.[3] so as to radiate 6 MW. While most parameters barely differ, there is a difference in the level of impurities necessary to radiate the required power (N_z/N_i equals 0.86% with N and 3.6% with C), and the density distribution is also different (N^z_{sol}/N^z_{tot} equals 67% with N and 38% with C). This is due, at least in part, to the broader radiation efficiency of N as a function of temperature.

The carbon sputtered from the main chamber is not the main cause of SOL contamination. When the sputtering is artificially switched off everywhere except in the divertor, in the case of no septum P_{rad} decreases from 6.3 MW to 5.9 MW, the impurity concentration from 3.7% to 3.3% and the maximum of Z_{eff} from 2 to 1.8.

VERTICAL VS. HORIZONTAL TARGETS

Another geometrical configuration being considered is that with horizontal targets (Fig. 3), for which again the septum makes little difference. It is found however that the horizontal configuration tends to enter less easily into the regime of detachment than the vertical one, by requiring a larger amount of seeded impurity to radiate (1.3% vs. 0.86% for $n_s=2\times10^{19}$ and P_{rad}=6MW with opaque septum), since the recycling of D neutrals from the vertical targets toward the separatrix tends to produce a wider region where radiation is effective. As a consequence, the larger amount of seeded nitrogen required in the horizontal target configuration produces Z_{eff} = 2.0 at the outer mid-plane at the separatrix, whereas Z_{eff} =1.7 in the vertical one.

The vertical configuration has also the obvious advantage of a wider spreading of the heat load over the target plates. This is especially important at high power. Fig. 4 compares the heat loading along the outer target for $n_s=2\times10^{19}m^{-3}$ and P_{rad}=3 MW. We note that the ratio of peak heat loads between the horizontal and vertical targets is worse than that expected from the consideration of the change in wetted target surface alone.

CONCLUSIONS

For given n_s and P_{rad}, the presence or the shape of the septum does not influence appreciably most hydrogenic plasma parameters. For a recycling impurity introduced to increase radiation, the septum details likewise have little effect on impurity content. The shape of the septum does affect, however, the content of an intrinsic impurity such as carbon, affecting the approach to detachment and core contamination. Little difference is found between carbon and nitrogen for fixed P_{rad} , except for the fact that more C than N is required to radiate the same amount. There is not enough D flow, resulting from pumping and leakage, for impurity entrainment in the divertor, the low level of C retention, in particular, being mainly due to transport and not to the sputtering from the vessel wall outside the divertor. These conclusions hold for both vertical and horizontal targets, but in addition the horizontal targets have to sustain a much

higher peak heat load. In any case, no solutions have been found with simultaneous detachment, high radiated power fraction and retention of impurities for Mark II GB in JET.

REFERENCES

[1] R Simonini, G Corrigan, G Radford, J Spence, A Taroni, Contrib. Plasma Phys. 34(1994)368

[2] E Deksnis, private communication

[3] A Pospieszczyk, et al., Proc. 22nd EPS Conf. 19-II(1995)309

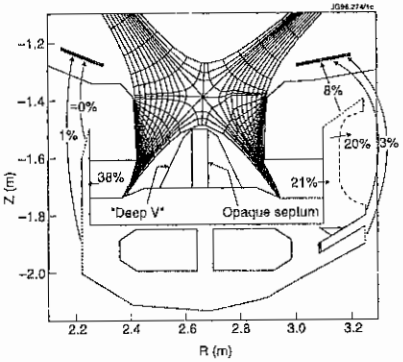

Fig.1. Vertical GB geometry, showing the three septum configurations, pumping and leakages

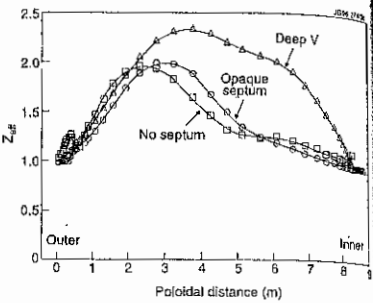

Fig.2. Poloidal profiles of Z_{eff} at separatrix with carbon as the radiating impurity for the three septum configurations, $n_e \sim 2\times10^{19}m^{-3}$, $P_i : P_e = 5MW$

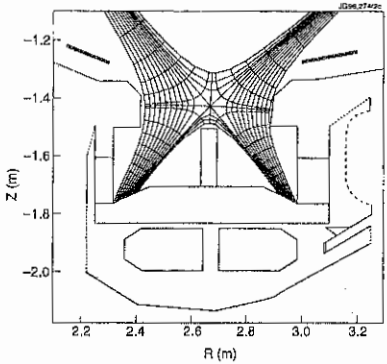

Fig.3. Horizontal GB divertor configuration

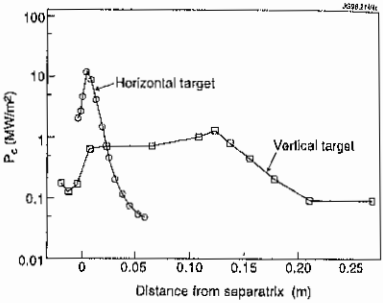

Fig.4. Heat loading on the outer divertor plate for the vertical and horizontal configurations, with nitrogen, $n_e \sim 2\times10^{19}m^{-3}$, $P_i : P_e$ 5MW, P_{rad} 3MW

STATISTICAL PROPERTIES OF TURBULENT TRANSPORT AND FLUCTUATIONS IN TOKAMAK AND STELLARATOR DEVICES

M.A. Pedrosa, C. Hidalgo, B. van Milligen, E. Sánchez, R. Balbín, I. García-Cortés
Asociación Euratom-Ciemat, 28040 Madrid, Spain

H. Niedermeyer, L. Giannone
IPP Association, Garching, Germany

INTRODUCTION

To go deeper into our understanding of plasma edge turbulence and into the mechanisms underlying anomalous transport, it is important to measure not only the fluctuation-induced transport but also the statistical properties of the time resolved turbulent flux [1].

The statistical properties of plasma fluctuations and turbulence transport have been investigated in the plasma bulk side and in the scrape off layer (SOL) side of the velocity shear layer of tokamak (TJ-I) and stellarator devices (TJ-IU). Comparative studies between the radial correlation of turbulent fluxes and fluctuations are under way in the TJ-IU torsatron.

EXPERIMENTAL SET UP

Measurements of fluctuations and turbulent flux have been carried out in the ohmically heated TJ-I tokamak (R=0.3 m, a=0.1 m, $\bar{n}_e \approx (1\text{-}3)\times10^{19}$ m^{-3}, $B_t \approx 1$ T, $I_p \approx 30$ kA) [2] and in the electron cyclotron resonance heating TJ-IU torsatron (ℓ=1, m=6, P_{ECRH}=200 kW, ν_{ECRH}=37.5 GHz, $\iota \approx 0.23$, R=0.6 m, $\bar{a} \approx 0.1$ m, $\bar{n}_e \approx 0.5\times10^{19}$ m^{-3}, B_t=0.67 T) [3] by means of Langmuir probes. One tip of the Langmuir probe array is used to measure ion saturation current (I_s) and two tips, aligned perpendicular to the magnetic field and poloidally separated $\Delta \approx 2$ mm, are used to deduce the poloidal electric field ($E_\theta \approx [\Phi(\theta_1)-\Phi(\theta_2)]/\Delta$) from the measured floating potential (Φ). Fluctuations in the poloidal electric field have been deduced from the floating potential fluctuation measurements and electron density fluctuations are given by $\tilde{n}_e \approx \tilde{I}_s$.

To determine the radial scale length of fluctuations and turbulent fluxes, we have designed a specific experimental set up. Two arrays of Langmuir probes 1 - 2 cm radially separated were used to obtain simultaneous measurements of fluctuations and turbulent transport at two radial positions. Probes were oriented with respect to the magnetic field direction in such a way that shadows between them were avoided (Fig. 1).

The influence of electron temperature fluctuations in the computation of the particle transport due to fluctuations has been investigated in the W7-AS stellarator. The fast sweeping Langmuir probe method has been used to determine the fluctuating spectra of the electron temperature fluctuations and their correlation with electron density fluctuations [4].

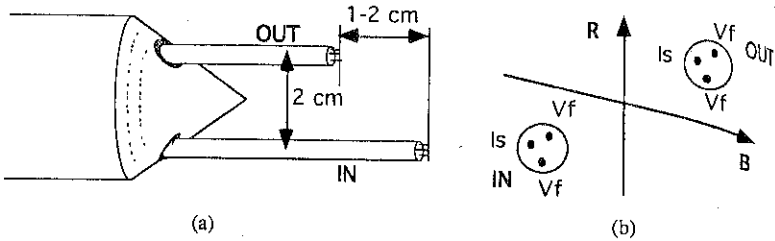

Fig. 1.- Experimental set up for radial correlation measurements. (a) Design of probes, (b) location of probes in the plasma (top view).

PROBABILITY DISTRIBUTION FUNCTION OF THE TURBULENT FLUX

The statistical properties of the radial turbulent particle flux, $\Gamma_T = \tilde{n}_e \tilde{E}_\theta / B_t$ (where $\tilde{n}_e$ and $\tilde{E}_\theta$ are the fluctuating density and poloidal electric field respectively), have been studied neglecting the electron temperature fluctuations effects in TJ-I and TJ-IU both in the plasma edge ($r<a_s$) and in the scrape off layer ($r>a_s$) regions, where a_s is the radial location of the velocity shear layer [3,5]. The shear layer location has been used as a reference point. The normalized turbulent radial flux results predominantly positive, that is on average the flux is outwards, and bursty. The local probability distribution function (PDF) of fluctuations and turbulent flux has been calculated. The local turbulent flux PDF results not symmetric. This asymmetry gives a measure of the average flux out compared to the maximum instantaneous fluxes. The local flux PDF presents a systematic variation as a function of the radial location (Fig. 2). Its non-Gaussian character is clearly seen: there exist large amplitude transport bursts that account for a significant part of the total flux. The PDF of the fluctuations, both density and electrostatic potential, have Gaussian character at the plasma edge. However the PDF of the ion saturation current fluctuations deviates from Gaussian in the SOL region.

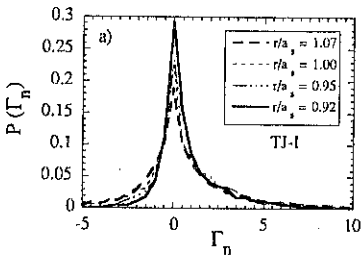

Fig. 2.- Flux PDF computed at different radial positions in TJ-I

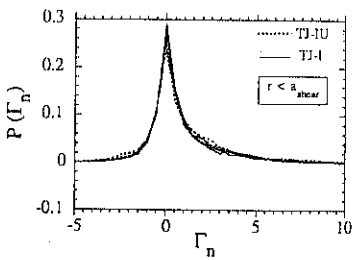

Fig. 3.- Comparison of flux PDF in the edge of TJ-I and TJ-IU.

To study changes in the statistical properties of the turbulent transport, related to global characteristics of the plasma (i.e. heating, current, electric field...), the local flux PDF for TJ-I and TJ-IU plasmas have been compared (Fig. 3). The structure of the local flux PDF appears very similar in both devices.

In the W7-AS stellarator the phase between density and electron temperature fluctuations is close to zero in the SOL and as a consequence the resulting turbulent flux is strikingly similar to the one calculated under the assumption $\tilde{T}_e/T_e = 0$ [6]. These results suggest that, although $\tilde{T}_e/T_e$ can be significant [7], the turbulent fluxes could be computed neglecting their effects.

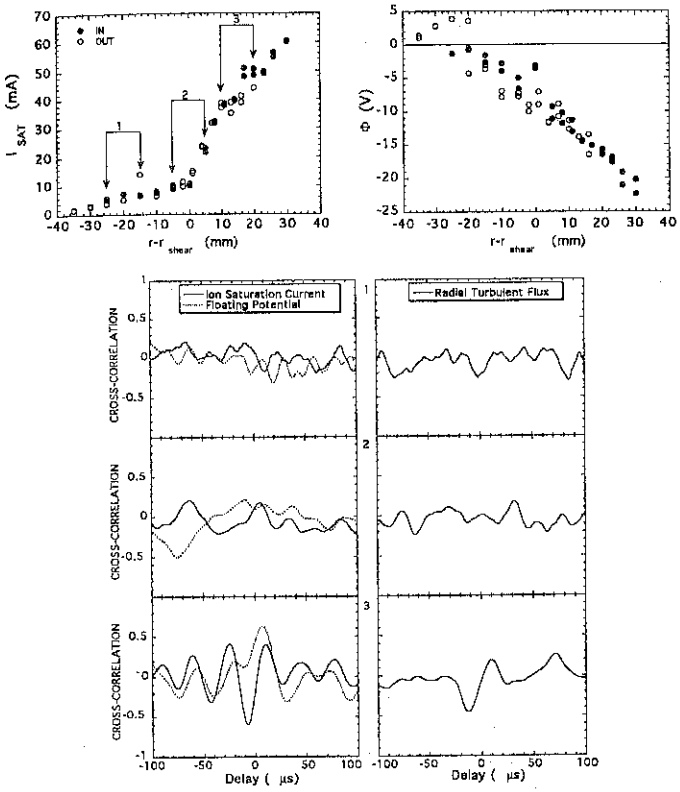

Fig. 4.- Radial profiles of the ion saturation current (I_{sat}) and of the floating potential (Φ) and radial cross-correlation (I_S-I_S, Φ-Φ, and T_e-T_e) measured at different probes positions: 1-both probes in the SOL, 2-one in the SOL and the other one in the bulk side of the shear layer, 3-both probes in the bulk side of the shear layer.

RADIAL SCALE LENGTH OF FLUCTUATIONS AND FLUXES

In order to compare the values of the characteristic radial scale length of turbulent fluxes and fluctuations, we have simultaneously measured the levels of fluctuations ($\tilde{I}_s$ and $\tilde{\Phi}$), and the turbulent fluxes have been computed, at two different radial locations ($\Delta r \approx 1$ - 2 cm) in the TJ-IU plasma boundary region. The obtained radial profiles of these magnitudes are shown in Fig. 4 together with the radial cross-correlation calculated for fluctuating signals and turbulent transport. Figure shows the correlation at different radial probes locations (marked by arrows in the profile). The value of the radial coherence associated with fluctuations and fluxes changes radially and increases going in towards in the plasma. Furthermore, for measurements taken at $\Delta r \approx 1$ cm, the radial coherence length associated with fluctuations is higher than the one associated with the turbulent flux. For probes located in the bulk side of the shear layer, the radial coherence, computed using wavelet analysis techniques [8], is intermittent, achieving occasionally values much higher than the time average value.

CONCLUSIONS

The statistical properties of fluctuations and turbulent transport change when moving radially from the scrape off side to the bulk side of the velocity shear layer. The local flux PDF shows the bursty character of flux and presents a systematic change as a function of the radial location.

There is a strong similarity between the statistical properties of the turbulent fluxes in different devices (TJ-I, TJ-IU). The comparison between these two devices suggests that the statistical properties of turbulent fluxes are not determined by plasma parameters like plasma current, magnetic shear, plasma density or magnetic field, and therefore, supports the universal character of plasma turbulence in magnetic confinement devices. This result emphasizes the importance of comparative studies between the structure of plasma turbulence in tokamak and stellarator plasmas to critically test edge turbulence models.

The value of radial coherence length associated with fluctuations and turbulent transport is strongly intermittent. For measurements taken at $\Delta r \approx 1$ cm in the plasma edge region of the TJ-IU torsatron, the radial coherence length associated with the turbulent flux proves to be not larger than the one associated with fluctuations. These comparative studies could provide a good criterion to distinguish between different mechanisms proposed to explain fast changes in transport [1].

[1] B.A. Carreras, C. Hidalgo, E. Sánchez at al. Phys. Plasmas (in press)
[2] I. García-Cortés, M.A. Pedrosa, C. Hidalgo et al. Phys. Fluids B 4,4007 (1992)
[3] E. Ascasíbar, C. Alejaldre, J. Alonso et al. *Proceedings of the 15th IAEA Conf. on Plasma Physics and Controlled Nuclear Fusion Research, in Seville (September 1994).* **1**, 749, IAEA Vienna (1995).
[4] L. Giannone, R. Balbín, H. Niedermeyer et al. Phys. Plasmas 1, 3614 (1994)
[5] M.A. Pedrosa, M.A. Ochando, J.A. Jiménez et al. Plasma Phys. Control. Fusion **38**, 365 (1996)
[6] R. Balbín, L. Giannone, C. Hidalgo, H. Niedermeyer, *Proceedings of the 10th International Conference on Stellarators*, EUR-CIEMAT 30, 93 (1995)
[7] C. Hidalgo Plasma Phys. Control. Fusion **37**, A53, (1995)
[8] B.Ph. van Milligen, C. Hidalgo, E. Sánchez Phys. Rev. Lett. **74**, 395 (1995)

CHARGED-PARTICLE DENSITY PROFILES NEAR THE WALL IN THE PRESENCE OF STRONG ELECTRIC FIELDS

I.Rogal', A.Zagorodny
Bogolyubov Institute for Theoretical Physics, 252143 Kiev, Ukraine

1. Introduction

The electric potentials in bounded plasmas are described by the Poisson equation and the relevant equations for particle distribution functions. It should be noted that due to the presence of plasma boundaries the kinetic equations contain appreciably, self-acting potentials which can not be disregarded.

The analytic solution of the nonlinear Boltzmann-Poisson equations for a plasma can be obtained only in the linear approximation. But the linear approach is invalid for the case of dauble-layer type structures with the potential discontinuity of the order of particle thermal energy. Such structures can appear under the action of strong electric intrinsic or external fields. For instance, linear solution can not he applied for the description of dusty plasmas with highly charged impurities.

The purpose of the present paper is to investigate particle density profiles near the plasma boundary by solving numerically the sell-consistent Poisson-Boltzmann equations.

2. Basic equations.

Let us consider a plasma half-space $z>0$ exposed to the external electric field. The equation for self-consistent potential is given by

$$\Delta\Phi(\vec{r}) = -4\pi \sum_{\sigma} e_{\sigma} f_{\sigma}(\vec{r},\vec{v}) \qquad (1)$$

where e_σ and f_σ are the charge and destribution function for particles of species σ satisfying he following equation

$$\left\{ \frac{\partial}{\partial t} + \vec{v}\frac{\partial}{\partial \vec{r}} - \frac{e_\sigma}{m_\sigma} \nabla\Phi(\vec{r})\frac{\partial}{\partial \vec{v}} \right\} f_\sigma(\vec{r},\vec{v},t) = I_{BL} + I_B. \qquad (2)$$

Here I_{BL} is the Balesku-Lenard collision term, I_B is the collision integral associated with the plasma boundary [1,2]. Stationary solution of Eg.(2) is

$$f_\sigma(\vec{r},\vec{v}) = n_\sigma \left(\frac{m_\sigma}{2\pi T}\right)^{3/2} exp\left\{ -\frac{m_\sigma \vec{v}^2}{2T} - \frac{e_\sigma\Phi(\vec{r}) + U_\sigma(\vec{r})}{T} \right\} \qquad (3)$$

where n_σ is the particle density for $z \to \infty$ and $U_\sigma(\vec{r})$ is the so-

called self-acting potential produced by the plasma boundary and associated with the deformation of the test charge Debye sphere near the boundary. This potential is described by the expression [2]

$$U_0(\vec{r}) = \frac{e_0^2}{2}\,\varphi_T(\vec{r},\vec{r}'), \quad \varphi_T(\vec{r},\vec{r}') = \varphi_B(\vec{r},\vec{r}') - \varphi_0(\vec{r},\vec{r}'), \quad (4)$$

where $\varphi_B(\vec{r},\vec{r}')$ and $\varphi_0(\vec{r},\vec{r}')$ are the unite test charge potential in bounded and unbounded systems, respectvely. In the case under consideration Eq.(3) yields

$$U_0(z) = \frac{e_0^2}{2}\int_0^{k_{max}} dk\,\frac{k\delta(k)}{\sqrt{k^2+k_D^2}}\,e^{-2z\sqrt{k^2+k_D^2}}, \quad (5)$$

$$\delta(k) = \left[\sqrt{k^2+k_D^2} - \tilde{\varepsilon}k\right]/\left[\sqrt{k^2+k_D^2} + \tilde{\varepsilon}k\right].$$

Here $\tilde{\varepsilon}$ is the deelectric permittivity of the medium occupying the half-spase $z<0$, $k_D^2 = \sum_\sigma 4\pi e_\sigma^2 n_\sigma/T$, $k_{max} = 1/r_{min}$, $r_{min} = e_0^2/3T$ is the minimum distance between the particle and its image reapproachment.

At large distance the plasma is neutral and for the self-consistent potential we have $\Phi(z)\big|_{z\to\infty} = 0$.

In what follow we consider two cases:

$$d\Phi/dz\big|_{z=0} = -\tilde{\varepsilon}E, \text{ or } \Phi(0) = \Phi_0.$$

where E is the external electric field strength.

3. Solving the nonlinear equation and numerical analysis.

The nonlinear set of Eqs (1),(3)-(5) can be solved by different numerical methods. In our studies we have used the Newton method, the method of small parameter and integral equation method.

Numerical results obteined on the basis of these methods are in good quantative agreement. The obtained solutions show the considerable dependence of particle density profeles on the plasma composition, dielectric properties of outer medium and the external electric field strength.

Let us consider, for example, potential and particle density distributions in the case of three component plasma consisting of electrons, single charged ($e_i/e_e = -1$) ions and highly charged dust particles ($e_d/e_e = 100$) at $\tilde{\varepsilon} = \infty$ (Figs.1,2). The figures show the dependences of the potential (in arbitrary units) $\varphi(\xi) = e_e\Phi/T$ and relative density deviatious from unperturbed valus $y_0(\xi) = (n_0(\xi) -$

$-\bar{n}_a)/\bar{n}_a$ on the dimensionless distance $\xi = k_D z$. Fig.1 is related to the values of $d\varphi(\xi)/d\xi\,|_{\xi=0} = \tilde{\varphi}'_0$ equal to: *1* - $\tilde{\varphi}'_0$=-0.1; *2* - $\tilde{\varphi}'_0$=-0.5; *3* - $\tilde{\varphi}'_0$ = -1 and *4* - $\tilde{\varphi}'_0$ = -2, respectively. The curves on Fig.2 are related to $\tilde{\varphi}'_0$ equl to: *1* - $\tilde{\varphi}'_0$=-1; *2* - $\tilde{\varphi}'_0$=-2; *3* - $\tilde{\varphi}'_0$=-5; *4* - $\tilde{\varphi}'_0$=-10. Thus, an encrease of the external field strength leads to nonlinear "saturation" of the distributions. An importaut feature of these destributions is that ion profiles differ from the homogenious level only for distanses of the order of few Debye lengthes, but unhomogeniety of electron density is considerable on much longer distance. As regard the dust particle profiles the presence of strong external feeld leads to the existance of the region in wluch dust particles are practically absent. With e_d/e_e encreases the boundary of such region becomes more steep.

The work is supparted by the Ukrainicen State Committee on Selence Technology and Industrial Policy and INTAS Program (project 94-2959).

References

1. A.G. Zagorodny, A.S. Usenko, I.P. Yakimenko. Dopovidi Akademiyi Nauk Ukrainskoyi RSR, № 3, p.51 (1984) (in Ukrainian).
2. A.S. Usenko, I.P. Yakimenko, A.G. Zagorodny. /hi: "Plasma Theory and Nonlinear and Turbulent Processes in Physics", Warld Scientific, Singapore, 1989, 2, p.721.

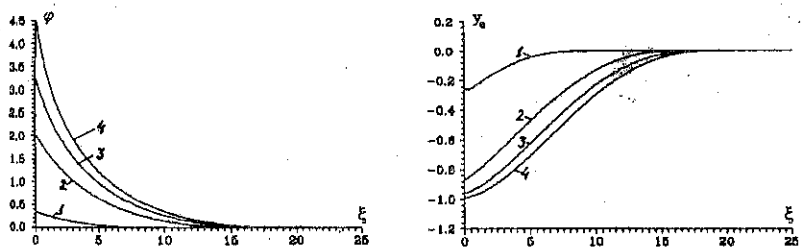

Fig. 1a

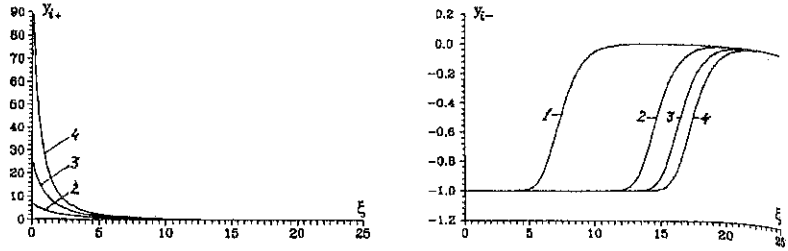

Fig. 1b

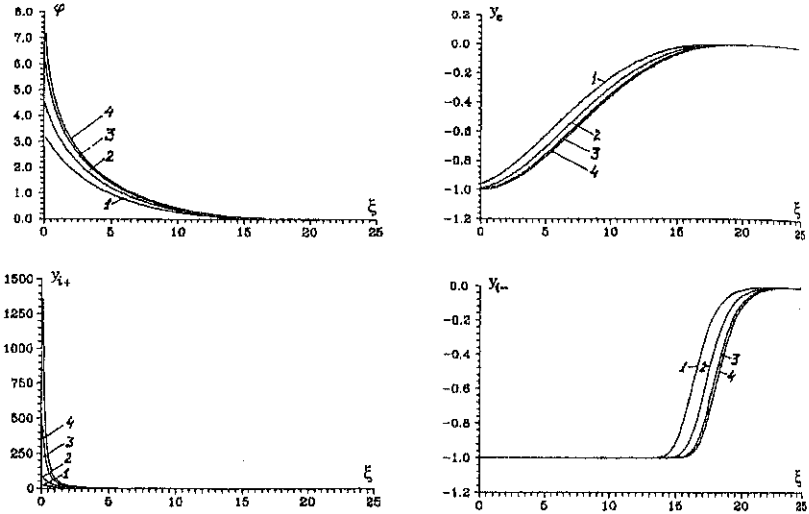

Fig. 2

Unstable Plasma-Surface Interaction as Edge Turbulence Driving Mechanism

I.V.Vizgalov, G.S.Kirnev, V.A.Kurnaev, D.V.Sarichev, V.G.Telkovsky
Moscow State Engineering Physics Institute, Moscow 115409, Russia

Abstract

In the previous experiments [1] it was shown that both the surface composition and the structure generated during interaction of plasma facing components (PFC) with incoming plasma flows play the principal role in dynamics of edge Debye layers. In particular, stable thin dielectric layers with enhanced emission of secondary electrons can appear on the surface contacting with hydrogen plasmas in presence of minor quantities of impurities. An unstable plasma-surface electric interaction is considered as one of possible mechanisms driving non-ambipolar target currents and edge turbulence.

Introduction

According to common approach, the anomalous transport in edge plasmas of fusion devices is determined by the turbulence. Although numerous turbulence driving mechanisms based on different types of instabilities have been proposed, the overall edge plasma behavior is not fully understood. One of the key features influencing turbulence in the scrape-off layer (SOL) is the presence of opened magnetic field lines striking the material surface (limiter or divertor PFC). It is significant that in SOL plasma-surface electrical interaction is, in general, locally non-ambipolar due to different reasons: toroidal drift, spatially unhomogeneous energy distributions of charged particles, externally forced target plate biasing, etc.

Under certain conditions PFC surface electron emissivity can also significantly influence the formation of sheath potential drop and non-ambipolar currents pattern. Secondary emission can be extremely large, provided SOL plasma flow has a hot electron component and the contact surface obtains enhanced electron-electron emissivity, for instance, as a result of dielectric layer formation. Simultaneous existence of PFC zones with different emissivity leads to appearance of transverse electron temperature and potential gradients accompanying with formation of current loops. In previous imitation experiments with the use of an electron beam-plasma discharge (BPD) it has been shown that under such test conditions collector plate obtains a non-linear N-shaped current-voltage characteristic (CVC) and plasma-surface potential drop in the sheath sets unstable with autogeneration of high-frequency electromagnetic oscillations [1]. The most pronounced instability of the sheath potential drop is observed in hydrogen plasmas in the presence of small admixtures of oxygen for materials which form oxides with enhanced emissivity of secondary electrons (W, Be, Al, Mg). The behavior of thin dielectric oxide layers on the surface of PFC materials (as in case of Be) has been modeled using samples made of aluminum alloy. The main emphasis in present experiments has been made on the study of the mentioned above instability as a possible driving mechanism influencing both the spatial pattern of non-ambipolar currents and their temporal modulation.

Experimental results.

Fig.1 shows schematic diagram of the target device. It involves two water cooled and electrically insulated target plates for modeling of inductance of transverse to magnetic fields currents according to non-ambipolar plasma-surface interaction processes described in the introduction. The end plate (5) interacts with central cylinder column of plasma beam in conditions similar to those for nearest to separatrix PFC zones. These zones are exposed to the most severe thermal and radiation loads and are supposed to have low secondary electron-electron emission coefficient (σ~1 in maximum) corresponding to pure bulk material. The periphery plate (4) has a central orifice and interacts only with outer ring layer of plasma flow. Its σ value can large (5-10 in maximum). The grounded diaphragm (2) limits the transverse flow dimensions and provides electrical contact of the periphery zone with vessel walls. Distribution of plasma flow between target plates can be varied according to dimensions of the apertures and/or by varying of the current in the correction coil (3). The plates are changeable for varying of test PFC materials. In particular, the target can work with a single plate.

One-plate collector. Typical experimental CVCs for aluminum and graphite in hydrogen plasma with admixture of O_2 and Ar (for modeling of chemical effects and physical sputtering on PFC surface) are presented in fig.2. They have a good qualitative agreement with calculated ones. High frequency autooscillations develop in collector circuit with LC contour for bias voltages corresponding to the negative resistance range of N-formed CVC. Autooscillations with amplitude of hundreds volts and frequency of up to 200MHz are observed.

It is worthy of note that during the slow varying of Al or W collector bias in Ar+O plasmas one can observe fast transitions between two states of the surface emissivity corresponding to appearing or removal of the oxide scales as a competition between their growth and sputtering. These transitions have a hysteresis character. As a typical example, fig.2 shows the current-voltage characteristics of aluminum and graphite collectors in H_2+Ar+O_2 working gas mixture. The curve 1 corresponds to the ion saturation current onto graphite collector plate and is similar to the ion branch of a conventional probe characteristic. Curve 2 represents the CVC for aluminum plate. The similar CVC behavior is observed for a wide range of working gas pressure $5\cdot10^{-5}\div10^{-3}$Torr. In pure hydrogen plasma with the oxygen impurity up to 1% the hysteresis isn't observed (presumably due to low sputtering effect).

When the collector bias working point is varied along the N-shaped CVC, the fluctuation level in plasma varies too. Typical potential fluctuations for Al collector plate are shown in fig.3. Collector bias appropriate to CVC portion with an abrupt current increase (fig.2, point B) stabilizes the plate potential and its fluctuation level is minimal (fig.3b). In the vicinity of floating potential (fig.2, point A) the level of fluctuations has an increase (fig.3a) according to the inflection of real CVC (caused by the change of oxide layer charging sign). The largest potential fluctuation amplitude is found to appear in negative biasing interval -100V - -300V (fig.2, point C), where positive feedback mechanism responsible for fluctuation boost is most effective (fig.3c). Experimentally observed radial contraction and broadening of

the BPD channel with the change of operating bias (time-averaged in oscillation regime) are correlated with the change of fluctuations level.

Two-plate collector. The appearance of surface currents between PFC zones with different emissivity states has been modeled by means of two-plate target device: *a priori* low emissive graphite central plate and Al peripheral plate. They are closed to one other through an ammeter and their potential bias can be externally varied from negative to positive values.

When plates are under a common floating potential, the first plate operates as a source of electromotive force and the second one - as a non-linear load, the plasma flow closing the non-ambipolar currents due to its longitudinal and transverse conductivity. It must be mentioned that induced self-correlated jxB forces and electric fields have an amplifying effect on the level of fluctuations and transverse drift. Moreover, a low emissive inner plate, operating as a converter of electron kinetic energy in collector regime, transmits an electric power along the current loop to high emissive periphery zones with generation of beam-plasma instabilities in re-emitted electron flows, so enhancing transverse energy transport. Providing working point of emissive plate with N-shaped CVC corresponds to the negative resistance (fig.2, point D, where absolute values of both plate currents are equal), additional amplifying of plasma potential fluctuations and autogeneration of new modes take place (fig.4d). As it is seen from the oscillograms, in this case the collector plate potential fluctuations are found to be excited more strongly compared with the one-plate aluminum collector scheme.

Summary.

Films with enhanced emission can appear and disappear on the surface of some PFC under rather specific conditions as a result of dynamic equilibrium between self-correlated processes of film synthesis and erosion. When zones with distinct electron emissive properties simultaneously exist on the PFC surface, emissivity driven effects sufficiently influence plasma flow turbulence and radial transport.

The discussed emissivity effects need additional investigations for a case of oblique incidence of magnetic field lines to the target surface. Preliminary estimations for realistic edge conditions (in accordance with models developed in [2,3]) show that effective suppression of secondary electrons emission emerges only for grazing angles lower than 10^0-15^0.

1. Vizgalov IV et al., 22 Conf. on Contr. Fusion and Plasma Phys., Bornemouth, 1995, v.III, p.285.

2. S.Mizoshita et al., J. Nucl. Mater. 220-222 (1995) 488.

3. Igithanov U.L.et al., In collected volume "Summaries of science and technology" (plasma physics), Moscow, 1990, v.11, pp.60-63.

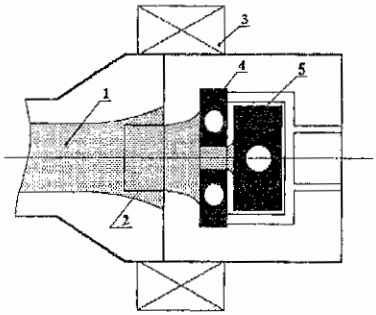

Fig.1. Scheme of the two-plate collector section. 1 - plasma flow, 2 - grounded diaphragm, 3 - correction coil, 4 - periphery aluminium plate, 5 - central graphite plate.

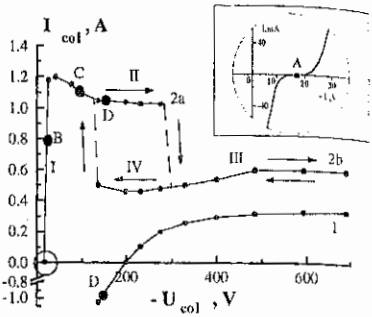

Fig.2. Current-voltage characteristics. $p=2*10^{-4}$ Torr, H_2 + admixture of Ar and O_2. 1 - graphite collector, 2a,2b - Al-collector.

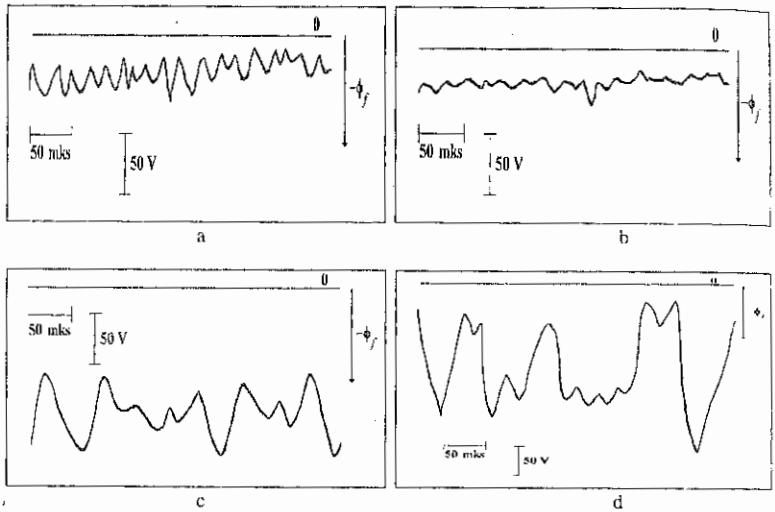

Fig.3. Oscillograms of the collector potential. Aluminium collector: a - floating potential, b - U_{col}=-30 V, c - U_{col} = -100 V; aluminium-graphite collector: d - floating potential.

INVESTIGATION OF THE EROSION COEFFICIENTS OF BORON CARBIDE AND TUNGSTEN IRRADIATED BY THE HIGH POWER PLASMA STREAMS

V.V.Chebotarev, **I.E.Garkusha**, G.P.Glazunov, O.E.Kazakov, V.G.Kotenko, D.G.Solyakov, V.I.Tereshin, N.T.Derepovskij, N.S.Poltavtsev

Institute of Plasma Physics of the National Science Center

"Kharkov Institute of Physics & Technology", 310108 Kharkov, Ukraine

1. Introduction

At the stage of current disruption in tokamak powerful thermal flows influence on a surface of elements, inverted to plasma. Under their influence serious damages of materials, first of all, connected with a thermal erosion and melting of a surface occur. Thus the pollution of plasma and level of losses through radiation essentially differs depending on kind of erosion element's material [1-3].

As a result of numerous experiments, carried out on various thermonuclear installations, beryllium and materials with low Z on basis of carbon considered as the most probable materials for divertor plates. Besides, tungsten, which has recordly low ion erosion, is also considered as a possible material for divertor plates [4].

Numerous researches of materials, which contain carbon, have shown, that the chemical erosion of a graphite can be reduced by addition of boron in it. It is not less important that the boron - carbon cover much better connects an oxygen, which becomes more often a main source of radiating losses from a plasma in use of graphite protection.

The investigations of influence of the plasma flows on erosion coefficient of a boron carbide and tungsten carried out in this work.

2. Experimental Installations

Boron carbide samples treated on a pulsed plasma accelerator "Prosvet". The accelerator represents a coaxial system of electrodes, with diameters 3 cm and 14 cm accordingly, which separated by figured isolator. Electrodes length is 70 cm. The pulsed electrodynamic valve, ensuring filling of the working gas, locates inside central electrode. The working gas (hydrogen) fills through three cross cracks, located on distance of 20 cm from the end of electrode . The power supply of the accelerator comes from the capacitor banks with

capacity of 111 μF. A maximum working voltage achieved 24 kV. Vacuum chamber is 120 cm in length and 100 cm in diameter. The accelerator generated plasma streams with density $n \approx 10^{14}$ cm $^{-3}$, average proton energy up to 2 keV and pulse duration 3÷5 μs. Specific plasma power density achieved 10 MW/cm^2.

The experiments with a tungsten carried out on the full-block quasistationary plasma accelerator QSPA Kh-50. The design of the accelerator is in detail described in [5]. The accelerator represents two-stage system with magnetic screening of solid-state electrode components and cold ion supplying from the anode side to provide ion current carrying in the main discharge. At the first stage ionization and preliminary acceleration of plasma, becoming then in the second (coaxial) stage, carried out. The limiting values of capacity banks, feeding the discharge in the main accelerating channel are as follows: U_C = 25 kV, C = 7200 μF, W = 2,2 MJ (U_C achieved up to now is 15 kV). The maximum parameters of plasma streams are as follows: plasma density (3 - 7) x 10^{16} cm^{-3}, proton energy 0.9 keV, quasistationary phase duration 0.15 ms (with pulse duration 300 μs). Average specific power of the plasma stream, generated by accelerator was P ≈ 16 MW/cm^2.

3. Experimental Results

The boron carbide samples were 90×90×8 mm head plates, which were made by method of vacuum hot pressing of boron carbide powder (B - 78.2% , C - 21.5%). These samples used as limiter plate material in torsatron "URAGAN-3M" device and had following characteristics: density 2.46 g/cm^3, heat conductivity 30 W/mK, electrical resistivity 10^{-2} Oh · m. The dependence of boron carbide erosion coefficient on average energy of incident particles in energy range E = 0.3-2 keV shown in Fig. 1. One can see from presented data that at energy of incident particles E = 0.3 keV the erosion coefficient is at the level S = 6 × 10^{-2} atom/ion. Further on, with increase E the erosion coefficient grows and reaches value S = 15 atom/ion at the energy E = 2 keV. The obtained values of erosion coefficient are sufficiently exceed the physical sputtering coefficients both of boron and carbon by ions of a hydrogen. Apparently, it is caused with radiation-stimulated sublimation of boron carbide, which takes place at the temperature of surface T ≥ 1600° K [6].

The specific outgasing rate carried out on the special test after 24- hours heating at 200°C in vacuum 4×10^{-9} Tor was ~ 10^{-11} Tor · l/s · cm^2.

Following step of researches have become experiments with tungsten samples, at which

radiation-stimulated sublimation is absent. Irradiation of tungsten samples carried out by hydrogen plasma streams with density of particles $n = 2 \times 10^{16}$ cm^{-3}, average energy of incident ions E = 0.3 keV and energy flux density in the near axis region in the plasma stream $\rho_W \approx 1$ kJ/cm^2. Tungsten samples had surface 3×8 cm^2 and thickness 1.5 mm.

The experiments have shown, that the quantity of eroded material decreased from pulse to pulse, and after 7 working discharges mass defect fallen down to the minimum level of an order 10^{-2} g (see Fig. 2). The valuation of average value of tungsten erosion coefficient gives the value $S = 6 \times 10^{-2}$ atom/ion, that also essentially higher of the physical sputtering coefficient of tungsten by protons ($S = 4 \times 10^{-4}$ atom /ion) [7].

X-ray analysis of surface of the irradiated samples has shown some reduction of spacing of a crystal lattice of tungsten. It has appeared equal a = 3.1627 Å, while for initial nonirradiated surface lattice spacing a_o = 3.1653 Å. Such reduction of spacing of a crystal lattice can be explained by occurrence of stretching stress of the 1-st kind or macrotensions, accompanied plastic deformation of a material. There existing of the macrotensions is confirmed by the cracks on the tungsten surface that appear after sample irradiation. The latter may be the reason of sufficient increasing the tungsten erosion for the account separation of large layers of a material. Besides on initial, nonirradiated samples primary orientation of crystals in perpendicular direction registered, which amplifies after plasma irradiation.

It follows from these experiments that under interaction of the powerful plasma streams with the boron carbide and tungsten samples the erosion of samples surfaces does not determine by the process of physical sputtering.

References

[1] Gudowska I, Bergsaker H, Emmoth B et al. 1990 *J. Nucl. Mater.* **176-177** 363-369

[2] Schneider U, Poschenrieder W, Hofmann J et al. 1990 *J. Nucl. Mater.* **176-177** 350

[3] Dylla F H, Bell M G, Hawryluk R J et al. 1990 *J. Nucl. Mater.* **176-177** 337-342

[4] Barabash V R, Mazul I V, Saksagansky G L et al.1991 *Voprosy Atomnoj Nauki I Techniki* (Moscow, Kurchatov Institute) **1(55)** 3-14 (in Russian)

[5] Tereshin V I. 1995 *Plasma Phys. Control. Fusion.* **37** A177-A190

[6] Pistunovich V I. 1991 *Fiz. Plazmy.* 17 560-575 (in Russian)

[7] Kalin B A et al. 1991 *Voprosy Atomnoj Nauki I Techniki* (Moscow, Kurchatov Institute) **1(55)** 108-112 (in Russian)

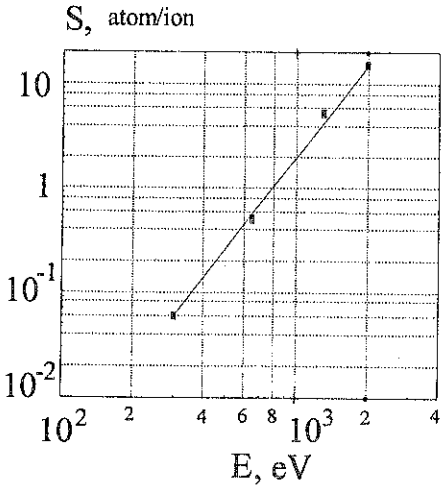

Fig. 1 Dependence of boron carbide erosion coefficient on protons energy.

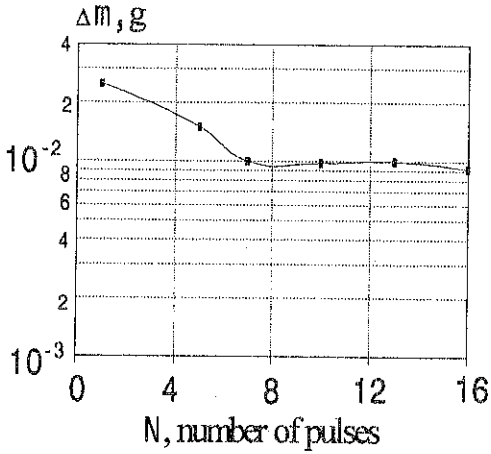

Fig. 2 Dependence of tungsten samples mass-defect on number of discharge pulses.

E

PLASMA HEATING AND CURRENT DRIVE

Current Amplification in the SPHEX Spheromak operated as a Helicity Injected Tight Aspect Ratio Tokamak

S.J.Gee, P.K.Browning, G.Cunningham, R.C.Duck, K.J.Gibson, J.Hugill, J.C.Sandeman, M.G.Rusbridge, S.Woodruff

Physics Department, UMIST, P.O.Box 88, Manchester, M60 1QD, U.K.

Introduction

Previously we have reported [1] the results of modifying the gun injected spheromak SPHEX [2] at UMIST to include an insulated current carrying rod along the geometric axis of the device (fig.1) demonstrating that a coaxial helicity source can form and sustain a plasma in an externally generated toroidal field. Here we present the effect of an improved rod and rod circuit design which allows a maximum rod current of 200 kA, four times greater than previously attained and with a time constant longer than the 1 ms plasma duration. The resulting aspect ratio is 1.07. The addition of the rod permits us to experimentally investigate the effectiveness of relaxation [3] and direct current helicity injection as the exclusive means (i.e. no externally applied loop voltage) of sustaining plasma current in a tokamak–like configuration.

Current density profiles and current amplification

Figure 2 shows contours of the current amplification (I_{tor}/I_{gun}) for fixed gun current $I_{gun} \sim 60$ kA in ψ_{gun} and I_{rod} space, where ψ_{gun} is the solenoid flux from the magnetised Marshall gun and I_{rod} is the rod current. The total circulating toroidal current I_{tor} was estimated by forming a weighted sum ($I_{tor} = \sum B_{pol}.\delta l/\mu_o$) of the poloidal flux density determined from a set of field coils on a single line of longitude located on the rod itself and on the flux conserver, coil positions are marked with an X in fig. 1; δl is the coil separation. Clearly the current amplification increases with increasing rod current, and toroidal currents of up to 450 kA are observed. We now need to ask how much of this increase occurs in the closed flux, where the current is indirectly driven, and how much on the open flux which is coupled to the gun and driven directly by it.

In figure 3 we compare the radial profile in the equatorial plane of the current density parallel to the local magnetic field measured by an insertable Rogowski loop [4] for $I_{rod} = 0$, $\psi_{gun} = 3$ mWb (this is the normal spheromak case) and for $I_{rod} = 83$ kA, $\psi_{gun} = 6$ mWb, in both cases $I_{gun} \sim 60$ kA. In the outer closed flux region, the current density increases by up to 50 % out to 20 cm and beyond 30 cm, whereas it decreases, also by about 50 %, near the magnetic axis. Thus the profile becomes increasingly hollow. It is not straightforward to calculate the change in the total current on the closed flux from the data, but it is clear that any increase is small, and is certainly not in proportion to the current amplification. The three fold increase in the current density for r<10 cm is primarily due to compression of the open flux by the toroidal field from the rod, confirmed by measurements of the floating potential showing that the radius of the

region of high average potential associated with the open flux [2] shrinks from ~ 13 cm to ~ 10 cm, with increasing rod current.

Although the current remains largely unaffected, the rod field does have a strong effect on the helical open flux tube (OFT) described in [5]. Evidence from field coils located on the rod show that the pitch of the OFT reduces with increasing rod current, consequently it passes through the line of longitude defined above more than once. Since we assume the current carried by the OFT is of the same order of magnitude as the gun current, this raises the current amplification in proportion to the wind up of the OFT, thus almost all of the increase in current is associated with the open flux.

The hollow current profile (fig.3) characteristic of the spheromak [4] persists as the external toroidal field is increased, and is different from the peaked current profile normally expected for a tokamak. Finally because the current density on the closed flux is unaffected by the action of the rod, whereas the magnetic field density increases, a strongly hollow $\mu = \mu_0 \mathbf{J} \cdot \mathbf{B}/B^2$ profile (fig.4) develops which barely spans the spheromak eigenvalue ($\mu_e \sim 11.1$ m^{-1}). In the spheromak, ($I_{rod} = 0$), μ must span μ_e for significant flux amplification to occur [6], but the additional toroidal field of the rod weakens this resonance condition and broadens it, so that significant flux amplification can occur even at lower values of μ.

Poloidal flux amplification

Figure 5 shows the contours of edge poloidal flux density measured at the flux conserver wall in the equatorial plane. To aid interpretation we divide this figure in to four distinct regions. Region 1 where no poloidal field is detected, is defined by the ejection limit from the Marshall gun and is goverened by a simple force balance at the gun muzzle [2]. In region 2, the plasma behaviour closely resembles that of the spheromak, with a well defined n=1 mode [1] characteristic of the spheromak. As we pass through region 3 towards region 4 the n=1 mode becomes less coherent, until finally in region 4 the edge poloidal field approaches zero even though plasma is ejected from the gun. Since the n=1 mode is a direct consequence of the rotation of the OFT through the surrounding plasma, it seems likely therefore in regions 3 and 4 where the mode is less coherent that the helical distortion of the OFT is also less distinct.

The implication of these changes is that the current drive also becomes less effective as we pass from region 2 to 4, until finally it fails altogether and provides further evidence that the n=1 mode is essential for the current drive process in SPHEX. It appears that even in region 2 the current drive may be less effective: the best overall measurement of the extent of relaxation obtainable from our data is the poloidal flux amplification ratio defined by

$$A_\psi = \frac{2\pi}{\psi_{gun}} \int_{geometric\,axis}^{magnetic\,axis} \mathbf{r} \cdot \mathbf{B}_{pol}\, \mathrm{d}\mathbf{r} \qquad (1)$$

This quantity shown in fig. 6 clearly decreases with increasing rod current, note here ψ_{gun} is increased in proportion to I_{rod} to follow the position of peak poloidal field defined by the dashed line in fig. 5. This fall in A_ψ from 4.5 characteristic of the spheromak

to about 3, may be due to a decreasing effectiveness of the dynamo: in [7] we show that the dynamo field (parallel to the local mean magnetic field) $\mathbf{E}_{d\parallel} = < \mathbf{v} \times \mathbf{b} > \cdot \mathbf{B}/B$ associated with broadband turbulence (i.e. with the n=1 mode and harmonics removed) is alone sufficient to drive current at the magnetic axis. Consistent with a reduction in $\mathbf{E}_{d\parallel}$, we see $\delta b/B$ fall from 7 % in the spheromak to 4 % with I_{rod}=83 kA and ψ_{gun}=6 mWb. Thus, we might expect the value of $\mathbf{E}_{d\parallel}$ to fall, although this has not yet been measured.

Finally, if we compare the contours of current amplification and edge poloidal flux density we see that they do not coincide, in particular the optimum values, shown as dashed lines, are very different. The current profile must therefore vary in different regions of the ψ_{gun}-I_{rod} parameter space. We can examine this by considering the individual contributions of the edge poloidal flux density used to calculate the toroidal current (fig. 7). The solid symbols show the contributions for a position of strong current amplification, but which also lies on the border of region 4 in fig. 5. A large poloidal flux density exists in the region of the rod, coils 6–11, but the flux density everywhere else has fallen. Although the current amplification is high, this is clearly an undesirable regime of operation because there is little if any poloidal flux amplification. The open circles show the corresponding distribution for optimum edge poloidal flux where a fully developed spheromak does form. I_{rod} = 83 kA in both cases.

Conclusions

We show in the presence of an externally generated toroidal field that DC helicity injection can form and sustain a plasma with μ barely spanning the spheromak eigenvalue μ_e. The current amplification ratio rises to ~ 7 as the external toroidal field is increased and circulating toroidal currents of order 450 kA are observed for the first time in SPHEX.

The observed hollow μ profiles, the fall in poloidal flux amplification and the relative fluctuation level all suggest that relaxation becomes less effective as the external toroidal field is increased, and there is evidence that the MHD dynamo fails altogether in certain regimes of operation. Compared with recent MHD simulations [8], however, our results show much stronger current drive at optimum ψ_{gun} values even with high rod current; this may in part be due to kinetic effects which we believe play an important part in the actual current drive process [9]. The SPHEX project is funded by EPSRC; the installation of the central conductor was funded by UKAEA Fusion.

[1] P.K.Browning *et al* Phys.Rev.Lett., **68**, 1722, (1992)
[2] P.K.Browning *et al* Phys.Rev.Lett., **68**, 1718, (1992)
[3] J.B.Taylor Phys.Rev.Lett., **33**, 1139, (1974)
[4] R.Martin *et al* Plas.Phys.Cont.Fus., **35**, 269, (1993)
[5] R.C.Duck *et al* 21st EPS Conf. on Cont.Fus. and Plas.Phys. (1994)
[6] D.A.Kitson *et al* Plas.Phys.Cont.Fus., **32**, 1265, (1990)
[7] A.Al-Kharky *et al* Phys.Rev.Lett., **70**, 1814, (1993)
[8] C.R.Sovinec *et al* Plas.Phys., **3**, 1038, (1996)
[9] M.G.Rusbridge *et al submitted to* Plasma Physics and Controlled Fusion

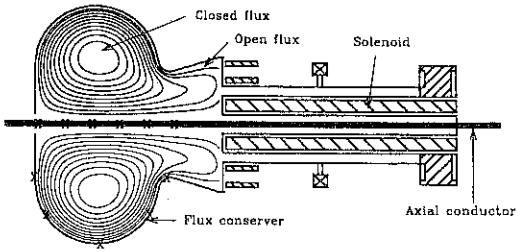

Fig. 1 Schematic of SPHEX

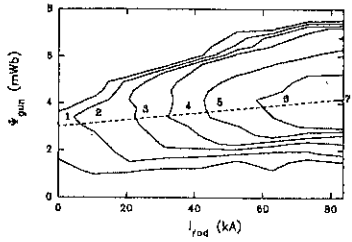

Fig. 2 Current Amplification (I_{tor}/I_{gun})

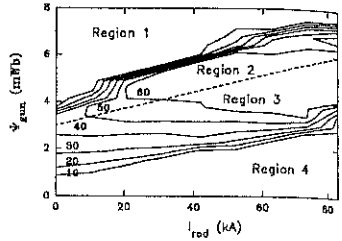

Fig. 5 Contours of edge poloidal field (mT)

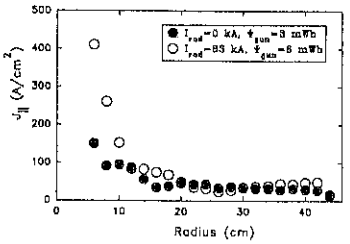

Fig. 3 Comparison of current density profiles

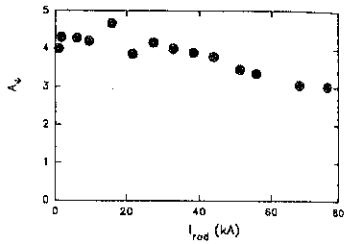

Fig. 6 Flux amplification

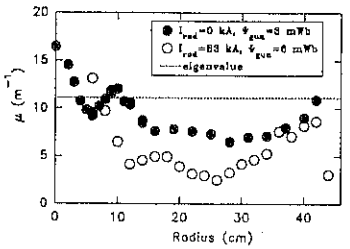

Fig. 4 Comparison of μ profiles

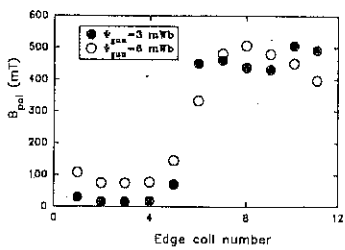

Fig. 7 Evidence of changing current profile

RESONANT AND NONRESONANT ELECTRON CYCLOTRON HEATING AT DENSITIES ABOVE THE PLASMA CUT-OFF BY O-X-B-MODE CONVERSION AT W7-AS.

H.P. Laqua, V. Erckmann, H. J. Hartfuß, W7-AS Team
Max-Planck-Institut für Plasmaphysik, EURATOM Ass.
D-85748 Garching, FRG,

ECRH-Group
Institut für Plasmaforschung, Univ. Stuttgart, D-70569 Stuttgart, FRG

H. Laqua
Institut für Meß- und Regelungstechnik, Univ. Karlruhe, D-76128 Karlsruhe, FRG

The O-X-B mode conversion process was proposed in 1973 [1] as a possibility to overcome the density limit for electron cyclotron resonance heating (ECRH). Here O, X, and B represent the ordinary, extraordinary and electron Bernstein mode. The essential part of this scheme is the conversion of the O-wave launched by an antenna from the low field side into an X-wave at the O-wave cut-off layer. This mode conversion requires an O-wave oblique launch near an optimal angle.

As shown in Fig. 1 the transverse refractive indices N_x of the O-wave and X-wave are connected at the optimal launch angle with a corresponding longitudinal (parallel B_0) index $N_{z,opt}=\sqrt{(Y)/(Y+1)}$ with $Y=\omega_{ce}/\omega$ (ω is the wave frequency, ω_{ce} is the electron cyclotron frequency) without passing a region of evanescence ($N_x{}^2<0$). For non-optimal launch an evanescent region always exists near the cut-off surface. The geometrical size of this evanescent region depends on the density scale length $L=n_e/(\partial n_e/\partial x)$, and a considerable fraction of the energy flux can be transmitted through this region, if L becomes small. The power transmission function $T(N_y,N_z)$ is [2]

$$T(N_y,N_z)=\exp\left\{-\pi\, k_0 L\sqrt{\frac{Y}{2}}\left[2(1+Y)\left(N_{z,opt}-N_z\right)^2+N_y^2\right]\right\},$$

where N_y and N_z are the poloidal and longitudinal components of the vacuum refractive index and k_0 the wave number. This angular dependence (N_z- dependence) was used in the experiments to identify the O-X-conversion process. After the O-X-conversion the X-wave propagates then back to the upper hybrid resonance (UHR) layer where the refractive index of the X-wave is connected to that of the electron Bernstein waves (EBW) as shown in Fig. 1 and a complete conversion into EBW's may take place. The EBW's propagate then towards the plasma centre where they are absorbed near the electron cyclotron resonance layer or in the nonresonant case by collisional multiple pass damping.

In our calculations, additionally, we take into account that in a real plasma the conversion layer is not a smooth surface but is due to density fluctuations rough and wavy. This introduces a beam divergence much higher than the intrinsic one and can reduce the O-X-conversion considerably.

With a statistic description of the poloidal cut-off surface roughness (toroidal fluctuations were neglected), the probability density function of the poloidal component N_y (similar to a poloidal beam divergence)

$$p(N_y) = \frac{\lambda_y}{\sqrt{2\pi}\sigma_x} \exp\left(-\frac{N_y^2 \lambda_y^2}{\left(1 - N_y^2\right) 2\sigma_x^2} \right) \left(1 - N_y^2\right)^{-\frac{3}{2}}$$

could be calculated as a function of the fluctuation amplitude standard deviation $\sigma_x = L\tilde{n}_e/n_e$ ($\tilde{n}_e/n_e$ is the relative fluctuation amplitude) and the poloidal correlation length λ_y. The modified power transmission function T_{mod} (O-X conversion efficiency) is then $T_{mod}(N_z) = \int T(N_y, N_z)\, p(N_y) dN_y$. In Fig. 2 the modified transmission is calculated as a function of the parameter $k_0 L$ for five different relative density fluctuation amplitudes. In all calculations the poloidal correlation length was assumed to be 2 cm. It can be clearly seen that a significant heating efficiency is obtained only at a very small density scale length or a very low fluctuation amplitude. The flexibility of W7-AS allows to investigate both extreme cases, i.e. target plasmas with $k_0 L \leq 10$ and with a relative density fluctuation amplitude of more than 20 % or peaked density profiles ($k_0 L = 60$) with a very low relative fluctuation amplitude of less than 2%. For both cases, high conversion efficiencies were experimentally measured and O-X-B mode conversion for plasma heating could be clearly shown for the first time.

Two 70 GHz beams were launched into a neutral beam (NBI) sustained target plasma at resonant (1.25 T) and nonresonant (1.75 T, 2.0 T) magnetic fields. The launch angle of the incident O-mode polarised wave was varied at fixed heating power (220 kW). An example of the nonresonant case is shown in Fig. 3. The increase of the total stored plasma energy (from the diamagnetic signal) depends strongly on the launch angle, which is typical for the O-X-conversion process, and fits well to the calculation. Here the power transmission function was normalised to the maximum energy increase. The central density was $1.5\ 10^{20}\ m^{-3}$, which is more than twice the cut-off density, the central electron temperature was 500 eV. Heating at the plasma edge could be excluded since at the nonresonant magnetic field of 1.75T no electron cyclotron resonance exist inside the plasma . Due to technical limitation of the maximum launch angle, only the left part of the reduced transmission function could be proved experimentally.

In the X-B-conversion process near the UHR parametric instabilities are expected, which generate decay waves with frequencies of the incident pump wave ω plus and minus the harmonics of the lower hybrid frequency ω_{LH} and the lower hybrid (LH) wave itself. With the electron cyclotron emission (ECE) receiver a spectrum of the decay waves with maxima at $\omega \pm n\omega_{LH}$ was measured for a resonant magnetic field of 1.25 T and is shown in Fig. 4. Note, that the pump wave is suppressed and the ECE-spectrum is clearly nonthermal since the density was twice the 70 GHz cut-off density. The low frequency LH-wave itself could be detected with a broad band loop antenna. A high degree of correlation between the high frequency decay waves and LH-wave was measured.

EBW's experience a cut-off layer ($N \rightarrow 0$) at the upper hybrid resonance (UHR) surface (see Fig. 1), which in the nonresonant or higher harmonic (n>1) field totally encloses the inner plasma. The radiation is then trapped inside the plasma like in a hohlraum. The EBW is either

reflected at the UHR surface in the case of an oblique angle of incidence or is back converted to the X-wave which is converted again to the EBW at its next contact with the UHR. The only way that radiation can escape out of the Plasma is the small angular window for O-X- and X-O-conversion, respectively. In the absence of an electron cyclotron resonance in the plasma the EBW's may be absorbed due to finite plasma conductivity after some reflections at the UHR-layer. Nonresonant heating was clearly observed at magnetic fields up to 2.0 T. At the maximum field the plasma energy content increased by about 1.5 kJ compared to a similar discharge with NBI only (see Fig. 5). Two 70 GHz beams in O-mode polarisation (110 kW power each) were launched with an angle of 40° with respect to the perpendicular launch into a NBI (800 kW) sustained target plasma with a central density of 1.6 10^{20} m^{-3} and a central temperature of 560 eV. More than 80% of the heating power was found in the plasma if the power scaling of the energy confinement ($P^{-0.6}$) was taken into account. Thus O-X-B-heating turned out to be very efficient.

Ray-tracing calculation were performed with newly developed code in order to get a more detailed insight into the O-X-B-scheme . Density, temperature and magnetic field profiles similar to that of a typical neutral beam sustained W7-AS plasma were used for model calculations for a straight plasma cylinder. We use the nonrelativistic hot dielectric tensor with a correction for electron ion collisions given by Stix [3] and an isotropic electron temperature. The ray trajectory in the x-z-plane is shown in Fig. 6 . The beam is launched from the low field side (LFS) and propagates through the cut-off, where it is converted into X-mode. Then it moves back to the UHR-layer, where the X-B-conversion takes place. The EBW´s are absorbed near the cyclotron resonance at the plasma centre. A small fraction of the beam power is lost at the UHR due to finite plasma conductivity. The power deposition zone for resonant heating strongly depends on the magnetic field and the electron temperature, but central power deposition seems possible. In calculations for the nonresonant case more than 40% of the beam power is absorbed due to finite plasma conductivity after six passes through the plasma.

In conclusion: efficient O-X-B heating with 70 GHz electron cyclotron waves was clearly demonstrated for the first time for resonant and nonresonant fields at W7-AS. Both, the angular dependence of the O-X-conversion and the parametric instability which is typical for X-B-conversion could be experimentally verified. Density fluctuations at the O-X-conversion layer play a significant role in the O-X-B-process and need to be taken into account.

With a newly developed three dimensional ray-tracing code for EBW's and improved measurement techniques of the power deposition profiles further investigations of the O-X-B-heating are envisaged to explore the potential of resonant and nonresonant O-X-B-heating for routine high density operation.

References

[1] J.Preinhaelter and V.Kopecký, J. Plasma Phys. 10 (1973) 1;

[2] E.Mjøhus, J. Plasma Phys. 31 (1984) 7;

[3]T.H.Stix:"THEORY OF PLASMA WAVES"; McGraw-Hill, 1962

Figures:

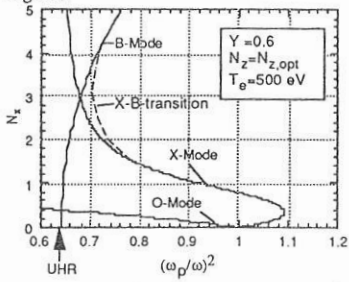

Fig. 1: Refractive index N_x versus ω_p^2/ω^2 for the O-X-B conversion process. The transition represents the connection of the X-mode and B-mode due to the hot dielectric tensor.

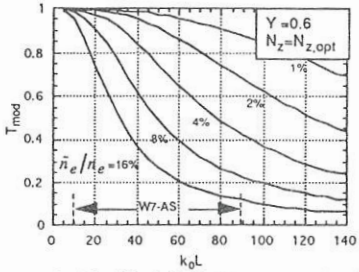

Fig. 2: Modified O-X-conversion in the presence of density fluctuations at the plasma cut-off layer versus normalised density scale length $k_0 L$ for different relative fluctuation amplitudes .

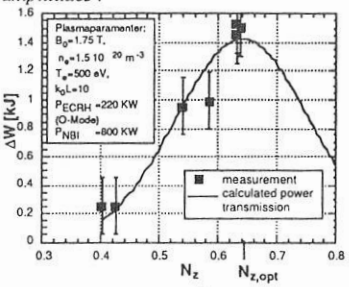

Fig. 3: Increase of the plasma energy content by O-X-B-heating versus the longitudinal vacuum refractive index N_z of the incident O-wave

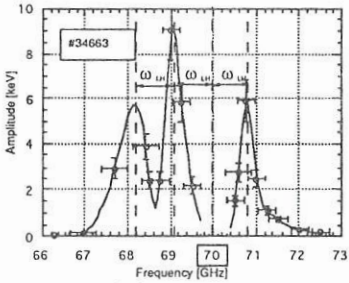

Fig. 4: High frequency spectrum of the parametric decay waves generated in the O-X-B-process. The incident wave frequency is 70 GHz and the LH frequency is about 900 MHz.

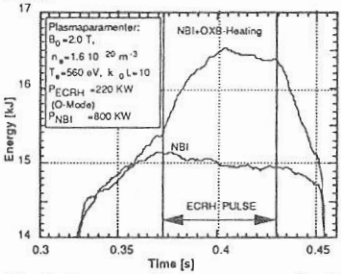

Fig. 5: Energy content (diamagnetic signal) of a NBI-discharge with and without nonresonant O-X-B-heating .

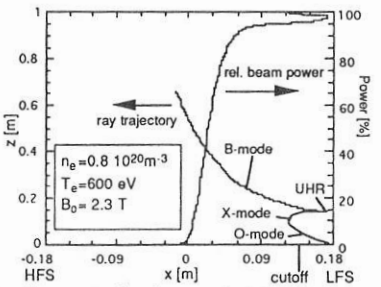

Fig. 6: Calculated ray trajectory in the x-z-plane and relative beam power for resonant O-X-B-heating .

EXTENSION OF THE RAY EQUATIONS OF GEOMETRIC OPTICS TO INCLUDE DIFFRACTION EFFECTS

A.G. Peeters

Max Planck Institut für Plasmaphysik, Euratom-IPP Association
Boltzmannstrasse 2 85748 Garching, Germany

The propagation of waves for which the wave length is small compared to the length scale over which the medium changes is usually treated within geometric optics. In this formalism the wave beam is represented by a number of rays which are independently traced through the medium. In the case of a focussed beam the rays can cross. The geometric optics approximation then leads to caustics, where the electric field amplitude is infinite. In the region where a caustic is formed the geometric optics approximation breaks down. For a correct description of the wave propagation, diffraction effects must then be taken into account.

In the literature several methods to include diffraction effects in the description of wave propagation in a magnetized plasma are given. A generalization of the method of S. Choudary and L.B. Felsen [1,2] was developped by E. Mazzucato [3]. This method uses a complex eikonal function, where the imaginary part describes the electric field profile of the beam. This method will be investigated in detail in this paper.

COMPLEX EIKONAL METHOD

In the eikonal method the electric field $\mathbf{E}$ is written in the form

$$\mathbf{E} = \mathbf{e}(\mathbf{x}) E_0(\mathbf{x}) \exp(\mathrm{i} S(\mathbf{x})), \tag{1}$$

where S is the eikonal function. Normally, this function is taken to be real and, consequently, the wave vector and frequency, defined by $\mathbf{k} \equiv \partial S/\partial \mathbf{x}$, $\omega \equiv -\partial S/\partial t$, are real. The functions $E_0(\mathbf{x})$ and $\mathbf{e}(\mathbf{x})$ give the amplitude and polarization of the wave. If the length scale over which the plasma parameters change is much larger than the wave length these functions change only slightly over a wave length. In the dispersion relation, which is derived through the substitution of Eq. (1) in the wave equation the terms which contain derivatives of these functions with respect to position can be neglected in comparison with the terms which contain derivatives of the eikonal function S. After deviding by $E_0(\mathbf{x})$, the wave equation and the dispersion relation do not contain any information on the profile of the wave amplitude. Because the ray equations of geometric optics are derived from the dispersion relation, no profile effects are retained in this description.

The method that uses a complex eikonal function intends to include effects of the profile in the description of the wave propagation. For this purpose an imaginary part of the function S is introduced $\mathrm{Im}(S(\mathbf{x})) = -\ln(E_0(\mathbf{x}))$. The complex eikonal function leads to a complex wave vector. The imaginary part $\mathbf{k}_i \equiv \mathrm{dIm}[S]/\mathrm{d}\mathbf{x}$ contains the profile information. The medium in which the wave propagates is assumed to be in steady state. The wave source is assumed to have constant frequency and strength. These assumptions make that the wave frequency in the medium is real and constant.

The same derivation that gave the ray equations of geometric optics can now be repeated. A dispersion relation is obtained which depends on the electric field

profile. From this dispersion relation ray equations, which include diffraction effects, are obtained.

Below the equations will be expanded in a small parameter to obtain a tractable set of equations. To be able to expand various quanitities in the same dimensionless small parameter δ, the velocity of light c and a frequency ω_0 close to the wave frequency will be used to make all length and time scales dimensionless.

Three different length scales are discerned, the wave length λ, the width w of the beam, and the length scale L over which the plasma parameters change. It is assumed that these length scales can be ordened in the following way

$$L \ : \ w \ : \ \lambda \ \sim \ \delta^{-2} \ : \ \delta^{-1} \ : \ 1, \tag{2}$$

where δ is a small parameter.

Because of the ordening (2) the imaginairy part of the wave vector $\mathbf{k}_i$ which describes the electric field profile, is of the order δ compared with the real part $\mathbf{k}_r$. Consistency with $w_0 \approx \delta^{-1}$, where w_0 is the waste of the beam, demands that the beam focussing is moderate. It turns out that the gradient $\mathrm{d}\mathbf{k}_r/\mathrm{d}\mathbf{x}$, which is related to the curvature of the phase front, must be taken of the order δ^2 or smaller to satisfy this demand. The imaginary part of the wave vector $\mathbf{k}_i$, its gradient $\mathrm{d}\mathbf{k}_i/\mathrm{d}\mathbf{x}$, and $\mathrm{d}\mathbf{k}_r/\mathrm{d}\mathbf{x}$ are allowed to vary over the width of the beam, i.e. $\mathrm{d}^n\mathbf{k}_i/\mathrm{d}\mathbf{x}^n = \mathcal{O}(\delta^{n+1})$ with $n \geq 0$, and $\mathrm{d}^n\mathbf{k}_r/\mathrm{d}\mathbf{x}^n = \mathcal{O}(\delta^{n+1})$ with $n \geq 1$.

DISPERSION RELATION

It will be shown below that the leading order description of diffraction effects requires an expansion of the dispersion relation up to and including second order terms in the small quantity $\delta = |\mathbf{k}_i|/|\mathbf{k}_r|$. It is clear that all terms of the order δ^2 in the dispersion relation can generate effects of the same order. The usual derivation of this relation assumes a homogeneous plasma and a constant wave vector. This assumption can no longer be made if the dispersion relation is to be derived including all terms of the order δ^2, because a consistent ordening of terms requires that both $\mathrm{d}\mathbf{k}_r/\mathrm{d}\mathbf{x}$ and $\mathrm{d}\mathbf{k}_i/\mathrm{d}\mathbf{x}$ are of the order δ^2.

A method to derive the dispersion relation including all second order terms in the small parameter δ is given in Ref. [4]. The final result can be written in the general form

$$\omega = \omega_0(\mathbf{k}, \mathbf{x}) + \mathrm{i}F_{\alpha\beta}(\omega_0(\mathbf{k}, \mathbf{x}), \mathbf{k}, \mathbf{x})\frac{\partial k_\alpha}{\partial x_\beta}, \tag{3}$$

where $\omega = \omega_0(\mathbf{k}, \mathbf{x})$ is the usual dispersion relation of the homogeneous medium with constant wave vector. This wave vector, however, now is complex and the dispersion relation must be evaluated as $\omega_0(\mathbf{k}_r + \mathrm{i}\mathbf{k}_i, \mathbf{x})$. The tensor $F_{\alpha\beta}$ is, like ω_0, of the order δ^0. Therefore, the second term of the right hand side of Eq. (3) is a correction of the order δ^2 to the usual dispersion relation.

THE RAY EQUATIONS

The dispersion relation can be written in the form $\omega = \omega(\mathbf{k}, \mathbf{x}, \partial\mathbf{k}/\partial\mathbf{x})$. The ray equations are derived from the demand that the dispersion relation is satisfied for all positions

$$\frac{\mathrm{d}\omega}{\mathrm{d}\mathbf{x}} = \left.\frac{\partial\omega}{\partial\mathbf{x}}\right|_{\mathbf{k},\mathrm{d}\mathbf{k}/\mathrm{d}\mathbf{x}} + \left.\frac{\partial\omega}{\partial\mathbf{k}}\right|_{\mathbf{x},\mathrm{d}\mathbf{k}/\mathrm{d}\mathbf{x}}\frac{\mathrm{d}\mathbf{k}}{\mathrm{d}\mathbf{x}} + \left.\frac{\partial\omega}{\partial(\partial\mathbf{k}/\partial\mathbf{x})}\right|_{\mathbf{k},\mathbf{x}}\frac{\mathrm{d}^2\mathbf{k}}{\mathrm{d}\mathbf{x}^2} = 0. \tag{4}$$

The ray equations can be derived from this equation by taking the real and imaginary part, taking the ray to propagate in the direction

$$\frac{\mathrm{d}\mathbf{x}}{\mathrm{d}\tau} = \mathbf{v} = \mathrm{Re}\left(\left.\frac{\partial\omega}{\partial\mathbf{k}}\right|_{\mathbf{x},\mathbf{dk}/\mathbf{dx}}\right), \tag{5}$$

and expanding the equations in the small parameter $\delta = |\mathbf{k}_i|/|\mathbf{k}_r|$. The final result can be written in the form [4]

$$\frac{\mathrm{d}x_\alpha}{\mathrm{d}\tau} = \frac{\partial\omega_r}{\partial k_{r,\alpha}} \tag{6a}$$

$$\underset{\delta^2}{\frac{\mathrm{d}k_{r,\alpha}}{\mathrm{d}\tau}} = \underset{\delta^2}{-\frac{\partial\omega_r}{\partial x_\alpha}} + \underset{\delta^3}{k_{i,\gamma}\frac{\partial^2\omega_r}{\partial k_{r,\gamma}\partial k_{r,\eta}}\frac{\mathrm{d}k_{i,\eta}}{\mathrm{d}x_\alpha}} + \underset{\delta^3}{F_{r,\gamma\eta}\frac{\mathrm{d}^2k_{i,\gamma}}{\mathrm{d}x_\eta\mathrm{d}x_\alpha}} \tag{6b}$$

$$\underset{\delta^3}{\frac{\mathrm{d}k_{i,\alpha}}{\mathrm{d}\tau}} = \underset{\delta^3}{-k_{i,\gamma}\frac{\partial^2\omega_r}{\partial k_{r,\gamma}\partial x_\alpha}} - \underset{\delta^3}{k_{i,\gamma}\frac{\partial^2\omega_r}{\partial k_{r,\gamma}\partial k_{r,\eta}}\frac{\mathrm{d}k_{r,\eta}}{\mathrm{d}x_\alpha}} - \underset{\delta^3}{F_{r,\gamma\eta}\frac{\mathrm{d}^2k_{r,\gamma}}{\mathrm{d}x_\eta\mathrm{d}x_\alpha}}, \tag{6c}$$

where

$$\omega_r = \omega_0(\mathbf{k}_r, \mathbf{x})$$

$$\overline{\mathbf{F}}_r = \overline{\mathbf{F}}(\omega_0(\mathbf{k}_r, \mathbf{x}), \mathbf{k}_r, \mathbf{x})$$

are real functions which do not depend on the imaginary part of the wave vector. To derive Eqs. (6) the dispersion relation (3) had to be expanded up to second order in the small quantity δ.

The first term on the right hand side of Eq. (6a), and the first term on the right hand side of Eq. (6b), are the terms of geometric optics. The other terms in these equations are at least one order in magnitude smaller. The direction of propagation of a ray is equal to that of geometric optics. The diffraction effects appear indirectly through a modification of the real part of the wave vector which is driven by the electric field profile through $\mathbf{k}_i$, $\mathrm{d}\mathbf{k}_i/\mathrm{dx}$, and $\mathrm{d}^2\mathbf{k}_i/\mathrm{dxdx}$. If the width of the beam decreases the gradient of the electric field profile increases and the second and third terms on the right hand side of Eq. (6b) become larger, causing more bending of the rays away from each other. The rays will, therefore, never cross and no caustics will be formed.

RELATION TO OTHER WORK

Using the complex eikonal method Mazzucato [3] derived a set of ray equations which include diffraction. It can be shown that his equations differ from the ray equations (Eqs. (6)) in this paper through the terms containing the tensor $\overline{\mathbf{F}}$. This tensor entered our equations through the correction on the dispersion relation that contains the gradients of the wave vector. In Ref. [3] it was assumed that the Altar-Appleton-Hartree dispersion relation is satisfied.

The statement that all terms of the order δ^2 have to be retained in the dispersion relation would be too strong. In principle, one could treat the effects of the gradient

of the wave vector in the transport of amplitude equation. This solution, however, is unnatural because effects of the same order are then treated in a different way. It also goes against the philosophy of the complex eikonal method, where the beam profile effects are introduced through the dispersion relation to derive ray equations that properly describe the diffraction effects. If the transport of amplitude equation has to be considered seperately one can just as well treat all diffraction effects in this equation.

It must be noted, however, that Ref. [3], applies the formalism to the treatment of a Gaussian beam. An example of the electric field of such a beam would be

$$\mathbf{E} = \frac{1}{w(z)} \exp\left[-\frac{x^2+y^2}{w^2(z)} + \mathrm{i}kz + \mathrm{i}k\frac{x^2+y^2}{2R(z)} - \mathrm{i}\omega t \right], \tag{7}$$

where the beam is assumed to propagate along the z-axis, $w(z)$ is the width of the beam and $R(z)$ is the radius of curvature. Both w and $1/R$ are assumed to vary on the long length scale $L = \delta^{-2}$. It can be verified that in this case $\mathrm{d}^2\mathbf{k}_i/\mathrm{d}\mathbf{x}^2 = \mathcal{O}(\delta^4)$, and $\mathrm{d}^2\mathbf{k}_r/\mathrm{d}\mathbf{x}^2 = \mathcal{O}(\delta^4)$. Therefore, all terms including the tensor $\overline{\mathbf{F}}_r$ can be neglected in Eqs. (6). In the set of Eqs. (6) then the function $\omega_r(\mathbf{k}_r, \mathbf{x})$ appears, and it is equivalent to that of Mazzucato.

In the case of a Gaussian beam the beam can be described entirely with a few parameters (width and radius of curvature of the phase front). In this case a reduced set of equations can be derived that gives the evolution of these parameters. Such a set is discussed in Refs. [4-6].

CONCLUSIONS

In this paper an extension of the ray equations of geometric optics to include diffraction effects for a wave beam propagating in a dispersive anisotropic medium is derived. The results of this paper extend the previous results to more general beams, and shed light on the conditions under which the assumptions made in previous work break down.

ACKNOWLEDGEMENT

Useful discussions with dr. G.V. Pereverzev and dr. E. Westerhof are gratefully acknowledged.

REFERENCES

[1] S. Choudhary, L.B. Felsen, IEEE Trans. Antennas Propagation, **Ap-21** 827 (1973).
[2] S. Choudhary, L.B. Felsen, Proc. IEEE **62**, 1530 (1974).
[3] E. Mazzucato, Phys. Fluids B **1**, 1855 (1989).
[4] A.G. Peeters, *Extension of the ray equations of geometric optics to include diffraction effects*, to appear in Phys. Plasmas.
[5] G.V. Pereverzev, *Paraxial WKB solution of a scalar wave equation*, Max Planck Institut für plasmaphysik report IPP 4/260 (1993).
[6] A.V. Timofeev, Plasma Phys. Reports **21**,646 (1995).

Microturbulence Behaviour Study during LH Heating in FT-2 Tokamak by CO_2-laser Scattering

V.N.Budnikov*, **V.V.Bulanin**, V.V.Dyachenko*, E.Z.Gusakov*, L.A.Esipov*, E.R.Its*, A.V.Petrov, A.V.Vers

State Technical University, St.Petersburg, Russia
* A.F.Ioffe Institute, St.Petersburg, Russia

1. Introduction

The detailed study of the transition from the LH current drive to the fast ion generation has been carried out in recent years on the FT-2 tokamak [1]. The parametric decay at low plasma density at $\omega_0 \approx 2\omega_{LH}(0)$ is conceded to be reasonable for the transition (Here: ω_0 is the frequency of the injected pump wave and $\omega_{LH}(0)$ is the lower-hybrid frequency evaluated at the plasma centre). The small-scale fluctuations behaviour during this transition has been studied with the collective CO_2-laser scattering. The concern experimental data are presented in this paper. The CO_2-laser scattering has been previously employed to investigate the short-wave fluctuations at the pump wave frequency [2] and at the ion gyrofrequency [3] presumably excited through the parametric mechanism. However, the study of the low frequency turbulence has not been attempted.

2. Experimental Setup

The FT-2 tokamak OH discharge in hydrogen (R = 55 cm, a = 8 cm, I_p up to 43 kA , B = 24 kGs) has been preceded the RF switch on [1]. The plasma parameters $\langle n_e \rangle = (1.3\text{-}4)\cdot 10^{13}$ cm^{-3}, T_e = 500-600 eV, T_i = 100 eV have been got at this moment. The RF power launched from the low magnetic field side with two-waveguide grill was from 20 to 140 kW at a frequency 920 MHz. The pulse duration was nearly 4 ms.

The incident CO_2-laser beam is directed along vertical chord of minor cross-section of the torus. The beam could be positioned at value x of 0, ±3, ±5, +6 cm (here $x = R - R_0$, where R_0 is the major radius of the device). For our case of near-forward scattering the laser beam couples only to fluctuation wavevectors $\mathbf{K}_\perp$ oriented nearly perpendicular to the incident beam. The diagnostic setup is able to gauge simultaneously the radiation scattered from fluctuations at four different $K_\perp$-values in the range from 8 to 40 cm^{-1} and in the frequency band up to 2 MHz. An optical mixing homodyne techniques was used for the detection. For super small scattering angles the length of scattering volume along the incident beam was about minor cross-section diameter. Thus the scattered signal power spectrum $P_s(K_\perp,\omega)$ can be conveniently regarded as an integral of local power spectrum of fluctuations along the laser beam direction.

3. Experimental Results.

The specific feature of the FT-2 tokamak experiment consists of the fact that the plasma density increase accompanying RF pulse makes it possible to observe the transition from the current drive to the fast ion generation in a single tokamak shot [1]. The typical traces of plasma parameters for such a discharge are shown in Fig 1. The waveforms for two different $K_\perp$-values represent the scattered power averaged in a frequency band 0.06-1 MHz and are plotted in the same arbitrary units to be compared between. One can see that the loop voltage drop associated with the current drive remains nearly fixed until the CX-flux is starting up. The

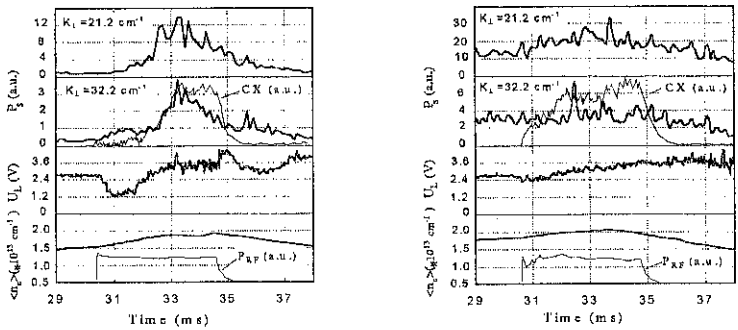

Fig.1. Time evolution of the scattering power P_S and plasma parameters for the different line averaged density ($<n_e>_{OH}$ preceded RF pulse; X = -3 cm, I_p = 30 kA.

drastic increase of the microturbulence has been observed just after the current drive switching off. The fluctuations behave in quite a different manner for the higher level of density (see Fig 1). For such a discharge the LH current is not driven. The CX-flux is starting from the beginning of the RF pulse. While the P_S value increase is not significant.

The observed turbulence was discovered to be excited only in the narrow range of plasma densities $(<n_e>)_{OH}$ preceding the RF pulse. This plasma density interval is correlated with the conditions when the current drive switch off and fast ion generation are observed simultaneously during a RF pulse. The fluctuation intensity increment ΔP_S over the OH level of P_S as a function of the initial density $(<n_e>)_{OH}$ are shown in Fig 2. It worth noticing that the experiments on the tokamaks of quite different geometry show the ion temperature increase [4] and the ion gyrofrequency short wave excitation [3] in the same narrow density range to satisfy the condition $\omega_0 \approx 2\omega_{LH}(0)$.

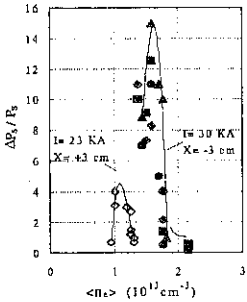

Fig 2. The relative increment of the scattering power versus $(<n_e>)_{OH}$. Different symbols correspond to different $K_\perp$-values.

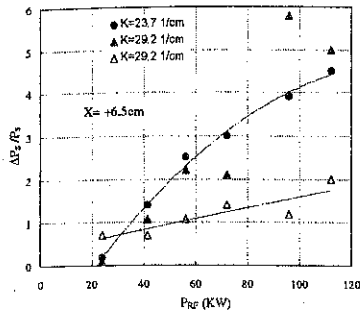

Fig 3. The relative increment of the scattering power versus injected RF power. Solid symbols correspond to $(\langle n_e \rangle)_{OH}=1.5\cdot10^{13}cm^{-3}$, *open -* $(\langle n_e \rangle)_{OH}=1.8\cdot10^{13}cm^{-3}$

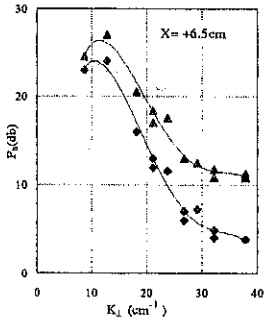

Fig 4. Power $K_\perp$ *-spectra for different periods of time: before RF pulse (squares) and after the current drive switch off (triangles).*

The ratio $\Delta P_s/P_s$ as a function of injected RF power is shown in Fig 3. The RF power threshold of nearly 20 kW is evidently seen for the case of low initial density $(\langle n_e \rangle)_{OH}$. At higher densities the threshold is not observed at all. A slight increase of fluctuations in these conditions may be merely accounted for plasma density increasing during RF pulse. The multichannel scattering detection has let to discover that shorter wave fluctuations are of greater rate increase as compared to the larger scale ones (see Fig 4).

The frequency integrated scattering power waveforms were found to be similar under the different incident laser beam x-positions. This refers equally to the different dependencies presented in Figs 2..4. However the frequency spectra are essentially dependent on the incident beam location. As the elongated scattering region is moved towards the plasma periphery, the scattering intensity is increased while the ω-spectra are shifted to lower frequency range. As an example two frequency spectra are shown in Fig 5 for the both central and peripheral scattering volume positions. One has to keep in mind that the orientation of **K**-vector relative to the plasma poloidal velocity $\mathbf{V}_\theta$ has to be changed under the incident beam displacement. Therefore the expected Doppler frequency shift $\mathbf{K}\cdot\mathbf{V}_\theta$ of scattering signal has to decrease as the laser beam chord is moved towards the plasma edge. This effect may be a reason of the observed ω-spectrum displacement to lower frequency range. It is particularly remarkable that an unusually sharp frequency spectra are discovered for the interval of $0 < |x| < 5$ cm. The peak nature of spectra remained quite appreciable even after the ensemble average. Thus the frequency peaks are accounted for the scattering from "quasicoherent" small-scale modes. These modes are to be associated with high frequency "quasicoherent" bursts which are evidently seen in output signals of detectors. These spectra are sampled in Fig 6 for $x = -3$ cm. Under the symmetrical probing ($x = +3$ cm) the spectra are found to be the same shaped accept the broadband background intensity.

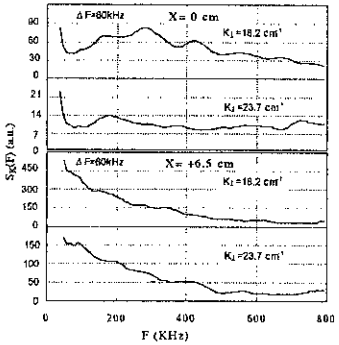

Fig 5. Comparison of the smoothed power spectra for different incident beam positions; I_p = 30 kA.

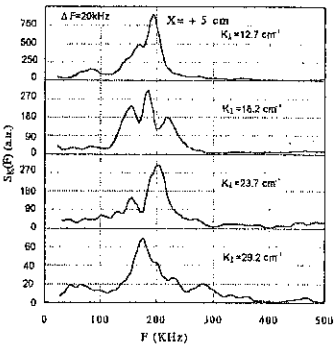

Fig 6. The smoothed power spectra for X= -5 cm; I_p = 40 kA.

4. Conclusion

The short-wave low-frequency turbulence with a "quasicoherent" mode is drastically increased just after LH current drive switch off. The increasing of electron density turbulence is strongly correlated with RF wave slowing down and ion generation appearance and exhibits the existence of RF power threshold. The intensive slowed down RF wave may be an immediate cause of fluctuation excitation or else indirect reason of drift turbulence enhancement through the evolution of plasma parameter radial profiles. However the fact that the small-scale fluctuations is increased faster then larger size ones is not characteristic of drift instability in tokamak. The most plausible process reasonable for this excitation is the pump wave decay into lower-hybrid and drift type waves [3]. It is possible as well that the RF wave is scattered from low-frequency fluctuations near plasma periphery [4], then RF wave is slowed down under the intensity increase. The non-linear interaction between this wave and interior plasma may cause a short -wave fluctuation enhancement.

5. Acknowledgements

This work was supported in part by INTAS Contract No 94-2236 and RFBR Contract No 94-02-04759-a.

Reference

[1] V.N.Budnikov et.al., 22nd EPS Conference, Bournemouth, 1995 ECA, vol. 19C, IV-385.

[2] C.M.Surko et.al., 2nd Joint Grenoble-Varenna Int. Symp. on Heating in Toroidal Plasmas (1980) vol. 1, p.393.

[3] Y.Takase et.al., Phys. Fluids, vol. 28, 983 (1985).

[4] J.J.Schuss et.al., Nuclear Fusion, vol. 21, 427 (1981).

INVESTIGATION OF THE DECAY WAVES AT $f = f_0 - n \cdot f_{ci}$ IN LH EXPERIMENTS ON THE FT-2 TOKAMAK.

V.N.Budnikov, V.V.Dyachenko, L.A.Esipov, E.R.Its, K.M.Novik, A.Yu.Stepanov.

IOFFE Physico-Technical Institute, 194021, St.Peterburg, Russia

Work supported by ISF #23000 and RFBR Grant #95-020-04072

Introduction

Parametric decay spectra with frequency $f = f_0 - n \cdot f_{ci}$ (where f_0 is the pumping wave frequency, $n \cdot f_{ci}$ is the ion cyclotron harmonic frequency) have been observed practically in all LH heating experiments in tokamaks. The most popular explanation was that there was a peripheral decay of pumping wave into a secondary LH wave (cold or warm) and into low frequency oscillations (ion cyclotron (IC) wave or IC quasi-mode) [1–6]. But some authors supposed that the process was essentially unfavorable for plasma heating because RF power dissipation at the periphery of the discharge [4–6], others believed that the decay was only an accompanying process, unimportant for ion heating [1–3].

Authors of the report would like to discuss an alternative point of view of the role of the above-mentioned decay in RF power transportation into the plasma. Main experimental evidences have been observed by the enhanced scattering diagnostics [7]. The high frequency extraordinary wave, which has an accessible upper hybrid resonance (UHR) surface, is used in this case. The back scattered wave gives local information about short wave length plasma oscillations in the vicinity of its UH resonance.

Experiments

Experiments have been carried out on the FT–2 Tokamak (R = 55 cm, a = 8 cm). Ohmic plasma parameters were as follows: B_T = (1.8–2.4)T, $I_p \cong$ 22 kA, n_{e0} = (0.5–2)·10^{13} cm $^{-3}$, $T_e(0) \cong$ 500 eV, $T_i(0) \cong$ 100 eV. LH wave was excited by the magnetron generator with operating frequency 920 MHz and the output power up to 300 kW. RF power is coupled into plasma by a two-waveguide grill placed at the low magnetic field side. Calculated $N_\parallel$ spectra lies within $N_\parallel$ = 2–3. The enhanced scattering and CX diagnostics were located in a tokamak cross-section displaced by one-quarter from the grill along the torus. Probing UH wave (f_0 = 59 GHz, P_{in} = 1 W) was emitted into the plasma from the high magnetic field side by a horn. Back scattered wave was received by the same horn. The location of the UHR surface was calculated using local value of $B_T(r)$ and $n_e(r)$. During RF pulse these parameters changed within some limits which provided scanning the UHR surface along the major radius R.

Spectrum of the scattered oscillations (Fig.1) included not only the pumping wave frequency f_0 = 920 MHz, but also the peaks shifted from f_0 by an ion cyclotron frequency f_{ci} and its 2nd and 3rd harmonics, where f_{ci} = 30 MHz corresponded to a local ion cyclotron frequency at the low field side of the torus on the radius r = 7–8 cm. There were no other peaks in the frequency range 450–1200 MHz.

Fig.2 represents the spatial distributions of: the electron density $n_e(r)$; the power of scattered radiation $P_s(r)$ summarized over all satellites; 1 keV CX flux for two values of central $n_e(0)$.

It should be noted that P_s radial profiles were measured in the equatorial plane, while the CX flux distribution was scanned vertically from the plasma center to the torus top. It was demonstrated that the oscillations at the shifted frequencies are localized at the radius r = (5–7) cm. The localization did not change while the local density varied by $(0.6–1.6)\cdot10^{13}$ cm^{-3}. In these cases the fast ion generation was observed from the central part of the plasma column.

Discussion

According to the back scattering condition $2k = q$ (where k and q are wave numbers of incident wave and measured oscillations respectively) maximum scattering wavelength for the probing wave at a frequency 59 GHz (λ_0 = 5 mm) is equal 2.5 mm. Transversal refractive index $N_\perp$ of the whistlers excited by the grill far from the LH resonance is estimated as $N_\perp = N_{\parallel}(n_e/n_{ecr})^{1/2}$, where n_{ecr} is the critical density (for f_0 = 920 MHz $n_{ecr} \cong 10^{10}$ cm^{-3}). It means that in our density range (at $N_\parallel \cong 2.5$) $N_\perp$ = 60–100, i.e. $\lambda_\perp$ = (5–3.3) mm. That is why the scattering on the pumping wave frequency f_0 must not be registered. Probably the broad, low amplitude peak at the frequency f_0 observed in the experiments is associated with some secondary processes such as pumping wave scattering on small-scale plasma oscillations. Further, if the satellites are produced by the parametric decay they can have higher $N_\parallel > N_{\parallel 0}$ as the decay threshold for high $N_\parallel$ daughter waves decreases. In our case, increase of $N_\parallel$ by two times is enough to investigate the satellites by the back scattering diagnostics. As higher $N_\parallel$ correspond to higher $N_\perp$ this process results in a more intensive amplitude of the scattered signal.

It was discovered that all satellites in this tokamak cross-section had the similar spatial location including the pump wave peak. It means that all registered oscillations had the same $N_\parallel$ spectrum, $N_\parallel \geq 5.0$. At the grill cross-section similar frequency peaks were observed by RF probes located near grill at the plasma surface at r = (7–8) cm. Though we could not observe low frequency daughter waves with $n\cdot f_{ci}$ for the lack of suitable equipment it is possible to suppose that parametric decay $L \rightarrow L' + IC$ took place in our experiments. Here L and L' are LH pump and daughter waves, IC are the ion cyclotron harmonics waves. Schematically the wave behavior is represented by Fig.3. Evidently the decay occurs at the plasma periphery near the grill and then the daughter wave L' goes away from the decay region and propagates along the torus and inside the plasma. As a result, in the next tokamak cross-section it is found at the radii r = (5–7) cm. As it was mentioned above, the parallel refractive index of LH daughter wave is higher than that of the pumping wave, $N_{\parallel D} > N_{\parallel 0}$. That is why its conversion region is located at a lower density $n_{LHD} = n_{LH}(f_0 - nf_{ci}) < n_{LH}(f_0)$, namely, they can be absorbed by ions due to the classical stochastic mechanism before they reach $n_{LH}(f_0)$.

In our case (for $N_\parallel$ = 2.5 and $T_e(0)$ = 500 eV) $n_{LH}(f_0)$ is equal to $4\cdot10^{13}$ cm^{-3}. For the maximal $N_{\parallel D}$ = 9 the lowest calculated n_{LH} is $2.3\cdot10^{13}$ cm^{-3}. Observed from the plasma center ion tail generation occurs at $n_e(0) = 1.8\cdot10^{13}$ cm$^{-3} \leq n_{LHD}$. The coincidence of the calculated and observed n_{LHD} takes place. The threshold of the parametric decay was not investigated in detail, but it had a low input

power level, $P_{th} \leq (20\text{–}30)$ kW. Because the threshold depends strongly on the electron temperature the simultaneous LH and EC heating experiment is planned.

Summary

Experimentally observed, parametrically excited wave with frequency $(f_0 - nf_{ci})$ is able to propagate from the periphery to a dense plasma and to be absorbed by ions in the vicinity of its local LH resonance.

The research has been supported by ISF #23000 and RFBR Grant #95-020-04072

References:

1. Pacher H. at all. In : Heating in Toroidal Plasmas, Como, 1980, vol.1, 329-541
2. D.Van Houtte at all. In: Heating in Toroidal Plasmas, Roma, 1984, vol.1, 554-570
3. Uehara K. and Nagashima T. In: Heating in Toroidal Plasmas, Grenoble, 1982, vol.2, 485-503
4. Cesario R., Pericoli-Ridolfini V. Nucl. Fusion, 1987, 27, p.435
5. Takase Y., Porkolab M. et al., Phys. Fluids, 1985, 28 p.983
6. Leuterer F. at all. Plasma Phys. and Contr. Nucl. Fusion Research., Proc. of 10th Conf., London, 12-19 September 1984, v.1, p. 597
7. Novik K.M., Piliya A.D. Plasma Physics and Controlled Fusion, v.35 (1993) 357-381.

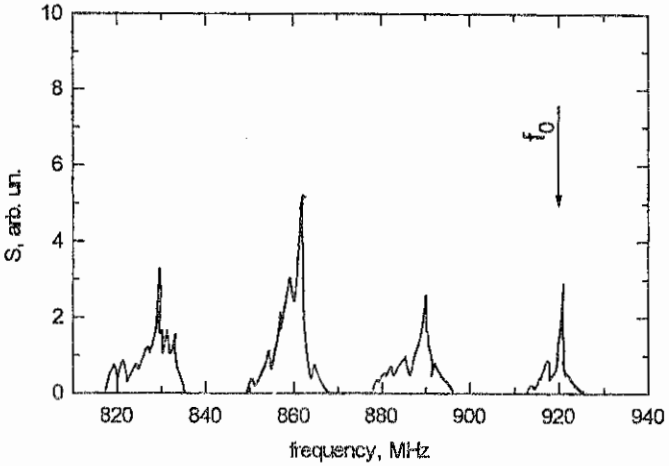

Fig. 1. Scatterred radiation spectra (f_0 - pump wave frequency).

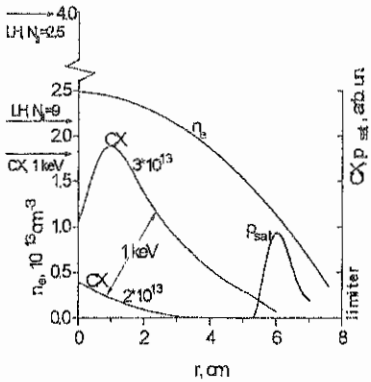

Fig. 2. Radial profiles of the enhanced scattering signal and charge exchange neutral beam (E = 1 keV).

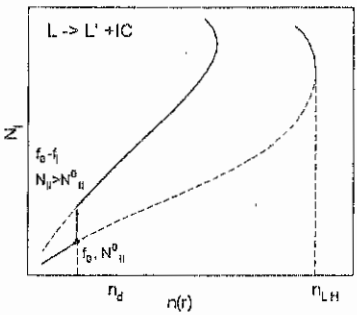

Fig. 3. Model of RF energy transport into the plasma.

Investigation of Lower Hybrid Wave Damping

S. Bernabei, A. Cardinali*, G. Giruzzi#, G.T. Hoang#, D. Ignat, R. Kaita, M. Okabayashi, F. Paoletti● and S. von Goeler

Plasma Physics Laboratory, Princeton University, Princeton NJ 08543 USA.
** Associazione Euratom-ENEA sulla Fusione, Frascati, Italy.*
 # Association Euratom-CEA sur la Fusion, Centre d'Etudes de Cadarache, France.
●Via dei Provoletti 69, Tor Bella Passera, Roma, Italy.

Introduction. The PBX-M experiment [1] is equipped with both a flexible Lower Hybrid (LH) wave launching system and a unique diagnostic set for the measurement of the spatial distribution of the superthermal electrons, which can be used to monitor the wave power deposition profile. This has made possible an extensive experimental and theoretical investigation of the LH wave damping in various physical regimes. The LH experiments have been performed with either indented or circular plasma configurations. Typical parameters were: plasma current $I_p \approx 180$ kA, density n_e=1 to 3×10^{19} m^{-3}, and RF power up to 800 kW at 4.6 GHz, delivered to the plasma through two fully-phased arrays of 32 waveguides each [2]. Partly because of the limited power available, steady state current drive was never achieved. Therefore, the loop voltage drop was used to determine the current drive (CD) efficiency , corrected for changes in current, resistivity and internal inductance, by means of a fitting method explained in the following section. The phase dependence of the damping has also been investigated. Some apparent anomalies have been encountered and explained by means of extensive computer modeling, performed by coupling a ray tracing code with a relativistic Fokker-Planck code.

Experimental results. Figure 1 shows the relative loop voltage drop $[-(V_{rf}-V_{oh})/V_{oh}]$ versus the RF power normalized to line averaged density, current and major radius of the plasma P/nI_pR. V_{oh} is the loop voltage in the purely ohmic plasma and V_{rf} is the residual loop voltage after application of RF power. The curve "rolls over" rather than increasing linearly with (P/nI_pR), because of the diminishing effect of the electric field as more current is driven by the RF and less by the OH system. The value of $(P/nI_pR)^{-1} = \eta_{lo}$ at which the curve crosses the line $-\Delta V/V_{oh}$=1 defines the efficiency of current drive at V_{loop} =0. In order to calculate the current drive efficiency η_{lo} at $V_{loop} = 0$, we follow the approach of Karney-Fisch [3] by plotting P_{el}/P_{abs} vs $u = c/(n_{\|abs}v_{Dreicer})$, where $P_{el} = V_{loop}I_{rf} = V_{loop}(-\Delta V_{loop}/V_{oh})I_p$ is the RF power converted into electromagnetic energy, $P_{abs} = \alpha P_{injected}$ is the fraction of RF power absorbed by the electrons, and $n_{\|abs} = \beta n_{\|0}$ is the value of $n_\|$ absorbed by the electrons, which is usually upshifted (due to toroidal effects [4]) relative to the injected value $n_{\|0}$. In this set of

equations, the parameters α and β are varied in order to have the experimental points fall between the curves for P_{cd}/P_{abs} vs. u corresponding to $Z_{eff} = 2$ and $Z_{eff} = 5$, obtained from the polynomial approximation given by Karney-Fisch to match the experimental value $Z_{eff} \approx 3$. Once α and β are determined, the efficiency at $V_{loop} = 0$ can then be calculated, since $\eta_o \propto \alpha/(\beta n_{\|0})^2$. Clearly, various combinations of α and β will fit the data between the Fisch-Karney curves, but the ratio α/β^2 is rather constant and η_o is well determined. For very low values of α, we obtain an $n_{\|abs}$ which is too low to be explained. On the other hand, values of α close to 1 would imply an $n_{\|abs}$ which is far too high. The choice of α=.65 produces a value for β in the case of total upshift of the spectrum to nearly $n_{\|abs} = 7$, which is what is calculated with the ray tracing code. The results are shown in Fig. 2, where η_o is plotted versus the injected value of $n_{\|o}$ for circular and indented configurations. For $n_{\|o} \geq 2.1$ the efficiency decreases as $n_{\|o}$ is increased as expected [5]. For values $n_{\|o} \leq 2.1$, the efficiency decreases with decreasing $n_{\|o}$. This is a surprising result since it is well known that faster phase velocity waves are more efficient in driving currents. The explanation can be seen in Fig. 3, where the value of $n_{\|abs}$ is plotted vs $n_{\|o}$. For $n_{\|o} \geq 2.1$, the upshift is modest and fairly constant, while for $n_{\|o} \leq 2.1$, the waves need a large upshift before damping. This points to two different damping regimes.

We have made extensive use of a 2-D Hard X-ray pinhole camera [6] to study the radial profile of the LH power deposition. In PBX-M, there are two perplexing results which counter the notion that a large spectral gap makes the damping of the LH waves independent of the original $n_{\|o}$. The location of the damping and the velocity of the fast electrons generated were observed to directly related to the value of $n_{\|o}$. Figure 4 shows the location where the maximum of the fast electron tail is formed, obtained from inverting the hard X-ray emission [7], as a function of $n_{\|o}$.The continuous line, obtained from ray tracing, is the locus of the maximum penetration of the wave in its first pass across the plasma. That the hard X-ray emission follows the first pass of the wave is a surprise, since at this location the value of $n_{\|}$ has changed very little from the launched value. Given that the typical temperature of the plasma is $\approx$ 1keV, the wave is far too fast for damping. Instead, the damping is expected close to r/a = 0.5, where the value of $n_{\|}$ is allowed to reach a maximum ($n_{\|} \approx 7$). The second anomaly concerns the effective temperature of the photon spectrum, deduced from the 2D hard X-ray camera measurements. As shown in fig. 5a, the photon temperature is approximately inversely proportional to $n_{\|o}$, for $n_{\|o} \geq 2.2$: this is what is normally expected since faster waves interact with faster electrons. Below $n_{\|o} = 2.2$ the situation is inverted and the photon temperature decreases for higher phase velocity.

Discussion. A mechanism is proposed which can explain how first pass damping is possible in situations with a large spectral gap. As the waves propagate in the plasma, they

must upshift in order to damp. As an electron tail is formed, enhanced by the electric field of the transformer, less upshift is needed for damping. Ultimately, even the incoming wave (with a practically unchanged $n_{||}$) can deposit some of its power into the tail. At equilibrium, the tail is maintained by a spectrum broader than the launched one: the value of the upshift is then intended as a 'weighted average' upshift of the various absorbed $n_{||}$. This scenario applies to the spectra centered at $n_{||o} \geq 2$. For values of $n_{||o} \leq 2$, the incoming wave with $n_{||} \approx n_{||o}$ is confined by accessibility to the outer portion of the plasma. For these faster waves, the spectral gap is too wide to be bridged, and only upshifted values of $n_{||}$ are damped. The waves with lower $n_{||}$ have the following characteristics: 1) efficiency is lower than for $n_{||o} \geq 2.1$; 2) damping location is not correlated to accessibility, but to upshift, which is largely independent of the original $n_{||o}$; 3) the photon temperature decreases as the phase velocity increases. If the photon temperature is plotted versus the absorbed value of $n_{||}$, an almost monotonic function is obtained (see figure 5b). The plausibility of this scenario has been confirmed by extensive 3-D Fokker-Planck simulations, including ray-tracing, to be presented elsewhere. An important role in this picture is played by radial diffusion. Fast electron diffusion coefficients of the order of 1 - 2 m^2/s have been estimated in similar PBX-M discharges [7]. It is possible to show that this level of diffusion is sufficient for flattening the fast electron profile in the region $r \leq a/2$, which could explain the observed hard X-ray profiles.

Acknowledgements. The authors gratefully acknowledge enlightening discussions with Dr. E. Barbato. Work supported by USDOE under contract AC02-76-CH0-3073

[1] R. Bell et al., Phys. Fluids B 2 (1990) 1271.
[2] N. Greenough et al., 14th IEEE Symp. on Fus. Eng. S. Diego (Oct 1991) vol. 1 p. 126.
[3] C. F. F. Karney and N. J. Fisch, Phys. Fluids 29 (1986) 181
[4] S. Bernabei and D. W. Ignat, Nucl. Fus., 22 (1982) 735.
[5] N. J. Fisch, Phys. Rev. Lett. 41 (1978) 873.
[6] S. von Goeler et al., Rev. Sci. Instrum. 65 (1994) 1621
[7] S. E. Jones et al., Phys. Plasmas 2 (1995) 1548.

Fig 1 Relative loop voltage drop $[-(V_{rf}-V_{oh})/V_{oh}]$ vs. RF power, normalized to average density $\bar{n}_e$, major radius R, plasma current I_p. The top scale is the inverse of the bottom one. full dots = LH in bean plasma configuration; circles = LH in circular plasma All the data for $n_{||injected} = 2.1$ The values at $-\Delta V/V_{oh}=1$ $[V_{rf}=0]$ are obtained from figure 4.

Fig 2 Current drive efficiency (InR/P) at $V_{loop}=0$ vs. injected value of $n_{||}$. full dots = LH in bean plasma configuration circles = LH in circular plasma.

Fig 3 $n_{||}$ absorbed vs. $n_{||}$ injected for the data of figure 4.

Fig 4 Radial location of the maximum of the HXR intensity, versus $n_{||injected}$. The line is the maximum accessibility of the wave at the first pass from LSC code. Plasma conditions are: Ip=180 kA, average density = $2.2x10^{13}$ cm^{-3}, B=1.7 T, $P_{RF} \approx 260$ kW, bean plasma configuration.

Fig 5 Photon temperature vs. $n_{||0}$ (a) and vs. $n_{||abs}$ (b) for the same shots of Fig. 2.

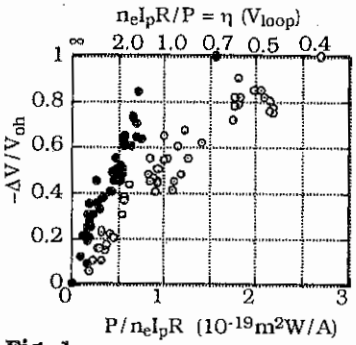

Fig. 1

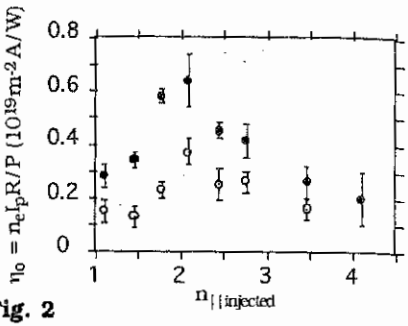

Fig. 2

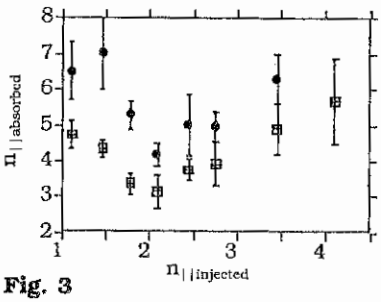

Fig. 3

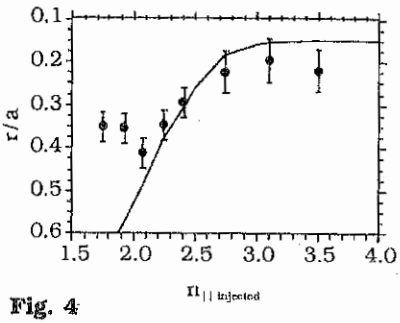

Fig. 4

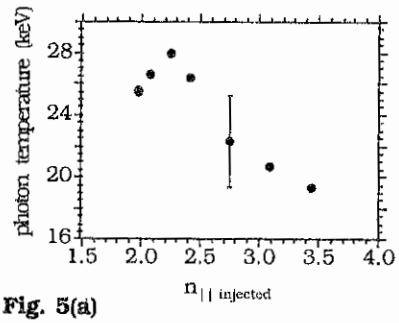

Fig. 5(a)

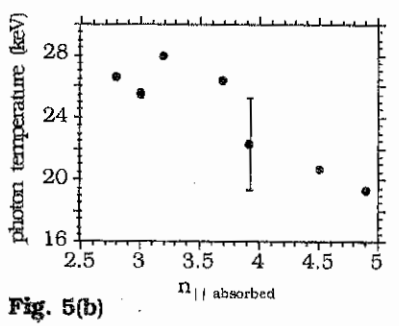

Fig. 5(b)

Effect of the radial drift of trapped suprathermal electrons on the ECRH power deposition profile

M. Romé, U. Gasparino, H.J. Hartfuß, H. Maaßberg, N. Marushchenko †

Max-Planck Institut für Plasmaphysik
EURATOM Association, D-85748 Garching, Germany
† *Institute of Plasma Physics, NSC-KhPTI, 310108 Kharkov, Ukraine*

Introduction.

The ECRH power deposition in low density, high temperature plasmas has been analyzed at W7-AS for different heating scenarios (fundamental O-mode and second harmonic X-mode) and different magnetic configurations. These are characterized by a different size of the toroidal ripple on the magnetic axis in the toroidal position of power launching (see Fig. 1), allowing to study the influence of (toroidally) trapped particles. The analysis has been limited to the case of perpendicular, on-axis heating.

The deposition profile has been estimated from the analysis of the electron heat transport in ECRH power modulation experiments, with the time dependent electron temperatures from ECE measurements. Peaked deposition profiles are usually obtained for both heating scenarios from a 3D Hamiltonian ray-tracing code based on the assumption of Maxwellian electron distribution function (single pass absorption). The heat transport analysis predicts the same peaked absorption profiles, but additionally a much broader contribution is present, whose width and relative integral contribution with respect to the "thermal" peaked part depends on the particular heating scenario and magnetic configuration.

The effect of the magnetic configuration on the electron distribution function in the different heating scenarios being considered, has been clearly demonstrated by means of a non-linear 2D bounce-averaged Fokker-Planck (FP) code, valid for the simplified magnetic field geometry close to the magnetic axis of W7-AS [1].

In a heuristic approach, the broadening of the thermal power deposition profile is expected to be related to the radial transport (determined by the ∇B-drift) of the locally trapped suprathermal electrons generated by the ECRH. The particles drift vertically in the local magnetic ripple, becoming passing particles by pitch angle scattering, and therefore contributing to the energy flux in the outer plasma region without direct ECRH deposition, through thermalization on the flux surfaces.

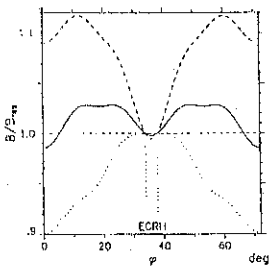

Fig. 1. *Magnetic field strength on-axis, normalized to the resonant field at the ECRH launching position, versus the toroidal angle within one field period for* $r_a \simeq 0.345$. *The solid line refers to the "standard" configuration of W7-AS, the dashed and the dotted lines correspond to the "minimum B" and the "maximum B" launching scenarios, respectively.*

Results of the power deposition analysis.

In Fig. 2a, the results of the power deposition analysis for scenarios at $B_0 = 2.5$ T in the "standard" configuration of W7-AS are summarized. The power deposition is clearly broadened for the lower densities both for fundamental O-mode (70 GHz) and for

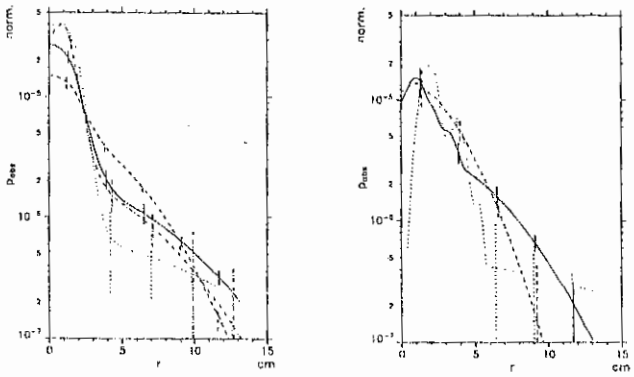

Fig. 2. *Power deposition profiles from ECRH power modulation experiments versus the effective radius r.* a: *$B_0 = 2.5$ T. The solid and the dashed lines refer to the fundamental O-mode heating (70 GHz), for $n_e = 2 \cdot 10^{19}$ m^{-3} and $n_e = 10^{19}$ m^{-3}, respectively. The dotted and the dash-dotted lines are the corresponding results for the second harmonic X-mode heating (140 GHz).* b: *$B_0 = 1.25$ T, and $n_e = 2 \cdot 10^{19}$ m^{-3}. The solid line refers to the "standard" configuration, the dashed and the dotted lines to the "minimum B" and the "maximum B" launching scenarios, respectively.*

second harmonic X-mode (140 GHz) launching. These findings support the picture of significant heat transport by suprathermal ripple trapped electrons since both the level of the suprathermal tail decreases and the collisional detrapping increases with density. The formation of the suprathermal tail in the ripple trapped electron distribution is expected to be more pronounced for X-mode launching [2], leading to a stronger broadening of the "effective" power deposition profile. For the O-mode scenarios, however, the lower single pass absorption and the effect of wall reflections may lead also to an enhanced broadening of the power deposition profile.

The effect of direct heating of ripple trapped electrons becomes more clear from Fig. 2b, which shows the results of a scan of the toroidal ripple, at $B_0 = 1.25$ T with second harmonic X-mode launching. In the "standard" case with 70 GHz launching, the deposition is broadened compared to the 140 GHz discharges of Fig. 2a, and this effect may be attributed to the stronger ∇B-drift of the trapped electrons. In the "maximum B" scenario, the deposition profile derived from the heat wave analysis is fairly close to the ray-tracing results, and the broadening of the deposition is of minor importance. For the "minimum B" scenario, a stronger broadening is found. All results on the power deposition are consistent with the heuristic model given above.

Convective Fokker-Planck model.

In order to simulate the broadening of the thermal power deposition profile, a simple FP model has been used, which describes the radial ∇B-drift of the toroidally trapped suprathermal electrons generated by the ECRH. In a first approach, collisional or collisionless detrapping can be treated as a loss term, i.e., the detrapped electrons are assumed to thermalize on the flux surfaces. Taking further trapping of these detrapped particles into account leads to a kind of *diffusive* modelling (with inward and outward ∇B-drifts). Neglecting this effect gives a *convective* model and the ECRH driven deviation of the trapped particle distribution from the Maxwellian defines the initial value for this *convective* FP

model. Both an analytical model and the solution of a time-dependent bounce-averaged FP code [1] are used for the initial distribution function. The drift of the suprathermal trapped electrons generated by the ECRH is described by means of the FP equation

$$< (v_{\nabla B})_z >_b \cdot \frac{\partial f_e^t}{\partial z} =< C^{lin}(f_e^t) >_b = C_w(f_e^t) + C_\lambda(f_e^t), \qquad (1)$$

where f_e^t represents the bounce-averaged distribution function of the trapped particles, $v_{\nabla B}$ the drift velocity due to the gradient of the magnetic field, and the angular brackets denote the bounce-averaging procedure, $< ... >_b \equiv \oint ...(ds/v_\parallel)/\oint(ds/v_\parallel)$, s being the coordinate along the magnetic field lines.
Stationary conditions are assumed. The presence of a radial electric field is omitted, so that the drift of the toroidally trapped electrons is mainly in the vertical direction z. The model is valid in the bulk part of the plasma axis, where the radial electric field is negligible. The collision operator is linearized by assuming a Maxwellian background. This assumption is quite reasonable outside of the ECRH deposition zone. The linearized collision operator, C^{lin}, is written as the sum of a diffusive term in $w \equiv mv^2/2T_e(z=0)$ ($\propto$ energy), and a diffusive term in $\lambda \equiv v_\perp^2 B/v^2 B_0$ ($\propto$ magnetic moment)

$$C_w(f_e^t) = \frac{2\nu_c(z)}{\sqrt{w}} \frac{\partial}{\partial w} \left\{ [2\eta(w_z) - \overline{\eta}(w_z)]\ f_e^t + \frac{T_e(z)}{T_e(0)} \sqrt{w} \frac{\partial}{\partial w} \frac{\eta(w_z)}{\sqrt{w}} f_e^t \right\},$$

$$C_\lambda(f_e^t) = 2\nu_c(z)\ \frac{\overline{\eta}(w_z) + Z_{eff}}{w^{3/2}}\ \frac{\partial}{\partial \lambda} \left[< \frac{1-\lambda\beta}{\beta} >_b\ \lambda\ \frac{\partial f_e^t}{\partial \lambda} \right],$$

respectively, with $\beta(s) \equiv B(s)/B_0$. $\nu_c(z) = \pi\sqrt{2}e^4\ n_e(z) \log\Lambda / m^{1/2} T_e^{3/2}(0)$ is the (local) collision frequency, with $\log\Lambda$ the Coulomb logarithm, $w_z = mv^2/2T_e(z)$, and

$$\eta(w_z) = \mathrm{erf}(\sqrt{w_z}) - \frac{2}{\sqrt{\pi}} \sqrt{w_z} \exp(-w_z) \quad , \quad \overline{\eta}(w_z) = \mathrm{erf}(\sqrt{w_z}) - \frac{\eta(w_z)}{2w_z}.$$

Eq. (1) is solved with difference schemes in w and λ (implicit difference formalism in z). The boundary condition $f_e^t(\lambda = \lambda_{lc}) = 0$ is used, where the function $\lambda_{lc}(z) = 1/\beta_M(z)$, represents the width of the trapped particle region, for different vertical positions z, β_M being the maximum value of the normalized magnetic field strength β. The derivative of the distribution function at the loss cone boundary, $\partial f_e^t/\partial\lambda(\lambda = \lambda_{lc})$, measures the collisional loss of the trapped electrons, while the collisionless detrapping is determined by the rate of changing of the function $\lambda_{lc}(z)$.
This model is well suited to describe the effect on the "broadening" of the ECRH power deposition profile of the loss cone size (i.e., the impact of the different magnetic field configurations), the magnetic field strength ($v_{\nabla B} \propto 1/B$), and the electron density, which enters via the initial value problem as well as via the loss rate due to collisional detrapping (the collisional slowing-down is of minor importance).

Simulations of W7-AS scenarios.
In the computations for W7-AS scenarios, the loss-cone width λ_{lc} has been assumed constant. Fig. 3a shows the power, normalized to the initial absorbed power, which is deposited at outer radii, in dependence of various parameters. The results are relevant to the "standard" configuration ($\lambda_{lc} \approx 0.97$). The behavior can be simply explained by the dependence of the ratio between the drift time, τ_D, and the collision time, $\tau_c = 1/\nu_c$, with respect to the magnetic field strength and the plasma parameters

$$\tau_D/\tau_c \propto n_e B_0 / T_e^{5/2} w^{5/2}, \qquad (2)$$

having neglected the variations with z of temperature and density, and the weak dependence of the Coulomb logarithm on the electron density. The broadening of the power

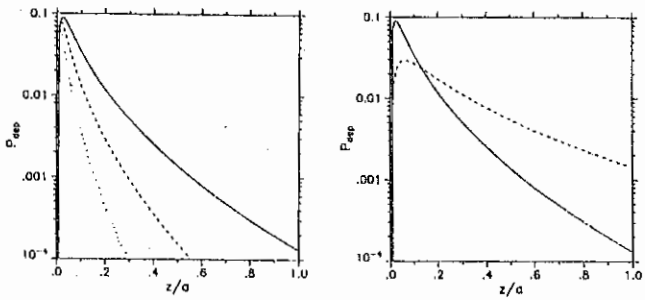

Fig. 3. *Fraction of the absorbed power deposited at the outer radii.* a: *"Standard" configuration. The solid line is the result for* $B_0 = 1.25$ *T, and* $n_e = 10^{19}$ m^{-3}, *the dashed line for* $B_0 = 2.5$ *T and* $n_e = 10^{19}$ m^{-3}, *and the dotted line for* $B_0 = 2.5$ *T and* $n_e = 2 \cdot 10^{19}$ m^{-3}. b: $B_0 = 1.25$ *T and* $n_e = 10^{19}$ m^{-3}. *The solid and the dashed lines are the results for the "standard" configuration and the "minimum B" scenario, respectively.*

deposition turns out to be larger in the case of low density and high temperature, and for decreasing magnetic field strength. Moreover, from Eq. (2) it results that the power deposition profile has a very strong dependence on the energy localization of the initial suprathermal trapped particles distribution function. The higher the velocity, where the EC resonance region is localized, the bigger is the effect of broadening of the power deposition profile.

In Fig. 3b the results for the power deposition in the case of the "standard" configuration ($\lambda_{lc} \approx 0.97$) and the "minimum B" launching ($\lambda_{lc} \approx 0.90$), are compared. Observe that for increasing loss cone width, the power is deposited on a broader radial range, and the particles could even be lost at the plasma boundary, before being thermalized. In the opposite limit of a narrow loss cone, the particles are detrapped by the pitch-angle scattering in a very short time, and in our model contribute to the power deposition only in a narrow region close to the axis. The theoretical predictions of this simplified model for the broadening of the power deposition profile, in particular its dependence on the plasma parameters and the magnetic field strength, are therefore consistent with the experimental findings.

In the case of decreasing $\lambda_{lc}(z)$, as it is the case, e.g., for the L2-stellarator, the detrapping effect of the pitch-angle scattering is weakened, so that the vertically drifting electrons remain trapped for a longer time [3]. As a consequence, less power is deposited than in the case of constant loss cone width. Depending on the rate of decreasing of λ_{lc} and on their energy, a significant fraction of the electrons may be lost at the plasma boundary. In this situation, it becomes important to take into account the presence of a radial electric field. Qualitatively, it can be observed that the effect of the electric potential is to deviate the trajectories of the particles inside the plasma, therefore increasing their confinement. Most of the absorbed power is released in any case in the central region of the plasma, with the deposition profile width being determined essentially by the initial loss cone size, and the velocity distribution.

References.

[1] N. Marushchenko *et al*, this conference
[2] M. Romé *et al.*, submitted for publication to Plasma Phys. Control. Fusion
[3] A.S. Sakharov and M.A. Tereshchenko, Plasma Phys. Rep. **21**, 93 (1995)

First ECRH Experiments in ASDEX-Upgrade

F. Leuterer, H. Brinkschulte, F. Monaco, M. Münich, A.G. Peeters,
G. Pereverzev, F. Ryter, W. Suttrop, ASDEX-Upgrade group,
Max Planck Institut für Plasmaphysik, 85740 Garching, Germany

G. Gantenbein, W. Kasparek, ECRH group, *Inst. f. Plasmaforschung Stuttgart*;
ECRH Group, *Inst. Appl. Physics, Nizhny Novgorod*;

Abstract

The variation of the global confinement time is found to depend on the radius of localized ECRH power deposition. Measurements of the risetime of electron temperature from ECE give broader profiles as the calculated ECRH deposition profiles. This is explained by diffusion within the time interval which is necessary for the measurement. Experiments with modulated ECRH for heat pulse propagation studies are described in a separate paper /1/.

1. The ECRH system

At ASDEX-Upgrade we are presently installing an ECRH system with a total power of 2 MW (resp. 2.8 MW) for a pulse length of 2 sec (resp. 1 sec), generated by 4 gyrotrons. The system is expected to be ready in spring 1997. The frequency is 140 GHz, the working mode is the second harmonic x-mode.

Two gyrotrons at a time are fed from one common power supply via one series modulator tube. This modulator is used for switching on and off the high voltage both for modulation (up to 1 kHz) and for safety reasons. Faster power modulation with a frequency up to 30 kHz is possible when the high voltage is reduced only by about 30%, which is sufficient to stop the oscillation in the gyrotron, but maintains the beam current.

The power is transmitted via four transmission lines partly quasioptical, and partly via a HE-11 waveguides /2/. The quasioptical part consists of beam correcting mirrors, polarization mirrors, elliptical and plane mirrors, and a mirror directional coupler within the beam matching box right after the gyrotron output. The waveguide part includes a mode coupling section to provide the necessary broad power density profile for transmission through the boron nitride torus window, and a mitre bend directional coupler just before the torus input. Both directional couplers give a clear signal free of interferences which can be calibrated for measuring the transmitted power. The launching is at the midplane from the low field side. Steerable mirrors (graphite with copper and gold coating) allow to vary the direction of the beam both poloidally (± 35°) and toroidally (± 25°) as necessary for localized on or off axis power deposition and current drive. The beam is focused such that without plasma the beam waist with w_o = 21.2 mm is located at half minor radius on the high field side.

In a first step we started experiments using another 140 GHz gyrotron with 0.5 MW / 0.5 sec of which 0.4 MW arrive at the torus input. The losses are due to power contained in higher order modes of the gyrotron output (estimated to 15%), which is not transmitted, and to ohmic losses in the mirrors and mitre bends (estimated to 7%). The adjustment of the mirror transmission line is without problems. However, the coupling of the quasioptical beam to the HE-11 mode in the waveguide turned out to be very sensitive to the quality of the Gaussian beam. Slight imperfections, like a rest of astigmatism, leads to excitation of additional waveguide modes, which, although containing only a small fraction of the power, can modify the power flow in the waveguides due to interferences and thus also the power density profile at the waveguide output and in the torus window. Improvement requires an accurate knowledge of the beam parameters.

2. ECRH heating in an ohmic plasma

Application of ECRH into ohmically heated plasmas leads to electron heating, and as a consequence to a drop in the loop voltage. However, this depends on the location of power deposition. In figs.1a and 1b we compare two shots where the power deposition was inside (r_{pol}<0.38), respectively outside (r_{pol}≈0.77), of the sawtooth inversion radius (r_{pol}≈0.4).

In the first case the loop voltage U_{loop} decreases very slowly, and at the end of the 0.5 sec pulse, the global confinement time τ_E, determined from the energy content W_{mhd} divided by the total power P_{tot}, reaches the same value as during the preceding ohmic phase. Thus τ_E seems not to be degraded with the increased total power input.

In the second case the loop voltage decreases faster, and the global confinement time at the end of the pulse reaches a constant value which is less than that in the ohmic phase, scaling as $\tau_{E,oh}/\tau_{E,ecrh} \approx (P_{tot}/P_{oh})^{-0.5}$, i.e. it shows the usual confinement degradation with power. The electron temperature increase in the central region (≈ 70 eV) is in this case less than in the first case (≈ 300 ev). The internal inductance and the sawtooth frequency remain constant, whereas they increase in the case of the central power deposition (l_i = 1.22 to 1.26). Such an increase of l_i indicates better confinement /3/.

We conclude that the influence of additional electron heating on confinement depends also on the localization of the power depositon.

3. Power deposition profile

The system is designed to achieve very localized power deposition. Calculations including diffraction effects /4/ show that we should get different power deposition profiles in the two cases of off axis heating as shown in fig. 2. In the case where the resonance magnetic field is off axis and the rf-beam arrives there perpendicular to the flux surface, the deposition profile is determined by the imaginary part of the wavevector. This leads to a very narrow profile with a full half width of ≈ 8 mm. On the other hand, if the ray is about tangent to the flux surface at the resonance, the deposition profile is determined mainly by the beam cross section, leading to a profile with full half width of ≈ 30 mm. In order to get an estimate of the experimental power deposition profile, we determine the rate of change of the electron temperature dT_e/dt at the switch on of the rf-power. Fig. 3 shows examples of ECE signals from different radii. The rise of T_e occurs instantaneously with the switch on, or delayed, depending on the radial position. In figs. 4 and 5 we plot dT_e/dt at the time where we observe an increase of T_e together with the delay Δt. We consider only those data points without measurable delay to represent a maximum estimated width of the deposition profile (dotted line). These profiles are, however, wider than the ones calculated for these particular shots, which are also shown in the figures as dashed lines. The difference in radial position between calculated and measured maximum may be due to calibration errors, and is not further discussed here. The measurements were taken at the low field side of the torus, while the power was deposited at the high field side (fig. 4) or in the upper part of the plasma (fig. 5) as shown in fig. 2.

The broader dT_e/dt-profiles can be understood by considering the one dimensional linearized heat diffusion equation. Assuming a Gaussian power deposition profile $\exp(-x^2/x_o^2)$, a step function for the time dependence and a constant electron heat diffusivity χ, we can calculate the temperature response as /5/:

$$\tilde{T}(x,t) = \text{const. } A \int_{(1+t/A)^{-1/2}}^{1} \exp(-(x/x_0)^2\zeta^2)/\zeta^2 d\zeta \qquad \text{equ.(1)}$$

Here the quantity $A = x_o^2/(4\chi)$ represents a characteristic time for diffusion. Numerical evaluation of equ.(1) shows that the heated zone widens by a factor of 2 within 10 characteristic

times. Taking for χ a value of 1 m^2/sec, we obtain A = 4 μsec in the case x_o = 4 mm, and A = 56 μsec for x_o = 15 mm. In ASDEX Upgrade it takes about 1 μsec for a 1 kV electron to run once around the torus. For deposition at r/a≈0.5 the poloidal circumference of the flux surface is ≈2.5 m and with a rf-beam diameter of 50 mm it takes about 50 μsec to heat all the flux surface. Furthermore, to determine dT_e/dt with sufficient reliability we need ≈500 μsec >> A. During this time considerable diffusion has occured. For the narrow profile in fig. 4 this corresponds to ≈120 A which leads, evaluating equ.(1), to a broadening by a factor of ≈5.5, and thus comes close to the measured width. Similarly, for the broader profile of fig. 5 the full flux surface is heated within one characteristic time, and the time for measurement corresponds to ≈10 A. In this case diffusion widens the heated zone to about two times the power deposition width, again similar to what we measure.
We conclude that the dT_e/dt-profiles cannot be simply taken as the power deposition profiles calculated from the wave absorption. Diffusion during the time which is necessary for the measurement of dT_e/dt must be taken into account.

References

/1/ Ryter F., this conference, paper OP3
/2/ Förster W., Proc. 9th. Workshop on ECE and ECRH, Borrego Springs, California, 1995, p. 565-573
/3/ Hoang G.T. et al., 19th EPS Conference on Controlled Fusion and Plasma Physics, Innsbruck 1992, Europhysics Conference Abstracts Vol. 16C, part 1, p.27
/4/ Peeters A.G., this conference
/5/ Tychonoff A.N., Samarski A.A., „Differetial Equations in mathematical Physics", VEB Dtsch. Verlag d. Wissenschaften, Berlin 1959

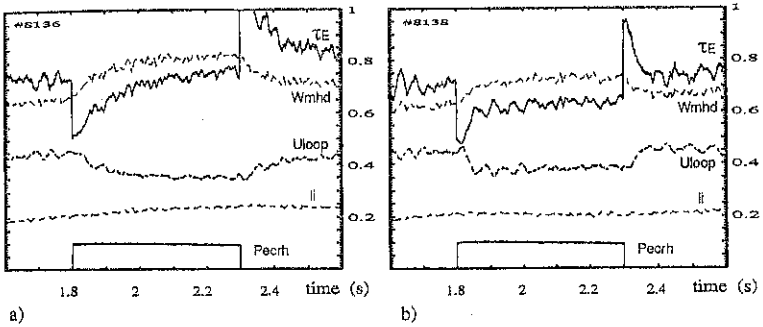

Fig. 1 Time traces of Pecrh, Uloop, Wmhd, li, τE for power deposition a) inside and b) far outside of the sawtooth inversion radius. Ip = 1 MA, ne = 4 10^19 m^-3, Bt = 2.5 T

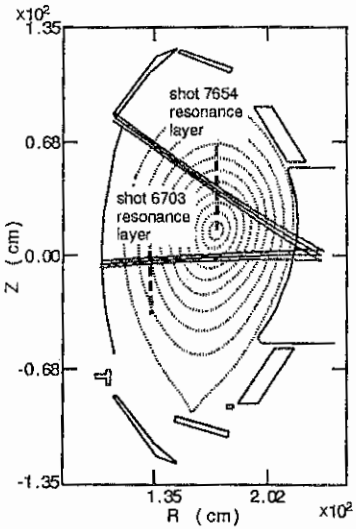

Fig. 2. Ray projections in the poloidal cross section for two cases of off-axis power deposition.

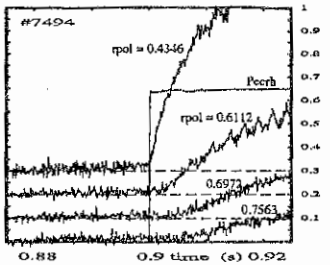

Fig.3 ECE time traces at different radii

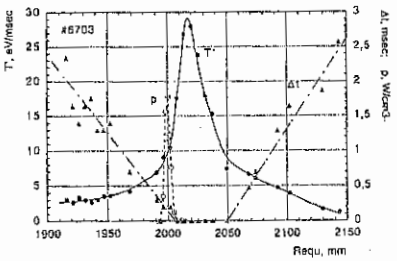

Fig.4 Calculated deposition profile p (dashed line), measured rate of temperature increase T' and measured delay time Δt; Bt = -2 T, phi = 0°

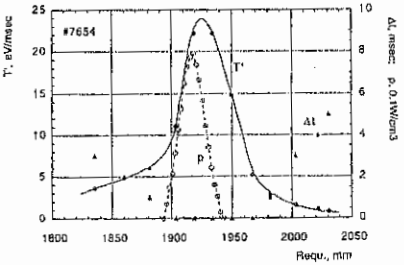

Fig.5 Calculated deposition profile p (dashed line), measured rate of temperature increase T', and measured delay time Δt; Bt = -2.5 T, phi = 30°

Simulations of Fast Particle Generation by LH Waves near the Grill

K. M. Rantamäki[1], T. J. H. Pättikangas[2], S. J. Karttunen[2],
X. Litaudon[3] and D. Moreau[3]
[1]Helsinki University of Technology, Association Euratom-TEKES,
FIN-02150 Espoo, Finland
[2]VTT Energy, Association Euratom–TEKES, P.O. Box 1604, FIN-02044 VTT, Finland
[3]Département de Recherches sur la Fusion Contrôlée, Association Euratom–CEA,
Centre d'Études de Cadarache, Saint Paul-les-Durance, France

1. Introduction

In recent lower hybrid (LH) current drive experiments, generation of carbon impurities in the grill region has been observed [1]. A possible explanation for the impurity production is the sputtering caused by the fast particles generated by the LH wave.

In this report, the absorption of LH waves and the generation of fast particles near the waveguide mouths is investigated with particle-in-cell (PIC) simulations. A model of a lower hybrid (LH) grill is included in the two-dimensional electrostatic PIC simulation code XPDP2 [2] and used for this purpose. The effect of extra spikes with high $n_\parallel$ in the LH spectrum on the production of fast electrons is studied in the edge plasma. The grill parameters in the simulation are chosen so that extra spikes with high values of $n_\parallel \simeq 6$ and $n_\parallel \simeq 18$ appear. The time evolution and acceleration of particles near the grill mouth is investigated by novel test particle diagnostics.

2. Particle-in-Cell Model for an LH Grill

The two-dimensional electrostatic particle-in-cell code XPDP2 [2] has been used for simulating the LH waves launched by an LH grill. The calculations are performed in a two-dimensional xy slab geometry; in velocity space the code is three-dimensional. The boundary conditions are periodic in the toroidal y direction and bounded in the radial x direction. The LH grill is located close to the $x = 0$ boundary, and the density is increasing linearly in the positive x direction. The grill mouth is along the periodic y axis, and the wave is launched from the antenna in the radial x direction. The magnetic field is in the y direction, and the electrostatic field lies in the xy plane. The length of the simulation box in the toroidal direction is $L_y = 8.4$ cm and in the radial direction $L_x = 2.3$ cm. Therefore, only small part of an LH grill can be simulated.

The waveguides of an LH grill are modelled as external charges oscillating on electrodes [3]. The external charge density describing the antenna is

$$\rho_{\mathrm{ext}} = \rho_{\mathrm{ext},0}\delta(x - x_{\mathrm{ext}}) \begin{cases} \sin(\omega_0 t - n\Delta\phi), & \text{for } n\ell < y - L_y + L_A < (n+1)\ell \\ 0, & \text{for } 0 < y < L_y - L_A \end{cases} \quad (1)$$

where $\rho_{\mathrm{ext},0}$ is the amplitude of the antenna, $n = 0, 1, 2, \ldots, N-1$, where N is the number of the waveguides, and $\Delta\phi$ is the phase difference between the adjacent waveguides. The width of the simulated grill section is L_A, and the width of a single waveguide is ℓ. In the

simulations presented below, the parameters $L_A = 4.2$ cm, $N = 12$ and $\Delta\phi = -\pi/2$ have been used.

In order to reduce noise typical of PIC codes, the signal oscillating with the grill frequency ω was picked from the wave potential by using so-called interferometer techniques [3]. The interferogram of the potential is here defined as

$$\phi_c(x, y, t) = \frac{2}{\tau_c} \int_{t-\tau_c}^{t} \sin(\omega\tau)\phi(x, y, \tau)\, d\tau. \tag{2}$$

In addition to noise, PIC codes have also another difficulty: there are only few particles in the tail of the Maxwellian distribution. This problem can be circumvented by using so-called test particles which contribute neither to the charge density nor to the wave potential. The test particles only move in the electrostatic field formed by the bulk electrons and ions.

In the simulations discussed below, the density at the plasma edge is $n_{e,\min} = 3 \times 10^{18}\mathrm{m}^{-3}$, and the linear density gradient is $\nabla n = 1.5 \times 10^{20}\mathrm{m}^{-4}$. At the high-density boundary of the plasma, a population of particles with an exponential density profile is added in order to avoid the reflection of the wave. The temperature is homogeneous with $T = 100$ eV and the magnetic field is $B_0 = 2.78$ T. The frequency of the antenna is 3.7 GHz. Mass ratio of $m_i/m_e = 100$ is assumed.

3. Fast Particle Generation

In Fig. 1, a contour plot is shown of the interferogram of the wave potential, Eq. (2). The section of a grill with twelve waveguides is located in the lower right corner at $x_{\mathrm{ext}} = 0.083$ cm. The propagation cone of the LH wave can be seen clearly, and it is bending slightly near the high density edge of the plasma. The test particles whose behaviour is analysed below are initially evenly distributed close to the grill, between $x = 0.6$ cm and $x = 0.8$ cm.

The Fourier sine transform of the grill, Eq. (1), is shown in Fig. 2. The parameters of the model grill have been chosen so that we obtain two spikes with high parallel refractive index in the spectrum: one at $n_\parallel = -5.8$ and another one at $n_\parallel = 18$. The spectrum changes rapidly as the wave penetrates into the plasma because of linear absorption and various non-linear mechanisms. Already in the region of the test particles, the spectrum has become much wider as can be seen in Fig. 3.

There are at least two reasons for the widening of the spectrum. First, in this case the power launched by the grill is $I = 76\ \mathrm{MW/m^2}$ which is rather high compared to typical values in present day experiments and may excite various non-linear processes. Second, the number of the modes in the spectrum is rather small because the mode spacing is determined by the length of the simulation box: $\Delta k_y = 2\pi/L_y$. Since the length of our simulation box is much smaller than the round trip around the torus, i.e., $L_y \ll 2\pi R$, the mode spacing is much larger than in a tokamak.

The spike of the LH spectrum at $n_\parallel \simeq 18$ has its phase velocity in the positive y direction, and it couples with the bulk electrons having velocities $v_y \simeq +1.5 \times 10^7$ m/s. The formation of a plateau in the velocity distribution of the bulk electrons can be seen clearly in Fig. 4. Fast electrons with velocities of $v_y \simeq 2.5 \times 10^7$ m/s are generated close to the grill mouth.

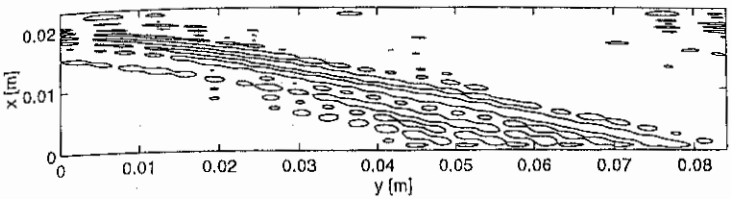

FIG. 1. Countour plot of the propagation cone obtained from the interferogram of the wave potential, Eq. (2).

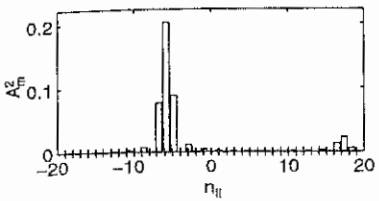

FIG. 2. The high $n_{||}$ spikes in the spectrum of the grill.

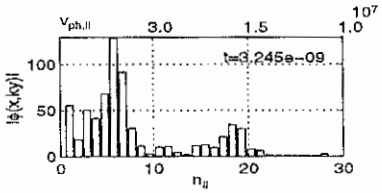

FIG. 3. The spectrum of the wave in the location of the test electrons at time t = 3.2 ns.

The modes generated by the high parallel refractive index spike at $n_{||} \simeq 6$ in the grill spectrum (see Fig. 2) have their phase velocities in the negative y direction. Their interaction with the plasma was investigated by following test electrons that were initially evenly distributed between $x = 0.6$ cm and $x = 0.8$ cm. Initially, their parallel velocities were evenly distributed around $v_y = -2 \times 10^7$ m/s^2, and the perpendicular velocities were thermal.

The time evolution of the test electrons in $y - v_y$ phase space is illustrated at two different times in Fig. 6. In Fig. 6(a), the initial loading of the test electrons can still be seen, as well as the early effect of the wave on them. The rapid acceleration of the particles in the parallel direction caused by the large-amplitude wave can be seen clearly in Fig. 6(b). The test electrons are accelerated even up to parallel velocities of $v_y \simeq 6^7$ m/s in a short time of 5 ns. Their total and parallel average energy increase by 30 % as can be seen in Fig. 5.

4. Summary and Discussion

Generation of fast electrons near the mouth of a lower hybrid grill has been investigated by particle-in-cell simulations when the LH spectrum contains spikes with very high values of $n_{||}$. A rapid generation of fast electrons is seen in the simulations when the LH wave is absorbed near the grill mouth.

The present model for the LH grill contains, however, several limitations, and therefore one should be cautious in interpreting the results. The noise inherent in PIC codes forces us to use high-amplitude waves in the simulations, which may give rise to some

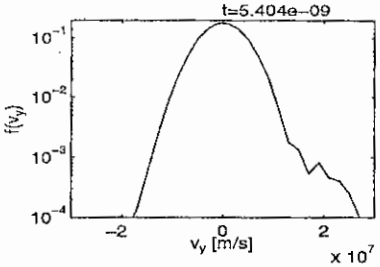

FIG. 4. The parallel velocity distribution of the bulk electrons at time $t = 5.4$ ns.

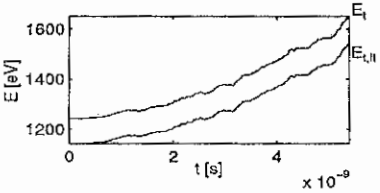

FIG. 5. The increase of the total (E_t) and parallel ($E_{t,\|}$) kinetic energy of the test electrons.

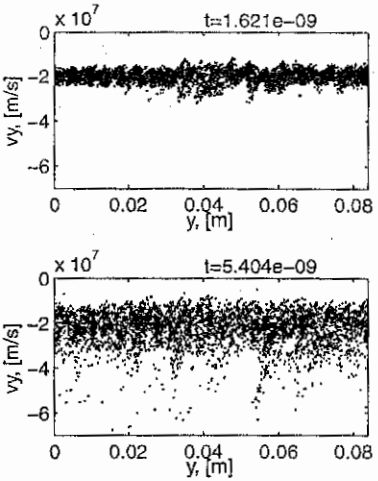

FIG. 6. $y - v_y$ phase space plots of the test electrons at time (a) $t = 1.6$ ns, and (b) $t = 5.4$ ns.

non-linear processes that are not present in real experiments. Another difficulty is the small size of the simulation region which makes the spacing of the Fourier modes launched by the grill larger than in real experiments. Therefore, furter refinements of the model are needed to resolve the connection between the fast particles produced by the LH waves and the experimentally observed impurity production near the grill.

Acknowledgements: We are grateful to the Plasma Theory and Simulation Group (Professor C. K. Birdsall, University of California, Berkeley) for providing us with their 2d3v PIC code XPDP2. In particular, we are grateful to David Cooperberg and Venkatesh Gopinath for helping us achieve initial runs with XPDP2.

[1] J. H. Harris, J. T. Hogan, M. Goniche, X. Litaudon, *et al.*, Europhys. Conf. Abstr., **19C**, Part IV (1995) 397.

[2] V. Vahedi, C. K. Birdsall, M. A. Lieberman, G. DiPeso and T. D. Rognlien, Phys. Fluids **B 5** (1993) 2719.

[3] Nakajima, N., Abe, H., Itatani, R., Phys. Fluids **25**, 2234, (1982).

A Study of ICRF Plasma Production for Tokamak Start-up and Wall Conditioning Purposes in TEXTOR-94

A.I.Lyssoivan[1], H.G.Esser[2], B.Giesen[2], R.Koch[1], A.Messiaen[1], G.Van Oost[1], J.Winter[2], J.A.Boedo[3], F.Durodié[1], M.Freisinger[2], P.Hüttemann[2], H.R.Koslowski[2], L.Könen[2], V.E.Moiseenko[4], O.Neubauer[2], J.Ongena[1], H.Reimer[2], J.Schwelberger[3], G.Telesca[2], D.Van Eester[1], M.Vervier[1], G.Waidmann[2]

[1] - Laboratoire de Physique des Plasmas - Laboratorium voor Plasmafysica, Association "Euratom-Belgian State", Ecole Royale Militaire - Koninklijke Militaire School, B-1000 Brussels, Belgium
[2] - Institut für Plasmaphysik, Forschungszentrum Jülich Gmbh, Association Euratom-KFA, D-52425 Jülich, Germany
[3] - University of California, San Diego, CA, USA
[4] - Institute for Plasma Physics, National Science Centre "Kharkov Institute of Physics and Technology", 310108 Kharkov, Ukraine

1. Introduction

Two applications of ICRF produced plasmas are studied on TEXTOR-94, with a view to reactor scale fusion devices, like ITER.

The first one is non-inductive preionisation and low loop voltage start-up. Such a scenario will be required for ITER, where the inductive electric field at start will be limited to values of E~0.3 V/m because of the limited current variations allowed by superconducting coils. To perform reliably tokamak start-up at low loop voltage, non-inductive preionisation, target plasma production and preheating are necessary.

The second one is wall conditioning. The presence of permanent magnetic fields produced by superconducting coils is not compatible with the application of standard glow discharge for cleaning and/or conditioning between discharges. A novel conditioning technique is therefore needed.

An alternative to plasma production by electron cyclotron heating is the use of radiofrequency power in the ion cyclotron range of frequencies (ICRF) developed earlier for stellarators [1] and proposed also for tokamaks [2]. Plasma production using ICRF power applied to conventional double-loop antennas has been successfully achieved in TEXTOR-94 [3-4] and TORE SUPRA [5].

In the present paper, we report the further study of ICRF plasma production in TEXTOR-94 and the first successful results on the applicability of RF plasma for tokamak start-up and wall conditioning purposes.

2. Experimental conditions

RF discharges in TEXTOR-94 (major radius 1.75 m, minor radius 0.46 m) have now been performed in $^4He_2$ instead of H_2 and D_2 [3]. High recycling gas was used to improve the reproducibility of plasma production in the presence of tokamak stray and/or correction poloidal fields in the case of start-up assisted by ICRF and to study the efficiency of ICRF wall cleaning. A mixture of helium and of a minority of reactive gas (silane) was also used to study the siliconisation efficiency in ICRF plasmas. RF power was applied using the existing ICRH system. This comprises two double-loop unshielded (A1) and shielded (A2) antennas [6]. Higher total power levels (P_{RF}≈350-700 kW at generators) have been coupled with antenna-plasma coupling efficiency $\eta=R_{pl}/(R_{pl}+R_v)\approx 60\%$. (Here R_{pl} is the antenna-plasma loading resistance, R_v is the antenna impedance in vacuum). The first experiments on ICRF assisted start-up and wall conditioning were performed at the normal magnetic field value B_T=2.24 T in the regime of standard 2nd harmonic ICRH scenario (f=32.5 MHz).

3. Characteristics of ICRF ($\omega \geq 2\omega_{CHe}$) plasmas produced in TEXTOR-94

3.1 Helium RF plasma production

The first experiments have been performed in pure toroidal magnetic field operation (U_{loop}=0). To find the range in B_T, where RF plasma production would be possible and

reliable, the first series of RF discharges was performed in multi-pulse regime, while B_T was ramped down in time (Fig.1a). Both antennas were excited simultaneously (A1 and A2 in π-phase) with time overlapped RF pulses. Helium plasma with central line averaged density $\bar{n}_{e0} \approx (1.2\text{-}1.7)\times10^{12}$ cm^{-3} was easily produced in a wide range of B_T (0.36 ÷ 2.24 T) at a gas pressure of 1.5×10^{-3} mbar starting with ≥50 kW of RF generator power. The last two pulses of RF discharge were performed with the unshielded antenna only. The figure demonstrates clearly the potential of ICRF plasma production for a large variety of He cyclotron harmonics ($2\omega_{CHe} \le \omega \le 12\omega_{CHe}$) without retuning the RF generator frequency. The lower and upper limits of B_T operation were not found so far. The typical central line averaged density ($\bar{n}_{e0} \approx 5\times10^{10} \div 3\times10^{12}$ cm^{-3}) was proportional to base gas pressure and RF power (Fig.2). The electron temperature (deduced from spectroscopic and electric probe measurements) was in the range 10 ÷ 40 eV, increasing in the low gas pressure case. The line averaged density profile, deduced from signals of the 9-channel HCN-interferometer, was broadened to the low field side (antenna locations) and peaked mainly in the centre (Fig.3).

A bright vertical radiating layer in the vicinity of the 2nd harmonic He cyclotron resonance was observed by a CCD camera looking tangentially at the plasma in the antenna A2 area (Fig.4). With B_T ramping down, the vertical column following the 2nd cyclotron harmonic layer was clearly seen to shift toward the inboard side of the tokamak vessel. The brightness of the layer was proportional to gas pressure. In this frequency range, the slow wave is strongly evanescent and the power is expected to be mostly collisionally dissipated in the ion Bernstein wave (IBW). Coupling with IBW may take place directly at the antenna or at the 2nd cyclotron harmonic layer, where the evanescent FW can convert to IBW. The observed phenomena may be attributed to increased energy dissipation near the 2nd cyclotron harmonic layer.

The presence of poloidal stray fields (even being compensated) strongly influenced antenna coupling and RF plasma stability. Their presence resulted in a lower density of the plasma produced during the ICRF preionisation phase (before applying loop voltage, t<0) as compared with the case of pure toroidal magnetic field operation. The typical density of RF target plasma was $\bar{n}_{e0} \approx (0.2\text{ - }0.8)\times10^{12}$ cm^{-3}, $P_{RF} \le 500$ kW at generators and the pressure $p_0 = (2\text{ - }5)\times10^{-5}$ mbar.

3.2 Multi-ion species RF plasma production

Two different types of behaviour of RF discharges in He - silane gas mixtures have been observed depending on the kind of silane and its concentration. In the case of normal silane (SiH_4), ICRF discharge was only possible with small (≤10 %) concentrations of reactive gas. The central line averaged electron density did not exceed the value of 10^{12} cm^{-3} because of strong disturbance of antenna-plasma coupling and high RF power reflection with SiH_4 concentration rise.

Using deuterated silane (SiD_4), ICRF discharges in gas mixture with higher concentration of silane (50%) have been realised for the first time (Fig.1b). RF multi-ion species plasma with density $n_{e0} \approx (1\div2)\times10^{12}$ cm^{-3} was reliably produced in a wide range of B_T (1.0 ÷ 2.25 T, $2\omega_{CHe} \le \omega \le 4\omega_{CHe}$) . No limitation in SiD_4 concentration in He was observed so far.

4. First results on ICRF assisted tokamak start-up (B_T=2.24 T, $U_{loop}\neq0$)

ICRF assisted start-up at the conventional loop voltage operation (~12 V) gives a significant reduction in the volt-second consumption: ~10% in the plasma and current start-up phase and up to 20% during plasma build-up and current ramp-up. ICRF preionisation also leads to a reduction of the radiated power by ~10% during current ramp-up and flat-top phases.

Successful ICRF assisted low voltage start-up has been demonstrated for the first time on TEXTOR. Plasma current ramping up to 400 kA during ~ 0.25 s was achieved at $U_{loop} \approx 5$V. Two features can be noticed: the presence of target ICRF plasma ($\bar{n}_{e0} \approx 0.8\times10^{12}$ cm^{-3}, t ≈ -0.02 s) before the plasma current start and of a low current plateau (Δt=0.15 s) before the current ramping. Low voltage start-up was only possible with assistance of ICRF power. The vertical stray field (compensated) was of the order of $|B_V| \approx$15-40 G and the gas pressure (2 - 5)$\times10^{-5}$ mbar.

5. First testing of ICRF wall conditioning (B_T=2.24 T, U_{loop}=0)

5.1 Wall cleaning by ICRF discharge

A progressive reduction of residual gas pressure was observed when successive RF discharges were performed after intentional initial loading of the first wall with an H-glow. Measurements with the quadrupole mass spectrometer confirmed that more than 90% of the pressure rise after each RF discharge was due to hydrogen. The total amount of gas desorbed during the five RF discharges is estimated to be about 6.5×10^{20} molecules. This corresponds to ~1 monolayer of the hole inner wall area of about 35 m^2 [4].

5.2 ICRF assisted thin film deposition

A good balance between the amount of Si disappearing from the gas phase during ICRF discharges in a gas mixture and that measured by post mortem surface analysis of wall samples was found. In the case of <10% SiH_4 concentration in He, about 1.2×10^{15} Si atoms/cm^2 were found in the wall sample inserted near the shielded antenna (A2) and ~7×10^{14} Si atoms/cm^2 in the sample placed mid-way between the antennas. For a total exposure time ~17 s, the deposition rate of the order of 1 monolayer/min was achieved which is comparable to the Si deposition efficiency in a standard DC glow discharge [4].

6. Conclusions

- He-plasma with density up to $\bar{n}_{e0} \approx 3 \times 10^{12}$ cm^{-3} and temperature $T_e \approx 10 \div 40$ eV is reliably produced in a wide range of $B_T \approx 0.36$ - 2.24 T without retuning the RF generator frequencies (f=32.5 MHz).
- Multi-ion species RF plasma can be produced in a gas mixture of He with reactive gases of different concentration: deuterated silane (SiD_4) - up to 50% (upper limit not reached so far); normal silane (SiH_4) - <10% (higher concentration disturbs antenna coupling).
- A bright vertical radiating layer is observed at the 2nd He cyclotron harmonic moving across the plasma when B_T changes.
- The presence of tokamak stray fields causes deleterious effects on antenna coupling and RF plasma stability.
- 10-20% reduction in the volt-second consumption in normal start-up operation ($U_{loop} \approx 12$V) has been achieved with assistance of ICRF power.
- ICRF assisted low voltage ($U_{loop} \approx 5$ V) current start-up has succeeded for the first time in a tokamak. Further experiments needed to improve the reproducibility and avoid delayed current ramping.
- A new ICRF conditioning technique has been successfully tested for the first time in a tokamak. Further study of the potential of ICRF discharges for purposes of gas desorption from the walls and thin film deposition is still needed.

Acknowledgements

We thank everyone in the TEXTOR-94 Team and the ICRF technical staff who have contributed to the present results.

References

[1] Shvets O.M., et al., *Proc. 4th Int. Symp. on Heating in Toroidal Plasmas, Roma 1984*, Vol.1, 513.
[2] Lyssoivan A.I., et al., *Nucl. Fusion* **32** (1992) 1361.
[3] Lyssoivan A.I., et al., *Proc. 22nd EPS Conf. on CFPP, Bournemouth 1995*, Vol.19C, Part III, 341.
[4] Esser H.G., et al., *12th Int. Conf. on PSI, St.Raphael 1996*, to be published in Journal Nucl.Mater.
[5] Gauthier E., et al., *12th Int. Conf. on PSI, St.Raphael 1996*, to be published in Journal Nucl.Mater.
[6] Van Nieuwenhove R, et al, *Nucl.Fusion* **32(11)** 1913 (1992).

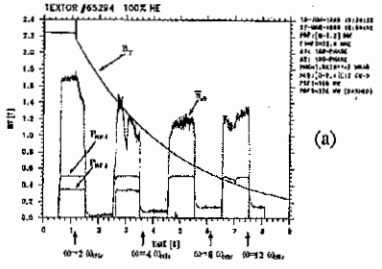

Fig.1 ICRF plasma production vs. toroidal magnetic field.

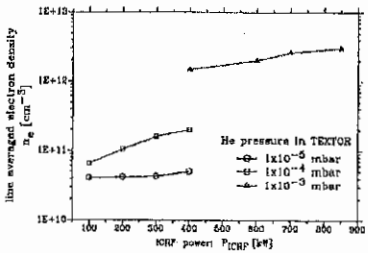

Fig.2 He-plasma density as function of RF power and gas pressure.

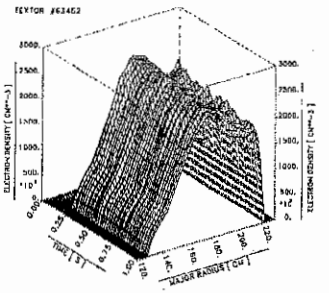

Fig.3 The line averaged density profile

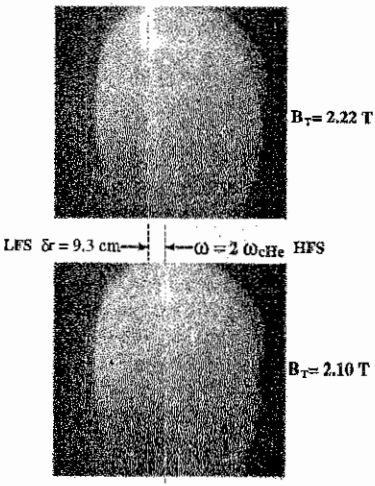

Fig.4 A bright vertical radiating layer at the 2nd harmonic He cyclotron resonance.

ELECTRON AND ION TEMPERATURE RESPONSE TO LOCALIZED ECRH AT 140 GHZ, 0.5 MW, FUNDAMENTAL RESONANCE, IN THE FTU TOKAMAK

S.Cirant, A.Bruschi, G.Granucci, S.Nowak, A.Simonetto, C.Sozzi, *Istituto di Fisica del Plasma, EURATOM/ENEA/CNR Association, Milano, ITALY*
G.Bracco, P.Buratti, **O.Tudisco**, V.Zanza, *Centro Ricerche Energia, Associazione EURATOM/ENEA sulla Fusione, CRE Frascati, C.P.65, 00044 Frascati, ITALY*

1. Introduction

The fast ON/OFF switching capability of the gyrotron tubes, and the high gain of the antenna launching the waves in the millimeter wavelength range, both allow precise localization in time and space of the electron heating in ECRH experiments in high magnetic field confinement devices. On the FTU tokamak [1], plasma heating at 140 GHz, 400 kW, was performed at 15 ms pulse length, preceding a full-scale ECRH experiment at 1.6 MW, 0.5 s.

Most attention was paid to the plasma thermal response, that was analyzed to infer the effective power deposition profile [2], and accurately compared with transport calculations in order to achieve further information on FTU thermal transport. Due to the limited pulse length, which is short compared to the confinement time of the ohmic plasma (in the range 28÷50 ms), the analysis is limited to the transient phase following an abrupt change of heating conditions. In the case of central heating of saw-teeth free discharges, it was observed [3] that the thermal response during ECRH can be described with a value of the electron heat diffusivity χ_e~0.4 m^2/s in the central region of the plasma. The present analysis indicates that this value is compatible with the value found during the ohmic phase, taking into account the large error bar due to the important role of the radiation in the plasma center. This result can be stressed as the ECRH produces a large increase of the local power density (20 times) and of the electron temperature gradient (10 times). The analysis is now also extended to off-axis ECW absorption, which provides both inward and outward thermal power flows, and to saw-toothing discharges.

The trasport calculations have been performed by means of a general transport code that solves the plasma energy diffusion equations averaged over the magnetic surfaces provided by the equilibrium reconstruction, based on the magnetic measurements.

2. Electron thermal energy increase

The discontinuity of the time derivative of the electron energy density after ECRH switching ON (or OFF) allows the estimate of the effective local value of the additional heating power density profile [2] (Fig.1,2), needed by the transport code used for modelling the electron and ion temperature response. By considering both ON and OFF transitions, the evolution of the power deposition profile can be monitored, Fig. 1.

At times later in the ECRH pulse, the experimental data have been compared with the predictions of the code. The χ_e profile obtained in the ohmic phase was used outside the central region, where it is undetermined, due to sawtooth or radiation effects. The Te(r,t) is well reproduced, both in the case of central and off-axis ECRH, Fig.3 and Fig.4 respectively, assuming a central χ_e value ≤ 0.5 m^2/s.

The same considerations hold for ECRH on discharges with saw-teeth, Fig.5.

3. Ion power balance analysis during ECRH

During on-axis ECRH a measurable increase of the neutron yield from D-D reactions is observed [4] at peak electron densities above 10^{20} m^{-3}, corresponding to an ion temperature increase up to 0.2 keV. The absolute increase of the neutron yield is reproduced by the simulation code using an anomaly enhancement factor of the Chang-Hinton ion thermal diffusivity in the range 1 to 2, Fig. 6 and Fig. 7, similarly to what has been previously obtained in the analysis of the ohmic plasma in stationary conditions [5]. The analysis of the time behaviour of the neutron yield in the transient phase during the ECRH permits in principle to discriminate between an anomaly factor applied to the ion thermal diffusivity or to the electron-ion energy transfer Q_{ei}, as shown in Fig. 7 where the time behaviours corresponding to the two different assumptions are reported. Even if in the case of Fig. 7 a better description is obtained by a decrease of the Q_{ei} term, no general conclusion can be drawn for the moment, due to the limited number of examined cases, to the uncertainty of the value of the central electron density and to the assumption of a constant Z_{eff} with time. However, a clear discrimination between χ_i and Q_{ei} effects will be possible when experiments with much longer pulse lengths and more power will be available.

4. Conclusions

The electron temperature in the transient phase of a preliminary series of ECRH shots on FTU can be described by a diffusive transport model, with χ_e in the range of values typical for ohmic discharges.

The enhanced neutron yield during ECRH at high density is consistent with the ion temperature increase obtained by the code under the assumption $\chi_i = (1\div2)\ \chi_{i,neoclassical}$.

1) S.Cirant et al.,Proc. 9th Joint Workshop on Electron Ciclotron Emission and Electron Cyclotron Resonance Heating, John Lohr Editor, 1995
2) G.Granucci et al., Proc. 22nd EPS Conference on Controlled Fusion and Plasma Physics, B.E.Keen, P.E.Stott, J.Winter Editors, 1995, v.19C, part I, p.361
3) G.Bracco et al., Proc. 22nd EPS Conference on Controlled Fusion and Plasma Physics, B.E.Keen, P.E.Stott, J.Winter Editors, 1995, v.19C, part III, p.021
4) S.Cirant et al., Proc. of 15th International Conference on Plasma Physic and Controlled Nuclear Fusion Research, Seville (Spain), Oct. 1994, IAEA/CN/60/G-P-6
5) F. Alladio et al., Proc. of 15th International Conference on Plasma Physic and Controlled Nuclear Fusion Research, Seville (Spain), Oct. 1994, IAEA/CN/60/A2/4-P-3

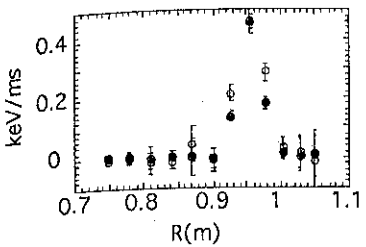

Fig.1 - dT_e/dt discontinuity at ON (closed dots) and OFF (open dots) transitions for a short on-axis ECRH pulse (2 ms).

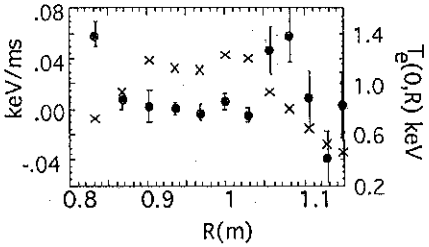

Fig.2 - dT_e/dt discontinuity (dots) and initial T_e profile for an ECRH pulse located at half minor radius..

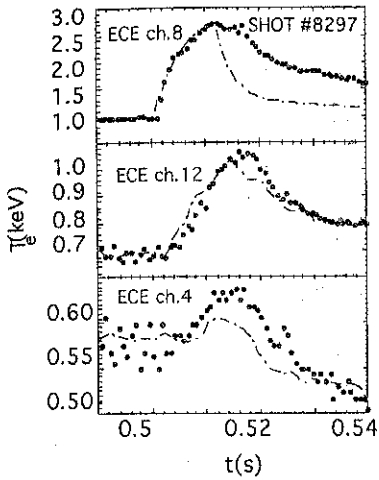

Fig.3 - Te(t) evolution at different radii in case of central ECRH (ECE ch.8 is on the magnetic axis, ch.12 and ch.4 are at 9.9 cm and 12.1 cm respectively). Experimental data are shown for comparison (dots).

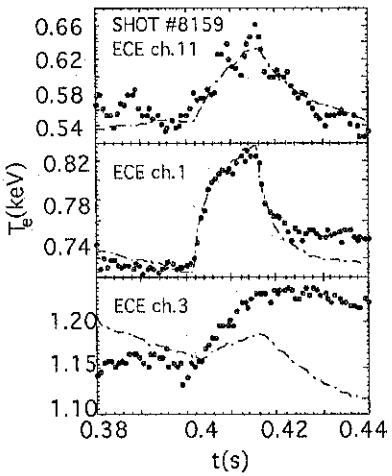

Fig.4 - Te(t) evolution at different radii in case of off-axis ECRH (ECE ch.1 is close to the resonance at 13.4 cm , ch.11 and ch.3 are at 16.2 c m and 6.3 cm respectively). Prediction (dashed line) and data (dots) are compared.

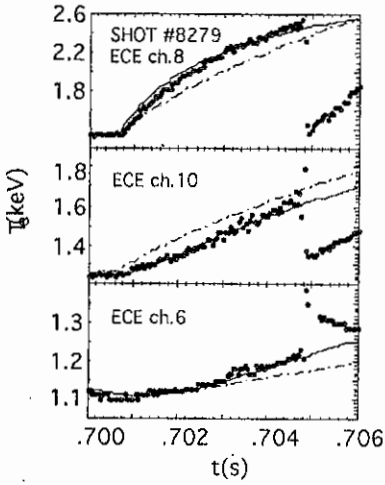

Fig.5 - Te(t) .evolution .at .different .radii in case of central ECRH (ECE ch.8 is 0.5 cm from the magnetic axis, ch.10 and ch.3 are at 4.3 c m and 6.5 cm respectively) on a saw-toothing discharge. ch.6 is outside the inversion radius. The continuous and dashed lines corespond to $\chi_{e,0}$=0.4 m^2/s and 0.1 m^2/s respectively

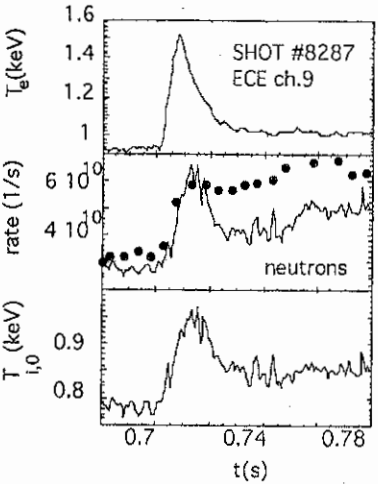

Fig.6 - Measured electron temperature, predicted neutron emission rate and ion temperature. Computation is made by assuming $\chi_i=\chi_{i,neoclassical}$, and $Q_{e,i}=Q_{e,i\text{-}collisional}$. Emission rate predictions are compared with experimental data (dots). Central electron density is 1.7 10^{20} m^{-3}.

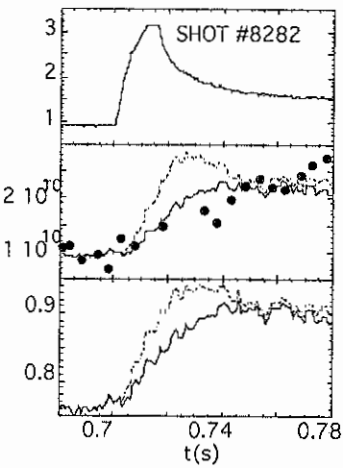

Fig.7 - Measured electron temperature, predicted neutron emission rate (experimental data in dots) and ion temperature. In this case: $\chi_i=2\chi_{i,neoclassical}$ (dashes) or $Q_{e,i}=0.5\ Q_{e,i\text{-}collisional}$ (continuous).. Central electron density is 0.95 10^{20} m^{-3}.

Numerical simulation of the coupling properties of advanced Lower Hybrid waves launchers

S. Berio, Ph. Bibet

Département de Recherche sur la Fusion Contrôlée
Association EURATOM-CEA
13108 St Paul lez Durance (France)

1. Introduction

Lower hybrid wave is an efficient tool to drive one part of the current in next grade tokamak [1] in such a way to improve confinement by profile control. Due to the size of next machines, the amount of power will be between 50 and 100 MW. To simplify antenna design, the study of the coupling to the slow wave from oversized waveguides arrays such as active/passive waveguide array [2] must be done. Especially since many modes can propagate, it is important to know the cross coupling coefficient between propagating modes in the case mainly of poloidal electron density inhomogeneities.

On different present machines, coupling measurements have been done and compared to theoretical values using SWAN code [3]. On Tokamak de Varennes [4], to reach a good agreement between the two, it has been necessary to suppose a vacuum gap at the plasma antenna interface. This can be explained by protruding limiters, by ponderomotive force, but it can also be due to the finite size of the rectangular waveguide which is not taken into account in SWAN. This leads necessarily to coupling coefficient change since the characteristic impedance of the modes are different [5].

On existing machine also, antennae are made of many poloidal rows of toroidal rectangular waveguide arrays. That leads necessarily to the existence of a poloidal wave number k_θ or index n_θ. This could be taken into account as input in a ray tracing code.

All these reasons has led to the necessity to write another code called ALOHA (Advanced LOwer Hybrid Antenna) to compute the coupling to the slow wave from oversized waveguides arrays.

2. Theory

The theory used stems from the one first developed by M. Brambilla [6]. Here, the finite size of the waveguide has been considered. To satisfy at the plasma antenna interface the condition of electric field parallel to the magnetic field (coupling to the slow wave), TE_{mn} and TM_{mn} modes are taken into account since the small size of the waveguide is considered to be less than half wavelength. Taking as coordinate z the toroidal axis, y the poloidal one and x the radial one, the total electromagnetic field in the antenna at the plasma antenna interface is given by the relation :

$$E_{zi}(x,y,z) = \sum_{i=1}^{N} \zeta_i(y)\,\theta_i(z)\,E_{zi}(x,y,z)$$

and :

$$H_{yi}(x,y,z) = \sum_{i=1}^{N} \zeta_i(y)\,\theta_i(z)\,H_{yi}(x,y,z)$$

where $\zeta_i(y)$ and $\theta_i(z)$ are equal to 1 on the waveguide i, and to 0 everywhere else. N is the number of waveguide.

$$E_{zi}(x,y,z) = \sum_{h,e}\sum_{\nu=0}^{\infty}\left(A_{i\nu}^{h,e}\,e^{-jk_{gi\nu}^{h,e}x} + B_{i\nu}^{h,e}\,e^{+jk_{gi\nu}^{h,e}x}\right) e_{zi\nu}^{h,e}(y,z)\,\sqrt{Z_{i\nu}^{h,e}}$$

$$H_{yi}(x,y,z) = \sum_{h,e}\sum_{\nu=0}^{\infty}\left(A_{i\nu}^{h,e}\,e^{-jk_{gi\nu}^{h,e}x} - B_{i\nu}^{h,e}\,e^{+jk_{gi\nu}^{h,e}x}\right) e_{yi\nu}^{h,e}(y,z)\,\sqrt{Y_{i\nu}^{h,e}}$$

E_{zi} and H_{yi} are the electric and magnetic field in the waveguide i :
with :

- $A_{i\nu}^{h,e}$ and $B_{i\nu}^{h,e}$ the complex amplitude of forward and backward wave of TE (h index) or TM (e index) mode with index $\nu = (m, n)$.
- $e_{zi\nu}^{h,e}$ and $h_{zi\nu}^{h,e}$ eigenfunction.
- $Z_{i\nu}^{h,e}$ and $Y_{i\nu}^{h,e}$ characteristic impedance and admittance.
- $k_{gi\nu}^{h,e}$ the waveguide wave number.

The electromagnetic fields inside the plasma are given by the Fourier integral :

$$E(x,y,z) = \frac{1}{(2\pi)^2}\int_{-\infty}^{\infty}\int \hat{E}(k_y,k_z)\,e^{j(k_x x + k_y y + k_z z)}\,dk_y\,dk_z$$

$$H(x,y,z) = \frac{1}{(2\pi)^2}\int_{-\infty}^{\infty}\int \hat{H}(k_y,k_z)\,e^{j(k_x x + k_y y + k_z z)}\,dk_y\,dk_z$$

The magnetic and electric field inside the plasma are linked by the plasma admittance tensor $\overline{\overline{Y}}_p$ [7] :

$$\hat{H}(k_y,k_z) = \overline{\overline{Y}}_p(k_y,k_z)\,\hat{E}(k_y,k_z)$$

As a first step only the coupling to the slow wave has been considered, the previous relation is simplified as :

$$\hat{H}_y(k_y, k_z) = -Y_0\, Y_s(k_z)\, \hat{E}(k_y, k_z)$$

where the plasma admittance is depending on the electron density n_e at the mouth, on the cutoff electron density n_{ec} and the electron density gradient ∇n_e

$$Y_s(k_z) = -\frac{A_i'(\eta_0)}{A_i(\eta_0)}\left(\frac{X_0}{\Delta_0}\right)^{1/3}\frac{e^{j\pi/6}}{\left(n_z^2-1\right)^{2/3}}$$

with : $n_z = \dfrac{k_z}{k_0}$

and :

$$\eta_0 = \eta_0(n_z) = e^{-j\pi/3}\left(n_z^2-1\right)^{1/3}\left(X_0-1\right)\left(\frac{\Delta_0}{X_0}\right)^{2/3}$$

$$X_0 = \frac{n_e}{n_{ec}} \quad \text{and} \quad \Delta_0 = \frac{k_0\, n_e}{\nabla n_e}$$

k_0 is the vacuum wave number and A_i, is Airy function, A_i' its derivative and Y_0 the vacuum admittance.

The continuity of the tangential component of the magnetic and electric fields using the orthonormality properties of eigenfunction leads to :

$$\sum_{t=h,e}\sqrt{Y_{iv}^t}\left(A_{iv}^t - B_{iv}^t\right)\delta_{ii'}\,\delta_{vv'} = \sum_{i=1}^{N}\sum_{t=e,h}\sum_{v=0}^{\infty} Y_{ii'vv'}^{tt'}\sqrt{Z_{iv}^t}\left(A_{iv}^t + B_{iv}^t\right)$$

where $Y_{ii'vv'}^{tt'}$ is the coupling coefficient between waveguide i and i' with mode of index v and v' and type h,e.

$$Y_{ii'vv'}^{tt'} = -\frac{1}{(2\pi)^2}\int_{-\infty}^{\infty}\int Y_0 Y_s(k_z)\, G_{iv}^t\, G_{i'v'}^{t'}{}^{*}\, dk_y\, dk_z$$

$$G_{iv}^t = f_{iv}^t\,\frac{m\pi/a}{k_y^2-(m\pi/a)^2}\left[1-(-1)^m e^{-jk_y a}\right]\frac{jk_z}{k_z^2-(n\pi/b_i)^2}\,e^{-jk_z z_i}\left[1-(-1)^n e^{-jk_z b_i}\right]$$

with : $f_{iv}^t\sqrt{\left(m^2\dfrac{b_i}{a}+n^2\dfrac{a}{b_i}\right)} = \pm\sqrt{\varepsilon_m\varepsilon_n}\,\dfrac{m}{a}$

if : $t = h$ and : $\pm\dfrac{2n}{b_i}$ if : $t = e$

$\varepsilon_p = 1$ if $m = 0,2$ if not

$v = (m,n)$

- sign - is for index i, and + is for index i'.
- b_i and z_i are the size and the position of waveguide i in the z direction.

The integral is done using a contour integral method. From these relations the plasma scattering matrix is deduced.

The radiated spectrum is given by the Poynting vector.

3. Numerical results

3.1. Comparison to SWAN code

First the plasma scattering matrix S given by the two codes has been compared on some cases. The main difference depends on the plasma parameters and is a factor 1.5 on the amplitude of the diagonal terms at 3.7 GHz for $n_e = 10^{12}$ cm^{-3} and $\nabla n_e = 10^{12}$ cm^{-4}. For the other terms the change is generally less than 16 %. The phase of the different terms are in agreement for the 2 codes. The difference leads to a variation of reflection coefficient for a given plasma parameters. An example is given on Fig. 1. The size of the waveguide and the mode index has also an influence on the S parameters as expected.

The radiated spectrum for one case is given by the 2 codes on Fig. 2 with no significant change. The computation of the radiated power seems to smooth the previous difference.

3.2. Radiating spectrum of antennae with multilayer of toroidal waveguide array

ALOHA code allows to consider many poloidal rows of toroidal waveguide array with different condition of feeding of the different arrays and also with different plasma parameters for each layers. For example Fig. 3 shows the radiated spectrum of an antenna made of 3 poloidal arrays fed differently : (1, $\pi/2$) for the first, (1, π) for the second and (1, $\pi/2$) for the third. The spectrum is plotted versus $n_{//}$ (n_z) and n_θ (n_y). The value at which the peaks occurs in the n_θ direction are depending on $m\pi/k_0$ (a+e) with a the poloidal size of waveguide and e the thickness between layers.

3.3. Influence of poloidal inhomogeneities on coupling between different propagating modes.

When the plasma electron density is homogeneous in the poloidal direction, the cross coupling between odd and even modes in poloidally oversized waveguide is null. In other case problems occur. To simulate the effect of these inhomogeneities in front of an oversized waveguide, the poloidal density variation which has been taken as : $n_e(y) = n_{e0} + \nabla_0 n_e\, y$ has been discretized in m steps for each propagating TE_{m0} mode with a density for each step : $n_e(j) = n_{e0} + \nabla_\theta n_e\, ja/(2\,m)$ ($j \in [1,m]$). The waveguide is divided in fictious in m waveguides with different plasma parameters for each one.

First results of computation done for one oversized waveguide of size 230 mm x 13.2 mm at a frequency of 3.7 GHz gives for a plasma with $n_{e0} = 4\,10^{11}$ cm^{-3} and $\nabla_\perp n_e = 10^{12}$ cm^{-4} $\nabla_\theta n_e = 2.6\ 10^{10}$ cm^{-4} cross coupling which are less than 5 %. It is observed in this

case that the cross coupling between odd and even modes is no more null.

4. New results on active/passive waveguide antenna

This work is a continuation of the study begun in [2] using SWAN code. Here multijunctions made of 2 waveguides with a 270 degrees phase shift are used to feed the active passive waveguide array. In this computation made at 5 GHz, 7 such bijunctions are considered. The toroidal periodicity is 11.25 mm with wall of 2 mm thickness, the depth of the passive waveguide is 15 mm. The bijunction are supposed to be fed independently. The variation of feeding phase from -180 to 180 degrees allows to realize symmetric spectrum for heating purpose and asymmetric one for current drive with a good directivity on a large scale of electron density (Fig. 4). The coupling is good and the power reflection stays less than 5 % even near the cutoff density (Fig. 5).

The maximum amplitude of the electric field is generally less than 1.8 times the incident electric field one (Fig. 6). To compare with Tore Supra multijunction, when the input reflection coefficient at the input is 5 % the maximum electric field amplitude is 2.2 times the incident one. That means that in spite of a less active radiating surface (around 2 times less) the injected power by active passive array can reach 70 to 80 % of the classical antenna using multijunctions.

5. Conclusion

A new code (called ALOHA) has been written and gives first results. It takes into account finite size and all propagating and some evanescent modes. At a first step only the coupling to the slow wave is considered. The whole admittance tensor is to be considered in the future.

It allows also to study many poloidal waveguides array with different feeding conditions and plasma parameters. Leading to the knowledge of the 2D radiated spectrum in $n_{//}$ and n_θ which can be an input for ray tracing code.

First studies of coupling between propagating modes due to poloidal inhomogeneities in front of an oversized waveguide shows that this problem doesn't seems to be too important. Further studies will be done to confirm.

New computations have been done on active passive array fed by multijunction showing very high flexibility and good coupling properties with an increase of the electric field which is less than in all active waveguide array.

Acknowledgment : We would like to thank D. Moreau for very fruitful discussions.

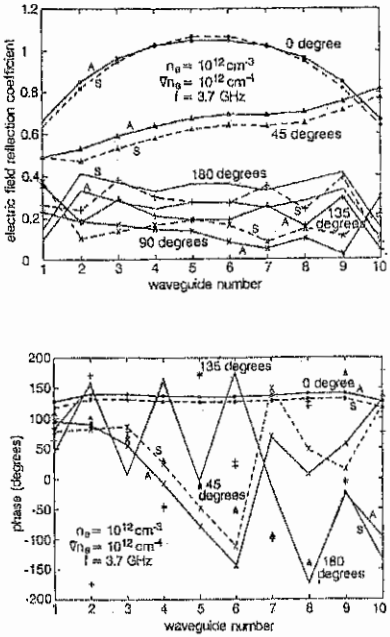

Fig. 1 : Comparison of the reflection coefficient results from SWAN and ALOHA code at the input of an array of 10 independently fed waveguides with plasma parameters $n_e = 10^{12}$ cm^{-3}, $\nabla n_e = 10^{12}$ cm^{-4}

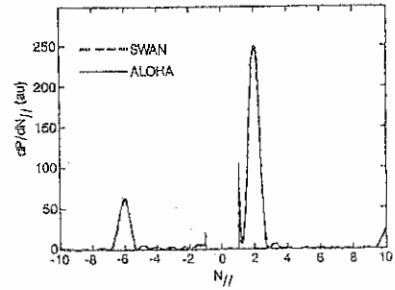

Fig. 2 : Comparison of the radiated $N_{//}$ spectrum given by SWAN and ALOHA code

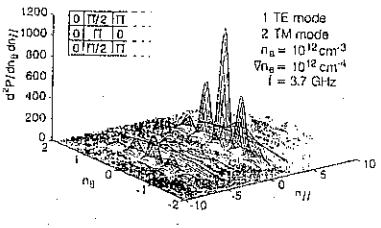

Fig. 3 : Radiated spectrum of 3 poloidal arrays of 10 waveguides of size : a = 72 mm, b = 8 mm, e = 2 mm, at a frequency f = 3.7 GHz fed with a 90 degrees phase shift for the first row, 180 degrees for the second, 90 degrees for the third with plasma parameters $n_e = 10^{12}$ cm^{-3}, $\nabla n_e = 10^{12}$ cm^{-4}

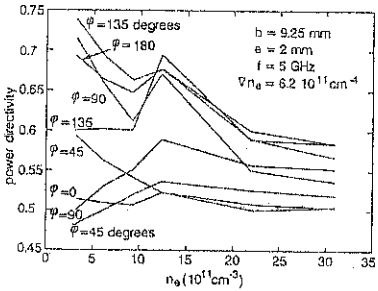

Fig. 4 : Directivity of an active passive antenna fed by seven 270 degrees multijunction versus the phase shift between multijunction and the density

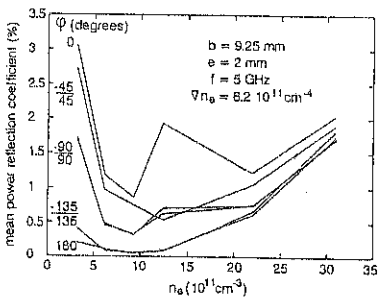

Fig. 5 : Coupling properties

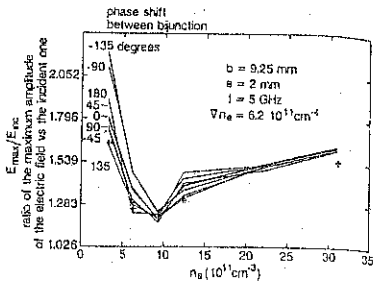

Fig. 6 : Maximum electric field

Reference

[1] Final Report on the ITER TASK IVA-LH : Lower Hybrid Heating and current drive operation scenario and system design.

[2] Conceptual study of a reflector waveguide array for launching Lower Hybrid waves in reactor grade plasmas. Ph. Bibet, X. Litaudon, D. Moreau, Nuclear Fusion, Vol. 35 (1995) pp. 1213-1223.

[3] Couplage de l'onde lente au voisinage de la fréquence hybride basse dans les grands Tokamaks, D. Moreau, T.K. Nguyen, Rapport EUR-CEA-FC-1246, 1984.

[4] LHCD Antenna Coupling Experiments on the TdV Tokamak, P. Jacquet et al. Proc. 11th topical conference on Radio Frequency Power in plasmas Palm Springs, CA, 1995, AIP conf. proceedings p. 122.

[5] Edge density profile effects for Lower Hybrid waveguide coupling. J. Stevens, M. Ono, R. Horton, J.R. Wilson, Nuclear Fusion, Vol. 21 n° 10 (1981) pp. 1259-1264.

[6] Slow wave launching at the lower hybrid frequency using a phased waveguide array, M. Brambilla, Nuclear Fusion, Vol. 16 n° 1 (1976) pp. 47-54.

[7] Three dimensional theory of waveguide plasma coupling, A. Bers, K.S. Theilhaber, Nuclear Fusion, Vol. 23, n° 1 (1983) pp. 41-48.

TURBULENT HEATING OF MAGNETIZED INHOMOGENEOUS PLASMA BY LOWER HYBRID RADIATION

V.N. Pavlenko, V.G. Panchenko, I.N. Rosum
Institute for Nuclear Research of Ukr.Acad.of Sci.
prospect Nauki 47, Kiev-28, Ukraine.

In this report on the base of the Klimontovich-Silin approach we develop the kinetic theory of fluctuations in the spatially inhomogeneous magnetoactive plasma in the presence of an HF pump wave field

$$\vec{E}_0(t) = E_0 \vec{y} \cos \omega_0 t$$

with frequency ω_0 near the lower hybrid frequency

$$\omega_{LH} = \omega_{pi} \left(1 + \omega_{pe}^2 / \Omega_e^2 \right)^{-1/2}$$

We have calculated the effective absorption length and found its dependence on the density gradient, plasma temperature, frequency and amplitude on the pump wave.

In such plasma we investigate the turbulent heating of magnetized inhomogeneous plasma by lower hybrid radiation when the parametric decay of pump wave into lower hybrid and electron drift waves occurs [1]:

$$\omega_0 = \omega_r + \omega_{ek} \qquad (1)$$

where the frequency ω_{ek} lies in the lower hybrid frequency region

$$\omega_{ek} = \omega_{LH} \left(1 + \frac{m_i}{m_e} \cos^2 \theta \right)^{1/2}$$

and the frequency ω_r is governed by [2]:

$$\omega_R = \omega_{*e} \left[1 - \frac{1}{2} k_x^2 \rho_i^2 \left(1 + \frac{T_e}{T_i} \right) \right] \qquad (2)$$

In formula (2) $\omega_{*e} = -k_y \partial T_e / m_e \Omega_e$ is the electron drift frequency. Note that we take into consideration a finite Larmor radius effect.

Accoding to (2) $\omega_R < \omega_{*e}$. This means that the interaction between the wave and the electrons is destabilising. We find that the ions will cause damping, but ion damping rate

usually be small. Since such universal instability for a long time considered to be unavoidable in a finite size plasma.

We note however that the ion Landau damping term will become important in a short device where $k_\parallel$ has to take rather large values. Moreover, in a device with magnetic shear, $k_\parallel$ can take small values only locally.

The efficiency of the pump wave energy absorption we can characterize by the length:

$$\ell_{eff.} \simeq v_{gr.} E_0^2 / 4\pi W \qquad (3)$$

where $v_{gr.}$ is the group velocity of the pump wave, $v_{gr.} = \omega_0 c / \omega_{pe}$ and W is the density of electromagnetic field energy absorbed by the plasma [3]:

$$W = \int \frac{dk}{(2\pi)^2} \int \frac{d\omega}{2\pi} \frac{\langle \widetilde{\delta E \, \delta E} \rangle_{\omega,k}}{4\pi} \cdot \omega \cdot \sum_\alpha \mathrm{Im}\, \chi_\alpha^0$$

Here $\langle \widetilde{\delta E \, \delta E} \rangle_{\omega,k}$ is the spectral density of the electrostatic field turbulent fluctuations in the region above instability threshold.

As a result we have:

$$\ell_{eff.} = 16 \frac{c}{\omega_{pe}} \left(\frac{B_0}{E_0}\right)^2 (k r_{De})^2 \frac{\omega_0^5 \cdot \gamma_{ek}}{\omega_{pe}^2 \cdot \omega_r \cdot \omega_{ek} \cdot (k_\perp c)^2} \qquad (4)$$

It is known [4] that the resonance parametric decay (1) occurs if $\omega_0 > 2\omega_{LH}$ and for typical plasma $k r_{De} \sim 10^{-1}$. We can choose the radiation with frequency $\omega_0 \simeq 3\omega_{LH}$ density energy $50\ kWt/sm^2$ and characteristic parameter for lower hybrid waves $\gamma_{ek}/\omega_{ek} \sim 10^{-3}$.

It follows from (4) that for the hot plasma with thermonuclear parameters $n_e = 5 \cdot 10^{13} sm^{-3}$, $T_e = 10\ keV$, $B_0 = 50\ kG$ the effective absorption length $\ell_{eff.} \simeq 3\ m$ i.e. is of same scale as plasma dimension that secures effective dissipation of the HF pump power.

References

1. Pavlenko V.N., Panchenko V.G., Revenchuk S.M. Plasma Phys. and Contr. Fusion, 1984, 26, 1221-1234.
2. Mikhailovskii A.B. Theory of Plasma Instabilities. Consultants Bureau, 1974.
3. Pavlenko V.N., Panchenko V.G., Revenchuk S.M. Sov. Phys. JETP, 1986, 64, 50-59.
4. Porkolab M. Phys. Fluids, 1977, 20, 2058-2072.

Modelling of Electron-Ion Parametric Turbulence for Ion Bernstein Waves

V.V. Olshansky, V.V. Demchenko[1], G. Kamelander[2], K.N. Stepanov
Institute of Plasma Physics National Science Center Kharkov Institute of Physics and Technology,310108, Kharkov, Ukraine;
[1] Technical University Graz, Austria;[2] Austrian Research Center Seibersdorf

Introduction

Our investigations [1] of the nonlinear stage of the parametric instability of plasma with two ion species under the strong alternating electric field (the relative velocity of the different species particles $u = |\vec{u}_\alpha - \vec{u}_\beta| >> v_{Ti}$) have shown that very fast turbulent heating of ions leads to the quick fall down of the ratio u/v_{Ti} as the turbulence approaches the stationary level at $u/v_{Ti} \sim 2$. At this stage the turbulent heating of ions practically ceases. However, in the region $u/v_{Ti} \leq 1$ the electron-ion instabilities [2] can be found essential. They are excited by the resonant electrons moving along the magnetic field with the velocity equal to the phase velocity of the beat wave formed by the unstable oscillations and the pumping wave. The frequencies and the growth rates of these oscillations are order of ion cyclotron frequency and characteristic transversal wave length is less or order of ion Larmor radius. These oscillations are ion cyclotron Bernstein modes modified by the oscillatory motion of electrons and ions in the electric field of the pumping wave.

The nonlinear theory of such parametric instability has been developed in the papers [3,4] for the weak pumping wave ($u << v_{Ti}$). In this case the oscillation level is equal to

$$W_{kin}/nT \sim \left(u/v_{Ti}\right)^4 . \qquad (1)$$

The growth rate of the longitudinal temperature $T_{e\|}$ of electrons and transversal temperature $T_{i\perp}$ of ions is determined by the expression ($T_{e\|} \sim T_{i\perp} \sim T$)

$$dT/dt = \eta_\alpha \left(u/v_{Ti}\right)^4 \cdot \omega_{ci} , \quad (\eta_\alpha \sim 1, \alpha = e,i) . \qquad (2)$$

The factor η_α should be obtained from the results of numerical simulation. The nonlinear broadening of cyclotron resonances becomes strong for turbulence level (1). This estimate can not be obtained on the ground of the weak turbulence theory even at $u << v_{Ti}$. The level of electron-ion cyclotron oscillations in the presence of the parametric instability, the temperature growth rate due to turbulent heating and the role of this turbulence in the plasma phenomena for problems of RF plasma heating can be determined by means of numerical simulation.

Formulation of the problem of electron-ion parametric instabilities simulation

The considered instabilitiy is basically three-dimensional. Although for electron-ion parametric instabilities considered below the longitudinal electric field is small ($E_\| \sim k_\| \varphi <<$

$E_\perp \sim k_\perp \varphi$) it plays a fundamental role in the excitation of unstable oscillations. To simplify this problem we suppose the unstable oscillations field $\vec{E}(x,z)$ to depend only on one coordinate x in the plane perpendicular to the magnetic field and on coordinate z along the magnetic field direction. Such simulation provides the pattern of two-dimensional turbulence which close to the pattern of a three-dimensional one [5]. Namely, the temperature growth rate due to the turbulent heating, evolution of the distribution functions over velocities and turbulence level are found to be close to ones obtained in the two-dimensional turbulence simulation. For electrons motion is considered to be strongly magnetized. Electrons move only along the magnetic field under the action of $\vec{E}_l(x,z)$. These assumptions simplify the problem significantly for numerical simulation.

The results of numerical simulation and discussion

For numerical simulation the 2D3V macroparticle Vlasov code has been used [6]. The calculations were carried out for the electron-ion plasma with mass relation $m_e/m_i=0.01$. Such choice of this relation reduces the time of the calculations as compared to a realistic one. The electric field of the unstable oscillations is supposed to be potential and periodic. Initial electron and ion temperatures are supposed to be equal. The ratio $\omega_{pe}^2/\omega_{ce}^2=0.0625$ is small enough and therefore the electrons are magnetized. The influence of their transversal motion on the dispersion is negligible. The pumping field frequency is chosen somewhat above the ion cyclotron frequency $\omega_0=1.2\omega_{ci}$. This range of frequencies corresponds to the ion cyclotron waves. When pumping field is absent and the frequency ω is close enough to $n\omega_{ci}$ the ion cyclotron damping of these waves occurs. The damping factor increases rapidly when ω tends to $n\omega_{ci}$. In the presence of the pumping field the current velocity u chosen for numerical simulation changes the waves dispersion significantly. We consider the case $u \sim v_{Ti}$ when this modification is the most essential. Then the frequencies themselves change by the value $\Delta\omega \sim 0.1\omega_{ci}$ and the parametric instability arises as a result of the competition between ion

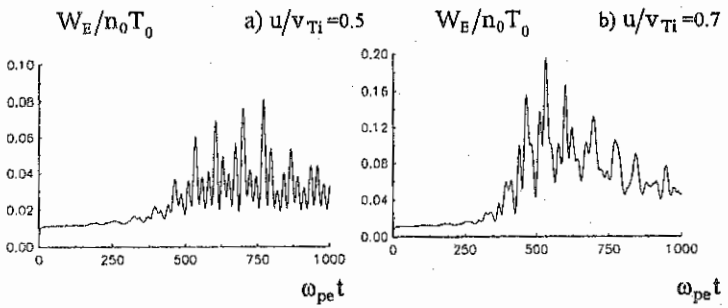

Fig. 1. Time dependence of the electric field energy density W_E.

cyclotron damping and the Cherenkov excitation of the waves by electrons and it has the growth rate order of $0.1\omega_{ci}$.

Fig. 1 shows the time dependence of the electric field energy density $W_E = \sum_k E_k^2/8\pi$ related to the initial thermal energy density of electrons (ions) n_0T_0 for the two values of u/v_{Ti}. One can see that even at u/v_{Ti}=0.7 the ratio W_E/n_0T_0 remains small. The energy W_E is quickly falling down when the ratio $u/v_{Ti}(t)$ decreases due to heating of ions. At the end of the considered time period the W_E value varies with time slowly almost approaching the quasistationary level.

For the cases considered the behavior of the energy density $W_{kin}(t)$ well corresponds to the theoretical estimate (1) obtained for the $u/v_{Ti} \ll 1$. For the maximum growth rate mode ($k\rho_{Li}$=2, $k_\perp u/\omega_0 \sim 1$, $z_e = \omega/\sqrt{2}k_\parallel v_{Te} \sim 1$) the next estimate follows from (1)

$$W_E(t)/n_0T_i(t) = (u/v_{Ti}(t))^3(\omega_{Ci}^2/\omega_{pi}^2)\left[1+T_i(t)/T_e(t)\left(1+i\sqrt{\pi}z_e W(z_e)\right)+k^2\rho_{Li}^2(\omega_{Ci}^2/\omega_{pi}^2)\right]^{-2}, \quad (3)$$

where $W(z)$ is the Kramp function. Formula (3) gives the values W_E/n_0T_0=0.03 and 0.07 for u/v_{Ti}=0.5 and 0.7 respectively. They are close to quasistationary state values of W_E/n_0T_i.

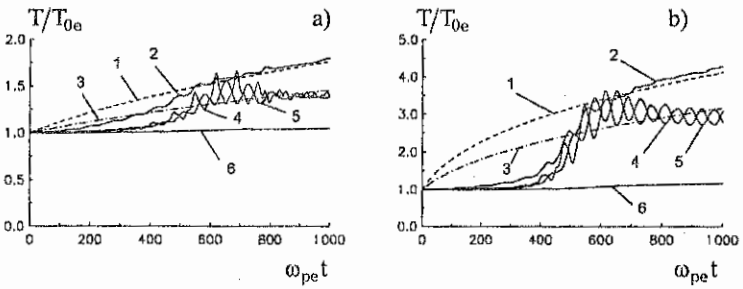

Fig. 2. Time dependence of the temperatures of particles. The curves 1,2,3,4,5,6 corresponds : 1,3- theoretical formula (4) for electrons and ions respectively; 2 - longitudinal temperature of electrons; 4,5 - transversal temperatures of ions; 6 - longitudinal temperature of ions.

a) u/v_{Ti}=0.5; b) u/v_{Ti}=0.7

At the nonlinear stage the turbulence is accompanied by fast electron and ion heating. From (2) we derive the time dependence of the temperature

$$T_\alpha(t)/T_0 = \left[1+2.5\eta_\alpha\left(u/v_{Ti}\right)^5\omega_{Ci}t\right]^{0.4}. \quad (4)$$

The formula (4) well approximates the temperature growth rate obtained by modelling (see Fig. 2a,b). The factor η_α values obtained in numerical simulation are the following: η_e=1, η_i=0.5 at u/v_{Ti}=0.5 and η_e=2, η_i=1 at u/v_{Ti}=0.7. One can see in the all considered cases that the growth of the longitudinal temperature of electrons is somewhat greater than the growth of the transversal temperatures of ions. Note that the both transversal temperatures of ions are close to each other. The growth of the longitudinal temperature of ions is negligible. The important feature is that the temperature of electrons grows all the time while the growth of ion temperature ceases after approaching some maximum value. Probably this is caused by switch- off of the nonlinear stochastic mechanism of interaction of ions and waves.

Conclusions

The modelling of nonlinear stage of the electron-ion parametric turbulence of plasma consisting of electrons and ions has shown that in the case of moderate pumping fields ($u/v_{Ti} \leq 1$) the ion cyclotron oscillations (ion Bernstein modes) are parametrically excited. These modes are modified due to the oscillations of the relative velocity of electrons and ions caused by the pumping wave and the parametric instability arising. The unstable oscillations considered strongly interact with electrons moving along the magnetic field if the Cherenkov resonance condition is met which leads to the waves excitation. In the other hand, waves interact with ions under the cyclotron resonance condition that leads to turbulent heating of ions and saturation of the oscillations level because of nonlinear broadening of the resonances. It was shown that the nonlinear estimate of turbulence level and temperature growth rate for the turbulent heating obtained earlier [3,4] for the weak pumping fields ($u \ll v_{Ti}$) holds well also in the case of the "moderate" pumping fields ($u \sim v_{Ti}$). The effect of cessation of the turbulent heating of ions is found when the ion temperature approaches some critical value.

Authors are grateful to Dr. S. Kasilov and Prof. V. Yegorenkov for discussions. The present work was partially supported by International Atomic Energy Agency (Contract No. 7116/R2/RB) and International Science Soros Education Program(Grant No. SPU042063).

References

1. Kitsenko A.B. et al Fizika Plasmi, 1995, Vol. 21, P. 159-166.

2. Kitsenko A.B.,Panchenko V.I.,Stepanov K.N. Zh. Tech. Fiz., 1973, Vol. 43, P. 1437-1444.

3. Mikhailenko V.S., Stepanov K.N. Zh. Ehksp Teor. Fiz., 1984, Vol 87, P. 161-176.

4. Mikhailenko V.S., Stepanov K.N. In Proc. Contrib. Papers of the Int. Conf. on Plasma Physics, Kiev, USSR, 6-7 April 1987; Kiev, Naukova Dumka, 1987, Vol. 1, P. 209-212.

5. Demyanov et al Ukrainian Journal of Physics,1991, Vol. 36, P. 369-377.

6. V. Olshansky Seibersdorf Report, Juli 1995, OEFZS-4752, Seibersdorf, Austria.

Splitting the Eigen Frequencies of Fast Magnetosonic and Alfven Waves with Bumpy Magnetic Field

I.O. Girka, **V.I. Lapshin** and K.N. Stepanov.
Kharkiv State University, 310077, Kharkiv, Ukraine.

The report is devoted to studying the effect of external steady magnetic field $\vec{B}_0$ ripple on dispersion properties of magnetohydrodynamic (MHD) waves. Plasma pressure is supposed to be small as compared to that of the magnetic field. Electron inertia can be neglected for fast magnetosonic (FMS) and Alfven branches of MHD waves in this case. In the laboratory [1] cylindrical plasma is often placed in a bumpy magnetic field, $\vec{B}_0 = B_{0r} \cdot \vec{e}_r + B_{0z} \cdot \vec{e}_z$ (in cylindrical coordinates),

$$B_{0z} = B_0 \cdot \left[1 + \varepsilon(r)\cos(k_b z)\right], \quad B_{0r} = B_0\left(\varepsilon'/k_b\right)\sin(k_b z), \tag{1}$$

here $|\varepsilon| << 1$, $\varepsilon' \equiv d\varepsilon/dr$, $k_b = 2\pi/L$, L is axial period of $\vec{B}_0$. Inhomogeneity (1) of $\vec{B}_0$ results usually [2] in a weak shift $\Delta\omega$ of the MHD waves eigen frequency ω, $\omega = \omega_0 + \Delta\omega$, where $\Delta\omega \sim \varepsilon^2 \cdot \omega_0$. Both the eigen frequency ω_0 determined in the zeroth approximation ($\varepsilon = 0$) and the shift $\Delta\omega$ are even functions of axial wave number k_z for nonresonant perturbations (the axial wave period is not close to the doubled ripple period), $\omega_0(k_z) = \omega_0(-k_z)$ and $\Delta\omega(k_z) = \Delta\omega(-k_z)$. It is shown here, that the splitting of eigen frequency, caused by resonant perturbation,

$$2\pi/k_z = 2L, \tag{2}$$

is determined as follows,

$$\omega = \omega_0 \pm \delta\omega. \tag{3}$$

The resonant shift $\delta\omega$ is $\delta\omega \sim \varepsilon \cdot \omega_0$.

In accordance with the symmetry of the problem (see (1)) we find the solution of Maxwell equations for the axial component of MHD wave magnetic field $B_z^{\sim}$ taking into account the small quantities of the first order in the following form:

$$B_z^{\sim} = \left[\left(C_0^{(+)} \cdot \psi_1^{(0)} + C_1^{(+)} \cdot \psi_1^{(+)}\right) \cdot e^{i \cdot k_z \cdot z} + \left(C_0^{(-)} \cdot \psi_1^{(0)} + C_1^{(-)} \cdot \psi_1^{(-)}\right) \cdot e^{-i \cdot k_z \cdot z} + \right.$$
$$\left. + C_3^{(+)} \cdot \psi_3^{(+)} \cdot e^{3i \cdot k_z \cdot z} + C_3^{(-)} \cdot \psi_3^{(-)} \cdot e^{-3i \cdot k_z \cdot z}\right] \cdot \exp\left[i \cdot (m \cdot \vartheta - \omega \cdot t)\right], \tag{4}$$

here m is azimuthal wave number, $C_{0,1,3}^{(\pm)}$ are integration constants. Solution $\psi_1^{(0)}$ of Maxwell equations for $B_z^{\sim}$ in the zeroth approximation is supposed to be known for a given plasma profile. Amplitudes of satellite harmonics are small as compared with that of the

fundamental harmonic, $\left|C_{1,3}^{(\pm)} \cdot \psi_{1,3}^{(\pm)}\right| \sim \left|\varepsilon \cdot C_0^{(\pm)} \cdot \psi_1^{(0)}\right|$, everywhere except the region of the fundamental Alfven resonance (AR), within which

$$\varepsilon_1^{(0)} = N_z^2, \tag{5}$$

and except the regions of satellite AR (SAR), within which

$$\varepsilon_1^{(0)} = \left(N_z \pm N_b\right)^2, \tag{6}$$

here $N_z = c \cdot k_z/\omega$ and $N_b = c \cdot k_b/\omega$. We derive below the explicit expressions for the frequency shift $\delta\omega$ in the case when these resonances do not take place in plasma using the perturbation theory for degenerated spectra.

Expressions for other components of MHD wave fields are analogous to (4). These expressions must satisfy the following boundary conditions. First, these fields must be finite inside the metallic chamber of radius $r = b$. Second, azimuthal component of electric field and longitudinal component of magnetic field, $B_3 = \left(\vec{B} \cdot \vec{B}_0\right)/\left|\vec{B}_0\right|$, must be continuous while crossing the outer magnetic surface,

$$r = a \cdot \left(1 + \varepsilon_a \cdot \cos\left(2k_z z\right)\right), \qquad \varepsilon_a = -a^{-2} \cdot \int_0^a r \cdot \varepsilon \cdot dr. \tag{7}$$

Third, the azimuthal component of MHD wave electric field must vanish at the metallic wall, $r = b$.

Functions $\psi_{1,3}^{(\pm)}$ are obtained using the perturbation theory. Coefficients $C_3^{(\pm)}$ are determined applying the boundary conditions to satellite harmonics.

Coefficients $C_1^{(\pm)}$ do not arise for plasma with a uniform density. Otherwise one constraint more is involved. It consists in the following. Energy of the electromagnetic field calculated using the expression (4) must be equal with accuracy up to small terms of the first order to that calculated in the zeroth approximation.

Applying the boundary conditions to the fundamental harmonics results in the following dispersion relation which is similar to a secular equation in the conventional perturbation theory,

$$D^{(0)2} - D^{(1)2} = 0, \tag{8}$$

Here $D_0\left(\omega_0\right) = 0$ is the MHD wave dispersion equation in a straight magnetic field, $\varepsilon = 0$. The MHD wave eigen frequency is obtained from (8) in the form (3). The frequency shift $\delta\omega$, caused by the weak inhomogeneity of $\vec{B}_0$, is equal to

$$\delta\omega = D^{(1)}\left(\partial D^{(0)}/\partial\omega\right)^{-1}_{|\omega=\omega_0}. \tag{9}$$

It means that MHD waves with axial period (2) exist in plasma cylinder with bumpy magnetic field (1) in the form of two standing waves, $C_0^{(+)} = \pm C_0^{(-)}$, with close frequencies (3). Crests

(or nodal points) of the standing wave with the higher (or lower) frequency are situated just in the middle of the coils of the longitudinal magnetic field. This fact is explained as follows. Eigen frequencies of FMSW and AW increase with the external magnetic field growing, and the standing wave with the crests (or nodal points) in the middle of the coils exists in those areas where the magnetic field is higher (or lower).

Beat waves arise as a result of superposition of these standing waves. Measurements of the frequency, $\delta\omega$, of these beat waves can be used for diagnostics of plasma density or the magnetic field. In tokamaks with eight coils of the toroidal magnetic field (in JET, for example) these beat waves have the axial wave number $k_z = 4/R$, here R is the large radius of a tokamak.

Simple analytical expressions are obtained for the shift $\delta\omega$ of eigen frequency in the case of MHD oscillations in the thin plasma cylinder with the uniform density separated from the metallic chamber by a narrow ($|m| \cdot (b-a) << a$) vacuum layer. For short wavelength ($k_A^2 << \kappa^2$) AW

$$\omega_0 = \omega_{ci}^{(0)} \cdot \left(1 - \left(|m| \cdot (b-a) \cdot k_A^2 / \left(a \cdot \kappa^2\right)\right)\right), \tag{10}$$

$$\delta\omega = \varepsilon(b) \cdot \omega_{ci}^{(0)} \cdot \left[\kappa^2 / k_\perp^2 - c \cdot a \cdot k_\perp^2 / \left(4 \cdot \omega_0 \cdot \left(2 \cdot |m| + 1\right)\right)\right], \tag{11}$$

here $\omega_{ci}^{(0)} = e \cdot B_0 / \left(m_i \cdot c\right)$, $k_A = \omega \cdot \omega_{pi} / \left(c \cdot \omega_{ci}^{(0)}\right)$ is the Alfven wave number, $\kappa^2 = k_z^2 - (\omega/c)^2$ is the vacuum wave number squared, $k_\perp$ is the transverse wave number,

$$k_\perp^2 = (\omega/c)^2 \cdot \left(\varepsilon_1^{(0)} - N_z^2\right) \cdot \left(1 - \mu^2\right), \quad \mu = \varepsilon_2^{(0)} / \left(\varepsilon_1^{(0)} - N_z^2\right), \tag{12}$$

$\varepsilon_{1,2}^{(0)}$ are components of the cold collisionless plasma permeability tensor. For FMSW with $k_A^2 >> \kappa^2$

$$\omega_0 = \left(\kappa \cdot c \cdot \omega_{ci}^{(0)} / \omega_{pi}\right) \cdot \sqrt{a / \left(|m| \cdot (b-a)\right)} << \omega_{ci}^{(0)}, \tag{13}$$

$$\delta\omega = \frac{-\varepsilon(b) \cdot a}{4 \cdot (b-a)} \cdot \left[1 + \frac{\kappa \cdot a}{2 \cdot |m| + 1} \cdot \sqrt{\frac{b-a}{|m| \cdot a}} \cdot \frac{\omega_{pi}}{\omega_{ci}^{(0)}}\right] \cdot \omega_0 . \tag{14}$$

In formulas (11) and (14) the ripple parameter ε is assumed to be uniform, $\varepsilon(r) = \varepsilon(b)$. Such assumption is true if $k_b \cdot b << 1$.

If a thin ($\kappa \cdot a << 1$, $k_\perp \cdot a << 1$) plasma cylinder is separated from the metal chamber by the wide ($\kappa \cdot b >> 1$) vacuum layer, then effect of $\tilde{B}_0$ inhomogeneity is important in the narrow layer $\Delta r \le \left(2 \cdot k_z\right)^{-1}$ near the magnetic coils. In this case the shift $\delta\omega$ is exponentially small. For example, for AW

$$\omega_0 = \omega_{ci}^{(0)} \cdot \left(1 - \left(k_A^2 / \left(2 \cdot \kappa^2\right)\right)\right), \tag{15}$$

$$\delta\omega = -\varepsilon(b)\cdot\exp\left(-2\cdot|k_z|\cdot(b-a)\right)\cdot\frac{N_z^2-1}{2\cdot|m|+1}\cdot\frac{\omega_{ci}^{(0)3}\cdot a}{\omega_{pi}^2\cdot c}\cdot\omega_0 . \qquad (16)$$

Splitting the eigen frequencies of FMS and AW with arbitrary axial wavelength occurs also in a current -carrying plasma cylinder (see, for example [3,4]). FMSW frequency shift caused by a longitudinal current is of the following order,

$$\delta\omega \sim \frac{2\cdot\omega_0^2\cdot k_z\cdot m}{\omega_{ci}^{(0)2}\cdot k_A^2\cdot a}\cdot\frac{B_{0\vartheta}(a)}{B_0}, \quad (m\neq 0). \qquad (17)$$

This effect is negligibly weak as compared with that considered in the present report for the waves with axial period $2L$ if

$$\frac{B_{0\vartheta}}{B_0} << \frac{\varepsilon\cdot N_A^2}{4\cdot m\cdot N_z} . \qquad (18)$$

As far as axially symmetrical ($m=0$) FMSW is concerned, splitting their spectrum in current -carrying plasma with uniform profiles of density and temperature is weak effect of the order which is higher than $(B_{0\vartheta}/B_0)^2$. Splitting the eigen frequencies of FMSW and AW with wave axial period $2L$, caused by $\tilde{B}_0$ inhomogeneity, on the contrary, takes place for axially symmetrical waves as well.

It was shown in [5] that SARs (6) can exist along with the fundamental Alfven resonance in cylindrical plasma placed in a bumpy magnetic field. In these SARs small satellite harmonics grow and are converted into small scale kinetic Alfven waves. The value of RF power absorbed in SAR regions is proportional in the nonresonant case to the product of ε^2 and the plasma density value in the SAR. For both satellite harmonics of the waves with $k_z = \pi/L$ SARs have the same location in the region where plasma density is 9 times greater than in the fundamental Alfven resonance. That is why plasma heating in SAR can be important in this case.

The authors thank Prof. Yegorenkov V.D. for helpful discussions. The report is supported by International Atomic Energy Agency, contact No 8931/RO and Science and Technology Center in Ukraine.

[1] Ryutov D.D.// Uspehi fizicheskih nauk. 1988. Vol.154. P.565. (in Russian)
[2] Girka I.A., Stepanov K.N.// Ukrainskij fizicheskij zhurnal.1988. Vol.37.P.69.(in Russian)
[3] Chance M.S., Perkins F.W., Sperling T. // Bull.Am.Phys.Soc. 1973. Vol.18. P.1273.
[4] Girka I.A., Stepanov K.N. //Reports of the Academy of Sciences of UkrSSR. Series A.1990.No 3. P.66. (in Russian)
[5] Girka I.A., Lapshin V.I., Stepanov K.N. // Plasma Phys. Reports, 1994, Vol. 20. P. 916.

QUASILOCAL CHERENKOV ABSORPTION OF MHD WAVES BY ELECTRONS IN A TOKAMAK

A.I.Pyatak*, S.V.Kasilov, K.N.Stepanov
*Kharkov State Automobile & Road Technical University
National Science Center "Kharkov Institute of Physics and Technology",
Akademicheskaya str. 1, 310108, Kharkov, Ukraine

1. Electron Cherenkov absorption may be used as one of basic mechanisms for the absorption of fast magnetosonic (FMSW) and Alfven (AW) waves for plasma heating and current drive in small β toroidal traps. The damping of these waves has been found in a uniform plasma immersed in a uniform magnetic field in Ref. [1](see also [2]) and for large scale tokamaks $(\omega a/v_A >> 1)$ in Ref. [3]. This damping includes Landau damping being due to the longitudinal wave electric field $E_\parallel$ together with TTMP (magnetic Landau damping) caused by the longitudinal wave magnetic field gradient action on a resonant particle (guiding centre) as well as the damping described by "oblique" electron components of the antihermitian part of the dielectric permeability tensor $\varepsilon_{ij} = \varepsilon_{ij}^H + i\varepsilon_{ij}^A$. This damping is described by complicated expressions for ε_{ij}^A containing the sums over bounce-resonances of terms being the integrals over particle energy and poloidal angle ϑ with elliptical functions entering the integrands [3]. Therefore the assessment of the damping may be impeded.

This report is devoted to studying the electron Cherenkov damping [3] for the short wavelength MHD waves for which the following condition is met

$$k_\parallel qR >> 1, \qquad (1)$$

where $k_\parallel$ is the longitudinal wavenumber, q is the tokamak safety factor, R is the large radius. Condition (1) is met practically always for MHD waves applied for plasma heating. In this case one is lucky to obtain simple expressions for ε_{ij}^A including the contributions from circulating and trapped electrons separately and to perform the analysis of MHD wave damping for various conditions.

2. Expressions for ε_{ij}^A contain the time integrals in the range $(-\infty, 0)$ whose integrands are proportional to $\exp[i\Phi(\tau)]$, where

$$\Phi(\tau) = \int_0^\tau k_\parallel v_\parallel(\tau')d\tau' - \omega\tau. \qquad (2)$$

The electron velocity along the trajectory is equal to

$$v_\parallel(\tau) = \pm v_0\sqrt{2\kappa^2 - 1 - \cos\vartheta(\tau)},\ v_0 = \sqrt{\frac{2\varepsilon_t E}{m_e}}\left[1 + \varepsilon_t\left(2\kappa^2 - 1\right)\right]^{-1}, \qquad (3)$$

where $\varepsilon_t = r/R$, $E = (1/2)m_e v^2$ is the particle energy, κ is the trapping parameter, $\vartheta(\tau)$ is the poloidal angle current value on the trajectory determined from the equation $d\vartheta/dt = v_\parallel(\tau)/qR$. The initial value $\vartheta = \vartheta(0)$ is the poloidal angle value at the observation point.

When the condition (1) is met, the time interval of efficient wave-particle interaction is small so that the velocity $v_\parallel(\tau)$ of resonant electrons may be simply changed for its value at the observation point $v_\parallel(\vartheta)$.(This substitution

corresponds to the local approximation.) The $v_\parallel(\tau)$ deviation from $v_\parallel(\vartheta)$ happens to be small. Indeed, at small τ

$$v_\parallel(\tau) = v_\parallel(\vartheta) + (1/2)\sin\vartheta\omega_0^2 qR\tau \quad (\omega_0 = v_0^2/qR). \qquad (4)$$

The electron-wave interaction time $\Delta\tau$ is estimated from the condition $|\Phi(\tau)| \sim 1$ (at $\omega \approx k_\parallel v_\parallel(\vartheta)$). In this case the deviation $\vartheta(\tau) - \vartheta$ is small

$$\Delta\vartheta = |\vartheta(\tau) - \vartheta| \sim \omega_0\Delta\tau \sim 1/\sqrt{k_\parallel qR|\sin\vartheta|} << 1. \qquad (5)$$

The second factor securing the applicability of such an approach is strong dephasing between the particle and the wave due to Coulomb conditions leading to the diffusional velocity spread

$\Delta v_\parallel : \overline{(\Delta v_\parallel)^2} = \nu_e v_\parallel^2 \tau$, where ν_e is the electron-ion Coulomb collision frequency. The resulting phase spread $\Delta\Phi = k_\parallel \int_0^\tau \Delta v_\parallel d\tau \sim k_\parallel v_\parallel \sqrt{\nu}\,\tau^2/2$.

The time the electron requires to pass the distance order of qR $\Delta\tau \sim qR/v_\parallel \sim 1/\omega_b$ due to the rotational transform may fall into a resonance region $\omega = k_\parallel v_\parallel$. The phase change during this time will amount to

$$\Delta\Phi \sim \frac{k_\parallel v_\parallel}{\omega_b}\sqrt{\frac{\nu_e}{\omega_b}} \sim \frac{\omega}{\omega_b}\sqrt{\frac{\nu_e}{\omega_b}}, \qquad (6)$$

ω_b is the bounce frequency. If the condition $\Delta\Phi > 1$ is met that is almost always the case for tokamaks with RF heating, then one can regard the separate passages through the resonant zone $\omega = k_\parallel v_\parallel$ to be statistically independent and, consequently, one can neglect the contributions from preceding passages the last one excepted . Thus we have $\int_{-\infty}^{0} \exp i\varphi(\tau)d\tau = \pi\delta\big(\omega - k_\parallel v_\parallel(\vartheta)\big)$. Applying this equality yields for ε_{ij}^A the expression

$$\varepsilon_{ij}^A = \varepsilon_{ij}^{(c)} + \varepsilon_{ij}^{(tr)}, \qquad (7)$$

the superscripts (c) and (tr) denoting the contributions of circulating and trapped electrons, respectively. The quantities $\varepsilon_{ij}^{(c,tr)}$ are

$$\varepsilon_{33}^{(c)} = \sqrt{\frac{\pi}{2}}\frac{\omega_{pe}^2\omega}{k_\parallel^3 v_{Te}^3}\Phi(\varsigma),$$

$$\varepsilon_{33}^{(t)} = \sqrt{\frac{\pi}{2}}\frac{\omega_{pe}^2\omega}{k_\parallel^3 v_{Te}^3}\big[1 - \Phi(\varsigma)\big],$$

$$\varepsilon_{23}^{(t)} = \varepsilon_{32}^{(t)} = \frac{i}{2\sqrt{2}}\frac{k_\perp\omega_{pe}^2\omega}{k_\parallel^3 v_{Te}^2\omega_{ce}\sqrt{\varepsilon_t}}\left\{\exp\big(-\varsigma^2\big) + \frac{\sqrt{\pi}}{\varsigma}\big[1 - \Phi(\varsigma)\big]\right\},$$

$$\varepsilon_{23}^{(c)} = \varepsilon_{32}^{(c)} = \frac{i}{2\sqrt{2}}\frac{k_\perp\omega_{pe}^2\omega}{k_\parallel^3 v_{Te}^2\omega_{ce}\sqrt{\varepsilon_t}}\left[-\exp\big(-\varsigma^2\big) + \frac{\sqrt{\pi}}{\varsigma}\Phi(\varsigma)\right], \qquad (8)$$

$$\varepsilon_{22}^{(t)} = \frac{1}{8}\sqrt{\frac{\pi}{2}}\frac{k_\perp^2\omega_{pe}^2\omega^5}{k_\parallel^7\omega_{ce}^2 v_{Te}^5\varepsilon_t^3}\frac{\partial^2}{\partial z^2}\left\{\frac{1}{z}\left[1-\Phi\left(\sqrt{\frac{z}{2}}\right)\right]\right\},$$

$$\varepsilon_{22}^{(c)} = \frac{1}{8}\sqrt{\frac{\pi}{2}}\frac{k_\perp^2\omega_{pe}^2\omega^5}{k_\parallel^7\omega_{ce}^2 v_{Te}^5\varepsilon_t^3}\frac{\partial^2}{\partial z^2}\left[\frac{1}{z}\Phi\left(\sqrt{\frac{z}{2}}\right)\right],$$

$$\Phi(\varsigma) = \frac{2}{\sqrt{\pi}}\int_0^\varsigma \exp\left(-t^2\right)dt,\ \varsigma = \frac{\omega}{2k_\parallel v_{Te}\sqrt{\varepsilon_t}},\ z = 2\varsigma^2.$$

Note that in this approximation the sum (7) exactly equals the antihermitian part of ε_{ij}^A for a plasma in the uniform magnetic field at $\omega/k_\parallel v_{Te} << 1$. It is natural, because in the local approximation during the interaction event $\omega \approx k_\parallel v_\parallel$ the particle is moving along a straight line and the change of $v_\parallel(\tau)$ due to the magnetic field nonuniformity is neglected. The splitting of ε_{ij}^A into the sum (7) permits to determine the contributions made by trapped and circulating electrons into the MHD wave damping under the condition (1).

The wave damping coefficient is equal to $\mathrm{Im}\,N = \mathrm{Im}\,N^{(c)} + \mathrm{Im}\,N^{(tr)}(k_r \approx k_\perp >> k_\vartheta)$, where

$$\frac{\mathrm{Im}\,N^{(a)}}{N} = \left[4\cos^2\theta N^4 - 2\left(1+\cos^2\theta\right)\varepsilon_1 N^2\right]^{-1} \times$$

$$\times\left\{\left(\cos^2\theta N^2 - \varepsilon_1\right)\left[\delta\varepsilon_{22}^a + \frac{\left(\varepsilon_{23}^H\right)^2}{\left(\varepsilon_{33}^H\right)^2}\varepsilon_{33}^a - \frac{1}{\varepsilon_{33}^H}\left(\varepsilon_{23}^H\varepsilon_{32}^a + \varepsilon_{23}^a\varepsilon_{32}^H\right)\right] + \right.$$

$$\left. + \frac{\varepsilon_1 N^4\sin^2\theta}{\left(\varepsilon_{33}^H\right)^2}\varepsilon_{33}^a - \frac{N^2\sin^2\theta}{\left(\varepsilon_{33}^H\right)^2}\left(\varepsilon_1^2 - \varepsilon_2^2\right)\varepsilon_{33}^a - \frac{\varepsilon_2\cos\theta\sin\theta N^2}{\varepsilon_{33}^H}\left(\varepsilon_{23}^a - \varepsilon_{32}^a\right)\right\}. \qquad (9)$$

The refractive index $N=kc/\omega$ is determined from the equation $\left(\cos^2\theta N^2 - \varepsilon_1\right)\left(N^2 - \varepsilon_1\right) = \varepsilon_2^2, \cos\theta = k_\parallel/k$

$$\varepsilon_1 = -\frac{\omega_{pi}^2}{\omega^2 - \omega_{ci}^2}, \varepsilon_2 = -\frac{\omega}{\omega_{ci}}\frac{\omega_{pi}^2}{\omega^2 - \omega_{ci}^2},$$

$$\varepsilon_{33}^H = \frac{\omega_{pe}^2}{k_\parallel^2 v_{Te}^2}, \varepsilon_{23}^H = \varepsilon_{32}^H = i\frac{\omega_{pe}^2}{\omega\omega_{ce}}\mathrm{tg}\theta.$$

If $\varsigma >> 1$ then the MHD wave damping is determined solely by strongly circulating particles, the contribution of trapped electrons being exponentially small. If $\varsigma \sim 1$ then trapped and circulating particles contribute equally to the damping coefficient to the order of magnitude. With $\varsigma << 1$ trapped electrons make the principal contribution to the damping.

For $\omega \geq \omega_{ci}$ and $k_\parallel \sim k \sim \omega/v_A$ the opacity barrier usually happens to be broad and MHD waves don't penetrate into the plasma core and such waves are absorbed by circulating electrons. Therefore below we treat the case $\omega << \omega_{ci}$ separately. In this case the AW and FMSW refractive indices,

respectively, $N^2 = \varepsilon_1/\cos^2\theta$, $N^2 = \varepsilon_1$.The damping (9) equals for AW and FMSW, respectively, to

$$\frac{(\mathrm{Im}\,N)^{(a)}}{N} = \frac{\varepsilon_1\varepsilon_{33}^a \sin^2\theta}{2\left(\varepsilon_{33}^H\right)^2\cos^2\theta}, \qquad (10)$$

$$\frac{(\mathrm{Im}\,N)^{(a)}}{N} = \left(\varepsilon_{22}^a\varepsilon_{33}^H + \frac{\varepsilon_{23}^{H2}}{\varepsilon_{33}^H}\varepsilon_{33}^a - 2\varepsilon_{23}^a\varepsilon_{23}^H\right)\left(2\varepsilon_1\varepsilon_{33}^H\right)^{-1}. \qquad (11)$$

When $x_0 = \left(\omega/k_\parallel v_{Te}\sqrt{2\varepsilon_t|\sin\vartheta|}\right)\left(k_\parallel qR\right)^{1/2} \le 1$, then only very slow trapped particles participate in the Cherenkov resonance. These particles make the dominant contribution to the damping at the trajectory sections near the turning points. Taking into account that also in this case the wave-particle interaction time is small, one can apply expression (4) for $v_\parallel(\tau)$. (One may call such an approximation a quasilocal one.) Then for ε_{33}^{tr} one obtains

$$\varepsilon_{33}^{tr} = \frac{\omega_{pe}^2\omega^3 qR}{\sqrt{8}\pi v_{Te}^5\varepsilon_t k_\parallel^4}\,\mathrm{Re}\int_0^{2\pi}\frac{d\vartheta}{|\sin\vartheta|}e^{i\alpha}\int_0^\infty\frac{dx}{x^4}\exp\left(-\frac{x_0^2}{x^2}\right)W\left[(x-1)e^{i\alpha}\right], \qquad (12)$$

where $\alpha = (\pi/4)\mathrm{sgn}\sin\vartheta$, $W(z) = \exp\left(-z^2\right)\left(1 + \frac{2i}{\sqrt{\pi}}\int_0^z\exp\left(t^2\right)dt\right)$.

For $x_0 \le 1$ the contribution to the damping of particles from the turning point region $\sqrt{k_\parallel qR} >> 1$ times exceeds that from all other trajectory sections far from the turning point. In this case, the spreaded function proportional to $W\left[(x-1)e^{i\alpha}\right]$ occupies the place of $\delta\left(\omega - k_\parallel v_\parallel\right)$. Only for $x_0 >> 1$ when the sections with $x>>1$ make the dominant contribution to the integral (12) one can substitute the function W in (12) by its asymptotic value for large arguments, in this case (12) coincides with (8).

For very low frequencies, $x_0 << 1$, the values $x<<1$ contribute to the integral over x. In this case expression (13) increases compared with (9):

$$\varepsilon_{33}^a = \frac{\sqrt{\pi}}{3}q_1\frac{\omega_{pe}^2\sqrt{\varepsilon_t}q^2R^2}{v_{Te}^2\left(k_\parallel qR\right)^{5/2}}, \quad q_1 = \frac{2}{\sqrt{\pi}}\int_0^1\left(\cos x^2 + \sqrt{3}\sin x^2\right)dx \approx 1.5\ldots$$

The AW damping increases by $1/x_0 >> 1$ compared with (10). The FMSW damping also increases by this factor compared with (11).

The work has been performed in part with the support from the International Science Foundation (grant U32200).

REFERENCES

1. K. N. Stepanov. Zhurn. Eksp. Teor. Fiz. (1960) v. 38, p. 265.
2. A. I Akhiezer et al. Collective Oscillations in Plasma. Pergamon Press. Oxford. 1967.
3. T. D. Kaladze et al. Fizika plazmy (1980) v. 8, p. 823.

Suprathermal Ion Generation at Fundamental Minority Cyclotron Resonance Heating

S.V.Kasilov, N.B.Marushchenko, A.I.Pyatak, K.N.Stepanov
Institute of Plasma Physics, National Science Center "Kharkov Institute of Physics and Technology", Akademicheskaya 1, 310108 Kharkov, Ukraine

1. Introduction. The generation of high energy tails of minority distribution function is a common feature of fast wave ICRF minority heating. E.g. the presence of fast ^3He ions with energy $\sim$ MeV is for a long time reported by JET [1].

Usually the minority distribution function is modelled with the help of bounce - averaged kinetic equation with quasilinear diffusion operator derived by Stix [2] within the local approach, which is modified by the account of toroidal trapping. The main assumption of such local theory is that different quasiplane waves or toroidal harmonics of the RF electromagnetic field $\sim \exp(im\vartheta + il\zeta)$, with ϑ and ζ being the poloidal and toroidal angles resp., contribute to quasilinear diffusion tensor independently. This assumption permits to obtain the correct expressions for quasilinear diffusion tensor almost everywhere in the phase space if the variation of the wave electromagnetic field with a poloidal angle ϑ is well described in the cyclotron resonance zone (CRZ) by one poloidal harmonic with given m [3]. Such a situation takes place if the minority density n_α is sufficiently less than critical density $n_{cr} = n_e k_{eff} v_{T\alpha}/\omega$, where $k_{eff} = max\left(k_\parallel, (\varepsilon_t \omega/qRv_{T\alpha})^{1/2}\right)$. Here n_e, ω, $k_\parallel$, $v_{T\alpha}$, ε_t, q and R are plasma density, wave frequency, parallel wavenumber, average velocity of minority ions, toroidicity and tokamak major radius respectively. Usually such a critical density is order of 1%.

The more typical for the experiments heating scenario is that with supercritical minority density $n_\alpha \gg n_{cr}$. In this case the wave polarization is strongly affected by the resonant minority particles, so that within CRZ the left hand side polarized component of the wave electric field E^+, which is responsible for the heating, is small and varies rapidly. For the case of weak wave absorption after one wave pass through CRZ, the nonlocal integral problem of finding E^+ in the CRZ was solved in Ref.[4], where the expressions for E^+ through slowly varying in the CRZ quantity $E_0^+/(\omega - \omega_{c\alpha}) \equiv A^+$ were obtained. Here E_0^+ is the solution to Maxwell equations with cold dielectric permittivity tensor. The corresponding nonlocal expressions for quasilinear diffusion tensor were obtained in Ref.[3], where the particles were assumed to be strongly passing, and the account of toroidal trapping was included to the nonlocal quasilinear theory in Ref.[5]. In this paper the results of numerical modelling of minority distribution function for the nonlocal quasilinear diffusion model are presented.

2. Calculation Model. The calculations were performed with 2D bounce-averaged Fokker-Planck code [6], modified here for tokamak geometry. For the Coulomb collision operator the distribution of the background particles was assumed Maxwellian. The bounce averaged quasilinear diffusion tensor in variables $v_\perp, v_\parallel$ being perpendicular and parallel velocity components in the minority cyclotron resonance point $\omega_{c\alpha}(\vartheta_{res}) = \omega$ has the only nonzero contravariant component which corresponds to the diffusion over perpendicular velocity. For the cases of subcritical and supercritical minority density this component is given respectively by

$$D_\perp = \frac{\pi e_\alpha^2 \left|E_0^+\right|^2 qR}{4m_\alpha^2 \varepsilon_t \omega \left|v_\parallel\right| \tau_b}, \quad n_\alpha \ll n_{cr}, \tag{1}$$

and

$$D_\perp = \frac{\pi e_\alpha^2 n_\alpha^2 k_\parallel^2 |A^+|^2 qR}{4m_\alpha^2 \varepsilon_t \omega |v_\parallel| \tau_b} \left| \int d^3v' \frac{f(v'_\perp, v'_\parallel)}{v'_\parallel - v_\parallel - i0} \right|^{-2}, \quad n_\alpha \gg n_{cr}. \qquad (2)$$

Here $\omega_{c\alpha}$, e_α, m_α and n_α are minority cyclotron frequency, charge, mass and density respectively, τ_b is a bounce time difined as particle return time to the minimum B point. Expressions (1) and (2) correspond to the case of E_0^+ and A^+ in the form of one toroidal harmonic in the CRZ vicinity. For the waves with broad spectrum over toroidal wavenumber l the diffusion coefficients (1) and (2) preserve the same form up to redefinition of constant in front (see their general form in Ref.[5]). The components of diffusion tensor for actually used in the code variables v and χ being particle velocity module and pitch angle in magnetic field minimum point, follow from correspondent covariant tensor transform. The square-root singularity in Eqs. (1) and (2) for trapped particles with the turning points in the CRZ vicinity was removed by change of $|v_\parallel|$ to $|v_\parallel^*| \equiv \left(v_\parallel^2 + \exp(-v_\parallel^2/\delta)\right)^{1/2}$, where $\delta \ll v_{T\alpha}^2$. This change simulates the saturation of diffusion tensor at $|v_\parallel| \to 0$, which has for such particles the expression through Airy function [7]. However this small group of particles is of minor importance for the result. The above change at the same time allows to use the same analytical formula for all kinds of trapped particles. It provides the exponential smallness of diffusion tensor for trapped particles which do not reach the CRZ ($v_\parallel^2 < 0$).

The diffusion coefficient (2) is the integral functional of the minority distribution function due to such a dependence of self-consistent wave electric field. The remarkable property of this coefficient is that it is increasing with parallel velocity as $v_\parallel^2$ for passing particles from the tail [3], thus providing much stronger diffusion of these particles than predicted by subcritical minority model (1).

3. Modelling results. The modelling was performed for ^3He minority cyclotron resonance heating in tokamak with the following parameters: major radius $R = 300\ cm$, toroidal magnetic field $B = 30\ kG$, plasma density $n_e = 10^{14}\ cm^{-3}$, plasma temperature $T_i = T_e = 7\ keV$, toroidicity $\varepsilon_t = 0.1$, surface averaged absorbed RF-power density $< p >= 0.5\ W/cm^3$, minority concentration $n_\alpha/n_e = 5\%$. The cyclotron resonance line $\omega_{c\alpha} = \omega$ was chosen to pass through the magnetic axis. Assuming $k_\parallel \sim 0.03\ cm^{-1}$, for the critical minority density we get $n_{cr}/n_e \sim 1\%$, i.e. minority is strongly supercritical. At the same time the wave absorption after one pass through the CRZ, which is characterized by the CRZ optical thickness

$$\tau \sim \frac{n_e}{n_\alpha} \frac{k_\parallel^2 v_{T\alpha}^2}{\omega^2} k_\perp R, \qquad (3)$$

where $k_\perp$ is characteristic perpendicular wavenumber of the fast magnetosonic wave (see e.g. Ref.[4]), is small, $\tau \sim 0.1 \ll 1$. Therefore the nonlocal supercritical minority heating model described by RF diffusion coefficient (2) is justified in the considered case. For the comparison we performed also the calculation for the same parameters set with subcritical minority model described by Eq. (1), which being however inapplicable to the considered case, is sometimes used for such a modelling.

In Figure 1 the contours of minority distribution function in the plane $(v_\perp, v_\parallel)$ are shown. Here $v_\perp = v \sin\chi$, $v_\parallel = v \cos\chi$ are the perpendicular and parallel velocity components in the magnetic field minimum point respectively. Fig.1a corresponds to subcritical minority model. The contours there tend to so-called "rabbit ears" picture (see Ref.[7]). The characteristic feature of this model is that most strongly heated particles are trapped

ones with turning points close to CRZ. The contours in Fig.1b correspond to supercritical minority model. The tails there are developing now in the region with higher parallel velocities. For intermediate energies this takes place mainly in the region of passing particles. The generation of the tails is more effective for supercritical minority model (both calculations correspond to the same RF power and minority densities). This is better seen from Figures 2, 3, and 4 where the distribution function is given as a function of energy for fixed value of pitch angle $\chi = 0°$, $90°$ and $64°$ respectively (the last value corresponds to trapped-passing boundary). This distribution has for supercritical minority model the distinct "two-temperature" structure, which is usually obtained at the modelling of second harmonic cyclotron resonance heating. The high energy tail has a higher energy contents for supercritical minority model, that is seen from Fig.5 where normalized to one particle energy contents $\mathcal{E}$ in the particles with energy below E is shown as a function of E ($\mathcal{E}(\infty)$ corresponds to average minority energy).

4. **Conclusions.**

- The self-consistent nonlocal quasilinear diffusion model predicts strong generation of high-energy particles at supercritical minority ion cyclotron heating.
- The modelling performed for JET-like parameters [1] provides the explanation of MeV-energy particles generation at relatively low RF power density levels.
- The modelling for PLT-like ICRF minority heating parameters has also been performed and showed the generation of particles with energy order of hundred keV. The detailed comparison was however impossible because of the absence in the literature of all necessary data belonging to the same experiment.
- The property of supercritical heating to heat mainly the passing particles shows that the efficiency of ICRF minority heating in stellarators may be higher than it was thought earlier, because the cone energy losses should be suppressed.

References

[1] D.F.H.Start et al. Proc. IAEA Technical Committee Meeting on Alpha-Particles in Fusion Research, Kiev, USSR, 1989, V. II, p.757.

[2] T.H.Stix. Nucl. Fusion, 1975, V.15, p.737.

[3] S.V.Kasilov, A.I.Pyatak, K.N.Stepanov. Fizika Plasmy (Sov. Journ. of Plasma Physics), 1990, V.16, p.959 (in Russian).

[4] S.V.Kasilov, A.I.Pyatak, K.N.Stepanov. Nucl. Fusion, 1990, V.30, p.2467.

[5] S.V.Kasilov, A.I.Pyatak, K.N.Stepanov. Proc. of the Joint Varenna-Lausanne Int. Workshop on "Theory of Fusion Plasma", Varenna, Italy, 1990. p.301.

[6] N.Marushchenko, U.Gasparino, H.Maaßberg, M.Romé. Report E041, this conference.

[7] G.D.Kerbel, M.G.McCoy. Phys. Fluids, 1985, V.28, p.3629.

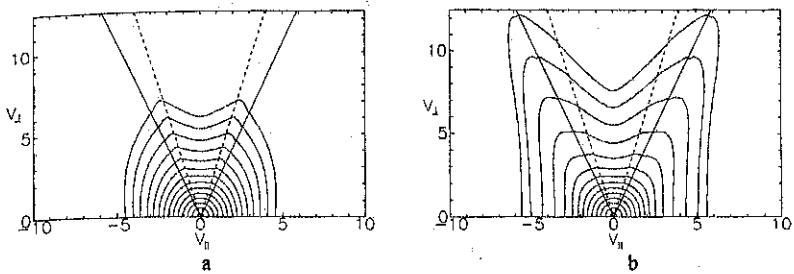

Fig.1. Contours of ^{3}He minority ion ditribution function computed for subcritical (a) and supercritical (b) minority models. Solid and dashed rays correspond to trapped-passing boundary and "maximum heating" line respectively.

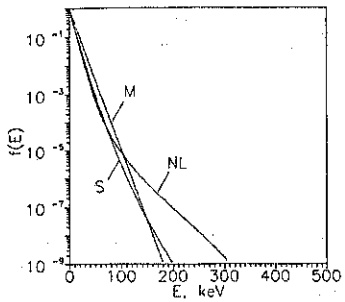

Fig.2. Minority distribution function over energies for particles with pitch angle in the magnetic field minimum $\chi = 0$. M - Maxwellian distribution, S - subcritical minority model, NL -supercritical minority model.

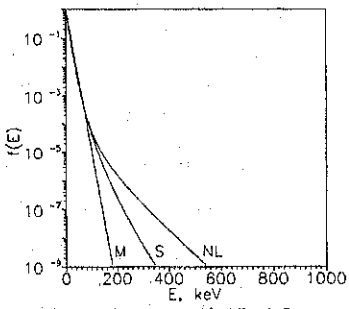

Fig.3. The same as in Fig.2 for $\chi = 90^o$ (zero parallel velocity).

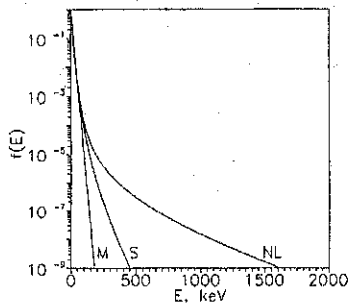

Fig.4. The same as in Fig.2 for $\chi = 64^o$ (trapped-passing boundary).

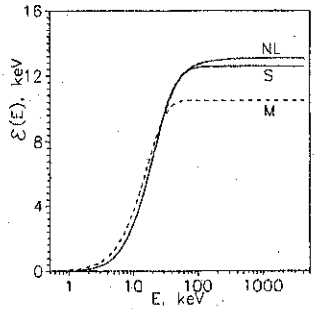

Fig.5. Total energy of the particles with energy below E normalized by the number of particles. M, S, NL mean the same as in Fig.2.

FAST WAVE HEATING AND CURRENT DRIVE IN TOKAMAK PLASMAS WITH NEGATIVE CENTRAL SHEAR*

C.B. Forest, C.C. Petty, F.W. Baity,† K.H. Burrell, J.S. deGrassie, A.W. Hyatt, R.I. Pinsker, M. Porkolab,‡ M. Murakami,† R. Prater, B.W. Rice,¤ and E.J. Strait

General Atomics, P.O. Box 85608, San Diego, California 92186-9784, U.S.A.

Fast waves provide an excellent tool for heating electrons and driving current in the central region of tokamak plasmas. In this paper, we report the use of centrally peaked electron heating and current drive to study transport in plasmas with negative central shear (NCS). Tokamak plasmas with NCS offer the potential of reduced energy transport and improved MHD stability properties, but will require non-inductive current drive to maintain the required current profiles. Fast waves, combined with neutral beam injection, provide the capability to change the central current density evolution and independently vary T_e and T_i for transport studies in these plasmas. Electron heating also reduces the collisional heat exchange between electrons and ions and reduces the power deposition from neutral beams into electrons, thus improving the certainty in the estimate of the electron heating. The first part of this paper analyzes electron and ion heat transport in the L–mode phase of NCS plasmas as the current profile resistively evolves. The second part of the paper discusses the changes that occur in electron as well as ion energy transport in this phase of improved core confinement associated with NCS.

Current drive and heating in L–mode plasmas with NCS

NCS formation. Plasmas with NCS are formed on DIII–D by heating the electrons with neutral beam injection during the current ramp-up phase of the discharge.[1,2] Operating at low density leads to high electron temperature and a long resistive diffusion time, freezing in a hollow current profile. Figure 1 shows time histories for a 1.6 MA discharge with 3.5 MW of neutral beam power injected during the current ramp. In this shot counter fast wave current drive (FWCD) was applied starting at 1.0 sec. The electron temperature immediately increases from 3 to 5.5 keV as the fast waves heat the electrons. There is also a small density rise associated with the rf. At the beginning of the rf injection, $q_{min} \approx 2.4$ and $q_0 \approx 3.0$ as measured by motional Stark effect spectroscopy.

Current profile modification. Counter current drive in the central region of the plasma enhances and maintains the shear reversal during the current profile relaxation. For comparison, q_{min} and $q_0 - q_{min}$ from a similar discharge with co current drive are also shown in Fig. 1. The current density is evolving towards a more peaked profile in both of these discharges as observed in the decreasing value of q_{min}. The difference between the time behaviors of q_{min} indicates centrally peaked counter current drive slows the rate at which the current profile peaks, while co current drive accelerates this process. The difference between the time behaviors of $q_{min} - q_0$, a quantity related to the degree of

*Work supported by the U.S. Department of Energy under Contracts DE-AC03-89ER51114, DE-AC05-96OR22464, and W-7405-ENG-48.

†Oak Ridge National Laboratory, Oak Ridge, Tennessee, U.S.A.

‡Massachusetts Institute of Technology, Cambridge, Massachusetts, U.S.A.

¤Lawrence Livermore National Laboratory, Livermore, California, U.S.A.

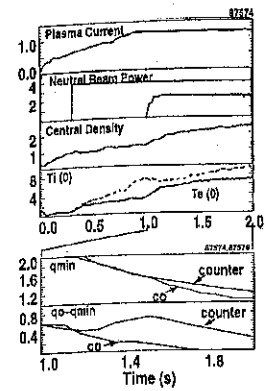

Fig. 1. Time histories for a L-mode NCS plasma with fast wave heating and counter current drive. q_0 and $q_0 - q_{min}$ are also shown for a shot with similar parameters but co current drive.

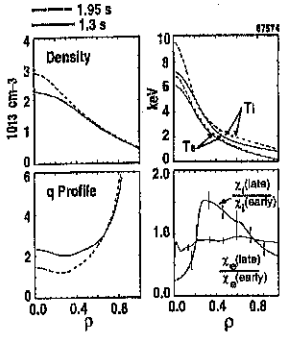

Fig. 2. Profiles at 1.3 sec (dashed) and 1.95 sec (solid) for the shot in Figure 1. The curves are spline fits to the data for T_e, T_i, and density. The q profiles are determined with an equilibrium reconstruction code and data from MSE. χ_e and χ_i are calculated from power balance using the transport code ONETWO.

central shear reversal, shows counter current drive maintains the negative shear for a longer duration than co.

q dependence of thermal transport. The scaling of global confinement with plasma current and internal inductance[3] implies that the local thermal transport is related to the poloidal field. Empirical T_e, T_i, density, q, and change in the thermal diffusivities χ_e, χ_i at 1.3 and 1.95 sec. Surprisingly, even though there is a large variation in q_{min}, from 1.8 to 1.0, χ_e drops by less than 15% over this time. Outside the NCS region, χ_i actually increases by 50%. This can be inferred from the profiles of T_e or T_i; $T_e$changes very little, while the slope of T_i flattens for $0.3 < \rho < 0.8$. The increase in T_i over this region is largely due to an improvement at the plasma edge. The increase in T_i and the corresponding drop in χ_i in the NCS region would appear to be correlated with the dropping q value, allowing the plasma to take on hot ion mode characteristics. The variation of transport at the location of q_{min} is interesting since the magnetic shear at this point is constant in time and equal to zero. This weak dependence of transport on q over much of the plasma cross section challenges previous explanations of the current scaling of transport.

Transport in NCS plasmas with improved core confinement and fast wave heating

Frequently, a reduction in the core transport is observed in the NCS configuration. A clear reduction in χ_i to neoclassical levels has been reported in neutral beam heated DIII–D plasmas,[4,5] as well as reduction of particle diffusivity for some NCS discharges. A small reduction in $\chi_e$was also inferred from DIII–D NCS discharges, but the uncertainty in the extent of the reduction was large because the direct heating of the electrons with neutral beams was small and significant uncertainty remained in the determination of the ion-electron heat transfer. Use of fast wave heating improves the certainty with which the electron heating is known.

Improved core confinement is found in 1.6 MA DIII–D plasmas when 5 MW of neutral beam injection is applied during the current ramp with low density ($< 1.5 \times 10^{13}\,cm^{-3}$), and an additional 2.5 MW is applied after flattop. The transition to improved core confinement occurs about 100 msec after the additional neutral beam power is applied and detected most easily in the central density, as

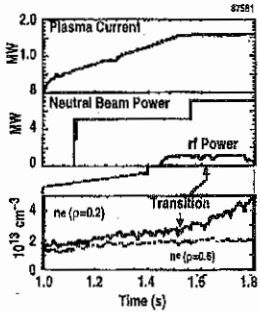

Fig. 3. Time histories for a NCS plasma with fast wave heating and improved core confinement starting at 1.55 sec.

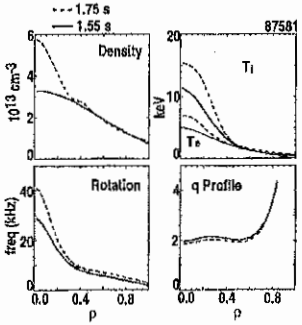

Fig. 4. Profiles before (1550 msec) and after (1750 msec) the transition in Fig. 3.

illustrated in Fig. 3. Coupling significant rf power to these L–mode plasmas has been difficult; H–mode transitions, triggered by additional rf heating, cause rapid changes in antenna loading which interfere with the transmitter operation. Nonetheless, 1.2 MW of rf power has been applied to this discharge starting before the additional neutral beam (shown in Fig. 3) and lasting through the transition to improved core confinement. This power level was sufficient to cause strong heating and peaking of the electron temperature inside the shear reversal region. Figure 4 shows the kinetic profiles at 1.55 and 1.75 sec, before and after the transition.

The fast wave power in the central region is the dominant source of electron heating in the power balance, but other terms are also important for accurately evaluating the change in χ_e. The transport analysis indicates that part of the apparent peaking is a result of the change in convective energy loss associated with the improved particle confinement after the transition. The change in the time derivative of the electron energy density and the increased ion-electron heat exchange are also important for evaluating the electron thermal transport. Figure 5 shows χ_e, χ_i, and χ_{mom} before and after the transition, with these effects properly accounted for. χ_i drops by an order of magnitude to neo-classical levels, while χ_e and χ_{mom} decrease by 50%, both remaining well above neoclassical levels. The physical mechanism causing ion thermal transport apparently causes some electron loss mechanism for these channels.

Role of q_{min} in the NCS transition. The phenomenology of the core transport barrier formation might be explained by various aspects of microturbulance theory.First, the negative magnetic shear allows stabilization of both macroscopic MHD modes (*e.g.*, sawteeth) and small scale MHD modes (*e.g.*, ballooning modes) in the plasma core. Then, according to one hypothesis, the microturbulence is stabilized by sheared $\vec{E}\times\vec{B}$ flow. As the pressure and plasma rotation in the plasma core build up, the radial electric field E_r also increases. If sufficient $\vec{E}\times\vec{B}$ shear develops, the rotational shear can stabilize microturbulence and a transport bifurcation can develop.[6,7] One criterion for the bifurcation is that the linear growth rate of the drift waves be offset by a shearing rate $\propto (p/q)(\partial/\partial p)(E_r/RB_p)$.[8] This shearing rate is most effective with low q_{min} and large momentum input. Another hypothesis suggests that the increased Shafranov shift associated with high-β_p in the central region of the plasma can lead to drift reversal of the trapped particles in that region, thereby stabilizing drift waves which are responsible for particle and

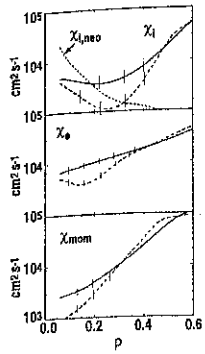

Fig. 5. χ_i, χ_e, and χ_{mom}, before and after the transition in Fig. 3.

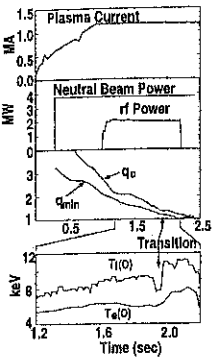

Fig. 6. Improved core confinement in an NCS discharge with a phase transition low q_{min} and substantial rf heating and counter current drive.

ion heat transport. The Shafranov shift of the central flux surfaces increases with q_{min}; thus, this model would predict that the transition would have a lower power threshold at high q_{min}, a different prediction than for rotational shear stabilization. Furthermore, this would be a potential mechanism for cases without momentum input such as balanced neutral beam injection.

NCS transitions at low NBI power, strong rf heating and low q_{min}. Spontaneous transitions to improved core confinement have been observed at lower neutral beam power using 2.2 MW of counter fast wave current drive and heating during the current flattop. Figure 6 shows time histories for the neutral beam power, rf power, and plasma current, and the central electron and ion temperature. At a time 1.95 sec, the T_e and T_i both increase, T_e increasing from 6 to 8 keV. Prior to and during the improved phase, the discharge has NCS, but with q_{min} just above 1. When q_{min} drops below 1 at 2.2 sec, the enhanced confinement mode is lost with the onset of sawteeth. T_e, T_i, and electron density all show reduced transport in the region of shear reversal. As above, the power balance analysis indicates that χ_e drops by less than 50%. The long delay between the turn on of the rf power and the transition in core confinement implies that the q profile is important for the transition; the low value of q_{min} makes the transition easier, thus implicating rotational shear stabilization as the mechanism for reduced transport.

References

[1]T.E. Strait, Phys. Rev. Lett. 75, 4421 (1995).
[2]B.W. Rice *et al.*, to appear in Plasma Phys. and Contr. Fusion (1996).
[3]J.R. Ferron *et al.*, Phys. Fluids B 5, 2532 (1993).
[4]L.L. Lao et al., Phys. Plasmas 3, 1951 (1996).
[5]B.W. Rice *et al.*, Phys. Plasmas 3, 1983 (1996).
[6]F.L. Hinton and G.M. Staebler, Phys. Fluids B 5, 1281 (1993).
[7]G.M. Staebler and F.L. Hinton, Phys. Plasmas 1, 99 (1994).
[8]R.E. Waltz, G.D. Kerbel, J. Milovich, and G. Hammett, Phys. Plasmas 2, 2408 (1995).

Efficient ICRF heating of D^+-H^+ plasma containing small boron admixture on T-11M tokamak.

Kovan I.A., Monakhov I.A., **Petrov Yu.V.**, Mirnov S.V.

Troitsk Institute of Innovative and Thermonuclear Investigations (TRINITI), 142092, Troitsk, Russia

Possibilities of ion heating by ICRF methods, based on fast waves (FW) excitation from the low magnetic field side (LFS) at frequencies $\omega_{cD}<\omega<\omega_{cH}$ in D-H plasma are believed to be questionable due to the effects of FW conversion to ion Bernstein waves (IBW) in the vicinity of ion-ion hybrid resonance. According to traditional approach (cut-off - resonance pair) FW-IBW conversion coefficient in this case should be small, moreover, IBW if excited should be damped quickly by electrons. In this paper we try to demonstrate that efficient central ion heating by LFS FW excitation in conditions of ion-ion hybrid resonance is still possible.

Basement of such statement is the following: recent theoretical analysis of FW-IBW conversion taking into account high magnetic field side (HFS) FW cut-off (cut-off-resonance-cut-off triplet treatment) has shown that 100% conversion can take place for certain values of wavenumbers $K_\parallel$ of FW excited from LFS [1,2]. I.e. experimental conditions are possible when internal plasma resonator formed by triplet cut-offs can be excited during LFS FW excitation with efficient energy transfer to IBW in conversion region. On the other hand, IBW can be efficiently damped by small fraction of third ion species if their cyclotron layer is located in the vicinity of the conversion region; subsequent energy transfer of this accelerated resonant admixture to major ions can cause their efficient central heating. Such method of ion heating was suggested in [3,4] for HFS excitation and second cyclotron harmonic of heavy Fe^{+23} (A=56) or Ne^{+10} (A=22) admixture in H-D plasma. We consider the lightweight, totally stripped ions of boron or beryllium to be more suitable for examined scenario. These elements enter into composition of the first wall coatings of majority of modern tokamaks, and ions of B^{+5} (A=11) or Be^{+4} (A=9) will inevitably present in central plasma. According to our estimates their quantity being small is not critical for IBW damping. Experiments on T-11M give some evidence that discussed method may be quite promising. Ion heating with efficiency up to $\eta_D=\Delta T_D(0)\cdot \bar{n}_e\cdot 10^{-13}/P_{RF}=15eV\cdot cm^{-3}/KW$ was registered during ICRF heating of D-H

plasma in conditions of L-H-like mode transition. (R_0/a_p=0.7m/0.19m, B_0=1.15T, I_p≈100kA, $\bar{n}_e \le 7\cdot10^{13}cm^{-3}$, $T_{e0}(OH)$≈400eV, $T_{i0}(OH)$≈150eV, n_H/n_D≈0.1÷0.15). Fast waves f=17.5MHz were injected from the low field side of the tokamak by poloidal loop antenna. The attained efficiency is 4-5 times higher than typical values for hydrogen minority ICRF heating regimes, which were observed earlier on a variety of tokamaks including T-11M [5] (Fig.1). High efficiency results were obtained on T-11M after the vacuum chamber wall boronization and coating of the main limiter and antenna Faraday screen with boron-containing films. Under these conditions the presence of a small boron admixture in D^+-H^+ plasma can lead to a strong IBW cyclotron damping at the layer of the second harmonic cyclotron resonance of fully ionized boron (Z=5, A=11, ionization potential 340eV) with subsequent efficient energy transfer to the bulk ion component. Important role in this case plays the choice of the optimum hydrogen content, which makes it possible to locate FW-IBW conversion layer in the vicinity of B^{+5} 2nd harmonic layer (X≈-6cm) and to avoid IBW electron damping.

Fig.2 shows the calculated dependence of conversion layer position (a) and fraction of IBW power, absorbed by plasma species (b), on relative hydrogen content. Because a full-wave modeling in conditions of ion-ion hybrid resonance is formidable task, the results of Fig.2(b) were calculated using 3D ray tracing code [6] for 15 IBW rays ($K_t=1/R_0 \div 15/R_0$) excited in tokamak midplane. Such calculations underestimate power absorption by hydrogen and deuterium at low n_H/n_e due to their direct cyclotron interaction with FW, nevertheless it is clear that at n_H/n_e≈10% the power input to B^{+5} ions can exceed significantly the power input to other plasma species. Numerical simulations predicted also very sharp profile of power absorbed by boron in vicinity of $\omega=2\omega_{cB+5}$. The fraction of IBW power, absorbed by B^{+5} appeared to be almost independent on boron concentration for n_{B+5}/n_e=0.3÷3%, it rises with electron concentration and inversely proportional to K_t. Thermalization characteristics of accelerated ions were also examined numerically according to Stix theory [7] for T-11M conditions. The shape of stationary distribution function of minority ions, formed under simultaneous action of RF-fields and Coulomb collisions, depends on parameter $\xi=\langle p\rangle/p_o$, where $\langle p\rangle$ is RF power absorbed by resonant ions per unit volume (averaged over magnetic surface) and $p_o=8\pi^{1/2}n_e n Z^2 e^4 \ln\Lambda/mV_e$ (n,Z,m refer to resonant ions). In stationary conditions, all the power gained by minority ions is delivered to bulk ions and electrons, so that

$\langle p \rangle = p_i + p_e$ where p_i - power density delivered from resonant ions to bulk ions, p_e - to electrons. Note that ξ is independent on minor ions concentration , because both $\langle p \rangle$ and p_e are proportional to it. Fig.3(a) shows energy distribution functions for various types of resonant minority ions: H^+, He^{++} (A=3) and B^{+5} (A=11) calculated according to [7], assuming fundamental harmonic heating and pitch-angle isotropy. The huge "tail" on H^+ - distribution function grows because of protons' bad drag on background ions which takes place at low Z and high RF power density levels. For such the distribution the main part of resonant ions energy is delivered to electrons, rather than to background ions. Fig.3(b) shows that there is a maximum value ξ^* for each type of resonant ions, before which ($\xi<\xi^*$) almost all the power gained by resonant ions is delivered to background ions ($\langle p \rangle \approx p_i$) , and after which ($\xi>\xi^*$) large fraction of $\langle p \rangle$ goes to electrons (undesirable region). According to our analytical consideration the value of ξ^* is proportional to $Z^4/A^{3/2}$, so it is clear that using B^{+5} is much more preferable for heating major ions than using H^+ or He^{++}. It should be noted that Fig.3 is valid for fundamental minority FW heating, rather than the 2nd harmonic IBW heating as in T-11M case. However, it is known that IBW heating does not cause strong resonant ions "tail" formation even at high cyclotron harmonics. So one should expect that in scenarios similar to that in T-11M the resonant minor ions would deliver their energy mainly to background ions even at higher values of ξ than it follows from Fig.3.

Thus, cyclotron acceleration of small fraction of totally stripped boron (beryllium) ions by IBW, converted from FW in the vicinity of ion-ion hybrid resonance looks quite promising method of central ion heating even for low magnetic field side FW excitation.

REFERENCES

[1] Majeski R., Phillips C.K., Wilson J.R., Phys.Rev.Lett., Vol.73, 2204 (1994).

[2] Ram A.K.,et.al., Contr.Fusion and Plasma Phys. (Proc.22 EPS Conf., Bournemout,1995), Eur.Phys.Society, Part IV,Vol 19C, 353 (1995).

[3] Longinov A.V., Stepanov K.N., in Soviet book "RF plasma heating", Gorky, 1983.

[4] Grekov D.L., D'yakov V.E., Longinov A.V., Contr.Fusion and Plasma Phys. (Proc.13 EPS Conf., Schlirsee,1986), Eur.Phys.Society, Part II, Vol 10C, 389 (1986).

[5] Azizov E.A., et al, Contr.Fusion and Plasma Phys. (Proc.19 EPS Conf., Innsbruck,1992), Eur.Phys.Society, Part I, Vol 16C, 47 (1992).

[6] Petrov Yu.V., Nuclear Fusion, Vol.34, 63 (1994).

[7] Stix T.H., Nuclear Fusion, Vol.15, 737 (1975).

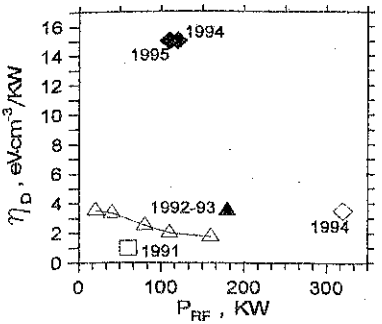

Fig.1 D^+ heating efficiency vs. injected RF power in different experimental campaigns; ■ - molybdenum first wall, limiter and antenna screen; ▲ - boronized first wall, molybdenum limiter and antenna screen; ◆ - boronized first wall, B_4C coated limiter and antenna screen. Hollow symbols refer to regimes without additional horizontal equilibrium control magnetic field.

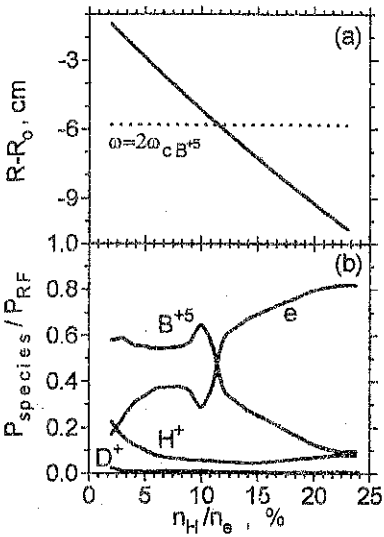

Fig.2 (a) - Location of FW-IBW conversion layer versus relative H^+-concentration, for $K_{||}=3/R_0$; horizontal line shows the location of 2nd harmonic cyclotron resonance layer of B^{+5} ions.

(b) - Fraction of RF-power delivered to different species of plasma versus relative hydrogen concentration.

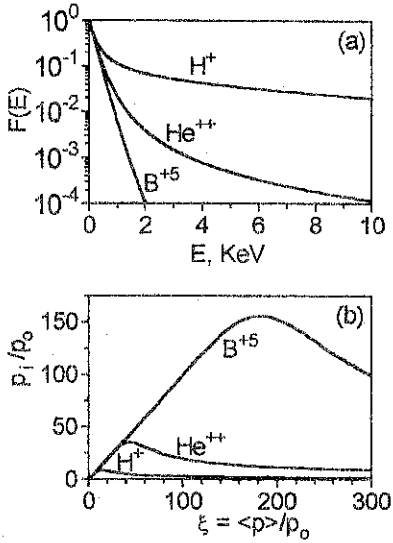

Fig.3 (a) - Stationary distribution functions for various types of resonant minor ions; fundamental harmonic FW heating is assumed; $\xi = <p>/p_o = 30$ for all curves.

(b) - Power density delivered from resonant ions to background ions through Coulomb collisions as a function of powerdensity <p> gained by resonant ions from RF field.

Effect of a Nonuniform Radial Electric Field on Sheared Toroidal Rotation and Bootstrap Current

Andrey A.Kabantsev
Budker Institute of Nuclear Physics
Lavrentyev avenue 11, Novosibirsk 630090, Russia

Introduction

Non-inductive current generation has important applications to future tokamak reactors like steady state operation and current density profile control. Recent results [1–3] point to the beneficial effects of negative magnetic shear on plasma confinement in tokamaks. The enhanced reversed shear (ERS) mode can be achieved only with a hollow current density profile which, in steady state operation, must be maintained by an external method of non-inductive current drive. The off-axis current maximum can be affected by the non-inductive bootstrap current generated by the pressure gradient. Bootstrap current is regarded as a serious candidate for non-inductively driving a significant fraction of the total current. High bootstrap fraction discharges have already been achieved and analyzed in several tokamaks, including JT-60 [4], TFTR [5] and DIII-D [6]. In this context, bootstrap current density profile distortion by any mechanism is essential for understanding ERS experiments and ultimately for implementing current profile control.

This paper presents a new current drive mechanism generated by a significant shear in toroidal rotation driven by non-uniform radial electric field. The physical origin of the mechanism lies in the difference of the mean toroidal drift velocities (E_r/B_θ) between the trapped electrons and ions due to the effect of the ion finite banana width coupled to the plasma pressure gradient ($\partial P/\partial r$) and electric field inhomogeneity ($\partial E_r/\partial r$). These result in a current along the magnetic field line, analogous to the neoclassical bootstrap current due to pressure gradient only. The high E_r and pressure gradients would generate a strong off-axis bootstrap current and sustain the hollow current density profile.

Recent experiments and theories show that both the radial electric field and the toroidal rotation play an important role in the L/H mode transition and have a dominant influence on the improvement of plasma confinement. In experiments it has been observed that the strong toroidal rotation is well correlated with the plasma confinement. These effects were attributed to the creation of edge radial electric field E_r and associated plasma potential shift much larger in magnitude than (T_i/e). Stabilization of turbulence by the sheared $\mathbf{E} \times \mathbf{B}$ flow associated with the strong rotational velocity shear may also play a role in creating the anomalous perpendicular viscosity, which is dominant in dictating the toroidal rotation in tokamaks.

The published theories of the bootstrap current neglect the radial electric field inhomogeneity encountered by the ion along its banana orbit. The negligence in the impact of this inhomogeneity on the ion toroidal drift velocity (E_r/B_θ) is valid if the E_r gradient scale length ($L_E \equiv \mid \nabla \ln E_r \mid^{-1}$) of the $E-$shear layer over which the velocity shear occurs is large compared with the width of the ion banana orbit, $\Delta_b = q\rho_i\epsilon^{-1/2}$. Here q

the safety factor, ρ_i the ion Larmor radius and $\epsilon = a/R$ the inverse aspect ratio. If L_E is comparable with ion banana width Δ_b, the shear of the radial electric field will strongly modify the toroidal rotation velocity and cannot be neglected. Since the ion banana width greatly exceeds the electron banana width, the impact of the E_r shear on the electron toroidal rotation velocity is therefore reduced. This change in relative velocity of electron and ions in their toroidal flow seems to be sufficient to produce a significant bootstrap current variation in a $E-$shear layer.

Equations

Charged particles in a magnetized toroidal plasma are forced to experience a high-frequency radial excursion due to their Larmor and banana orbits. As a consequence, in the presence of a pressure gradient the bootstrap current j_{bs} arises, that scales as [7]

$$j_{bs} \approx -\frac{\epsilon^{1/2}}{B_\theta}\frac{\partial P}{\partial r}. \tag{1}$$

To evaluate the effect of the non-uniform profile $E_r(r)$ on bootstrap current distortion in a E_r-shear layer we apply a simple model integrating the radial electric field along the ion banana orbits. Consider the magnetic surface at radial position ($r_O \gg \Delta_b$). In the presence of plasma density and radial electric field gradients the instantaneous toroidal rotation profile differs from the guiding center profile. The effect is proportional to the radial excursion squared, so it is negligible for electrons with respect to ions. As a consequence, the electrons feel the bare field $E_r(r_0)$ and so their toroidal flow component, connected with the $E_r \times B_\theta$ drift, is $n_e u_e(r_0) = n_e(r_0)E_r(r_0)/B_\theta$. The same component of the ion toroidal flow on this magnetic surface, averaged over a banana orbit, is given by

$$\langle n_i u_i(r_0)\rangle \approx n_i(r_0)\frac{E_r(r_0)}{B_\theta}(1 + \alpha \cdot \Delta_b^2 \cdot \nabla \ln n \cdot \nabla \ln E_r). \tag{2}$$

Here α is the geometric factor of order unity depending on the banana orbit configuration and it is assumed that the second- or higher-order derivatives of $n(r)$ and $E_r(r)$ are relatively small. A large shear of the E_r would also imply on appreciable squeezing of banana orbits, but in the present paper these details will not be included for simplicity. Thus, in the present model we have a difference in the net toroidal flow velocities between the electrons and trapped ions.

Hence, the additional current component δj_{bs}, correcting the neoclassical bootstrap current j_{bs}, may be written in the following useful form using the Eqs.(1),(2).

$$\delta j_{bs} = -\alpha \cdot \Delta_b^2 \cdot \frac{e}{T_i} \cdot \frac{\partial E_r}{\partial r} \cdot j_{bs}. \tag{3}$$

Here e is the charge of ions. For $(\partial E_r/\partial r < 0)$ the ions drift in the direction of the bootstrap current (co-direction) in the $\mathbf{E}_r \times \mathbf{B}_\theta$ drifting frame of the electrons.

Relevant parameter range, experimental data

It can be seen from Eq.(3), that in the case of strong fall of the edge radial electric field, where T_i is relatively small and the T_i gradient scale length $L_i \equiv T_i/(\partial T_i/\partial r)$ and, consequently, the thickness L_E of $E-$shear layer become comparable to the ion poloidal

gyroradius (banana width), the current term δj_{bs} corresponding to the sheared toroidal rotation can be comparable with j_{bs} at a radius where the $E_r(r)$ gradient is largest. By comparison with Eq.(3), we see that this specific condition is equivalent to assuming the thin layer L_E (on the order of the ion poloidal gyroradius) of the strong radial electric field E_r:

$$eE_r\Delta_b \cdot \frac{\Delta_b}{L_E} \sim T_i. \tag{4}$$

A key issue of this model is how one can obtain the strongly sheared toroidal rotation in tokamak plasmas. A physical mechanism for the onset of thin layer of strong radial electric field in torus plasma assumes that the radial electric field and its structure are produced not by the momentum input but by a radial current associated to ion orbit losses. This current is balanced by a neutralizing current, whose expression is not universally accepted in literature, and which may be due collisions with neutrals [8] or to plateau neoclassical contributions [9], or to ion–ion viscosity [10]. The ion orbit loss current and the neutralizing current are depend on the electric field amplitude. Above a critical electric field $E_{cr} = v_{Ti}B_\theta$ the effective radial conductivity drops abruptly, so a thin layer of high radial electric field and an associated non-uniform $\mathbf{E} \times \mathbf{B}$ drift velocity profile is formed at the plasma. These effects were attributed to the creation of edge radial electric field E_r and associated plasma potential shift much larger in magnitude than (T_i/e). Nevertheless, it is still uncertain the question of how the radial electric field is determined in the quasi-steady state of non-ambipolar fluxes in axysimmetric systems. However, it is clear that the plasma can have a negative potential and that the sheared toroidal rotation due to this occurs without any direct momentum input but to the radial electric field induced by loss of ions. A detailed discussion of this process, as well as the other processes determining toroidal rotation, is beyond the scope of the present paper.

A relevant example of the strongly non-uniform radial profiles of the E_r and the sheared toroidal rotation velocity were observed in experiments with perpendicular neutral beam injection in JIPP TII-U [11]. The plasma rotation profile was hollow and was significantly different from that observed on plasmas heated with tangential neutral beams. The direction and the radial structure of the toroidal rotation velocity cannot be explained by the momentum input of NBI. Our estimations of value of $(\delta j_{bs}/j_{bs})$ for these experiments show that it reaches $0.2 \div 0.5$ at a radius $r \approx (2/3)a$, that help to quantify the effects of non-uniform toroidal rotation on the plasma behavior.

The anomalous axial current behavior suggesting the influence of the current, driven by the sheared axial $E_r \times B_\theta$ drift has also been observed in open trap AMBAL-M experiment [12]. At the steady state the axial current over a wide central plasma region is many times as much as initially effused from plasma source seed current [not yet published].

Besides this direct influence of sheared toroidal rotation on bootstrap current in the shear layer, under some circumstances it may be as the case of Kelvin-Helmholtz instability, which will provide the anomalous velocity of radial diffusion [13] and thus will affect on bootstrap current value due to the fact that the bootstrap current is related to the radial velocity of diffusion as $j_{bs} \sim V_{r,diff}B_\theta$.

An important component of the considered current drive mechanism is the source of a thin shear layer ($L_E \sim \Delta_b$) of a nonuniform radial electric field. There are presently two plausible mechanism which have the strong influence on the radial electric field distribution and so they have the potential to provide a spatially tunable current source. Some recent experiments [11] show that both the neutral beam injection and the ICRF pulse can create a sufficient radial electric shear. There is some degree of control of rotation

profiles primarily through neutral beam heating. However, the detailed analysis of these processes, as well as the other processes determining toroidal rotation, is beyond the scope of the present report.

Summary

Thus, it might be important to take the effect of non-uniform radial electric field on bootstrap current into account for comparing with theory the results of shear reversal experiment with high bootstrap current fraction. The non-inductive current component proportional to radial electric field gradient becomes large in case of $(\partial E_r/\partial r)\Delta_b{}^2 \sim (T_i/e)$. Electron root ($\partial E_r/\partial r > 0$) and ion root ($\partial E_r/\partial r < 0$) correspond to the reduction and enhancement of the bootstrap current, respectively. The high E_r and pressure gradients can to generate a strong off-axis bootstrap current and to sustain the hollow current density profile.

Finally, a series of experiments on NB and ICRF-driven strong sheared toroidal rotation plasmas were performed on JIPP TII-U [11] and DIII-D [6] tokamaks. Results are still being analyzed and will be reported elsewhere, but preliminary analysis indicates that significant distortion of the neoclassical bootstrap current was achieved.

References

[1] E.A.Lazarus *et al, Phys. Fluids B* **3** 2220 (1991)
[2] M.Hugon *et al, Nucl. Fusion* **32** 33 (1992)
[3] S.H.Batha *et al, Proc. 22nd EPS Conf. Plasma Physics* **II** 113 (1995)
[4] M.Kikuchi *ISPP-16 "Piero Caldirola"* SIF, Bologna, 1994
[5] M.C.Zarnstorff *et al, Phys. Fluids B* **2** 1852 (1990)
[6] B.W.Rice *Physics of Plasmas* **3** 1983 (1996)
[7] A.A.Galeev, R.Z.Sagdeev, in *Rev. of Plasma Physics*, ed. by M.A.Leontovich Vol. 7, Consultants Bureau, New York, 1979
[8] H.Xiao *et al, Phys. Fluids B* **5** 4499 (1993)
[9] T.E.Stringer, *Nucl. Fusion* **33** 1249 (1993)
[10] R.R.Weinants *et al, Nucl. Fusion* **32** 837 (1992)
[11] K.Ida *et al, Nucl. Fusion* **31** 943 (1991)
[12] T.D.Akhmetov *et al, Characteristics and Mechanisms of Hot Initial Plasma Creation in the End System of AMBAL-M,* this conference
[13] A.A.Kabantsev, S.Yu.Taskaev, *Soviet J. of Plasma Physics* **16** 406 (1990)

LOCALISED GLOBAL EIGENMODES AND MODE CONVERSION ZONES IN ICRF

V.E.Moiseenko* and E.Tennfors

The Royal Institute of Technology, S-100 44 Stockholm, Sweden

*Permanent affiliation: IPP NSC Kharkov Institute of Physics and Technology, 310108 Kharkov, Ukraine

As is well known, the Alfvén wave forms a continuum spectrum in a tokamak plasma. It has gaps in which specific global modes -Toroidicity Induced Alfvén Eigenmodes (TAE) - have been found [1]. The Alfvén continuum has the extension to ICRF. It is studied for some limiting cases in [2-4]. Like the Alfvén continuum, it has gaps and extremum points in the vicinity of which localized global eigenmodes can be found [4]. In the present report, the study of the ICRF continuum and localized eigenmodes is presented.

To describe local resonances (continnum spectrum) and localized eigenmodes, the near - magnetic surface approach [4] can be used. We assume infinite conductivity along magnetic field lines: $\vec{B}_0 \cdot \hat{\varepsilon} \cdot \vec{B}_0 = \infty$ ($\hat{\varepsilon}$ is a dielectric tensor) and that the ion Larmor radius is small. Both local resonances and TAE-like modes are characterised by sharp spatial dependence of the electric field components in the radial direction. In this approximation, Maxwell's equations can be reduced to the following form:

$$\frac{d^2u}{d\vartheta^2} + G \cdot u = C, \qquad (1)$$

with $G = \frac{\omega^2}{c^2}\frac{B_0^2}{B_\varphi^2} q^2 \varepsilon_\perp R^2$, $\varepsilon_\perp = \varepsilon_{rr}$, $u = \exp(i\beta\vartheta)\cdot E_r$, $\beta = nq$, n is the toroidal Fourier mode number and q is the tokamak safety factor. In the Eq.(1), the poloidal inhomogeneity, which originates from the curvilinear toroidal geometry, is neglected because the inhomogeneity of $\varepsilon_\perp$ is more strong in ICRF.

The general solution of equation (1) is

$$u = u_C + A_1 \cdot u_1 + A_2 \cdot u_2, \qquad (2)$$

where u_C is the specific solution, driven by the right-hand part of the equation (2), u_1 and u_2 are linearly independent solutions of the homogeneous equation. Coefficients A_1 and A_2 can be defined after applying of the periodic boundary conditions for E_r.

$$A_1 = (d_C' \cdot d_2 - d_C \cdot d_2')/D, \quad A_2 = (d_C \cdot d_1' - d_C' \cdot d_1)/D, \text{ where } D = d_1 \cdot d_2' - d_1' \cdot d_2; \qquad (3)$$

$$d_i = \exp(-i\pi\beta)\cdot u_i\big|_{\vartheta=\pi} - \exp(i\pi\beta)\cdot u_i\big|_{\vartheta=-\pi},$$
$$d_i' = \exp(-i\pi\beta)\cdot du_i/d\vartheta\big|_{\vartheta=\pi} - \exp(i\pi\beta)\cdot du_i/d\vartheta\big|_{\vartheta=-\pi}, \qquad i=1,\ 2,\ C \qquad (4)$$

For most fusion devices the condition $|G| >> 1$ is realised in the major part of the plasma column. Therefore, the WKB approximation is valid there. In the region where it is less accurate or breaks, we use parabolic cylinder functions (we assume that there are no

cyclotron resonances on the magnetic surface under consideration). In this approximation, the expressions (3) can be written in the following form:

$$D = 4i \cdot \left[\cos(\Gamma) - T \cdot \cos(2\pi\beta)\right], \tag{5}$$

$$A_{1,2} = 2i \frac{S \cdot \exp(i\Gamma) \cdot V_{1,2} + i\left[T\exp(i\Gamma) - \exp(\mp 2i\pi\beta)\right] \cdot V_{2,1}}{D}, \tag{6}$$

where $\Gamma = \int\limits_{\mathrm{Re}G>0} \gamma \cdot d\vartheta$, $V_{1,2} = \int\limits_{-\pi}^{\pi} u_{1,2} C d\vartheta$, $\gamma = \sqrt{\pm G}$ (the sign should be chosen so that real part of the expression under the root is positive); S and T are the reflection and transmission coefficients $S = (k^2 - 1)/(k^2 + 1)$, $T = 2k/(k^2 + 1)$, $k = \sqrt{1 + \exp(2a)} - \exp(a)$; if $\mathrm{Re}\,G \geq 0$, $a = -\pi G/\sqrt{2G''}$ in the point of G minimum; if there is a region on the magnetic surface where $\mathrm{Re}\,G < 0$, $a = \int\limits_{\vartheta_l}^{\vartheta_r} \gamma \cdot d\vartheta$. $\vartheta_{r,l}$ should be derived from the equation: $\mathrm{Re}G\big|_{\vartheta=\vartheta_{r,l}} = 0$.

Because we do not write the complicated expressions for the two linearly independent solutions, it must be specified here that u_1 describes the transmission and reflection of the wave launched in the positive ϑ direction, while u_2 - in the negative.

To study local resonances or localised eigenmodes, the first to look for is points where determinant D is close to zero. If $D = 0$ and $\partial D/\partial r \neq 0$. there is a local resonance (continuum wave) at this point. If

$$D = 0; \quad \partial D/\partial r = 0, \tag{7}$$

there are two possibilities: splitting of local resonances or localized eigenmode.

Resuming the analysis of formulas (5) and (6), it is necessary to mention that Γ and β are phases. They appear in the expressions only as arguments of circular functions. Unlike them T controls the amplitude of the functions. Therefore, concerning T behaviour, there are the three following cases.

The first case is $T \equiv 1$. This case implies that $\varepsilon_\perp > 0$ on the magnetic surface and WKB approximation is accurate. From formulas (2), (5) and (6) we have

$$u \approx \frac{u_2 V_1}{2 \cdot \sin(\pi\beta + \Gamma/2)} - \frac{u_1 V_2}{2 \cdot \sin(\pi\beta - \Gamma/2)}. \tag{8}$$

This means that modes u_1 and u_2 are uncoupled. Every mode has its own denominator and, therefore, its own local resonances and local eigenmodes. Zeros of denominators give the same local resonance conditions as for the Alfvén resonance:

$$m + nq = \pm \frac{\omega}{c} \sqrt{\varepsilon_\perp} qR. \tag{9}$$

For localised eigenmodes it is necessary to meet the additional condition mentioned above (see Eq.(7))

$$\partial(\pi\beta \pm \Gamma/2)/\partial r \approx 0. \tag{10}$$

The Eqs. (9) and (10) together determine a pair of eigenvalues: ω and r, forming a discrete spectrum. It is evident that they have a solution r=0. It corresponds to the global resonance of the fast Alfvén wave - GAE- the Global Alfvén Eigenmode [5] in ICRF.

If $T \neq 1$, the first that should be mentioned is the appearance of gaps in the continuous spectrum. The condition for the appearance of gaps follows from Eq.(5)

$$|\cos(\Gamma)| > T. \qquad (11)$$

If this condition is met the determinant D never turns to zero for any toroidal mode number n. From the RF heating point of view (fixed frequency) Eq.(11) determines the "forbidden" zones in the plasma column.

One can expect new phenomena when a local resonance in the WKB case (T=1), becomes a forbidden zone for $T \neq 1$. This is the case when $\cos(\Gamma) \approx \cos(2\pi\beta) \approx \pm 1$. This condition means that the resonances for u_1 and u_2 modes are very close to each other (see the Eq.(8)). The physical nature of the effects in the forbidden zone can be understood as coupling of these two modes because of reflections from the region where the WKB approximation is not valid.

The mentioned conditions can be written in another more conventional form

$$\int_{-\pi}^{\pi} \frac{\omega}{c} r \cdot \csc\alpha \cdot \sqrt{\varepsilon_\perp} \cdot d\vartheta \cong \pi(m_1 - m_2); \quad 2nq \cong -(m_1 + m_2), \qquad (12)$$

where m_1 and m_2 are coupled poloidal mode numbers. These conditions are similar to those for the TAE mode in the Alfvén range of frequencies [1]. Note that the conditions (12) mean nothing more that enhanced coupling. The result becomes clear from the analysis of the expression (5) for the determinant.

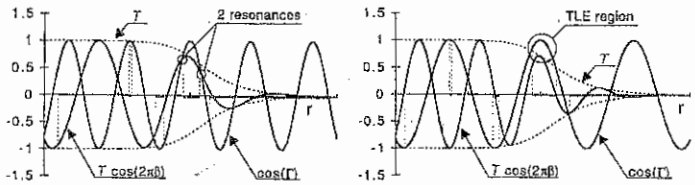

Fig.1 The radial behaviour of the terms which the equation (5) comprises for the two cases: (a)-- $\partial\Gamma/\partial r > \partial(2\pi\beta)/\partial r$ - the splitting resonance case; (b)-- $\partial\Gamma/\partial r < \partial(2\pi\beta)/\partial r$ - TLE case. Forbidden zones are indicated by shaded marks along the r-axis.

Fig.1 displays the behaviour of the two terms this expression. If their curves intersect each other, there is a pole in E_r, i.e. a local resonance. If the curves come close without intersection, this can be interpreted as localised mode. There are two cases in respect to the ratio of radial derivative of cosine phases Γ and $2\pi\beta$ in the resonant point. It is evident from Fig.1, that if $\partial\Gamma/\partial r > \partial(2\pi\beta)/\partial r$ the mode coupling leads to splitting of local resonances. In other words, the local resonances are moved from the forbidden zone to the left and to the right. In the opposite case, $\partial\Gamma/\partial r < \partial(2\pi\beta)/\partial r$, the two coincident resonances, which existed in the case of T=1, dissapear. The determinant D does not turn to zero but have a close to zero extremum near the resonant point, which means a local increase of the

electromagnetic field. It can be interpreted as a TLE – TAE-like eigenmode [4]. When the transmission coefficient T is close to unity the field distribution in this mode is the following:

$$u \propto \left(V_1 u_1 + V_2 u_2\right)/D. \tag{13}$$

It is very specific that the numerator of this formula does not contain diagonal terms (compare with formula (8)), but only transverse ones. So, each mode is driven mainly by the coupled one. It is necessary to mention, that in the framework of the present consideration the relation between V_1 and V_2, which depends on boundary conditions cannot be resolved. Therefore, the relative amplitude of the two modes which TLE consists in remains undefined here.

Note that the transmission coefficient T and, therefore, the coupling power, does not depend on the poloidal numbers of coupled modes. So, and this is the difference between TAE and TLE, the coupling of modes with very different m_1 and m_2 becomes possible.

The third case which we consider is $T \approx 0$. This is a case of deep (in WKB sense) $\varepsilon_\perp < 0$ zone. The pair of solutions u_1 and u_2 has the Wronskian proportional to T. This means that they are degenerate and we have a single-mode case. This is the eigenmode of the Eq.(1) which is trapped in the region $\varepsilon_\perp > 0$. It is little sensitive to the external periodic boundary conditions because the reflections from the $\varepsilon_\perp < 0$ zone are more important.

The asymptote of the transmission coefficient is

$$T \approx \exp(-a). \tag{14}$$

With this expression for T the continuum condition D=0 is the similar to that studied in papers [2-4]. In the zero order expansion over T we have for this eigenmode

$$u = i\frac{\left[V_1 - \exp(-2i\pi\beta)\cdot\sin(\Gamma)\cdot V_2\right]\cdot\left[\sin(\Gamma)\cdot u_1 - \exp(2i\pi\beta)\cdot u_2\right]}{2\cdot\cos(\Gamma)}. \tag{15}$$

Note that near the determinant zeros the ratio between u_1 and u_2 is fixed, which is characteristic for the one-mode case. Thus, nothing like TAE can be expected here.

However, the conditions (7) can be met together for this case. This is because Γ usually has one maximum over r. This means that the localised eigenmode can exist. In [4] it was called OHE (Original Hybrid Eigenmode). In the polarisation and radial dependence of electric field, this eigenmode is similar to the fast Alfvén wave global eigenmode considered above for the case T=1. The main difference is that while the second one is a travelling wave along the magnetic field line, the OHE is a standing wave. The dispersion of these waves are also different.

REFERENCES

[1] Chance M S and Cheng C Z 1986 *Phys. Fluids* **29** 3695
[2] Tennfors E 1986 *Plasma Phys Control. Fus.* **28** 1483
[3] Moiseenko V E 1989 *Sov. J. Plasma Phys.* **15** 214
[4] Moiseenko V E 1994 21st EPS Conf. on Contr. Fusion and Plasma Phys., Montpellier, France, Vol.18B, part I, P.50
[5] Appert K, Gruber R, Troyon F and Vaclavik J 1982 *Plasma Phys.* **24** 1147

PLASMA PRODUCTION BELOW THE ION CYCLOTRON FREQUENCY WITH CRANKSHAFT TYPE ANTENNA.

V.E. Moiseenko, **V.V. Plyusnin**, A.I. Lyssoivan*, E.D. Volkov, N.I. Nazarov, S.V. Kasilov, A.P. Litvinov.

Institute for Plasma Physics, National Science Center "Kharkov Institute of Physics and Technology", 310108 Kharkov, Ukraine
* - Laboratoire de Physique des Plasmas-Laboratorium voor Plasmafysica, Association "Euratom-Belgian State", Ecole Royale Militaire-Koninklijke Militaire School, B-1000 Brussels, Belgium.

INTRODUCTION. Recent plasma RF production and heating experiments [1] with three-half-turn (THT) antenna [2] showed that it could be effectively used only for plasma heating and density ramp-up. However, it requires the additional source of low density plasma ($n_e \geq 4 \times 10^{11}$ cm^{-3}). Such a scenario with two different sources of RF power for one purpose looks complicated. To avoid this disadvantage and to enable the reliable production and heating of dense ($n_e \geq 2 \times 10^{13}$cm^{-3}) plasma in the range of frequencies $\omega < \omega_{ci}$ the crankshaft antenna has been proposed and optimized for the URAGAN-3M (U-3M) torsatron [3]. This antenna is a combination of THT and 4 frame antennae [3] resulting in a curved, like a crankshaft, form of the central strap of antenna. RF current in the central strap has a double value and opposite phase with respect to the currents in the side straps. As it was shown in [3] the addition of crankshaft modulation to the central strap of antenna leads to strong increase of the RF power coupled to plasma at the low density stage and enables the nearly constant rate of plasma build-up process. From the other hand, the efficiency of this antenna at the stages of dense plasma production and heating is very close to the THT antenna's. The increase of the crankshaft antenna efficiency at the plasma break-down stage is a result of excitation of slow modes with high azimuthal wave numbers.

The optimization of crankshaft antenna to the conditions of the U-3M experiments has been performed by 1-D RF code [3]. Fig.1 shows the schematic view of crankshaft type antenna which has been manufactured, installed and tested during plasma production experiments in the U-3M torsatron.

This paper presents the first experimental results on plasma production by crankshaft antenna in the U-3M torsatron. Using the optimization technique [3], similar to used for U-3M and for the TEXTOR tokamak [4], a crankshaft antenna version is proposed for ICRF assisted plasma start-up in the ASDEX-UPGRADE tokamak.

ANALYSIS OF THE FIRST EXPERIMENTS ON PLASMA PRODUCTION WITH THE CRANKSHAFT ANTENNA IN THE URAGAN-3M TORSATRON. The URAGAN-3M device is an l =3, m=9 torsatron with major radius R=1 m, average plasma radius a=12 cm and range of magnetic field values B_0 = 0.1-1.1 T. A characteristic feature of device is that its magnetic system (helical winding and 4 coils of vertical magnetic field) together with the supporting construction is enclosed into a large vacuum tank for ensuring the open helical divertor operation [5]. The crankshaft antenna with optimal sizes [1-3] (l_z =24 cm and l_φ =40 cm) has been installed at the average minor radius r=16 cm from the low field side.

The antenna is covered by thin layer of TiN in order to reduce metal impurities release from its surfaces into the plasma. The plasma production scenario in the range of frequencies $\omega<\omega_{ci}$ has been realized at the heating frequency f = 8.3 MHz and confining magnetic field range of 0.6 T $\leq B_0 \leq$0.8 T. The experiments have been carried out with the steady-state neutral hydrogen puffing into vacuum chamber.

Fig.2 presents one of the typical shots in the first experimental session with the crankshaft antenna. The temporal evolution of plasma density and RF current in the crankshaft antenna are shown. The plasma with density about of 10^{13} cm^{-3} was successfully produced by crankshaft antenna without any additional pre-ionization. Fig.3 presents the results of crankshaft antenna testing when the confining magnetic field and neutral gas pressure values have been varied.

The dynamics of plasma build-up at the stages of breakdown and neutral gas burn out observed in experiments has been analyzed using 0-D transport code [6,7]. By means of this code the nature of plasma density limitation in the experiments was studied. The termination of the growth of plasma density (even its decay) during the RF pulse (Fig.2) is illustrating the typical situation for the first shots which are characterized by the strong light impurity release from poorly conditioned inner metallic surfaces of U-3M [8]. In this case, the concentration of light impurities was too high, and the RF input power was not sufficient to overcome the impurity radiation losses barrier. Note that in these experiments the RF power input has been limited by arcing in the antenna circuit, so that total RF voltage on the antenna could not be higher than 15 kV ($P_{rf} \leq$ 200 kW). The influence of the impurities on the dynamics of plasma build-up was modeled by introduction of additional losses from the impurity with the same radiation capability to hydrogen atom. The comparison of experimental time trace of plasma density to the computed by 0-D code one showed the qualitative agreement between them (Fig.4). For 25% of radiating impurity saturates of plasma density at the level of 10^{13} cm^{-3} for RF power input 200 kW while the same density without impurities is obtained at 30 kW. The accomplishment of plasma production experiments in a good conditioned device with increased (up to 500-600 kW) RF power and comparison of their results with numerical simulation remain to be done.

STUDIES OF THE RF ASSISTED PLASMA START-UP IN THE ASDEX-UPGRADE TOKAMAK. To analyze the plasma RF build up scenario in the range of frequencies $\omega<\omega_{ci}$ by the double-loop antenna installed in the ASDEX-Upgrade tokamak [9] and with proposed crankshaft one, we use a numerical modeling which combines self-consistently 1-D RF and 0-D transport codes [3,6,7]. The geometry of crankshaft antenna with optimized size of crankshaft modulation of the central strap (dS=4 cm) [3] has been adapted to the sizes of ASDEX-Upgrade double-loop antenna box [9]. Note, that the chosen crankshaft antenna sizes (l_z=48 cm and l_φ=90 cm) are very close to those which provide the most effective wave excitation in plasma column [2].

In 1-D RF code the plasma dielectric tensor taking into account collisional energy dissipation as well as electron Landau damping is used. Ion gyroradius has been assumed to be zero. The model describes correctly the excitation, propagation and mutual conversion of slow and fast waves, while kinetic ion-cyclotron wave (IBW) is neglected. Here, the antenna is modeled by divergence-free external currents. Therefore, the electrostatic mechanism of wave excitation is disabled.

The 1-D code predicts a much better coupling for the crankshaft antenna as compared to the double-loop one (Fig.5) making the crankshaft antenna more favorable for plasma start up. However, the plasma production ability of double-loop antenna can be increased by changing of angle between the antenna currents and steady magnetic field from 90 degrees [4]. The computations indicate a strong sensitivity of the RF power coupling to variation of this angle. It can be explained by increase of slow waves excitation efficiency in low density plasma. Such antenna tilt could be realized by its rotation or by applying of the vertical magnetic field ($B_V \approx 10 \div 100$ Gs).

The 0-D simulations of the plasma start up have been carried out taking into account the RF power coupling efficiency as a function of density (Fig.5) for fixed density of the neutral hydrogen in the vacuum chamber of ASDEX-Upgrade. The scenarios of plasma RF start up in the ASDEX-Upgrade tokamak with different RF power values have been analyzed for double-loop and crankshaft antennae (Fig.6a,b). It was assumed that only a fraction of total RF power was coupled to the plasma, with the other part being dissipated ohmically in antenna. Small increase of double-loop antenna tilt leads to significant reduction of necessary RF power for reliable realization of plasma start up (from 800 kW for 0.5 degree of the antenna tilt to the 500 kW for 1 degree, see Fig.6a). However, the RF power value, even in the case of 500 kW input, remains high enough with the long duration of the neutral gas burn out stage. The scenario of plasma production with the crankshaft antenna takes significantly less time and needs much less RF power for a reliable start up as well (Fig.6b). Here, 200 kW of RF power should be considered as a threshold value for the chosen antenna, magnetic field configuration and density of hydrogen in vacuum chamber.

The above results show the possibility of initial plasma production (n_e up to (2-4)x10^{12} cm^{-3}) and electron pre-heating which should facilitate the further Ohmic discharge [7] in the ASDEX-Upgrade tokamak.

CONCLUSIONS. The results obtained can be summarized as follows:

1) The first tests of the crankshaft antenna in the URAGAN-3M torsatron showed the possibility to produce plasma with density up to 10^{13} cm^{-3} in the range of frequencies $\omega<\omega_{ci}$ without any pre-ionization assistance in a wide range of parameters.

2) The experimental results are in qualitative agreement with the numerical modeling.

3) Two scenarios of the initial plasma RF production in the range of frequencies $\omega<\omega_{ci}$ were considered for the ASDEX-Upgrade tokamak.

ACKNOWLEDGMENT. This work was supported in part by International Science Foundation (Grants No.UA7000 and UA7200).

REFERENCES:

[1] A.I. Lysoivan et al. Fusion Engineering and Design 26 (1995) 185
[2] V.E. Moiseenko. 8th Stellarator Workshop, 1991, Kharkov, IAEA, Vienna (1991) 207.
[3] V.E. Moiseenko et al, 21st EPS Conference, Montpellier, ECA, 1994, V18B, 980.
[4] A.I. Lyssoivan et al. 22nd EPS Conference, Bournemouth, ECA, 1995, PIII, 341.
[5] E.D. Volkov et al. 14th Int. Conference, Wurzburg 1992, IAEA, Vienna (1993) vol.2, 679.
[6] V.E. Moiseenko et al. Fusion Engineering and Design 26 (1995) 203
[7] A.I. Lysoivan et al. Nuclear Fusion, 32 (1992) 1361
[8] N.I. Nazarov et al. Fizika Plazmy (Sov.Journal of Plasma Physics), 13 (1987) No.12, 1511.
[9] J.-M. Noterdaeme et al. Fusion Eng. and Design. 24 (1994) 65-74.

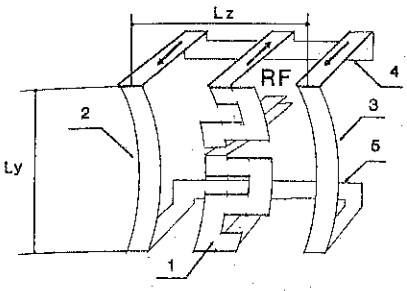

Fig.1: URAGAN-3M. Crankshaft antenna view
1 - Crankshaft strap ($l/f=2l$)
2,3 - side straps ($l/f = l$)
4,5 - longitudinal conductors

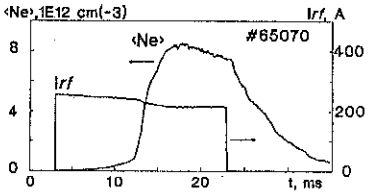

Fig.2: URAGAN-3M, Plasma RF build up experiment. Crankshaft antenna, B=0.64 T, f=8.3 MHz, Hydrogen

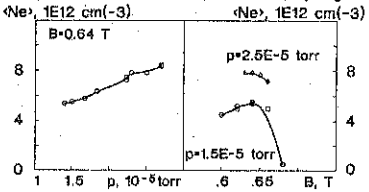

Fig.3: URAGAN-3M Produced plasma density ve gas pressure and confining magnetic field values.

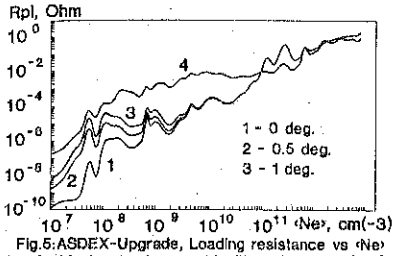

Fig.5:ASDEX-Upgrade, Loading resistance vs ‹Ne› for double-loop antenna with tilt angle varied (1-3) and crankshaft antenna(4). B=2.5 T, f=30 MHz

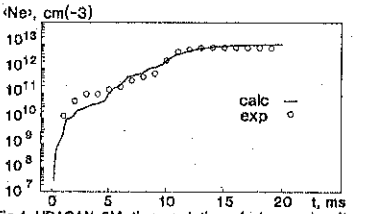

Fig.4: URAGAN-3M, time evolution of plasma density in experiment (#65070) and calculated by 0-D code

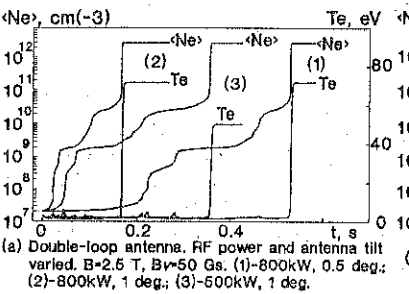

(a) Double-loop antenna. RF power and antenna tilt varied. B=2.5 T, Bv=50 Gs. (1)-800kW, 0.5 deg.; (2)-800kW, 1 deg.; (3)-600kW, 1 deg.

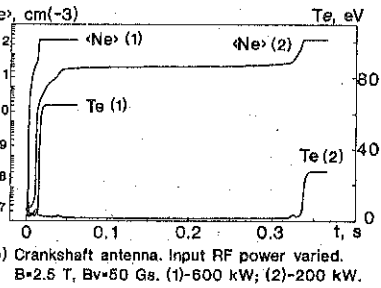

(b) Crankshaft antenna. Input RF power varied. B=2.5 T, Bv=50 Gs. (1)-600 kW; (2)-200 kW.

Fig.6: ASDEX-Upgrade. Plasma RF start up numerical calculations for double-loop and crankshaft antennae.

Bipolar Modification of Bootstrap Current Density by Localized RF Heating

J.A. Heikkinen[1] and S.K. Sipilä[2]

TEKES–Euratom Fusion Association
[1]VTT Energy, P.O. Box 1604, FIN–02044 VTT, Finland
[2]Helsinki University of Technology, FIN–02150 Espoo, Finland

Abstract
A simple, fast model is presented for the minority ion bootstrap current in the presence of ion cyclotron heating in tokamaks. The bipolar trapped ion diamagnetic current appears to dominate over other minority current generation mechanisms in a significant parameter range. The current profile, the dependence on wave intensity, and the increase of the current generation efficiency with electron temperature and with the second power of the inverse major radius are well reproduced by fully toroidal Monte Carlo simulations.

1. Introduction

Shaping the plasma current profile in a tokamak is considered an important tool in entering the second stable regime for short-wavelength ballooning instabilities, stabilization of sawtooth instabilities, and for improving the energy confinement in the plasma core by stabilizing microinstabilities. Only a small auxiliary perturbation in the current density may be required to shape the current profile properly.

The Doppler resonance condition $\omega - n\Omega = k_{\|} v_{\|}$ for a wave of frequency ω implies that the particles resonate with the wave of given parallel wave number $k_{\|}$ with opposite parallel velocity $v_{\|}$ on opposite sides of the resonance for inhomogeneous magnetic field. Recently, much attention has been devoted to the diamagnetic source current of heated ions around the ion cyclotron resonance [1,2,3] which accompanies and can even dominate the current from the Doppler condition. This well-localized current of bipolar profile is excited even with symmetric $k_{\|}$ spectrum, thus requiring no directivity in the antenna system.

Models for the RF–induced diamagnetic current have been recently developed for the ICRF–heated minority ions [2] and for alpha particles heated by lower hybrid waves [4], in which the reduced-order Fokker–Planck equation is solved in the small bounce time limit with respect to the collisional or RF time scale in a thin-orbit approximation. In the present work, the ICRF model is further developed to facilitate detailed comparisons of the current density profile with the results of toroidal 3D Monte Carlo guiding-center simulations. The model is presented in Section II, and the comparison with the toroidal simulation is given in Section III. The results are summarised in Section IV.

2. Bootstrap Current by ICRF Heating

Starting from the steady-state drift equation [5] within a thin-orbit approximation in an axisymmetric tokamak with circular cross-section, and approximating $\rho_L/L \ll 1$ and $\tau_B/\tau_s \ll 1$, where ρ_L is the poloidal Larmor radius of the fast ions, L is the gradient scale length for the plasma and wave parameters, τ_B is the bounce time of the ion banana orbits, and τ_s^{-1} is the inverse slowing-down time of the ions by the electron drag, one can

derive a flux-surface averaged expression for the bootstrap current j_B of the fast particles (see refs. [6,7,2,4] for related expressions)

$$j_B = -\frac{m}{B_\theta}\int_0^{2\pi}\int_0^{\infty}\int_{1-\epsilon}^{h}\sqrt{1-\lambda/h}\frac{\partial f_0(r,v,\lambda)}{\partial r}v^3 d\lambda dv d\theta, \tag{1}$$

where m is the particle mass, $h = 1+\epsilon\cos\theta$, $\epsilon = r/R$ is the inverse aspect ratio at plasma radius r, R is the major radius of the tokamak, B_θ is the poloidal magnetic field and $\lambda = hv_\perp^2/v^2$ with $v_\perp$ and v denoting the perpendicular and total velocity. Only trapped ions are taken into account in Eq. 1. The collisional and RF operators are assumed independent of the sign of the parallel velocity $v_\parallel$.

While most ICRF heated ions become trapped with $\lambda = 1+\epsilon\cos\theta_{IC}$, where θ_{IC} is the poloidal angle of the crossing of the radius r with the cyclotron resonance layer, the anisotropic effects to f_0 are here modelled by adopting an angle-dependent distribution function where λ is uniformly distributed between h and $1-\epsilon$, which takes into account all trapped particles. After averaging over θ, the bootstrap current becomes

$$j_B = -\epsilon\frac{m}{3B_\theta}\frac{\int_{-\pi}^{\pi}[(1+\cos\theta)^{3/2}/h]d\theta}{\int_{-\pi}^{\pi}[(1+\cos\theta)^{1/2}\sqrt{h}]d\theta}\int_0^{\infty}\frac{\partial f_0(r,v)}{\partial r}4\pi v^4 dv. \tag{2}$$

$f_0(r,v)$ is obtained from a flux-surface and pitch averaged equation [8] as

$$f_0(r,v) = f_0(r,0)\exp\left[-\int_0^v dv\frac{-\alpha v^2 + (1/2)(\partial/\partial v)(\beta v^2)}{v^2 D_{IC} + \beta v^2/2}\right], \tag{3}$$

and normalized as $\int_0^\infty 4\pi v^2 dv f_0(r,v) = n(r)$ with $n(r)$ denoting the minority ion density. $\alpha(r,v)$ and $\beta(r,v)$ are the Coulomb diffusion coefficients [8], and $D_{IC}(r,v)$ is the pitch symmetrized ion cyclotron diffusion operator [9]. It should be noted that the present solution is a variant of the expression of Taguchi [2], where f_0 was described as a delta function of λ at $1+\epsilon\cos\theta_{IC}$.

In the presence of finite orbit effects by toroidicity, the expression (3) may give too peaked distributions in radius when the RF diffusion coefficient D_{IC} is calculated from the local values of the diffusion coefficient. In order to compare the present analytical model with toroidal simulation results, we replace D_{IC} by

$$D_{IC}(r) = P_c(r)/3mn(r), \tag{4}$$

where $P_c(r)$ is the density of collisional power transfer from the fast ions to the bulk particles obtained from the simulation. With this replacement, the finite orbit broadening effects can be incorporated into the model without the need to describe the orbit trajectories analytically.

3. Comparison with Toroidal Simulations

In the calculations, the profile of the wave intensity is assumed to behave as e^{-z^2/s^2}, where z is a vertical coordinate along the cyclotron resonance from the equatorial plane, and

s is a given exponential length. The resonance position is determined from the Doppler condition for a particle of parallel velocity $v_{\|}$, for preassumed magnetic background, and for a wave with a given wave vector. As reference parameters, the reactor-scale values $R = 7.75$ m, $a = 2.8$ m, $B = 6.2$ T, $I = 15$ MA, $T_{e,i} = 20$ keV, $n_e = 0.84 \times 10^{20}$ m^{-3} with equal deuterium and tritium concentrations, and a hydrogen minority concentration $n_H = 2 \times 10^{18}$ m^{-3} are assumed. Here, B is the toroidal magnetic field on the axis, I is the total plasma current, and T_i is the ion temperature for each ion species. The plasma density and temperature are assumed to have radial dependencies $n, T = n_0, T_0 \times (1 - r^2/a^2)^{\alpha_n, \alpha_T}$ with $\alpha_n = \alpha_T = 0.5$. Circular plasma cross section with a parabolic current profile is adopted. In the reference case, the wave parameters are $E_+ = 3000$ V/m, $|E_-/E_+| = 0$, $k_\perp = 30$ m^{-1}, $k_{\|} = 0$, and $s = 1$ m. Here, E_+ and E_- are the left-handed and right-handed electric field components of the wave, respectively. The cyclotron resonance layer $\omega = \Omega$ intersects the equatorial plane at $r_{IC} = 0.8$ m on the outboard side of the axis. The case with $k_{\|} = 0$ is considered to eliminate other current sources except the diamagnetic one.

Fig. 1 shows the current density of the hydrogen ions obtained from the Monte Carlo simulation for the reference case with varying $k_{\|}$. It is observed that the finite $k_{\|}$ broadens the bipolar diamagnetic current density profile by the wave-induced drift [3] and by the broadened resonance regime. The total integrated current is found to increase for increasing $k_{\|}$. However, only small changes in the maxima nor minima of the current density around the cyclotron resonance are found in the present parameter range, thus indicating that the diamagnetic bipolar current density seen for $k_{\|} = 0$ dominates the shape and magnitude of the current profile also for $k_{\|} \neq 0$. Analytical estimates of the current profiles, calculated by recording the collisionally transferred power density from the heated ions to the bulk and substituting this in Eq. (4), are also given. A good agreement in both magnitude and profile is found. The analytical model slightly underestimates the current density outside the cyclotron resonance, which is caused by the bootstrap current contribution by thermal minority ions not included in the present analytical model. The found agreement in Fig. 1 demonstrates the rough validity of the approximations made for the present parameters.

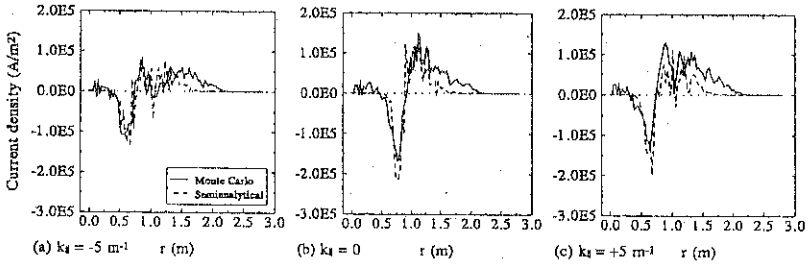

Fig. 1: The minority ion current density profile obtained from the Monte Carlo simulation for $k_{\|} = 0$, and for $k_{\|} = \pm 5$ m^{-1} with outboard resonance position. The analytical result is shown for comparison.

4. Summary

A model for the minority ion bootstrap current in the presence of ion cyclotron heating is presented for tokamaks making possible the fast estimate of the current with reduced-order Fokker–Planck solution of the ion distribution. The model should be further improved by a more rigorous treatment of the pitch dependence of the distribution function. The bipolar trapped ion diamagnetic current attractive for current profile modification appears to dominate over other minority current generation mechanisms in a significant parameter range. The current profile, the dependence on wave intensity, and the increase of the current generation efficiency with electron temperature and with the second power of the inverse major radius are well reproduced by fully toroidal Monte Carlo simulations. The current generation power efficiency is optimized for small aspect ratio, small major radius, high electron temperature, and for low wave field.

The RF current opposes the plasma current inside the IC resonance and enhances it at outer radii. No directivity of the waves is needed to produce the bipolar diamagnetic current profile. However, by inclusion of finite $k_{\|}$, it is possible to enhance or suppress the RF modification of the plasma current, depending on the sign of asymmetry of the $k_{\|}$ spectrum.

The present analytical model does not take into account the effect of the resonance position in R to current generation, which is demonstrated in the toroidal Monte Carlo simulations. The bootstrap current obtained here should also be corrected to account for the electron back current opposing the minority current. This factor may vary between, say, 0.25 and 0.75 around the mid-radius of a reactor depending on the effective charge of the plasma and the charge number of the minority ions. In the simulations, the ICRF wave diffusion operator has been assumed fixed with Gaussian profiles. The inclusion of realistic operator forms based on a spectrum of waves obtained by wave codes with full absorption models (including both electron and ion damping) is important.

References

[1] W.G.F. Core and G.A. Cottrell, Nucl. Fusion **32**, 1637 (1992).

[2] M. Taguchi, in Controlled Fusion and Plasma Physics (Proc. 21th Eur. Conf. Montpellier, 1994) Vol. 18B, Part III, European Physical Society 1142 (1994).

[3] T. Hellsten, J. Carlsson, and L.-G. Eriksson, Phys. Rev. Lett. **74**, 3612 (1995).

[4] J.A. Heikkinen and S.K. Sipilä, "Alpha Current Driven by Lower Hybrid heating of Thermonuclear Alpha Particles in Tokamak Fusion Reactors", to appear in Nucl. Fusion.

[5] M.N. Rosenbluth, R.D. Hazeltine, and F.L. Hinton, Phys. Fluids **15**, 116 (1972).

[6] A. Nocentini; M. Tessarotto, F. Engelmann, Nucl. Fusion **15**, 359 (1975).

[7] C.T. Hsu, P.J. Catto, and D.J. Sigmar, Phys. Fluids B **2**, 280 (1990); C.T. Hsu, K.C. Shaing, R.P. Gormley, and D.J. Sigmar, Phys. Fluids B **4**, 4023 (1992); M. Taguchi, J. Phys. Soc. Japan **61**, 4443 (1992).

[8] T.H. Stix, Nucl. Fusion **15**, 737 (1975).

[9] D. Anderson, W. Core, L.-G. Eriksson, H. Hamnén, T. Hellsten, and M. Lisak, Nucl. Fusion **27**, 911 (1987).

ECCD Experiments in RTP

R.W. Polman, E. Westerhof, J. Lok, F.A Karelse, O.G. Kruyt, A.A.M. Oomens,
F.C. Schüller, and the RTP-team
FOM-Instituut voor Plasmafysica 'Rijnhuizen', Association Euratom-FOM,
P.O. Box 1207, 3430 BE Nieuwegein, The Netherlands.

Abstract

Electron Cyclotron Current Drive (ECCD) experiments on the Rijnhuizen tokamak RTP have been performed utilizing 60 GHz waves launched from the high field side of the torus. The ECCD efficiency as a function of the position of the cold resonance layer has been measured and compared with Fokker-Planck simulations. The experimental results are consistent with these simulations.

Introduction

ECCD is accomplished by preferentially heating electrons moving in one toroidal direction. Their reduced collissionality results in a toroidal current.

In the present RTP experiments the total toroidal plasma current, I_p, was kept constant by a feedback circuit. In fact, I_p can be assumed to be the sum of four components: the inductive current drive, a current due to bootstrap effects, ECCD, and an inductively driven extra current due to an additional conductivity created by ECRH via energetic electrons. Thus $I_p = I_{cond} + I_{boot} + I_{ECCD} + I_{syn}$. The established ECCD is not large enough to drive all of I_p. The loop voltage is only reduced below its Ohmic value (Fig. 1) and the driven current must be obtained indirectly. The voltage reduction results from both ECCD and the lowered global plasma resistance. The latter is due to the thermal T_e increase plus the enhancing extra contribution by the synergetically ECH created conductivity. The four contributions to I_p do not have the same current density distribution. The bootstrap current flows off-axis in the pressure-gradient region while the other components are centered about the plasma axis but can have strongly different profile widths. Until now, the exact experimental profiles can not be known directly and one has to rely on calculations or indirect methods.

This paper aims to identify the I_{ECCD} dependency on the location of the resonance layer and on the toroidal launch angle.

Experimental set-up

The RTP tokamak ($R_0 = 0.72$ m, $a_{lim} = 0.165$ m, $B_T \leq 2.5$ T, boronized SS first wall) is equipped with two 60 GHz, 200 kW, 100 ms gyrotrons, and a single 110 GHz, 200 ms, 500 kW gyrotron. One of the 60 GHz gyrotrons is connected by a wave guide transmission line to the high field side of the tokamak to achieve ECCD in the down shifted resonance scheme. The waves are obliquely launched from a flat steerable mirror, located halfway the equatorial plane and the top. The launch angles ranged from -30° to +30° off-perpendicular. The power was directed towards the magnetic axis. The polarization of the waves is linear. The injected power

couples for 80% or more to the X-mode. For the experiments reported here, this system has been operated at a power level of about 130 kW and pulse lengths of up to 100 ms. In some discharges the second 60 GHz gyrotron, injecting O-mode perpendicularly from the low field side, was used to get higher temperatures of the target plasma. The working gas was hydrogen. The density was feedback controlled. The EC driven current is derived from a comparison of the residual loop voltages for co- and counter-drive discharges. If one relies on the assumption that by reversing the toroidal direction of the EC wave injection only I_{ECCD} changes sign and that the other components remain the same for co- and counter drive, then the RF driven current is simply the total plasma current multiplied by half the fractional change in loop voltage: $I_{ECCD} = [(V_{cntr} - V_{co}) / (V_{cntr} + V_{co})] (I_p - I_{boot})$, where V_{cntr} and V_{co} represent the loop voltages during counter- and co-drive, respectively. This expression has been used here; further, I_{boot} is taken zero. The approach is accepted in ECCD research. Knowledge of the current density profiles through polarimetry should provide results of a more local quality.

Standard diagnostics, a 19-channel interferometer, 20- channel ECE, a high-resolution multi-position Thomson Scattering system and other multi-channel diagnostics are available at RTP. Very recently a polarimeter has been implemented on the 19-channel interferometer.

Experimental results

First results on ECCD in RTP have been reported in [1]; driven current fractions were found up to 20%. Since then the parameter range studied has been expanded, but the ECCD efficiency itself could not be pushed up further. The experimental results are shown in Fig. 2.

Most experiments were done with $I_p = 60$ kA, and $\langle n_e \rangle \approx (1.0 - 1.3) \times 10^{19}$ m^{-3}; B_T was varied between 2.1 and 2.5 T. The standard toroidal launch directions were +30° and -30° off-perpendicular. The diffuse Doppler-shifted absorption zone is to the high field side of the cold resonance position, which is at 2.14 T for 60 GHz radiation. Hence the driven current depends on B_T. Linear theory predicts the scaling $I_{ECCD} \sim T_e/n_e$ with temperature and density; Fokker-Planck simulations suggest for the parameter regime of the experiment an even stronger influence of the density: $I_{ECCD} \sim T_e/n_e^{1.5}$ (see the next section). The temperature effect is clearly demonstrated in Fig. 2. The maximum driven current (11 kA) was obtained at $B_T = 2.33$ T for $T_e \approx 3$ keV (obtained with 2 gyrotrons), and $\langle n_e \rangle \approx 1.0 \times 10^{19}$ m^{-3}. This is consistent with the largest possible resonance downshift at the plasma centre while still retaining efficient central heating. For one gyrotron the maximum temperature reached is lower ($T_e \approx 1.5$ keV) and the I_{ECCD} shows a maximum (≈ 6 kA) at B_T around 2.30 T. For a further increased magnetic field (2.46 T) the off-axis heating leads to a lower central temperature than in the Ohmic heating phase; this resembles 2X-mode off-axis heating results with the 110 GHz gyrotron [3].

Current drive results at the non-standard injection angles ±23°, and ±11°, and with plasma currents $I_p = 40$ and 80 kA are not distinguishable from the others, while modeling for the steeper ±11° injection case predicts an I_{ECCD} maximum for B_T around 2.25 T (see Fig. 3).

Experimental data so far are qualitatively in agreement with predictions (see figs. 2 and 3). However, ECCD is sensitive to the density, which should be low to get a measurable rf current

drive. At the more perpendicular injection, as well as for 80 kA plasmas, the density increases in an uncontrolled way with about 20%. This makes a quantitative comparison difficult.

Current density profiles from polarimetry should show the current drive straight-forwardly, in contrast with the indirect loop voltage method. The preliminary results support the expected dependencies qualitatively and look promising. However, the low density and the modest amount of I_{ECCD} result in a Faraday rotation around 1°, which is not high enough above the experimental error bars to draw clear conclusions at this moment.

Theoretical results

Detailed Fokker-Planck code simulations have been performed for the experimental parameters covered by the experiments (i.e. $T_e(0) \approx 1.5 - 3.0$ keV, $n_e(0) \approx 1.7 - 2.4\ 10^{19}$ m^{-3}, $B_{axis} \approx 2.10 - 2.40$ T, toroidal injection angle $\phi \approx 11° - 30°$). The results are given in figure 3.
The scaling of the EC driven current with density and temperature is approximately $\sim T_e / n_e^{1.5}$. However, the temperature scaling may be complicated by a dependence on the magnetic field on axis, B_{axis}. Further, I_{ECCD} is a strong function of both B_{axis} and the injection angle: for an injection angle of 30° and with $T_e(0) \approx 1.5$ keV a maximum is obtained around $B_{axis} \approx 2.30$ T. At higher T_e the maximum shifts to higher values of B_{axis}, but for $B_{axis} > 2.35$ T these will no longer be consistent with sufficient central power deposition required to achieve such temperatures. Therefore these conditions are experimentally inaccessible in RTP. Decreasing the injection angle leads to lower efficiencies and a small shift of the maximum towards lower magnetic fields: for $\phi \approx 11°$ a relatively sharp maximum is obtained at $B_{axis} \approx 2.25$ T.

In the absence of radial transport, the Fokker-Planck calculations predict the generation of large local energetic electron populations. In many cases, these nonthermal electrons may locally even account for an equal or even much higher energy density than the thermal plasma. When radial transport is included in the calculations, the highly localized non-thermal electrons are redistributed, such that globally the contribution of non-thermal electrons is almost the same. The total EC driven current is found to drop by at most 20% as a consequence of radial diffusion. This effect of radial transport on the local nonthermal electrons has important consequences for comparisons with various other plasma diagnostics [2].

These calculations are roughly consistent with the experimentally derived EC driven currents of Fig. 2, in particular the B_{axis} dependence. Though, the experiments have not yet been able to confirm the drop in efficiency for the smaller injection angles.

Acknowledgment

We are grateful to the ECRH-, Thomson scattering-, and the diagnostic teams, as well as to the technical staff of RTP for their skilful contributions. This work was performed under the Euratom-FOM Association agreement with financial support from NWO and Euratom.

References

[1] E. Westerhof et al., 22nd EPS Conference, Bournemouth, 1995, Vol 19C, I-385.

[2] A.G. Peeters, and E. Westerhof, Phys. Plasmas **6**, 1628 (1996)

[3] A.A.M. Oomens et al., IAEA-CN-60 / A3-8, Sevilla, 1994, Vol. 1, 481.

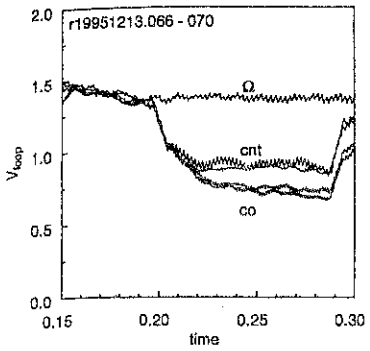

Fig. 1
V_{loop} time-traces of 5 discharges in a row overlaid: 1 Ohmic, 2 co- and 2 counter current drive cases.
I_p = 60 kA, P_{ECH} = 130 kW, injection ±30°, $\langle ne \rangle = 1.0 \times 10^{19} m^{-3}$.
Oscillations are due to the chopper regulated power supply for the vertical field coils.

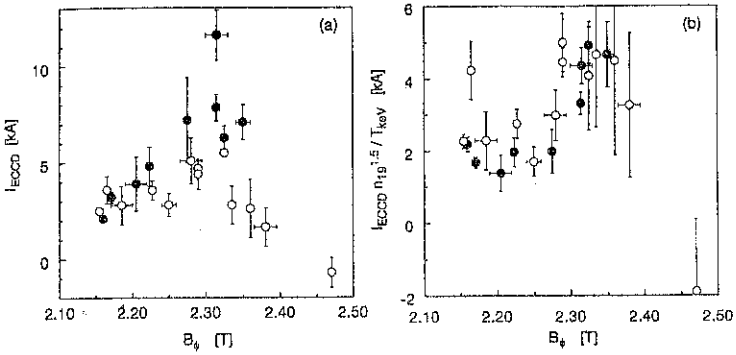

Fig. 2
Experimental I_{ECCD} as a function of B_T, for 30° off-perpendicular injection.
Full points: 2 gyrotrons
a) I_{ECCD}
b) normalized with a scaling factor $n^{1.5}/T$

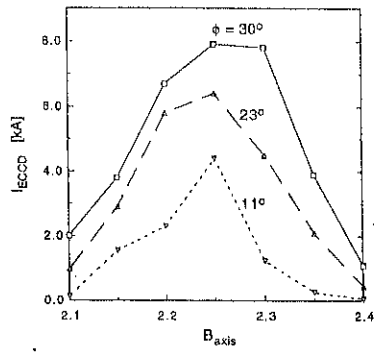

Fig. 3
Simulated I_{ECCD} as a function of B_{axis}, for 11°, 23°,and 30° off-perpendicular injection.
Plasma parameters: $T_e(0)$ = 1.5 keV, $n_e(0)$ = 1.7×10^{19} m^{-3}. EC power: 135 kW X-mode.

Propagation of a Wave Beam through Cyclotron Resonance

E. Westerhof

FOM-Instituut voor Plasmafysica 'Rijnhuizen'
Association EURATOM-FOM
Postbus 1207, 3430 BE Nieuwegein – Nederland

1. Introduction

Wave propagation in regions of resonant absorption is a long standing problem [1], and waves at cyclotron (harmonic) resonance are no exception. The applicability near resonance of standard dielectric expressions for wave energy density and flux is questionable, and directly related to this is the problem of ray-tracing in dissipative media. After all, rays are supposed to represent trajectories of wave energy. Although methods have been proposed for ray-tracing in dissipative media (see e.g. [2]), their applicability to cyclotron resonance remains to be proven.

2. O-mode Quasi-Perpendicular Propagation

The problems for the O-mode in case of propagation close to perpendicular with respect to the equilibrium magnetic field is well illustrated by the (weakly relativistic) quasi-perpendicular approximation of the O-mode dispersion relation

$$D = 1 - \omega_p^2/\omega^2 - N_\perp^2\left(1 + \tfrac{1}{2}\mathcal{F}_{7/2}\frac{\omega_p^2}{\omega_c^2}\right) = 0 \qquad (1)$$

valid for $|N_\parallel| \lesssim v_t/c \ll 1$. All symbols have their usual meaning, $v_t \equiv \sqrt{kT_e/m_e}$, and $\mathcal{F}_q(z;N_\parallel)$ denotes the so-called Shkarofsky function of half-integer index q and argument $z = (c^2/v_t)^2(1-\omega_c/\omega)$ [3,4]. The corresponding dielectric wave energy fluxes are [5]

$$F_\perp = N_\perp\frac{c|E_z|^2}{4\pi}\left(1 + \tfrac{1}{2}\mathcal{F}'_{7/2}\frac{\omega_p^2}{\omega_c^2}\right) \quad F_\parallel = N_\parallel N_\perp^2\frac{c|E_z|^2}{16\pi}\frac{c^2}{v_t^2}\frac{\omega_p^2}{\omega_c^2}\frac{\partial}{\partial z}(\mathcal{F}'_{5/2} - \mathcal{F}'_{3/2}). \qquad (2)$$

Note the convention used in this paper of a prime denoting the real part. Both contain a 'sloshing' contribution due to the resonant term in the dispersion relation. Especially, the parallel sloshing flux can be large, of order $(c^2/v_t^2)N_\parallel(\omega_p^2/\omega_c^2)$, and has an oscillatory behaviour near the resonance. The question remains whether the dielectric energy fluxes provide a good description of a wave trajectory.

Also ray-tracing according to the method of Friedland and Bernstein [2] is not without problems. They propose to use, instead of the full complex dispersion relation, the approximate dispersion relation with real roots

$$\Phi_\omega \equiv (\partial D D^*/\partial\omega) = 0 \qquad (3)$$

where D^* is the complex conjugate of the exact dispersion relation. When one applies this approximation to the dispersion relation (1), a bi-quadratic equation for $N_\perp$ is obtained, where one of the roots approximates the O-mode dispersion. However, when $(\omega_p/\omega) \gtrsim 3v_t/c$, the approximation can be shown to become very poor close to the resonance. This is a consequence of the derivative of the resonant terms in the dispersion relation. Approximation (3) appears to be useful only in a restricted parameter range.

3. Propagation in a Plane Slab: a numerical approach

The question of the trajectory of a wave beam near cyclotron resonance thus remains open. To simplify the problem, we consider wave propagation in a plasma slab, which is inhomogeneous only in the x-direction and in which the magnetic field is directed along z varying as $B(x) = B(0)/(1 + x/R)$. A beam with frequency ω is injected from the low field side at $x = a$ with $k_\parallel$-spectrum:

$$E(k_\parallel) \propto \exp\Big(-(k_\parallel - k_0)^2/\big((\Delta k)^2 + 2i(1 - k_0^2)\mathcal{R}^{-1}\big)\Big) \tag{4}$$

where $k_0 = \sin\theta$ gives the initial direction of propagation, Δk determines the Gaussian half width of the initial beam power profile as $\Delta z = \sqrt{2}/\Delta k_\parallel$, and $\mathcal{R}$ is the curvature of the initial phase front (negative for a focussed beam). Since the equilibrium is independent of z, $k_\parallel$ is a conserved quantity. Thus, using the WKB approximation the beam profile at any x is obtained straightforwardly as

$$E(x,z) \propto \int dk_\parallel\, E(k_\parallel) \exp\big(-i\omega t + ik_\parallel z + \int_a^x k_\perp dx\big) \tag{5}$$

where the complex $k_\perp$ is to be determined from the local dispersion relation [6]. An approximate evaluation of the beam trajectory (analogous to the derivation of the group velocity) results in an equation for 'group trajectory' of the beam maximum $z_{\max}(x)$

$$(dz_{\max}/dx) \propto -(dk'_\perp/dk_\parallel). \tag{6}$$

The validity of this result, has been studied by numerical calculations on the basis of Eq.s (4) and (5). The results of such a calculation are presented in Fig.s 1 to 3. The parameters are $T_e = 1$ keV, $\omega_p^2/\omega^2 = 0.7$, and injection direction of 2.3°, such that $N_\parallel \approx v_t/c$. The spectral width is varied from $\Delta k = .0175, .035$, to $.07$, corresponding to beam divergences of 1°, 2°, and 4°, respectively. Results as presented in Fig.s 1 to 3 are independent of the particular choice for a and R. In the following, distances will be normalized to $c/\omega = \lambda/2\pi$.

Figure 1 gives the O-mode solution for the real part of $k_\perp$ from the (exact) weakly relativistic dispersion relation as a function of $k_\parallel$ and x (here represented in terms of

ω/ω_c). The structure of the surface traced out by $k'_\perp$ as a function of $N_\parallel$ and ω/ω_c together with Eq. (6) explains the behaviour of the beam trajectory as depicted in Fig. 2. However, the full warm plasma effects are realized only in case of the smallest beam divergence. When the spectral width of the beam is larger, $\Delta N_\parallel \gtrsim v_t/c$, the warm plasma effects on the wings of the beam differ significantly from those at the beam centre, and beam diffraction effects tend to suppress the warm plasma effects. Wave absorption is seen to hardly affect the beam trajectory. The angle of propagation, $\arctan(dz/dx)$, of the wave beam, is given in Fig. 3 for the case of $\Delta k = .0175$. It is compared with propagation angles according to the dielectric fluxes (from the full dispersion relation) and to Eq. (6). Clearly, the dielectric energy fluxes do not properly approximate the direction of propagation. In contrast, the group trajectory (6) is consistent with the numerical results (provided the beam divergence is sufficiently small).

A second example with $a = 2\,10^2$ and $R = 10^4$ for perpendicular propagation and beam width $\Delta k = .06$ (i.e. 3.4 degrees) is shown in Fig. 4, giving contours of power levels at each x normalized to the local maximum, in order to correct for absorption. Just at resonance the beam experiences subsequently strong defocussing and focussing.

Most of these effects are accompanied by significant absorption. A notable exception here is the change in ray trajectory on the low field side of the resonance, where absorption is still absent but the proximity of the resonance nevertheless affects the trajectory strongly. In more general geometry, this could lead to changes in the position of power deposition or even to beam reflection before reaching the resonance. Such an effect was noted in Ref. [7] from ray-tracing of second harmonic X-mode in TCV.

4. Conclusion

Neither the approximate dispersion relation proposed in Ref. [2], nor the standard dielectric expressions for the wave energy fluxes forms a sufficient basis for the calculation of beam trajectories near cyclotron resonance. The observations presented above, in particular, the negligible effect of absorption on the trajectory of the beam maximum, suggests the use for ray tracing of the following dispersion relation

$$D = k^2 - {k'_\perp}^2(\boldsymbol{x}, k_\parallel) - k_\parallel^2(\boldsymbol{x}, \boldsymbol{k}) = 0, \tag{7}$$

where ${k'_\perp}^2(x)$ is the real part of the solution of the exact warm plasma dispersion relation and $k_\parallel(x)$ is the appropriate projection of the wave vector on the magnetic field. Absorption then immediately follows from the imaginary part of $k_\perp$ obtained from the exact dispersion relation. As noted above, diffraction effects may reduce the warm plasma effects significantly, requiring extension of standard ray-tracing as in Ref. [8].

Acknowledgement This work was performed under the Euratom–FOM Association agreement with financial support from NWO and Euratom.

[1] L. Brillouin, *Wave propagation and group velocity*, Academic Press, New York (1960). [2] L. Friedland, I.B. Bernstein, Phys. Rev. A **22**, 1680 (1980). [3] I.P. Shkarofsky, Phys. Fluids **9**, 561 (1966). [4] P.A. Robinson, J. Math. Phys. **27**, 1206 (1986). [5] E. Westerhof, *Theory of Fusion Plasmas*, Proceedings Joint Varenna-Lausanne International Workshop, 22-26 August 1994, Varenna (It), p. 115. [6] I. Fidone, G. Granata, R.L. Meyer, Phys. Fluids **25**, 2249 (1982). [7] A. Pochelon, et al., 20^{th} *EPS Conference on Controlled Fusion and Plasma Physics*, Lisboa (1993), Part III p. 1029. [8] E. Mazzucato, Phys. Fluids B **1**, 1855 (1989).

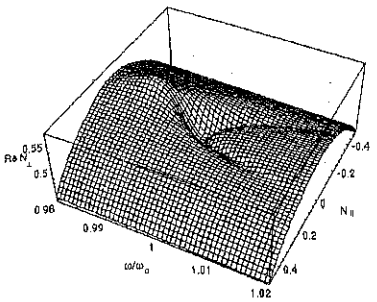

Figure 1. Real part of $N_\perp$ from the O-mode dispersion relation with T_e = 1 keV, $\omega_p^2/\omega^2 = 0.7$.

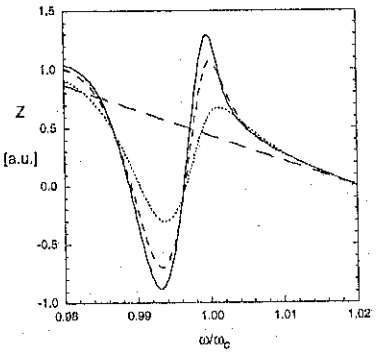

Figure 2. Beam trajectory. Parameters as Fig. 1, injection angle 2.3°. Full curve Δk = .0175, dashed Δk = .035, dotted Δk = .07, and long dashed cold plasma dispersion.

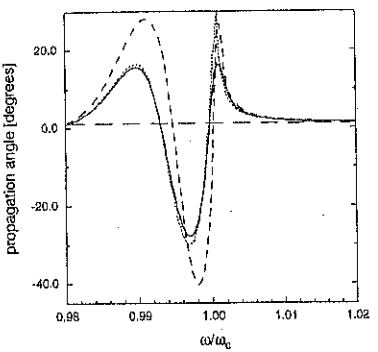

Figure 3. Propagation angle. Parameters as for Fig. 1. The full curve corresponds to Δk = .0175 case, long dashed to cold plasma dispersion, dotted to Eq. (6), dashed to $\arctan(F_\parallel/F_\perp)$.

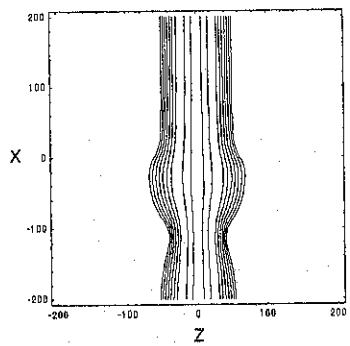

Figure 4. Perpendicular beam. Contours equally spaced in $\ln|E|^2$. *Parameters: T_e = 1 keV, $\omega_p^2/\omega^2 = 0.7$, Δk = .06, $a = 2\,10^2$ and $R = 10^4$.*

STUDY OF THE 2D FAST ELECTRON MOMENTUM DYNAMICS DURING LOWER HYBRID CURRENT DRIVE

Y.Peysson, R.Arslanbekov, G.T.Hoang, X.Litaudon, E.Sébelin, I.P.Shkarofsky* and M.Shoucri*

DRFC, CE Cadarache, F-13108 St-Paul-Lez-Durance, France,
**CCFM, Varennes, Canada.*

1. Introduction

The knowledge of the two-dimensional (2D) fast electron dynamics in momentum space during Lower Hybrid (LH) current drive experiments is of great importance in view to control accurately the non-inductive current density profile in the plasma and to achieve a significant enhancement of tokamak performances in a steady-state regime. Moreover, in combined scenarios with Fast Wave Electron Heating (FWEH), 2D effects on the non-thermal electron population are expected to be large, according to theoretical predictions. The fast electron dynamics is analysed in detail from the suprathermal bremsstrahlung emission, which provides a quite direct insight of the non-thermal electron distribution function in both configuration and momentum spaces. Quantitative simulations of experimental results obtained on TORE SUPRA are carried out for various plasma conditions based on toroidal ray-tracing combined with self-consistent 2D relativistic Fokker-Planck calculations. As the studied photon energy range lies mainly in the region above the plateau of quasilinear diffusion, a careful attention is paid to the fast electron dynamics in momentum space whose accurate description must take into account of the full two-dimensional nature of pitch-angle scattering.

2. Modeling of LH experiments

Recent experiments have been carried out on the TORE SUPRA tokamak in view to control in a stationary manner the current density profile flowing in the plasma [1]. Such a goal has been achieved by launching LH waves in poor accessibility conditions, so that much of the power is expected to be absorbed off-axis. In this case, the absorption due to Landau damping is weak, because of the moderate electron temperature in the plasma region where the wave packet propagates. As a consequence, the wave makes many passes in the discharge and undergoes numerous reflections between cut-off and caustics before the initial $n_{//}$ spectrum is upshifted to sufficiently large values for an efficient damping on bulk electrons to take place, i.e. $n_{//} \approx 7.0/\sqrt{T_e[keV]}$. Though the current drive efficiency is rather low in such conditions, it turns out that this multipass regime has lead routinely to stationary reversed magnetic shear in the plasma core, when the LH power is large enough to drive the full current. A critical issue in such scenarios is the accurate determination of the power deposition profile, in connection with the possible existence of a transport barrier in the plasma layer where the magnetic shear becomes negative. Indeed, it has been observed experimentally a significant rise of the electron temperature in the

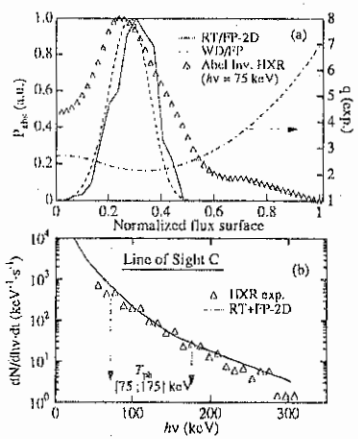

Fig. 1. Power deposition profile (#14386)

core of the plasma, few seconds after the onset of the LH power, which may be ascribed to a transition towards a new plasma state with enhanced global confinement. Because of the non-linear dependence of the LH power deposition profile with the current density profile, an accurate assessment of a core transport barrier is based on quantitative comparisons between theoretical predictions and experimental observations. Such an approach has been considered in detail using the non-thermal bremsstrahlung emission in the hard x-ray (HXR) energy range, which allows a quite direct estimate of the localisation of the fast electrons interacting resonantly with the LH wave, both in configuration and momentum spaces. As simulations of the bremsstralung emission requires a careful description of the perpendicular electron dynamics, it has been determined by a standard method based on the use of a toroidal ray-tracing combined with a 2D relativistic Fokker-Planck module [2,3]. In the calculations, the quasi-linear diffusion coefficient is determined self-consistently with the power deposition profile from the wave absorption by averaging $\partial f(p_{//},p_{\perp})/\partial p_{//}$ over the perpendicular direction. Fokker-Planck calculations are carried out using the relativistic Beliaev-Budker collision operator, including the first Legendre harmonic reaction term, which plays an important role for an accurate determination of the shape of the fast electron tail [4].

As shown in Fig.1, the predicted LH power deposition profile is clearly off-axis and in fair agreement with Abel inverted HXR measurements between 50 and 100 keV. Plasma conditions - #14386, $I_p = 0.4$ MA, $B_t = 2$T, $T_{e0} = 3.5$ keV, $n_{e0} = 3.0\times10^{+19}$ m^{-3} - correspond to a strong multipass regime for which the plasma core is inaccessible to the initial wave packet. In this case, it is possible to give a statistical description of the wave dynamics, a complementary approach to the standard ray-tracing technique [5]. The main advantage of this method is that mechanisms involved in producing of wave diffusion (WD) in the phase space need not to be specified, and results of the LH modeling become robust and insensitive to various assumptions (magnetic equilibrium, scattering effects, antenna extension and position...). A very good agreement between the two descriptions of the LH wave dynamics is found, as shown in Fig.1, even if a one-dimensional Fokker-Planck solver has been used for the wave diffusion approach. It is interesting to note that the safety factor profile deduced from time evolution of various magnetic measurements is non monotonic, taking into account of the bootstrap fraction, as observed experimentally from polarimetry measurements (Fig.1). The fact that both the minimum q-value and the LH power deposition take place in the same plasma region gives confidence to the consistency of the whole analysis. This conclusion is reinforced by the very good quantitative agreement found between the experimental HXR energy spectrum, and numerical predictions using self-consistent ray-tracing and 2D Fokker-Planck calculations (Fig.1). Not only the slope of the HXR spectrum (given by the photon temperature T_{ph} [6]), but also the absolute level of the signal over a wide photon energy range are reproduced. Calculations of T_{ph} have also been carried out for various TORE SUPRA plasma conditions, and compared to experimental estimates determined in the same energy window 75-175 keV. In Fig.2, calculated and measured T_{ph}, for three different chords A, B, C [6], are reported as a function of the accessibility parameter $n_{//acc} = 1+\left(\omega_{pe}/\Omega_{ce}\right)^2$ where ω_{pe} and Ω_{ce} are respectively the electron plasma frequency and the electron gyrofrequency. A very good agreement is observed, and in particular the decrease of T_{ph} when $n_{//acc}$ increases, i.e. when B_t is reduced, is well reproduced. Such a dependence may be explained by the fact that at lower magnetic fields, less energetic electrons are accelerated by the LH waves, leading to a degradation of the current drive efficiency, and lower T_{ph} values.

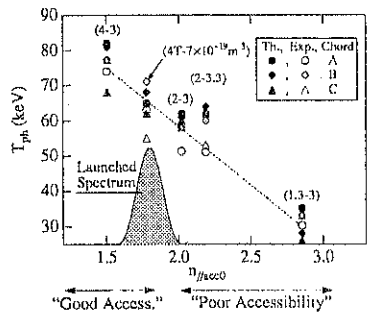

Fig. 2. Photon temperature for various LH wave accessibility conditions.

3.Fast electron dynamics above the plateau region

As shown in the previous section, it is possible to account for most characteristics of full current drive discharges sustained by means of LH waves with self-consistent ray-tracing + 2D relativistic Fokker-Planck calculations. In particular, a good quantitative description of the non-thermal bremsstrahlung emission is possible for a broad set of plasma conditions, even if the dominant contribution to the HXR emission arises from fast electrons whose energy is well beyond the quasilinear plateau (Fig.3). In this case, an accurate description of the perpendicular dynamics in momentum space is critical. In order to simplify the 2D analysis in momentum space, the 2D distribution function is represented by its two moments $F_0(p_{//}) = 2\pi\int_0^\infty p_\perp f(p_{//},p_\perp)dp_\perp$ and $F_2(p_{//}) = 2\pi\int_0^\infty p_\perp^3 f(p_{//},p_\perp)dp_\perp$ with respect to the perpendicular direction, and by the perpendicular temperature defined by the ratio $T_\perp(p_{//}) = F_2/2F_0$, which is a measure of the broadening of the distribution function in $p_\perp$ as a result of the combined effects of collisional slowing-down, pitch-angle scattering and quasi-linear diffusion. The suprathermal distribution function $f(p_{//},p_\perp)$ may be then approximated by

$$f(p_{//},p_\perp) = \frac{F_0(p_{//})}{2\pi T_\perp(p_{//})}\exp\left[-\frac{p_\perp^2}{2T_\perp(p_{//})}\right].$$

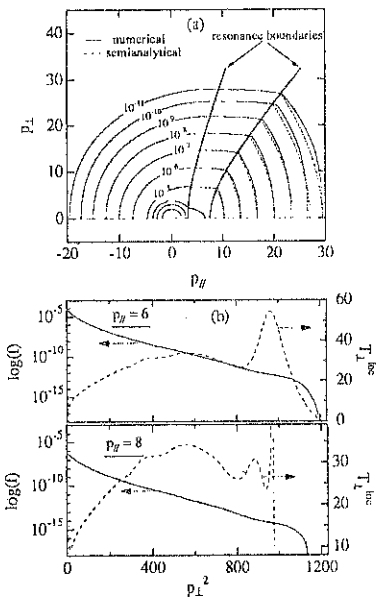

Fig. 3. (a) Contour plot of the 2D electron distribution function, (b) slope analysis.

As expected from theoretical predictions [7,8], $T_\perp$ is nearly constant over the plateau region as a function of $p_{//}$, because the average escape time is roughly given by the slowing-down time scale. In the region above the plateau, a non monotonic dependence of $T_\perp$ with $p_{//}$ is observed numerically, as shown in Fig.4, which first corresponds to an increase and is then followed by a strong decrease as far as $p_{//}$ becomes larger. The dependence of $T_\perp$ as a function of $p_{//}$ has been investigated by solving the Langevin equations which give the trajectory of a test electron in momentum space. In the case of no electric field, the Langevin approach becomes particularly simple and analytical solutions may be obtained, from the knowledge of initial values on given boundaries. Above the plateau region, it is straightforward to calculate that in the non-relativistic limit, the relationship between an initial point of the trajectory defined by $(p_{//0},p_{\perp 0})$ and $(p_{//},p_\perp)$ is given by $p_{\perp 0}^2 = \left(p_{//}^2 + p_\perp^2\right)\left(\frac{p_{//}^2}{p_{//0}^2}\right)^{\frac{1}{Z}} - p_{//0}^2$, where Z is the ion charge. If $f(p_{//},p_\perp)$ is a Maxwellian function of $p_\perp$ at the upper boundary of the plateau region, it can be shown that the perpendicular temperature above the plateau $T_\perp(p_{//}) = T_\perp(p_{//0})\left(\frac{p_{//}^2}{p_{//0}^2}\right)^{\frac{1}{Z}}$ is a decreasing function

of $p_{//}^2$, a dependence which is in disagreement with numerical computations (Fig.4). In the limit of $T_\perp \to \infty$, which corresponds to strong pitch-angle scattering, $T_\perp^* = T_\perp$ since iso-f contours in momentum phase space are circles in this case. The increase of $T_\perp$ as a function of $p_{//}$ above the plateau region is deeply related to the local slope of the distribution function in the perpendicular direction. From the definition of a local perpendicular temperature $T_\perp^{loc}(p_{//}, p_\perp) = -\frac{1}{2}\left(\frac{\partial \ln f(p_{//}, p_\perp)}{\partial p_\perp^2}\right)^{-1}$, the non-Maxwellian nature of the electron distribution function as a function of $p_\perp$ may be clearly observed, as reported in Fig.3 for two different values of $p_{//}$. If $T_\perp^{loc}(p_{//}, p_\perp)$ is roughly approximated by a linear function of $p_\perp^2$ in the domain where it increases with $p_\perp$, then it can be shown that the strong increase of $T_\perp$ above the plateau region as a function of $p_{//}$ observed numerically may be well reproduced (Fig.4). Similar results may be obtained by a numerical integration of the Langevin equations, from the upper boundary of the plateau. In particular, iso-f contours are well described (Fig.3), as well as the $p_{//}$ dependence of $T_\perp$ (Fig.4). The rise of $T_\perp$ may be explained by several mechanisms. It arises likely from the much easier momentum transfer between the LH wave and high $p_\perp$ electrons because of their low collisionality as compared to electrons with low perpendicular energy. Finally, the saturation of $T_\perp$ with $p_{//}$ is analysed as a spurious effect which is a result of the finite size of the mesh over which the 2D Fokker-Planck equation is solved. Indeed, its position is an increasing function of the upper limit of the momentum grid from 35 to 55 as shown in Fig.4, and therefore is not an intrinsic characteristic of the fast electron dynamics at high energy. It is worth to note that this numerical error arises mainly because of the relativistic corrections at high energy. Indeed, the condition of no flux at the external boundary of the mesh is no more fulfilled (Fig.4), leading to a spurious loss term in the calculations and a rapid decrease of $T_\perp$ with $p_{//}$. As a consequence, it turns out that even if the mesh over which the Fokker-Planck equation is solved extends up to p = 30, the electron distribution function has the correct shape for $p \leq 20$ - 25 only. Therefore, a detailed study of the distribution function at high energy requires a very large momentum domain, for accurate calculations.

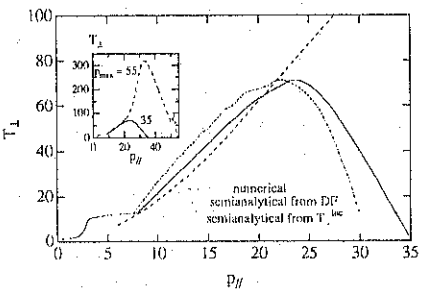

Fig. 4. Perpendicular temperature $T_\perp$ as a function of $p_{//}$. In the insert, calculations for different values of the upper limit of the momentum grid.

References

[1] X.Litaudon et al., Proc. 11th Top. Conf. on Radio Frequency Power in Plasmas, Palm Springs, USA (AIP, New York) 355 (1995) 90.

[2] R.Arslanbekov et al., Proc. 22th EPS Conf. on Controlled Fusion and Plasma Physics, Bornemouth, United Kingdom, Vol.IV (1995) 393.

[3] Y.Peysson et al., Proc. 11th Top. Conf. on Radio Frequency Power in Plasmas, Palm Springs, USA (AIP, New York) 355 (1995) 102.

[4] M.Shoucri, I.Shkarofsky, Comp. Phys. Comm. 82 (1994) 287.

[5] K.Kupfer et al., Phys. Fluids B, 5 (1993) 4391.

[6] J.P.Bizarro et al., Phys. Fluids B, 5 (1993) 3276.

[7] V.Fuchs et al., Phys. Fluids 28 (1985) 3619.

[8] I.Shkarofsky et al., Proc. 9th Top. Conf. on Radio Frequency Power in Plasmas, Charlestone, USA (AIP, New York) 244 (1991) 280.

Study of the Waveguide Antenna Coupling of the Ion Bernstein Wave Experiment on FTU

R. Cesario, O. Sauter *
Associazione Euratom-ENEA sulla Fusione, Centro Ricerche Frascati
00044 Frascati, Rome, Italy
*Ecole Politechnique Federale de Lausanne, Centre de Recherches en Physique des Plasmas
Lausanne, Switzerland

The waveguide grill antenna, routinely used in the lower hybrid (LH) current drive experiments, was also proposed for coupling the ion Bernstein waves (IBW) to tokamak plasmas [1]. This type of antenna has been first employed in the IBW plasma heating experiment on FTU [2]. With 1.5 MW of rf power at a frequency of 433 MHz, and a toroidal magnetic field of about 8 Tesla, this experiment, which is starting now, operates with the 4th ion cyclotron harmonic of a hydrogen plasma near the plasma centre. The scheme of the IBW plasma coupling is shown in Fig. 1, in a slab plasma geometry with x, y, z, corresponding to the radial, poloidal and toroidal directions, respectively. The trend of the wavevector component perpendicular to the toroidal magnetic field is shown against the radial abscissa in the scrape-off plasma region, near the slow wave antenna. The electron plasma waves with parallel refractive index $n_{//} \geq n_{//cr}$ (typically is $n_{//cr} \approx 2$, for standard tokamak plasma parameters), mode-converts into the lowest-temperature ion Bernstein mode, near the lower hybrid frequency [3]. The IBW propagates in the plasma centre and is absorbed on the plasma particle near the ion cyclotron harmonic. This scheme is similar to the original lower hybrid launching proposed by Stix [4], with the difference that the operating frequency is lower, occurring in the range of the ion cyclotron frequency.

In order to estimate the antenna-plasma coupling, the wave equations must be solved for determining the surface plasma impedance. The wave equation problem allows analytical

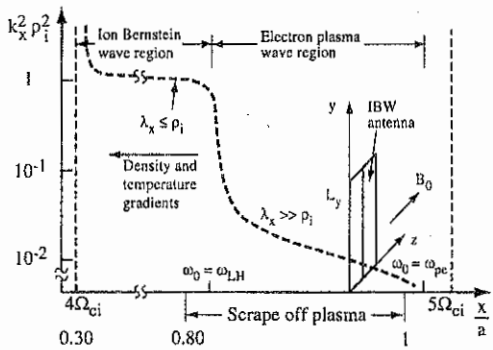

Fig. 1. Scheme of the IBW coupling following the linear wave dispersion relation. k_X is the wavevector component perpendicular to the toroidal magnetic field, ρ_i is the ion Larmor radius. Slab plasma geometry with x, y, z the radial, poloidal and toroidal directions respectively. The FTU hydrogen plasma are considered: major radius R = 0.93 m, minor radius a = 0.33 m, parallel refractive index n_Z = 5, toroidal magnetic field 8 T, operating frequency f_0=433 MHz.

solution only in the range $\omega_{ci}/\omega_0 \leq 2$ of the ion cyclotron harmonic frequency [5]. For the high harmonic range: $\omega_{ci}/\omega_0 \geq 4$, $k_{perp}\,\rho_{oi} \geq 1$, relevant for the IBW experiment on FTU, a full-wave model and a numerical solution of the wave equations should be considered (ω_{ci}, ω_0 are the ion cyclotron and the operating frequency, k_{perp} is the wavevector component perpendicular to the toroidal magnetic field and ρ_{oi} is the ion Larmor radius). In the present paper, we show the antenna-coupling results obtained by the numerical solution of the surface plasma impedance, by considering the plasma parameters relevant for the IBW-FTU experiment. The present full-wave analysis of the surface plasma impedance has been carried out by the SEMAL code [6], which solves the integro-differential equations for the wave electric field in the wavevector space, for any value of ω_{ci}/ω_0 and $k_{perp}\rho_{oi}$, and for any assumed profile of plasma density, temperature and magnetic field, in the antenna coupling region. The surface plasma impedance $Z_p(n_y,n_z)$, given for each partial wave of the Fourier spectrum by :

$$\underline{E}_{perp}(n_y,n_z) = \underline{\underline{Z}}_p(n_y,n_z)\,\underline{B}_{perp}(n_y,n_z),\quad \underline{E}_{perp} = E_y\underline{e}_y + E_z\underline{e}_z,\quad \underline{B}_{perp} = B_z\underline{e}_y - B_y\underline{e}_z$$

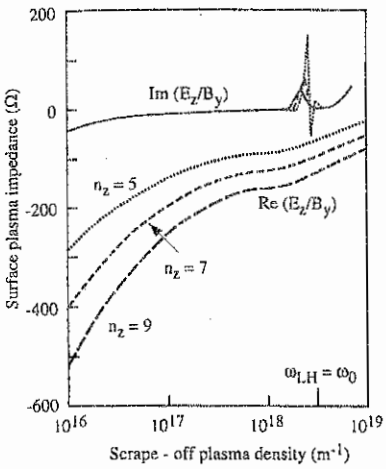

Fig. 2. Plasma surface impedance vs. the local density of the scrape-off plasma at the antenna mouth, with the parallel refractive index as parameter. Same plasma parameters as in Fig. 1.

can be evaluated at any antenna position in the scrape-off plasma, also near the EPW-IBW mode-conversion layer, without losing precision of the solution ($n_y = k_y/c\omega_0$, $n_z = k_z/c\omega_0$, are the components of the wave refractive index in the poloidal and toroidal directions). The E_z/B_y component, of the surface plasma impedance is shown in Fig. 2, versus the local plasma density. The FTU scrape-off plasma parameters have been assumed, and some n_z values in the range corresponding to the maximum emitted rf power by the waveguide antenna for 0-π phasing, are considered. This impedance component is relevant for the wave electric field polarisation of the fundamental TE_{01} waveguide mode. The waveguide antenna coupling has been determined by evaluating the reflection coefficients of each waveguide, due to the reflected fundamental TE_{01} and all the evanescent higher modes, for a given transmission coefficient of the fundamental TE_{01} incident mode (see Fig. 3). In the analysis of the vacuum fields in the waveguides, we have taken into account the waveguide finite extension

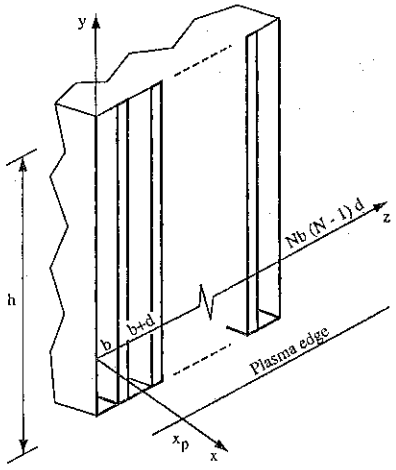

Fig. 3. Sketch of the antenna-plasma interface.

in the poloidal (y) direction, due to the low operating frequency of the IBW experiment, so that the field wavelengths are comparable to the antenna dimensions. The calculated total reflected rf power versus the local plasma density at the antenna mouth, expected for standard positions of the antenna in the scrape-off layer, is shown in Fig. 4. The two waveguide antenna of the FTU experiment, with dimensions l_y=0.4 m, l_z=0.08 m, is considered. Two relative phasing between the waveguides, 0° and 180°, have been considered. We observe that very high reflection of the rf power for the 0° phasing is expected, and a good antenna coupling is possible with 180°. All these results are obtained by calculating at any position the plasma surface impedance matrix, in the wavenumber range: $-0.5 \le n_y \le 0.5$, $0 < n_z \le 100$, in order to obtain a sufficient wave field reconstruction by the Fourier spectrum.

Recent IBW heating experiments of tokamak plasmas showed that a good antenna coupling was not sufficient for having the coupling and the propagation of the IBW in the plasma interior. No plasma heating was observed during the IBW experiment on DIII-D, despite of an optimum antenna coupling. Parametric instabilities observed from the scrape-off plasma were invoked as responsible of the poor wave penetration into the plasma interior [7]. A possibility of reducing the parametric instability intensity was found by operating at high local plasma density near the antenna, during the IBW heating experiment on PBX-M [8]. This result was in agreement with a model of convective losses of the parametric instability due to the plasma inhomogeneity [9]. Following that model, the rf power threshold of the parametric instability expected in the IBW experiment on FTU has been calculated, and the result is shown in Fig. 4. The rf induced insta-

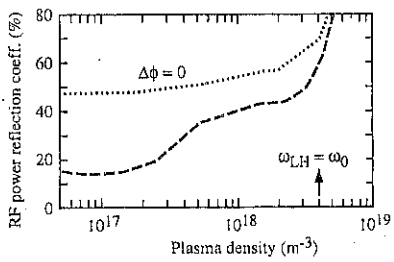

Fig. 4. Calculated reflection coefficient of the rf power of the IBW waveguide antenna vs. the plasma density at the antenna mouth, for waveguide phasing $\Delta\phi$=0, $\Delta\phi$=π. The scrape-off plasma parameters as in Fig. 1 are considered. The antenna consists of N=2 waveguides of height h=40 cm, transverse dimension b=3.6 cm, separated by cm thick metallic wall, d=0.2 cm.

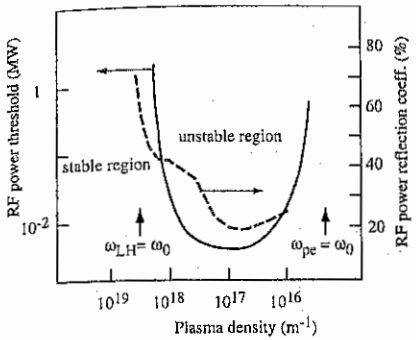

Fig. 5. RF power threshold of the parametric instability (continuous line) and RF power reflection coefficient (dotted line) vs the local plasma density at the antenna mouth. Same plasma parameters as in Fig. 1

bility, which occurs in the scrape-off plasma near the antenna, can be strongly reduced by operating at high local plasma densities at the antenna-plasma interface, so as $0.7 \leq (\omega_{LH\ local}/\omega_0) < 1$, where a marginal antenna coupling (~40%) is expected. We can conclude that the IBW antenna coupling to a tokamak plasma is mainly dependent on the local plasma density at the antenna mouth, for a given operating frequency. For low local plasma densities, so as $\omega_{LH\ local} << \omega_0$, we have found a good waveguide antenna coupling, with a rf power reflection coefficient less than 20%. In this condition, corresponding to a distance of many wavelengths between the antenna and the IBW mode conversion layer, a similar result can be recovered by the Brambilla's lower hybrid grill code. Moreover, a marginal coupling of 30-40% reflected rf power is found, by assuming higher local plasma densities, so as $0.3\ \omega_0 \leq \omega_{LH\ local} \leq 0.7\ \omega_0$. These conditions should be useful for operating with a low activity of the parametric instabilities, which can affect the wave propagation beyond the scrape-off plasma. Moreover, by operating with the antenna located beyond the IBW mode conversion layer, so as $\omega_{LH\ local} \geq \omega_0$, a very high power reflection is expected, which shows that the direct coupling of the ion Bernstein wave to the plasma, without launching the buffer electron plasma wave, cannot be obtained.

References

[1] S. Puri, Phys. Fluids **22** (1979) 1716; M. Ono, Heating in Toroidal Plasmas, Como (Italy) 1980, **1**, 593, Ed. by the Commission of the European Communities, Brussells (Belgium)

[2] P. Papitto, R. Cesario, F. De Marco, G.L. Ravera, M. Sassi, in Fusion Technology 1992, Rome, Elsevier Science Publishers B.V. 1993

[3] H.T. Stix, Waves in Plasmas, American Institute of Physics, New York, 1992, p. 301

[4] H.T. Stix, Phys. Rev. Letters, **15** (1965) 878

[5] M. Brambilla, Nuclear Fusion, 28 (1988) 549)

[6] O. Sauter, J.Vaclavik, Nucl Fusion, **22**, n. 8 (1992) 1455

[7] Pinsker R. et al., in Radiofrequency Power in Plasmas (Proc. 9th Top. Conf. Charlston, 1991) AIP, New York (1991) 105

[8] Cesario, R., et al., Nucl. Fusion **34** (1994) 261

[9] Cardinali, A., Cesario, R., De Marco, F., Sauter, O., in Radiofrequency Heating and Current Drive of Fusion Devices, EPS Top. Conf., Brussels, 1992, **16E**, p. 153.

Bounce Averaged Fokker-Planck Code for the Simulation of ECRH at W7-AS

N Marushchenko
Institute of Plasma Physics, NSC KIPT, 310108 Kharkov, Ukraine

U Gasparino, H Maaßberg, M Romé
Max-Planck Institut für Plasmaphysik, EURATOM Association, D-85748 Garching, Germany

For the modelling of low density ECRH discharges a full kinetic description is needed. The basic equation describing the electron distribution function, f_e, is the gyro-averaged Fokker-Planck (FP) equation in a 5-dimensional phase space with the quasi-linear diffusion term. So far, a fully self-consistent solution of this problem is clearly outside the bounds of numerical possibilities.

At sufficiently low collision frequencies, the phase space dimension can be reduced by bounce-averaging of the kinetic equation. The bounce-averaging procedure is based on the existence of a very fast time scale, relevant to the quasi recurrent motion of the particles along the field lines. In a locally periodic magnetic field a particle can be reflected (trapped particles), or it can suffer a periodic variation of its parallel velocity, without changing the direction of its motion (passing particles). The bounce-averaging procedure is explicitly defined, for an arbitrary function A, as $< A >_b \equiv \tau_b^{-1} \oint A\, ds/v_\parallel$, where $\tau_b \equiv \oint ds/v_\parallel$ is the "bounce time". The integrals are defined over a complete bounce orbit for trapped particles (i.e., from one turning point to the other, and back), and over a complete period of the magnetic field for passing particles.

For a general magnetic field configuration the bounce-averaging has to be performed numerically for every particle population (trapped and passing), and trapping/detrapping mechanisms have to be formulated by suitable boundary conditions. In the axisymmetric (tokamak) case, only one population of trapped particles exists. Moreover, the conservation of the toroidal momentum allows a further reduction of the dimensionality of the problem, and the FP equation can be solved in a 3-dimensional phase space of invariants (energy, magnetic moment, and toroidal momentum) [1]. A general stellarator magnetic field configuration is characterized, on the contrary, by the existence of local (helical and toroidal) mirrors, and there is no rigorous way to define the different trapped particle populations.

Limiting the analysis to the treatment of central (*on-axis*) ECRH, a bounce-averaged FP model can be introduced, which is well suited to treat the specific magnetic configuration effects of W7-AS close to the axis, where the toroidal mirror term dominates in the Fourier expansion of B. Here the radial and poloidal variations of B are disregarded. The problem is finally formulated as a time-dependent 2D Fokker-Planck equation, for the different populations of trapped particles and passing particles. The FP equation is written as

$$\frac{\partial f_{e0}^i}{\partial t} = < C(f_{e0}^i) >_b + < S_{ql}(f_{e0}^i) >_b + < S_{dc}(f_{e0}^i) >_b + < S_{loss}(f_{e0}^i) >_b . \qquad (1)$$

f_{e0}^i represents the bounce-averaged electron distribution function, which has to be considered as a function of time and two invariants of motion. The index $i = \pm, n$ labels the different particle populations: passing particles, with positive (+) or negative (−) parallel

velocity, and trapped particles ($n = 1, \ldots, N_r$, with N_r the number of toroidal ripples being considered). $C = \sum_\alpha C^{e,\alpha}$ represents the Fokker-Planck collision term, where the sum is performed over the particle species α (electrons and ions) existing in the plasma, S_{ql} is the quasi-linear diffusion operator describing the absorption of the EC waves in local approach,

$$S_{ql} = \frac{1}{v_\perp}\frac{\partial}{\partial v_\perp} v_\perp Q_{\perp\perp} \frac{\partial}{\partial v_\perp}, \tag{2}$$

with $Q_{\perp\perp}$ the dominant component of the quasi-linear diffusion tensor, $S_{dc} \propto E_\parallel \partial/\partial v_\parallel$ is a term representing the effect of a dc electric field, and S_{loss} is a general source and loss term allowing for particle and energy conservation in order to obtain stationary conditions, and, in general, for modelling of the *anomalous* electron energy transport. This kind of modelling conserves the essential features of both the quasi-linear diffusion driven by the ECRH absorption and the effect of the power loss term in velocity space.

A numerical code has been developed to solve Eq. (1) taking into account the simplified magnetic field geometry close to the axis of W7-AS. The code allows to consider an arbitrary number of toroidally trapped particle populations (in the case of W7-AS, $N_r = 5$). Several particle populations are physically distinguished: two populations of passing particles, particles being trapped in the toroidal mirror where the ECRH is launched, and particles being trapped in the other toroidal mirrors. The boundary condition between the trapped populations and the common populations of passing particles is given by the continuity of the distribution function and the conservation of the total particle flux.

The numerical solution of Eq. (1) is found by means of a conservative alternating direction implicit scheme [2]. The Coulomb coefficients and the parameters of the source and loss terms are recalculated at each time step. Polar coordinates are used in velocity space. Note that these are the most natural coordinates for the collision term, while the RF and the electric field terms are represented more naturally in cylindrical coordinates. As a consequence, convergence problems could appear for situations with very strong RF heating, localized in velocity space close to the boundary between passing and trapped particles. The code has been bench-marked with the FPPAC code [3], where a homogeneous magnetic field is used, by reducing the size of the trapped particle region in velocity space. Full agreement has been obtained.

The time-dependent solution allows the simulation of quite different situations, e.g., the iteration of the heating and power losses with respect to a fixed temperature, defined, e.g., by the slope of distribution function in the limit $v \to 0$.

In the collision operator, the ion distribution functions are assumed to be Maxwellian with constant temperatures, while the non-linear electron-electron part, $C^{e,e}$, includes the first two Legendre harmonic terms in p, allowing for conservation of total momentum and energy. Note that a nonlinear treatment of the collision term is mandatory in order to describe the energy flux in phase space. The non negativeness of the distribution function is also assured.

Note, that using of the local quasilinear operator as base for obtaining the bounce averaged one, which was formulated and studied in [4] with taken into account nonlocal effects, can be done when the width of the RF beam b is small enough, i.e. if the change of the phase of wave-particle interaction due to the magnetic field inhomogenity is small during crossing RF beam by particle, $\delta\Phi \sim N_r^2 \epsilon_t b^3/(\rho_e R^2) \ll 1$, where ϵ_t, ρ_e, R are the toroidal modulation, electron gyroradius and big radius of device, respectively.

The specification of the quasi-linear diffusion coefficient requires, in general, the knowl-

edge of amplitude and spectrum of the local RF fields. These are determined by the propagation characteristics of the waves involved. In particular, the amplitude of a component of the wave spectrum at a given point depends on the amount of damping it experiences while propagating through the plasma. This, in turn, is a complicated function of the electron distribution function along the path of the wave. Thus, in general, the determination of the electron distribution function and the quasi-linear diffusion coefficient must be made simultaneously. The most common approach is to use Maxwellian absorption rates calculated for a uniform magnetic field. Following this approach, the quasi-linear diffusion coefficient has been computed by means of a 3D Hamiltonian ray-tracing code. In particular, only the $Q_{\perp\perp}$ component of the diffusion tensor, has been taken into account, the acceleration due to the EC waves being mainly in the perpendicular velocity direction. The diffusion coefficient is averaged on a small magnetic flux tube around the axis. This is equivalent to describe the effect of the heating by means of an "effective" quasi-linear diffusion coefficient independent of the radial and poloidal coordinates. The toroidal dependence (a Gaussian profile is assumed) of the injected beam is retained for the bounce-averaging. This simplified approach is justified for focused EC beams.

In the low density ECRH discharges, radiative losses as well as collisional electron-ion power transfer are fairly small, and the radial electron energy transport plays the dominant role. In general, the so called *anomalous* transport, i.e., a mechanism being not understood, has to be formulated as a power sink in phase space for the Fokker-Planck modelling, in order to attain stationary conditions. The resultant distribution function depends sensitively on the form of this power loss term. Quite different loss models can be tested, e.g. a *convective* term, defined only in the trapped particle region, for the simulation of fast losses of energetic trapped electrons due to the radial drift [5], a loss model at low $v_\perp$ simulating the parallel power losses in case of strong magnetic turbulence, or a simple isotropic loss term, proportional to $(v^2 - < v^2 >) f_{e0}$.

The code allows to study the deviation of the stationary electron distribution function from the Maxwellian for the different populations in many different physical situations, e.g., in terms of the field ripple, the heating power density, the heating scenario (fundamental O-mode and second harmonic X-mode), and the electron density [5].

Here we report only two examples of applications of the code. Perpendicular ECRH at the second harmonic X-mode with a minimum of B at the launching position, leads to very high power densities for the electrons being trapped in the local mirror at the launching plane. The formation of a strong tail is found by the FP simulations for this population of electrons. Fig. 1 shows the bounce-averaged electron distribution function f_{e0}, as a function of the parallel and perpendicular velocities computed in the toroidal position of minimum B. Note that a deviation from the initial Maxwellian distribution, though much smaller, can be observed in the other toroidal ripples, due to the collisional energy transfer. The distribution of passing particles remains close to the initial Maxwellian distribution.

The code allows also to study scenarios with oblique RF injections, and therefore to estimate the EC driven current. In the example shown in Fig. 2, the most part of the input power is absorbed by barely passing particles, with a definite sign of the parallel velocity. The trapping as a consequence of their acceleration in the perpendicular velocity, determines a loss of momentum of this population of passing particles, and the toroidal induced current turns out to be in the direction opposite to that of launching [6]. A similar scenario has been experimentally studied, as reported in Ref. [7].

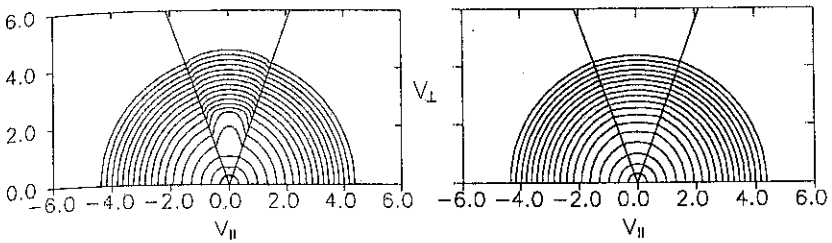

Fig.1. 2nd harmonic X-mode, "*minimum B*" scenario: isoline plots of the bounce-averaged electron distribution function with trapped electron population within the ECRH launching plane (**right**) and for the other field periods (**left**). Parameters are following: $n_e = 1 \cdot 10^{13} cm^{-3}$, $T_e = 1.5keV$, $P_{abs} = 10W/cm^3$ (corresponds to 400kW of total inputed RF power).

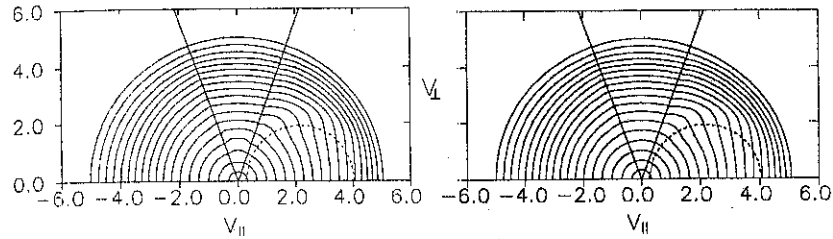

Fig.2. Case of oblique launching of RF beam for "*minimum B*" scenario (**right** and **left** are the same as above). Dotted line is the resonant line on axis at minimum B point. Parameters are following: $n_e = 1.5 \cdot 10^{13} cm^{-3}$, $T_e = 1.5keV$, $P_{abs} = 10W/cm^3$, $N_{||} = 0.185$, $n\omega_{ce}/\omega = 0.996$. Note, that due to effect of trapping of some part of passing electrons the resultant current ($\langle \overline{v_{||}} \rangle = -0.012 v_{Te}$) has the opposite to sign of $N_{||}$. The local coefficient of quasilinear RF diffusion is given from 3D ray-tracing modelling.

References.

[1] F.S. Zaitsev, M.R. O'Brien, and M. Cox, Phys. Fluids B **5**, 509 (1993)

[2] Ju.N. Dnestrovsky, D.P. Kostomarov, *Mathematical Simulation of Plasma*, Springer-Verlag, New York (1985)

[3] J. Killeen, G.D. Kerbel, M.G. McCoy, and A.A. Mirin, *Computational Methods for Kinetic Models of Magnetically Confined Plasmas*, Springer-Verlag, New York (1986)

[4] Kuyanov A.Yu., Skovoroda A.A., Timofeev A.V., Plasma Phys. Rep. **19**, 683 (1993)

[5] M. Romé *et al.*, submitted for publication to Plasma Phys. Control. Fusion

[6] R.H.Cohen, Phys. Fluids **30**, 2442 (1987).

[7] V. Erckmann *et al.*, Fusion Eng. Design **26**, 141 (1995)

Characterization of LHCD Suprathermal Electron Distributions on TdeV [1]

P. Brooker, D. Boyd*, C. Côté
M. Shoucri, I. Shkarofsky, Y. Peysson** V. Fuchs, R.A. Cairns†
A. Côté, Y. Demers, F. Skiff*

Centre canadien de fusion magnétique, Varennes, Canada J3X 1S1
*Univ. of Maryland, USA **CEA-Cadarache, France †Univ. of St-Andrews, U.K.

1:Introduction

Measurements performed on TdeV, [B = 1.5-1.9 T, R = .86m, a = .25m, I_p = 140-200 kA], have been used to deduce properties of the suprathermal electron distribution generated during Lower Hybrid Current Drive (LHCD) [1]. Such measurements are important because correct modelling of LHCD suprathermal electrons is necessary for the design of future advanced tokamaks that are proposing to use LHCD to maintain the reverse magnetic shear required for enhanced confinement operation.

Three diagnostics sensitive to the presence of LHCD suprathermal electrons are used; the electron cyclotron transmission (ECT) diagnostic[2], a hard X-ray camera and a filtered soft X-ray tomographic array. Data from these 3 diagnostics are presented below along with comparisons to Fokker Planck simulations.

2:ECT Measurements

The ECT diagnostic measures $f_{//}(|p_{//}|)$ which is the asymmetric part of the parallel electron momentum distribution; $f_{//}(|p_{//}|) = f(p_{//}) - f(-p_{//})$. Measurements have been made along two chords, at r/a = 0 and r/a ~ ½ . Fig. 1 shows the results of the off-axis channel for shot 27654, [I_p = 142kA, n_{eo}=2.0×10^{19}m^{-3}, $N_{//0}$ = 3.0, V_{loop}= .05Volts , T_{eo} = 2.2 keV, q_o = 0.8, P_{rf} = 680 kW]. The distribution is flat which is more representative of a RF "quasilinear plateau" than that of a runaway tail. Also, the end of the plateau is at least 95 keV which is well beyond $E_{//}$=30 keV which corresponds to the injected $N_{//0}$=3. Since V_{loop}=.05V for this shot, the effect of electric field cannot explain this extended tail.

The value of $N_{//}$ associated with a resonant energy of 95 keV is 1.9 . This

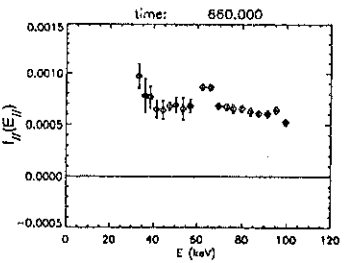

Figure 1 ECT signal for 27654

[1] *Supported by the Canadian Government, Hydro-Québec and INRS*

can be related to the values of $N_{//}$ allowed by the requirement of non evanescent wave propagation. Requiring $N_{\perp}^2 \geq 0$ in the infinite, magnetized, cold plasma dispersion relation, $P_4 N_{\perp}^4 + P_2 N_{\perp}^2 + P_0 = 0$, one finds that there exists a lower bound on $N_{//}$. The ECT signal sensitivity increases with density so one would expect that the maximum contribution to the off axis signal would come around the horizontal midplane. Fig.2 plots the lower bound on $N_{//}$ for the $z = 0$ horizontal midplane. From the graph, the lower bound on $N_{//}$ for r/a =½ is 2.3 which corresponds to a resonant energy $E_{//}$ = 48 keV. This implies that all lower hybrid waves that are resonant with electrons with parallel energies greater than 48 keV would be evanescent and hence not allowed to exist, in contrast to the ECT data.

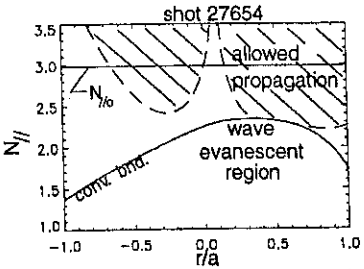

Fig.2 Conversion Boundary and lower propagation boundary.

There are various hypothesises to explain this fact. One hypothesis is that although the ECT signal implies that there are 100 keV electrons present at $(r/a, z) = (½, 0)$, these high energy electrons could be produced by lower hybrid waves resonant at some place else on the same or neighbouring flux surface. For example, the position $(r/a, z) = (-½, 0)$ is on the same flux surface as the position $(r/a, z) = (½, 0)$. From Fig.2 we see that for $r/a = -½$, the conversion boundary is at $N_{//} = 1.85$. This corresponds to a resonant energy of $E_{//} = 96$ keV which is consistent with what is measured by the ECT signal.

In Fig.2, $N_{//} = 1.85$ at $r/a = -½$, is outside of what is marked as the allowed propagation region. All lower hybrid rays are expected to be confined in this region which is bounded by $k_r=0$ cut-offs and caustics[3]. If the 100 keV electrons are accelerated from such waves, it would imply that the rays tunnel through the propagation boundary. Evidence of waves outside the propagation boundaries has also been seen on PBX-M[4].

The distribution measured by the ECT signal in Fig. 1 occurred during a 8 msec time window centred around 660 msec. Often, the distribution changes dramatically from one 8 msec scan to the next. This indicates that the distribution is not as steady state as is usually assumed. These changes in the distribution are not correlated with either the loop voltage or the bremsstrahlung X-ray emission from the plasma measured by the X-ray diagnostics mentioned later. One candidate to explain this behaviour is the anomalous doppler instability. In this, a distribution which is very asymmetric in the parallel direction, symmetrizes itself in the parallel direction by pitch angle scattering.

3: Hard X-ray Camera

The hard X-ray camera consists of 4 Cd-Te detectors viewing the plasma along perpendicular impact parameters of 0,-6,-12,-18 cms. The results of shot 27654 are shown

below in fig.3. The X-ray emission energy spectrum is centrally peaked and decays exponentially with energy. The heavy line is for impact parameter -12 cm which corresponds to r/a ~ ½ which is the same as the off axis channel of the ECT. The fact that this channel shows photons with energy at least to 90 keV is consistent with the high energy electrons seen by the ECT off axis channel. The exponential decay constants, referred to as the photon temperatures, range from 13 to 16 keV.

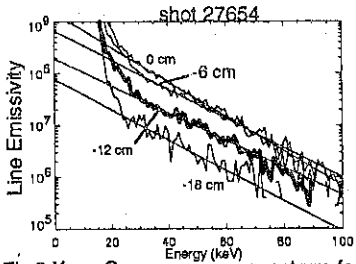

Fig.3 X-ray Camera energy spectrum for impact parameters of 0,-6,-12,-18 cm. Em. units are photons/sec/keV/GF[cm^2]

4: Filtered X-ray Tomographic Array

This diagnostic consists of a linear array of silicon photodiodes that view the plasma through 1.5 atm of argon gas. In contrast to the X-ray camera above that measures an energy spectrum up to 100 keV, the filtered array's detectors are only sensitive to radiation between 9 and 15 keV. Fig.4 shows data for shot 27821 which is typical. [I_p=180kA, P_{rf}=700kW, $N_{//}$ = 2.5, $n_e = 1.6\times10^{19}m^{-3}$]. The diamonds are the experimental line integrated X-ray intensities. Note that there is significant emission all the way up to 18 cm, consistent with the signal from the X-ray camera. The other two curves are the results of Fokker-Plank simulations that will be discussed in the next section.

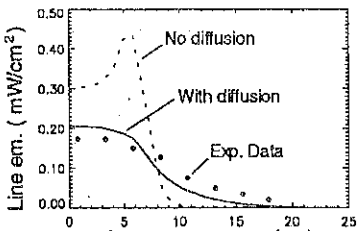

Fig.4 X-ray line integrated emissivity

5: Fokker Planck (FP) Simulations

Simulations from a circular flux surface toroidal ray-tracing code[5] consistently coupled to a fast 2D FP solver[6], predicted power deposition in only a narrow radial range of $0.1 \le r/a \le 0.3$. Consequently, zero signals are predicted for the ECT off axis channel and both the X-ray camera and filtered array for impact parameters $r/a \ge ½$. This is in contradiction to all three diagnostics. This disagreement is partly due to the fact that this code does not include radial diffusion. Furthermore, the code predicts that the ECT signal should drop off rapidly for energies above the injected $N_{//}$. The simulation does predict a photon temperature of 19 keV for the bremsstrahlung emission[7] for impact parameters ≤ 6 cm compared to experimental values 13-15 keV measured by the X-ray camera.

Recently, simulations have been made that use the power deposition profile outputs of the 1½D ACCOME[3] code as inputs to a fast 2D FP solver[8] that includes radial diffusion. The results of this simulation are plotted in Fig.4. for no radial diffusion and for

a diffusion coefficient of $0.1 \cdot v_{//} / v_{th}$ m^2/sec, assuming the diffusion is due to magnetic turbulence[9]. In general, the distributions predict the signal measured by the filtered array fairly well near the centre of the plasma but underestimates the emission for impact parameters greater than mid radius.

There is no doubt that radial diffusion plays an important role in TdeV based on measurements of suprathermal edge losses. However, when simulations are run with a diffusion coefficient large enough to reproduce the edge losses, the resulting hot population radial profile still does not give enough suprathermals to match the measured X-ray emissivities at large radii as in Fig.4. This suggests that the experimental power deposition profile is broader than what the codes are predicting. If, in fact, the level of magnetic fluctuations is high enough to affect radial transport significantly, it has been shown that the same fluctuations (with possible contribution from density fluctuations) can broaden the power deposition profile because of their effect on lower hybrid wave propagation[10]. Collisionless diffusion of accelerated particles across field lines is another mechanism that should be considered[11].

5. Conclusions

The ECT diagnostic has shown that there exists a plateau in the distribution function that extends well beyond the resonance energy of the injected $N_{//}$ and this is consistent with the bremsstrahlung energy spectrum of the X-ray camera. A hypothesis was presented that indicates that the concept of propagation boundaries might not be right. Perhaps one or more of the assumptions used in the calculation is at fault.

The Fokker-Planck simulations predict power deposition in only a narrow radial range of $0.1 \leq r/a \leq 0.3$. Consequently, radial diffusion is required to place suprathermal electrons beyond $r/a \geq \frac{1}{2}$, which is in line with all three diagnostics sensitive to the suprathermal electrons. Furthermore, there is evidence that the power deposition profile is broader than that predicted by the coupled ray tracing-FP simulations.

References

[1]Y. Demers, A. Côté et al., Proc. of 21st EPS, Montpellier, France, Vol. 18B (1994) 1086.
[2]D. Boyd, F. Skiff and S. Gulick, to be pub. in Rev. Sci. Instr., HTPD-1996, Monterey.
[3]V. Fuchs, P. Bonoli, I. Shkarofsky *et al.* , Nuclear Fusion **35** (1995) 1.
[4]H. Takahashi *et al.*, 20th EPS conference, Lisboa, 26-30 July,1993, p. III-901
[5]J. Bizarro, Y. Peysson *et al.*, Phys. Fluids B **5** (1993) 3276.
[6]M. Shoucri, I. Shkarofsky, Computer Physics Communications **82** (1994) 287.
[7]MATLAB bremsstrahlung module compliments of Y. Peysson, TORE SUPRA
[8]I. Shkarofsky, M. Shoucri, CCFM internal report RI 462e.
[9]G. Giruzzi, Plasma Phys. Control. Fusion **35** (1993) A123.
[10]G. Vahala, L. Vahala, P. Bonoli, Phys. Fluids B **4** (1992) 4033.
[11]G. Manfredi, M. Shoucri *et al.*, Fusion Technology **29** (1996) 244.

EFFICIENT IMPURITY EXTRACTION WITH MODERATE POWER OFF-AXIS ICRF HEATING IN A RIPPLED TOKAMAK

Marchenko V.S.
Institute for Nuclear Research, Kiev, Ukraine

Central impurity accumulation can be very detrimental to fusion plasmas and raises doubt about the use of the H-mode in a reactor [1]. So there is a long-standing interest in the possibilities to reverse the normal inward flux of impurities in tokamak plasmas. The possibility of using directed neutral-beam injection (NBI) has been extensively discussed in the literature [2,3]. Here an alternative method is proposed, which is based on the strong enhancement of convective ripple transport of resonating ions in the presence of moderate power off-axis ICRF heating. The mechanism of this enhancement could be described as follows.

Let the resonant surface $\omega=\omega_{BI}$ (here ω is applied frequency, ω_{BI} is impurity cyclotron frequency) be located in the domain, where ripple wells occupy plasma cross-section vertically (Fig.1). Then impurity ions on those magnetic surfaces, which intersect resonant chord, accumulate on the banana orbits shown in Fig.1. Such banana particles will eventually become trapped into the ripple well. In the absence of ICRF a particle, wich is locally trapped in region 1, drifts vertically until it escapes from the local well on the same magnetic surface where it has been trapped. The situation changes considerably in the presence of ICRF. Then the drifting impurity ion remains in resonance when bouncing in the local well. Thus it accelerates vertically and moves down to the bottom of the ripple well. The condition that a locally trapped particle will not escape from the ripple well until it leaves the plasma could be written in the form

$$(\vec{v}_d \nabla)J_s < (dJ_l/dt)_{RF}, \qquad (1)$$

where $\vec{v}_d=\vec{e}_z(v^2+v_\parallel^2)/2\omega_{BI}R$ is the toroidal drift velocity, J_s is the phase volume confined by the ripple well separatrix, $J_l=\oint v_\parallel dl$ is the longitudional adiabatic invariant of the

locally trapped particle, and $(dJ_l/dt)_{RF}$ represents damping of J_l due to ICRF heating in the local well. For typical parameters an ICRF electric field amplitude of $E\sim 10$ V/cm is sufficient to satisfy (1).

The calculated impurity outflux is given by

$$\Gamma_I^{RF} \simeq \frac{3}{2}\frac{n_I T_* |\sin\theta_0|}{m_I \omega R_{res}} \qquad (2)$$

where n_I, m_I are impurity density and mass respectively, θ_0 is poloidal angle at which the given magnetic surface intersects resonant chord $R=R_{res}$, $T_*=(D_b/\lambda)^{1/2}$, D_b is the banana bounce-averaged RF diffusion coefficient in velocity space [4], $\nu_{ad}=\lambda v^2$, ν_{ad} is the rate of trapping into the local well [5]. For typical parameters of the edge tokamak plasma and total input power $P_{RF}\sim 100$kW Eq.(2) gives $\Gamma_I^{RF}\sim 10^{15}\,cm^{-2}sec^{-1}$. For comparison, with about 600kW NB co-injection in the PLT tokamak, an impurity outflux of $\Gamma_I^{NBI}\sim 10^{12}\,cm^{-2}sec^{-1}$ was obtained with close values of edge plasma parameters [6].

REFERENCES

[1] Muller, E.R., et al., Nucl.Fusion 27 (1987) 1817.
[2] Stacey, W.M., Jr., Sigmar, D.J., Nucl.Fusion 19 (1979) 1665.
[3] Stacey, W.M., Jr., Sigmar, D.J., Phys.Fluids 27 (1984) 2076.
[4] Chang, C.S., Colestock, P., Phys.Fluids B 2 (1990) 310.
[5] Goldston, R.J., Towner, H.H., J.Plasma Phys. 26 (1981) 283.
[6] Stacey, W.M., Jr., et al., Nucl.Fusion 25 (1985) 463.

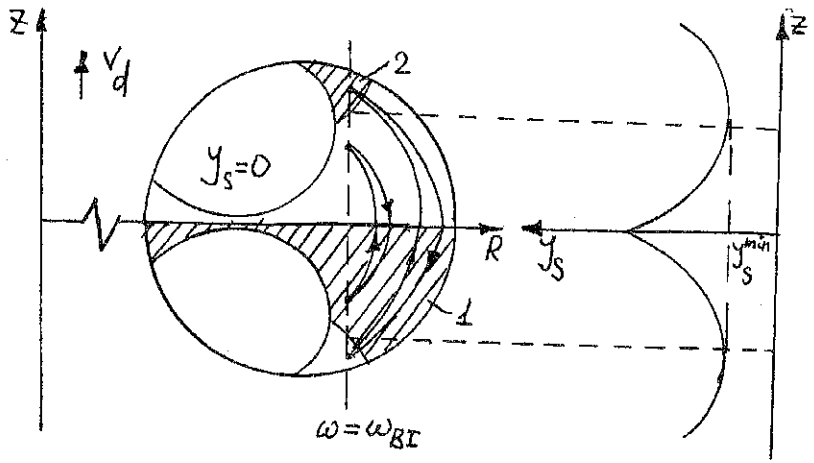

Fig.1 Guiding center orbits of resonant impurity shown in poloidal projection. The hatched regions 1,2 correspond to $(\vec{v}_d\nabla)J_a > 0$, where trapping of banana particles into the local wells is possible.

Cold front propagation and fast non−local temperature response in pellet injected Heliotron E plasma

H.Zushi, Y.Kanda*,M.Hosotsubo*,T.Okamoto*, M.Nakasuga,K.Kondo, S.Sudo** , F.Sano#, T.Mizuuchi#, H.Okada#, K.Nagasaki#, T.Senju#, K.Sakamoto#, C.Christou, Y.Nakamura, M.Wakatani, T.Obiki#, **K.N.Sato****

Department of Fundamental Energy Science, Faculty of Energy Science, Kyoto University, Gokasho Uji 611, Japan
#Institute of Advanced Energy, Kyoto University
*Dept. of Nuclear Engineering, Faculty of Engineering, Kyoto Univ.
** National Institute for Fusion Science, Nagoya 464−01

1. Introduction

An interesting problem related to pellet injection is the transient plasma response to the pellet perturbation. Two types of precooling phenomena have been reported on several tokamaks[1−6]. In first, the temperature inside a particular magnetic surface drops suddenly when a pellet arrives at it. The second shows a cold front propagating faster than the pellet itself. So far the effects of pellet injection on the destruction of magnetic surfaces and a relation to these phenomena have not yet been reported. In this paper, fast response of ECE to pellet injection is described from the point of view of non−local electron enhanced transport triggered by the local perturbation. Particularly, we study (1) how the plasmoid propagates around the torus from the injection port until a new equilibrium state is established, and (2) how the pellet perturbs the electron temperature profile in this short time−scale ($<< \tau_E$). We will discuss the strong magnetic bursts during the ablation phase.

2. Experimental Arrangement and Diagnostics

The particle content and velocity of the pellet are $\sim 6 \times 10^{19}$ particles and $\sim$ 400m/s, respectively. The pellet is injected on the horizontal plane from the outboard side of the torus along the longer axis ($\sim$30cm) of the elliptic plasma. The position of the pellet is deduced by the time trace of H_α emissions from the cloud, which are measured both at the opposite (inboard side) port along the pellet path and at the next inboard port with a sight line crossing the pellet path. The electron density is measured with a 7ch FIR interferometer at the opposite torus port ($\Delta\Phi \sim 180°$) and therefore the density rise due to pellet injection is usually delayed by at least 250 ± 150 μs. A soft X−ray tomography is taken at $\Delta\Phi \sim 47°$ between the pellet and FIR ports. Four arrays with

20 ch detectors(X−ray energy: 0.2∼30 keV) view a plasmoid vertically. A 48 ch ECE system is used to measure the time delay at which the electron temperature starts to decay. The cyclotron emission is detected along the vertical direction along which the magnetic field strength is decreased. This system is located close to the pellet port($\Delta\Phi\sim9.5°$). The magnetic bursts are measured with 120 pick−up coils at several locations around the torus. All these data are recorded at every 3 μs. A target plasma is initiated at B=1.9T by 2nd harmonic ECRH(f=106GHz) with 350 kW, and then NBI with 3MW is performed. Three injection timings are chosen during ECRH and NBI, and after ECRH is turned−off (post−ECRH).

3. Toroidal Propagation of the Plasmoid

Typically dips are observed on H_α emission from the cloud[7]. In order to identify the local position of the travelling pellet, we compare the dip position with some rational surfaces(q=1 and q=2/3). The result for the q=1 surface is shown in Fig. 1. Based on this knowledge, the toroidal propagation of the high density plasmoid is investigated.

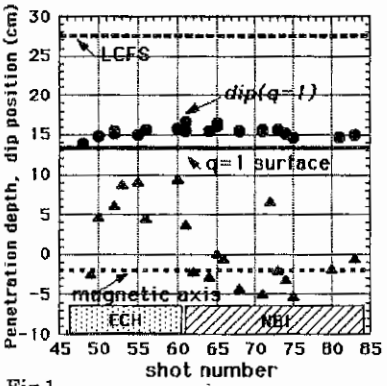

Fig.1

Penetration depths(triangles) and dip positions(circles) are plotted for ECRH and NBI plasmas. Vertical axis indicates the distance from the center of the chamber. In this configuration the magnetic axis is slightly shifted inside.

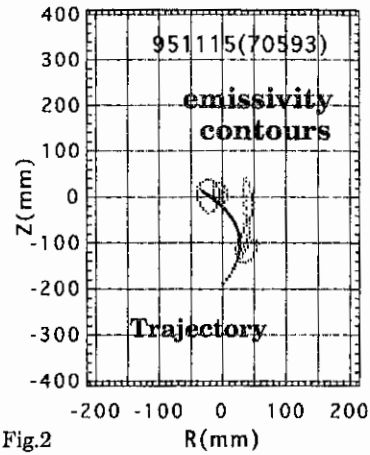

Fig.2

Time sliced X−ray emissivity contours at the peak are plotted. Field line trajectory is also shown by dots. The center of the chamber is R=0 and Z=0.

A density pulse preceding the gradual density rise is observed on the most inner viewing FIR chord [8]. From the comparison with the field line tracing, this pulse agrees well with the trajectory if the high density plasmoid starts around the region between

q=2/3 and q=1, and propagates along the filed lines. This assumption is qualitatively supported by soft X-ray tomography. Figure 2 shows the trajectory of the field lines starting from near the q=1 surface to near the axis along the pellet path. A Li pellet is injected in this case. Five contours around the peak of the emissivity at several times are also shown for 0.5 ms. Agreement between them is fairly good. Thus it is considered that the high density plasmoid propagates along the field lines, when a pellet is ablated at least for $r \lesssim r_s(q=1)$.

4. Cold-Front and Non-Local Response

It is found that there are two types of ECE response. One shows a very short delay time($\sim$100 μs) independent of the plasma radius. The other is the case that the delay time increases with decreasing radius, as shown in Fig.3. Here t=0 is defined as the time at which the pellet arrives at the plasma edge. We call the former "non-local" response, and the latter "cold-front" response. In Fig.3 three ECE signals are taken inside the q=1 surface.

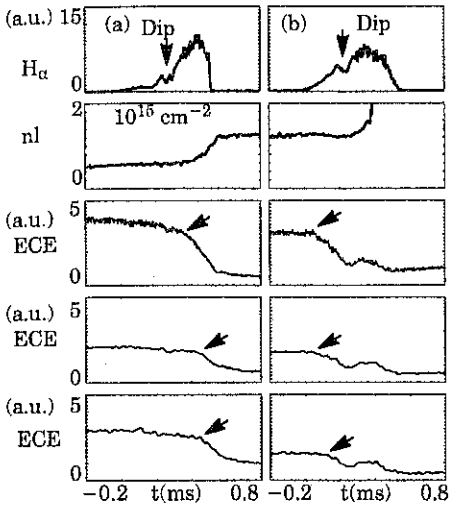

Fig.3 Two types of ECE response (a) "cold-front", and (b) "non-local". H_α, line density, ECE signals (<r>$\sim$9.2cm,4.2cm,0 cm,respectively) are plotted for two (a) post-ECRH and (b) NBI plasmas.

Figure 4 shows the delay time as a function of frequency(radius), which are obtained in ECRH and post-ECRH plasmas. In case of "non-local" response, the ECE signals near the axis start to decay when the pellet penetrates just $\sim$ 4cm from the edge. The radial propagation velocity is 2.5 km/s. On the other hand, the "cold-front" also propagates with a velocity of 500 m/s, which is slightly faster than the pellet velocity. The possibility of the interference with the ECE signals by a high density plasmoid is carefully checked.

From the field line tracing the ECE viewing chord is far from the trajectory of the plasmoid, and on the basis of the toroidal propagation measurement (§3), we consider that ECE is not interfered with the plasmoid. We note that the "cold-front" type is frequently observed in " post- ECRH" plasmas. In ECRH and NBI plasmas, however, the

"non−local" type is usually obtained, although the ablation behavior(at least penetration depth) is quite different, as shown in Fig.1. It is left to the future whether the heating source itself and related effects lead to the "non−local" response, or not.

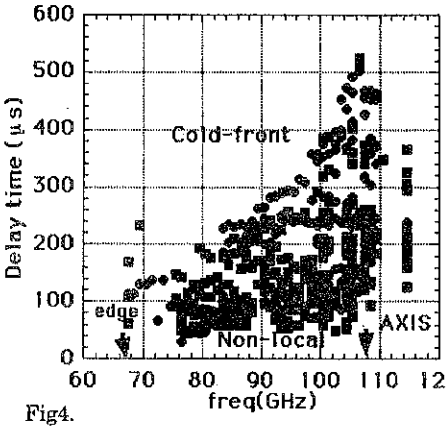

Fig4.
Delay time versus the ECE frequency(the axis corresponds to 107GHz and the edge 67 GHz, respectively) Circles and squares are taken in "post−ECRH" and during ECRH plasmas.

5. Discussion

Regarding the pellet generated magnetic perturbations, we would like to mention that only during the ablation phase(~0.5 ms) strong magnetic bursts are observed. Several modes (poloidal mode number m=1−4) are excited in the frequency range from 5kHz to 80kHz. The amplitude reaches up to 1 Gauss[9]. As shown in Fig.1, dips are found on the H_α trace and the widths of the dips are well correlated with these bursts intensities. In this sense, the islands, if the width is associated with islands[10], are transiently created by pellet injection itself.

Thus it is suggested that island− formation precedes the local pellet position. Then a relation between the mode surface position and penetration depth is investigated. For example, bursts with m=2 are excited when the penetration position is far from the q=2 surface, which is expected to be associated with the mode. This indicates that the core magnetic surfaces are perturbed even when the pellet stays at the edge.

References

[1] A.D. Cheetham, et al., Proc. 14th Eur. Conf. on Control. Fusion and Plasma Phys. Madrid 1987, Vol.11D, Part I 205
[2] M.Sakamoto, K.N.Sato, et al., Plasma Phys. Control. Fusion **33** (1991) 583
[3] TFR Group, Nucl. Fusion **27** (1987) 1975
[4] M.Greenwald et al., 10th IAEA Conf. on Plasma Phys. and Control. Nucl. Fusion Research Vol.1 (1985) 45
[5] G.Vlases, Proc. 11th Eur. Conf. on Control. Fusion and Plasma Phys. Vol. 7D, Part I (1983) 127
[6] W.Liu, M.Talvard Nucl. Fusion **34** (1994) 337
[7] S.Sudo et al., Nucl. Fusion **27** (1987) 1401
[8] H.Zushi et al., Proc. 20th Eur. Conf. on Control. Fusion and Plasma Phys., 1993, Part 2 715
[9] H.Zushi et al., Proc. 18th Eur. Conf. on Control. Fusion and Plasma Phys. , 1991, Part2 153
[10] B.Pegourie, M.A.Dubois, Nucl. Fusion, **29** (1989) 745

Self-consistent currents on ICRH antenna and screen parts taking into account magnetic shielding

S. Pécoul, S. Heuraux, R. Koch* and G. Leclert.
Laboratoire de Physique des Milieux Ionisés, URA CNRS 835,
Université Henri Poincaré, Nancy I, BP 239, 54506 Vandœuvre Cedex (France)
*Laboratoire de Physique des Plasmas - Laboratorium voor Plasmafysica, Association "Euratom-Etat Belge" - Associatie "Euratom-Belgische Staat",
Ecole Royale Militaire -Koninklijke Militaire School 1040 Brussels (Belgium)

1.The Slab Coupling Model and Implementation of the ICANT code

The ICANT code solves the antenna radiation problem using a finite boundary element technique combined with a spectral solution of the interior problem[1]. The slab approximation is used and periodicity in y and z directions is introduced to account for toroidal geometry. The boundary conditions between the plasma and the vacuum can be easily related to the spectral surface impedance matrix[1] ξ. That is to say, the Fourier components of the fields at x=-v are related by the expression $(E_y,E_z)= \omega\xi.(B_z,B_y)$. We assume for simplicity that the plasma is modelled by a density step with a surface impedance matrix resulting from the magnetosonic wave dispersion relation, $k_\perp^2 = u(1 - \mu^2)$, $u = \varepsilon_1 - n_z^2$, $\mu = \varepsilon_2/u$, where ε_1 and ε_2 are the xx and xy components of the dielectric tensor.

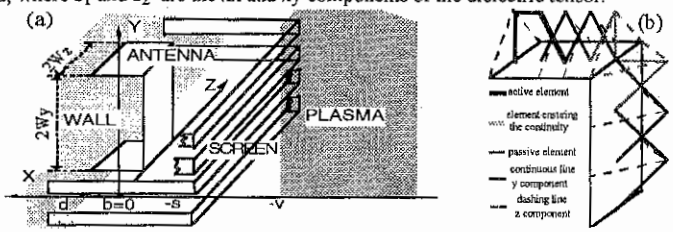

Fig 1: Geometry of the system antenna-plasma (a) and a finite element representation of the current (b).

We choose a finite element representation of the current $\mathbf{J}=\Sigma\, c_i\, \mathbf{T}_i$ where the finite current element $\mathbf{T}_i$ automatically ensures the current continuity (see gray lines on Fig. 1b). The current profile is built self consistently by imposing the vanishing of the tangential electric field on the antenna surface as the conditions $\int_v {}^d\mathbf{E}.\mathbf{T}_i\, dx = 0$. From the set of c_j which determines the current on the antenna we can obtain the needed parameters to characterise the antenna (radiated power, impedance, electric field,...).

The new version of ICANT can now solve cases with fully metallic conductors, i.e. with isotropic conductivity on the surface. To have realistic results, the finite element representation has to be properly chosen. Also more complicated antenna shape like "trombone-type" antennas, with an x-dependence of the current J_x, will be investigated with the present version of ICANT.

2.On the determination of the current profiles on a "trombone-like" antenna.

In the conventional models, the question of how to choose the current distribution on the different parts of the trombone is always problematic. Consider for instance the simple case of Fig. 2a. On that antenna part with a return conductor, two TEM coaxial modes exist that need to be appropriately combined. The self-consistent solution has been analysed for different geometrical parameters of the antenna. This simple case illustrates the deviation from a cosine on each part of the antenna that results from selfconsistency. However ICANT code can describe the effects of particular relevance to antennae like that used in JET or ASDEX-Upgrade.

In the following parts, we have chosen the fixed parameters: R_0= 4 m major radius, r_0= 2 m minor radius, B_T= 6 T toroidal magnetic field for the Tokamak characteristics. For the strap antenna in front of the screen or plasma, we take w_y= 1.2 m strap length, w_z= 0.2 m strap wide and d_1= 0.1 m the distance between wall and strap. Here, the back strap between the main strap and the wall has the same wide and its length ℓ takes different values. The current profiles (Fig. 2b-c) are given versus the distance between the main and back straps when this type of antenna radiates in vacuum. It is easy to see that the current profile on the strap departs from the usual assumption (cosine variation) even for small values of ℓ and d_2=.5d_1 (Fig. 2b).

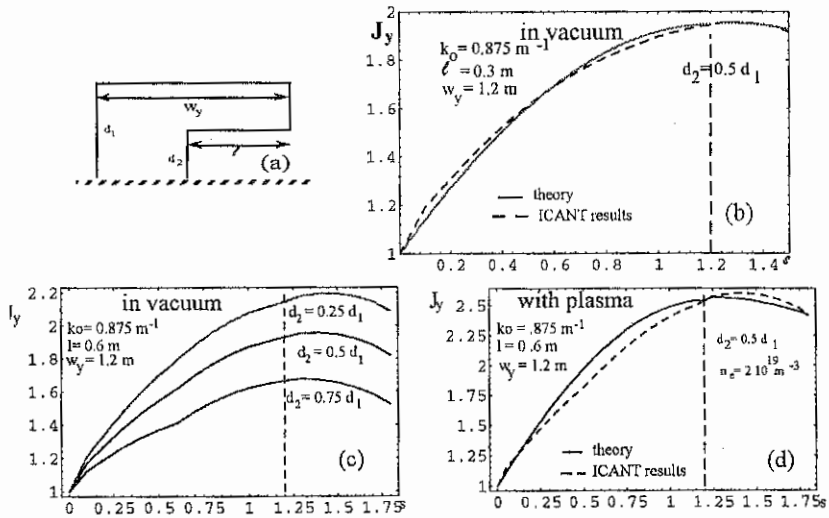

Fig 2. Trombone like antenne: description of the antenna (a). Evolution of the current profile J_y versus curviline coordinate s (b) , J_y versus back strap position (c) and $J_y(s)$ current profile on the antenna with plasma.

In vacuum, the ß values change drastically with the position of the back part of the trombone antenna and the current profile on the main strap is strongly distorted in the region located

above the connection to the wall. In the presence of a plasma, the current profile on the strap is no longer a cosine as shown on Fig.2d. Furthermore the ß value evaluated in vacuum would lead to inconsistent results if it were used in the plasma case.

3. Effects of the position of the screen above or below the strap.

We assume during this part of the work that the screen blades have anisotropic conductivity that is correct if the blades are small enough. This assumption will be discussed in the next paragraph. As shown elsewhere[1], in the case of a single antenna facing a metallic wall, there are resonances of the selfconsistent propagation constant ß. These spurious resonances occur at each zero of $k_y^2+k_z^2-k_0^2$ and are related to the existence of a current J_x perpendicular to the wall. In the presence of plasma, these resonances still exist but they do not contribute significantly to the radiated power and give only small discontinuities of ß when the density is greater than 5. 10^{18} m^{-3}.

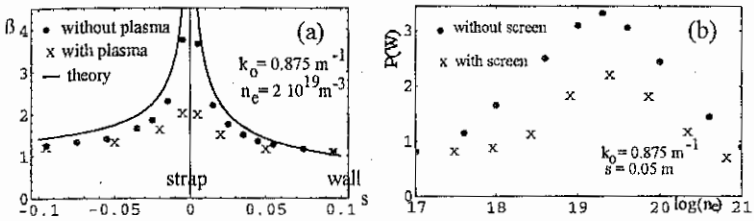

Fig 3 : a) ß versus screen position s, b) radiated power versus plasma density

The system was first tested in vacuum, for a screen made of contiguous blades. It was found that both when the screen is above the central conductor and when it is located between the central conductor and the back wall, the self-consistent ß values (see Fig 3a) agree well with the classical formulae in the plane capacitor limits: (i) screen between strap and wall $ß=\sqrt{d/s}$ and (ii) screen above strap $ß=\sqrt{(d+s)/s}$. For a finite screen with a plasma in front of the antenna the evolution ß versus the position s of the screen is similar but the values are smaller because the screen transparency is now 0.5. The radiated power for a given density and with small values of k_0R_0 depends only weakly on the screen position. The radiated power versus density exihibits a peak as a single antenna[1] but the radiated power is smaller. This peak does not exist when the impedance matrix is deduced from an inhomogenous plasma model.

4. Magnetic shielding effects.

The most basic effect of the so-called magnetic shielding is to distribute the current on the central conductor, as opposed to the conventional model where the current on the strap is assumed unidirectional. Examples of such current distributions, that prevent field lines to

cross the strap, are shown Fig. 4. Similar current loop distributions exist on individual screen blades that exclude the magnetic field from the conductor area.

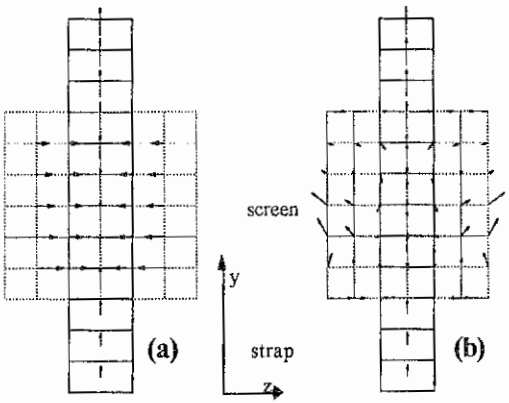

Fig; 4 Current vectorfield on the plate screen and the antenna for anisotropic (a) and isotropic (b) conductivity.

The currents induced on the screen result from two effects. One can be associated to the electric shielding of the strap (as seen for an anisotropic case on Fig. 4a), and the other, associated with magnetic shielding, causes the occurence of current loops (as shown on Fig.b). The fact that the current J_y on the central part of the screen is in the opposite direction of the current on the strap is characteristics of the magnetic shielding. In order to clearly demonstrate the existence of magnetic shielding effects, the next step is to compute the magnetic field generated by the antenna with a screen.

References:

[1] Pécoul S, Heuraux S, Koch R and Leclert G, in *11th Radiofrequency Power in plasmas*, Palm Springs, AIP Conf Proc.**355**, 409 (1995) .

[2] Pécoul S, Heuraux S, Koch R and Leclert G, *22nd EPS Conf. on Controlled Fusion and plasma physics* Bournemouth **19C**, II-337, (1995) .

PROFILE CONTROL IN JET WITH OFF-AXIS LOWER HYBRID CURRENT DRIVE

A. Ekedahl[1], Y. Baranov, J. Dobbing, B. Fischer, C. Gormezano, M. Lennholm,
V. Pericoli-Ridolfini[2], F. Rimini, J. Romero, P. Schild, F. Söldner.
JET Joint Undertaking, Abingdon, Oxfordshire, OX14 3EA, UK.
[1] Electromagn. Field Theory, Chalmers Univ. of Technology, S-412 96 Göteborg, Sweden.
[2] ENEA, Centro Ricerche Energia Frascati, Via E. Fermi 27, 00044 Frascati (Roma), Italy.

1 Introduction

The full Lower Hybrid Current Drive (LHCD) system in JET was brought into operation in the 1994/95 experimental campaign. The maximum LH power coupled to divertor plasmas reached 7.3MW, using 8.2MW generated power. In profile control experiments 13s long LH pulses were applied, delivering a maximum energy of 68MJ to the plasma. Full current drive and sawtooth suppression have been obtained up to 3MA and analysis suggests that overdriving of the current is taking place in low density discharges with high LH power. For I_p>2MA the fast electron profile and LH driven current profile, as deduced from Fast Electron Bremsstrahlung (FEB) measurements, are peaked at approximately mid radius, as is suitable for current profile control. High power LHCD before the Neutral Beam heating phase has been used to study the effect of profile control on Hot-Ion H-modes.

2 Current Drive Efficiency

Full current drive with LHCD alone has been achieved in X-point configuration in the range I_p=0.7-3.0MA and $\bar{n}_e$=0.7-2.0×10^{19}m^{-3}. Fig. 1a shows the theoretical current drive efficiency, calculated for the experimental conditions by a ray-tracing + Fokker-Planck code (LHCD code), against volume averaged electron temperature $\langle T_e \rangle$. No DC electric field effect was taken into account in these calculations. Fig. 1b shows the experimental current drive efficiency for discharges where full replacement of the plasma current was obtained, i.e. with zero resistive surface loop voltage. The variation in Z_{eff} was small and has not been taken into account in the graphs. For line averaged density $\bar{n}_e$>1.1×10^{19}m^{-3} the experimental and theoretical efficiency are in agreement. The efficiency reaches η_{CD}=0.25-0.30×10^{20}m^{-2}A/W, a value which is in accordance with the requirements for advanced tokamak scenarios in ITER. The calculated efficiency (Fig. 1a) saturates above $\langle T_e \rangle$≈1.5keV and for $\bar{n}_e$<1.1×10^{19}m^{-3} the

efficiency drops slightly. An explanation for this behaviour is a shift of the absorption towards lower energy electrons, i.e. $n_{\parallel}$ upshifts, once a saturated plateau in the electron distribution function has been formed. The experimental efficiency (Fig. 1b) deduced from measurements of the surface loop voltage decreases with temperature for $\langle T_e \rangle > 1.5$keV and $\bar{n}_e < 1.1\times10^{19}$m^{-3}. In addition, the hard X-ray emission from the fast electrons appears lower than expected, especially at high LH power (P_{LH}>5MW). A plausible explanation for the observed result is the local overdriving of the current in discharges with excessive LH power. A negative DC electric field, which counteracts the LH wave field, is then induced in the plasma region at approximately mid radius where the LH power is deposited.

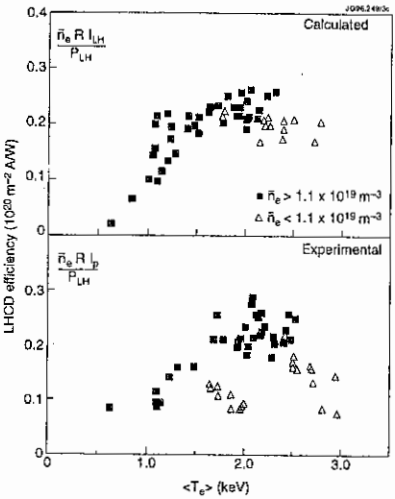

Fig. 1. a) Theoretical η_{CD} without DC electric field effect, calculated by the LHCD code. b) Experimental η_{CD} for full current drive shots.

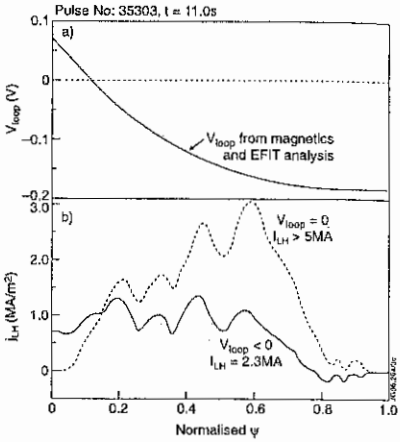

Fig. 2. a) Loop voltage profile from j(ρ)-analysis. b) Calculated LH current profiles for V_{loop}<0 (from j(ρ)-analysis) and V_{loop}=0.

The radial profile of the parallel electric field has been calculated, applying the technique by Forest et al. [1]. The method utilises the radial current profile, j(ρ), determined by magnetic measurements, including Faraday rotation, and EFIT equilibrium reconstruction. The parallel electric field profile can be obtained by evaluating the time derivative of the poloidal flux. Fig. 2a shows the loop voltage profile for a 2MA discharge with

$\bar{n}_e = 0.7\times10^{19}m^{-3}$ and P_{LH}=5.5MW. A reversed loop voltage is obtained in the region $0.1<\psi<1.0$ and in the region outside ψ=0.5 the loop voltage is ~−0.15V, which suggests that the current is being overdriven. There is a discrepancy between the evaluated loop voltage at ψ=1.0, which is almost −0.2V, and the measured surface loop voltage, which remains close to zero. A possible reason is that the measured surface loop voltage is not representative of the value at the plasma surface itself, but at a point further outside the plasma.

The loop voltage profile shown in Fig. 2a was used as input for a simulation of the discharge with the ray-tracing + 2D Fokker-Planck code. The hot conductivity term reached a maximum of $1.6\times\sigma_{Spitzer}$ at ψ=0.6 and the resulting current was 2.3MA. For comparison, when V_{loop}=0 was used in the calculation the driven current amounted to >5MA, see Fig. 2b. The output of the code was then used to calculate the expected FEB emission and to compare it with the measured emission. A reasonable agreement between experimental and calculated line averaged brightness was obtained when the current profile corresponding to 2.3MA and V_{loop}<0 was used. This analysis suggests that the current is being overdriven, but an accurate calculation is difficult in these conditions and there are still discrepancies between measured and calculated current drive efficiency in some discharges.

3 Profile Control Experiments

Full suppression of sawteeth has been achieved with LHCD up to 3MA in conditions close to full current drive (Fig. 3). At low density, a peaked electron temperature profile and high central electron temperature (T_{e0} above 8keV) have been obtained. This high temperature phase is characterised by very low MHD activity.

LHCD has been used to modify the current profile before the formation of Hot-Ion H-modes in order to raise q_0 above unity and to suppress sawteeth during the high power NBI or NBI+ICRH phase. In a first campaign the ELM-free period was reduced when preceding LH profile control was used, probably due to the decrease in edge shear and triangularity associated with the broadening of the current profile. In a second campaign the plasma configuration was modified to keep a higher edge shear, with the result that the length of the ELM-free period was similar both with an without LH profile control. Fig. 4 shows the result of the second experiment. The sawteeth were suppressed during the NBI phase and in some cases there was a softening of the MHD activity, which prevented the decrease of the neutron yield. The ELM which terminated the high performance phase was delayed.

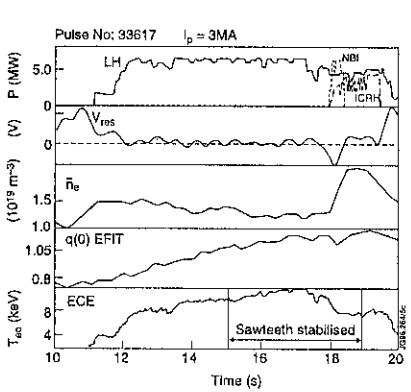

Fig. 3. Sawtooth stabilisation with LH profile control in a 3MA discharge. Full current drive is also obtained.

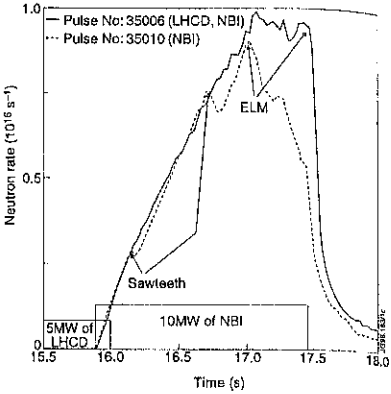

Fig. 4. Time evolution of the neutron rate in Hot-Ion H-modes with and without preceding LH profile control.

4 Summary

Full current drive with LHCD alone has been obtained up to 3MA, resulting in current drive efficiency η_{CD}=0.25-0.30×10^{20}m^{-2}A/W. Analysis suggests that overdriving of the current is taking place in low density discharges ($\bar{n}_e$ <1.1×10^{19}m^{-3}) with high LH power (P_{LH}>5MW), but there are still discrepancies between experimental and calculated current drive efficiency in some discharges.

Sawtooth suppression and strong peaking of the electron temperature profile have been obtained up to 3MA in low density discharges. Promising results have been achieved with LH profile control before Hot-Ion H-modes and forthcoming LHCD experiments will aim at improving MHD stability and confinement of Hot-Ion H-modes and at studying shear optimised scenarios.

Acknowledgement - The authors thank Drs C. Petty and W. Zwingmann for help in the analysis of the loop voltage profiles.

Reference

[1] C.B. Forest et al., Phys. Rev. Lett. 73 (1994) 18.

Dynamics of ECRH Current Drive in the Presence of Source Frequency Tuning

J.A. Heikkinen[1], H. Bindslev[3], and O. Dumbrajs[2]

TEKES-Euratom Fusion Association
[1]VTT Energy, P.O. Box 1604, FIN–02044 VTT, Finland
[2]Helsinki University of Technology, FIN–02150 Espoo, Finland
[3]JET Joint Undertaking, Oxon OX14 3EA, England

Abstract
The various time scales of current generation by electron cyclotron waves are qualitatively investigated for the localized off-axis current drive needed for profile control and plasma stabilization in tokamaks. These are compared with the source frequency tuning rate offered by the present technology. The competition of bootstrap current perturbation created by localized ECRH heating with the conventional electron cyclotron current drive mechanism is also addressed.

1. Introduction

Shaping the plasma current profile in a tokamak is considered an important tool in entering the second stable regime for short-wavelength ballooning instabilities, stabilization of sawtooth instabilities, and for improving the energy confinement in the plasma core by stabilizing microinstabilities. For ECRH control, frequency tuning of the source may be needed to locate the electron cyclotron resonance in proper position. This may be needed even in real time for feedback. To investigate the limits of such frequency tuning for moving the current generation region, the current rise and decay times have to be evaluated and to be compared with the tuning rate. In the same context, the role of diffusion broadening of the current profile and its rate have to be assessed. Such an analysis requires solutions of the electron kinetic equations in the tokamak configuration in response to the fast moving cyclotron resonance region, which work is in progress. In the present work, we report on the results of a parameter study to construct a satisfactory model for a more complete analysis.

Parameter study

The quasilinear diffusion coefficient D for the electron interaction with the microwave is evaluated from [1]

$$D = \frac{\pi}{16\tau}[(\frac{eE_{\parallel}}{m})^2(\frac{k_{\perp}v_{\parallel}}{\omega})^2\frac{e^{-2y^2/L^2}}{Wv_{\parallel}^3}]_{\theta_{res}}\frac{K}{\oint d\theta/v_{\parallel}}, \qquad (1)$$

where $E_{\parallel}$ is the parallel wave field component with respect to the magnetic field, K is the resonance integral, τ is the average time between successive passes through the RF, θ is the poloidal angle, θ_{res} indicates the angle at which the resonance condition $\omega - \Omega_0(r,v,\theta) - k_{\parallel}v_{\parallel}$ is satisfied at radius r, $y = r\sin\theta_{res}$, L is the radius of the microwave beam, e,m denote the electron charge and mass, $v_{\perp}$ and $v_{\parallel}$ are the electron

perpendicular and parallel velocity with respect to the magnetic field, respectively, $\oint d\theta$ denotes the integral over one complete bounce in the particle orbits, and one has defined $W^2 = \sin^4\alpha/L^4 + (\Omega_T'/2v_\parallel)^2$. Here, ordinary wave mode propagation is assumed having fundamental cyclotron resonance with the electrons, ω is the wave angular frequency, Ω is the relativistically corrected cyclotron frequency, $k_\parallel$ and $k_\perp$ are the parallel and perpendicular wavenumber components, respectively, $\Omega_T' = (\Omega_c y/qR^2)(1-k_\parallel v_\perp^2/2\Omega_c v_\parallel)$, Ω_c is the cyclotron frequency at $\theta = \pi/2$, R is the major radius, and q is the safety factor, α is the wave propagation angle with respect to the magnetic field. The above diffusion coefficient is limited by relativistic heating out, giving the maximum $D = (c^2\Delta k_\parallel v_\parallel/L\omega v_\perp)^2/(2\tau_1)$, where $\Delta k_\parallel$ is the spread in the parallel wavenumber spectrum, and $\tau_1 = \tau 2\pi Rq/L$.

In the present model the wave power absorption density p_{RF} is determined from

$$p_{RF} = \int_0^c 4\pi m \frac{\partial}{\partial v}(v^3 \hat{D}) f dv, \tag{2}$$

with the distribution function $f(r,v)$ obtained from the isotropized Fokker–Planck equation

$$\frac{\partial f}{\partial t} = \frac{1}{v^2}\frac{\partial}{\partial v} v^2 \hat{D} \frac{\partial f}{\partial v} + \frac{\partial f}{\partial t}_{coll}, \tag{3}$$

where $(\partial f/\partial t)_{coll}$ denotes the electron-electron collision operator, v is the total electron velocity, and $\hat{D} = (1/2)\int_{-1}^{1}(1-\mu^2) D d\mu$ is the pitch angle averaged diffusion coefficient with $\mu = v_\parallel/v$.

For quantitative calculations, reactor-scale parameters $R = 7.75$ m, $a = 2.8$ m, $B_c = 6.2$ T, $I = 15$ MA, centre density $n_e = 0.84 \times 10^{20}$ m^{-3}, and centre temperature $T_e = 20$ keV with profiles $(1-(r/a)^2)^{0.5}$ are adopted. The cyclotron resonance (in the low velocity limit) is taken at $r = 0.8$ m, and the beam radius is $L = 0.1$ m. For reference, fifty 2 MW beams are considered with almost perpendicular propagation ($k_\parallel = 200$ m^{-1} with $\delta k_\parallel = 60$ m^{-1}). Fig. 1a shows the profile of the absorption density which is well localized near the resonance. The diffusion coefficient $\hat{D}$ is depicted as a function of velocity in Fig. 1b at the radius of maximum absorption density. The distribution function remains here nearly Maxwellian with slowly increasing temperature. This is the consequence of relatively weak diffusion coefficient with respect to the energy diffusion term in the collision operator in the present case. For the present parameters with nearly perpendicular propagation, the current generation might be expected to be small as based on the mechanism of reduced collisionality described in Ref. [2]. For more oblique propagation, the efficiency has been expected to improve to find $j[\mathrm{A/m^2}]/p_{RF}[\mathrm{W/m^3}] \approx 1$. As the magnitude of the diffusion coefficient would not change much with changing propagation angle, characteristic time scale of current generation might stay in the range of a few milliseconds characteristic to the collisional time scale.

Bootstrap current

The local heating of the fast particles can create a local perturbation of the bootstrap

current which has a bidirectional form, as has been found for ICRF and LH heated fast ions [3]. Here, in our reference case no significant fast tail formation is found, but because of the localized heating of thermal electrons similar bidirectional perturbation can arise. By including the thermal diffusion operator $(1/r)(\partial/\partial r)r\chi_e\partial T_e/\partial r$ we have solved from Eq. (3) the evolution of the electron temperature profile with the given power source and have evaluated the corresponding perturbation in the bootstrap current profile. The temperature and bootstrap current profiles for different times are depicted in Figs. 2a and 2b for $\chi = 1$ m^2/s. It can be seen that the ensuing bootstrap current perturbation can amount to a significant level of the created current around the resonance, but its growth might be somewhat slower than the one ensuing from the asymmetry in $k_\parallel$. It should be emphasized that this well-localized bootstrap current of bipolar profile is excited even with symmetric $k_\parallel$ spectrum, thus requiring no directivity in the antenna system, and that it is not degraded by the trapped particle effect but is even enhanced by it. The profile and magnitude of this current are strongly affected by the magnitude of the thermal conductivity. It is interesting to note that for some recently observed reversed shear configurations where the thermal diffusion rate has been decreased to the neoclassical level, the local heating and the ensuing bootstrap current perturbation as presented here would be strongly enhanced (in the absence of any deteriorating mechanisms) with possible beneficial effects for sustaining the reversed shear configuration.

Gyrotron tuning rate

It has been demonstrated that the frequency of a high-power gyrotron can be changed even in microseconds by changing the operating voltage. Fast changes from about 145 GHz to 135 GHz in steps about 2.7 GHz by changing the accelerating voltage from 80 to 125 kV and the modulation voltage can be realized for gyrotrons with coaxial rods. The time scale for variation of the magnetic field even by 2%, resulting in the frequency change by the same amount, would be much longer and of the order of 0.1 s which for some applications is too slow. From the above analysis, the current generation time would be of the order of milliseconds. Obviously, the fast frequency tuning in a much shorter time scale might help to profile the ensuing current profile by sweeping the resonance position appropriately for each application.

Summary

Gyrotrons with fast tuning in frequency can be used for fine tuning of the absorption point in electron cyclotron heating and current drive, enabling their efficiency optimization. The tuning in the range discussed above would be particularly attractive in the MHD mode stabilization and profile control. However, care has to be taken to account for the finite rise time of the driven current, and, interestingly, for the accompanying bootstrap current perturbation which is tied to the local heating and thermal diffusivity. It has been demonstrated that this current which ensues without any wave directivity may be comparable to the current created by the asymmetry in wave spectrum.

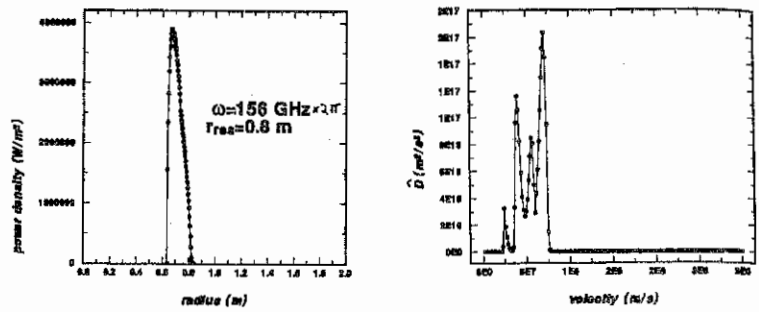

Fig. 1. (a) The power absorption profile and (b) the diffusion coefficient $\hat{D}$ for the ordinary wave propagation with 100 MW input power.

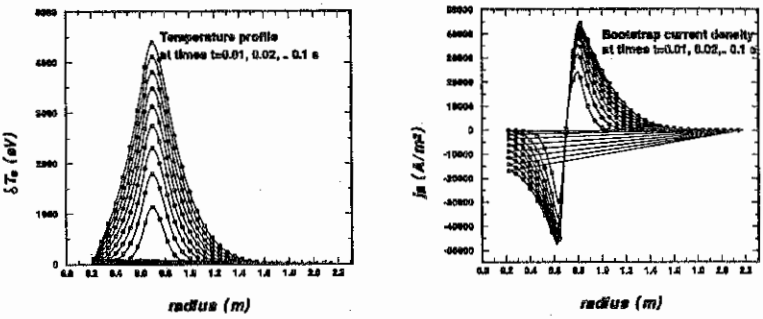

Fig. 2 (a) The temperature and (b) the bootstrap current density evolution for the power source of Fig. 1 with the thermal diffusivity $\chi = 1$ m^2/s for various times.

References

[1] M.R. O'Brian et al., Nucl. Fusion **26** (1986) 1625.
[2] C.F.F. Karney and N.J. Fisch, Nucl. Fusion **21** (1981) 1549.
[3] J.A. Heikkinen and S.K. Sipilä, "Bipolar Modification of Bootstrap Current Density by Localized RF Heating", this meeting; J.A. Heikkinen and S.K. Sipilä, "Alpha Current Driven by Lower Hybrid heating of Thermonuclear Alpha Particles in Tokamak Fusion Reactors", to appear in Nuclear Fusion.

Anomalous resistivity and energy release in the low-β electromagnetoplasma

Yurii M. Voitenko
Department of Space Plasma Physics, Main Astronomical Observatory, Golosiiv, Kyiv-22, 252650, Ukraine
e-mail: voitenko@mao.gluk.apc.org

1. Introduction

We study anomalous resistivity and turbulent heating of a low-β magnetoplasma with electric field $\mathbf{E}_0 \parallel \mathbf{B}_0$ (here $\beta < 1$ is the plasma/magnetic field pressure ratio and B_0 is the background magnetic field). Quasi-steady E_0 and current density, j_0, should be related by Ohm's law with an anomalous resistivity, the nature and magnitude of which in many cases are uncertain today. The problem of anomalous heating mechanisms is of particular importance for both laboratory and space plasmas, because it is that which allows - or doesn't allow - fast energy release in the plasma with rare collisions. It is believed that the fast energy release onset occurs as soon as current density exceeds a threshold, determined by the turn-on condition for the favourable instability, producing turbulent limitation of the field-aligned currents. Ion-cyclotron, ion-acoustic, and lower-hybrid-drift instabilities have been widelly discussed (see, e.g., Huba 1985).

Here the kinetic theory of the E_0-driven instability of the kinetic Alfvén waves (KAW) is developed and consequent anomalous transport mechanism in low-β electromagnetoplasma is discussed. Also, a possible role of a new mechanism for the KAWs excitation by external electric field E_0 due to the AME-effect is proposed and analytical expressions for the terms describing both SME and AME effects in E_0-driven KAW instability are derived (Voitenko 1996).

2. Perturbed Distribution Function

We search for the linear response of the one-particle distribution function on the plane waves with electromagnetic wave potentials $(\phi(\mathbf{r},t), A_z(\mathbf{r},t)) = (\tilde{\phi}, \tilde{A}_z) \times \exp(i\mathbf{kr} - i\omega t)$, $k_\perp \gg k_z$, $\mathbf{k}_\perp \perp \mathbf{B}_0 \parallel \mathbf{z}$,

Let us start with the Boltzman kinetic equation for one-particle distribution function F. To the guiding center variables $(t; \mathbf{r}_g; V_z; V_\perp^2; \theta)$ it reads as

$$\frac{\partial F}{\partial t} + \dot{\mathbf{r}}_g \frac{\partial F}{\partial \mathbf{r}_g} + \dot{V}_z \frac{\partial F}{\partial V_z} + \dot{\theta} \frac{\partial F}{\partial \theta} = C^c(F), \qquad (1)$$

where $C^c(F)$ is integral Landau, accounting for the pair Coulomb collisions (see, e.g., Akhiezer et al.), and $\dot{\mathbf{r}}_g$, $\dot{V}_z$ and $\dot{\theta}$ are determined by equations of particle motion in the electromagnetic fields, including self-consistent wave electromagnetic fields and external electric, E_0, and magnetic, B_0, fields. Here and below where we drop the plasma component index all expressions are applicable for any component.

It is convenient to present one-particle distribution function F as a sum of slowly varying under the actions of pair Coulomb and wave-particle collisions (quasilinear) part F_0, fast linear response on the wave fields f^L, and fast nonlinear response f^{NL}.

Substituting for $F = F_0 + f^L + f^{NL}$ and ordering (1) with respect to electromagnetic disturbances, one can obtain equations for f^L and f^{NL}. Using for f_L expansion

$$f^L = \sum_{\mathbf{k}} \sum_n f_n \exp\left(-in(\theta - \chi)\right) \exp(-i\omega t + i\mathbf{k}\mathbf{r}_g), \tag{2}$$

where χ is angle between x-axis and $\mathbf{k}_\perp$, after some algebra we obtain the equation for f_n as

$$i\frac{eE_0/m}{\omega - i\nu - k_z V_z - n\Omega}\frac{\partial f_n}{\partial V_z} + f_n = f_n^0. \tag{3}$$

Only term $-\nu f$ is taken into account for $C^e(f)$. The solution f_n^0 for the case of $E_0 = 0$ is:

$$f_n^0 = -\frac{e}{m}\frac{J_n}{\omega - i\nu - k_z V_z - n\Omega}\left(k_z(\tilde{\phi} - \frac{\omega}{k_z c}\tilde{A}_z)\frac{\partial F_0}{\partial V_z} + n\Omega(\frac{\tilde{A}_z}{c}\frac{\partial F_0}{V_z} + (\tilde{\phi} - \frac{V_z}{c}\tilde{A}_z)\frac{\partial F_0}{V_\perp \partial V_\perp}\right) \tag{4}$$

where $J_n = J_n(k_\perp V_\perp/\Omega)$ is the Bessel function.

For the wavelengths obeying $eE_0/k_z < m_e V_{Te}^2$, we obtain solution of (5) as

$$f_n = (1 - \frac{ieE_o}{m}\frac{1}{\omega - i\nu - k_z V_z - n\Omega}\frac{\partial}{\partial V_z})f_n^0. \tag{5}$$

In the case of $E_0 = 0$, $\nu = 0$ and Maxwellian distribution function, expression (5) reproduces that obtained by Sharma & Tripathi (1988). Expression (2) with (5) and (4) for f_n f_n^0 gives plasma linear response on the shear (magnetically noncompressible) EM waves with $B_z = 0$.

The same expansion as (2) we use for nonlinear response f^{NL}:

$$f^{NL} = \sum_{\mathbf{k}} \sum_n f_n^{NL} \exp\left(-in(\theta - \chi)\right) \exp(-i\omega t + i\mathbf{k}\mathbf{r}_g). \tag{6}$$

Substituting (6) and (2) into second-order (1) and solving it with respect to series amplitude, f_n^{NL}, one obtains

$$f_n^{NL} = \frac{ie^2}{m^2\Omega k_z}\frac{J_n}{V_z - V_k + n\Omega/k_z}\sum_{\mathbf{k_1},\mathbf{k_2}} \delta(\mathbf{k} - \mathbf{k_1} - \mathbf{k_2})\delta(n - j - l) \times$$

$$\exp(-i\chi n + i\chi_1 j + i\chi_2 l)\left([\mathbf{k}_1 \times \mathbf{k}_2]_z(\tilde{\phi}_1 - \frac{V_z}{c}\tilde{A}_{1z}) + \frac{E_0}{B_0}(\mathbf{k_1} * \mathbf{k_2})\tilde{A}_{1z}\right) \times$$

$$\left((\tilde{\phi}_2 - \frac{V_z}{c}\tilde{A}_{2z})\frac{\partial F_0}{\partial V_z} + \frac{l\Omega}{k_{2z}}(\frac{\tilde{A}_{2z}}{c}\frac{\partial F_0}{V_z} + (\tilde{\phi}_2 - \frac{V_z}{c}\tilde{A}_{2z})\frac{\partial F_0}{V_\perp \partial V_\perp})\right)\frac{J_j(1)J_2}{V_z - V_{2k} + l\Omega/k_{2z}}, \tag{7}$$

where terms describing influence of E_0 on three-wave interaction are included through $\mathbf{r}_g$, and only dominant terms, discibing three-wave interaction, are kept. The above expressions provide full kinetic description of the KAW weak turbulence generation by external electric field (see Voitenko 1996).

3. Anomalous Transport Produced by KAWs

In the low-β plasma the threshold of SME KAW instability, $E_{0cr}/E_{Dr} \leq 0.1$, is well below that of the ion-acoustic, $E_{0cr}/E_{Dr} \approx 0.8$, and ion-cyclotron, $E_{0cr}/E_{Dr} \approx 0.3$, instabilities, discussed before.

Thus, in this section we discuss anomalous transport produced by SME KAW turbulence. In mane cases (see Belikov, Kolesnichenko & Plotnik 1982) one can suppose scattering (target) particles in C^c to be Maxwellian and to take the averaged 'slow part' of Boltzman equation (1) in the form $F_0 = f_M(V_\perp)f(V_z)$, where f_M is Maxwellian distribution. Keeping terms $\sim \overline{E_z f^L}$ and integrating (1) over $V_\perp$, we obtain Fokker-Plank diffusion equation for one-dimensional function f:

$$\frac{\partial f}{\partial t} + \frac{eE_o}{m}\frac{\partial f}{\partial V_z} = \frac{\partial}{\partial V_z} D^C \left(\frac{V_z}{V_T^2} f + \frac{\partial f}{\partial V_z}\right) + \frac{\partial}{\partial V_z} D^{QL} \frac{\partial f}{\partial V_z}, \tag{8}$$

where quasilinear and Coulomb diffusion coefficients are:

$$D^{QL}(V_z) = \frac{\pi e^2}{m^2} \sum_{\mathbf{k}} \delta(\omega_k - k_z V_z) \Lambda_0(\kappa) |E_{z\mathbf{k}}|^2; \tag{9}$$

$$D^C = \nu_c V_T^2. \tag{10}$$

Here $\Lambda_0 = I_0(\kappa^2)\exp(-\kappa^2)$ and $I_0(\kappa^2)$ with
$\nu_c = 2(\pi - 1)\sqrt{2\pi} n e^4 L_C/(m_e^2 V_{Te}^3)$ is derived from the Landau integral with Maxwellian scattering centers.

The first moment of equation () for electron component is Ohm's law:

$$\frac{4\pi}{\omega_{pi}^2}\frac{\partial j_z}{\partial t} = E_0 + \frac{4\pi\nu_{ei}}{\omega_{pi}^2} j_z + \frac{4\pi\nu_{ew}}{\omega_{pi}^2} j_z \tag{11}$$

with anomalous e-wave collision frequency

$$\nu_{ew} \approx \int dV_z D^{QL} \frac{\partial f_e}{\partial V_z} / \left(\int dV_z V_z f_e\right), \tag{12}$$

Here D^{QL} includes the normalised energy of KAWs spectrum, determined by nonlinear three-wave interaction of KAWs (Voitenko 1996). The saturation of KAW turbulence may be also caused by quasilinear relaxation of the unstable distribution function. Since KAWs' longitudinal phase velocities usually occupy a little part in the electron velocity space, $V_1 < V_k < V_2$, with $V_A \leq V_1$, $V_2 < V_{Te}$, we can restrict ourselves by studying only resonant electrons suggesting the other electrons to be Maxwellian. Integral of equation () from the point outside (but close to) resonant region, $V_z = V_1 - 0$, where $D^{QL} = 0$ and $f_e \approx f_e^M$ (f_e^M is Maxwellian distribution) to the point inside $V_z = V_k$), gives us the relation between turbulence level and slop of distribution function there:

$$\left(\frac{D^{QL}}{\nu V_{Te}} + 1\right)\frac{\partial f_e}{\partial V_z} = \frac{\partial f_e^M}{\partial V_z}_{V_z \approx V_A}. \tag{13}$$

Combining this relation and (12), we finally obtain anomalous collision frequency in the approximation of strong turbulent diffusion:

$$\nu_{ew} \approx \frac{(V_0 - V_A)^2}{V_0 V_{Te}} \nu_{ei} \tag{14}$$

From the above expression one can see that for sub-Dreicer electric fields e-wave collision frequency due to SME-effect is less than thermal collision frequency, $\nu_{ew} \approx E_0/E_{Dr}\nu_{ei}$, and cannot provide enough collisions to maintain current system in marginall stable regime $j_z = j_A$. At the same time, with growing E_0/E_{Dr} SME KAW instability may provide sufficient friction force due to it's action only on the resonant electrons, and the electric field much greater than the Dreicer field may be achieved owing to the corrugation developed in $f_e(V_z)$, producing a friction force distributed over all electrons, preventing their escape. In short, electrons accelerated by E_0 with velocities greater than those decelerated by the original instability, begin to form separate group with a secondary positive slope in $f_e(V_z)$, resulting in a secondary instability (and correspondent friction force) development, and so on. For every individual hump with thermal spread $S_\mu = S_{Te}/p$ and density $n_\mu = n/p$ (p is number of humps) we have asselerating/decelerating force balance

$$eE_0/m = S_\mu \nu_\mu, \tag{15}$$

where $\nu_\mu = (4\pi e^4 L_{C\mu}/(m_e^2 V_{Te}^3)(L_{C\mu} n_\mu / S_\mu^3$ is effective 'thermal' collision frequence of hump with number μ.

The number of humps, $p_m = 0.4L_C + 1 \approx 8$, provides near-marginal current limitation for electric fields up to

$$E_0^m/E_{Dr} = (1 - 2.5 \ln p_m)p_m \geq 10^2. \tag{16}$$

The problem of escaping electrons at the tail of distribution function may by alleviated with the development of AME KAW instability, which has negative feedback influence on the *all* electrons, asselerated by E_0.

The instability of kinetic Alfvén waves may be operative for the cases of fast energy release in discharges and current sheets in the tokamaks, spheromaks, and in the solar and earth's magnetospheres.

Acknowledgments

I wish to thank the company 'Drenaj' and personaly Director Badio M. F. for the financial support.

References

1. Belikov, V. S., Kolesnichenko Ya. I., & Plotnik, I. S.: 1982, *Nucl. Fusion* **22**, 1559.
2. Hasegawa, A.: 1980, *Nucl. Fusion* **20**, 1158.
3. Huba, J.D.: 1985, in M.R.Kundu, and G.D.Holman (eds.) *Unstable current systems and plasma instabilities in Astrophysics*, D.Reidel Publ.Co., Dordrecht, Holland, p.315.
4. Sharma, A. & Tripathi, V. K.: 1988, *Phys. Fluids* **31**, 12, 3697.
5. Voitenko, Yu. M.: 1996, this Proceedings.

ON PLASMA ROTATION DRIVEN BY PONDEROMOTIVE FORCES

Julio J. Martinell
Instituto de Ciencias Nucleares, UNAM
A. Postal 70-543, 04510 Mexico D. F., MEXICO

Abstract

The conditions for driving plasma rotation by the effect of ponderomotive forces are evaluated analyzing different mechanisms that may be produced by some types of high-power radiofrequency waves commonly used for heating and current drive in toroidal devices. Particular attention is paid to lower hybrid waves, as they are the ones that have been observed to produce plasma rotation. A comparison is made with the resonant mechanism which can also drive plasma rotation from the oscillating wave fields. The results are then discussed in relation to the possible production of an L-H transition.

Introduction.

When high-power radiofrequency (RF) waves are injected into a toroidal plasma, the nonlinear ponderomotive (PM) forces become important and are able to influence the plasma dynamics. This forces are the result of time-averaging the momentum equation over the fast oscillation time-scale, and are completely nonlinear in nature, thereby manifesting themselves prominently in high amplitude electromagnetic waves. PM forces are of primary importance in dealing with the interaction of high intensity lasers with a plasma, such as in the case of inertial confinement research with lasers. In magnetic confinement, the present requirements for RF heating and current drive in large devices already have an RF power high enough to take the nonlinear effects into account. Having powers of a few tens of MW, the effect of PM forces on the plasma dynamics should be important. On the other hand, there is experimental evidence that RF waves, in particular lower-hybrid waves, can influence the dynamics of a toroidal plasma as a whole, by producing bulk rotation [1]. This rotation may well be driven by nonlinear forces by giving momentum to the plasma ions in a preferential direction. Plasma rotation is also of major relevance in the transition from the L to the H mode, where it is now clear that a poloidal rotation near the plasma edge is intimately linked to the establishment of the H mode. In that respect RF waves may be used to induce an L-H transition, and that can be accomplished in two ways: by a resonant mechanism [2] and by the non-resonant ponderomotive force, which is the one considered here.

The idea of driving rotation by a PM force has been already analyzed by a number of authors [3-5]. They have considered the basic expression of the PM force obtained originally by Klima [6], which essentially consists of a ponderomotive potential and an induced magnetization. There is also a time dependent contribution which is usually neglected for the time scales normally involved, although it should be pointed out that in L-H transition the variation of the electric field amplitude may be fast enough to make the time dependent term important. Now, the way this ponderomotive force can drive rotation varies in the different models proposed. In one mechanism the drift velocity due to the radial component of the PM force is mainly directed in the poloidal direction and is able to move the ions in this direction [3]. Other mechanism considers the angular (toroidal or poloidal) component of the PM force and relies on a radial convection of plasma which is gaining momentum from the PM force, to produce a sheared plasma rotation [4]. In those two models, the PM force is balanced by non-dissipative terms in

the momentum equation; in the first case it is the Lorentz force, while in the second the convective term is considered. It is expected, however, that viscosity should play an important role in determining the rotation, since it is precisely this effect which prevents the plasma to rotate poloidally as a whole in standard neoclassical theory. Tsypin et al. [5] have included this dissipative term in computing the rotation produced by Alvfén waves, using a viscosity of the Burnett type.

We are here interested in studying a model that includes the different nonlinear effects, since it is quite likely that all of them are of similar order. First the dynamics is studied without the viscous effects, just to evaluate the feasibility this model and the relative contribution of the various terms. In this non-dissipative model we can also compare with the results obtained previously in [2] with a resonant momentum transfer to the plasma ions, since that was also the case considered there. Then we discuss the effect of a viscous term in a qualitative way. We note that such a scenario may cause the edge poloidal rotation necessary for inducing a transition to the H mode.

Model analysis.

Using a multifluid description of the plasma, the averaged momentum balance equation for particles of species j in steady state may be written as [5],

$$m_j n_j \mathbf{v}_j \cdot \nabla \mathbf{v}_j = \frac{q_j}{c} n_j \mathbf{v}_j \times \mathbf{B} - \nabla \cdot \mathbf{P}_j + \mathbf{R}_j + \mathbf{F}_{ip}, \tag{1}$$

where $\mathbf{P}_j$ is the stress tensor for j-particles, $\mathbf{F}_{ip}$ is the ponderomotive force, $\mathbf{R}_j$ the averaged friction forces and all other variables have their usual meaning. No steady electrostatic field is assumed. The ponderomotive force has different representations depending on the way it is derived, including a possible time dependence. Ignoring this possibility, the PM force of an electromagnetic field oscillating at frequency ω can be written as,

$$\mathbf{F}_{jp} = \frac{1}{2}\mathrm{Re}\left\{ \frac{i}{\omega}\nabla \mathbf{E}^*_\omega \cdot \mathbf{j}_{j\omega} - \nabla \cdot \left[\mathbf{j}_{j\omega} \left(\frac{i}{\omega}\mathbf{E}^*_\omega + \frac{4\pi \mathbf{j}^*_{j\omega}}{\omega^2_{pj}} \right) \right] \right\}, \tag{2}$$

where $\mathbf{j}_{j\omega}$ is the current of j-particles induced by the spectral component of the electric field $\mathbf{E}_j$. We will rather use a more convenient expression in terms of the dielectric tensor ϵ_{ik} which makes it easier to introduce the special kind of waves being considered. This is given as the addition of a PM potential term and an induced magnetization,

$$\mathbf{F}_{jp} = -n_j \nabla \Phi + \mathbf{B} \times (\nabla \times \mathbf{M}), \tag{3}$$

with

$$\Phi = \frac{1}{16\pi n_j}(\delta_{ik} - \epsilon_{ik}) E^*_i E_k, \qquad \mathbf{M} = \frac{1}{16\pi} \frac{\partial \epsilon_{ik}}{\partial \mathbf{B}} e^*_i E_k.$$

Let us for the moment neglect the terms $\mathbf{P}_j$ and $\mathbf{R}_j$ in Eq.(1). When only the right hand side term is taken to balance the PM force one has the case considered in [4] and [7]; a convective momentum transfer to the plasma edge. If the first term on the right hand side is assumed to balance the PM force, then the situation is the one considered in [3] and [8]. We take the three terms together. From the radial and poloidal components

of Eq.(1) in cylindrical coordinates we can obtain two coupled equations for v_{jr} and $v_{j\theta}$, which, for axisymmetric configurations, take the form,

$$\omega_{Bj} v_{j\theta} + \frac{F_{jpr}}{m_j n_j} = v_{jr} \frac{\partial v_{jr}}{\partial r} + \frac{v_{j\theta}}{r} \frac{\partial v_{jr}}{\partial \theta} - \frac{v_{j\theta}^2}{r}, \tag{4}$$

$$-\omega_{Bj} v_{jr} + \frac{F_{jp\theta}}{m_j n_j} = v_{jr} \frac{\partial v_{j\theta}}{\partial r} + \frac{v_{j\theta}}{r} \frac{\partial v_{j\theta}}{\partial \theta} + \frac{v_{j\theta} v_{jr}}{r}, \tag{5}$$

where $\omega_{Bj} = q_j B/m_j c$. Let us assume now that the amplitude of the wave is only dependent on the radial coordinate, varying as it penetrates the plasma. In that case $F_{jp\theta} = 0$, and if we also assume poloidal symmetry (which is not necessary always true), the equations can be decoupled obtaining the velocities,

$$v_{j\theta} = -\frac{\omega_{Bj} r}{2}, \qquad v_{jr} = \left[\frac{2BM_z}{m_j n_j} - \frac{2\Phi}{m_j} - \omega_{Bj}^2 \frac{r^2}{2} \right]^{1/2}, \tag{6}$$

which corresponds to a rigid rotation together with a radial flux due to the PM force, since without it there are no real solutions for v_{jr}. On the other hand, if $v_{jr} = 0$ Eq.(4) gives a quadratic equation for $v_{j\theta}$ which has two solutions, that for $F_{jp} \ll m_j n_j \omega_{Bj}^2 r$, correspond to the rigid rotation $v_{j\theta} = -\omega_{Bj} r$ and to the smaller velocity solution given in [3],

$$v_{j\theta} = \frac{1}{\omega_{Bj}} \left(\frac{1}{m_j} \frac{d\Phi}{dr} - \frac{B}{m_j n_j} \frac{dM_z}{dr} \right) = \frac{\omega_{jp}(\omega^2 + \omega_{Bj}^2)}{16\pi m_j n_j \omega_{Bj} (\omega^2 - \omega_{Bj}^2)^2} \frac{dE_0^2}{dr} \tag{7}$$

where the last expression corresponds to lower hibrid waves having a dielectric constant $\epsilon = 1 - \omega_{jp}^2/(\omega^2 - \omega_{Bj})$ with ω_{jp} the plasma frequency. In the opposite limit, $F_{jp} \gg m_j n_j \omega_{Bj}^2 r$, the dependence on the wave power gets weaker, scaling as,

$$v_{j\theta} = \sqrt{r} \left(\frac{1}{m_j} \frac{d\Phi}{dr} - \frac{B}{m_j n_j} \frac{dM_z}{dr} \right)^{1/2} \sim \left[\frac{dE_0^2}{dr} \right]^{1/2}. \tag{8}$$

When there is a poloidal component of the PM force, Eq.(5) can produce a poloidal rotation by a direct drive balanced by the convective force [4,7], for which a radial velocity is needed. If v_{jr} is known then the poloidal rotation is given by,

$$v_{j\theta} = \frac{1}{m_j n_j r v_{jr}} \int F_{jp\theta} r dr - \frac{r\omega_{Bj}}{2}, \tag{9}$$

which again represents a superposition of the rigid rotation due to the magnetic force and a term that depend on the actual form od the poloidal PM force. At this point we compare these results with those obtained in [2] from a resonant mechanism for momentum transfer. It was found that, the rotation induced by a single wave had a scaling with the wave power W, that was weaker as the power increased. For low powers there was a linear scaling $v_{j\theta} \sim W$, which then turns to $v_{j\theta} \sim W^{1/3}$ and finally to $v_{j\theta} \sim W^{1/5}$ for the largest energies. For these large powers the PM force becomes important and the scaling for this mechanism also weakens as the power rises, as one can see from Eqs.(7) and (8), going from the linear scaling to $v_{j\theta} \sim W^{1/2}$.

Finally, we can briefly mention the effect viscosity would have on our results by including in Eq.(1) the term $\mathbf{P}_j = -\mu_j \nabla \mathbf{v}_j$. In this case, viscosity can be the balancing term for the PM force without the need of the other terms, which was the situation considered in [5]. This scenario is also obtained when $v_{jr} = 0$ in Eq.(5), and the resulting expression for $v_{j\theta}$ will also be proportional to the power as in Eq.(9). The general case is not tractable in an analytical way.

Conclusions.

The analysis of the different possibilities for driving a poloidal rotation in a plasma, by effect of the ponderomotive force of an injected high frequency wave, shows that various combinations of PM force components with the plasma dynamics may produce such a rotation. It is found that the resulting rotation is less sensitive to the wave energy as this energy increases, but the weakening is not as prominent as the one found for resonant wave absorption. It is important to mention the relevance this way of rotating a plasma could have on the confinement, since by externally injecting RF waves it would be possible to induce an L-H transition. It is not necessary to increase the RF power too much since its effect on the rotation gets weaker.

References.

[1] S. Tsuji et al., Phys. Rev. Lett. **64**, 1023 (1990)
[2] I.A. Voitsekhovitch, M. Coronado and J.J. Martinell, Phys. Plasmas **2**, 3667 (1995).
[3] Q. Gao, L. Bai, X. Peng, J. Zhang, S. Wang, C. Liu and X.M. Qiu, Proc. 15th Int. Conf. Plasma Phys. and Controlled Nucl. Fusion Res., Seville, D-P-I-10 (1994); X.M. Qiu, L. Bai, Chin. Phys. Lett. **11**, 677 (1994)
[4] R. Van Nieuwenhove, V. Petrzilka and J.A. Tataronis, J. Plasma Phys. **54**, 245 (1995).
[5] V.S. Tsypin, A.G. Elfimov, C.A. de Azevedo and A.S. de Asis, Phys. Plasmas 3 No. 7 (1996)
[6] R. Klima, Czech. J. Phys. B **18**, 1280 (1968); R. Klima, Czech. J. Phys. B **30**, 874 (1980)
[7] R. Klima and V.A. Petrzilka, Czech. J. Phys. B **30**, 1002 (1980)
[8] J. Vaclavik, M.L. Sawley and F. Anderegg, Phys. Fluids **29**, 2034 (1986)

INDEX

Зам.107 Формат 60×90 /16 Обл.-вид. арк. 33,5

Підписано до друку 5.11.96 Тираж 400 прим.

Поліграфічна дільниця ІТФ ім.М.М.Боголюбова НАН України